

MAX PLANCK INSTITUTE FOR POLYMER RESEARCH

JOHANNES GUTENBERG UNIVERSITY MAINZ

Investigation in Linker Functionality of Main-Chain Thermally
Activated Delayed Fluorescence Polymers
and Through-Space Charge Transfer in Supramolecular Polymers

DISSERTATION

zur Erlangung des Grades

„Doktor rerum naturalium“

am Fachbereich Chemie, Pharmazie und Geowissenschaften

der Johannes Gutenberg-Universität und in Kooperation

mit dem Max-Planck-Institut für Polymerforschung

in Mainz

Kai Philipps

geboren in Oberwesel

Mainz, den 13.04.2021

Die vorliegende Dissertation wurde in der Zeit von Juni 2017 bis April 2021 am Max-Planck-Institut für Polymerforschung in Mainz unter Betreuung von Prof. Dr. Paul Blom angefertigt.

Dekan: [REDACTED], Johannes Gutenberg-Universität Mainz

1. Gutachter: Prof. Dr. Paul Blom, Max-Planck-Institut für Polymerforschung, Mainz

2. Gutachter: [REDACTED], Johannes Gutenberg-Universität Mainz

Tag der mündlichen Prüfung: 31.05.2021

Für Lea, Lenne und meine zukünftigen Kinder

Abstract

In recent years, organic light-emitting diodes (OLED) using thermally activated delayed fluorescence (TADF) emitters were shown to be one of the most promising technologies for display and lighting applications. The TADF mechanism enables the utilization of both singlet and triplet excitons for light generation based on a thermal upconversion resulting from a small energy difference (ΔE_{ST}) between the lowest excited triplet and singlet states. While excellent performances have been reported for small molecule TADF emitters, the necessary vacuum processing makes large-area device fabrication difficult and expensive, explaining the high research interest in the development of polymeric TADF emitters enabling solution processing.

The focus of this dissertation was on the systematic investigation of the influence of the linker moiety on the photophysical properties and performance in optoelectronic devices in main-chain TADF polymers. Two sets of yellowish-green emitting polymers with alkyl spacers of different lengths as well as a conjugated biphenyl linker were synthesized and compared to structurally equivalent small molecules. While the charge transfer (CT) character of the excited state and the ΔE_{ST} showed no linker dependent change, all polymeric materials were identified to suffer from a pronounced concentration quenching effect in a film, reducing their photoluminescence quantum yield (PLQY) and performance in OLEDs. This adverse effect was successfully suppressed by diluting the materials with polystyrene in blended films, resulting in the TADF polymers with nonconjugated linkers showing similarly high PLQY values as well as efficiencies in OLEDs compared to the small molecule emitter. Furthermore, with regard to device performance they were observed to be superior to their conjugated polymer counterpart.

In the second part of this dissertation, the field of use of TADF emitters was expanded by incorporating donor and acceptor moieties into peptide-polymer conjugates capable of pH-responsive self-assembly. Upon increasing pH in aqueous solution, a supramolecular polymer is formed leading

to donor and acceptor coming in close proximity to one another exhibiting a through-space charge transfer (TSCT) indicated by a significant red-shift in photoluminescence (PL).

Zusammenfassung

In den letzten Jahren haben sich organische Leuchtdioden (OLED) mit thermisch aktivierten Emittern mit verzögerter Fluoreszenz (TADF) als eine der vielversprechendsten Technologien für Display- und Beleuchtungsanwendungen erwiesen. Der TADF-Mechanismus ermöglicht die Verwendung von Singulett- und Triplett-Exzitonen zur Lichterzeugung basierend auf einer thermischen Aufwärtskonvertierung, die aus einer kleinen Energiedifferenz (ΔE_{ST}) zwischen den niedrigsten angeregten Triplett- und Singulettzuständen resultiert. Während für niedermolekulare TADF-Emitter hervorragende Leistungen berichtet wurden, macht die erforderliche Vakuumverarbeitung die Herstellung großflächiger Bauelemente schwierig und teuer, was das hohe Forschungsinteresse an der Entwicklung polymerer TADF-Emitter erklärt, die eine Lösungsverarbeitung ermöglichen.

Der Schwerpunkt dieser Dissertation lag auf der systematischen Untersuchung des Einflusses der Verknüpfungseinheit auf die photophysikalischen Eigenschaften und die Effizienz optoelektronischer Bauelemente bei TADF-Hauptkettenpolymeren. Eine Reihe gelblich-grün emittierender Polymere mit unterschiedlich langen Alkylspacern sowie einem konjugierten Biphenyllinker wurden synthetisiert und mit strukturäquivalenten kleinen Molekülen verglichen. Während der Ladungstransfer(CT)-Charakter des angeregten Zustands und des ΔE_{ST} keine linkerabhängige Änderung aufwiesen, wurde festgestellt, dass alle Polymermaterialien im Filmzustand unter einem ausgeprägten Konzentrationslöschungseffekt leiden, der ihre Photolumineszenzquantenausbeute (PLQY) und Effizienz in OLEDs verringert. Dieser nachteilige Effekt wurde erfolgreich unterdrückt, indem die Materialien mit Polystyrol in gemischten Filmen verdünnt wurden, was dazu führte, dass die TADF-Polymere mit nicht konjugierten Linkern ähnlich hohe PLQY-Werte sowie Wirkungsgrade in OLEDs im Vergleich zum niedermolekularen Emitter zeigten, und sie zeigten sich des Weiteren als überlegen gegenüber ihres konjugierten Polymer-Gegenstücks.

Im zweiten Teil dieser Dissertation wurde das Anwendungsgebiet von TADF-Emittern erweitert, indem Donor- und Akzeptoreinheiten in Peptidpolymerkonjugate eingebaut wurden, die zur pH-induzierten Selbstorganisation fähig sind. Bei Erhöhung des pH-Werts in wässriger Lösung wird ein supramolekulares Polymer gebildet, das dazu führt, dass Donor und Akzeptor nahe beieinander liegen und einen Ladungstransfer (TSCT) durch den Raum zeigen, der durch eine signifikante Rotverschiebung der Photolumineszenz (PL) angezeigt wird.

I hereby declare that I wrote the dissertation submitted without any unauthorized external assistance and used only sources acknowledged in the work. All textual passages, which are appropriated verbatim or paraphrased from published and unpublished texts as well as all information obtained from oral sources are duly indicated and listed in accordance with bibliographical rules. In carrying out this research, I complied with the rules of standard scientific practice as formulated in the statutes of Johannes Gutenberg-University Mainz to insure standard scientific practice.

Date, Place, Signature

Table of Content

1.	Introduction	1
1.1.	Organic Light-Emitting Diodes	2
1.2.	Transition between Electronic States	5
1.2.1.	Performance Characterization of OLEDs	7
1.2.2.	Emissive Processes in OLEDs.....	8
1.3.	Thermally Activated Delayed Fluorescence Emitters	10
1.3.1.	TADF Mechanism and Molecular Design Principle	10
1.3.2.	Small Molecule TADF Emitters.....	11
1.3.3.	Polymer TADF Emitters.....	12
1.3.4.	TADF Polymer Architectures.....	15
1.4.	Supramolecular Polymers.....	19
2.	Objectives.....	21
3.	Molecular Design and Synthesis of TADF Main-Chain Polymers	24
3.1.	Introduction	24
3.2.	Molecular Design and Computational Results	25
3.3.	Synthesis of Main-Chain TADF Polymers and Small Molecules	32
3.4.	Thermal Properties of the TADF Materials.....	41
3.5.	Estimation of HOMO and LUMO of the TADF materials.....	43
3.6.	Conclusion.....	50
3.7.	Appendix of Chapter 3	51

3.7.1.	Contributions to Chapter 3	51
4.	Photophysical Characterization.....	53
4.1.	Steady State Photophysical Properties in Solution	53
4.2.	Steady State Photophysical Properties in Film State	66
4.3.	Transient Photophysical Characterization.....	79
4.4.	Conclusion	94
4.5.	Appendix of Chapter 4.....	96
4.5.1.	Contributions to Chapter 4.....	96
4.5.2.	Figures and Tables	97
4.5.3.	Discussion of the Artifact Observed in Figure 4.15d.....	112
4.5.4.	Temperature-dependent TRPL of the TADF Materials in Pristine Film	113
4.5.5.	Estimation of Rate Constants for Arrhenius Plot.....	115
5.	Characterization in Optoelectronic Devices.....	117
5.1.	Hole Transport Characteristics.....	117
5.1.	Electron Transport Characteristics	124
5.2.	Organic Light-Emitting Diode Performances	130
5.2.1.	OLEDs with PS Host	132
5.2.2.	OLEDs with Small Molecule Host	145
5.3.	Conclusion	149
5.4.	Appendix of Chapter 5.....	151
5.4.1.	Contributions to Chapter 5.....	151

5.4.2.	Figures and Tables.....	151
6.	Supramolecular TADF Polymer.....	161
6.1.	Synthesis of D-PSar-D and D-PSar-A.....	162
6.2.	Self-Assembly Investigation via Transmission Electron Microscopy (TEM).....	173
6.3.	Photophysical Characterization.....	178
6.4.	Conclusion and Outlook.....	183
6.5.	Appendix of Chapter 6.....	184
6.5.1.	Contributions to Chapter 6.....	184
7.	General Methods.....	186
7.1.	Synthetic, Purification and Sample Preparation Methods.....	186
7.1.1.	Solvents and Chemicals.....	186
7.1.2.	Reaction Methods.....	186
7.1.3.	Solid Phase Peptide Synthesis.....	186
7.1.4.	pH-Electrodes.....	187
7.1.5.	Soxhlet Purification.....	187
7.1.6.	Chromatography.....	188
7.1.7.	Sublimation.....	189
7.1.8.	Film Preparation.....	190
7.2.	Analytical Methods.....	192
7.2.1.	Nuclear Magnetic Resonance.....	192
7.2.2.	Mass Spectrometry.....	193

7.2.3.	Differential Scanning Calorimetry	193
7.2.4.	Cyclic Voltammetry	193
7.2.5.	Ultraviolet Photoelectron Spectroscopy.....	194
7.2.6.	Ultraviolet-Visible Absorption Spectroscopy	195
7.2.7.	Steady State Photoluminescence Spectroscopy	196
7.2.8.	Time Resolved Photoluminescence Spectroscopy	198
7.2.9.	Profilometer	202
7.2.10.	Atomic Force Microscopy	203
7.2.11.	Transmission Electron Microscopy	203
7.2.12.	Analytical Size Exclusion Chromatography	204
7.3.	Theoretical Computation.....	204
7.4.	Fabrication of Optoelectronic Devices.....	204
7.4.1.	Characterization of Optoelectronic Devices	207
8.	Synthetic Procedures and Characterization.....	209
8.1.	Standard Operating Procedures (SOP).....	209
8.1.1.	Synthesis of Peptides via SPPS (SOP1).....	209
8.1.2.	Coupling of Carboxylic Acid-functionalized Dye to Peptide-loaded Resin and Cleavage from Resin (SOP2).....	210
8.1.3.	End Group Modification and Deprotection of Polymer-peptide Conjugates (SOP3).....	210
8.2.	Synthesis of Methyl 2-(phenylamino) benzoate (1).....	211
8.3.	Synthesis of 7-(2-(Phenylamino)phenyl)tridecan-7-ol (2).....	212
8.4.	Synthesis of 9,9-Dihexyl-9,10-dihydroacridine (3b)	213

8.5.	Synthesis of 1-(9,9-Dimethyl-9,10-dihydroacridin-2-yl)-2-ethylhexan-1-one (4a)	214
8.6.	Synthesis of 2-(2-Ethylhexyl)-9,9-dimethyl-9,10-dihydroacridine (5a).....	216
8.7.	Synthesis of Bis(4-(2-(2-ethylhexyl)-9,9-dimethylacridin-10(9H)-yl)phenyl)methanone (6a) 217	
8.8.	Synthesis of Bis(4-(2-bromo-7-(2-ethylhexyl)-9,9-dimethylacridin-10(9H)- yl)phenyl)methanone (7a).....	219
8.9.	Synthesis of Tol-MAc-BP	220
8.10.	Synthesis of P(C2-MAc-BP)	222
8.11.	Synthesis of P(C6-MAc-BP)	224
8.12.	Synthesis of P(Ph-MAc-BP).....	226
8.13.	Synthesis of 1,6-Bis(4-bromophenyl)hexane-1,6-dione (8)	228
8.14.	Synthesis of 1,6-Bis(4-bromophenyl)hexane (9).....	229
8.15.	Synthesis of 4,4,5,5-Tetramethyl-2-(4-(6-(4-(4,4,5-trimethyl-1,3,2-dioxaborolan-2- yl)phenyl)hexyl)phenyl)-1,3,2-dioxaborolane (10e).....	230
8.16.	Synthesis of 1-(9,9-Dihexyl-9,10-dihydroacridin-2-yl)-2-ethylhexan-1-one (4b)	231
8.17.	Synthesis of -(2-Ethylhexyl)-9,9-dihexyl-9,10-dihydroacridine (5b).....	232
8.18.	Synthesis of Bis(4-(2-(2-ethylhexyl)-9,9-dihexylacridin-10(9H)-yl)phenyl)methanone (6b) 234	
8.19.	Synthesis of Bis(4-(2-(2-ethylhexyl)-9,9-dihexyl-7-iodoacridin-10(9H)- yl)phenyl)methanone (7b).....	236
8.20.	Synthesis of Tol-HAc-BP	238
8.21.	Synthesis of P(C2-HAc-BP).....	240

8.1.	Synthesis of P(C6-HAc-BP)	242
8.1.	Synthesis of P(Ph-HAc-BP).....	244
8.1.	Synthesis of 10-(3-Iodophenyl)-9,9-dimethyl-9,10-dihydroacridine (12)	246
8.2.	Synthesis of Methyl 6-(3-(9,9-dimethylacridin-10(9H)-yl)phenyl)hex-5-ynoate (14)	247
8.3.	Synthesis of Methyl 6-(3-(4,6-diphenyl-1,3,5-triazin-2-yl)phenyl)hexanoate (15)	248
8.4.	Synthesis of 6-(3-(9,9-Dimethylacridin-10(9H)-yl)phenyl)hexanoic acid (16).....	250
8.5.	Synthesis of <i>tert</i> -Butyl (5-(3-(9,9-dimethylacridin-10(9H)-yl)phenyl)pent-4-yn-1-yl)carbamate (18)	251
8.6.	Synthesis of <i>tert</i> -Butyl (5-(3-(9,9-dimethylacridin-10(9H)-yl)phenyl)pentyl)carbamate (19)	252
8.7.	Synthesis of 5-(3-(9,9-Dimethylacridin-10(9H)-yl)phenyl)pentan-1-amine (20).....	254
8.8.	Synthesis of Methyl-6-(3-bromophenyl)hex-5-ynoate (21).....	255
8.9.	Synthesis of Methyl 6-(3-bromophenyl)hexanoate (22)	256
8.10.	Synthesis of Methyl 6-(3-(4,4,5,5-tetramethyl-1,3,2-dioxaborolan-2-yl)phenyl)hexanoate (23)	257
8.11.	Synthesis of 6-(3-(4,6-Diphenyl-1,3,5-triazin-2-yl)phenyl)hexanoic acid (26).....	258
8.12.	Synthesis of <i>tert</i> -Butyl (5-(3-bromophenyl)pent-4-yn-1-yl)carbamate (27).....	259
8.13.	Synthesis of <i>tert</i> -Butyl (5-(3-(4,4,5,5-tetramethyl-1,3,2-dioxaborolan-2-yl)phenyl)pent-4-yn-1-yl)carbamate (28)	261
8.14.	Synthesis of <i>tert</i> -Butyl (5-(3-(4,6-diphenyl-1,3,5-triazin-2-yl)phenyl)pent-4-yn-1-yl)carbamate (29)	262

8.15.	Synthesis of <i>tert</i> -Butyl (5-(3-(4,6-diphenyl-1,3,5-triazin-2-yl)phenyl)pentyl)carbamate (30) 263	
8.16.	Synthesis of 5-(3-(4,6-Diphenyl-1,3,5-triazin-2-yl)phenyl)pentan-1-amine (31)	264
8.17.	Synthesis of H ₂ N-L-Phe-L-His(Trt)-L-Phe-L-His(Trt)-L-Phe-Ahx-[L-Gly]-resin (32)	265
8.18.	Synthesis of 6-(3-(9,9-Dimethylacridin-10(9H)-yl)phenyl)hexanoyl-L-Phe-L-His(Trt)-L-Phe-L-His(Trt)-L-Phe-Ahx-L-Gly-OH (33)	266
8.19.	Synthesis of 6-(3-(4,6-Diphenyl-1,3,5-triazin-2-yl)phenyl)hexanoyl-L-Phe-L-His(Trt)-L-Phe-L-His(Trt)-L-Phe-Ahx-L-Gly-OH (34)	267
8.20.	Synthesis of 6-(3-(9,9-Dimethylacridin-10(9H)-yl)phenyl)hexanoyl-L-Phe-L-His(Trt)-L-Phe-L-His(Trt)-L-Phe-Ahx-L-Gly-Ethylenediamine-Fmoc (36).....	268
8.21.	Synthesis of 6-(3-(9,9-Dimethylacridin-10(9H)-yl)phenyl)hexanoyl-L-Phe-L-His(Trt)-L-Phe-L-His(Trt)-L-Phe-Ahx-L-Gly-Ethylenediamine-NH ₂ (37).....	269
8.22.	Synthesis of 6-(3-(9,9-Dimethylacridin-10(9H)-yl)phenyl)hexanoyl-L-Phe-L-His(Trt)-L-Phe-L-His(Trt)-L-Phe-Ahx-L-Gly-Ethylenediamine-NH-Poly(sarcosine)-COCH ₂ NCH ₃ H (39).....	270
8.23.	Synthesis of 6-(3-(9,9-Dimethylacridin-10(9H)-yl)phenyl)hexanoyl-L-Phe-L-His-L-Phe-L-His-L-Phe-Ahx-L-Gly-Ethylenediamine-NH-Poly(sarcosine)-L-Gly-Ahx-L-Phe-L-His-L-Phe-L-His-L-Phe-6-(3-(9,9-dimethylacridin-10(9H)-yl)phenyl)hexanoyl (D-PSar-D).....	272
8.24.	Synthesis of 6-(3-(9,9-Dimethylacridin-10(9H)-yl)phenyl)hexanoyl-L-Phe-L-His-L-Phe-L-His-L-Phe-Ahx-L-Gly-Ethylenediamine-NH-Poly(sarcosine)-L-Gly-Ahx-L-Phe-L-His-L-Phe-L-His-L-Phe-6-(3-(4,6-diphenyl-1,3,5-triazin-2-yl)phenyl)hexanoyl (D-PSar-A).....	273
9.	Appendix	274
9.1.	NMR Spectra	274
9.2.	MALDI-TOF Spectra	320

9.3.	ESI HRMS Spectra	328
10.	Acknowledgement	330
11.	Publications and Presentations.....	332
12.	References.....	333

Abbreviations

δ	chemical shift	DF	delayed fluorescence
σ	standard deviation	DFT	density functional theory
A	acceptor	DHAC	9,9-dihexyl-9,10-dihydroacridine
Ac	9,9-dimethyl-10-phenyl-acridine	DI	deionized (water)
acc	acceleration	DMAC	9,9-dimethyl-9,10-dihydroacridine
AFM	atomic force microscopy	D_n	number average diameter
Ahx	amniohexanoic acid	DIPEA	N,N-diisopropylethylamine
Ar	aromatic ring	DMF	dimethylformamide
Boc	butyloxycarbonyl	DOOS	density of occupied states
br	broad	DOS	density of states
CBP	4,4'-bis(N-carbazolyl)-1,1'-biphenyl	DSC	differential scanning calorimetry
iCCD	intensified charge-coupled device	EA	electron affinity
CE	current efficiency	E_B	electron-hole pair binding energy
CIE	Commission Internationale de L'Eclairage (chromaticity)	EGDM	Extended-Gaussian-Disorder-Model
CT	charge transfer	EIL	electron injection layer
CV	cyclic voltammetry	EL	electroluminescence
d	doublet	EML	emission layer
D	donor	EO	electron-only (device)
\mathcal{D}	dispersity	EQE	external quantum efficiency
DCM	dichloromethane	ESI	electrospray ionization
DCTB	trans-2- [3- (4-tert-butylphenyl) -2-methylpropenylidene] malodinitrile	EtHex	2-ethylhexyl
DET	Dexter energy transfer	ETL	electron transport layer
		Et ₂ O	diethylether
		EtOAc	ethylacetate

EtOH	ethanol	<i>IP</i>	ionization potential
F	phenylalanine	IPES	inverse photoelectron spectroscopy
Fc	ferrocene		
Fmoc	fluorenylmethoxycarbonyl	IQE	internal quantum efficiency
FRET	Förster Energy Transfer	IRF	instrument response function
FWHM	full width at half maximum	ISC	intersystem-crossing
G	glycine	ITO	indium tin oxide
Gly	Glycine	<i>J</i>	current density
H	histidine	LED	light-emitting diode
HBTU	2-(1H-benzotriazol-1-yl)-1,1,3,3-tetramethyluronium-hexafluorophosphat	<i>l</i>	angular momentum number
Hex	Hexane/ hexyl	<i>L</i>	luminance
HFIP	hexafluoroisopropanol	LE	locally excited state
HIL	hole injection layer	L-M	Lippert-Mataga
His	histidine	L_n	number average length
HMBC	heteronuclear multiple bond correlation	LUMO	lowest unoccupied molecular orbital
HO	hole-only (devices)	L_w	weight average polymer length
HOBt	1-hydroxybenzotriazol	<i>m</i>	multiplicity
HOMO	highest occupied molecular orbital	<i>M/I</i>	monomer to initiator ratio
HRMS	high resolution mass spectrometry	MALDI	matrix-assisted laser desorption ionization
HSQC	heteronuclear single quantum coherence	mCP	<i>m</i> -bis(N-carbazolyl)benzene
HT	high temperature furnace	m	multiplet
HTL	hole transport layer	MeOH	methanol
IC	internal conversion	m_l	magnetic moment number
		M_n	number average molecular weight
		m_s	spin quantum number

III

M_w	weight average molecular weight	TADF	thermally activated delayed
n	principal quantum number		fluorescent
NCA	N-carboxyanhydride	TAPC	1,1-bis[(di-4-
NMR	nuclear magnetic resonance		tolylamino)phenyl]cyclohexane
OLED	organic light-emitting diode	TBAc	9,9-bis(1,3- ditert-butylphenyl)-
PE	power efficiency		10-phenyl-acridine
PEG	polyethylene glycole	TCTA	tris(4-carbazoyl-9-
PF	prompt fluorescence		ylphenyl)amine
PH	phosphorescence	T_d	decomposition temperature
Phe	phenylalanine	TD-DFT	time-dependent density functional
PL	photoluminescence		theory
PLQY	photoluminescence quantum yield	TFA	trifluoroacetate
		TFE	2,2,2-trifluoroethanol
PMMA	poly(methyl methacrylate)	T_g	glass transition temperatures
PMT	photomultiplier tube	TGA	thermogravimetric analysis
Ppm	parts per million	THF	tetrahydrofuran
PPV	poly(p-phenylene vinylene)	TIPS	triisopropylsilane
PS	polystyrene	TLC	thin-layer chromatography
PSar	polysarcosine	ToF	time-of-flight
PTFE	polytetrafluoroethylene	TPA	triplet-polaron annihilation
RISC	reverse intersystem-crossing	TPBi	2,2',2''-(1,3,5-Benzinetriyl)-
rpm	revolutions per minute		tris(1-phenyl-1-H-
s	singlet		benzimidazole)
S	total spin angular momentum	TRPL	time-resolved photoluminescence
SEC	size exclusion chromatography	TSA	triplet-singlet annihilation
SOC	spin-orbit coupling	Trt	trityl
SPPS	solid-phase peptide synthesis	TRZ	2,4,6-triphenyl-1,3,5-triazine
t	triplet	TSCT	through-space charge transfer

TTA	triplet-triplet annihilation
UPS	ultraviolet photoelectron spectroscopy
UV-vis	ultraviolet-visible spectroscopy
V	voltage
X_n	degree of polymerization

1. Introduction

Since the invention of the incandescent light bulb by Thomas Edison in 1879, electrical lighting plays an important role in modern life. Despite the low efficiencies on light output due to heat generation as a major loss process, the working principle of applied electrical current leading to a light-emitting glowing wire was still the basis of a major part of lighting devices more than a century later. The incandescent light bulb was later fully replaced by fluorescent tubes and the smaller compact fluorescent tubes due to their superior power efficiency. This transition to more efficient energy usage was promoted by the increasing awareness of the greenhouse effect. While fluorescent tubes technology meets this criterion, the mercury gas in them poses an environmental and health hazard leading to a steady replacement with inorganic light emitting diodes (LED). Not only do LEDs show superior efficiencies, high stabilities and do not contain mercury in comparison to fluorescent tubes but their small device size also enables a wide variety of mobile and display applications. The light emission in these LED devices is based on recombination at a p-n junction of crystalline semiconductors making them point light sources,^[1] which is a disadvantage for spherical lighting applications. Their rigidity further hinders their application on flexible substrates. In contrast to inorganic LEDs, organic light-emitting diodes (OLEDs) can be processed into flexible, thin film devices emitting over a large area.^[2] While it took about 30 years since the first report of an organic electroluminescent device by Tang and VanSlyke,^[3] the OLED technology found widespread application in displays of televisions and mobile electronic devices due to performance and stability improvements. Despite the advantages of a large area OLED achieving high brightness without glare (see **Figure 1.1**), their more common application in lighting is hindered by a higher price in comparison to inorganic LEDs.

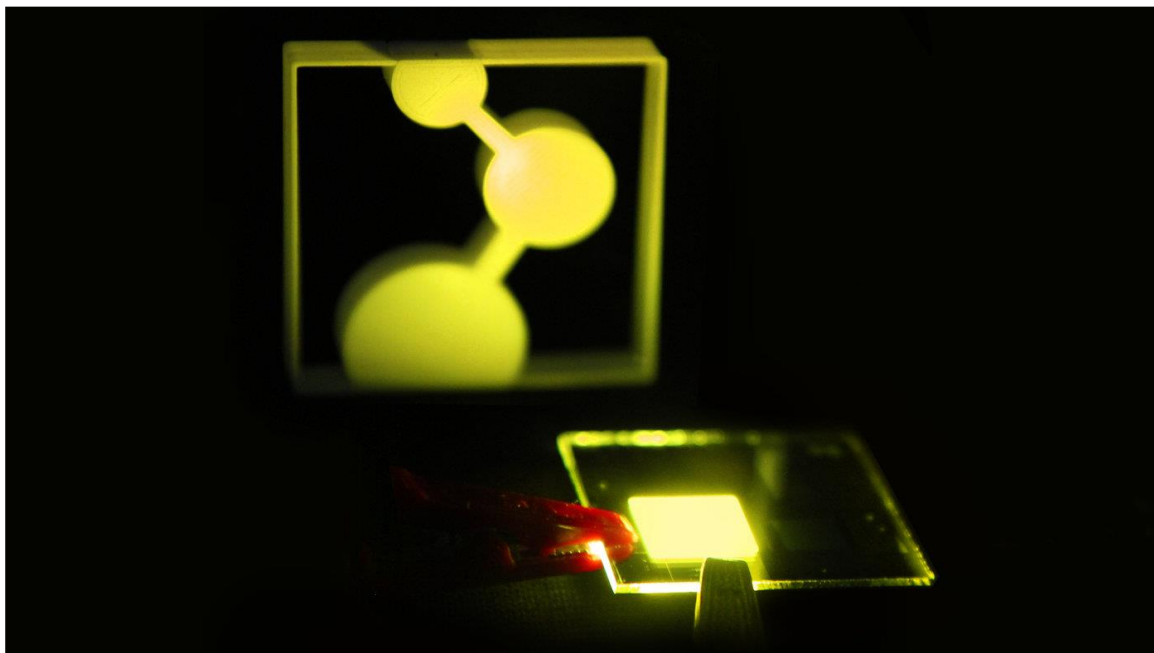


Figure 1.1. Photograph of a organic light-emitting diode emitting yellow light. Reprinted with permission, copyright MPIP Mainz.

1.1. Organic Light-Emitting Diodes

The working principle of an OLED is explained on a simplified single-layer device of an organic semiconductor between two electrodes (see **Figure 1.2**). Upon applying a voltage, electrons are injected from the cathode into the lowest unoccupied molecular orbital (LUMO) of the organic semiconductor, while holes are injected into the highest occupied molecular orbital (HOMO) from the anode. Both charge carriers then move through the emissive layer (EML) via a so-called hopping process driven by the electrical field. As soon as holes and electrons meet in the EML, an exciton is formed. This quasiparticle consists of a bound pair of a hole and an electron. Upon so-called Langevin-type recombination of an exciton, a photon is created. In order to contribute to the light emitted by the OLED the photon has to leave the EML through the transparent electrode used.

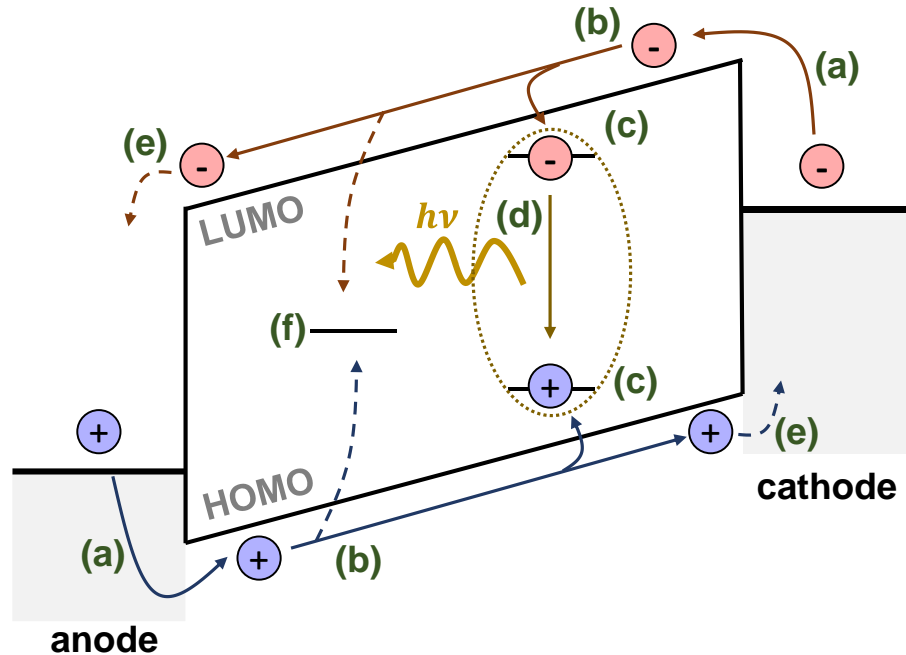


Figure 1.2. Schematic band diagram of a single layer OLED under forward bias visualizing the processes: (a) Charge injection, (b) charge transport, (c) excitons formation, (d) radiative excitons recombination, (e) electrode quenching and (f) nonradiative recombination mediated by traps.

Loss processes that are in competition with the radiative recombination in the OLED can lead to significant reduction in efficiency and stability of the light-emitting devices, motivating the introduction of several functional layers in order to suppress them (see **Figure 1.3**). A prerequisite for an efficient charge injection is the right choice of electrode material. While for the cathode a low work function material like Ba, Li, or Ca is usually applied via thermal evaporation in the device fabrication,^[4] a transparent and conductive anode has to be chosen with indium tin oxide being mostly used.^[5] The cathode work function should not be too high in comparison to the LUMO of the next layer or EML in order to prevent the creation of an injection barrier. The same is the case for a low work function anode leading to an insufficient hole injection into the HOMO of the emissive layer. In order to improve the charge injection properties on each side a hole and electron injection layer (HIL and EIL respectively) can be introduced. In a similar way can the introduction of a hole transport layer (HTL)

to the anode side or an electron transport layer (ETL) to the cathode side of the device architecture lead to an enhancement of charge transport. These layers further prevent the electrode quenching observed for devices with imbalanced transport. If the hole and electron transport properties are significantly higher than their counterpart for the EML material used, the dominant charge carrier species can diffuse to the counter electrode and be directly quenched.^[6] The introduction of an ETL for example can in the case of dominant hole transport cause a reduction of cathode quenching based on an accumulation of the holes at the EML-ETL interface.^[7] If the ETL further has a deep HOMO level, then the hole transfer to the cathode can be hindered and the ETL acts as a so-called hole blocking layer, which is sometimes introduced as a separate layer.^[8] Within the EML, non-radiative trap assisted recombination of holes and electrons (see **Figure 1.2f**) can further reduce the efficiency significantly. These traps can originate from molecular defects in the emissive material itself, but can also stem from impurities from the synthesis^[9] like side products or catalyst residue or are introduced during device fabrication like water or oxygen.^[10] In order to reduce the density of traps,^[11] increase the charge conduction and suppress nonradiative decay paths, the emitters are often dispersed in a host.^[12]

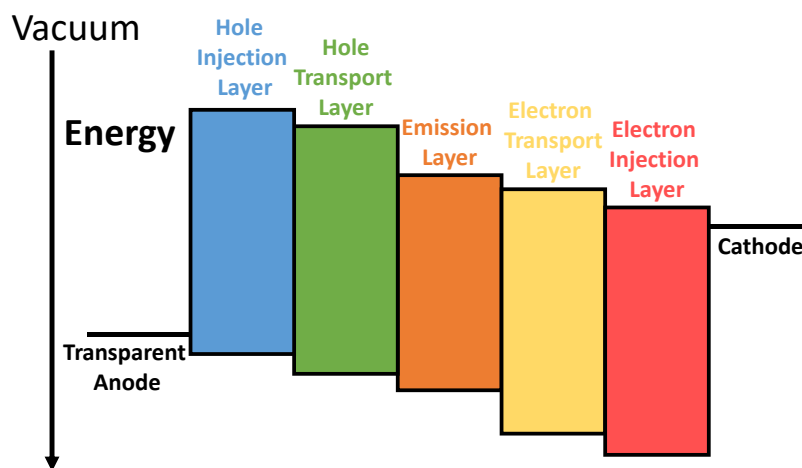


Figure 1.3. Schematic representations of a typical OLED with energy level diagram.

1.2. Transition between Electronic States

In order to describe electronic states in an atom or molecule, the electron is characterized by quantum numbers. While the principal quantum number (n) describes the principal shell of an electron, the angular momentum number (l) its subshell and the magnetic moment number (m_l) its orbital, the spin quantum number (m_s) describes its intrinsic spin angular momentum that can be either $+\frac{1}{2}$ or $-\frac{1}{2}$ which is usually referred to as up (\uparrow) or down (\downarrow) spin. An orbital can only be occupied by two electrons and their spin has to be opposite to one another. The total spin angular momentum (S) of an atom or molecule with several electrons is the sum of all electron spins. A molecule in the ground state usually has a complete electron shell having no unpaired electrons, resulting in a total $S = 0$. The number of near-degenerate levels that only differ in the spin-orbit interaction energy is called multiplicity (m) and is defined as $m = 2S + 1$, characterizing the ground state of most molecules as singlet state ($m = 1$)^[13] (see **Figure 1.4**).

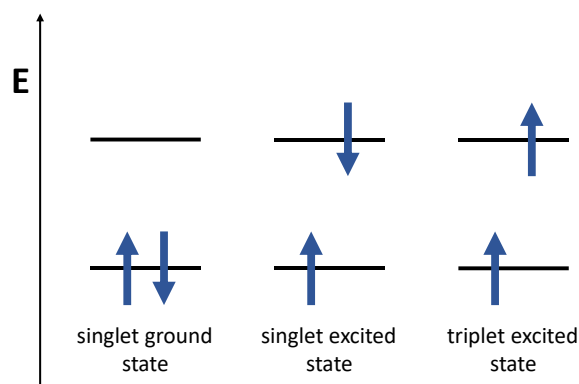


Figure 1.4. Schematic representation of singlet and triplet states.

Upon photoexcitation of a molecule, an electron transfers to a higher energy level while the spin orientation is preserved. In this case, an excited state with the same multiplicity is formed (**Figure 1.5**). There are several possible decay paths for this singlet excited state: The radiative transition to the ground state is called fluorescence but it is also possible for this high energy state to decay

nonradiatively by internal conversion (IC) or intersystem-crossing (ISC). In IC, the excited state decays back to the ground state losing its excess energy via vibronic relaxation. ISC is the transition of the electron to an excited state with a multiplicity of $m = 3$ undergoing a spin flip. The probability of this process into a so-called triplet state is low for most molecules stemming due to the required spin flip, making it a forbidden transition according to the spin selection rule. This triplet excited state can again either decay radiatively via phosphorescence (PH) or nonradiatively via vibrational relaxation. Phosphorescence lifetimes are usually in a millisecond to second time range, which is long in comparison to the fast fluorescent (nanosecond) and even faster absorption processes (femtosecond). The efficiency of light-emitting materials upon photoexcitation is defined by the photoluminescence quantum yield (PLQY), which is the number of photons emitted as a fraction of the number of photons absorbed.

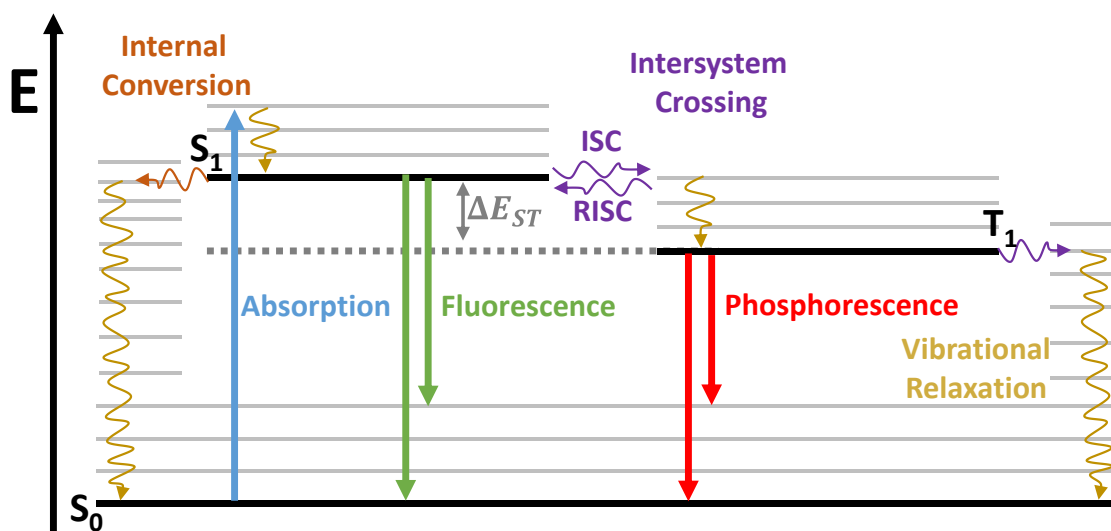


Figure 1.5. Jablonski diagram showing photophysical processes.

1.2.1. Performance Characterization of OLEDs

In order to evaluate the performance of an OLED device, the quantum efficiency can be described in a variety of different key performance indicators: For display applications, the external quantum efficiency (EQE) is often of the highest interest and is defined by the relation

$$\eta_{EQE} = \gamma \cdot \eta_{IQE} \cdot \eta_{out} \cdot \quad (1)$$

where γ is the charge carrier balance with an ambipolar transport of holes and electrons being $\gamma = 1$, η_{IQE} is the internal quantum efficiency (IQE) and η_{out} is the outcoupling efficiency.^[14] The IQE characterizes the percentage of electron hole pair that end up recombining under light emission. Therefore, this variable takes the ratio between radiative and nonradiative processes, which the singlet and triplet excitons undergo, into account. Whether the light generation of an OLED is based on the singlet or triplet excitons depends on the material used and is described in detail in the next section 1.2.2.

The so-called outcoupling efficiency is determined by the percentage of photons that leave the OLED device through the transparent substrate, which is an important measure for display applications. Reflection at the interfaces within the device and absorption of the generated photons makes inefficient outcoupling a major loss process.^[15] For a flat substrate without outcoupling enhancing modifications, an η_{out} of 20 % - 30 % is often assumed.^[16] While **Equation 1** describes the theoretical basis of the EQE, for its calculation upon device characterization the following equation is used:

$$\eta_{EQE} = \frac{\int F_{\lambda} \cdot \lambda \cdot h^{-1} \cdot c^{-1} d\lambda}{J \cdot e^{-1}}, \quad (2)$$

Where λ is the wavelength and F_{λ} is the luminous flux of each wavelength of the electroluminescent (EL) spectrum, h is the Planck constant, c is the speed of light, J is the current density and e is the elementary charge. The term J/e in this equation stands for the number of charges injected.

Another important parameter for the characterization of OLED performance is the power efficiency (PE) that describes the ratio of luminous flux (F) and the electrical power (P):^[17]

$$\eta_{PE} = \frac{F}{P} = \frac{F}{J \cdot V} \quad (3)$$

where J is the current and V is the voltage. The luminous flux is defined as

$$F = K_m \int V(\lambda) F_\lambda d\lambda \quad (4)$$

where K_m is the photonic constant and $V(\lambda)$ is the luminous efficiency function that describes the characteristic wavelength-dependent sensitivity of human vision. A third often used parameter is the current efficiency (CE) that is defined as the luminance (L) divided by the current density (J)

$$CE = \frac{L}{J} \quad (5)$$

1.2.2. Emissive Processes in OLEDs

The first generation of OLEDs used fluorescent emitters with which despite high PLQYs suffer from a theoretical maximum in EQE of about 5 % assuming 20 % outcoupling efficiency.^[18] The limiting factor of their performance stems from the ratio of 1:3 between singlet and triplet excitons formed upon charge injection (see **Figure 1.6**). While in the combination of two electrons just one antiparallel configuration leads to a singlet state, there are three different combinations leading to triplet states described by the magnetic spin quantum numbers $m_s = -1, 0, 1$.^[13] The triplet excitons formed in the device not only do not contribute to the light output of the OLED but can furthermore enhance the degradation process.^[19] Triplet excitons can recombine nonradiatively and produce heat via vibrational relaxation or form high energy ('hot') charge carriers that can break chemical bonds and form trap states.^[20,21]

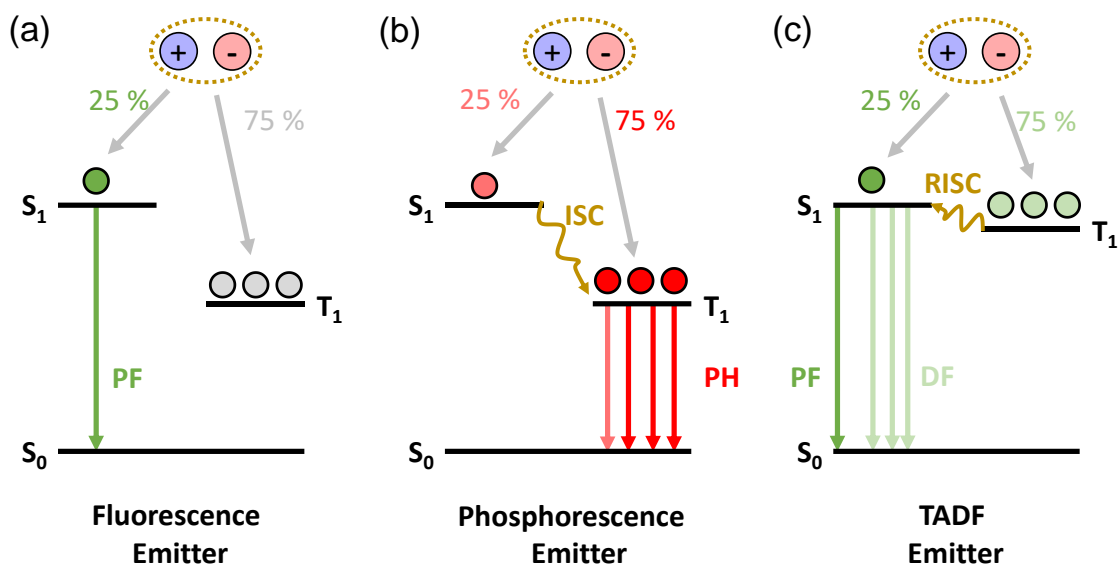


Figure 1.6. Radiative pathways in fluorescent, phosphorescent and TADF materials.

In order to harvest both singlet and triplet excitons, a second generation of OLEDs using phosphorescence as light-emitting process were developed. Those phosphorescent emitters can achieve an internal quantum efficiency of 100 % (see **Figure 1.6b**) based on increasing the spin-orbit coupling (SOC) between the exciton spin angular momentum and the orbital angular momentum upon introduction of heavy metals.^[22] A disadvantage is that most phosphorescent emitters contain heavy transition metals like iridium, which are by nature scarce, expensive^[23] and often toxic.

While the phosphorescent OLED emission is based on the conversion of all excitons into triplet states, the third generation of OLED emitters achieves a transition in the opposite direction: In thermally activated delayed fluorescent (TADF) emitters the triplet excitons transition into singlet excitons via reverse intersystem crossing (RISC; see **Figure 1.6c**). While the 25 % of directly created singlet excitons usually decay radiatively within nanoseconds giving the so-called prompt fluorescence (PF), triplets converting to singlet states lead to a delayed fluorescence (DF) in the microsecond time window. In TADF materials RISC is facilitated by a small energy difference between the singlet and triplet excited state (ΔE_{ST}) and promoted by the thermal energy at room temperature being higher than its

activation energy.^[24] The detailed mechanism and molecular requirements of TADF emitters are described in the next section 1.3.1.

1.3. Thermally Activated Delayed Fluorescence Emitters

1.3.1. TADF Mechanism and Molecular Design Principle

In order to achieve a small ΔE_{ST} necessary for efficient TADF, the exchange energy (J_e) has to be minimized as seen in **Equations 6 – 8**.^[25]

$$E_S = E_{HOMO} - E_{LUMO} + J_e \quad (6)$$

$$E_T = E_{HOMO} - E_{LUMO} - J_e \quad (7)$$

$$\Delta E_{ST} = E_S - E_T = 2J_e \quad (8)$$

Where E_{HOMO} is the energy of the highest occupied molecular orbital and E_{LUMO} is the energy of the lowest unoccupied molecular orbital. The magnitude of the exchange energy depends on the wave function overlap between the ground state and the excited state, i.e. between HOMO and LUMO. Minimizing this overlap can be achieved by connecting electron rich donor (D) and electron deficient acceptor (A) moieties to one another in combination with an almost perpendicular arrangement between them, leading to a highly localized HOMO on the donor and LUMO on the acceptor.^[26] While a small overlap is favorable for a small ΔE_{ST} , full orthogonality on the other hand leads to a strong decrease in PLQY.^[27]

The use of donor and acceptor moieties further introduces two separate types of excited states: The first is a locally excited state (LE) usually based on a π - π^* excitation of the donor and a second excited state of charge transfer character (CT) resulting from an electron transfer from the donor to the acceptor.^[28] The singlet excited states of both types (1LE and 1CT) can emit light undergoing fluorescent decay, which enables it to differentiate between them upon changing the polarity of the surrounding: While the emission from an LE state shows little to no shift in solvents of different polarity, CT emission exhibit a solvatochromic shift.^[29] While there are also triplet states with both

excited state characteristics (^3LE and ^3CT), a direct RISC from ^3CT to ^1CT via SOC is forbidden and therefore of low probability.^[30] Therefore, the interplay between CT and LE singlet and triplet states is crucial for the efficiency of TADF. While the conversion from ^3LE to ^1CT via RISC is usually slow, a vibronic coupling between ^3LE and ^3CT , also called mixing, significantly enhances this process facilitating efficient TADF (see **Figure 1.7**).^[31] The importance of this vibronic coupling for an efficient RISC was further demonstrated upon sterically hindering the D-A dihedral angles. This restriction effectively suppressed the vibronic coupling and resulted in emitters showing room temperature phosphorescence.^[32]

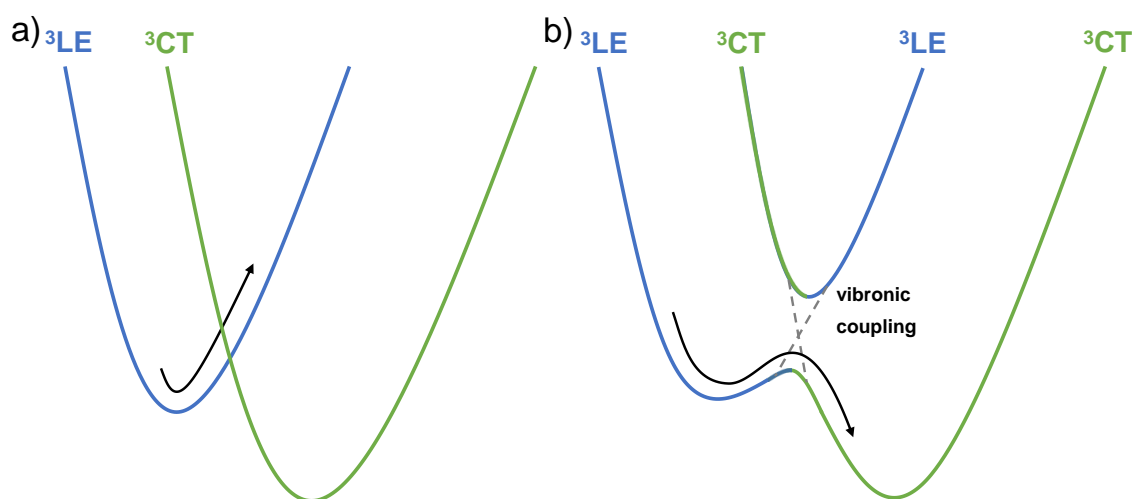


Figure 1.7. Schematic representation (a) a crossing of ^3LE and ^3CT states and (b) a mixing between them based on a vibronic coupling.

1.3.2. Small Molecule TADF Emitters

TADF was first utilized in electroluminescence using organometallic compounds^[33] and a variety of high performance TADF emitters based on for example copper (I),^[34] silver(I) and gold(I and III)^[35] were developed, since the first reported by Endo et al.^[26] The highest research interest in recent years was focused on fully organic small molecule TADF emitters. This first full organic OLED emitter already exceeded the theoretical EQE limit of conventional fluorescent emitters (5 %) reaching 5.3 %

and in subsequent improvements in molecular design high EQEs above 20 %^[36] have been reported with exceptionally examples reaching close to 30 %^[37] and beyond.^[38] Apart from improving EQE, research interests are focusing on the improvement of color purity by achieving narrow emission spectra,^[39-41] increasing the stability of TADF OLEDs (especially of blue emitters),^[42] further understanding the TADF mechanism^[24,43] and optimizing the device architectures^[44,45].

1.3.3. Polymer TADF Emitters

Despite major advances in all performance trait achieved in the field of small molecular TADF emitters, vacuum deposition, which is commonly applied as fabrication method, limits scalability and has high associated costs.^[46] Although there are a few solution-processable small molecules reported,^[47,48] these emitters usually show low solubility, crystallization and poor film formation properties.^[49] Polymers in comparison to small molecules usually form excellent films in wet processing methods, such as ink-jet printing, and can easily be scaled up and are of low cost.^[49]

Despite solution-processed TADF polymers and dendrimers being promising to solve cost and scaling issues, these materials largely lag behind on OLED performance in comparison to their small molecule counterparts.^[50] TADF polymeric emitters often suffer from structural defects, as well as residual impurities stemming from purification difficulties.^[27] Furthermore, it turns out that designing an efficient TADF polymer is challenging: Not only is a rigid structure between D and A required to ensure a low ΔE_{ST} , but at the same time nonradiative internal conversion needs to be suppressed to achieve a high PLQY,^[27] which is more difficult with an increasing number of atoms.^[51] This number is further growing due to the introduction of solubilizing and linker-moieties that are usually necessary.

Another major factor for this inferiority stems from a strong concentration quenching effect that, although also found in pristine films of small molecule TADF emitters, is more prone to polymeric materials.^[27] Concentration quenching is usually used as an umbrella term and includes several different singlet and triplet deactivation processes that are observed at high emitter concentration as for example

in pristine films or solutions of low dilution. For conventional fluorescent and phosphorescent emitters the concentration quenching is dominated by long-ranging Förster Energy Transfer (FRET).^[52] This process is based on dipole-dipole interactions and requires an overlap of absorption and emission spectra, which is due to the intense Stokes shift based on the CT characteristics of TADF emitters usually not the case. The energy transfer processes occurring in host-guest films of TADF chromophores at high and low doping concentrations are shown schematically in **Figure 1.8** with 4,4'-bis(N-carbazolyl)-1,1'-biphenyl (CBP) as host and the TADF emitter 1,2,3,5-tetrakis(carbazol-9-yl)-4,6-dicyano-benzene (4CzIPN) as guest. While the aforementioned Stokes shift leads to an ineffective FRET between the TADF molecules, the same energy transfer can be effective from host to guest depending on the host chosen. Recently the concentration quenching observed in TADF chromophores was identified to be dominated by Dexter energy transfer (DET) mechanism between the TADF emitter molecules,^[52,53] leading to nonradiative quenching pathways competing with the RISC^[52-54]. Furthermore due to this DET, triplet excitons are more prone to undergo bimolecular quenching like triplet-triplet annihilation (TTA), triplet-singlet annihilation (TSA) and triplet-polaron annihilation (TPA) based on their long lifetimes in a range of microseconds in concentrated films.^[27,55] This triplet quenching processes become dominant at high triplet exciton densities, for example at high luminance in OLEDs leading to an EQE roll-off at high operating voltages.^[56]

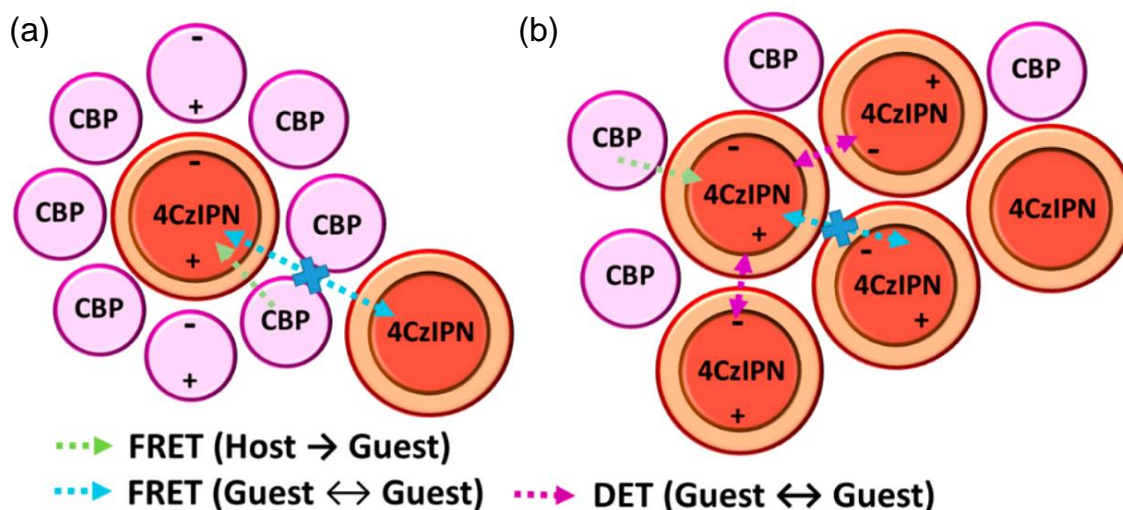


Figure 1.8. (a) Schematic representation of an ideal host–guest system of CBP (host) and 4CzIPN (TADF chromophore guest). (b) Schematic representation of CBP-4CzIPN host–guest system with high emitter content leading to concentration quenching based on DET between the 4CzIPN molecules itself (right). Reprinted with permission from Ref. 52. Copyright 2017 American Chemical Society.

The short-range characteristics of DET promises the reduction of concentration quenching by introducing spatial distance between separate D-A pairs in the form of embedding the TADF materials in a host matrix (see **Figure 1.8a**).^[46] For small molecule emitters most commonly a small molecule host is employed and the emissive layer is formed via co-evaporation,^[57] whereas the TADF polymers are usually blended with a host during solution processing.^[58–60] However, blending a polymer with a host is much more challenging than for a small molecule, due to the reduction in translational entropy, in particular if the host is also polymeric.^[61] The host material should be chosen carefully to avoid phase separation and aggregation.^[49] While dilution successfully suppresses this loss process for TADF small molecules, in case of their polymer counterparts not only intermolecular but also intramolecular quenching of neighboring TADF units within the polymer has to be taken into account.^[62]

1.3.4. TADF Polymer Architectures

In order to minimize these adverse effects and increase the performance in polymer based OLEDs, a variety of different polymer structures and molecular design principles have been developed in recent years.^[46] These can be divided into groups according to the position of D and A in the polymer architecture, as well as the presence or absence of an insulating spacer which interrupts the conjugation between the TADF units (see **Figure 1.9**). Following this categorization, D-A alternating and fully conjugated^[59,63] as well as spacer-separated main-chain polymers^[58,60,64] exhibiting high external quantum efficiencies have been reported. Other design classes are backbone-donor/ pendent-acceptor polymers,^[65-68] backbone-acceptor/ pendent-donor polymers,^[69] as well as polymers with a nonconjugated backbone bearing the DA chromophores grafted as side moieties. The latter can be further divided into directly connected D-A structures^[70-73] and through-space charge transfer (TSCT) polymers with D and A positioned separately at different (neighboring) monomer units.^[74-76] Another class of macromolecular TADF chromophores are dendrimers, which usually have a TADF core and can be divided in conjugated^[77,78] and nonconjugated shell.^[79,80]

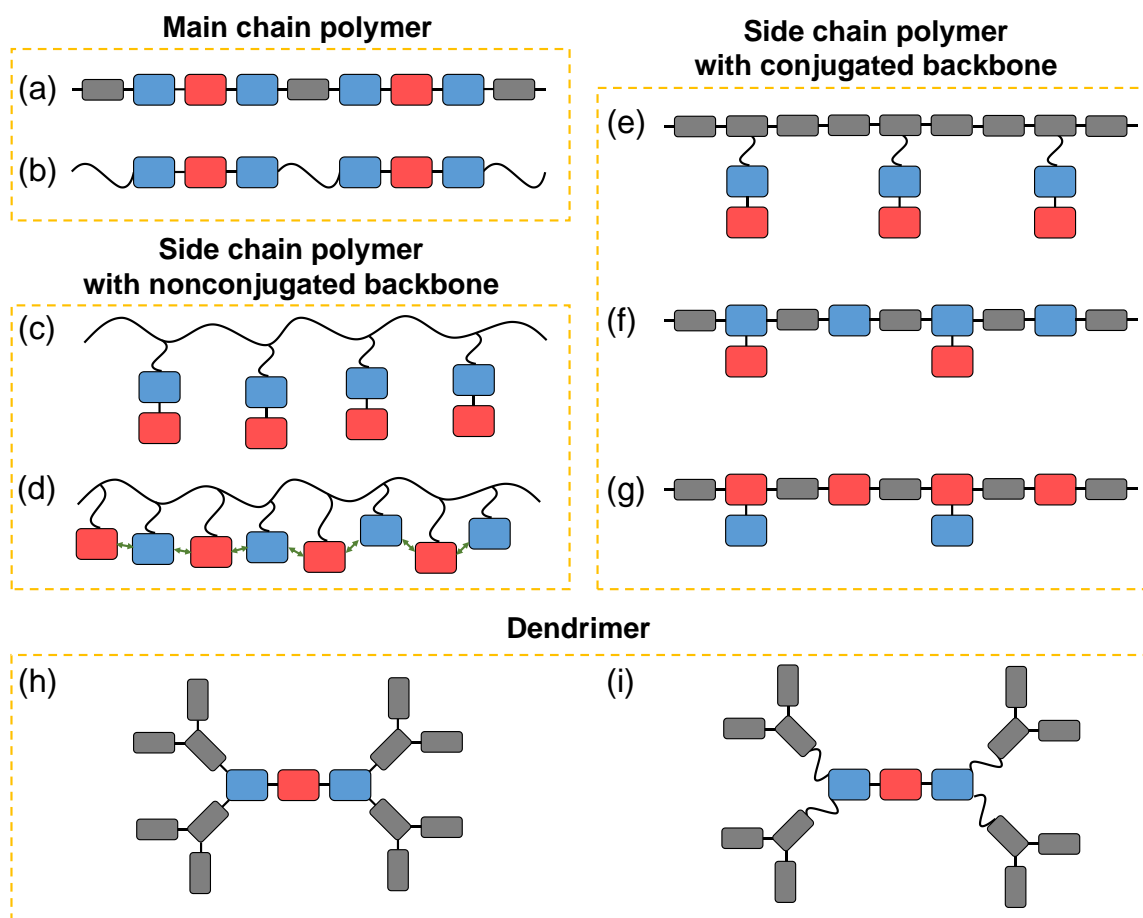


Figure 1.9. The structural diagram of TADF polymers architectures. The blocks represent donor (blue) and acceptor moieties (red) of the TADF, as well as host moieties (gray). (a) Conjugated and (b) nonconjugated main chain TADF polymers, nonconjugated backbone with (c) TADF unit in side chain and (d) donor and acceptor separately in side chain (through-space TADF), conjugated backbone with (e) TADF unit in side chain, (f) backbone-donor/ pendent-acceptor and (g) acceptor backbone-acceptor/ pendent-donor and (h) Conjugated and (i) nonconjugated dendrimers.

In parallel with developing and evaluating these various polymer architectures, another strategy emerged to suppress concentration quenching: By reducing the ratio of A in comparison to D in the polymer structure, the aforementioned spatial distance between the TADF chromophores can be obtained and the short-range concentration quenching effectively suppressed,^[54] while avoiding phase separation issues of host-guest polymer blends. The same effect can be achieved by including moieties into the polymer structure that act as host.^[72] Such structural control is achieved by tuning the feeding ratio of the comonomers during synthesis.^[54,81] and due to the universal nature of these self-hosting

strategies they were already successfully applied to a variety of the aforementioned polymer architectures.^[54,76,82,83] But this method also shows a trade-off in the transport properties resulting in a performance drop of the OLEDs at low amount of A. Due to the reduction of electron accepting moieties, the electron charge transport decreases leading to an unbalanced charge transport.^[54] A similar trend can be observed for the second strategy for which impairing device performances, usually accompanied with a second emission stemming from the host, indicate an incomplete charge transfer from the host to the TADF chromophore at low ratios.^[82,84] Both polymer designs therefore require the synthesis of a set of polymers with varying contents in order to identify the optimized ratio. As an example, the synthesis of poly(9-(heptadecan-9-yl)-9H-carbazole-co-9,9-dihexal-10-(4-(4,6-di-tert-butyl-1,3,5-triazin-2-yl)phenyl)-9,10-dihydroacridine (PCzAPT_x) is shown in **Figure 1.10**. Upon dilution of the TADF subunits by changing the feeding ratio of the polymerization from 1:1 to 1:9 between the TADF chromophore (M₁) and the host monomers (M₂ and M₃) monomer the maximum EQE was improved from 13.6 % to 16.9 %.^[54]

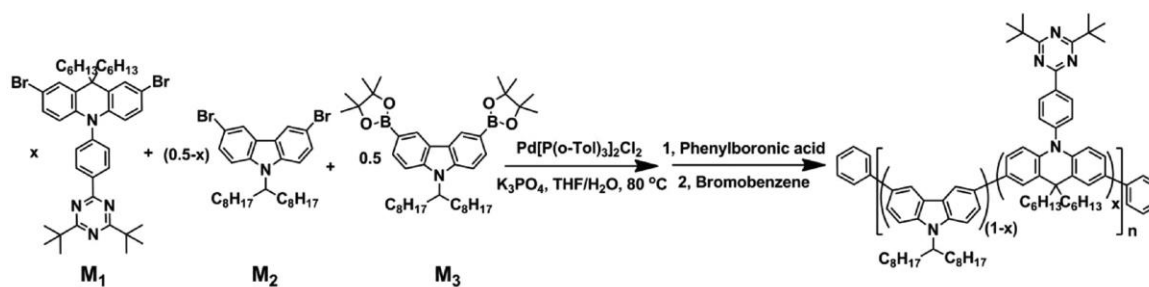


Figure 1.10. Synthetic route of the TADF polymers PCzAPT_x. Reprinted from Ref. 54 with permission from Wiley [Copyright © 2018 WILEY-VCH Verlag GmbH Co. KGaA, Weinheim].

In contrast to most TADF polymers with donor and acceptor directly connected via covalent bonds, TADF emission can also be achieved based on a through-space charge transfer mechanism. While donor and acceptor are molecularly separated by for example being incorporated in different side chains, charge transfer based on spatial π - π interactions can occur.^[27] Absence of a conjugated

connection between donor and acceptor in this design strategy leads to fully separated HOMO and LUMO distributions and a resulting small ΔE_{ST} and simultaneously avoids a decrease in oscillator strength at almost perpendicular D-A orientation.^[76] Applying this concept, Shao et al. first reported a blue emitting TSCT polymer reaching 3.1 % EQE in OLEDs with 9,9-dimethyl-10-phenyl-acridine acting as donor (Ac) and 2,4,6-triphenyl-1,3,5-triazine (TRZ) as acceptor moieties (see **Figure 1.11**).^[76] Although a close proximity of donor and acceptor is needed for the TSCT, concentration quenching was identified as a major loss process and an improvement in EQE to 12.1 % EQE was achieved by reducing the acceptor to donor monomer feeding ratio in the polymer synthesis to 1:19. The importance of the orbital overlap between donor and acceptor was further demonstrated by the suppression of delayed emission upon exchanging the Ac donor by a more sterically hindered 9,9-bis(1,3-ditert-butylphenyl)-10-phenyl-acridine (TBAc). Since this first report a wide variety of TSCT emitters have been developed ranging across the whole color spectrum.^[75,85]

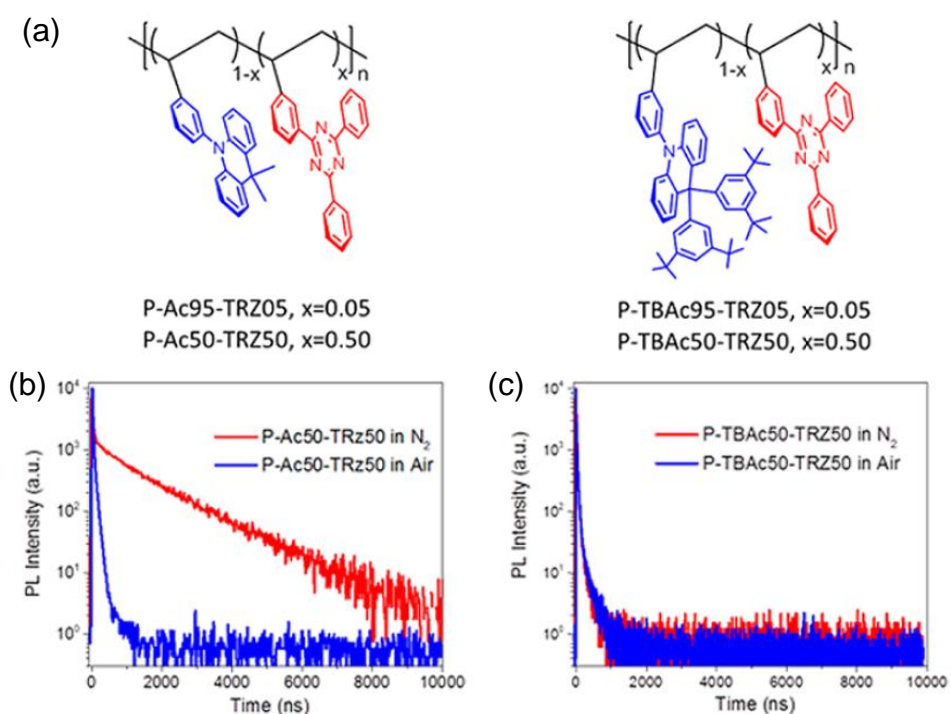


Figure 1.11. (a) Molecular structure of P-Ac-TRZ and P-TBAc-TRZ with different donor and acceptor ratios shown in percent as number. PL decay curves of (b) P-Ac50-TRZ50 and (c) P-TBAc50-TRZ50 in nitrogen and in air atmosphere in toluene solution. Reprinted with permission from Ref. 76. Copyright 2017 American Chemical Society.

1.4. Supramolecular Polymers

In contrast to “classical” organic chemistry that focusses on forming and cleaving covalent bonds, the field of supramolecular chemistry deals with noncovalent interactions between molecules. These interactions include electrostatic, π - π and Van der Waals interactions, as well as the hydrophobic effect and hydrogen bonds and can lead to aggregation, repulsion or attraction between specific moieties or molecules. Self-organization and self-assembly of molecules based on these, often classified as weak interactions, are of crucial importance for the dynamic processes happening in biological systems. Through clever molecular design, it is possible to tune attractive and repulsive interactions leading to a high selectivity in positioning complementary structural motifs with a supramolecular complex.^[86] In material science, the awareness of these interactions and their manipulation enabled the development of self-healing and stimuli-responsive materials for a wide variety of applications.^[87]

A subsection of supramolecular chemistry is concerned with the supramolecular polymerization, which similarly to their covalent counterpart, is based on forming macromolecules from monomers. While most covalent polymerizations are irreversible and in order to overcome the entropy loss, originating from the reduction of the number of molecules, require exothermic polymerization reactions, supramolecular polymerizations are typically dynamic and reversible stemming from the weak nature of the interactions.^[88] Depending on the specific interactions responsible causing a self-assembly of the monomers, polymerization and/or depolymerization can be initiated with external stimuli like pH,^[89,90] temperature,^[91,92] redox reactions,^[93,94] and many more.^[95]

With the objective of achieving high control over the supramolecular properties of responsive materials, a variety of molecular structures were adapted from nature. One of these examples are peptide-polymer conjugates, in which the peptide moieties enable a controlled self-assembly.^[96,97] The selectivity of the interactions between peptide chains is based on the directional nature of hydrogen bonds, which leads to the formation of secondary structures in proteins like beta sheets or alpha helices.

Additional to the hydrogen bond interactions, the specific choice of the amino acids used in the peptide sequence further enables fine tuning of the responsive stimuli for self-assembly.^[97] As an example, the supramolecular polymer system adapted in chapter 6 and developed in the Besenius group contains a pentapeptide with an alternating sequence of phenylalanine (F) and histidine (H).^[98,99] While the π - π interactions and hydrophobicity of the FHFHF peptide moiety facilitate the β -sheet directed folding at neutral and basic pH, the pKa of the imidazole side chain in H of 6.0 leads to its protonation in acidic conditions.^[100] The positive charges results in a disassembly based on coulomb repulsion between the monomers. Two of these pentapeptides are connected by a polyethylene glycol (PEG) or polysarcosine (PSar) polymer affording ABA-type polymer-peptide conjugates.^[98] The PSar enables a solubility in aqueous solution and forms a polymer shell around the self-assembled rod-like nanostructures formed in solution at pH higher than 6.

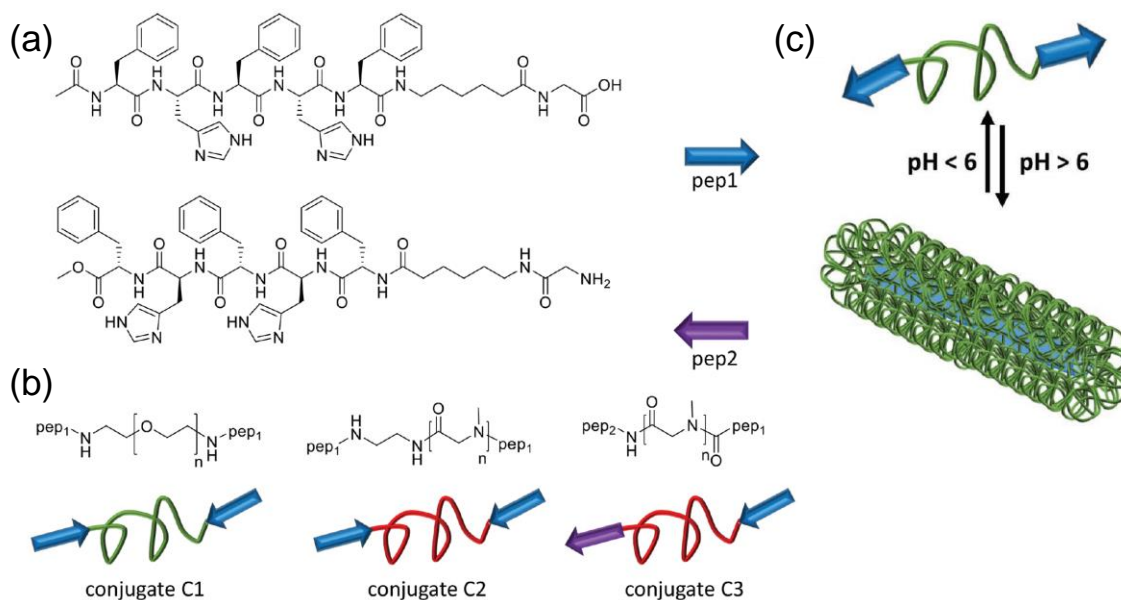


Figure 1.12. Chemical structures of (a) the peptide building blocks pep1 and pep2 and (b) of peptide-polymer conjugates C1, C2, and C3. (c) Schematic representation of the pH-dependent formation of supramolecular rod-like polymers. Reprinted from Ref. 98 with permission from Wiley [Copyright © 2018 WILEY-VCH Verlag GmbH Co. KGaA, Weinheim].

2. Objectives

Artificial lighting is crucially important in everyday life and is responsible for 1/6 to 1/5 of the overall electrical energy consumption.^[101] This motivates scientists all over the world into developing more efficient lighting technologies to reduce the carbon footprint. Other important traits necessary for the widespread application of these technologies are the use of eco-friendly materials and production methods, as well as cheap fabrication. These characteristics make OLEDs based on all-organic TADF materials a promising candidate for a wide variety of display and lighting applications, due to their lack of expensive and ecologically harmful components like rare earth metals and mercury. An important factor that still has to be improved are the fabrication costs associated with multilayer vacuum processing, which incentivizes the high research interest in device structure optimization as well as the development of solution processable TADF polymers.

While also observed for small molecule TADF emitters, TADF polymers are more prone to concentration quenching,^[27] which is a major loss process leading to reduced efficiencies and life times of OLEDs devices. In order to suppress this nonradiative process, which is thought to be based on a short-range Dexter energy transfer,^[52,53] the emitters are usually diluted in a small molecular host or by introducing host moieties into the polymer structure. However, the use of a small molecular material as host can lead to declining film formation properties. The choice of the linker moiety and position within the polymer architecture can also have a significant effect on the performance of the obtained TADF polymer. Despite the fact that a wide variety of polymer architectures and linkers have been developed, the direct influence of the type of linker applied independent of the TADF units used is still lacking.

In order to gain insight into the differences in TADF properties and the extent of concentration quenching, the objective of this work was to synthesize TADF polymers solely differing in the linker moiety. Incorporating an identical TADF chromophore enabled identification of any difference in photophysical properties and device performance as a function of linker. For this investigation, one

conjugated and two nonconjugated alkyl linkers of different length as well as a structure equivalent small molecule had to be synthesized using a main chain polymer architecture (chapter 3). In order to additionally evaluate the effect of solubilizing side chains on the TADF properties, a second set of materials with identical polymer structure but longer alkyl chains at the donor moiety should be synthesized, too. The photophysical characterization (chapter 4) in solution and film state in steady state was to be performed in order to assess the CT character of the excited state, estimate the ΔE_{ST} , and determine the PLQY. The magnitude of concentration quenching had to be determined by investigating the change in PL intensity with dilution in an insulating material. The impact of the linker strategy used was to be investigated in detail using time-resolved spectroscopy, which is necessary to differentiate between prompt and delayed fluorescence.

After fully characterizing the photophysical properties between the different materials, their device performance, starting with single charge carrier mobilities, had to be determined (chapter 5). An optimization of device architecture had to be performed enabling a comparison in electroluminescent properties between the different linkers applied. By using an insulating host material, the concentration quenching effect on the device performance of the materials was to be investigated, independent from host effects based on the charge transport of the host. In order to assess the effect of the insulator in the devices, small molecule hosts were to be used in the fabrication of reference OLEDs.

While TADF emitters gained a lot of attention in recent years based on OLEDs, the photophysical properties of these chromophores make them also interesting for sensing applications: In TADF materials based on a TSCT mechanism, a close proximity between donor and acceptor are necessary to obtain a CT excited state. The CT characteristics of this emissive state leads to a red-shift in PL upon increasing polarity of the environment (as for example shown in solvatochromism) and the contribution of triplet states to the PL emission furthermore results in a high sensitivity of the PL intensity on oxygen that quenches the triplet excited state upon singlet oxygen generation. All of the aforementioned effects combined therefore enable a qualitative analysis of the distance between donor

and acceptor, the polarity of the environment and the presence of oxygen based on the observed PL spectrum.

In order to utilize these characteristic photophysical properties in a responsive material, a donor and an acceptor moiety known to show TADF based on TSCT had to be incorporated into a pH-responsive supramolecular polymer system (chapter 6). At first, the supramolecular monomers containing donor and acceptor moieties had to be synthesized and their self-assembly in aqueous solutions had to be investigated. Subsequently the change in photophysical properties upon aggregation in solution had to be determined. In order to fully characterize the emissive states, identify DF and investigate oxygen responsivity of the triplet excited state of the self-assembled supramolecular polymer, time-resolved photoluminescence spectroscopy should be performed as a last step.

3. Molecular Design and Synthesis of TADF Main-Chain Polymers

3.1. Introduction

Despite being one of the more simplistic polymer architectures, there are just a few examples of main-chain TADF polymers in literature, in which donor and acceptor are embedded into the polymer backbone. Achieving an almost orthogonal dihedral angle between donor and acceptor necessary for a small ΔE_{ST} is challenging in an alternating D-A polymer, which usually exhibits a planar geometry.^[102] In order to prevent this disadvantageous conformation, a linker unit is often introduced into the molecular structure that separates the TADF units from one another. Due to the importance of this additional moiety for the efficiency of the TADF and therefore performance in OLEDs, focus in the research field of main-chain TADF polymers was directed to the development of new linker moieties.^[58,60,103]

Wang and coworkers recently proposed a “TADF + Linker” strategy^[60] that promises a simple synthesis of new TADF polymers. This is achieved by connecting highly efficient small molecules that are already known from literature with a tetramethyl phenylene linker that does not negatively influence the RISC rate and the resulting harvest of triplet states in OLEDs. Prior to this, Kim et al. used a nonconjugated diphenylcyclohexane linker^[58] and Liu et al. a 1,4-dihydroxybenzene and a bisphenol A moiety as a linker^[103] applying a similar concept. Although in all three examples the TADF polymers showed high maximum external quantum efficiencies in OLEDs (EQE of 13.2 %, ^[103] 15.4 %^[58] and 23.5 %^[60]), the concentration quenching effect observed required dilution in a host in order to achieve them.

Despite these promising examples for the development of efficient TADF polymers with various linkers, a systematic study using the same TADF unit for conjugated and nonconjugated linkers is missing. Therefore, in this chapter the synthesis as well as thermal and electronic characterization of two sets of main-chain polymeric TADF emitters either flexible non-conjugated (alkyl moieties, both short and long) or rigid conjugated (phenyl) linkers is described and compared to a structure equivalent small molecule. The photophysical characterization as well as characterization in OLED devices is described in chapters 4 and 5.

3.2. Molecular Design and Computational Results

Bis[4-(9,9-dimethyl-9,10-dihydroacridine)phenyl]methanone (DMAC-BP) was selected as TADF unit for this systematic investigation and it consists of a benzophenone as acceptor and 9,9-dimethyl-9,10-dihydroacridine as donor (see **Figure 3.1a**). This choice was motivated by the extremely small ΔE_{ST} of 7 meV and a high PLQY of 0.85 in neat film, showing only a small concentration quenching (0.90 for 10 wt% diluted in *m*-bis(N-carbazolyl)benzene (mCP) film).^[104] The authors ascribe the limitation of concentration quenching to the inhibited interaction between the donors due to the methyl substitution of the DMAC groups leading to high PLQYs.^[104] Furthermore, the same combination of donors and acceptors used in DMAC-BP was also utilized as TADF chromophore in several polymers of different architectures^[59,60,67] and dendrimers.^[78] While concentration quenching was suppressed in the reported dendrimeric emitters due to a self-hosting nature of this polymer architecture, the effect was more pronounced for the TADF polymers and a dilution in a host was applied. The aforementioned properties and the fact that DMAC-BP as well as its polymeric derivatives are already well studied, makes it a perfect model compound for the systematic investigation of the influence of the linker in main chain TADF polymers.

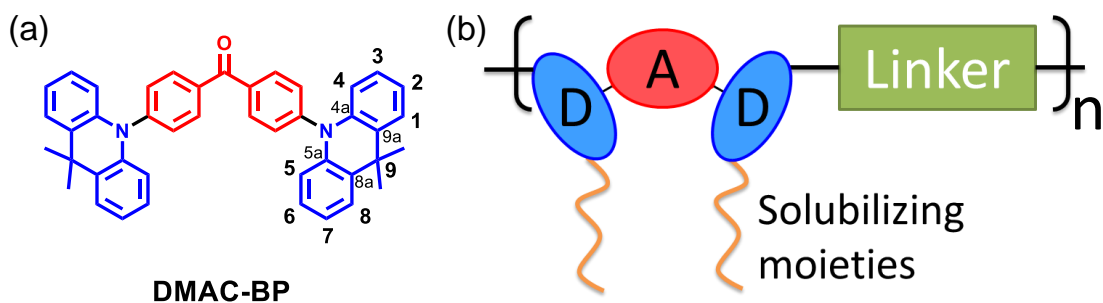


Figure 3.1. (a) Chemical structure of DMAC-BP with acridine substitution numbering shown. (b) Schematic representation of the polymer design with assigned roles.

In order to design a TADF polymer based on DMAC-BP, a main chain polymer structure was chosen connecting the acridine donors at the 2-position with a linker moiety (see **Figure 3.1**). This way the D-A-D triad is in the polymer backbone leading to an identical chemical substitution for both donors and their electronic uniformity. Furthermore, 2-ethylhexyl (EtHex) side chains were introduced as solubilizing moieties to the 7-position of the acridine Ds to ensure solution processability of the polymers.

For comparison of the opposing linker strategies described in the introduction, a conjugated as well as two nonconjugated spacers were selected to connect the donors in the main-chain polymers. The set of materials (**Figure 3.2**) consists of a fully conjugated polymer **P(Ph-MAc-BP)** with a 1,1'-biphenyl linker as well as two nonconjugated polymers **P(C2-MAc-BP)** and **P(C6-MAc-BP)** with 1,2-diphenylethane and 1,6-diphenylhexane linker moieties, respectively. The nonconjugated linkers selected differ in the length of the alkyl chain, from a shorter and stiffer ethyl moiety for **P(C2-MAc-BP)** to a longer and more flexible hexyl spacer for **P(C6-MAc-BP)**. In order to compare the polymer properties to a TADF small molecule the structurally equivalent **Tol-MAc-BP** with identical solubilizing groups and a tolyl substitution of the donor moieties was selected/synthesized. Using the same TADF unit in all polymers enables the investigation of the influence of the type of linkage on the concentration quenching in an isolated way. In addition, a second set of materials with the same linker moieties but 9,9-dihexyl-9,10-dihydroacridine (DHAC) as donor were selected. Although Adachi and coworkers ascribed the limited concentration quenching exhibited by DMAC-BP^[104] to the methyl groups of DMAC, concentration quenching was still a major loss process observed in polymers using an similar or identical donor moiety.^[59,60,67] In the second set of materials (**Tol-HAc-BP**, **P(C2-HAc-BP)**, **P(C6-HAc-BP)** and **P(Ph-HAc-BP)**) the even bulkier and longer alkyl chains at the 9-position promised the inhibition of D-D interactions while simultaneously further increasing the solubility.

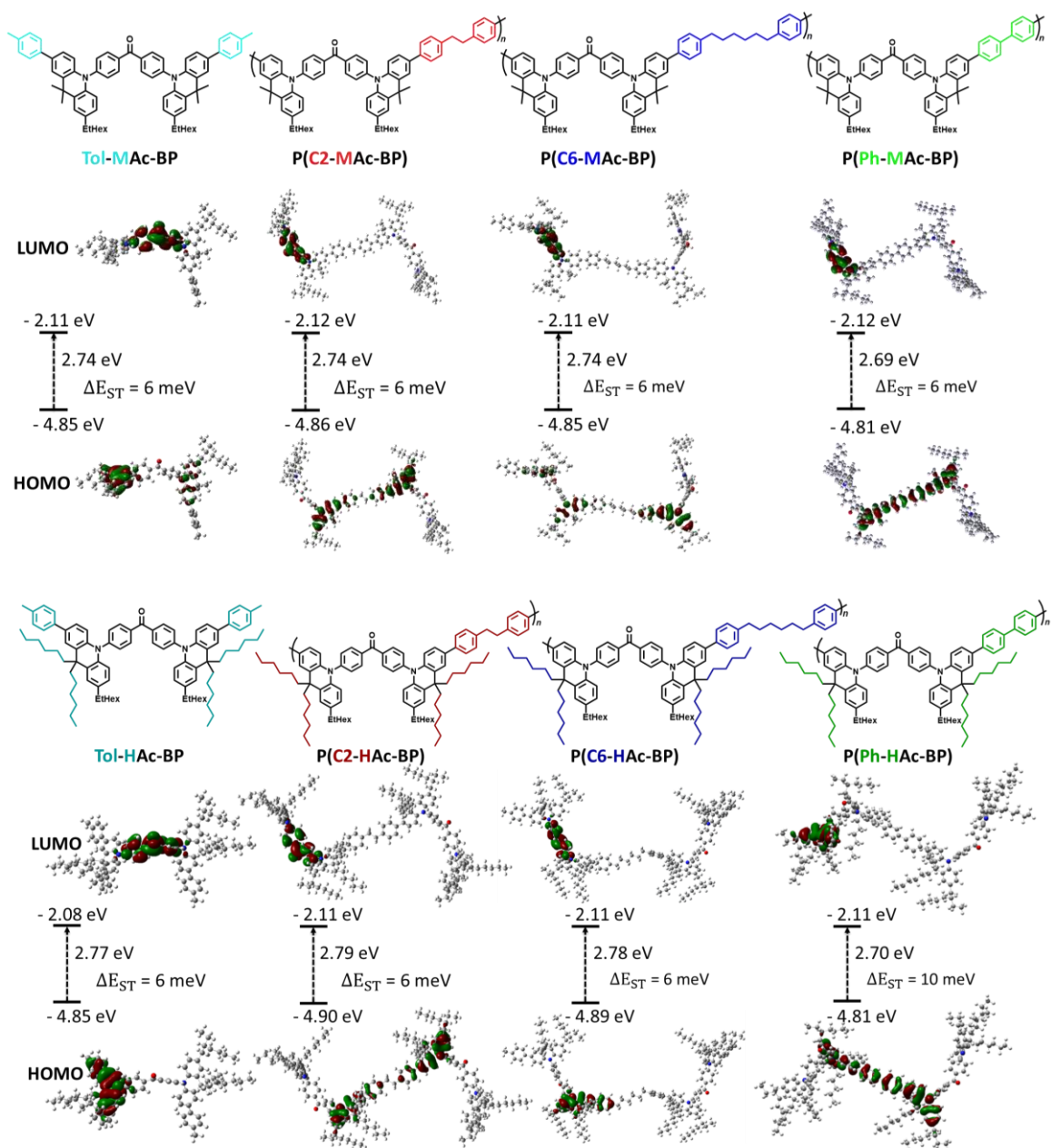


Figure 3.2. Molecular structures and frontier orbital distribution of the TADF polymers and small molecules.

As a first step the electronic properties were investigated using density functional theory (DFT) to ensure that the HOMO and LUMO distributions and the ΔE_{ST} is not adversely affected by the choice of linker, ethylhexyl substitution as solubilizing moiety and the integration of hexyl side chains. In order to reduce the number of atoms for the computations, fragment molecules consisting of the linkers connecting two D-A-D triads were used. The ground-state geometries were optimized at B3LYP/6-31G(d,p) level of theory and in subsequent time-dependent DFT (TD-DFT) calculations the energies of S_1 and T_1 were determined. The computational results are summarized in **Table 3.1**.

Table 3.1. Summary of computational data.

Compound	E_{HOMO} [eV]	E_{LUMO} [eV]	$\Delta E_{\text{HOMO-LUMO}}$ [eV]	E_{S_1} [eV]	E_{T_1} [eV]	ΔE_{ST} [meV]	Θ_{D-A}^a [°]	Θ_D^b [°]
Tol-MAc-BP	4.847	2.109	2.739	2.241	2.235	6	89.2	179.3
P(C2-MAc-BP)	4.861	2.116	2.746	2.254	2.248	6	89.1	179.3
P(C6-MAc-BP)	4.853	2.112	2.741	2.245	2.239	6	89.3	178.8
P(Ph-MAc-BP)	4.805	2.120	2.685	2.235	2.229	6	88.2	179.6
Tol-HAc-BP	4.847	2.076	2.771	2.270	2.264	6	82.5	158.3
P(C2-HAc-BP)	4.900	2.110	2.790	2.303	2.297	6	82.8	163.8
P(C6-HAc-BP)	4.892	2.113	2.779	2.293	2.287	6	83.1	162.5
P(Ph-HAc-BP)	4.805	2.106	2.699	2.272	2.262	10	85.1	165.0

^a Average of dihedral angles between donor and acceptor in the D-A-D triad. ^b Average of dihedral angles along N-C^{4a} and N-C^{5a} bond in D.

Except for a small increase of the HOMO for the fully conjugated linker in the fragment molecules representing **P(Ph-MAc-BP)** and **P(Ph-HAc-BP)** no significant difference in HOMO and LUMO energies between the different linkers and the small molecules were observed. The HOMO energies range from -4.805 eV to -4.900 eV with a LUMO from -2.076 eV to -2.120 eV. The high similarity furthermore results in a similar energy difference between HOMO and LUMO $\Delta E_{HOMO LUMO}$ of -2.685 eV to -2.790 eV. Due to the connection of the TADF units via the donors, the linker strategy only has an influence on the HOMO. For **P(Ph-MAc-BP)** and **P(Ph-HAc-BP)**, the HOMO's orbital distribution expands from one acridine donor to the next through the biphenyl linker, while an interruption of the conjugation caused by the alkyl linkers in the nonconjugated polymers leads to an expected gap in molecular orbital distribution of the HOMO (see **Figure 3.2**). The frontier orbital distributions further show a strong localization of the HOMO on the donor and the LUMO on the acceptor moieties, fulfilling an important prerequisite for TADF (see **Figure 3.2**).

The small overlap necessary for this localization is associated with the dihedral angles (θ_{D-A}) close to 90° between donor and acceptor (see **Figure 3.3**). Overall, the hexyl substituted TADF fragments representing **Tol-HAc-BP**, **P(C2-HAc-BP)**, **P(C6-HAc-BP)** and **P(Ph-HAc-BP)** show a slightly smaller θ_{D-A} of 82.5 - 85.1° in comparison to their methyl substituted counterparts, ranging from 88.2 to 89.2° (see **Table 3.1**). Taking a closer look at the molecular conformation revealed that this lower D-A angle for the second set of materials is caused by a deformation of the hexyl substituted acridine donor structure (see **Figure 3.3**). While the dihedral angle within the donor (θ_D) is close to 180° for the methyl substituted materials indicating planarity, the introduction of hexyl chains to the 9-position seems to deform the donor to θ_D angles between 158.3 - 165.0° . Despite this difference in donor conformation, the computational results point to an extremely small ΔE_{ST} of 10 meV for **P(Ph-HAc-BP)** and 6 meV for all the other materials. Overall, the computational results show no significant change in electronic structure based on the linkers and alkyl chains introduced. Furthermore, the electronic prerequisites for TADF, namely an almost perpendicular D-A structure, high localization of HOMO on the donor and LUMO on the acceptor and a small ΔE_{ST} , were preserved making this set of materials viable for systematic investigation of the influence of the linker moiety.

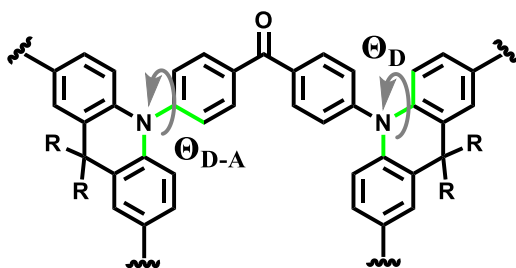
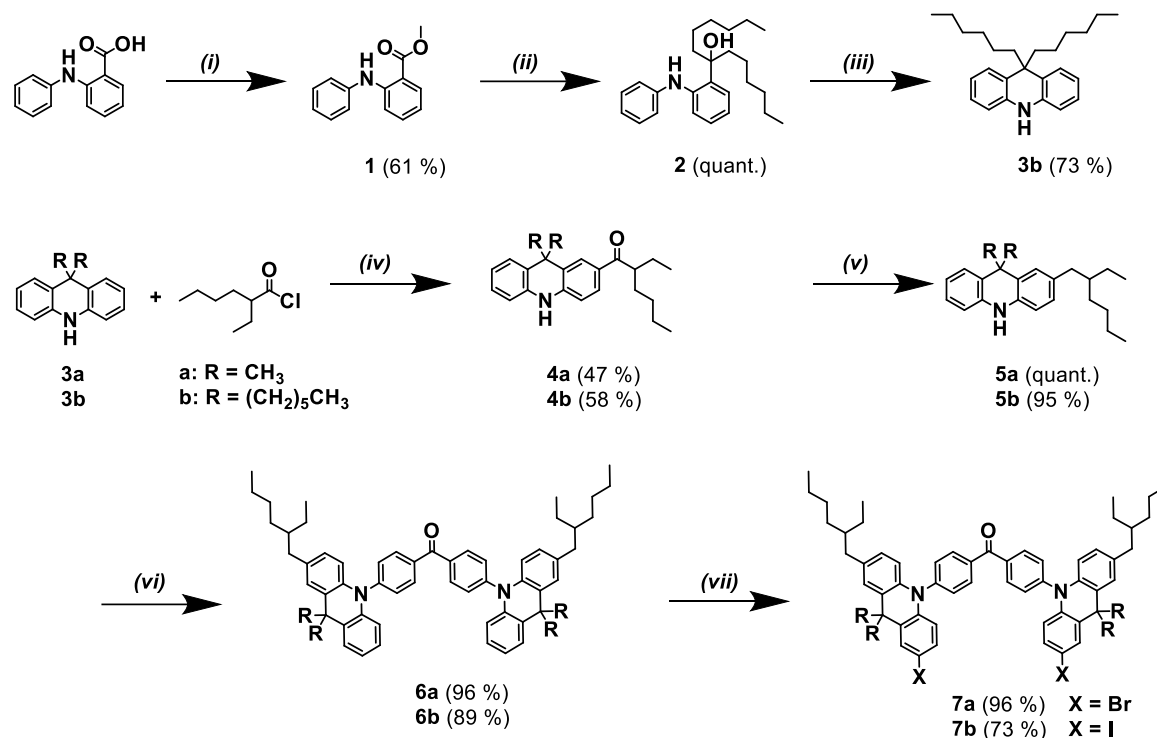


Figure 3.3. Visualization of the dihedral angle between D and A (θ_{D-A}) and within the acridine D (θ_D) as a measure for its planarity.

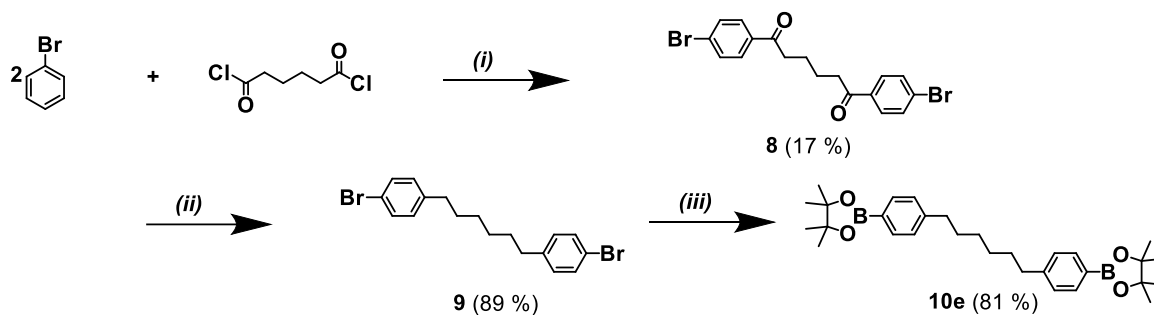
3.3. Synthesis of Main-Chain TADF Polymers and Small Molecules

The synthetic route can be divided in three parts: The syntheses of the comonomers, one containing the TADF unit (**7a** and **7b** in **Scheme 3.1**) and the other one being one of the linkers (**Scheme 3.2**), as well as the subsequent polymerization (**Scheme 3.3**). While the donor 9,10-dihydro-9,9-dimethylacridine (**3a**) was commercially available, its hexyl derivative **3b** had to be synthesized: As a first step (phenylamino)benzoic acid was converted to **1** by esterification. In the next step, this ester moiety was alkylated in two subsequent Grignard reactions obtaining the alcohol **2**. Heating this compound under acidic conditions caused a cyclization reaction affording 9,10-dihydro-9,9-dihexylacridine (**3b**). Both acridine derivatives **3a** and **3b** were substituted with 2-ethylhexanoyl chloride via Friedel–Crafts acylation to obtain **4a** and **4b**. After a reduction of the ketones, to yield **5a** and **5b**, Buchwald-Hartwig aminations with 4,4'-dibromobenzophenone were carried out to produce the donor-acceptor-donor molecules **6a** and **6b**. In a subsequent halogenation, the brominated comonomer **7a** and iodinated comonomer **7b** were obtained with an overall yield of 43 % and 16 %, respectively. While **7a** had shown sufficient reactivity in Suzuki–Miyaura polycondensation in literature,^[59] iodide was chosen as an even better leaving group for **7b** in order to ensure polymer formation.



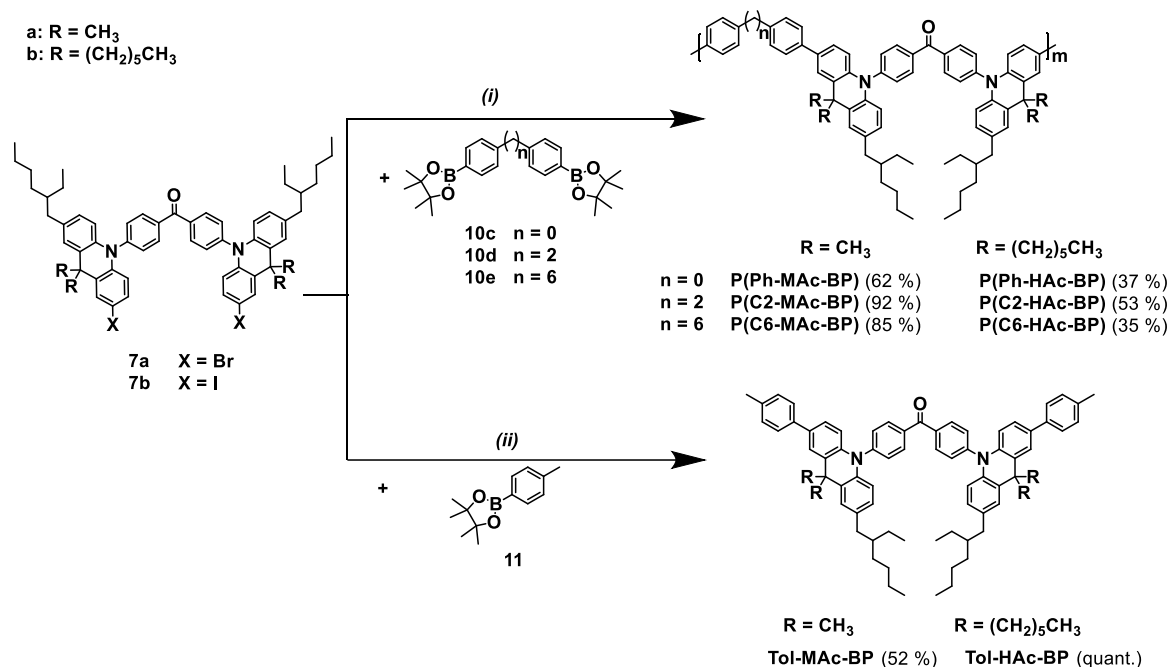
Scheme 3.1. Synthesis of comonomers **7a** and **7b**: i) thionylchloride, MeOH, 0 °C → reflux; ii) hexylmagnesium bromide, tetrahydrofuran (THF), r.t.; iii) HCl, acetic acid, reflux; iv) AlCl₃, CH₂Cl₂, -20 °C → r.t.; v) LiAlH₄, AlCl₃, THF, 0 °C → r.t.; vi) 4,4'-dibromobenzophenone, Pd(*t*-Bu₃P)₂, K₂CO₃, toluene, 100 °C; vii) a) N-bromosuccinimide, THF, r.t. b) N-iodosuccinimide, THF, r.t.

In order to connect the TADF units with the aforementioned linkers, the second comonomer contains two boronic acid pinacol ester moieties that facilitate the cross-coupling reaction. In contrast to the functionalized comonomers **10c** and **10d** for the 1,1'-biphenyl linker as well as the 1,2-diphenylethane linker, **10e** was not commercially available and had to be synthesized. Starting from bromobenzene and adipoyl dichloride **8** was formed in two Friedel–Crafts acylations in *para* position to bromide. In a second step, the ketones were reduced to obtain **9**. In a final step, the bromide was substituted with a boronic acid pinacol ester group affording comonomer **10e** with an overall yield of 12 %.



Scheme 3.2. Synthesis of comonomer **10e**: i) AlCl_3 , 50 °C; ii) trifluoroacetate (TFA), triethylsilane, DCM, r.t.; iii) 1) *n*-butyl lithium, THF, -78 °C 2) 2-isopropoxy-4,4,5,5-tetramethyl-1,3,2-dioxaborolane, -78 °C \rightarrow r.t.

In a final Suzuki–Miyaura polycondensation between boronic esters **10c–e** and **11** and the halogenated TADF units **7a** and **7b**, the two sets TADF materials were synthesized (see **Scheme 3.3**). This reaction was performed in a sealed pressure tube for 72h with a multiphase solvent mixture of toluene, water and ethanol. The small molecules **Tol-MAC-BP** and **Tol-HAc-BP** were obtained with a 52 % and quantitative yield, respectively. For the polymers, an additional step was performed right after the 72 h by adding **11**, fresh catalyst and another 24 h of reaction time. The motivation for this end-capping procedure is based on the different electronic properties of the halogenated end-group leading to the formation of traps and quenching the excited state resulting in significantly reduced efficiencies in OLEDs.^[9] After purification via Soxhlet extraction as well as a subsequent preparative size exclusion chromatography (SEC) described in detail on the following pages, the DMAC- and DHAC-based polymers were obtained in high to moderate yields of 62-92 % and moderate to low yields of 35-53 %, respectively.



Scheme 3.3. Syntheses of TADF small molecules **Tol-MAc-BP** and **Tol-HAc-BP**, as well as TADF polymers **P(C2-MAc-BP)**, **P(C6-MAc-BP)**, **P(Ph-MAc-BP)**, **P(C2-HAc-BP)**, **P(C6-HAc-BP)** and **P(Ph-HAc-BP)**: i) 1) **6a-6c**, Pd(PPh₃)₄, Na₂CO₃, toluene/EtOH/H₂O, 120 °C, 2) **11**, Pd(PPh₃)₄, 120 °C; ii) **11**, Pd(PPh₃)₄, Na₂CO₃, toluene/EtOH/H₂O, 120 °C.

The molecular weight distributions of both sets of polymer materials were determined via size exclusion chromatography (SEC) in THF as a solvent using polystyrene (PS) calibration. After a Soxhlet purification both sets of polymers showed broad multimodal molecular weight distributions (see **Table 3.2** and **Figure 3.4**, dashed lines). The polymers **P(C2-MAc-BP)**, **P(C6-MAc-BP)** and **P(Ph-MAc-BP)** show a broader molecular weight distribution with dispersities (D) of 2.34-2.41 than their hexyl substituted counterparts (D of 1.58-1.91). The first set of polymers furthermore display higher number average molecular weights (M_n) of 4.7-5.2 kg/mol in comparison to 2.6-3.3 kg/mol for the second set.

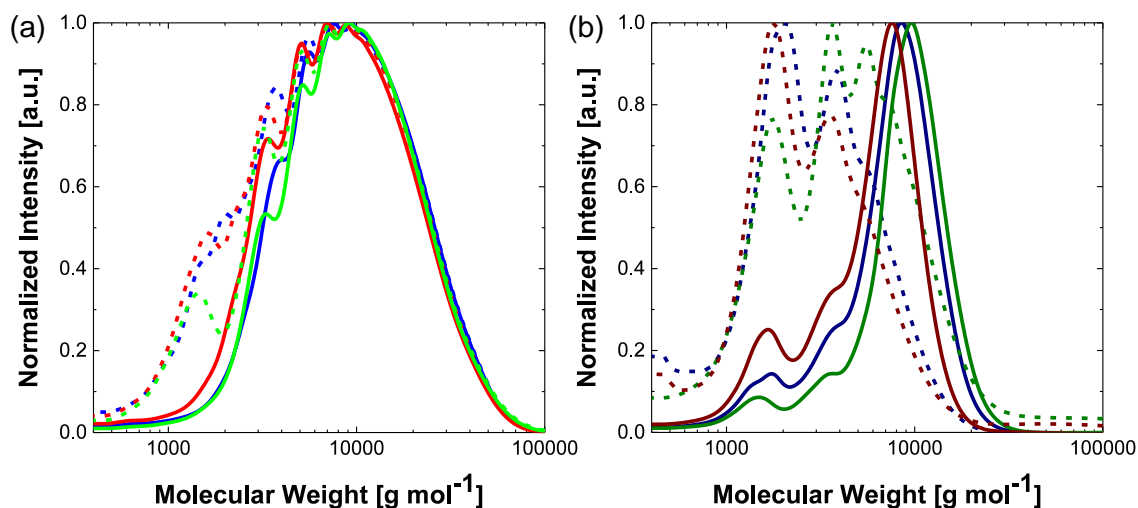


Figure 3.4. Molecular weight distribution after Soxhlet purification (dashed lines) and preparative SEC (solid lines) from SEC in THF calibrated via PS standard of (a) **P(C2-MAc-BP)** (red), **P(C6-MAc-BP)** (blue) and **P(Ph-MAc-BP)** (green) (b) **P(C2-MAc-BP)** (dark red), **P(C6-MAc-BP)** (dark blue) and **P(Ph-MAc-BP)** (dark green) using UV detection (254 nm).

Although a higher reactivity was expected for the polymers based on **7b** in comparison to the bromide-substituted **7a** due to the iodide as leaving group, the opposite was the case. A possible explanation is the steric hindrance resulting from the hexyl chain in combination with the bigger iodine. Another possible reason is the higher difficulty of controlling the stoichiometry in the polymerization for the comonomer **7b**. Although **7b** was dried in high vacuum over several hours, small impurities of hexane remained. Due to the fact that the molecular weights achieved in step-growth polymerizations is highly dependent on the stoichiometry and conversion, a small difference in amount of the comonomers used can decrease the molecular weight significantly and high conversions are further required. The average degree of polymerization (X_n) describing the average number of repeating units of a polymer sample can be calculated for bifunctional monomers with two identical polymerization moieties (A-A reacting with B-B) with

$$X_n = \frac{(1 + r_{A,B})}{(1 + r_{A,B} - 2pr_{A,B})} \quad (9)$$

where p is the conversion and the stoichiometric imbalance $r_{A,B}$ represents the ratio between the number of moiety A ($N_{A,0}$) and of B ($N_{B,0}$) before the reaction:^[61]

$$r_{A,B} = \frac{N_{A,0}}{N_{B,0}} \quad (10)$$

Equation 9 shows the sensitivity of the step growth polymerization to p and $r_{A,B}$ explaining the low molecular weights obtained. In order to be able to increase the comparability of two sets of polymers, all materials were further purified with a semi-preparative SEC with chloroform as a solvent (see **Figure 3.4**, solid lines). The final M_n values of the polymers further investigated range from 4.7 kg mol⁻¹ to 7.1 kg mol⁻¹ with D of 1.49-1.86 (see **Table 3.2**).

Table 3.2. Summary of molecular weight characteristics of the TADF polymers.

Compound	after Soxhlet purification			after preparative SEC		
	M_n	M_w	D	M_n	M_w	D
	[kg mol ⁻¹]	[kg mol ⁻¹]		[kg mol ⁻¹]	[kg mol ⁻¹]	
P(C2-MAc-BP)	4.7	11.4	2.41	6.6	12.2	1.86
P(C6-MAc-BP)	4.9	11.6	2.38	7.2	13.3	1.84
P(Ph-MAc-BP)	5.2	12.1	2.34	7.3	13.3	1.83
P(C2-HAc-BP)	2.6	4.1	1.58	4.7	7.2	1.55
P(C6-HAc-BP)	2.8	4.4	1.58	5.9	9.0	1.53
P(Ph-HAc-BP)	3.3	6.3	1.91	7.1	10.5	1.49

The TADF materials were fully characterized via ^1H NMR spectroscopy, ^{13}C NMR spectroscopy and for **Tol-Mac-BP** and **Tol-HAc-BP** also MALDI-MS. The ^1H NMR spectra are shown in **Figure 3.5** and **Figure 3.6** and all protons of the repeating units could be assigned. The chemical shifts of the TADF materials with identical linker are similar to one another and only differ in the additional alkyl signals stemming from the hexyl substitution. Despite the same shifts, the DMAC-based polymers show well resolved signals with matching integration in contrast to their DHAC counterparts with broader unresolved signals. This signal broadening might be caused by the non-planarity of the donors introducing a more inhomogeneous chemical environment for the H atoms.

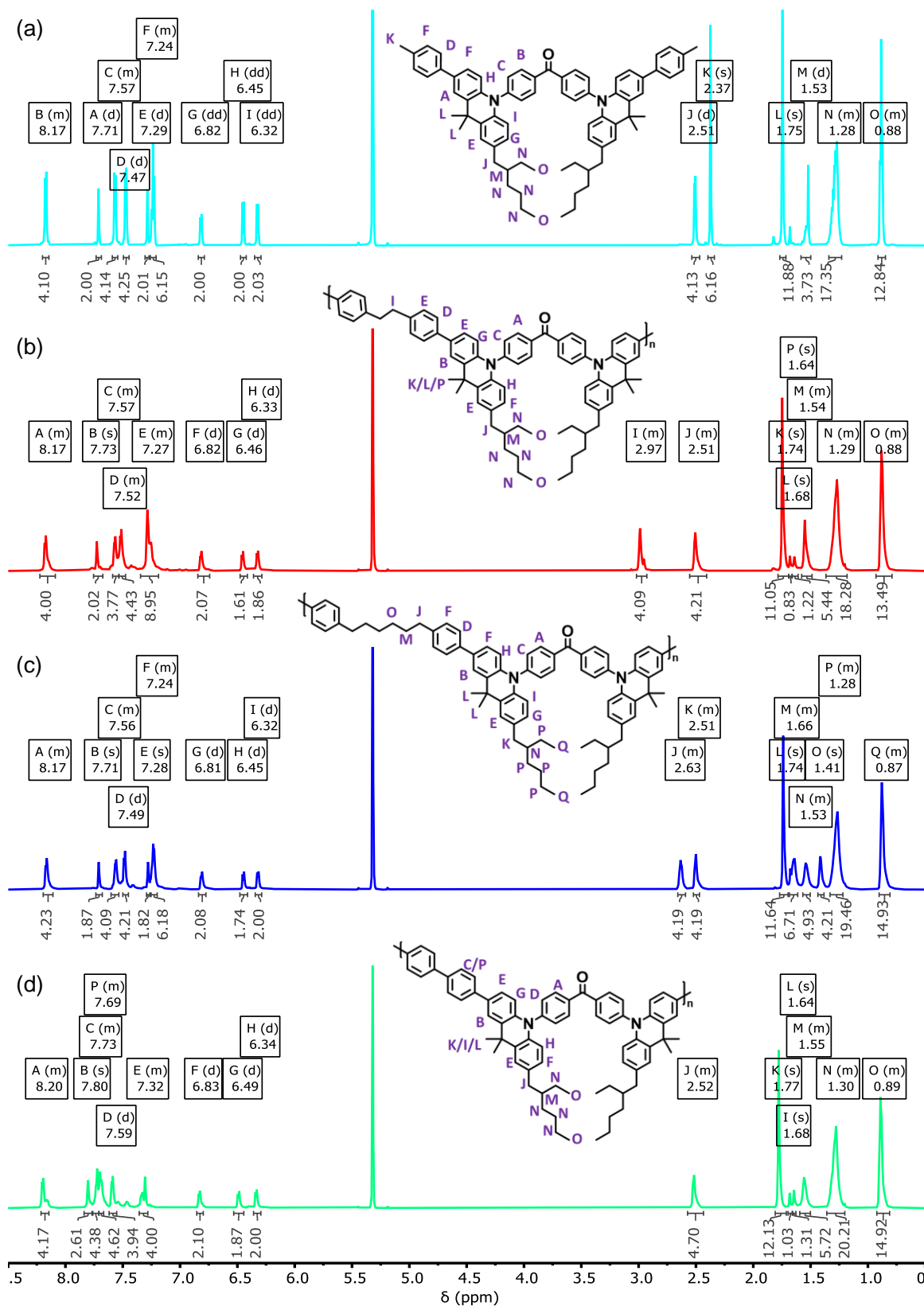


Figure 3.5. ^1H NMR spectra of (a) Tol-Mac-BP, (b) P(C2-Mac-BP), (c) P(C6-Mac-BP) and (d) P(Ph-Mac-BP) in methylene chloride- d_2 .

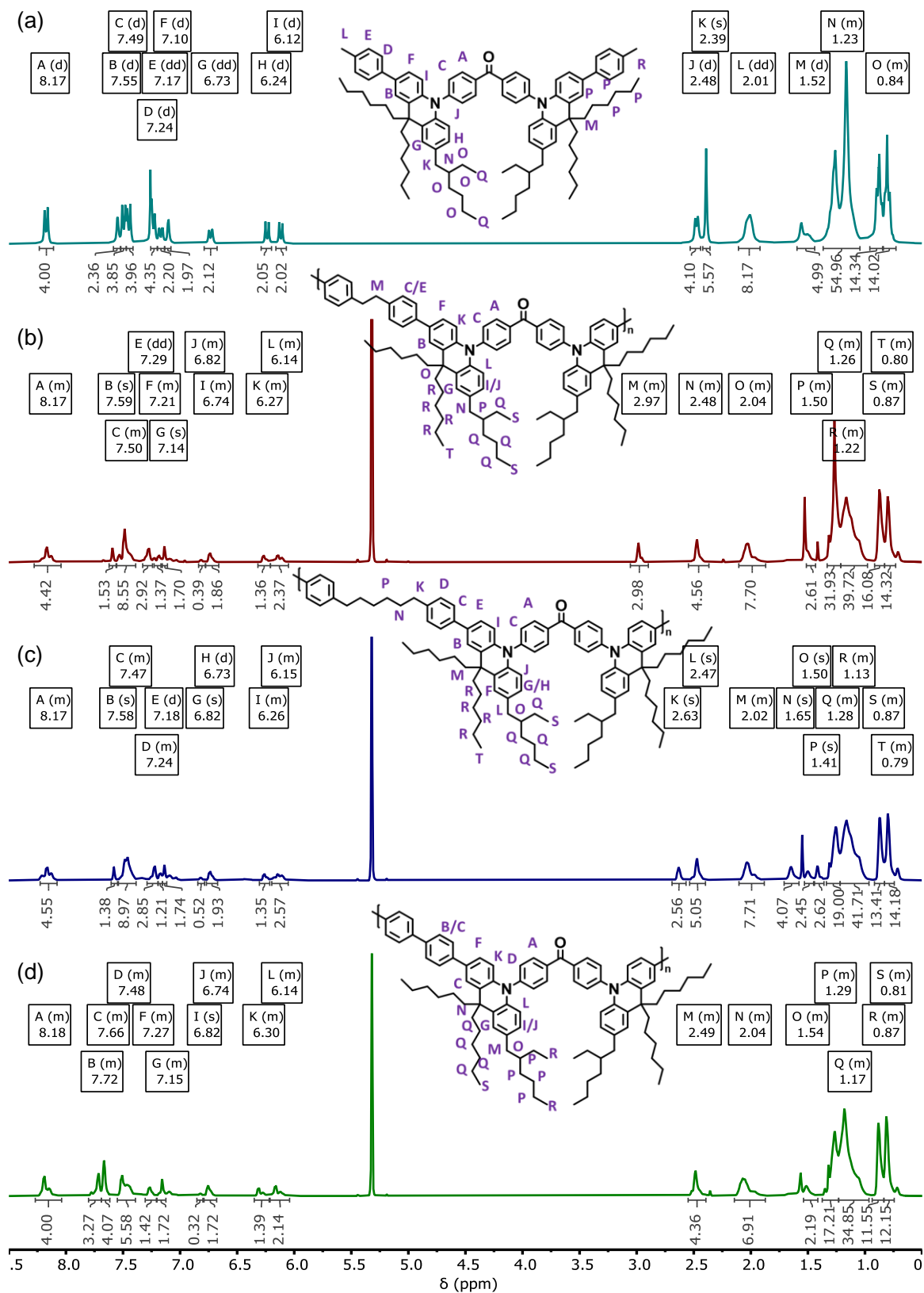


Figure 3.6. ^1H NMR spectra of (a) Tol-HAc-BP in chloroform-*d* and (b) P(C2-HAc-BP), (c) P(C6-HAc-BP) and (d) P(Ph-HAc-BP) in methylene chloride-*d*₂.

3.4. Thermal Properties of the TADF Materials

A prerequisite for a long OLED life time is a sufficient thermal stability.^[105] The thermal properties of the synthesized polymers, as well as their small molecule counterparts, were analyzed using thermogravimetric analysis (TGA) and differential scanning calorimetry (DSC) (see **Figure 3.7** and **Table 3.3**). An important measure for the thermal stability of compounds is the decomposition temperature (T_d). This is the temperature at which a weight loss of >5 % in nitrogen atmosphere is observed in TGA. Both sets of materials show high thermal stability with T_d s of 425-432 °C for **Tol-MAc-BP**, **P(C2-MAc-BP)**, **P(C6-MAc-BP)** and **P(Ph-MAc-BP)** and 371-379 °C for the hexyl-substituted derivatives. This decrease of about 50 °C in T_d was observed for the polymers as well as the small molecules. The fact that this trend was observed independent on the linker and the molecular weight points to lowered thermal stability specifically due to the *n*-hexyl chains.

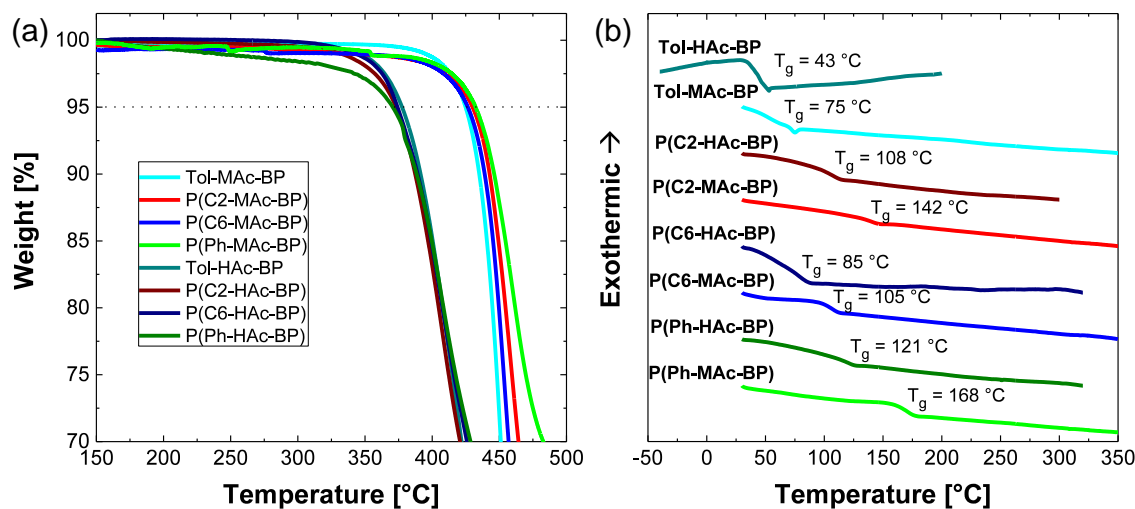


Figure 3.7. (a) Thermogravimetric analysis (TGA) and (b) differential scanning calorimetry (DSC) of the small molecules and polymers.

A higher density of long alkyl chains also reduces the glass transition temperatures (T_g) of polymers, stemming from a higher atomic mobility^[106] and can be observed as a step or kink in DSC (see **Figure 3.7b**). In contrast, aromatic structures are more rigid and as a result the T_g values decrease from the fully conjugated **P(Ph-MAc-BP)** (165 °C), to the nonconjugated **P(C2-MAc-BP)** and **P(C6-MAc-BP)** (142 °C and 105 °C, respectively) with increasing alkyl linker length. The lowest T_g are recorded for the small molecule **Tol-MAc-BP** (75 °C). The same trend can be observed for the hexyl-substituted materials, showing T_g s lowered by 20 °C or more in comparison to their DMAC-based counterparts. The DSC furthermore shows no signs of crystallization, which is advantageous for the use in solution processed OLEDs owing to a reduced tendency to aggregate.

Table 3.3. Summary of thermal properties of **Tol-MAc-BP**, **P(C2-MAc-BP)**, **P(C6-MAc-BP)** and **P(Ph-MAc-BP)**.

Compound	T_d [°C]	T_g [°C]	Compound	T_d [°C]	T_g [°C]
Tol-MAc-BP	425	75	Tol-HAc-BP	379	43
P(C2-MAc-BP)	430	142	P(C2-HAc-BP)	373	108
P(C6-MAc-BP)	427	105	P(C6-HAc-BP)	374	85
P(Ph-MAc-BP)	432	168	P(Ph-HAc-BP)	371	121

3.5. Estimation of HOMO and LUMO of the TADF materials

In order to be able to utilize a material in OLED application, the determination of HOMO and LUMO levels are of high importance for the selection of hole as well as electron injection layer material. HOMO and LUMO were measured using cyclic voltammetry (CV) as well as ultraviolet photoelectron spectroscopy (UPS). In CV, HOMO and LUMO energies cannot directly be measured. Instead, with CV one obtains the reduction and oxidation potentials in solution, also called electron affinity (*EA*) and ionization potential (*IP*) respectively, which approximate the HOMO and LUMO.^[107] The CV measurements were performed in dichloromethane (DCM) solutions using Bu_4NPF_6 as a supporting electrolyte and ferrocene (Fc) as an internal reference (shown in **Figure 3.8** with **P(C2-HAc-BP)**).

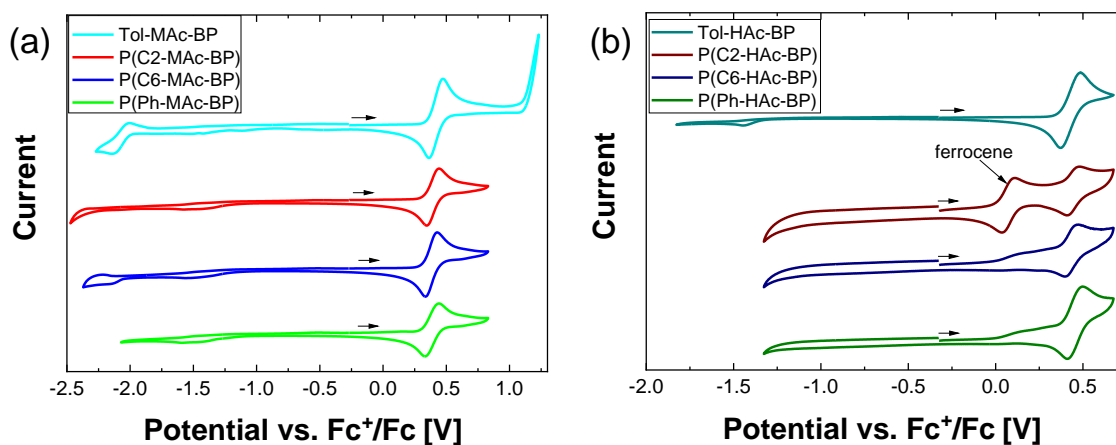


Figure 3.8. Cyclic voltammogram of (a) **Tol-MAc-BP**, **P(C2-MAc-BP)**, **P(C6-MAc-BP)** and **P(Ph-MAc-BP)** as well as (b) **Tol-HAc-BP**, **P(C2-HAc-BP)**, **P(C6-HAc-BP)** and **P(Ph-HAc-BP)** in CH_2Cl_2 with 0.1 M Bu_4NPF_6 as supporting electrolyte. The ferrocene internal reference was added after the scan and the CV was measured again (as seen for **P(C2-HAc-BP)**).

The shape of the oxidations and reduction curves in the cyclic voltammograms already allows a conclusion. All materials show a positive peak for the oxidation on the forward scan and negative peak of similar magnitude on the back scan, representing a reversible oxidation. Furthermore, there was no

reduction peak observed except for **Tol-MAc-BP** and **P(C6-MAc-BP)** stemming from the reduction potential being beyond the recommended potential window for CV in DCM solution.^[108]

The IP_{CV} can be calculated by comparing the onset of oxidation of the analyte ($E_{Ox}(onset)$) with the standard used. This allows the estimation of the HOMO energy due to the known oxidation potential of this standard ($E_{HOMO,Fc} = -4.8$ eV) using the equation

$$IP_{CV} = -e \cdot [(E_{Ox}(onset) - E_{Fc/Fc+}) - E_{HOMO,Fc}] \quad (11)$$

with the elementary charge e .^[109] The calibrated cyclic voltammograms are shown in **Figure 3.8** and they enable the calculation of the EA_{CV} energy level if a reduction can be measured:

$$EA_{CV} = -e \cdot [(E_{Red}(onset) - E_{Fc/Fc+}) - E_{HOMO,Fc}] \quad (12)$$

Although there was no reduction peak recorded for most of the samples except for **Tol-MAc-BP** and **P(C6-MAc-BP)**, the LUMO energy can still be estimated by adding energy of the optical bandgap (E_g^{opt}) derived from the onset of the absorption (see section 4.2) to the HOMO energy:

$$E_{LUMO} = E_{HOMO} + E_g^{opt} \quad (13)$$

The obtained IP values are similar for both sets of materials ranging from -5.10 eV to -5.17 eV and appear to be independent of the type of linker moiety (see **Table 3.4**). The LUMO energies derived from **Equation 13** show a comparable deviation between one another of -2.48 eV to -2.63 eV as a result of the highly similar optical bandgap. The EA_{CV} determined from the reduction signal in CV that was only observed for **Tol-MAc-BP** and **P(C6-MAc-BP)** is with -2.79 eV and -2.82 eV slightly lower.

Table 3.4. Summary of CV and UPS results of Tol-MAc-BP, P(C2-MAc-BP), P(C6-MAc-BP) and P(Ph-MAc-BP).

Compound	E_g^{opt} [eV]	IP_{CV} [eV]	EA_{CV} [eV]	$E_{cut\ off}$ [eV]	$E_{HOMO\ edge}$ [eV]	IP_{UPS} [eV]	EA_{UPS} [eV]
Tol-MAc-BP	2.60	-5.14	-2.79 ^a , -2.60 ^b	17.14	1.24	-5.32	-2.72 ^b
P(C2-MAc-BP)	2.61	-5.17	-2.63 ^b	17.16	1.29	-5.35	-2.74 ^b
P(C6-MAc-BP)	2.61	-5.12	-2.61 ^b	17.15	1.31	-5.38	-2.77 ^b
P(Ph-MAc-BP)	2.63	-5.17	-2.82 ^a , -2.61 ^b	17.11	1.27	-5.38	-2.75 ^b
Tol-HAc-BP	2.63	-5.17	-2.54 ^b	17.06	1.67	-5.82	-3.19 ^b
P(C2-HAc-BP)	2.62	-5.10	-2.48 ^b	17.06	1.68	-5.84	-3.22 ^b
P(C6-HAc-BP)	2.61	-5.14	-2.52 ^b	17.12	1.56	-5.66	-3.05 ^b
P(Ph-HAc-BP)	2.65	-5.16	-2.51 ^b	18.35	2.58	-5.45	-2.80 ^b

^a Obtained from cyclic voltammetry in CH₂Cl₂. ^b Calculated with **Equation 13**.

In order to see if there is a significant difference in solid state, both sets of materials were further investigated in UPS. In this method, thin films of the materials on a silicon wafer covered with 2 nm of chromium and 50 nm of gold are exposed to ultraviolet light. Upon absorption of this high energetic light by an electron, it is excited to the vacuum level and exits the material with excess kinetic energies. The exact amount of kinetic energy of an electron depends on its energetic state within the material, *i.e.* the binding energy. The emitted photoelectrons are detected as a function of their excess kinetic energy, allowing the determination of their binding energy in the analyzed material. The resulting UPS spectrum shows the intensity of the detected electrons plotted against the binding energy. For each of the samples, three UPS spectra were recorded for different spots of the film to increase accuracy (see **Figure 3.9** and **Figure 3.10**).

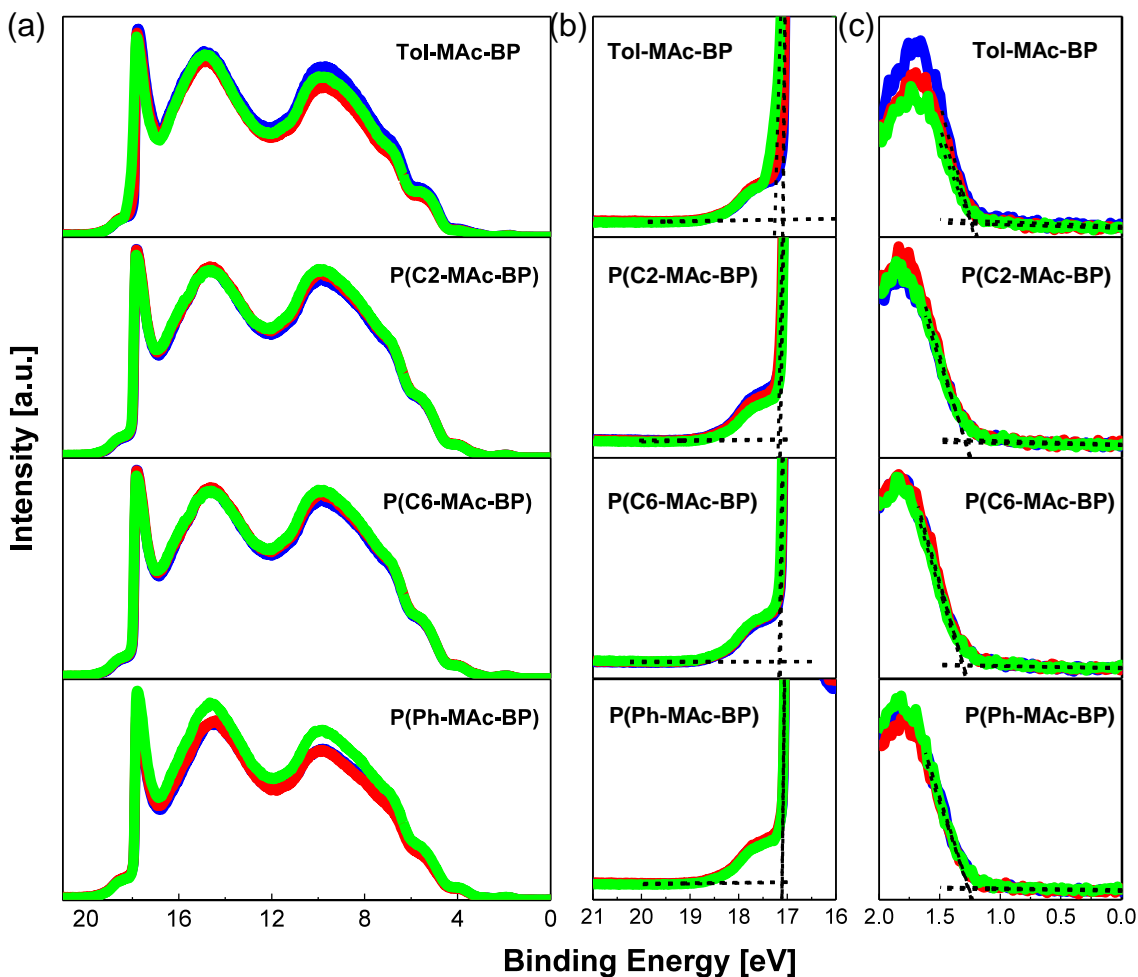


Figure 3.9. Ultraviolet photoelectron spectra of **Tol-MAC-BP**, **P(C2-MAC-BP)**, and **P(Ph-MAC-BP)** films shown in (a) full range, (b) zoom on the secondary electron cut-off with visualized onset fit (dashed lines) and (c) zoom on the HOMO edge with visualized onset fit (dashed lines). The red, green and blue spectra have been measured at different locations in the films.

Internal comparison of the UPS spectra shows high similarity between the small molecule **Tol-MAC-BP**, and the polymers **P(C2-MAC-BP)**, **P(C6-MAC-BP)** and **P(Ph-MAC-BP)** independent of the difference in linker moiety (see **Figure 3.9**). For the evaluation and calculation of the ionization potential, the onsets on both ends of the spectra were obtained from the intersection of two linear fits (see **Figure 3.9b-c**). At high binding energies close to the energy of the excitation light, the so-called secondary electron cut-off ($E_{cut\ off}$) can be obtained from the UPS spectrum. A small deviation of 0.05

eV between the DMAC-based materials has been observed. Similarly, the energies of the HOMO edge ($E_{HOMO\ edge}$) on the other end of the spectra range from 1.24 eV to 1.31 eV and stem from the excitation of electrons at the ground state. The hexyl substituted materials **Tol-HAc-BP**, **P(C2-HAc-BP)** and show $E_{cut\ off}$ values similar to the first set of materials of 17.06-17.12 eV and shifted energies of the HOMO edge to 1.56-1.68 eV (see **Figure 3.10**). In contrast to all other materials, **P(Ph-MAc-BP)** exhibits a strong shift of both values to higher binding energies.

With $E_{cut\ off}$ and $E_{HOMO\ edge}$, the ionization potential can be calculated from using the equation

$$IP_{UPS} = h\nu - (E_{cut\ off} - E_{HOMO\ edge}), \quad (14)$$

with h being the Planck constant and ν is the frequency of the excitation radiation. Using **Equation 13** furthermore enables the estimation of the LUMO level by adding the optical gap to IP_{UPS} (see **Table 3.4**). For **Tol-MAc-BP**, **P(C2-MAc-BP)**, **P(C6-MAc-BP)** and **P(Ph-MAc-BP)** similar IP_{UPS} values independent of the linker between -5.32 eV to -5.38 eV and were obtained resulting in approximated LUMO energies of -2.72 eV to -2.77 eV. In contrast, the UPS results show a significantly higher IP from -5.45 eV for **P(Ph-HAc-BP)** and -5.66 eV for **P(C6-HAc-BP)** to -5.84 eV and -5.82 eV for **P(C2-HAc-BP)** and **Tol-HAc-BP**, respectively.

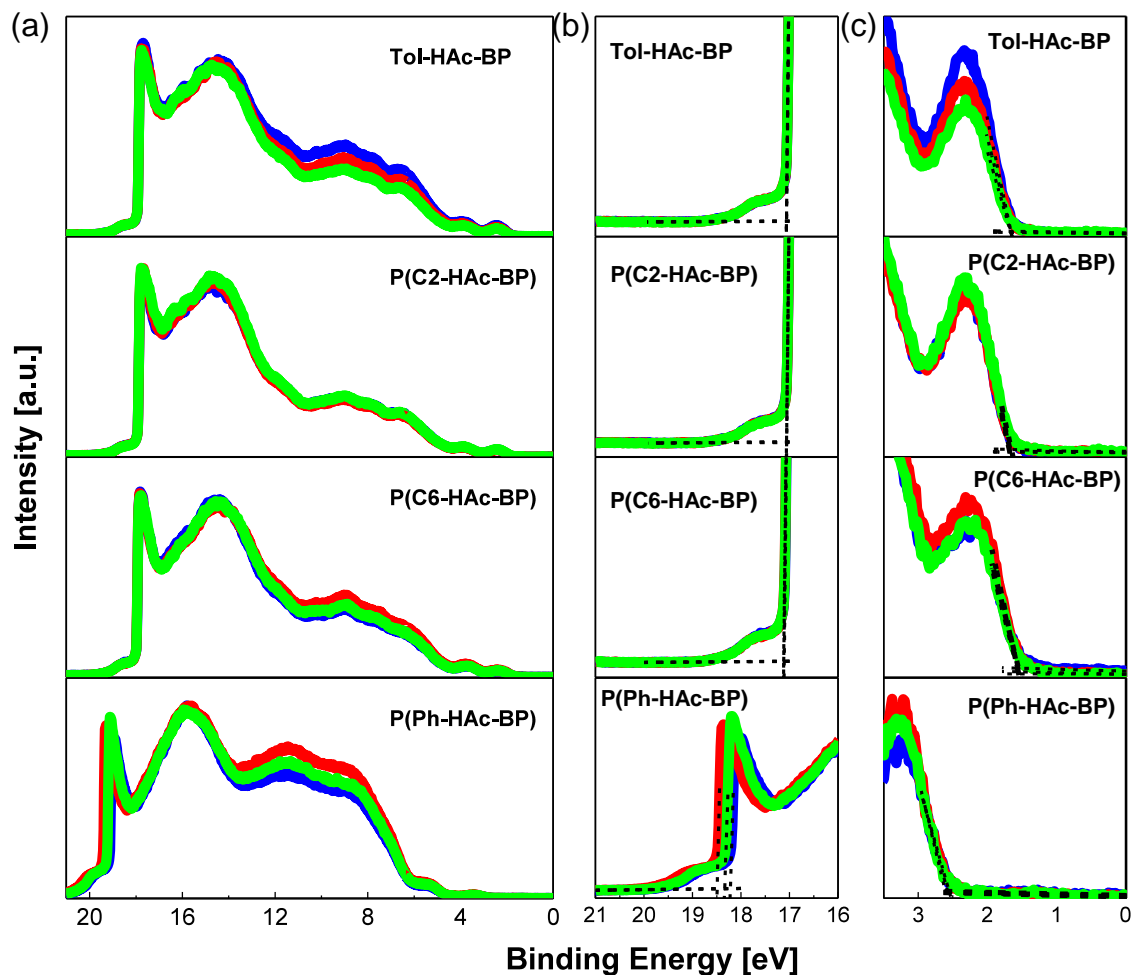


Figure 3.10. Ultraviolet photoelectron spectra of **Tol-HAc-BP**, **P(C2-HAc-BP)**, and **P(Ph-HAc-BP)** films shown in (a) full range, (b) zoom on the secondary electron cut-off with visualized onset fit (dashed lines) and (c) zoom on the HOMO edge with visualized onset fit (dashed lines). The red, green and blue spectra have been measured at different locations in the films.

The approximations of the HOMO and LUMO energies obtained from CV and UPS are in good agreement with one another for **Tol-MAc-BP**, **P(C2-MAc-BP)**, **P(C6-MAc-BP)** and **P(Ph-MAc-BP)** (see **Figure 3.11**) and indicate to not significantly influenced by the linker moieties. In contrast to the uniformity of the results obtained for the MAc series, the hexyl substituted materials **Tol-HAc-BP**, **P(C2-HAc-BP)**, **P(C6-HAc-BP)** and **P(Ph-HAc-BP)** not only show lower similarity between the CV and UPS results, but also a higher difference in HOMO and LUMO between one another. While the

HOMO estimated by CV for all materials is similar to the first set of materials, the UPS results show a significantly higher *IP*.

The generally slightly higher *IP* determined by CV can be explained by the difference between polarization energy in the solid state and solvation energy in solution.^[110] This leads to a systematic underestimation of the energy of both the HOMO and the LUMO in CV (also called ‘electrochemical gap’) in comparison to UPS/IPES (inverse photoelectron spectroscopy) that determines the so-called transport gap.^[110] Furthermore, a systematic underestimation of the LUMO energy based on the optical bandgap used for its determination has to be taken into account. The difference between the optical gap and the so-called fundamental gap between HOMO and LUMO is the electron–hole pair binding energy (E_B) included in the latter.^[107]

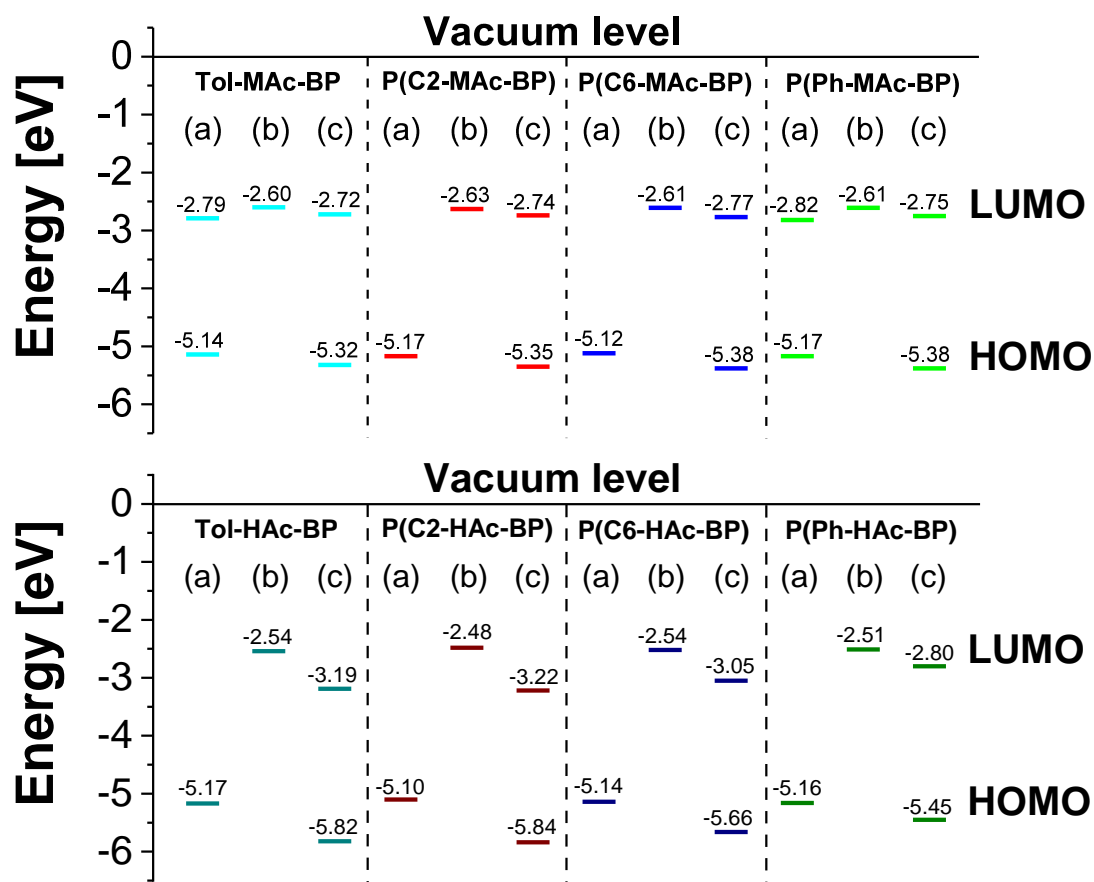


Figure 3.11. Energies of HOMO and LUMO level in the two material sets estimated from (a) IP_{CV} and EA_{CV} of cyclic voltammetry in DCM, (b) calculated with $EA = IP_{CV} + E_g^{opt}$ and (c) IP_{UPS} of ultraviolet photoelectron spectroscopy and calculated with $EA_{UPS} = IP_{UPS} + E_g^{opt}$.

3.6. Conclusion


In this chapter, the syntheses of two sets of the TADF polymers as well as their small molecule counterparts were described. Based on the known TADF chromophore DMAC-BP,^[104] two nonconjugated TADF polymers with a short (ethyl) and a longer (hexyl) linker, as well as one conjugated TADF polymer were synthesized for the investigation of the influence of the linker moiety on the polymer properties. A second set with an identical linker strategy but hexyl substituted acridine donors was synthesized as well, to gain insight into the effect of the 9-position substitution of the donor. DFT calculations of representative fragments of the polymer structures showed a preservation of the

small ΔE_{ST} of 6-10 meV necessary for efficient TADF independent of the linker moiety introduced and alkyl substitution applied. All materials were successfully obtained via multistep synthesis and the polymers exhibit similar molecular weights of $M_n = 5.9-7.3$ kg/mol with $D_s = 1.49-1.86$, increasing their comparability by excluding the influence of the polymer chain length. The thermal properties showed an expected decrease in T_g and T_d with increasing alkyl proportions. **Tol-MAc-BP**, **P(C2-MAc-BP)**, and **P(Ph-MAc-BP)** displayed very similar HOMO and LUMO energy level estimations based on CV and UPS measurements, ranging from -5.12 to -5.38 eV and from -2.60 to -2.82 eV, respectively, indicating no significant electronic change stemming from polymerization with the different linker strategies. In contrast, their hexyl-substituted counterparts showed a higher deviation in HOMO and LUMO level, ranging from -5.10 eV to -5.82 eV and from -2.48 eV to -3.22 eV.

3.7. Appendix of Chapter 3

3.7.1. Contributions to Chapter 3

The syntheses of **Tol-HAc-BP**, **P(C2-HAc-BP)**, **P(C6-HAc-BP)** and **P(Ph-HAc-BP)**, the DFT calculations and CV measurements were performed by Kai Philipps (Molecular Electronics Department, MPIP Mainz). The syntheses of **Tol-MAc-BP**, **P(C2-MAc-BP)**, **P(C6-MAc-BP)** and **P(Ph-MAc-BP)** was performed by [REDACTED] (The Institute of Scientific and Industrial Research (ISIR), Osaka University). The UPS measurements were performed by [REDACTED] (Molecular Spectroscopy Department, MPIP Mainz). The TGA and DSC measurements were performed by [REDACTED] (Molecular Electronics Department, MPIP Mainz). The MALDI as well as SEC measurements were performed by the polymer analytics group at the MPIP Mainz. Experimental results were regularly discussed with Paul Blom (Molecular Electronics Department, MPIP Mainz), Jasper Michels (Molecular Electronics Department, MPIP Mainz), [REDACTED] (Faculty of Science, Vrije

Universiteit Amsterdam and Molecular Electronics Department, MPIP Mainz) and 

(Molecular Electronics Department, MPIP Mainz).

4. Photophysical Characterization

In order to analyze any influence of the hexyl substitution as well as the linker strategy on the photophysical properties, the materials were characterized using a variety of spectroscopic methods. Starting with steady state absorption and photoluminescence spectroscopy of solutions (section 4.1) and in solid films (section 4.2). Subsequently, the TADF properties were extensively studied using time-resolved photoluminescence spectroscopy (section 4.3).

4.1. Steady State Photophysical Properties in Solution

As a first step, the absorption of all materials was measured in toluene solution (see **Figure 4.1a** and **c**). The molar absorption coefficients ($\epsilon(\lambda)$) for all materials were determined by recording the absorbance for a series of solutions with known concentrations. By plotting the absorbance of a chosen wavelength (usually absorbance maximum) of each of these spectra versus their concentration and fitting these data points with a straight line, ϵ can be determined for each of the materials with a high accuracy (plots shown in Appendix 4.5). The molar absorption coefficients of the full range of the spectrum can be calculated relative to this value. It has to be noted that the number average molecular weight was used in calculating the concentration of the TADF polymer solutions in order to compare with the results obtained for solutions of the small molecules **Tol-MAc-BP** and **Tol-HAc-BP**.

The absorption maxima of **Tol-MAc-BP**, **P(C2-MAc-BP)**, **P(C6-MAc-BP)** as well as their hexyl-substituted counterparts **Tol-HAc-BP**, **P(C2-HAc-BP)**, **P(C6-HAc-BP)** in toluene solution are very close to one another at around 316 nm. In contrast, the conjugated polymers **P(Ph-MAc-BP)** and **P(Ph-HAc-BP)** show a significantly red-shifted absorption band peaking at 353 nm. This shift can be assigned to the increased conjugation length caused by the biphenyl linker, effectively connecting two acridine donors to one donor, as indicated by the extent of the HOMO in the computational results (see **Figure 3.2**). The molar absorption coefficients at maximum absorbance are similar for the small

molecules, $7.3 \times 10^4 \text{ M}^{-1} \text{ cm}^{-1}$ and $6.4 \times 10^4 \text{ M}^{-1} \text{ cm}^{-1}$ for **Tol-MAc-BP** and **Tol-HAc-BP**, respectively. As expected, the polymers show higher ϵ values because there are several TADF chromophores embedded in the polymer backbone. In case of quantifying the absorption of polymers, it makes more sense to compare the mass absorption coefficient (ϵ_{mass}) than the molar absorption coefficient, especially in terms of materials with a broad molecular weight distribution (high dispersity; spectra shown in Appendix 4.5). The mass absorption coefficients of the small molecules **Tol-MAc-BP** and **Tol-HAc-BP** are higher with $72.5 \text{ L g}^{-1} \text{ cm}^{-1}$ and $50.3 \text{ L g}^{-1} \text{ cm}^{-1}$ than their polymer counterparts based on the additional linker group increasing the molecular weight of the repeating unit. The ϵ_{mass} values of both sets of polymers range from $22.9 \text{ L g}^{-1} \text{ cm}^{-1}$ to $56.1 \text{ L g}^{-1} \text{ cm}^{-1}$ and therefore are in the same order of magnitude indicating no significant enhancement or quenching effect of the absorption upon polymerization. All DMAC-based materials further exhibit a broad and relatively weak absorption band at low energies. The maxima of this absorption range from 382 nm to 404 nm for the nonconjugated polymers and the small molecules, and from 422 nm to 424 nm for **P(Ph-MAc-BP)** and **P(Ph-HAc-BP)**, respectively.

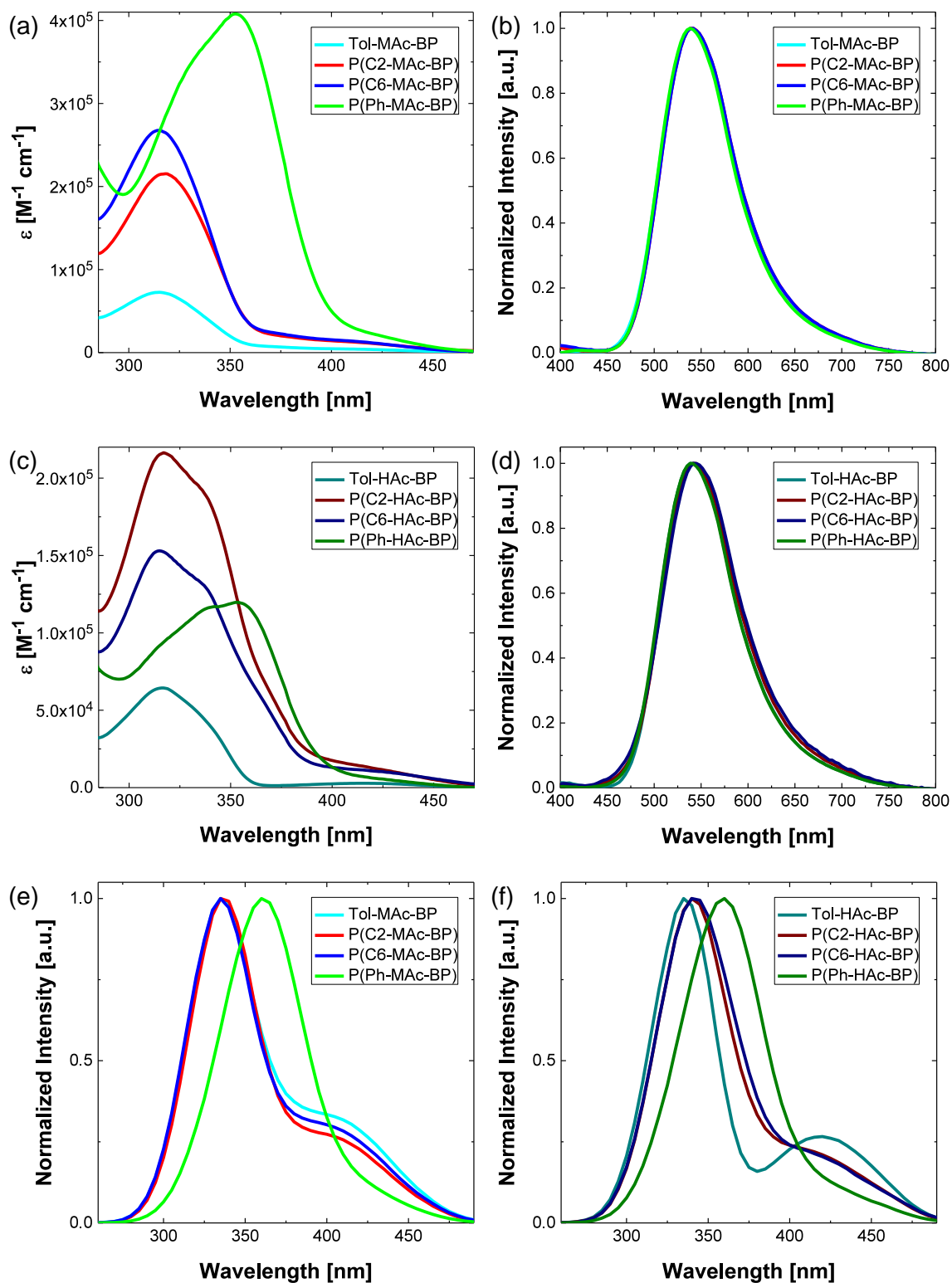


Figure 4.1. (a) Molar absorption coefficient (b) photoluminescence and (e) excitation spectra of **Tol-MAc-BP**, **P(C2-MAc-BP)**, and **P(Ph-MAc-BP)** in toluene solution. (c) Absorption, (d) photoluminescence and (f) excitation spectra of **Tol-HAc-BP**, **P(C2-HAc-BP)**, and **P(Ph-HAc-BP)** in toluene solution. The PL spectra were recorded at $\lambda_{exc} = 355$ nm. The excitation spectra were recorded at PL maximum shown in (b) and (d).

In direct comparison of the compounds with the same linker (see **Figure 4.1a** and **c**), the two sets of materials show similar absorption spectra except for additional lower energy bands observed between 320 nm and 380 nm for the hexyl-substituted materials **Tol-HAc-BP**, **P(C2-HAc-BP)** and **P(C6-HAc-BP)**. In order to determine the maxima of the superimposed absorption bands, a Gaussian deconvolution of the spectra was performed (see deconvolution described in Appendix 4.5 and absorption maxima in **Table 4.1**). The deconvolution revealed one additional absorption band for **Tol-HAc-BP** peaking at 339 nm and two for **P(C2-HAc-BP)** and **P(C6-HAc-BP)** with a maximum at 344 nm and 364 nm as well as 341 nm and 360 nm, respectively. A possible explanation for these supplementary absorption bands is a non-planarity of the acridine donor induced by hexyl substitution, as predicted in the computational calculations (see **Figure 3.2**).

Table 4.1. Summary of steady state photophysical properties of **Tol-MAc-BP**, **P(C2-MAc-BP)**, **P(C6-MAc-BP)**, **P(Ph-MAc-BP)**, **Tol-HAc-BP**, **P(C2-HAc-BP)**, **P(C6-HAc-BP)** and **P(Ph-HAc-BP)** in solution.

Compound	$\lambda_{Abs,max}^a$ [nm] in toluene	ϵ_{max} [$10^4 \text{ M}^{-1} \text{ cm}^{-1}$] in toluene	$\epsilon_{mass,max}$ [$\text{L g}^{-1} \text{ cm}^{-1}$] in toluene	$\lambda_{PL,max}$ [nm] in toluene	$\lambda_{exc,max}$ [nm] in toluene	Slope [10^3 cm^{-1}] L-M-Plot	PLQY in toluene ambient/ N ₂
Tol-MAc-BP	315, 397 ^b	7.3 ± 0.1	72.5 ± 0.6	538	334, 398 ^b	17.6 ± 4	0.08/ 0.26
P(C2-MAc-BP)	319, 404 ^b	21.5 ± 0.3	32.8 ± 0.4	540	335, 399 ^b	11.1 ± 7	0.07/ 0.21
P(C6-MAc-BP)	315, 401 ^b	26.7 ± 0.4	37.0 ± 0.5	542	335, 397 ^b	10.9 ± 7	0.14/ 0.45
P(Ph-MAc-BP)	336 ^b , 353, 424 ^b	40.8 ± 0.2	56.1 ± 0.3	538	360, 429 ^b	11.1 ± 7	0.18/ 0.35
Tol-HAc-BP	316, 339 ^b , 415	6.4 ± 0.1	50.3 ± 0.2	539	335, 421	17.5 ± 4	0.09/ 0.57
P(C2-HAc-BP)	316, 344 ^b , 364 ^b , 382 ^b	21.6 ± 0.3	38.9 ± 0.6	541	340, 406 ^b	4.8 ± 2	0.08/ 0.21
P(C6-HAc-BP)	315, 341 ^b , 360 ^b , 401 ^b	15.3 ± 0.2	30.0 ± 0.3	542	342, 405 ^b	4.4 ± 1	0.08/ 0.29
P(Ph-HAc-BP)	330 ^b , 353, 422 ^b	12.0 ± 0.3	22.9 ± 0.6	539	360, 432 ^b	9.2 ± 2	0.12/ 0.38

^a $\lambda_{exc} = 355 \text{ nm}$. ^bDerived from spectral deconvolution (see Appendix 4.5)

Upon excitation at 335 nm, all compounds exhibit a green emission with a maximum around 540 nm showing an almost identical broad Gaussian band shape indicating a CT emission (see **Figure 4.1b** and **d**). This high similarity shows that the energy of the emissive state is not affected by the differences in molecular structure of these TADF emitters in toluene solution. In order to link the absorption bands to the emission, excitation spectra were recorded (**Figure 4.1e-f**). These spectra demonstrate a maximum of the CT emission at excitation wavelengths of 334 nm to 342 nm for the small molecules and non-conjugated polymers, as well as 360 nm for **P(Ph-MAc-BP)** and **P(Ph-HAc-BP)**, which corresponds to the $\pi \rightarrow \pi^*$ excitation. Upon excitation at these wavelengths a LE state is formed and a transition into an emissive CT state driven by the solvent relaxation occurs.^[111] In contrast to the shoulder observed in the absorption spectrum of **Tol-HAc-BP**, **P(C2-HAc-BP)** and **P(C6-HAc-BP)**, the absorption maximum of this excitation is not clearly identifiable due to a superimposed absorption band. All materials further show an increase in PL emission intensity approaching the low energy absorption maximum, proving this to be the direct intramolecular charge transfer excitation often observed in D-A internal charge transfer emitters and thus in TADF emitters.^[112,113]

Now that the absorption bands and emissive state are identified, the interplay between LE and CT states are further investigated by changing to a variety of solvents. The solubilizing groups introduced into the molecular structure enable the solubility of all polymers in toluene, THF, chloroform and DCM. Furthermore, the hexyl moieties of **P(C2-HAc-BP)**, **P(C6-HAc-BP)** and **P(Ph-HAc-BP)** allowed a sufficient solubility in hexane and the small molecules **Tol-MAc-BP** and **Tol-HAc-BP** were further measured in dimethylformamide (DMF) solution. The normalized absorption and photoluminescence spectra are shown in **Figure 4.2**, as well as a photograph of the solutions under UV radiation. While the absorption bands identified as $\pi \rightarrow \pi^*$ excitations for the hexyl substituted polymers display a significant bathochromic shift with increasing solvent polarity, just a slight shift in absorption is apparent for **P(C2-MAc-BP)**, **P(C6-MAc-BP)** and **P(Ph-MAc-BP)**. This observation reinforces the conclusion that the $\pi \rightarrow \pi^*$ excitations of the DMAC-based polymers are

found within the broad absorption band exhibiting maximum absorbance. This so-called positive solvatochromism, identified by a bathochromic shift at higher solvent polarities, stems from an increase in dipole moment between ground state and excited state upon excitation.^[114] The solvent molecules adapt to the change in dipole moment of the solute molecule usually within picoseconds and reorganize. This effect is far more pronounced in the emission spectra than in the absorption due the longer life times of the excited state (usually in nanosecond time scale) in comparison to the solvent reorganization.^[115]

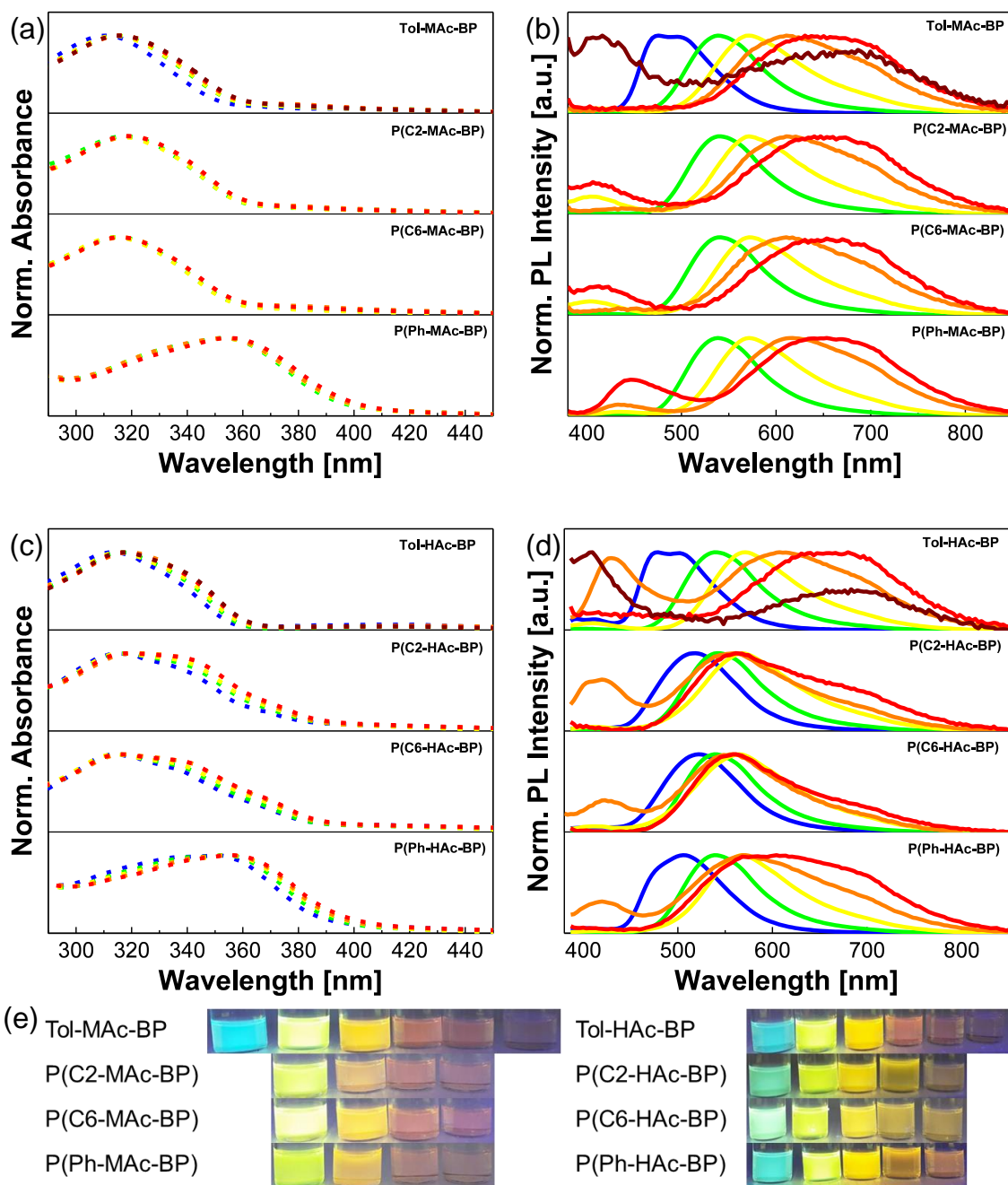


Figure 4.2. (a) UV-vis absorption and (b) PL spectra of **Tol-MAc-BP**, **P(C2-MAc-BP)**, **P(C6-MAc-BP)** and **P(Ph-MAc-BP)** as well as (c) UV-vis absorption and (d) PL spectra of **Tol-HAc-BP**, **P(C2-HAc-BP)**, **P(C6-HAc-BP)** and **P(Ph-HAc-BP)** in hexane (blue), toluene (green), THF (yellow), CHCl_3 (orange), DCM (red) and DMF (dark red) solution. (e) Photograph of the solutions measured in a)-d) under UV radiation (356 nm) in the order mentioned in the caption.

As expected, a strong positive solvatochromism was observed for both sets of materials ranging from blue to red emission in hexane and chloroform, respectively (see **Figure 4.2b, d and e**). The broad Gaussian line shape in solvents with high and low polarity indicates a CT character of the emission. Due to a strong electronic coupling between the LE and CT states,^[116] a transition to a bimodal PL emission can only be observed in like hexane, indicating a mixed CT/LE character. The fact that this vibronic feature is just observed in an extremely apolar solvent is a sign for a strong CT character often found for compounds with a small ΔE_{ST} .^[117] Furthermore, an additional emission at higher energies can be observed for some of the compounds in solution with higher polarity than toluene. This dual emission phenomenon stems from an incomplete transition from the LE to the CT excited state. The interpretation of solvent-dependent emission spectra is complex^[115] and would require a detailed study to ensure correct conclusions. Nonetheless, there are a few possible explanations previously given in literature for D-A-D molecules that are similar to the materials studied:

For **Tol-MAc-BP**, the LE emission is only observed in DMF solution in which it is the dominant emissive state. This observation is likely caused by very different radiative emission rates (k_r) for both emissions depending on the solvent:^[111]

$$k_r = \frac{\phi_{PL}}{\tau_{PL}}, \quad (15)$$

where ϕ_{PL} is the PLQY and τ_{PL} the life time of the emissive state.^[117] With higher polarity, the PLQY of the CT emission conformation usually decreases drastically in comparison to the LE emission. This quenching of the CT excited state is based on the energy gap law. It describes the increase in nonradiative deactivation rate (k_{nr}) in solvents of higher polarity due to the reduction in Franck-Condon energy, which results in an increase in vibrational wavefunction overlap.^[118] In particular in D-A-D molecules with almost perpendicular orientation between donor and acceptor, a more distorted structure is often observed in polar solvents leading to a decrease in spatial overlap of the orbitals involved in the electronic transition, further reducing the PLQY.^[81] Another effect contributing is the dependency of the solvent relaxation kinetics. Especially in solvents with a relatively long molecular

reorientation time, a fast LE decay facilitates a high LE emission intensity by disfavoring the relaxation to a CT excited state.

The combination of these effects can lead to an inversion in the LE-CT emission intensity ratio in high polarity solvents for a D-A-D small molecule like **Tol-MAc-BP** and **Tol-HAc-BP**. In contrast, the polymers **P(C2-MAc-BP)**, **P(C6-MAc-BP)** and **P(Ph-MAc-BP)** exhibit an increasing LE emission with increasing polarity also in THF, DCM and chloroform. This result indicates an adverse effect on the transition efficiency from LE to CT excited state in the polymer in comparison to the structurally equivalent small molecule. A possible explanation could be a conformational restriction stemming from the incorporation of the D-A-D chromophore into a polymer backbone. Surprisingly, the hexyl-substituted materials **Tol-HAc-BP**, **P(C2-HAc-BP)**, **P(C6-HAc-BP)** and **P(Ph-HAc-BP)** only show an additional LE emission in chloroform solutions.

In direct comparison, the spectra recorded for **Tol-MAc-BP**, **P(C2-MAc-BP)**, **P(C6-MAc-BP)** and **P(Ph-MAc-BP)** show almost identical CT emissions indicating a similar CT characteristic of the excited state, independent of the molecular differences. While **Tol-HAc-BP** also exhibits high similarity to the DMAC-based materials, **P(C2-HAc-BP)**, **P(C6-HAc-BP)** and **P(Ph-HAc-BP)** differ in terms of a significantly smaller solvatochromic shift (see **Figure 4.2d**). The emission maximum of the hexyl-substituted polymers **P(C2-HAc-BP)**, **P(C6-HAc-BP)** in DCM solution is hypsochromically shifted by about 95 nm in comparison to **P(C2-MAc-BP)**, **P(C6-MAc-BP)** and shows a non-Gaussian shape skewed to long wavelength. Two separate PL emissions were identified using Gaussian deconvolution of the PL spectrum, indicating the existence of two emissive CT states (see **Figure 4.3**). This second CT emission in DCM solution was not observed for the DMAC-based materials, which links it directly to the hexyl substitution of the acridine donor. A second conformer could be the explanation of this second emissive state, most likely caused by the deformation of the donor, as also observed in the DFT calculations (see **Figure 3.2**).

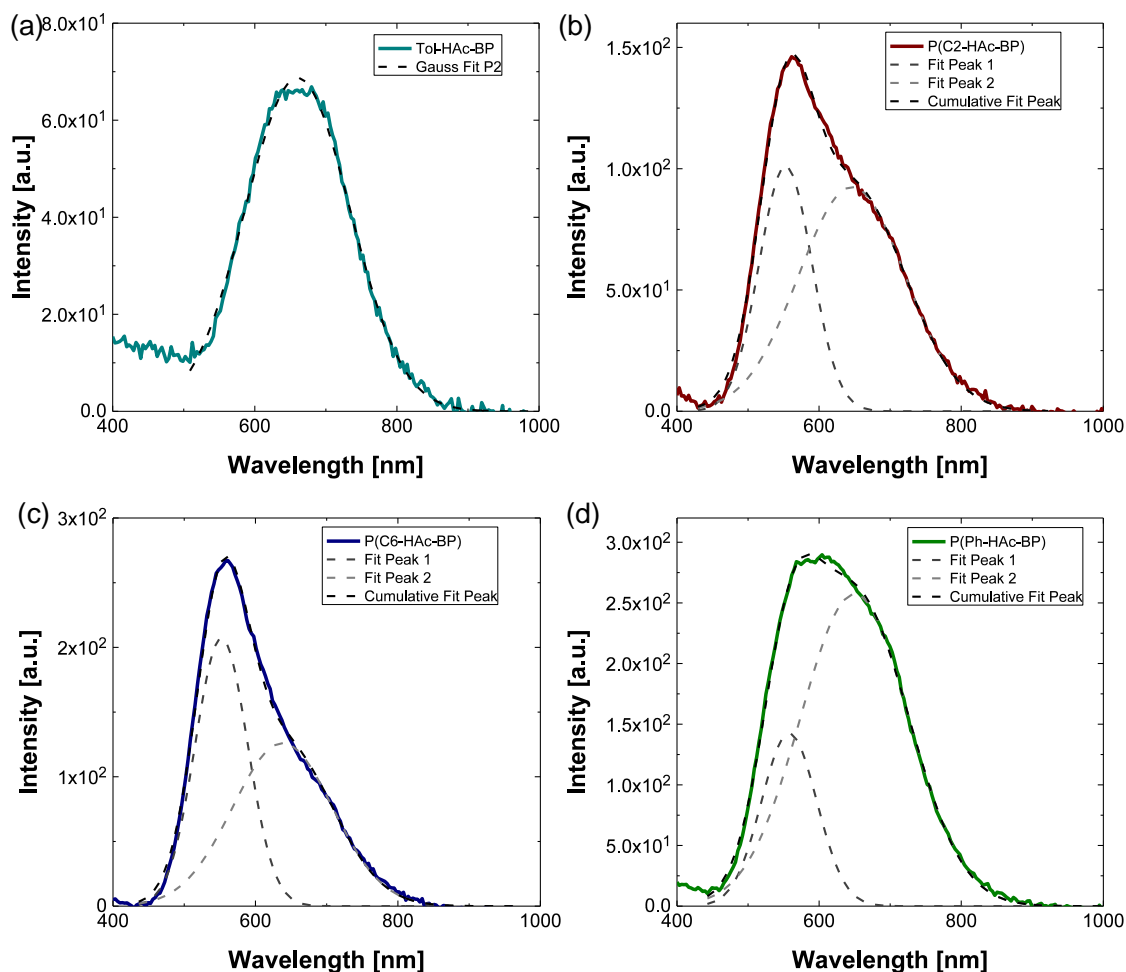


Figure 4.3. Gaussian deconvolution of (a) Tol-HAc-BP, (b) P(C2-HAc-BP), (c) P(C6-HAc-BP) and (d) P(Ph-HAc-BP) of DCM solutions excited at 355 nm.

In order to compare to quantify the solvatochromic shifts observed, the Stokes shift, which is the energy difference between absorption ($\bar{\nu}_A$) and emission band maxima ($\bar{\nu}_E$), is plotted against the orientation polarizability (Δf) in a so-called Lippert-Mataga (L-M) plot (see **Figure 4.4**) based on the Lippert equation

$$\bar{\nu}_A - \bar{\nu}_E = \frac{2}{hc} \Delta f \frac{(\mu_E - \mu_G)^2}{a^3} + \text{constant} \quad (16)$$

with h being Planck's constant, c the speed of light, a the radius of the cavity in which the chromophore is found, and μ_E and μ_G the dipole moment of the excited state and ground state, respectively. The

cavity radius a is based on the so-called Onsager's model, in which a solute molecule is approximated as a polarizable point dipole within a spherical cavity.^[119] Due to the fact that estimating this cavity is difficult for complex molecules, the slope of the Lippert-Mataga plot was compared between the different materials and no dipole moment was calculated based on the Onsager radius. Δf is defined by the relation

$$\Delta f = \frac{\varepsilon-1}{2\varepsilon+1} - \frac{n^2-1}{2n^2+1}, \quad (17)$$

where ε is the dielectric constant and n is the refractive index of the solvent and it describes the amount of solvent motion in reorientation after a change in electric field by the solute upon excitation.^[120] By fitting the data points with a straight line, the Lippert-Mataga plot enables the characterization of the CT characteristics of the emissive state. The change in dipole moment between ground state and excited state can be estimated from the slope of this linear fit.

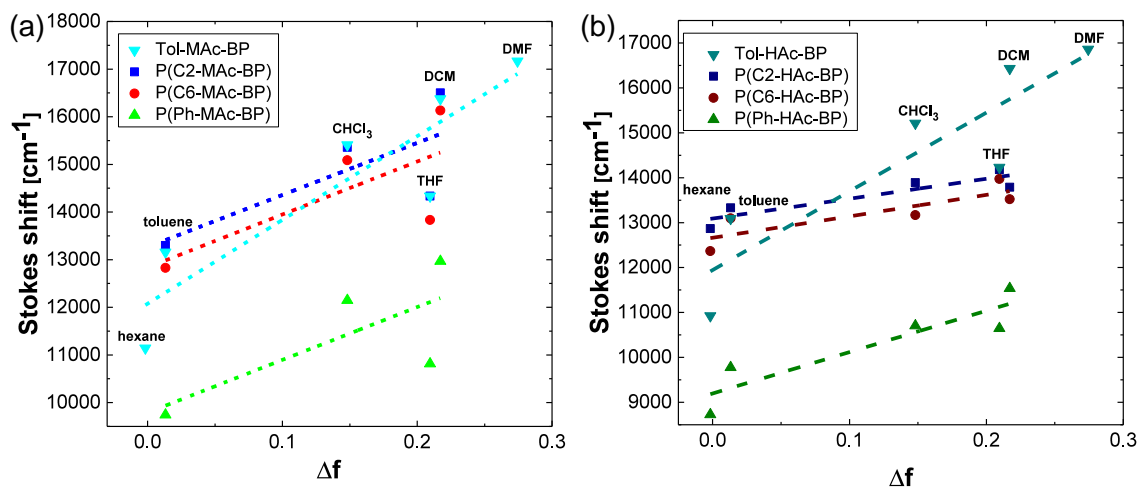


Figure 4.4. Lippert-Mataga-plot of (a) Tol-MAc-BP, P(C2-MAc-BP), P(C6-MAc-BP) and P(Ph-MAc-BP) and (b) of Tol-HAc-BP, P(C2-HAc-BP), P(C6-HAc-BP) and P(Ph-HAc-BP): Correlation of the Stokes shift and the orientation polarizability (Δf) in various solvents.

The previously mentioned high similarity of the solvatochromic shifts of **P(C2-MAc-BP)**, **P(C6-MAc-BP)** and **P(Ph-MAc-BP)** is reflected by the similar slopes ranging from $10.9 - 11.1 \times 10^3$

cm^{-1} . While these highly similar shifts were also observed for **Tol-MAc-BP** and **Tol-HAc-BP**, the significantly higher slope of about $17.5 \times 10^3 \text{ cm}^{-1}$ is caused by a smaller Stokes shift in hexane solution. This outlying position of the shift in hexane in the Lippert-Mataga plot can be explained by the mixture of LE and CT leading to a more hypsochromically shifted emission than from a pure CT state. In comparison to their DMAC-based counterparts, the slopes of **P(C2-HAc-BP)**, **P(C6-HAc-BP)** are with $4.8 \times 10^3 \text{ cm}^{-1}$ and $4.4 \times 10^3 \text{ cm}^{-1}$ reduced by more than half due to the second emissive species described earlier. The slope of $9.2 \times 10^3 \text{ cm}^{-1}$ in the Lippert-Mataga plot for **P(Ph-HAc-BP)** is based on a similarly intense emission of both of the CT states, leading to broad emission with a maximum at 604 nm. Although THF gives rise to a similar orientation polarizability as DCM ($\Delta f(\text{DCM})=0.22$), the Stokes shift is significantly lower. Explaining this specific effect would require further investigation,^[115] which is beyond the scope of this thesis. Although THF and hexane solutions do not exactly follow a linear trend, the slopes in the Lippert-Mataga plot reveal a higher change in dipole moment between the ground and excited state for the first set of materials and the small molecule Tol-HAc-BP with almost identical Stokes shifts in contrast to a smaller shift for **P(C2-HAc-BP)**, **P(C6-HAc-BP)** and **P(Ph-HAc-BP)**.

Now that the absorption bands leading to a CT emission and the solvent polarity effect on the PL emission have been identified, the influence of the linker incorporation into the polymer backbone and donor substitution on the PLQY in solution was studied. Toluene solutions were chosen for the PLQY comparison between the various TADF materials. The measurement method requires an integrating sphere and the procedure is described in detail in section 7.2.7. All materials exhibit low to moderate PLQYs ranging from 21 % to 57 % in degassed toluene solution solutions showing no clear trend with molecular structure (see **Figure 4.5**). Due to the efficient triplet quenching effect of oxygen, it is easy to prove the role of triplet states to the emission. This is accomplished by comparing the PLQY between degassed solutions and ambient conditions, in which the triplet states are practically fully quenched by oxygen dissolved in solution.^[117] For this purpose, the solutions were flushed with air after the PLQY measurement in degassed solution and characterized again. The PLQY values measured

under ambient conditions were found to be quite similar for the different materials, i.e. in the range of 7 %-18 %. The strong rise in PLQY upon exclusion of oxygen ranges from 2-fold increase for **P(C2-MAc-BP)** to a 6-fold for **Tol-HAc-BP** and indicates a high involvement of a triplet excited state of all materials, as expected for TADF emitters (see **Figure 4.5**).

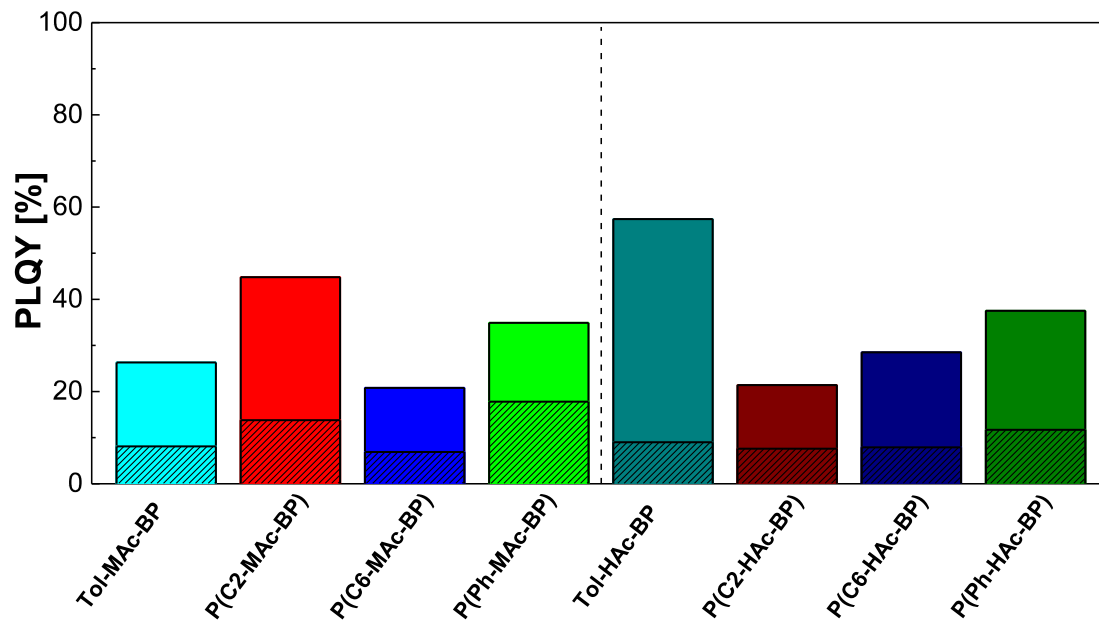


Figure 4.5. Bar chart of PLQY of Tol-MAc-BP, P(C2-MAc-BP), P(C6-MAc-BP), P(Ph-MAc-BP), Tol-HAc-BP, P(C2-HAc-BP), P(C6-HAc-BP) and P(Ph-HAc-BP) in degassed toluene solution (no pattern) and under ambient conditions (hatched area).

4.2. Steady State Photophysical Properties in Thin Films

While the characterization of both sets of materials in solution in the previous section enabled the assessment of the CT characteristics, the photophysical properties in thin films are of higher importance due to their application in OLEDs. In a next step the absorption and emission in pristine solid films is evaluated (see **Figure 4.6**). For all materials, the absorption spectra are very similar to the UV-vis spectra measured in solution with no additional band present. The only difference seems to be

a slightly more pronounced direct CT excitation band in pristine films with about 10 % absorbance in comparison to the absorption maximum. Upon excitation, all compounds exhibit an almost identical PL emission in pristine film with a maximum at 533-538 nm.

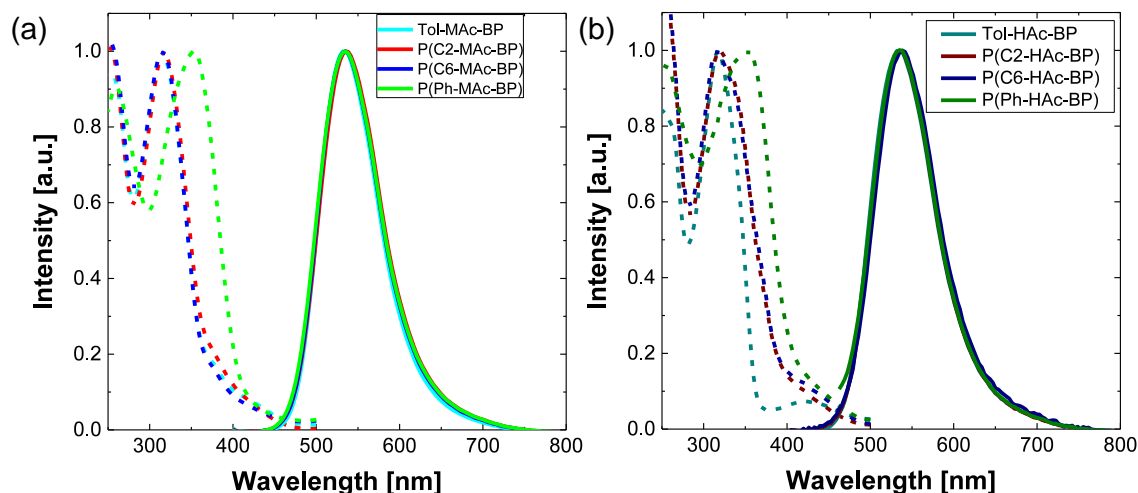


Figure 4.6. Normalized Absorption (dashed lines) and PL spectra (solid lines) of pristine films (a) of **Tol-MAc-BP**, **P(C2-MAc-BP)**, and **P(Ph-MAc-BP)**, as well as (b) of **Tol-HAc-BP**, **P(C2-HAc-BP)**, and **P(Ph-HAc-BP)** on quartz substrate.

As next step, their TADF properties were investigated. While there are various possibilities in steady state PL spectroscopy to do so, the easiest is analogous to the PLQY determination in solution in the previous section, to compare the PL intensity in the presence and absence of oxygen. This was performed by measuring the PL spectrum in ambient condition in a cryostat and comparing it with the spectrum obtained from the same sample upon evacuation of the cryostat, reaching high vacuum with a pressure of down to 10^{-4} mbar without changing film position (see **Figure 4.7a** and **b**). It is further possible to calculate the ratio between delayed and prompt fluorescence (Φ_{DF}/Φ_{PF}) by comparing the integration of the PL intensity under oxygen free conditions ($I_{O_2\ free}$) and in ambient with oxygen being present (I_{O_2}) using the relation^[117]

$$\frac{\int I_{O_2\ free}(\lambda)d\lambda}{\int I_{O_2}(\lambda)d\lambda} = \frac{(\Phi_{PF} + \Phi_{DF})}{\Phi_{PF}} = 1 + \frac{\Phi_{DF}}{\Phi_{PF}}, \quad (18)$$

where Φ_{DF} is the quantum yield of the delayed fluorescence and Φ_{PF} is the quantum yield of the prompt fluorescence. All values are listed in **Table 4.2**. It has to be noted that these Φ_{DF}/Φ_{PF} ratios via steady state PL spectroscopy can only act as an estimation because it is not possible to differentiate between PF and DF. Furthermore, this equation is only valid under the assumption that the triplet states are fully quenched by oxygen in film state in ambient atmosphere.

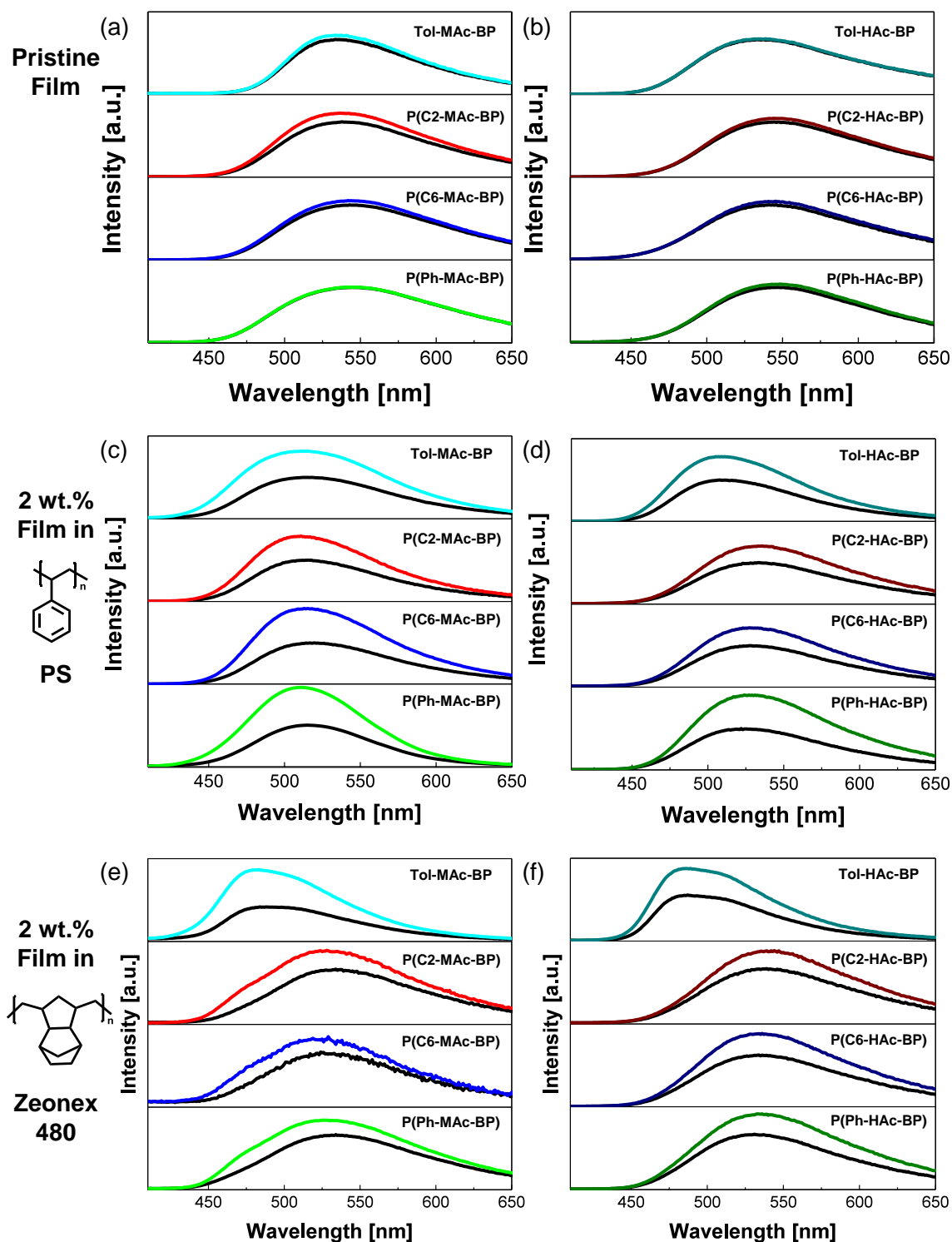


Figure 4.7. PL spectra under ambient conditions (black) and in vacuum of Tol-MAc-BP (cyan), P(C2-MAc-BP) (red), P(C6-MAc-BP) (blue) and P(Ph-MAc-BP) (green) in (a) pristine film, (c) film of 2 wt% in PS and (e) film of 2 wt% in Zeonex® 480. PL spectra under ambient conditions (black) and in vacuum of Tol-HAc-BP (dark cyan), P(C2-HAc-BP) (dark red), P(C6-HAc-BP) (dark blue) and P(Ph-HAc-BP) (dark green) in (b) pristine film, (d) film of 2 wt% in PS and (f) film of 2 wt% in Zeonex® 480.

While a strong triplet state involvement was observed in analogous measurements in solution, the pristine films show little to no change with and without oxygen being present leading to Φ_{DF}/Φ_{PF} values between 0.01 and 0.17. A possible reason for this is a limited oxygen permeability of the film already preventing an efficient quenching of triplet states below the surface of the film. A concentration quenching effect dominating in thin film could also reduce the DF contribution significantly. In order to eliminate both of the mentioned effects and to evaluate the ratio between DF and PF in film state, polystyrene ($M_w = 174$ kg/mol, $D = 1.06$, atactic), as well as the cyclic olefin polymer Zeonex® 480 were selected as host polymers (molecular structure see **Figure 4.7c** and **d**). While both form transparent films and are known to exhibit sufficient oxygen permeability,^[25] PS is slightly more polar (0.13 D^[121]) than Zeonex® 480 (0 D). Blend films in Zeonex® 480 and PS were fabricated for both sets of compounds using a high dilution of 2 wt% of the TADF materials in order to prevent possible concentration quenching.

Table 4.2. Summary of steady-state photophysical properties of **Tol-MAc-BP**, **P(C2-MAc-BP)**, **P(C6-MAc-BP)**, **P(Ph-MAc-BP)**, **Tol-HAc-BP**, **P(C2-HAc-BP)**, **P(C6-HAc-BP)** and **P(Ph-HAc-BP)** in film state.

Compound	λ_{PL}^a			Φ_{DF}/Φ_{PF}			ΔE_a^{TADF} [meV]
	[nm]			pristine	2 wt% in		
	pristine	2 wt% in PS	2 wt% in Zeonex® 480		PS	Zeonex® 480	
Tol-MAc-BP	534	508	486	0.07	0.67	0.93	61.3 ± 5.0
P(C2-MAc-BP)	535	517	529	0.17	0.57	0.38	24.8 ± 2.3
P(C6-MAc-BP)	535	515	528	0.08	0.79	0.28	15.0 ± 0.7
P(Ph-MAc-BP)	535	518	528	0.01	0.82	0.30	28.9 ± 0.8
Tol-HAc-BP	535	512	489	0.01	0.58	0.59	26.5 ± 0.3
P(C2-HAc-BP)	535	532	535	0.07	0.41	0.31	-
P(C6-HAc-BP)	538	532	532	0.06	0.43	0.41	-
P(Ph-HAc-BP)	535	530	532	0.06	0.82	0.39	63.4 ± 7.5

^a $\lambda_{exc} = 350$ nm.

In contrast to pristine films, a significant increase in emission intensity upon exclusion of oxygen is observed for all compounds in both polymer hosts (see **Figure 4.7c** and **d**). Starting with the evaluation of the TADF blended with PS, Φ_{DF}/Φ_{PF} values ranging from 0.41 to 0.82 were obtained. The emission shows a hypsochromic shift in comparison to the pristine films to 515-518 nm for **P(C2-MAc-BP)**, **P(C6-MAc-BP)** and **P(Ph-MAc-BP)** based on the change in polarizability (i.e. dielectric coefficient) of the host.^[122,123] Although this effect appears similar to the solvatochromism, it is not caused by any reorientation of the host as it is the case for solvent molecules. It is based on the static interaction between the dipole moment of the CT state and the host. This effectively changes the energy of the CT state while having no influence on the LE excited state.^[122] An even more intense

shift was observed for the small molecules **Tol-MAc-BP** and **Tol-HAc-BP** with a PL maximum at 508 and 512 nm, respectively. In contrast, the DHAC-based polymers show only a small shift to 530-532 nm. A possible reason can be a phase separation due to their more aliphatic nature than **P(C2-MAc-BP)**, **P(C6-MAc-BP)** and **P(Ph-MAc-BP)**.

In direct comparison with to the PS host polymer, the films of both sets of materials blended in Zeonex® 480 also showed a significant increase in PL intensity changing from ambient to vacuum atmosphere. Ratios between DF and PF of 0.28-0.93 were obtained, which is similar to results obtained for the PS blended films. As expected for a very apolar host, an even stronger hypsochromic shift to 486 and 489 nm was observed for the small molecules **Tol-MAc-BP** and **Tol-HAc-BP**, respectively. In contrast, the polymer compounds showed a smaller shift than expected to 528-529 nm for **P(C2-MAc-BP)**, **P(C6-MAc-BP)** and **P(Ph-MAc-BP)** and for **P(C2-HAc-BP)**, **P(C6-HAc-BP)** and **P(Ph-HAc-BP)** there was even no change occurring.

This observation is most likely based on phase separation, which was confirmed by atomic force microscopy (AFM) measurements on the films of **Tol-MAc-BP** and **P(C6-MAc-BP)** in both host polymers (see **Figure 4.8**). The AFM surface topography of the blended films of both materials in PS and of **Tol-MAc-BP** in Zeonex® 480 was determined to be smooth and featureless, giving no indication of demixing in the films. In contrast, the AFM images of a film of **P(C6-MAc-BP)** in PS shows a pattern of drop-like features (see **Figure 4.8d**). The dark spots in this image can be assigned to **P(C6-MAc-BP)**-rich domains within the Zeonex® film most likely resulting from liquid-liquid demixing upon film formation. This phase separation leads to the TADF chromophores in the polymer backbone having the same environment and polarizability as in pristine films. Furthermore, the line shape of the emission spectra in Zeonex® 480 differs from pristine and from the PS blended films for the DMAC-based polymers in showing a bimodal profile. This observation can be explained by the low polarizability of Zeonex® 480 host polymer shifting the energy of the CT excited state closer to the LE excited state resulting in state mixing, analogous to the PL emission recorded in hexane solution.

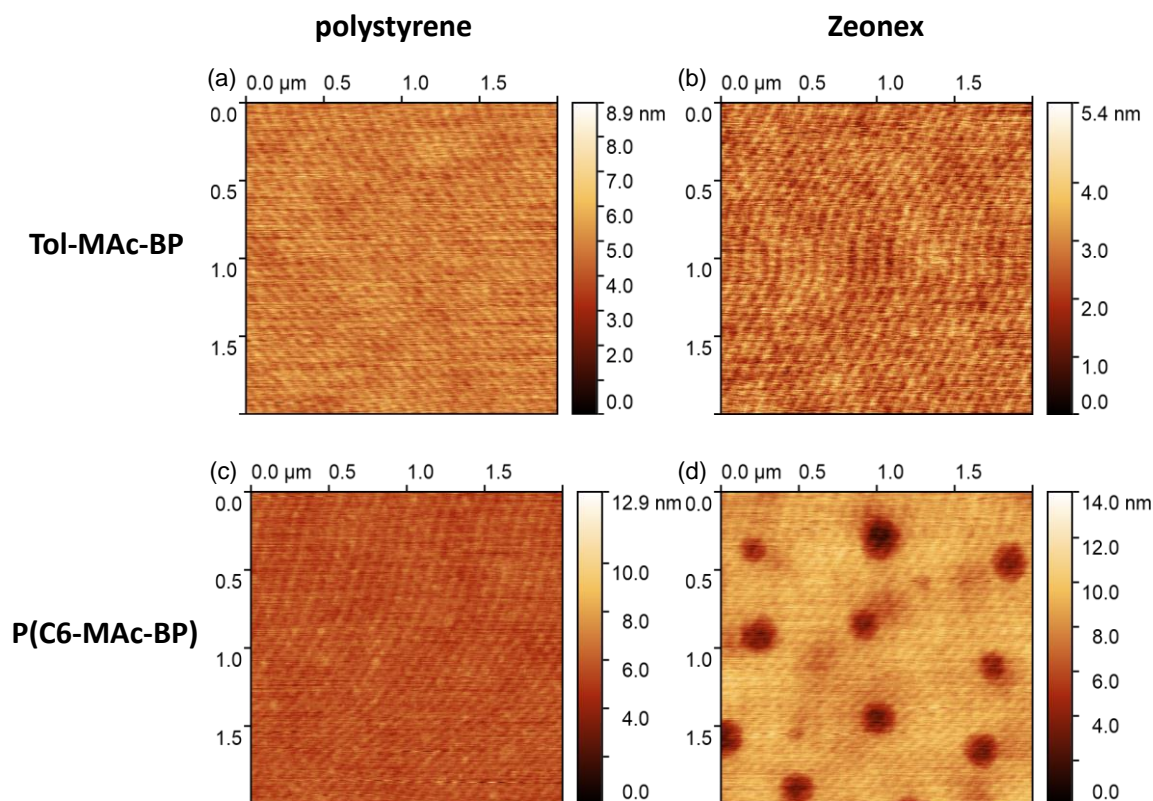


Figure 4.8. Topology AFM images (2 μm x 2 μm) of 2 wt% **Tol-Mac-BP** in (a) PS and (b) Zeonex® 480 host as well as **P(C6-Mac-BP)** in (c) PS and (d) Zeonex® 480 host.

Although all compounds showed a significant increase in emission intensity upon exclusion of oxygen, effectively proving strong triplet state involvement in the PL in diluted film state, the origin of the absence of this effect in pristine film was still not clear. To be able to differentiate between a low oxygen permeability, dominating concentration quenching or a combination of these effects as reason for the insensitivity of the pristine films to oxygen, the PL was measured as a function of temperature. The rate of the RISC that is the basis of the triplet to singlet conversion in TADF emitters depends on the thermal energy in comparison to the ΔE_{ST} , leading to an increasing DF contribution with rising temperatures as a direct consequence. The pristine film samples (**Figure 4.9**) as well as the diluted compounds in the PS host (**Figure 4.10**) were chosen for this characterization and the temperature was changed in steps of 20 K from room temperature down to 77 K.

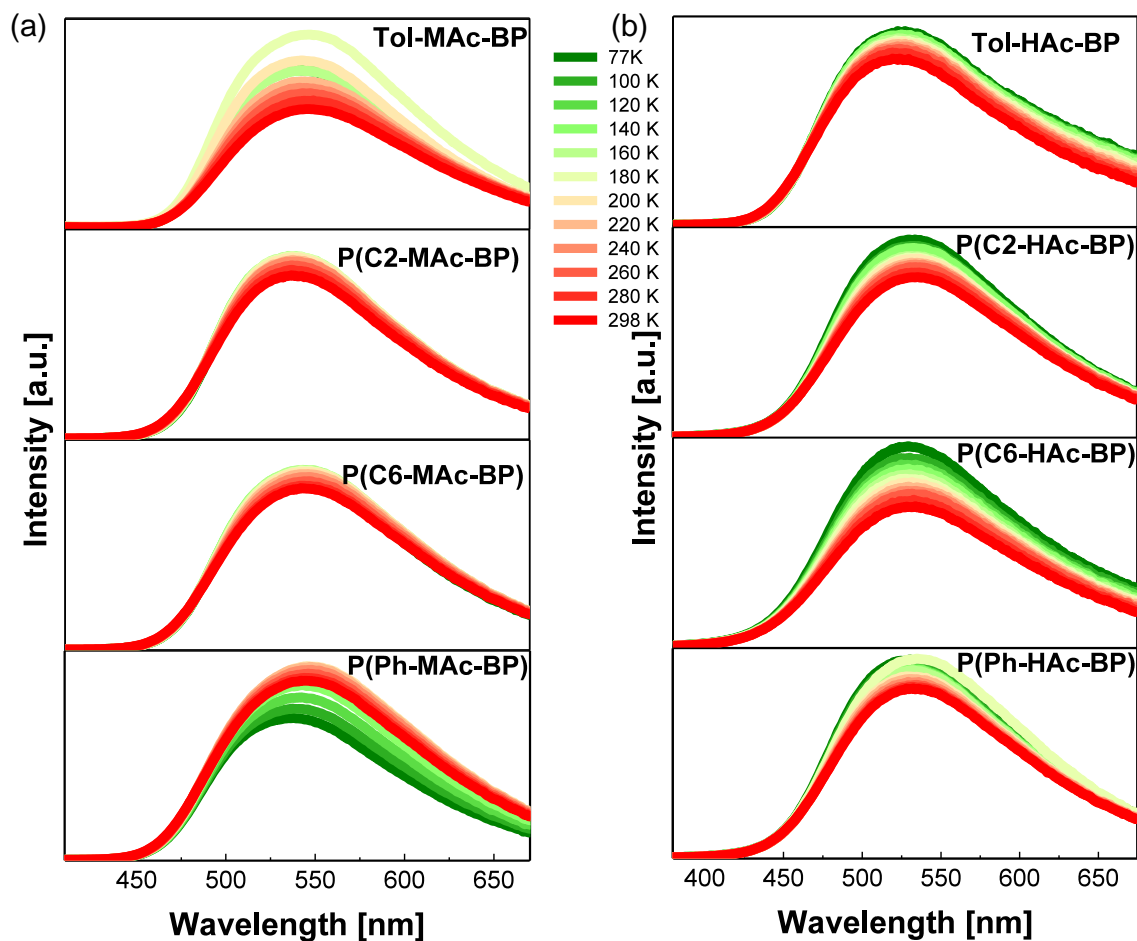


Figure 4.9. PL spectra of pristine films of (a) Tol-MAc-BP, P(C2-MAc-BP), P(C6-MAc-BP) and P(Ph-MAc-BP), as well as (b) Tol-HAc-BP, P(C2-HAc-BP), P(C6-HAc-BP) and P(Ph-HAc-BP) under vacuum at different temperatures ($\lambda_{exc} = 350$ nm).

While the expected trend was only observed for the pristine film of **P(Ph-MAc-BP)**, an inverse trend was shown by the pristine films of all other compounds: This increase in PL emission upon cooling may be partly based on the reduction of nonradiative processes such as internal conversion at lower temperatures^[24] and indicates a dominant concentration quenching effect.^[124] In contrast, the same measurements performed with the TADF materials diluted in PS polymer host show a steady decrease in PL intensity upon lowering the temperature as expected for TADF emitters with limited concentration quenching. Surprisingly the films of **P(C2-HAc-BP)** and **P(C6-HAc-BP)** in PS differ

from the rest of the compounds: The change in PL intensity in these two samples does not follow a clear trend across the temperature range. A possible explanation is that due to the phase separation the concentration quenching is not sufficiently suppressed.

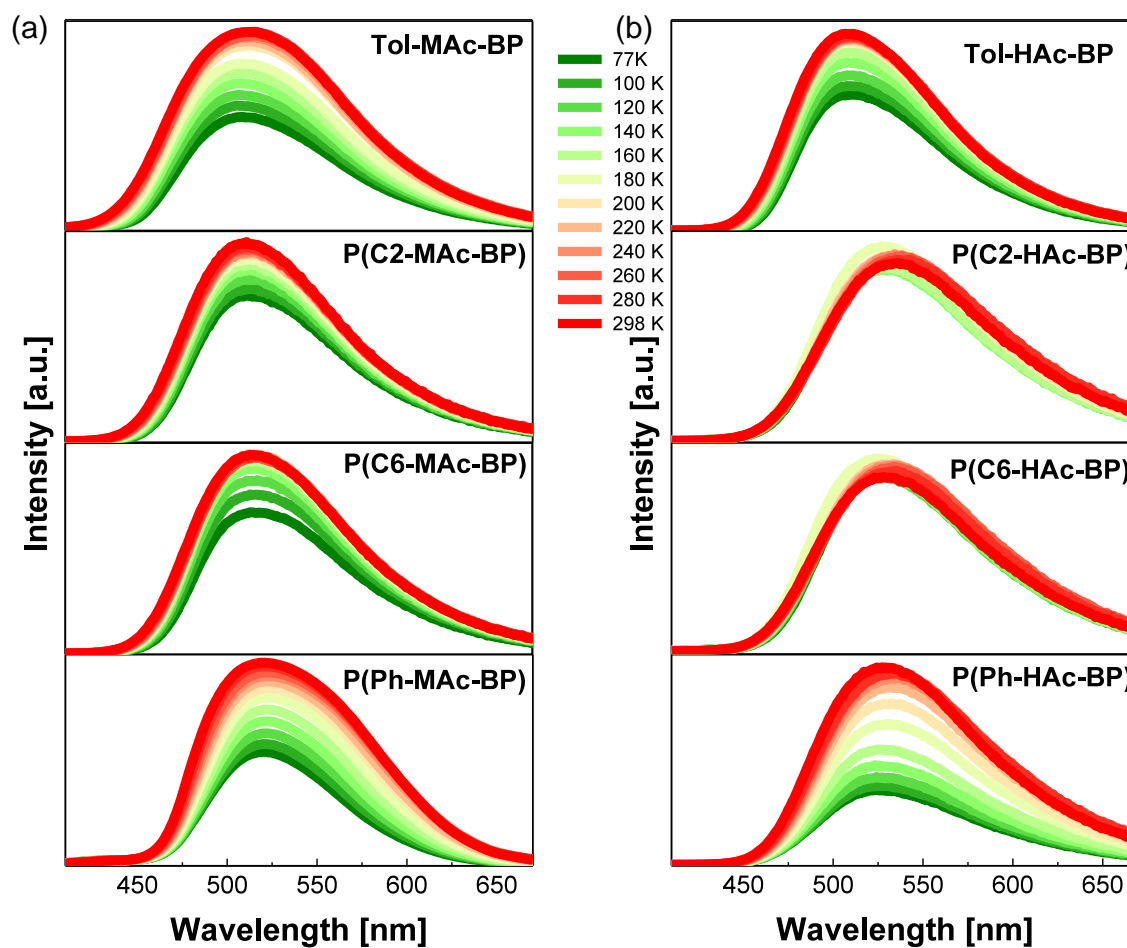


Figure 4.10. PL spectra of blended films of 2 wt% (a) Tol-MAc-BP, P(C2-MAc-BP), P(C6-MAc-BP) and P(Ph-MAc-BP), as well as (b) Tol-HAc-BP, P(C2-HAc-BP), P(C6-HAc-BP) and P(Ph-HAc-BP) in PS under vacuum at different temperatures ($\lambda_{exc} = 350$ nm).

Under the assumption that an increase in DF intensity (I_{DF}) with temperature is solely stemming from TADF and not significantly influenced by additional processes in the diluted films, the

activation energy of the TADF (ΔE_a^{TADF}) can be determined as an estimation for the ΔE_{ST} using the Arrhenius relation:

$$\ln(\int I_{DF}(\lambda)d\lambda) = \frac{-E_a^{TADF}}{k_B} \cdot \frac{1}{T} \quad (19)$$

where k_B is the Boltzmann constant, λ is the wavelength. Because the PL intensity (I_{PL}) recorded in steady state consists of both PF and DF and it cannot be differentiated between them, the integrated DF intensity can only be estimated via

$$\int I_{DF}(\lambda)d\lambda = \int I_{PL}(\lambda)d\lambda - \int I_{PL,O_2}(\lambda)d\lambda, \quad (20)$$

where I_{PL,O_2} is the intensity of the steady state PL spectrum in the presence of oxygen. This equation is only valid under the assumption that the triplet excited states are fully quenched under exposure to oxygen at ambient conditions and the PL spectrum measured stems solely from PF and the results can therefore only act as a rough estimation.

In an Arrhenius plot, the natural logarithm of the integrated DF intensity derived from **Equation 20** was plotted against the reciprocal temperature and a subsequent fit with a straight line enables the calculation of ΔE_a^{TADF} (see **Figure 4.11**). For all materials except **P(C2-HAc-BP)** and **P(C6-HAc-BP)** small TADF activation energies of 15.0 – 63.4 meV were determined, being higher than the singlet-triplet energy difference of 6-10 meV calculated by TD-DFT computations. The small ΔE_{ST} of the first set of materials effectively proves the preservation of a small ΔE_{ST} upon polymerization. Furthermore, no adverse effect based on the type of linker for the activation energy of RISC was observed making the linking of Ds in a main-chain polymer a robust approach. The nonlinear change in PL intensity upon changing the temperature for **P(C2-HAc-BP)** and **P(C6-HAc-BP)** is most likely a consequence of phase separation in the blended films.

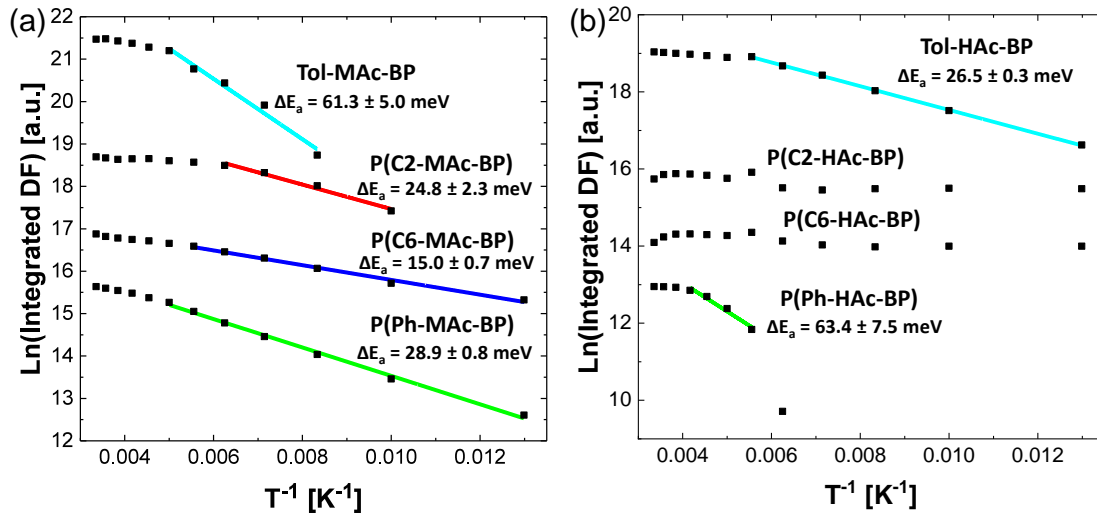


Figure 4.11. Arrhenius plot of blended films of 2 wt% (a) **Tol-MAc-BP**, **P(C2-MAc-BP)**, **P(C6-MAc-BP)** and **P(Ph-MAc-BP)**, as well as (b) **Tol-HAc-BP**, **P(C2-HAc-BP)**, **P(C6-HAc-BP)** and **P(Ph-HAc-BP)** in PS under vacuum at different temperatures ($\lambda_{exc} = 350$ nm).

Although the direct comparison of the TADF materials in pristine and 2 wt% blended film proved the presence of concentration quenching, those two films represent the far ends of blending ratios. In order to quantify the influence of concentration quenching on the PL efficiency of the different polymer linker strategies, the PLQY was determined for **Tol-MAc-BP**, **P(C2-MAc-BP)**, **P(C6-MAc-BP)** and **P(Ph-MAc-BP)** with varying blending ratio with PS (see **Figure 4.12**) in nitrogen atmosphere (method described in detail in section 7.2.7). For this experiment only the first set of materials (DMAC-series) was selected based on their better blending properties and small estimated ΔE_{ST} . Furthermore, a PS polymer with a lower molecular weight of $M_w = 1.100$ g/mol ($D = 1.15$, atactic) was used as a host in order to prevent phase separation, as observed previously.

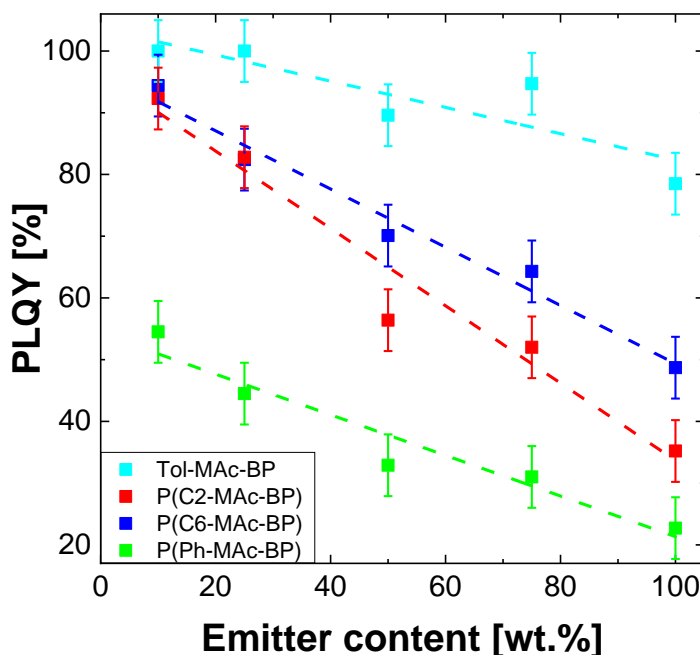


Figure 4.12. PLQY of films of **Tol-MAc-BP**, **P(C2-MAc-BP)**, **P(C6-MAc-BP)** and **P(Ph-MAc-BP)** in various blending ratios with PS.

The PLQY values of the polymers **P(C2-MAc-BP)**, **P(C6-MAc-BP)** and **P(Ph-MAc-BP)** in pristine films are clearly lower than for the small molecule **Tol-MAc-BP** having a high PLQY of 0.79 ± 0.05 similar to the model compound DMAC-BP ($\Phi_{PL} = 0.85$)^[104]. The lowest quantum yield in pristine film of 0.23 ± 0.05 can be found for the fully conjugated **P(Ph-MAc-BP)** with an increase in PLQY with a slightly increasing alkyl linker length from 0.35 ± 0.05 for **P(C2-MAc-BP)** to 0.49 ± 0.05 for **P(C6-MAc-BP)**. Upon increasing blending ratios, all materials show a significant increase in PLQY based on the reduction of concentration quenching (**Figure 4.12**). Although **Tol-MAc-BP** already was showing a high PLQY in neat film in comparison to the TADF polymers, an even higher PLQY of 1.00 ± 0.05 was obtained upon blending with PS. Thus, the PLQY increases for the polymers by 94 %-163 % going from neat films to 10 wt% dilution resulting in PLQYs of 0.92 ± 0.05 for **P(C2-MAc-BP)**, 0.94 ± 0.05 for **P(C6-MAc-BP)** and 0.55 ± 0.05 for **P(Ph-MAc-BP)**. Although the ΔE_{ST} of the polymers are similar to one another, the PLQY of **P(Ph-MAc-BP)** is

significantly lower than of their nonconjugated counterparts pointing to a higher quenching rate for the conjugated linker. This result can be explained by a more intense coupling between the lowest electronically excited and the vibrational states which is well known for extended conjugated systems.^[125] Comparing the two nonconjugated polymers with one another shows that for **P(C6-MAc-BP)** higher PLQYs have been determined than for **P(C2-MAc-BP)** ranging from pristine to 1:1 blending ratios. A possible explanation is a better spatial distance between the TADF units due to the longer and more flexible alkyl chain preventing short-range quenching more efficiently. However, this small beneficial effect seems to vanish at a dilution of 1:3 and the determined PLQYs for both polymers are on top of each other.

4.3. Transient Photophysical Characterization

The steady state characterization in solution and film state revealed a preservation of the small ΔE_{ST} upon polymerization and a strong influence of concentration quenching on the PLQY of the TADF polymers. In order to investigate this loss process in detail and its connection to the type of linker, time-resolved photoluminescence (TRPL) measurements were performed. This enables to distinguish between PF and DF. As a first step the pristine films, in which a dominance of the concentration quenching is expected, were characterized and the decay curves are shown in **Figure 4.13**.

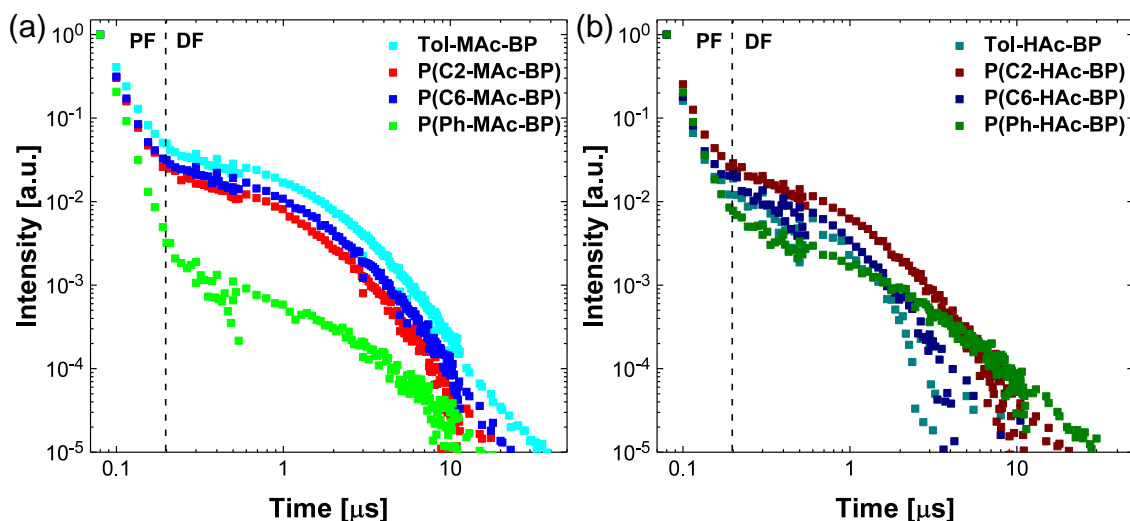


Figure 4.13. Decay curves of pristine films of (a) Tol-MAc-BP, P(C2-MAc-BP), P(C6-MAc-BP) and P(Ph-MAc-BP), as well as (b) Tol-HAc-BP, P(C2-HAc-BP), P(C6-HAc-BP) and P(Ph-HAc-BP) at room temperature ($\lambda_{exc} = 355$ nm).

The decay curves in these log-log plots at room temperature can be separated into two regions (see **Figure 4.13a-b** separated by a dashed line). The first region ranging from the PL intensity maximum to 200 ns shows a fast nanosecond decay that can be attributed to the PF. Following a turning point of the decay curve at a delay of around 200 ns, the second region is characterized by a slow microsecond decay caused by DF indicating the first clear evidence of TADF in pristine film. Due to the fact that the decay curves are normalized to the maximum intensity resulting from the PF, the differences in the DF contribution to the PL emission between the TADF materials can be compared qualitatively by looking at the intensity of the DF: For the DMAC-based materials, **Tol-MAc-BP** has the highest DF intensity followed by the nonconjugated polymers **P(C2-MAc-BP)** and **P(C6-MAc-BP)**. A significantly lower PL intensity is observed by the fully conjugated **P(Ph-MAc-BP)**, which also shows a steeper PF decay. This inferiority of **P(Ph-MAc-BP)** is in agreement with the lower PLQY derived in steady state in the previous section 4.2. In direct comparison to the DMAC-based materials, the PL decay curves of the DHAC-based materials are more similar to one another. In terms of DF intensity, the fully conjugated polymer **P(HAc-BP)** again is found to be at

the lower end with **Tol-MAc-BP**, **P(C2-MAc-BP)** and **P(C6-MAc-BP)** showing more DF contribution.

In order to determine PF and DF lifetimes (τ_{PF} and τ_{DF}), both regions of the transient PL curves were fitted with exponential decay functions. In contrast to the fluorescence decay of TADF molecules in solution that can often be described by a sum of two exponential decays (monoexponential PF and monoexponential DF decay), fitting the PL decay of film samples is often more complex.^[24] This complexity stems from the heterogeneity of the D-A dihedral angles due to the restricted motion in the solid film resulting in a distribution of conformations with different fluorescence decays. Nonetheless, in order to be able to determine a lifetime of PF and DF in films, the fluorescence decay is fitted with a sum of exponential decay functions for the PF and DF regions using

$$I(t) = \sum_i^n A_i e^{-\frac{t}{\tau_i}}, \quad (21)$$

Where $I(t)$ is intensity at time t and A_i is the initial intensity decaying with the lifetime of τ_i . For the separate fitting of PF and DF, the time window around the turning point (see **Figure 4.13** dashed line) of the decay curve has to be omitted. The PF could be fitted with a monoexponential decay and the DF with a sum of two exponential decays. The fit curves are shown in the Appendix 4.5 (**Figure A4.11**) and the fit parameters are summarized in **Table 4.3**. In order to be able to compare the lifetimes of the triplet state, an average lifetime (τ_{av}) of the DF was calculated using the equation

$$\tau_{av} = \frac{\sum A_i \tau_i^2}{\sum A_i \tau_i}. \quad (22)$$

Similarly the average initial intensity (A_{av}) of the exponential fits can be calculated using

$$A_{av} = \frac{\sum A_i^2 \tau_i}{\sum A_i \tau_i}, \quad (23)$$

Which enables the calculation of the ratio between quantum yield of DF and PF:

$$\frac{\Phi_{DF}}{\Phi_{PF}} = \frac{A_{DF} \tau_{DF}}{A_{PF} \tau_{PF}}. \quad (24)$$

Table 4.3. Summary of transient PL decay fitting parameters of PF and DF of **Tol-MAc-BP**, **P(C2-MAc-BP)**, **P(C6-MAc-BP)**, **P(Ph-MAc-BP)**, **Tol-HAc-BP**, **P(C2-HAc-BP)**, **P(C6-HAc-BP)** and **P(Ph-HAc-BP)** in pristine film.

Compound	A_{PF}	τ_{PF}	$A_{DF,1}$	$\tau_{DF,1}$	$A_{DF,2}$	$\tau_{DF,2}$	$\tau_{DF,av}$	Φ_{DF}/Φ_{PF}
		[ns]	[10 ⁻³]	[μ s]	[10 ⁻³]	[μ s]	[μ s]	
Tol-MAc-BP	24.5	24.9	34.8	1.20	2.3	4.60	1.88	0.09
P(C2-MAc-BP)	80.1	18.2	19.4	0.74	3.8	2.16	1.26	0.01
P(C6-MAc-BP)	65.9	19.1	23.1	0.91	3.5	2.73	1.48	0.02
P(Ph-MAc-BP)	411.9	13.3	2.4	0.33	0.7	2.49	1.79	<0.01
Tol-HAc-BP	1085.4	11.4	57.1	0.10	7.8	0.76	0.44	<0.01
P(C2-HAc-BP)	160.6	15.7	20.3	0.76	1.4	2.65	1.12	0.01
P(C6-HAc-BP)	650.2	12.4	7.0	0.84	21.2	0.36	0.57	<0.01
P(Ph-HAc-BP)	428.8	13.2	4.6	0.66	1.1	3.42	2.19	<0.01

The PF lifetimes of the pristine films range from 13.3 ns to 24.9 ns for the DMAC-based and from 11.4 ns to 15.7 ns for the DHAC-based TADF materials. In case of the DF lifetimes, a significant difference between the two sets of TADF materials was observed. While the DMAC-based materials show a similar $\tau_{DF,av}$ of 1.26-1.88 μ s, the differences in DF lifetimes within the DHAC-based materials are more significant. Where **P(C2-HAc-BP)** and **P(Ph-HAc-BP)** exhibit intermediate DF lifetimes of 1.12 μ s and 2.19 μ s, respectively, a very fast decay was found for **Tol-HAc-BP** and **P(C6-HAc-BP)** with 0.44 μ s and 0.57 μ s. The ratios between DF and PF calculated for the pristine films is low and in agreement with the values estimated in steady state assuming oxygen-based quenching of the triplet state (see **Table 4.2**).

Now that the PF and DF lifetimes of the pristine films have been determined as a starting point, the change upon dilution in PS is further investigated. Due to the higher DF contribution the DMAC-based materials, **Tol-MAc-BP**, **P(C2-MAc-BP)**, **P(C6-MAc-BP)** and **P(Ph-MAc-BP)** were chosen for a more detailed investigation of the concentration quenching effect. Using the same blending

ratios as in the PLQY determination in section 4.2 further enables correlating the significant change in PLQY upon dilution in PS to the results in transient PL.

Before investigating the influence of dilution on the PF and DF lifetimes and their contribution to the overall PL emission, the spectral shifts in PL exhibited by the films and caused by the PS host at different blending ratios were analyzed. In order to differentiate between the shift in PF and DF, **Figure 4.14** shows the PL emission spectrum integrated at the fast decaying PL maximum and with a delay of 1 μ s, respectively. The PF and DF spectra of each sample are almost on top of each other proving an emission from the same excited state. The PL maxima of DF and PF of the **Tol-MAc-BP**, **P(C2-MAc-BP)**, **P(C6-MAc-BP)** and **P(Ph-MAc-BP)** films are almost identical for the same blending ratio and shift from 540 nm to 518 nm for both, PF and DF, with increasing dilution. This proves that the emission is independent of the linker and mainly depends on the host:guest ratio and dielectric constant of the host. Both emission spectra show a gradual hypsochromic shift with increasing PS content.

This change in the PL maximum stems from the change in polarizability of the surroundings of the TADF chromophore, similarly to the solvatochromism observed in solution. PS exhibits a low dipole moment (0.13 D^[121]) resulting in the charge transfer excited state of the TADF materials being less stabilized in the apolar host polymer than in the pristine film. The films with 10 wt% emitter content in PS further showed similar PL maxima in comparison to the blended films with only 2 wt% that were characterized in steady state PL (see **Table 4.2**). While an ongoing shift to 508 nm was observed for the PL in the 2 wt% film of **Tol-MAc-BP**, the TADF polymers show almost no change upon further dilution in PS ($\lambda_{PL,max} = 515\text{-}518$ nm). A plausible explanation of this observation is the close intramolecular distance between the TADF units in the polymer structure, making a complete surrounding of the chromophore with apolar PS impossible in comparison to the small molecule **Tol-MAc-BP**.

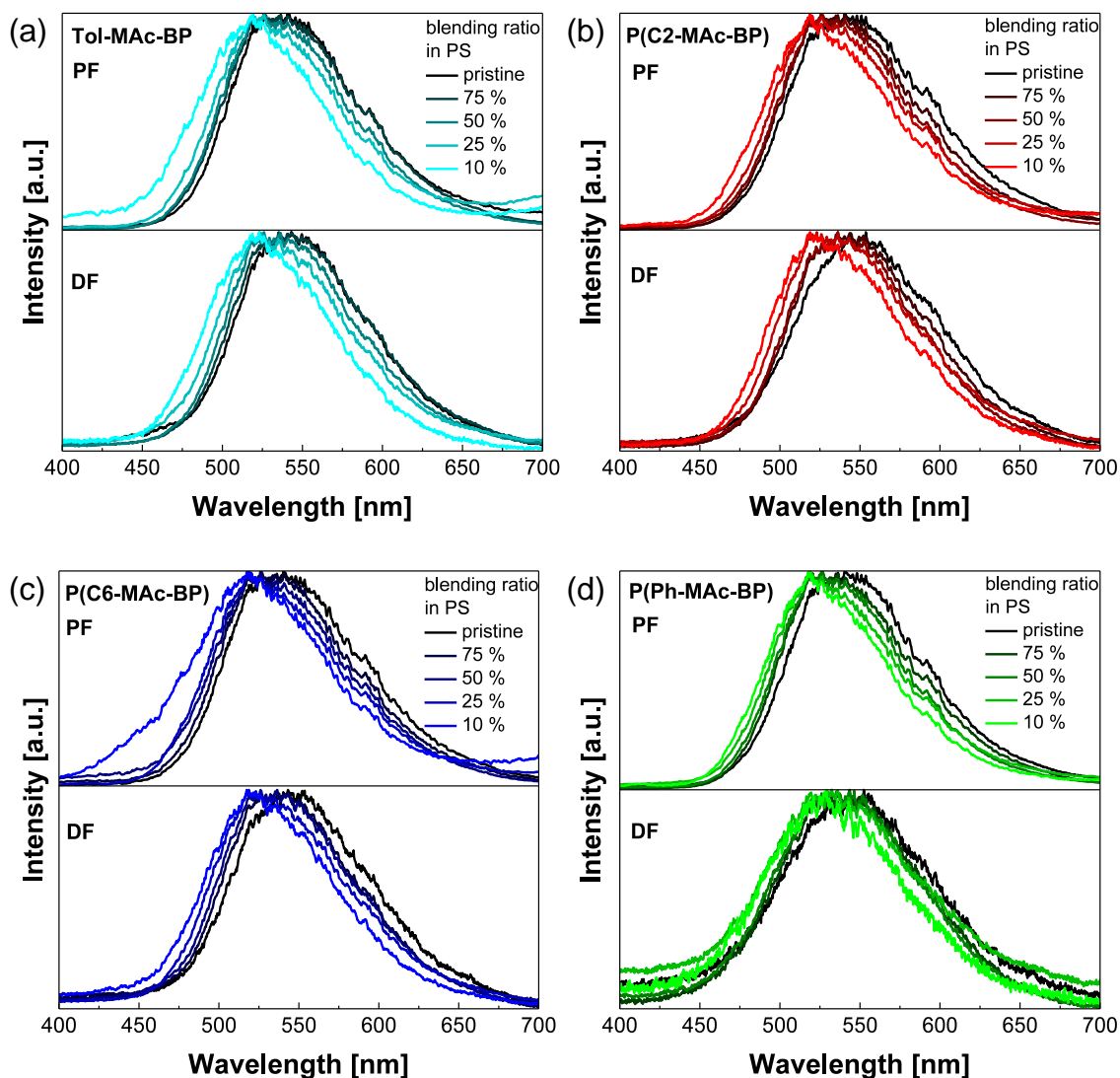


Figure 4.14. Normalized PF and DF spectra of (a) Tol-MAc-BP, (b) P(C2-MAc-BP) (c) P(C6-MAc-BP) and (d) P(Ph-MAc-BP) in film state in a variety of blending ratios in PS ($\lambda_{exc} = 400$ nm).

While the decay curves obtained for pristine films shown in **Figure 4.13** were mainly used to compare the different TADF materials with one another, the TRPL investigation of the DMAC-based materials with changing emitter content in PS gives an insight into the influence of concentration quenching on PF and DF in particular (see **Figure 4.15a-d**). An increase in contribution of the DF to the overall emission with higher dilution was observed for all materials. In contrast, the decay curve of PF appears to be quite similar throughout the different blending ratios and at first glance a significant

change is only observed between the pristine and diluted films for the TADF polymers (see **Figure 4.15a-d** inset). These observations indicate that the increase in PLQY upon blending mainly stems from a rise in DF emission. In order to determine the lifetimes of PF and DF, the decay curves were both fitted using a sum of two exponential functions utilizing **Equation 21**. The fit curves are shown in the Appendix 4.5 (**Figure A4.12** and **Figure A4.13**) and the average lifetimes are summarized in **Table 4.4**.

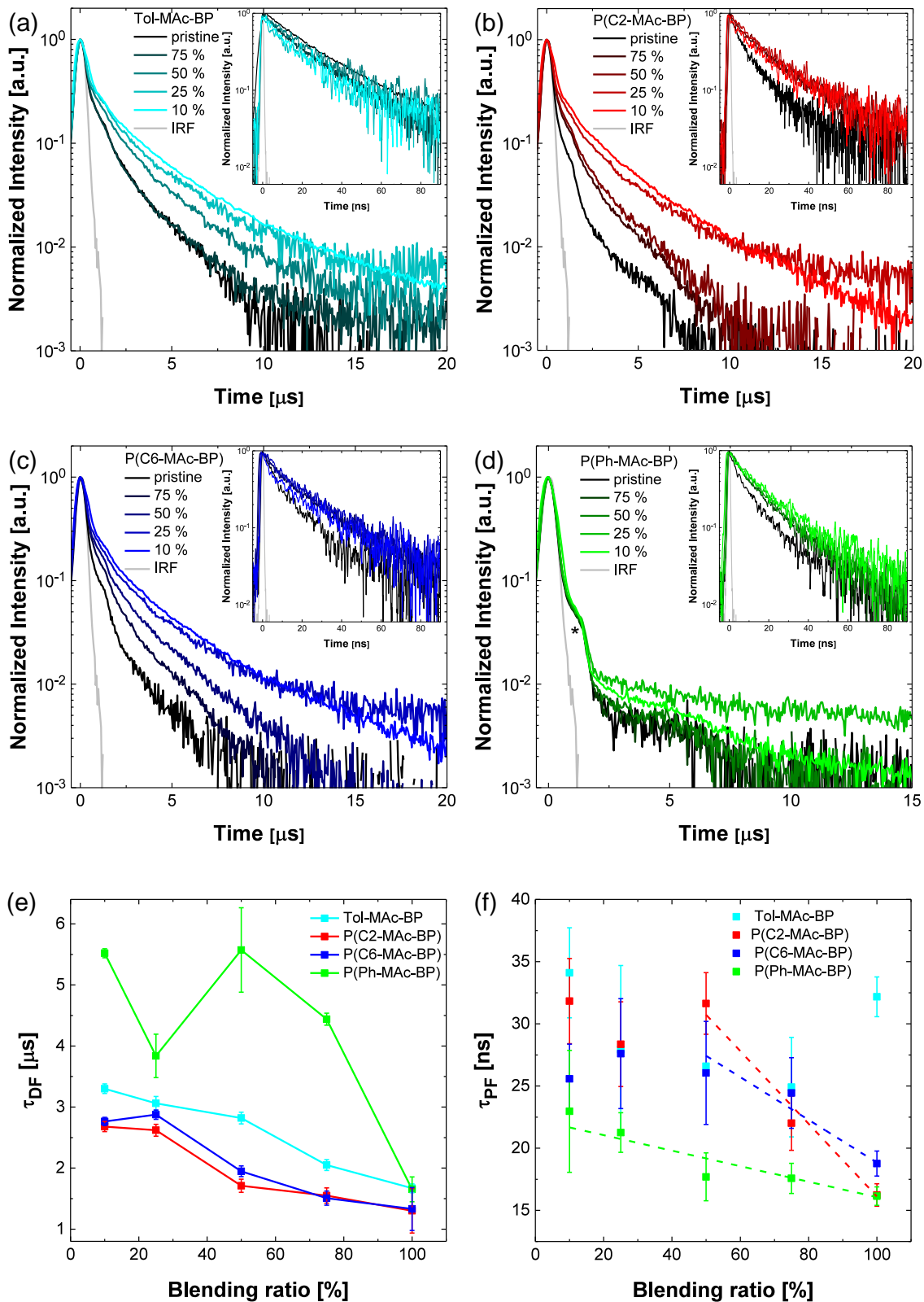


Figure 4.15. Normalized transient PL curves of films of various blending ratios in PS at r.t. in N_2 atmosphere of (a) Tol-MAC-BP, (b) P(C2-MAC-BP), (c) P(C6-MAC-BP) and (d) P(Ph-MAC-BP). The transient PL measured in nanosecond scale are shown in the inset. (e) DF lifetimes and (f) PF lifetimes of films of Tol-MAC-BP, P(C2-MAC-BP), P(C6-MAC-BP) and P(Ph-MAC-BP) in various blending ratios with PS as a host derived from the transient PL curves in a-d. In (d), * indicates an artifact described in Appendix 4.5.3.

Concomitantly with the increase in DF intensity going to high dilutions, an increase in delayed fluorescence lifetimes was observed (see **Figure 4.15e**). Between the pristine and 10 wt% films in PS, DF lifetimes for the small molecule **Tol-MAc-BP** changed from 1.67 μs to 3.30 μs , as well as from 1.30 μs to 2.68 μs and 1.33 μs to 2.76 μs for the nonconjugated polymers **P(C2-MAc-BP)** and **P(C6-MAc-BP)**, respectively. This simultaneous rise in DF lifetime and PLQY (see **Figure 4.12**) with dilution in PS can be explained by the aforementioned nonradiative, DET-based triplet quenching process (see **Figure 1.8**) competing with the RISC,^[54] which is suppressed upon decreasing the emitter content in the blended films.

Despite a small $\Delta E_{\alpha,SS}^{TADF}$ of 28.9 meV similar to the other materials in highly diluted film state (see **Figure 4.11**), the fully conjugated polymer **P(Ph-MAc-BP)** shows a significantly smaller DF contribution to the overall emission. Furthermore, τ_{DF} rises from 1.64 μs to 5.52 μs between the pristine and the 10 wt% blended film. It has to be noted that the determined DF lifetimes are less reliable and furthermore an artifact was observed in the decay curves (see **Figure 4.15d**), which is described in detail in Appendix 4.5.3. The even longer DF lifetimes of **P(Ph-MAc-BP)** compared to the other TADF materials can be assigned to the increased conjugation extending across two donor moieties. The longer DF lifetimes of **P(Ph-MAc-BP)** indicate a lower RISC rate from the triplet to the radiative singlet excited state in comparison to the other TADF materials. This lower RISC rate competing with nonradiative processes like vibronic relaxation leads to a lower DF contribution and the long triplet excited state lifetimes further facilitate quenching processes like TTA, that depend on the triplet exciton concentration.^[126]

Table 4.4. PLQY and lifetimes of PF and DF of blended films of **Tol-MAc-BP**, **P(C2-MAc-BP)**, **P(C6-MAc-BP)** and **P(Ph-MAc-BP)** in PS in N₂ atmosphere.

Compound	100 %	75 %	50 %	25 %	10 %
	$\tau_{PF}^a / \tau_{DF}^a / \Phi_{PL}^b$	$\tau_{PF}^a / \tau_{DF}^a / \Phi_{PL}^b$	$\tau_{PF}^a / \tau_{DF}^a / \Phi_{PL}^b$	$\tau_{PF}^a / \tau_{DF}^a / \Phi_{PL}^b$	$\tau_{PF}^a / \tau_{DF}^a / \Phi_{PL}^b$
	[ns]/ [μs]/ -	[ns]/ [μs]/ -	[ns]/ [μs]/ -	[ns]/ [μs]/ -	[ns]/ [μs]/ -
Tol-MAc-BP	32.2/ 1.67/ 0.79	24.9/ 2.05/ 0.95	27.9/ 2.82/ 0.90	27.9/ 3.06/ 1.00	34.1/ 3.30/ 1.00
P(C2-MAc-BP)	16.2/ 1.30/ 0.35	22.0/ 1.55/ 0.52	31.6/ 1.71/ 0.56	28.4/ 2.62/ 0.83	31.8/ 2.68/ 0.92
P(C6-MAc-BP)	18.8/ 1.33/ 0.49	24.4/ 1.51/ 0.64	26.0/ 1.95/ 0.70	27.6/ 2.88/ 0.82	25.6/ 2.76/ 0.94
P(Ph-MAc-BP)	16.1/ 1.65 ^c / 0.23	17.6/ 4.44 ^{c,d} / 0.31	17.7/ 5.57 ^c / 0.33	21.3/ 3.84 ^{c,d} / 0.45	23.0/ 5.52 ^c / 0.55

^aAverage lifetimes based on biexponential fit calculated via the following equation: $\tau_{av} = \Sigma A_i \tau_i^2 / \Sigma A_i \tau_i$. ^b $\Delta \Phi_{PL} = \pm 0.05$.^[127]
^cLifetimes based on monoexponential fit. ^dFit with R² between 0.8 and 0.9.

While the pronounced triplet excited state quenching was identified to be the main reason for the low PLQYs at high emitter content, an increase of the PF lifetimes upon blending indicates an influence of the blending ratio also on the singlet excited states. In contrast to **Tol-MAc-BP**, an increase in PF lifetime from pristine to blended films with raising PS:guest ratio was observed for all TADF polymers (see **Figure 4.15f**). Whereas τ_{PF} of **P(Ph-MAc-BP)** rises slightly and steadily from 16.1 ns in pristine film to 23.0 ns in 1:9 dilution, **P(C2-MAc-BP)** and **P(C6-MAc-BP)** display a steeper increase from 16.2 ns and 18.8 ns in pristine films to 31.6 ns and 26.0 ns in 1:1 blended films. Furthermore, the nonconjugated polymers exhibit a more or less constant PF lifetime at dilutions of 1:1 and higher. The increase in PF lifetime with dilution observed for the TADF polymers can be attributed to the suppression of nonradiative singlet exciton processes: According to literature, this singlet exciton quenching most likely stems from an electronic stabilization of the excited state based on the high dipole moment of the TADF materials in comparison to the host.^[52] The high polarizability of the surrounding TADF units at high emitter content leads to a decrease in excited state energy, which can be observed as spectral shift of the PL emission depending on the PS:guest ratio (see **Figure 4.14**). Based on the energy gap law described earlier when discussing solvatochromism (see section 4.1), the

small optical gap leads to a higher overlap of the vibronic wave functions, which promotes the nonradiative singlet excited state processes (IC and ISC) explaining the decrease in PF lifetime.

The direct comparison of the decay curves of films with 1:9 blending ratio (see **Figure 4.16**) indicates that the photophysical properties of the nonconjugated polymers **P(C2-MAc-BP)** and **P(C6-MAc-BP)** become very similar to the small molecule **Tol-MAc-BP** at high dilution. This shows that quenching processes can be suppressed almost completely by decreasing the emitter content in the blends. No significant difference based on the length of the alkyl linker can be observed between the decay curves of **P(C2-MAc-BP)** and **P(C6-MAc-BP)** at dilutions of 1:3 as well as 1:9. This observation is in agreement with the PLQY results and shows that intrachain quenching between neighboring TADF units is not significantly influenced by the length of the alkyl linker at high dilution or plays a minor role in comparison to interchain quenching.

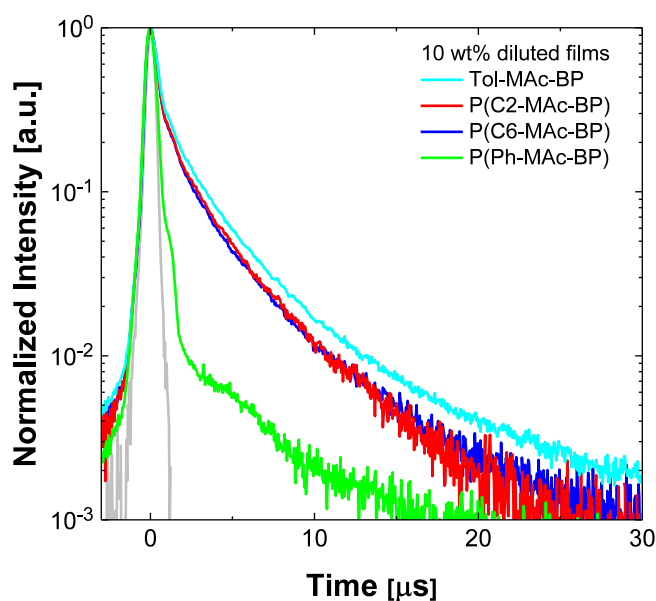


Figure 4.16. Normalized transient PL curves of 10 wt% films of **Tol-MAc-BP** (cyan), **P(C2-MAc-BP)** (red), **P(C6-MAc-BP)** (blue) and **P(Ph-MAc-BP)** (green) with PS as a host ($\lambda_{exc} = 400$ nm).

Before the temperature-dependent TRPL characterization of the films with 10 % emitter content, the excitation power dependence of the DF was measured. This experiment enables it to identify if the DF stems from TADF, TTA or if both upconversion mechanisms take place. Due to fact that TTA is a bimolecular process, it is characterized by a quadratic dependence of the DF intensity at low laser powers.^[128,129] In contrast, TADF is based on a monomolecular process resulting in a slope of unity over the whole range of excitation powers. For this measurement, the DF emission was recorded with a delay of 1 μs (see **Figure 4.17**).

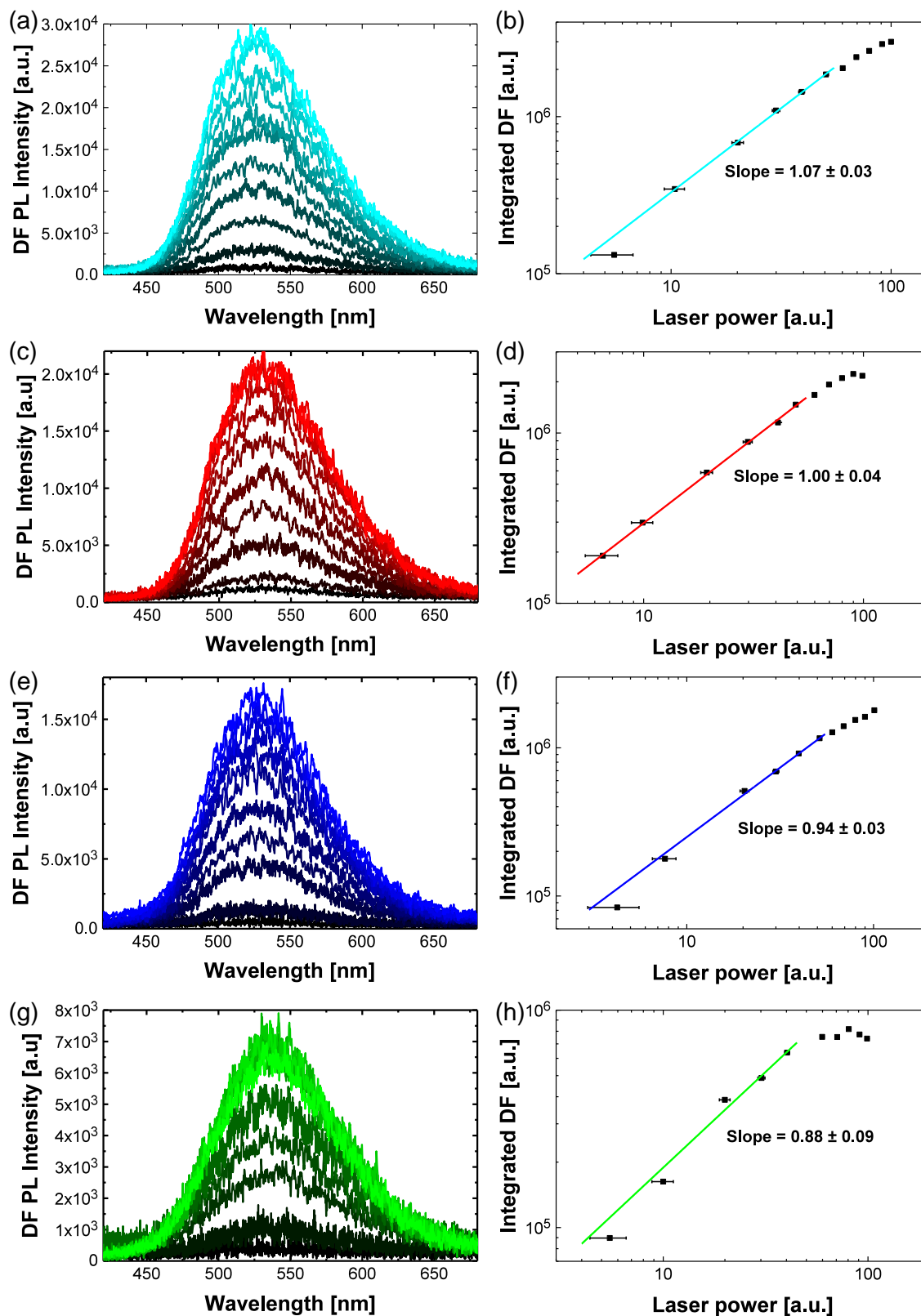


Figure 4.17. Power dependence of the delayed fluorescence in blended films of 10 wt% in PS ($\lambda_{exc} = 400$ nm): DF spectra with increasing laser power and linear fit of log-log plot of DF intensity as a function of excitation power of (a, b) Tol-Mac-BP (black \rightarrow cyan), (c, d) P(C2-Mac-BP) (black \rightarrow red), (e, f) P(C6-Mac-BP) (black \rightarrow blue) and (g, h) P(Ph-Mac-BP) (black \rightarrow green). The laser power in (b), (d), (f) and (h) is plotted in arbitrary units because the excitation laser light also contained laser light of 800 nm passing through the frequency doubling crystal.

None of the TADF materials in the blended films showed any change in spectral line shape of the DF emission within the range of excitation laser power used indicating no additional emissive species occurring. Linear proportionalities between the logarithms of the integrated DF and the excitation power with slopes around unity for all the materials and over the whole power range indicate a single photon upconversion process proving TADF as the main origin of the DF. The decrease in PL intensity at high laser powers for all materials can be attributed to irreversible bleaching of the sample. This bleaching was visible to the naked eye after the measurement upon excitation with a UV lamp showing a stronger emission of the film surrounding the bleached spot.

In order to compare the nonconjugated polymers **P(C2-MAc-BP)** and **P(C6-MAc-BP)** with the small molecule reference **Tol-MAc-BP**, transient PL spectra of films of 10 wt% emitter content in PS were measured as a function of temperature (**Figure 4.18a-c**). In contrast to the transient PL decay curves of pristine films (see Appendix 4.5.4; **Figure A4.15** and **Figure A4.16**), which did not show any significant change in DF intensity at different temperatures, the DF intensity in films of the diluted chromophores clearly decreases upon cooling. The observed decrease of the DF intensity at lower temperatures is based on the reduction in thermal energy responsible for RISC and therefore expected for a TADF emitter. Furthermore, the DF remained apparent at 10 K for all materials in the 1:9 polymer blends, consistent with a small ΔE_{ST} .

Fitting the PF and DF decays for the 10 wt% diluted films was achieved with two decay times each (see Appendix 4.5; fits are shown in **Figure A4.14** and parameters are summarized in **Table A4.2**), which enables the determination of the Φ_{DF}/Φ_{PF} ratio as well as the ΔE_a^{TADF} . By using **Equation 24**, the ratio between DF and PF can be calculated from the decay curves showing a significantly higher DF contribution to the PL emission than determined in the steady state measurements (2 wt% in PS, see **Table 4.2**). The Φ_{DF}/Φ_{PF} values of **Tol-MAc-BP** and **P(C6-MAc-BP)** are similar to one another with 2.06 and 2.03, respectively and an even higher ratio of 3.36 was obtained for **P(C2-MAc-BP)**. The ratio determined for **P(C2-MAc-BP)** seems to be an overestimation because it does not reflect the previous results showing a slightly higher DF contribution from **Tol-MAc-BP** (see **Figure 4.16**).

Nonetheless, the difference to the steady state measurements films of 2 wt% emitter content in PS, in which it is not possible to distinguish between DF and PF and a triplet state quenching by oxygen had to be assumed, is more than a factor two. This indicates that triplet quenching in ambient conditions in these previous experiments was incomplete making them less reliable (see **Figure 4.7**). The high DF contribution to the PL reflects the strongly promoted RISC process due to the small ΔE_{ST} .

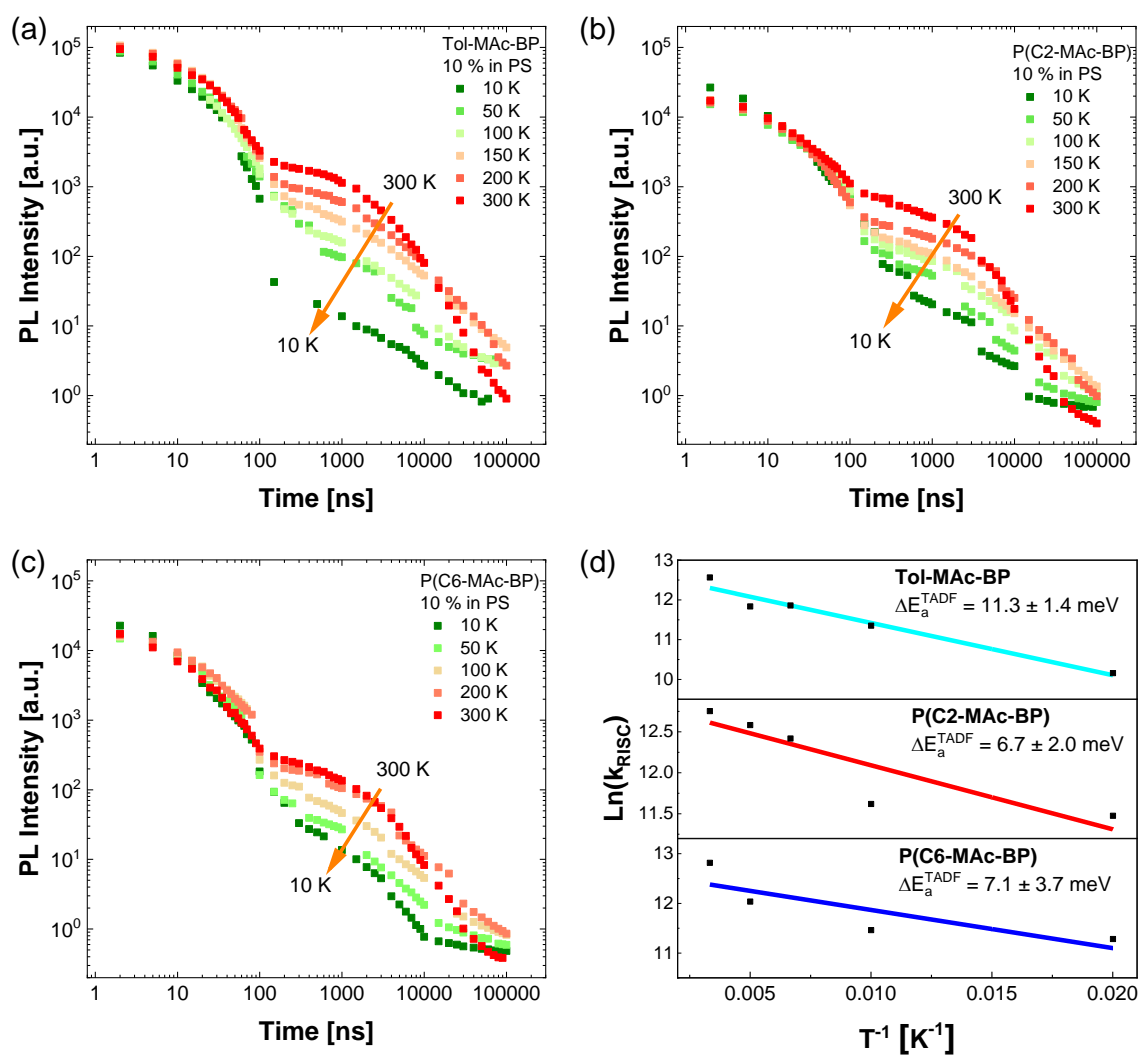


Figure 4.18. Transient PL decay curves of films of 10 % blending ratio in PS of (a) Tol-Mac-BP, (b) P(C2-Mac-BP) and (c) P(C6-Mac-BP) at different temperatures in He atmosphere. (d) Arrhenius plot of the RISC rate of Tol-Mac-BP, P(C2-Mac-BP) and P(C6-Mac-BP) derived from a-c and fitted with a straight line.

While the estimation of the ΔE_{ST} in steady state was based on the assumption that the increase in PL intensity stems solely from the DF and that the DF is fully quenched by oxygen in the PS:guest blend, in transient PL measurements it is possible to directly distinguish between PF and DF. For the determination of the activation energy for TADF, the natural logarithm of the RISC rate (k_{RISC}) is plotted against the reciprocal temperature (see **Figure 4.18d**) using a modified version of **Equation 19**:

$$\ln(k_{RISC}) = \frac{-E_a^{TADF}}{k_B} \cdot \frac{1}{T} \quad (25)$$

k_{RISC} can be calculated using

$$k_{RISC} = \frac{k_{PF}k_{DF}\Phi_{DF}}{k_{ISC}\Phi_{PF}}, \quad (26)$$

where k_{PF} , k_{DF} and k_{ISC} are the rate constants of PF, DF and ISC. k_{ISC} was derived from

$$k_{ISC} = \frac{k_r}{\Phi_{PF}} - k_r - k_{IC} \quad (27)$$

where k_{IC} is the IC rate constant. The equations and calculated rate constants are shown in detail in Appendix 4.5.5. The TADF activation energy for **Tol-MAc-BP**, **P(C2-MAc-BP)** and **P(C6-MAc-BP)** derived from the transient PL curves range from 6.7 meV to 11.3 meV and are in good agreement with the computational results ($\Delta E_{ST} = 6-10$ meV; **Table 3.1**) while being lower than the activation energy determined in the rough estimation performed in steady state ($\Delta E_{a,SS}^{TADF} = 15.0 - 61.3$ meV; **Figure 4.11**). The low $\Delta E_{a,TRPL}^{TADF}$ values determined for **P(C2-MAc-BP)** and **P(C6-MAc-BP)** reveal that the energy difference between the singlet and triplet excited states, which is the crucially important for efficiency of the TADF, was not influenced upon polymerization using a nonconjugated alkyl linker.

4.4. Conclusion

In summary, in this chapter the photophysical properties of **Tol-MAc-BP**, **P(C2-MAc-BP)**, **P(C6-MAc-BP)** and **P(Ph-MAc-BP)** and their hexyl substituted counterparts **Tol-HAc-BP**, **P(C2-HAc-BP)**, **P(C6-HAc-BP)** and **P(Ph-HAc-BP)** were investigated. All materials showed an almost identical yellowish-green PL emission with a maximum at 535 nm in pristine film when excited

in the $\pi \rightarrow \pi^*$ and direct CT excitation identified in absorption spectroscopy in solution and film state. Both sets of materials exhibit positive solvatochromism with **Tol-MAc-BP**, **P(C2-MAc-BP)**, **P(C6-MAc-BP)**, **P(Ph-MAc-BP)** and **Tol-HAc-BP** showing no change in CT characteristics of the excited state. Therefore, the linker strategy did not influence the CT characteristics but a decrease bathochromic shift and a second CT emission was observed for the hexyl substituted polymers **P(C2-HAc-BP)**, **P(C6-HAc-BP)**, **P(Ph-HAc-BP)**. The solvatochromism further revealed a strong electronic coupling between the LE and CT states.

Steady state and transient PL spectroscopy showed a dominating concentration quenching effect in pristine film of the DMAC-based materials limiting their PLQY. The concentration quenching of the TADF materials was suppressed upon dilution in PS blends increasing the PLQY by 94 %-163 % going from pristine films to a blending ratio of 1:9. Small ΔE_a^{TADF} values of 28.9 meV for **P(Ph-MAc-BP)** and below 12 meV for **Tol-MAc-BP**, **P(C2-MAc-BP)**, **P(C6-MAc-BP)** were determined, indicating that the low ΔE_{ST} was preserved upon polymerization. The change in PF and DF lifetimes with increasing PS ratio in PS:guest films revealed singlet as well as triplet exciton quenching being the origin of the low PLQY and DF emission in pristine films of **Tol-MAc-BP**, **P(C2-MAc-BP)**, **P(C6-MAc-BP)** and **P(Ph-MAc-BP)**. In 10 wt% films, the nonconjugated linker strategy applied in **P(C2-MAc-BP)** and **P(C6-MAc-BP)** showed excellent PLQY with 0.92 ± 0.05 and 0.94 ± 0.05 similar to the small molecule **Tol-MAc-BP** (1.00 ± 0.05) proving it to be superior to a conjugated linker as in **P(Ph-MAc-BP)** with 0.55 ± 0.05 . Although the PLQY for the longer hexyl linker in **P(C6-MAc-BP)** is higher in low dilution in comparison to **P(C2-MAc-BP)**, this small beneficial effect of the alkyl length becomes insignificant at blending ratios of 1:3 and higher. The efficient TADF and high PLQY values acquired from these materials when embedded in a host are further investigated in their application in OLEDs in chapter 5.

4.5. Appendix of Chapter 4

4.5.1. Contributions to Chapter 4

The temperature dependent TRPL measurements of pristine films were performed by [REDACTED] (Molecular Electronics Department, MPIP Mainz) and Kai Philipps (Molecular Electronics Department, MPIP Mainz). All other steady state and time-resolved photoluminescence as well as AFM measurements of this chapter were performed by Kai Philipps. Experimental results were regularly discussed with Paul Blom (Molecular Electronics Department, MPIP Mainz), Jasper Michels (Molecular Electronics Department, MPIP Mainz), [REDACTED] (Faculty of Science, Vrije Universiteit Amsterdam and Molecular Electronics Department, MPIP Mainz) and [REDACTED] (Molecular Electronics Department, MPIP Mainz).

4.5.2. Figures and Tables

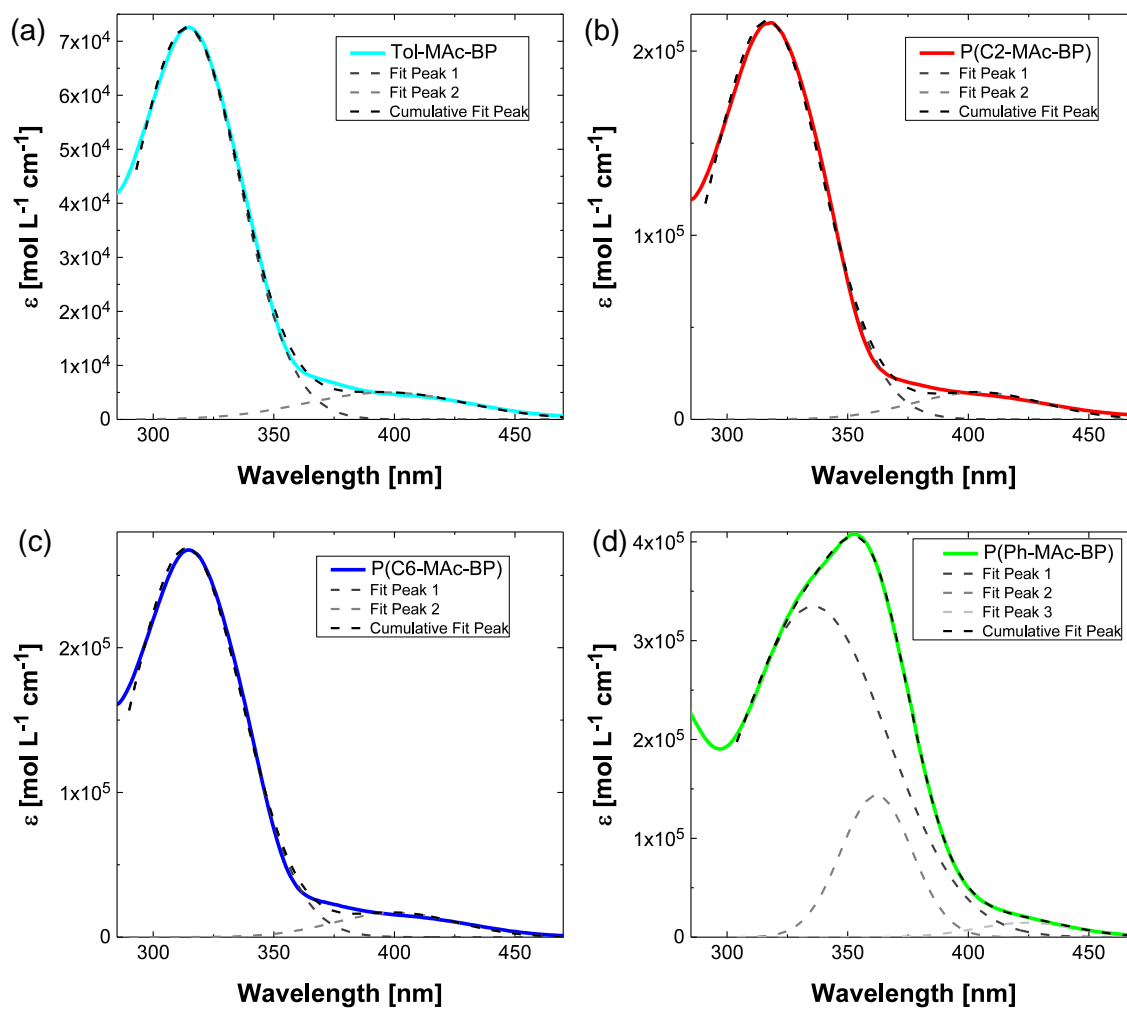


Figure A4.1. Gaussian deconvolution of the molar absorption coefficient spectra of (a) Tol-MAc-BP, (b) P(C2-MAc-P), (c) P(C6-MAc-BP) and (d) P(Ph-MAc-BP) in toluene.

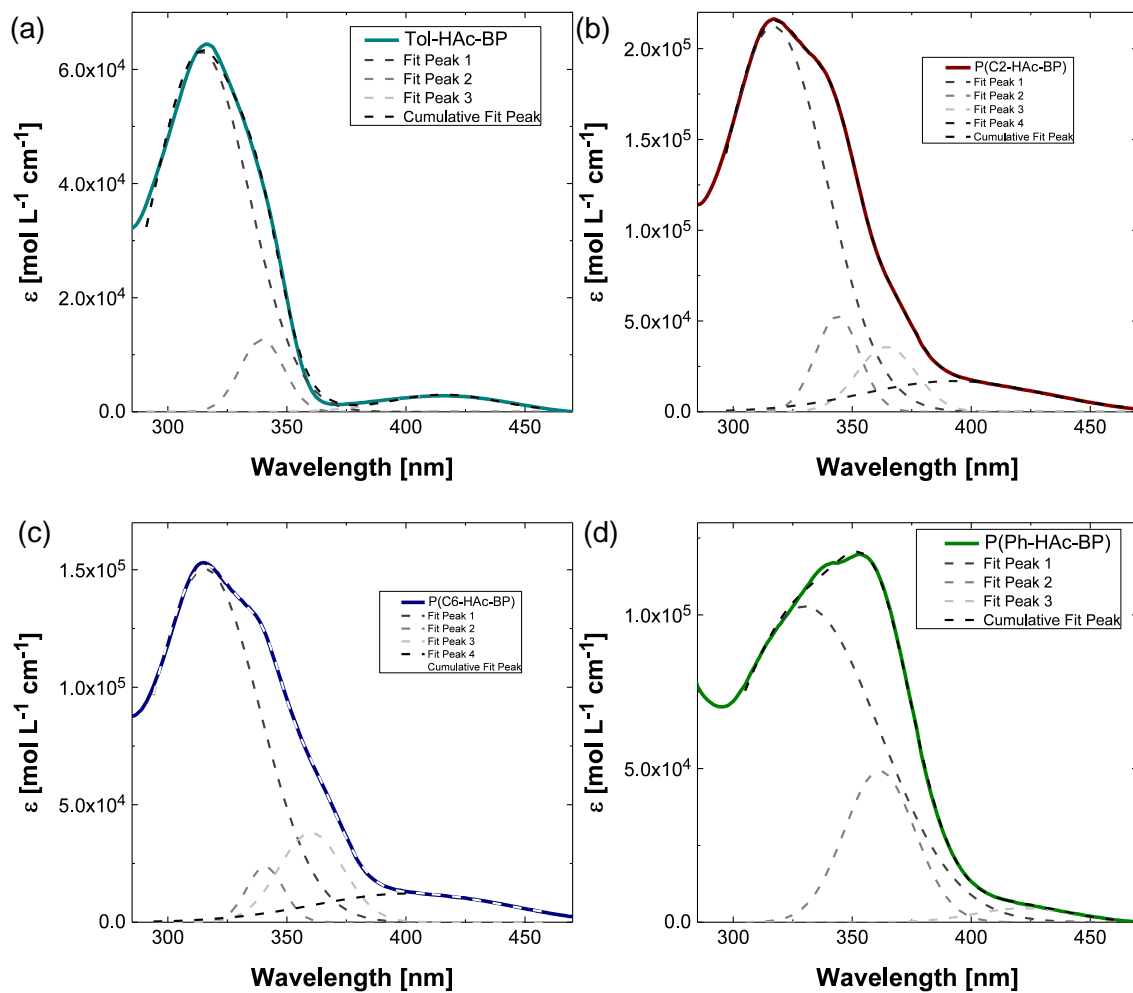


Figure A4.2. Gaussian deconvolution of the molar absorption coefficient spectra of (a) Tol-HAc-BP, (b) P(C2-HAc-BP), (c) P(C6-HAc-BP) and (d) P(Ph-HAc-BP) in toluene.

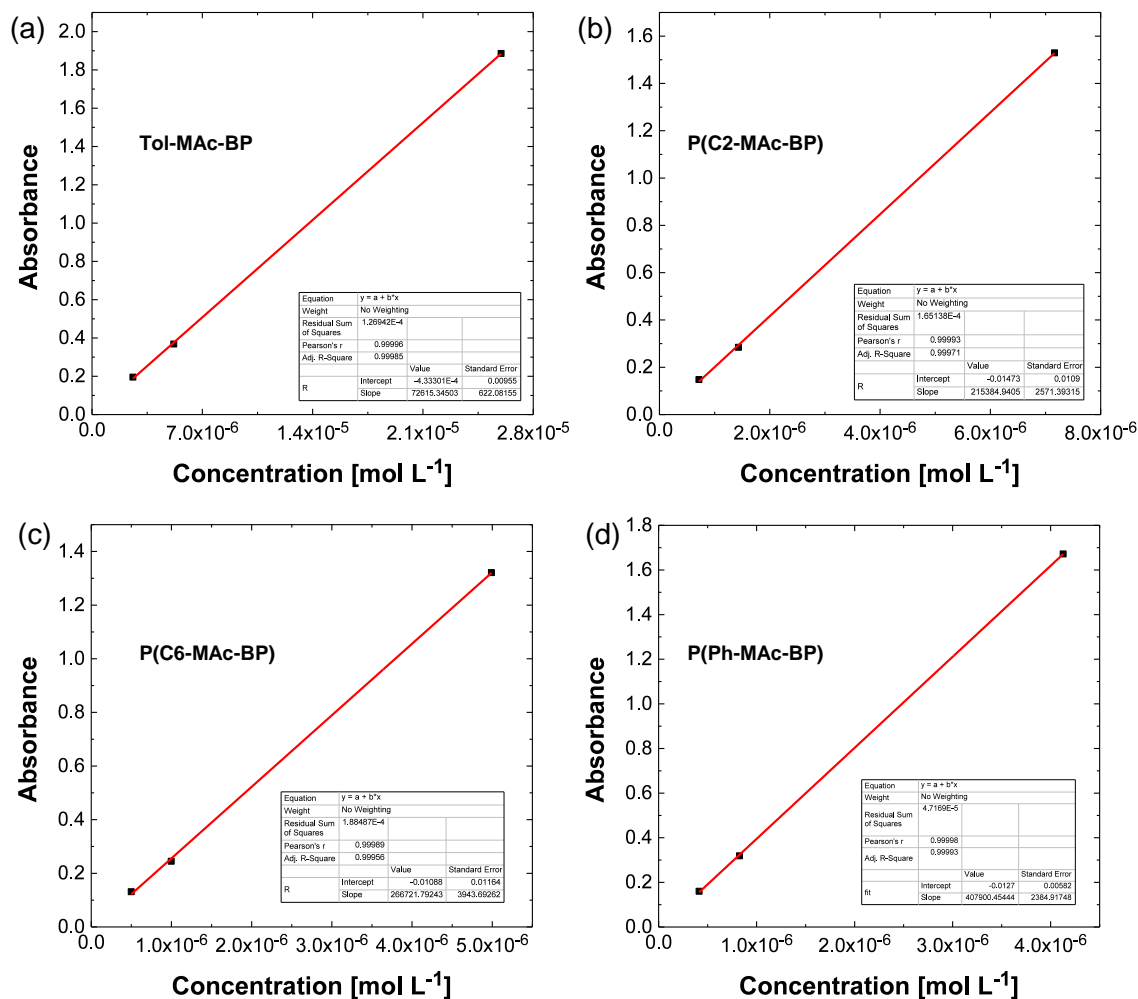


Figure A4.3. Absorbance against concentration plot of absorption maximum of (a) Tol-MAC-BP, (b) P(C2-MAC-BP), (c) P(C6-MAC-BP) and (d) P(Ph-MAC-BP) in toluene fitted with a straight line to obtain the molar absorption coefficient.

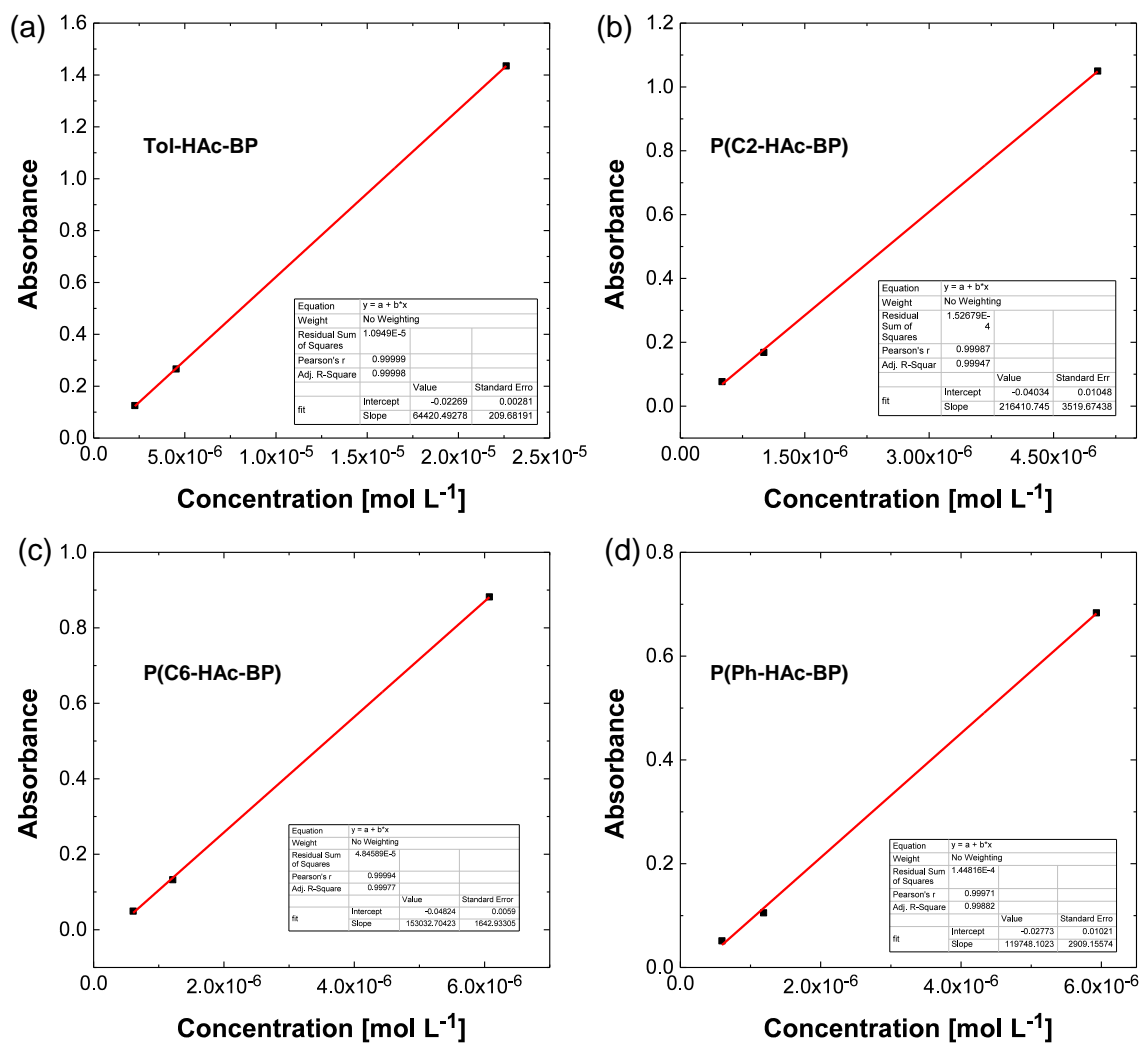


Figure A4.4. Absorbance against concentration plot of absorption maximum of (a) **Tol-HAc-BP**, (b) **P(C2-HAc-BP)**, (c) **P(C6-HAc-BP)** and (d) **P(Ph-HAc-BP)** in toluene fitted with a straight line to obtain the molar absorption coefficient.

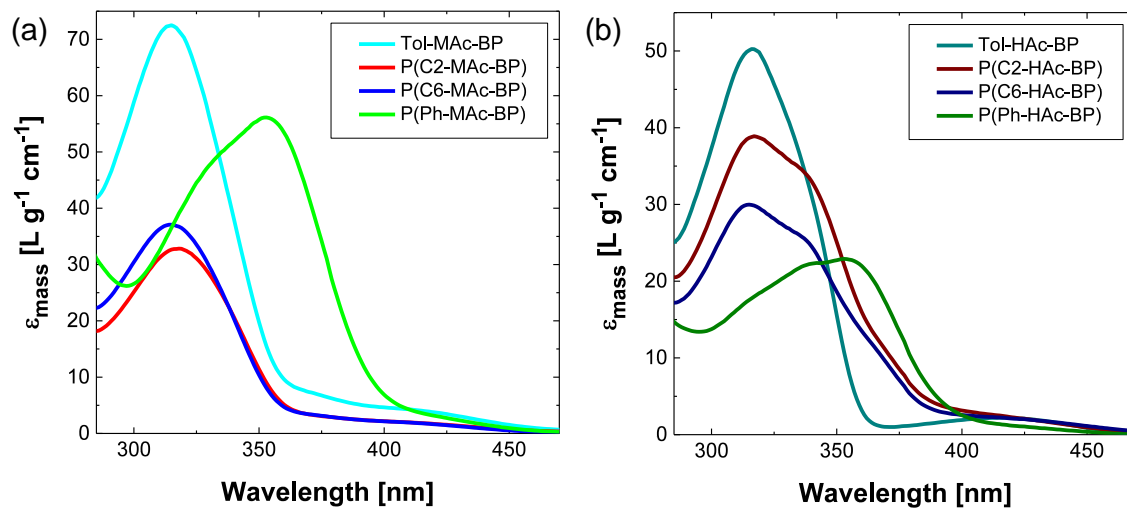


Figure A4.5. Mass absorption coefficient spectra of (a) Tol-MAc-BP, P(C2-MAc-BP), P(C6-MAc-BP) and P(Ph-MAc-BP) as well as (b) Tol-HAc-BP, P(C2-HAc-BP), P(C6-HAc-BP) and P(Ph-HAc-BP) in toluene.

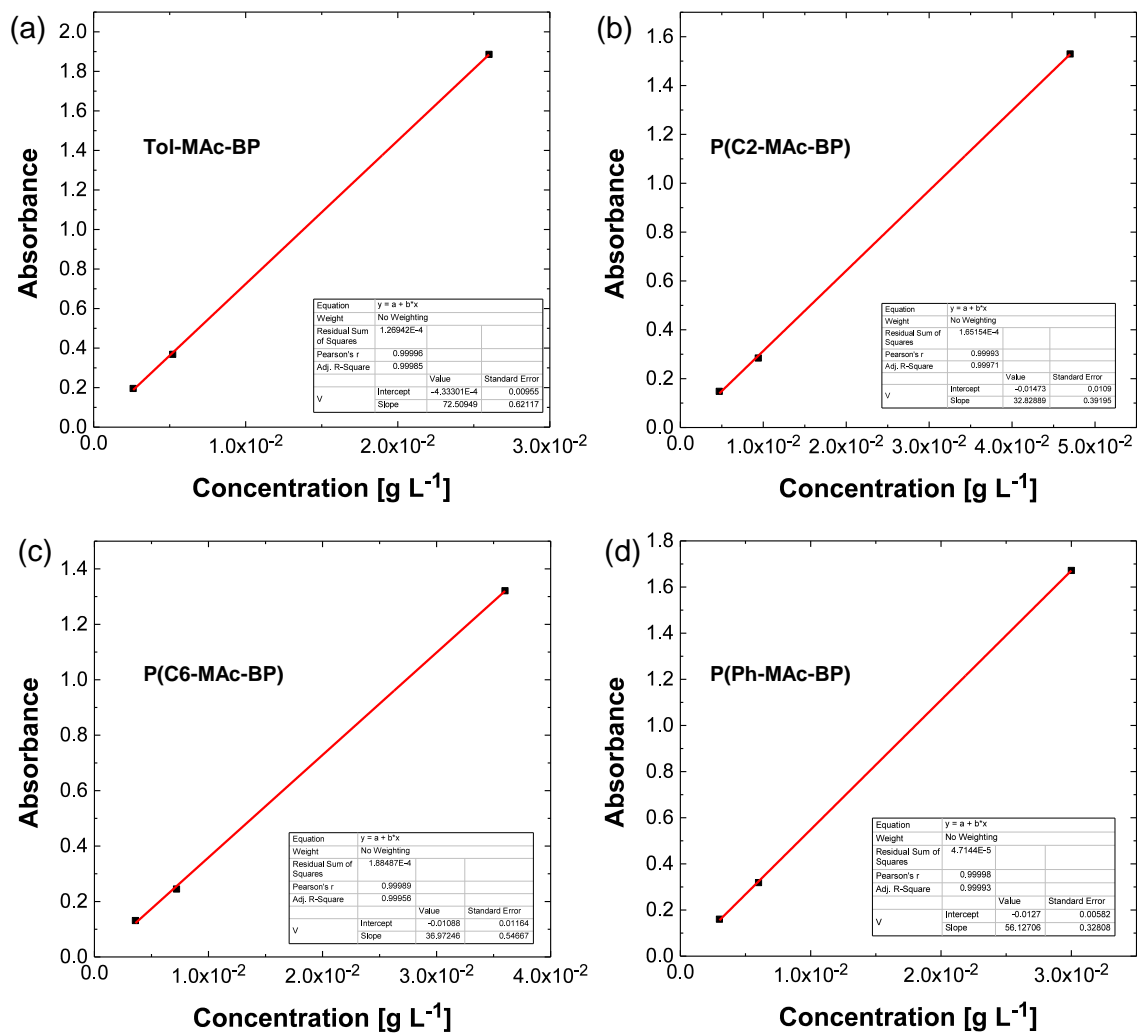


Figure A4.6. Absorbance against mass concentration plot of absorption maximum of (a) **Tol-Mac-BP**, (b) **P(C2-Mac-BP)**, (c) **P(C6-Mac-BP)** and (d) **P(Ph-Mac-BP)** in toluene fitted with a straight line to obtain the mass absorption coefficient.

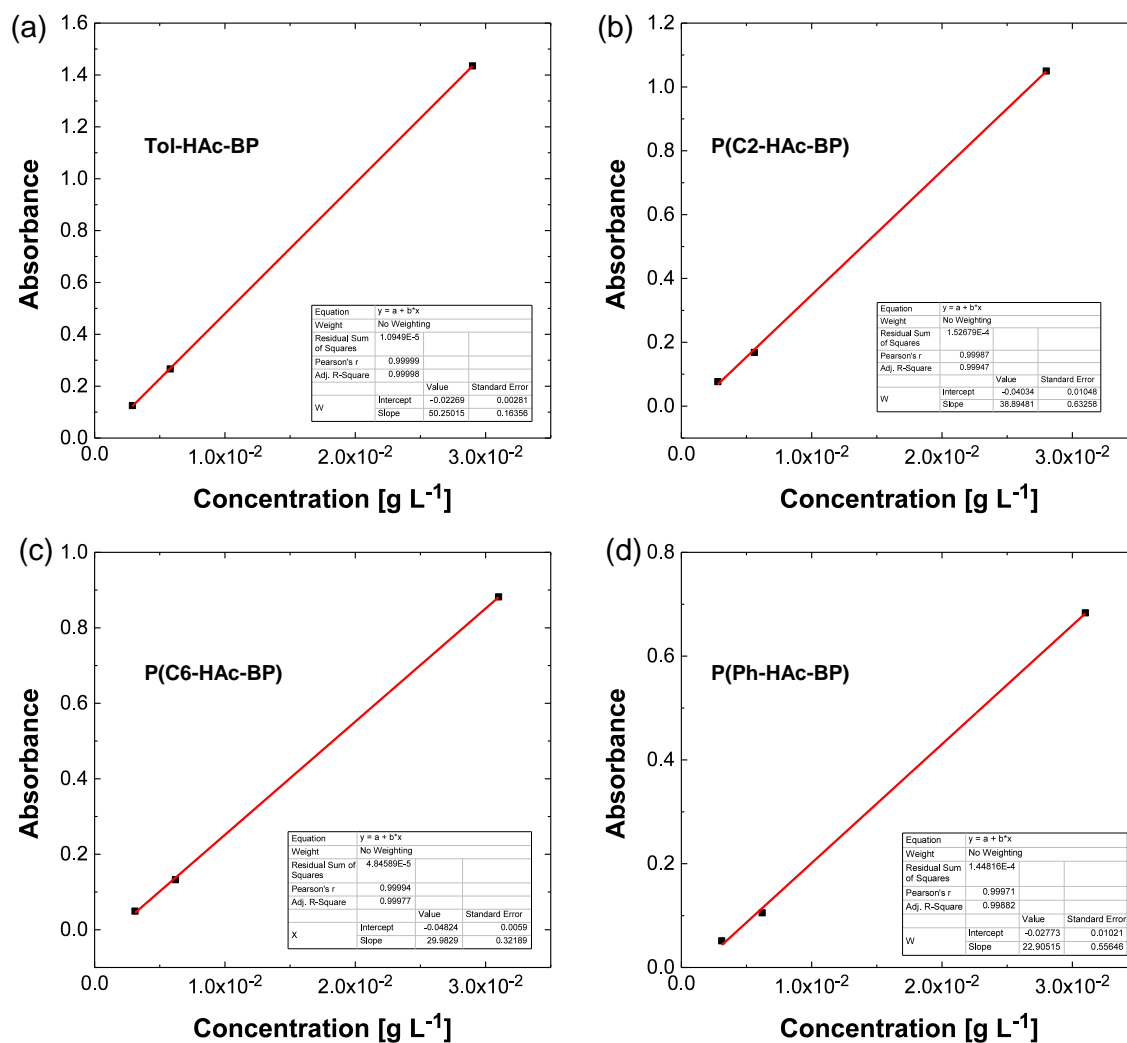


Figure A4.7. Absorbance against mass concentration plot of absorption maximum of (a) **Tol-HAc-BP**, (b) **P(C2-HAc-BP)**, (c) **P(C6-HAc-BP)** and (d) **P(Ph-HAc-BP)** in toluene fitted with a straight line to obtain the mass absorption coefficient.

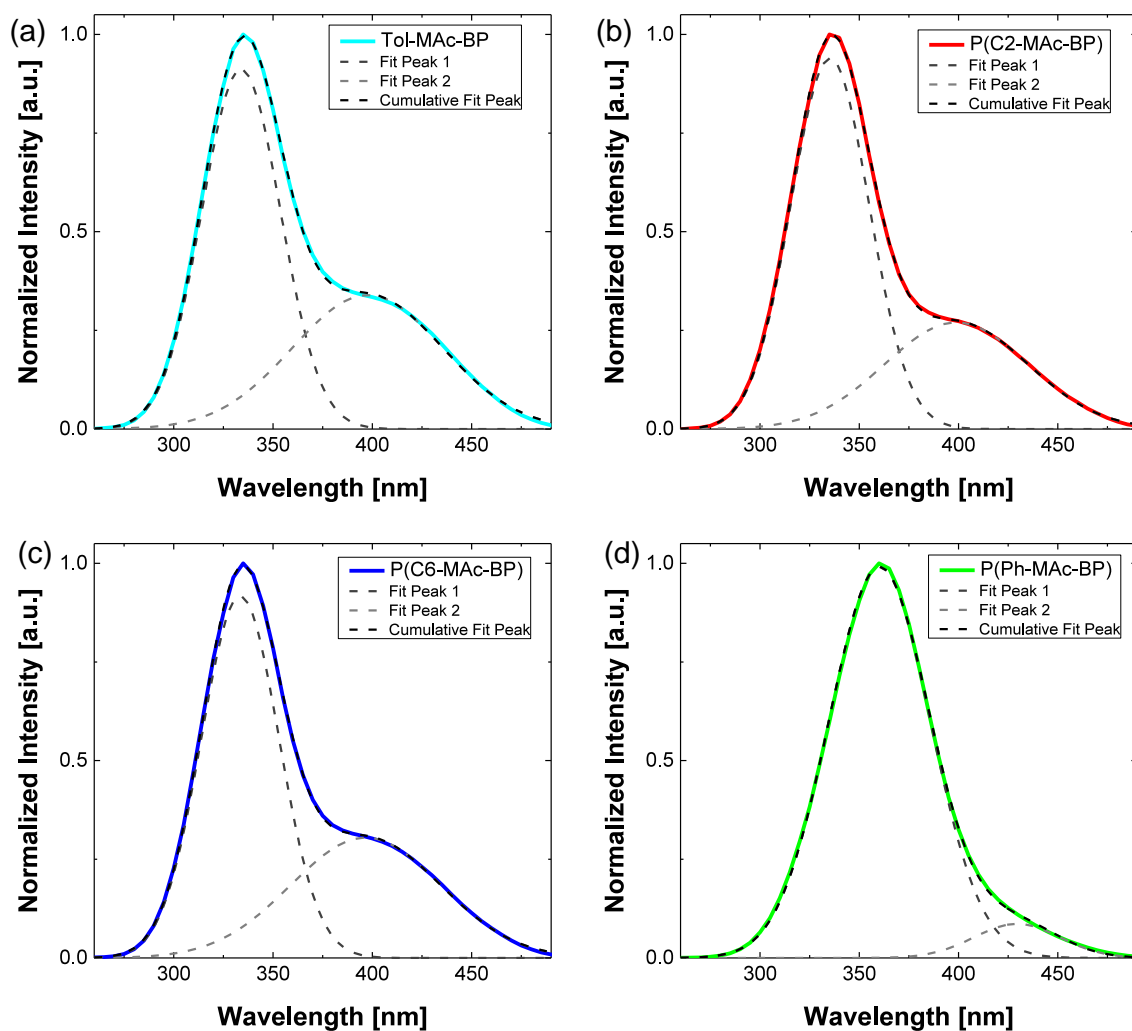


Figure A4.8. Gaussian deconvolution of the excitation spectra of the PL emission maximum at 535 nm of (a) Tol-MAc-BP, (b) P(C2-MAc-BP), (c) P(C6-MAc-BP) and (d) P(Ph-MAc-BP) in toluene.

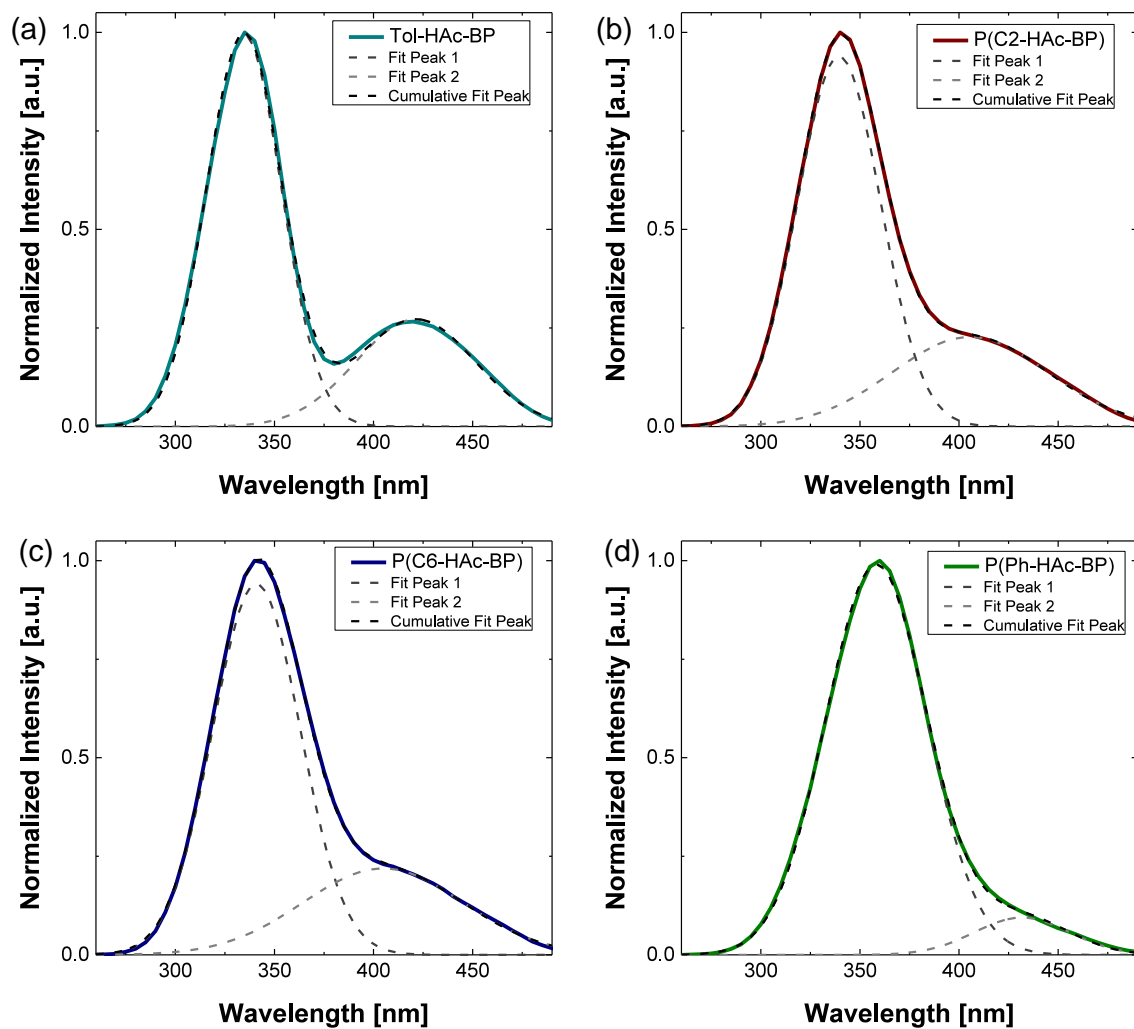


Figure A4.9. Gaussian deconvolution of the excitation spectra of the PL emission maximum at 535 nm of (a) Tol-HAc-BP, (b) P(C2-HAc-BP), (c) P(C6-HAc-BP) and (d) P(Ph-HAc-BP) in toluene.

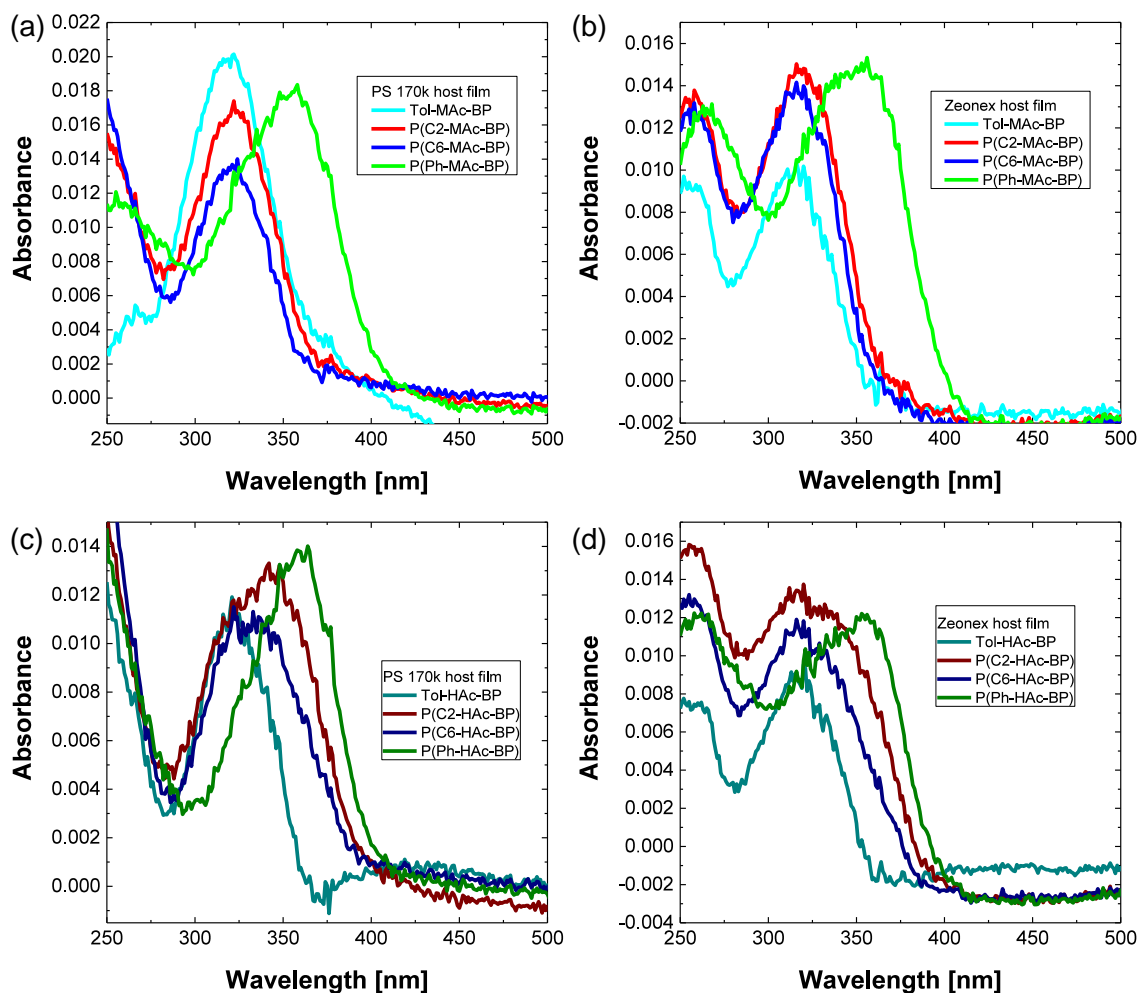


Figure A4.10. Absorption spectra of blended films of **Tol-MAc-BP**, **P(C2-MAc-BP)**, **P(C6-MAc-BP)** and **P(Ph-MAc-BP)** of 2 wt% in (a) PS and (b) Zeonex® 480. Absorption spectra of blended films of **Tol-HAc-BP**, **P(C2-HAc-BP)**, **P(C6-HAc-BP)** and **P(Ph-HAc-BP)** of 2 wt% in (c) PS and (d) Zeonex® 480 on quartz substrate.

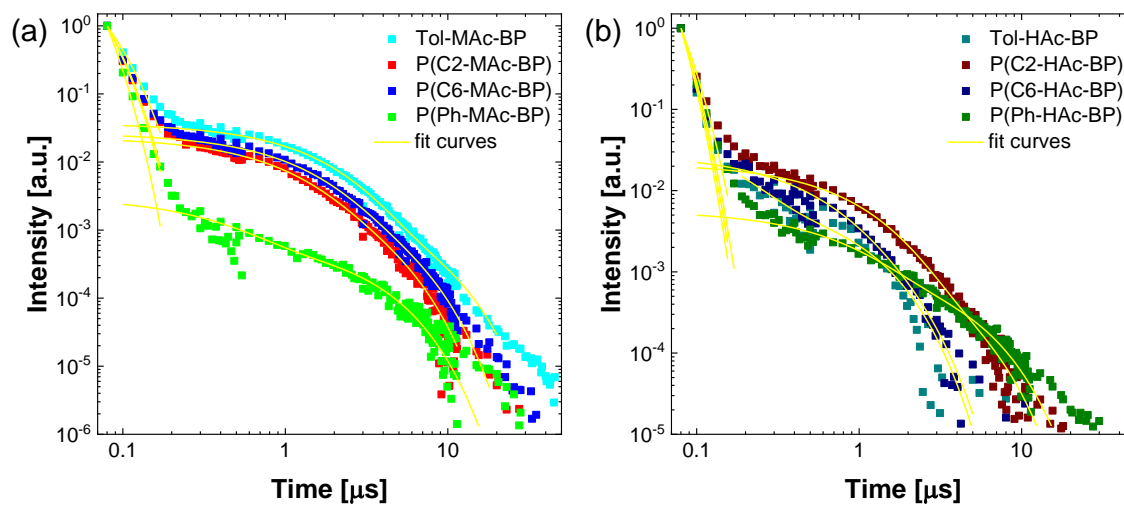


Figure A4.11. Decay curves of pristine films of (a) Tol-MAc-BP, P(C2-MAc-BP), P(C6-MAc-BP) and P(Ph-MAc-BP), as well as (b) Tol-HAc-BP, P(C2-HAc-BP), P(C6-HAc-BP) and P(Ph-HAc-BP) at room temperature ($\lambda_{\text{exc}} = 355 \text{ nm}$) with visualized biexponential fit.

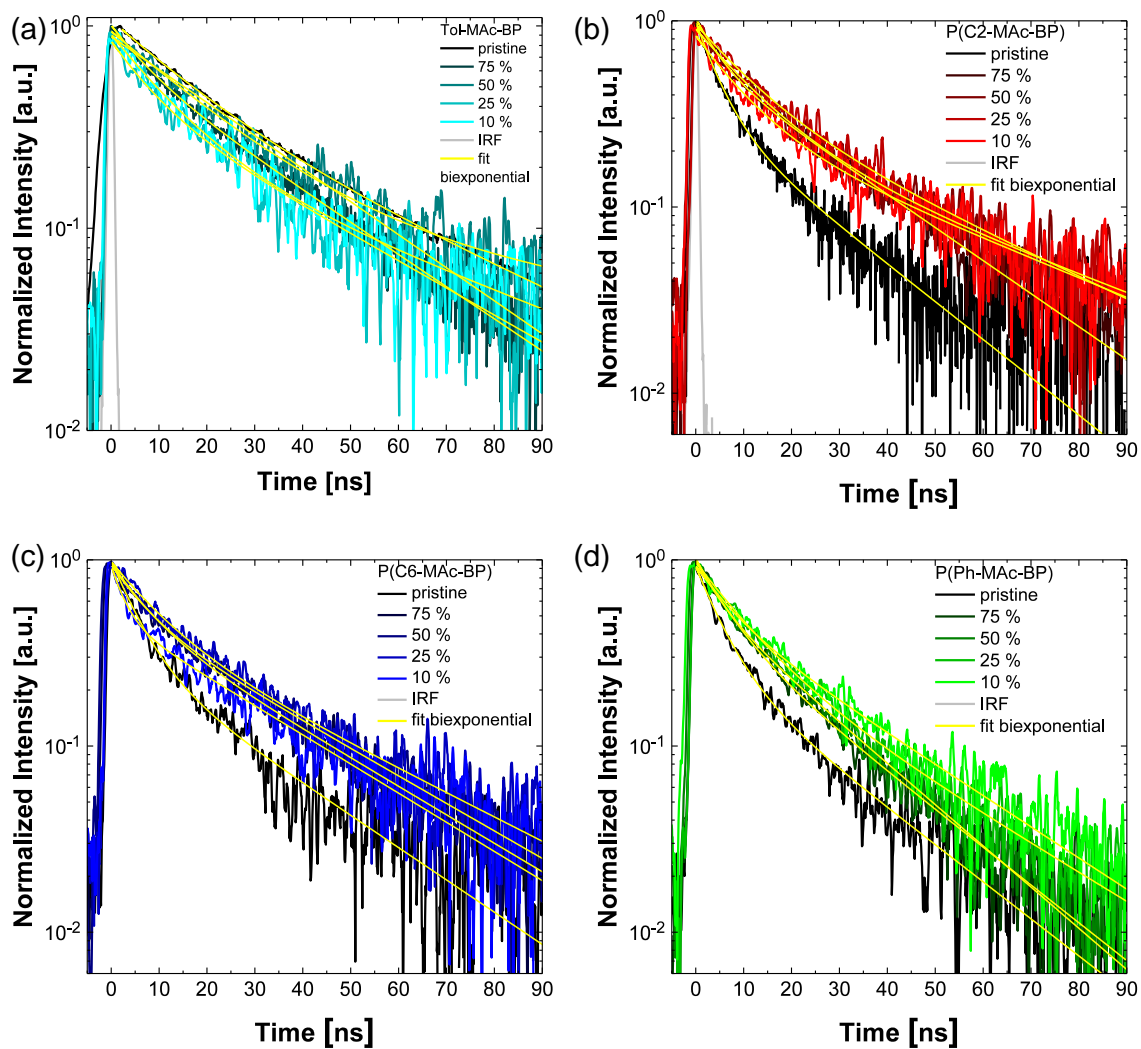


Figure A4.12. Normalized transient PL curves of films of various blending ratios in PS at r.t. in N_2 atmosphere of (a) Tol-Mac-BP, (b) P(C2-Mac-BP), (c) P(C6-Mac-BP) and (d) P(Ph-Mac-BP) in nanosecond scale with visualized biexponential fit.

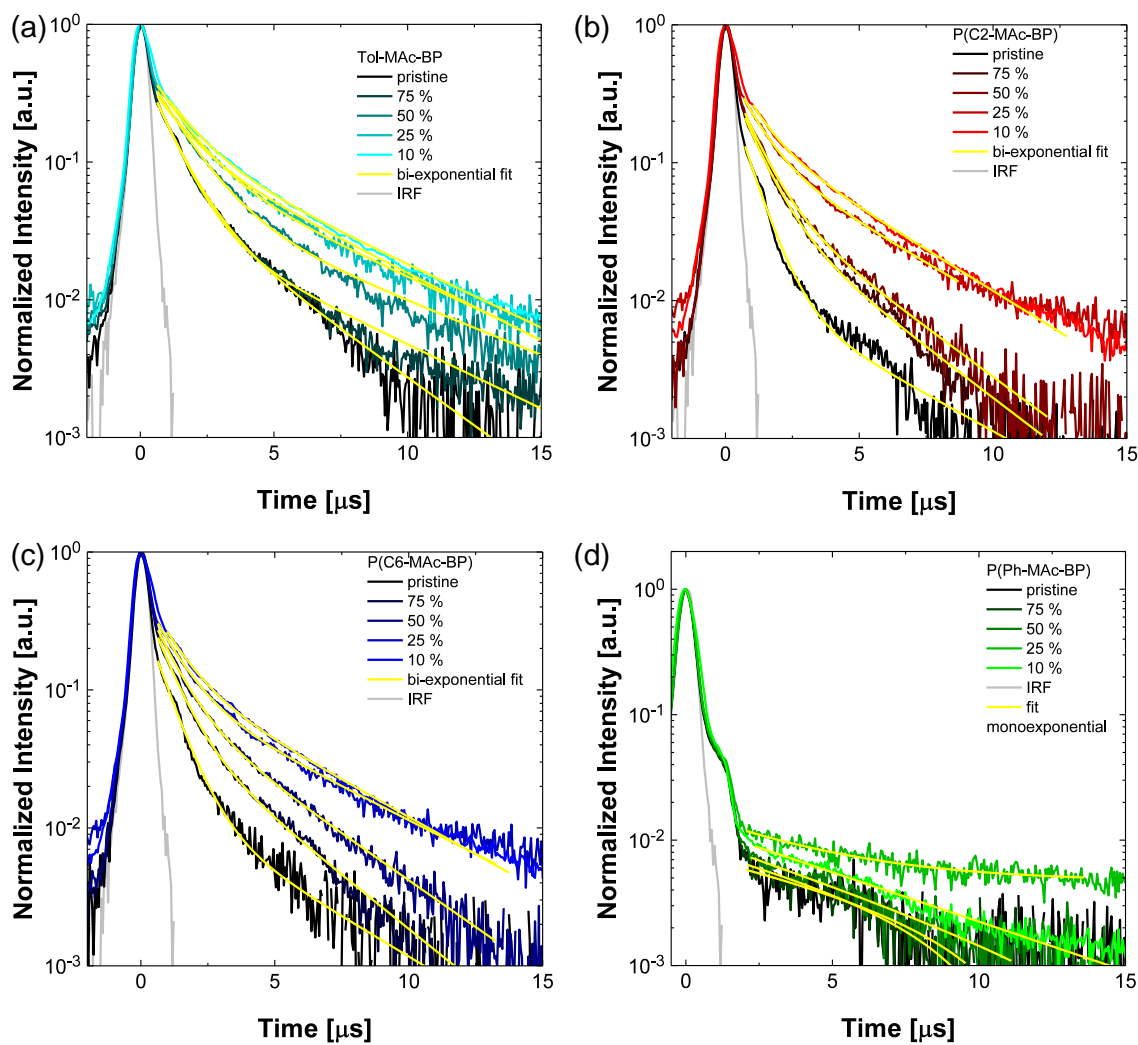


Figure A4.13. Normalized transient PL curves of films of various blending ratios in PS at r.t. in N_2 atmosphere of (a) Tol-MAc-BP, (b) P(C2-MAc-BP), (c) P(C6-MAc-BP) and (d) P(Ph-MAc-BP) in microsecond scale with visualized biexponential fit.

Table A4.1. Parameters of biexponential fits for PF and DF in various blending ratios in PS at r.t. in N₂ atmosphere of Tol-MAc-BP, P(C2-MAc-BP), P(C6-MAc-BP) and P(Ph-MAc-BP) shown in **Figure A4.12** and **Figure A4.13**.

Compound	Blending ratio	A _{1, PF}	τ _{1, PF}	A _{2, PF}	τ _{2, PF}	A _{1, DF}	τ _{1, DF}	A _{2, DF}	τ _{2, DF}
			[ns]		[ns]		[μs]		[μs]
Tol-MAc-BP	100 %	0.63	15.6	0.44	41.2	0.44	0.88	0.07	3.11
	75 %	0.34	7.3	0.67	27.3	0.48	0.90	0.04	4.66
	50 %	0.88	26.6	-	-	0.46	1.22	0.06	5.53
	25 %	0.41	8.0	0.44	32.5	0.45	1.17	0.11	4.88
	10 %	0.65	11.6	0.26	47.6	0.40	1.21	0.15	4.73
P(C2-MAc-BP)	100 %	0.67	4.5	0.32	21.37	0.35	0.69	0.01	4.04
	75 %	0.43	4.8	0.60	24.5	0.40	0.82	0.06	2.94
	50 %	0.64	11.5	0.26	44.5	0.42	0.82	0.08	3.03
	25 %	0.57	10.7	0.39	36.2	0.40	0.88	0.13	3.82
	10 %	0.54	9.1	0.29	41.2	0.41	0.85	0.19	3.62
P(C6-MAc-BP)	100 %	0.68	5.4	0.31	25.1	0.35	0.74	0.02	3.73
	75 %	0.46	7.1	0.50	28.4	0.42	0.77	0.07	2.77
	50 %	0.41	6.6	0.53	29.4	0.41	0.86	0.10	3.20
	25 %	0.52	9.2	0.45	33.4	0.41	0.97	0.11	4.44
	10 %	0.45	2.9	0.49	27.7	0.42	0.97	0.14	4.02
P(Ph-MAc-BP)	100 %	0.63	5.3	0.29	21.8	-	-	-	-
	75 %	0.54	6.4	0.47	21.4	0.01	4.4	-	-
	50 %	0.38	4.8	0.62	19.6	0.01	5.6	-	-
	25 %	0.61	9.7	0.36	28.0	0.01	3.8	-	-
	10 %	0.38	6.9	0.55	25.9	0.01	5.5	-	-

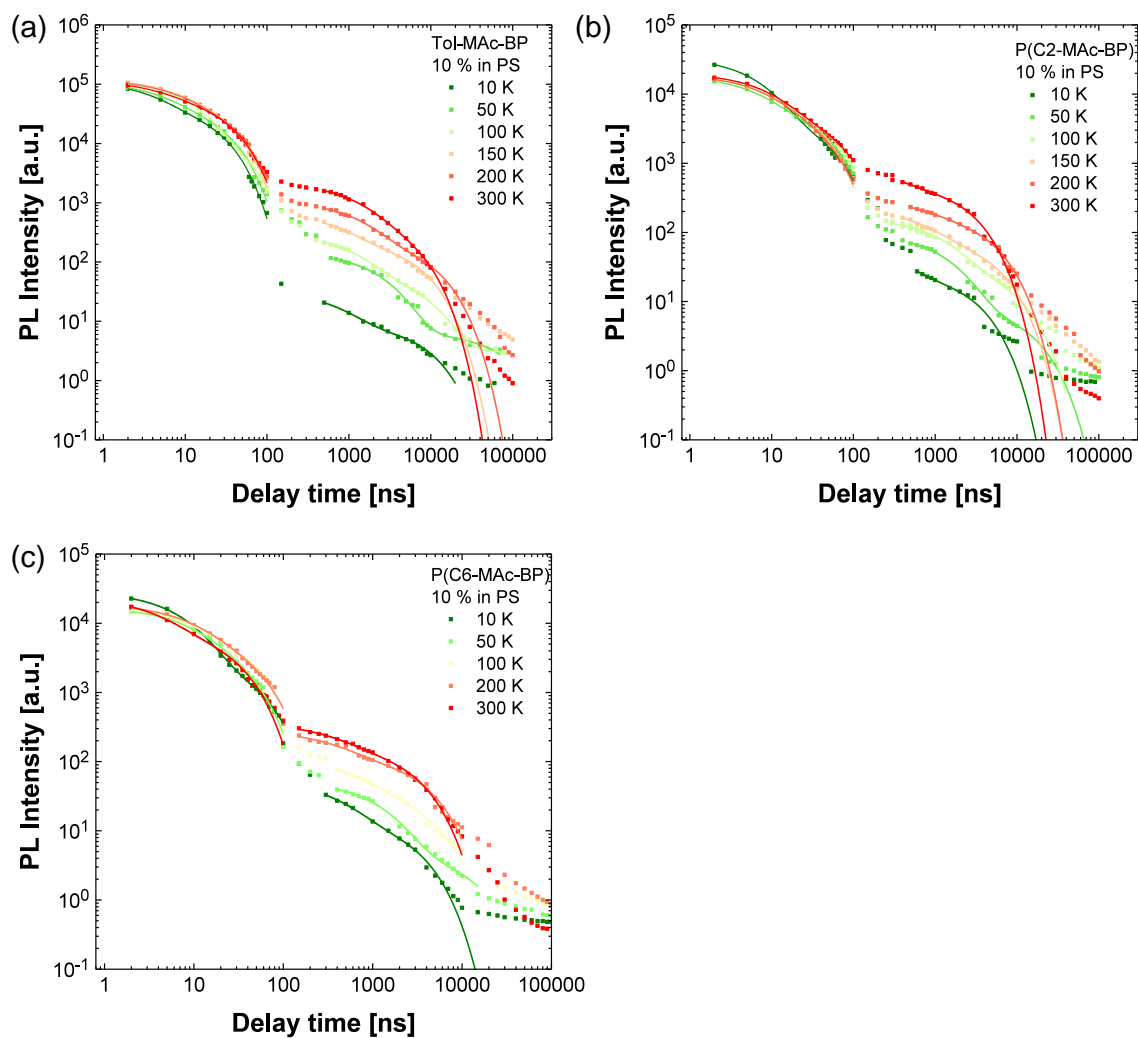


Figure A4.14. Transient PL decay curves of films of 10 % blending ratio in PS of (a) **Tol-MAc-BP**, (b) **P(C2-MAc-BP)** and (c) **P(C6-MAc-BP)** at different temperatures in He atmosphere with visualized biexponential fit.

Table A4.2. Parameters of biexponential fits for PF and DF in 10 wt% blending ratio in PS at various temperatures in He atmosphere of **Tol-MAc-BP**, **P(C2-MAc-BP)** and **P(C6-MAc-BP)** shown in **Figure A4.14**.

Compound	Temperature	$A_{1, PF}$	$\tau_{1, PF}$	$A_{2, PF}$	$\tau_{2, PF}$	$A_{1, DF}$	$\tau_{1, DF}$	$A_{2, DF}$	$\tau_{2, DF}$
		[10 ³]	[ns]	[10 ³]	[ns]		[μ s]		[μ s]
Tol-MAc-BP	10 K	73.0	3.5	46.3	22.4	50	0.32	12	6.53
10 % in PS	50 K	63.9	4.7	49.1	25.9	140	2.35	7	79.8
	100 K	100.4	10.8	16.7	45.1	236	1.06	67	7.45
	150 K	53.0	5.5	75.2	26.4	485	0.71	231	6.61
	200 K	60.7	6.8	60.7	31.0	859	1.26	236	9.69
	300 K	53.9	4.6	64.1	29.4	1582	1.15	627	4.89
P(C2-MAc-BP)	10 K	29.2	6.6	5.2	44.5	42	0.31	25	3.08
10 % in PS	50 K	12.3	6.6	6.5	44.5	88	1.39	9	14.7
	100 K	12.3	7.1	7.2	46.9	130	1.23	33	9.32
	150 K	11.3	6.7	9.7	32.3	146	0.68	86	5.36
	200 K	11.9	7.9	7.4	36.7	129	0.64	189	4.81
	300 K	14493	9.23	5858	58.58	457	0.26	510	2.66
P(C6-MAc-BP)	10 K	26022	7.08	3269	44.98	41	0.39	15	2.78
10 % in PS	50 K	10443	7.98	7107	29.85	49	1.16	5	12.7
	100 K	10523	7.46	8093	37.66	71	0.65	41	4.04
	200 K	12001	8.57	7447	39.26	161	0.37	127	3.54
	300 K	15959	3.75	8506	25.69	198	0.34	175	2.72

4.5.3. Discussion of the Artifact Observed in Figure 4.15d

The fast decay around 2 μ s in **Figure 4.15d** can be ascribed as an artifact of the set-up used based on the fact that this fast decay was not observed in the transient PL decays of pristine films recorded at another set-up (see **Figure A4.15d**). This signal is only visible due to its the small DF intensity of the **P(Ph-MAc-BP)** films. Furthermore, the pristine films of **Tol-MAc-BP**, **P(C2-MAc-BP)** and **P(C6-MAc-BP)** in **Figure 4.15a-c** that also show a low DF intensity at this delay time, exhibit

a small kink in the decay curves at this position showing the low intensity of this artifact in comparison to their exhibited DF.

4.5.4. Temperature-dependent TRPL of the TADF Materials in Pristine Film

The transient PL decay curves of the pristine films are shown in **Figure A4.15** and **Figure A4.16** as a function of temperature.

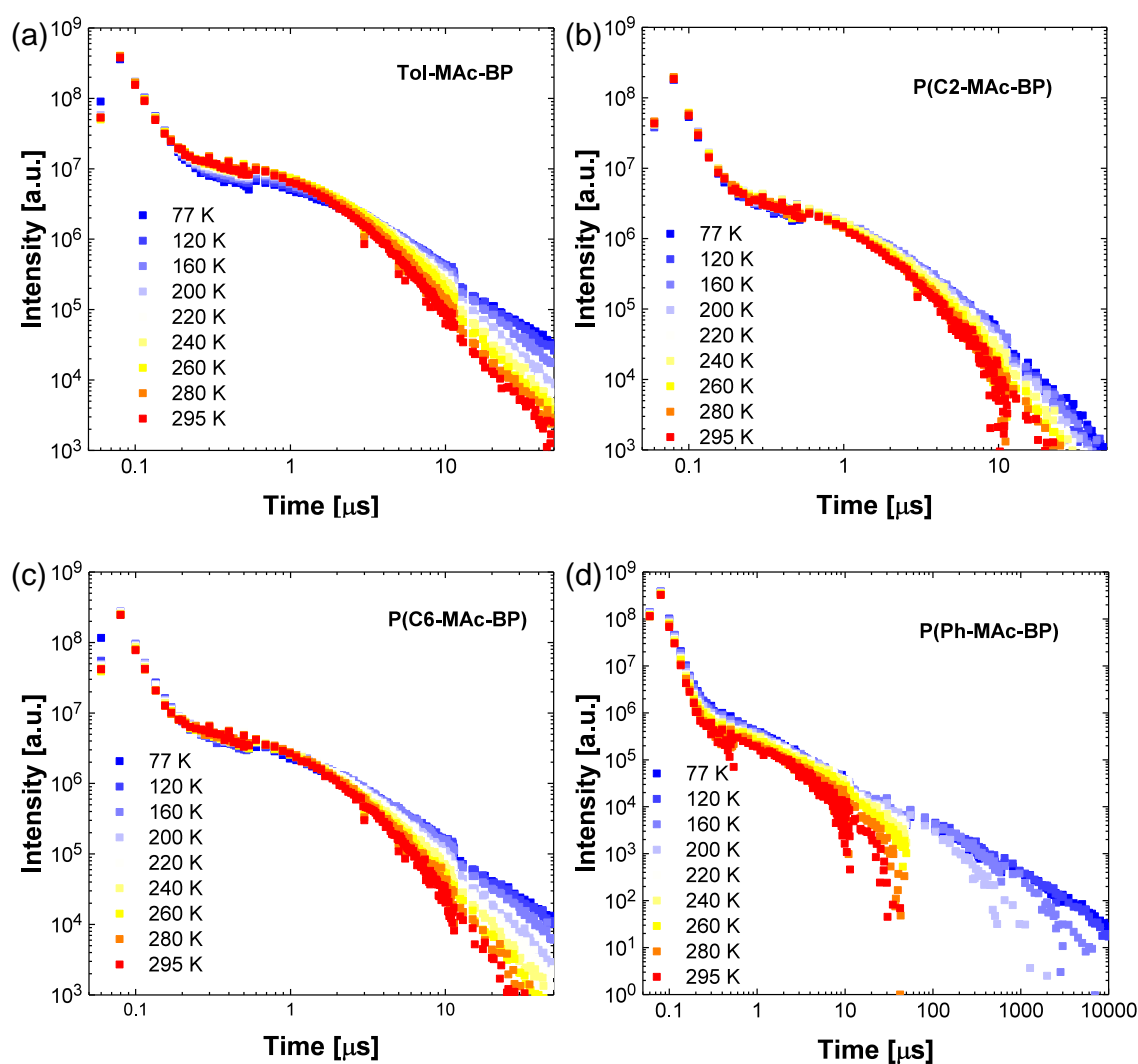


Figure A4.15. Transient PL curves of pristine films of (a) Tol-MAc-BP, (b) P(C2-MAc-BP), (c) P(C6-MAc-BP) and (d) P(Ph-MAc-BP) under vacuum at various temperatures.

All decay curves show only a small to no change in PF intensity as a function of temperature and changes were only observed in the DF region of the plot. In contrast to a TADF emitter not affected by concentration quenching, the DF intensity is not gradually decreasing with lower temperatures.^[24] Furthermore, in cases like **Tol-MAc-BP**, in which a decrease in DF intensity near its maximum can be observed (see **Figure A4.15a**), the change is small and not in orders of magnitude as usually found for TADF emitters without concentration quenching effect. For all pristine films measured, the DF decay curves become less steep with lowering temperature indicating an increase in DF lifetimes based on a reduction of non-radiative decay processes.

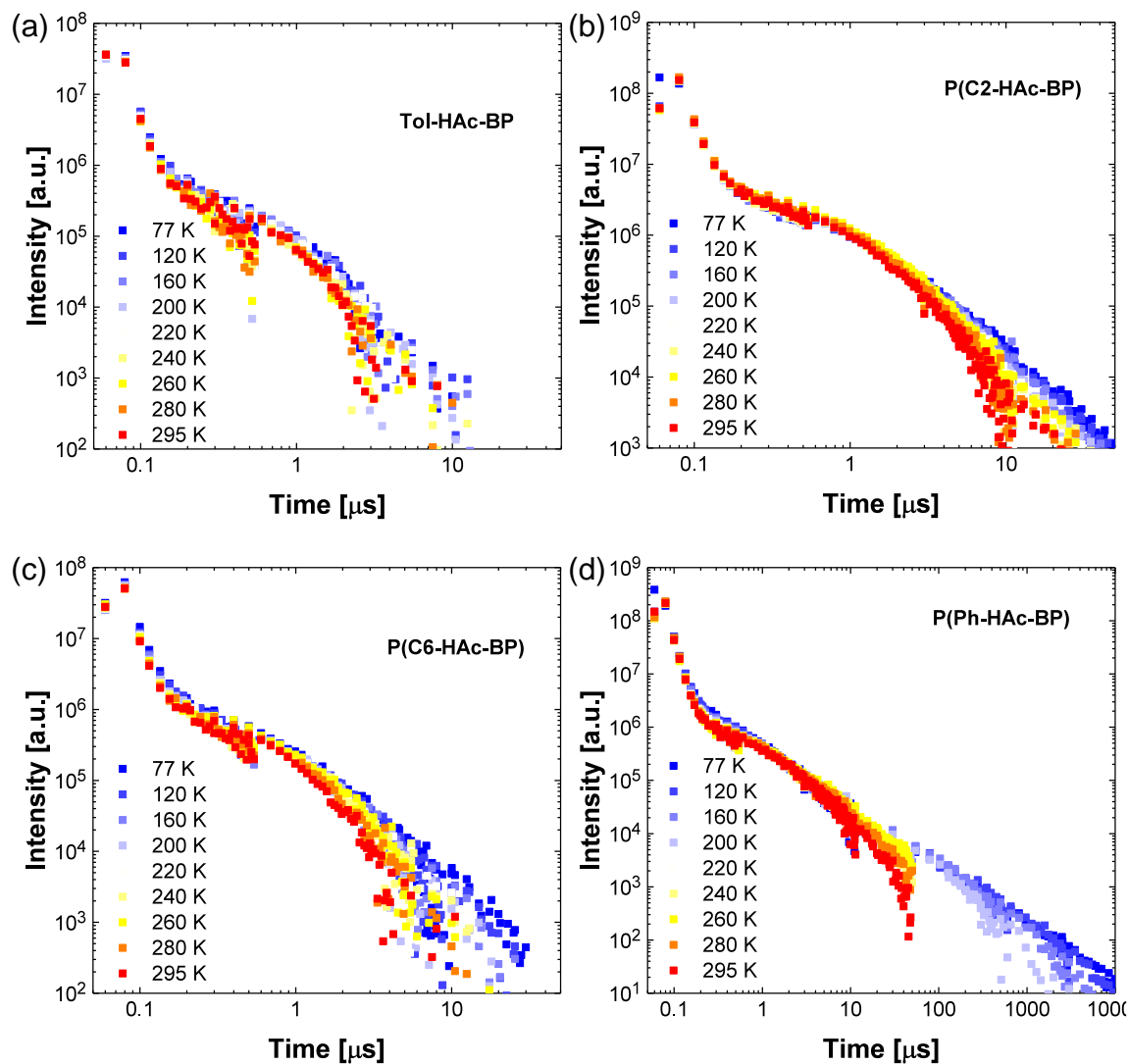


Figure A4.16. Transient PL curves of pristine films of (a) Tol-HAc-BP, (b) P(C2-HAc-BP), (c) P(C6-HAc-BP) and (d) (Ph-HAc-BP) under vacuum at various temperatures.

4.5.5. Estimation of Rate Constants for Arrhenius Plot

For the Arrhenius plot shown in **Figure 4.18d** the following calculation path in agreement with literature was used:^[40,130] As a first step Φ_{PF} and Φ_{DF} were calculated with **Equation 24** and the relation

$$\Phi_{PL} = \Phi_{PF} + \Phi_{DF} \quad (28)$$

using the PLQY values determined in steady state (**Table 4.4** and **Figure 4.12**). As a next step the radiative emission rate of the fluorescence was calculated with

$$k_r = \frac{\Phi_{PF}}{k_{PF}}, \quad (29)$$

where the k_{PF} was determined by

$$k_{PF} = \frac{1}{\tau_{PF}}. \quad (30)$$

In subsequent calculations k_{IC} , k_{ISC} , Φ_{IC} , Φ_{ISC} and k_{TADF} were determined using **Equations 31, 27** as well as **32-34**:

$$\Phi_{PL} = \frac{k_r}{k_r + k_{IC}} \Leftrightarrow k_{IC} = \frac{k_r}{\Phi_{PL}} - k_r \quad (31)$$

$$\Phi_{IC} = \frac{k_{IC}}{k_r + k_{IC} + k_{ISC}} \quad (32)$$

$$\Phi_{ISC} = 1 - \Phi_{PF} - \Phi_{IC} = \frac{k_{ISC}}{k_r + k_{IC} + k_{ISC}} \quad (33)$$

$$k_{TADF} = \frac{\Phi_{DF}}{\Phi_{ISC}\tau_{DF}} \quad (34)$$

k_{ISC} derived from the decay curve of 300 K of the different polymers was used in all subsequent calculations of k_{RISC} at lower temperatures using **Equation 26** in agreement with literature method.^[130]

The parameters are summarized in **Table A4.3**.

Table A4.3. Rate constants and quantum yields of **Tol-MAc-BP**, **P(C2-MAc-BP)** and **P(C6-MAc-BP)** at 300 K.

Compound	Φ_{PF}	Φ_{DF}	k_r [$\times 10^7$]	k_{IC} [$\times 10^5$]	k_{ISC} [$\times 10^7$]	Φ_{IC}	Φ_{ISC}	k_{TADF} [$\times 10^5$]	k_{RISC} [$\times 10^5$]
Tol-MAc-BP	0.33	0.67	1.23	0	2.54	0.00	0.67	2.86	2.86
P(C2-MAc-BP)	0.21	0.71	0.47	3.94	1.72	0.02	0.77	3.74	3.46
P(C6-MAc-BP)	0.31	0.63	1.48	8.81	3.19	0.02	0.67	3.90	3.68

5. Characterization in Optoelectronic Devices

In the photophysical characterization (chapter 4), the nonconjugated polymers **P(C2-MAc-BP)** and **P(C6-MAc-BP)** were observed to be superior to **P(Ph-MAc-BP)** in terms of PLQY and DF contribution to the overall PL emission. While concentration quenching was identified as a dominating loss process in pristine films, high PLQYs of 0.92 and 0.94 were achieved for **P(C2-MAc-BP)** and **P(C6-MAc-BP)** upon blending in PS as an insulator host, similar to the small molecule **Tol-MAc-BP** (PLQY of 1.00).

Although these results are promising for their application in highly efficient OLEDs, various factors besides a high PLQY and efficient RISC play a role in the device performance. For instance, Ohmic charge injection from the electrodes into the EML is necessary for an efficient OLED, which can be challenging for emitters with either deep LUMO- and/or HOMO-levels.^[131] An imbalance in the mobility of holes and electrons can further limit the EQE and reduce the device lifetime due to a narrow recombination zone.^[44] Such an imbalance in mobilities is likely to occur, since the two charge carrier types are transported through different moieties of the TADF molecule. Another frequently observed cause of imbalanced transport is the presence of charge traps, which are localized states situated in the bandgap of the emitter. These traps immobilize charge carriers, hindering charge transport, as well as acting as (non-radiative) recombination centers in an OLED. These traps may originate from water/oxygen-related impurities or chemical defects in the molecular structure.^[132-135] Therefore, in order to better understand charge injection and charge transport in the emitters, single-carrier devices were investigated first, before their application in an OLED.

5.1. Hole Transport Characteristics

In order to investigate hole injection and hole mobility characteristics of **Tol-MAc-BP**, **P(C2-MAc-BP)**, **P(C6-MAc-BP)** and **P(Ph-MAc-BP)** hole-only devices (HO) were fabricated using

the device structure glass/indium tin oxide (ITO; 100 nm)/ poly(3,4-ethylenedioxythiophene): poly(styrene sulfonic acid) (PEDOT:PSS; 60 nm)/ TADF emitter/ MoO₃ (10 nm)/Al (100 nm); see HO-A in **Figure 5.1**). The substrates used for the device fabrication consist of glass with a patterned structure of ITO as transparent conductor, forming the bottom electrodes for 4 OLEDs of different pixel sizes (8.1 mm², 14.82 mm², 34.81 mm² and 97 mm²). PEDOT:PSS was used as a hole injection layer and was applied by spin-coating from aqueous solution. After annealing the PEDOT:PSS layer does not redissolve in apolar organic solvents, enabling subsequent spin coating of emitter layers. Due to its ease of application, high work function, and improving device yield, PEDOT:PSS has become one of the most used HIL layers in solution-processed organic electronics.^[136] On top of PEDOT:PSS, **Tol-MAc-BP**, **P(C2-MAc-BP)**, **P(C6-MAc-BP)** and **P(Ph-MAc-BP)** were spin coated from a chlorobenzene solution. Subsequently, a 10 nm layer of molybdenum oxide (MoO₃) was evaporated as a high work function hole injection layer, covered with a 100 nm aluminum top electrode. This device structure enables the comparison of hole injection between PEDOT:PSS and MoO₃, which due to its high work function of 6.9 eV, acts as an efficient hole injector.^[137]

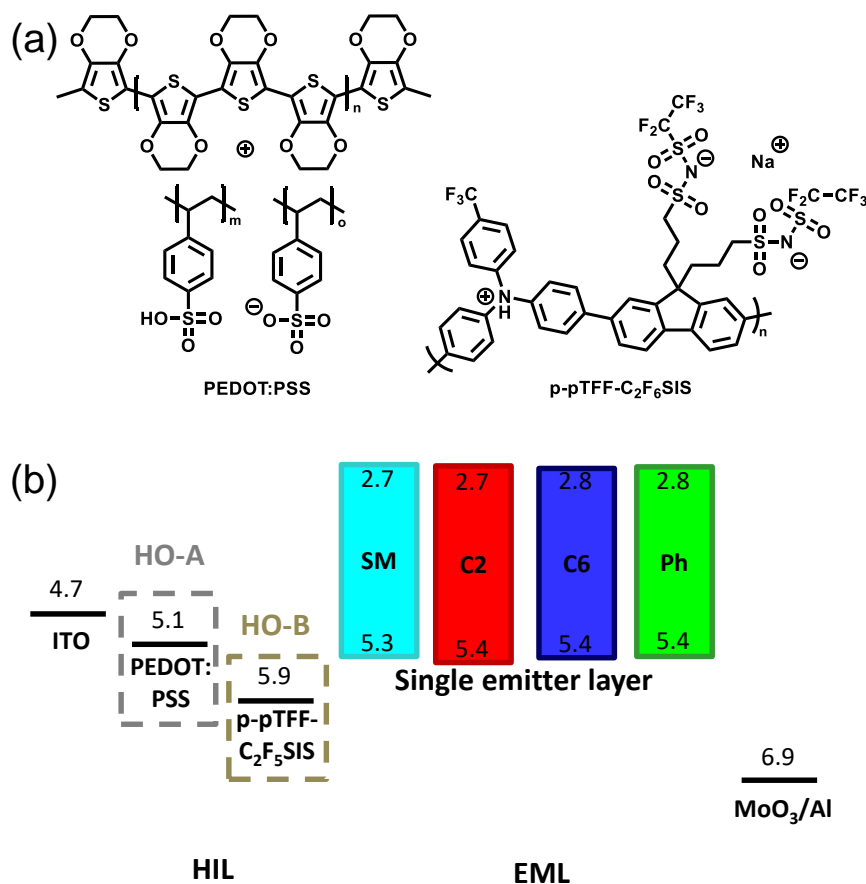


Figure 5.1. (a) Chemical structures of the HIL materials PEDOT:PSS and p-pTFF-C₂F₆SIS. (b) Energy level diagram showing the HOMO/LUMO levels and structures of the hole-only devices HO-A and HO-B.

The current density (J) versus voltage (V) characteristics of the HO devices are shown in **Figure 5.2**. While the efficient injection of holes from the MoO₃ electrode (i.e. negative bias) results in high current densities ranging from 94 A m⁻² to 433 A m⁻² at -8 V for the whole set of materials at room temperature, the hole injection from PEDOT:PSS is significantly hindered, reaching one or two orders of magnitude lower current densities of 39 A m⁻² at 8 V. This significant difference in current indicates a high injection barrier for holes when using PEDOT:PSS as HIL, as expected from the energy level misalignment (**Figure 5.1b**). To further characterize the charge transport, the devices were also measured at lower temperatures. While the current injected from MoO₃ (reverse bias) shows a steady decrease in current density upon cooling, the J - V characteristics remain hardly affected in forward bias,

indicating that the measured current is entirely dominated by leakage current. Leakage current stems from discontinuities in the film, resulting in a local charge transport between cathode and anode.^[138] The dominance of leakage current in forward bias indicates that the injected current from PEDOT:PSS is lower than the leakage current, stemming from a relatively large injection barrier. Therefore, PEDOT:PSS was exchanged for a different HIL layer with a higher work function to reduce the injection barrier.

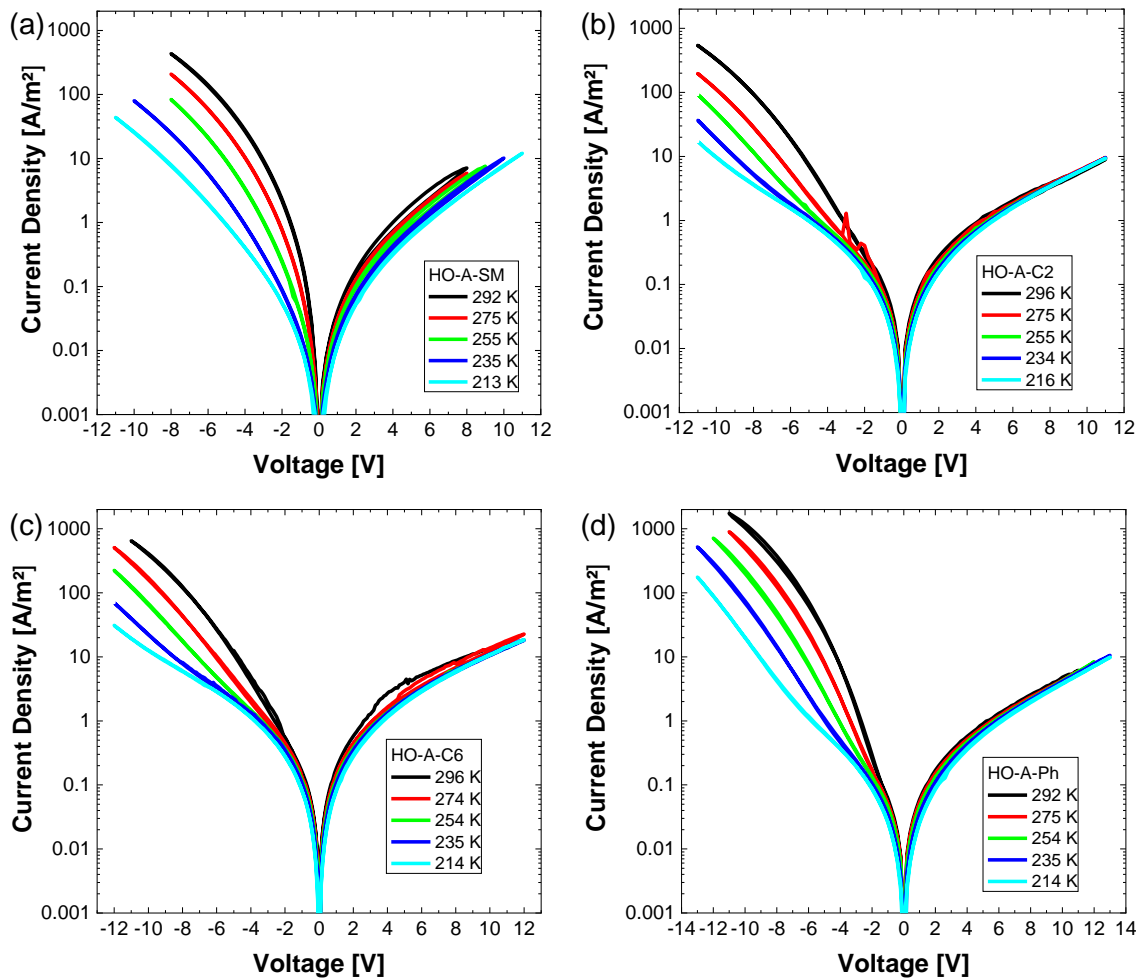


Figure 5.2. J-V characteristics of the hole only devices HO-A with PEDOT:PSS as HIL layer of (a) **Tol-Mac-BP** (100 nm), (b) **P(C2-Mac-BP)** (123 nm), (c) **P(C6-Mac-BP)** (135 nm) and (d) **P(Ph-Mac-BP)** (112 nm) at various temperatures.

As an alternative HIL material, p-doped poly(9,9-bis(3-(pentafluoroethanesulfonylimidosulfonyl)propyl)fluorine-2,7-diylalt-1,4-phenylene-(p-trifluoromethylphenylimino)-1,4-phenylene) sodium salt (p-pTFF-C₂F₅SIS)^[139] was chosen to substitute PEDOT:PSS, yielding the device structure (glass/ ITO (100 nm)/ p-pTFF-C₂F₅SIS (40 nm)/TADF emitter/ MoO₃ (10 nm)/Al (100 nm); see HO-B in **Figure 5.1**). The p-doping is obtained by the use of the strong acceptor nitrosonium hexafluoroantimonate (NOSbF₆). This material is applied via spin coating from acetonitrile, obtaining a film thickness of 40 nm. P-pTFF-C₂F₅SIS is a HIL material with a very high work function of 5.85 eV, promising efficient hole injection. In contrast to the hole-only devices using PEDOT:PSS as HIL, the *J-V* characteristics of the HO-B devices show significantly more symmetric curves (see **Figure 5.3**), indicating successful removal of the injection barrier from the bottom electrode. In case of **Tol-Mac-BP**, the current in reverse bias is even lower than in forward bias, most probably caused by an interface or morphological effect near the MoO₃ layer, leading to an injection barrier. Comparing the different TADF materials, the hole currents of the polymers are quite similar with current densities of 18-45 A m⁻² at 7 V, the device thickness being 76-77 nm. By contrast, the current density measured for the device HO-B of the small molecule **Tol-Mac-BP** is approximately one order of magnitude higher at 436 A m⁻² at 7 V, while the layer thickness of 191 nm is a factor of 2.5 higher compared to the polymer devices. The observation of a higher current for a much thicker layer indicates substantially better hole transport in the case of the small molecule. This indicates that polymerization leads to a significant decrease in hole conduction properties, independent of the type of linker applied. Using a conjugated linker as in **P(Ph-Mac-BP)** furthermore did not show any significant improvement in charge transport.

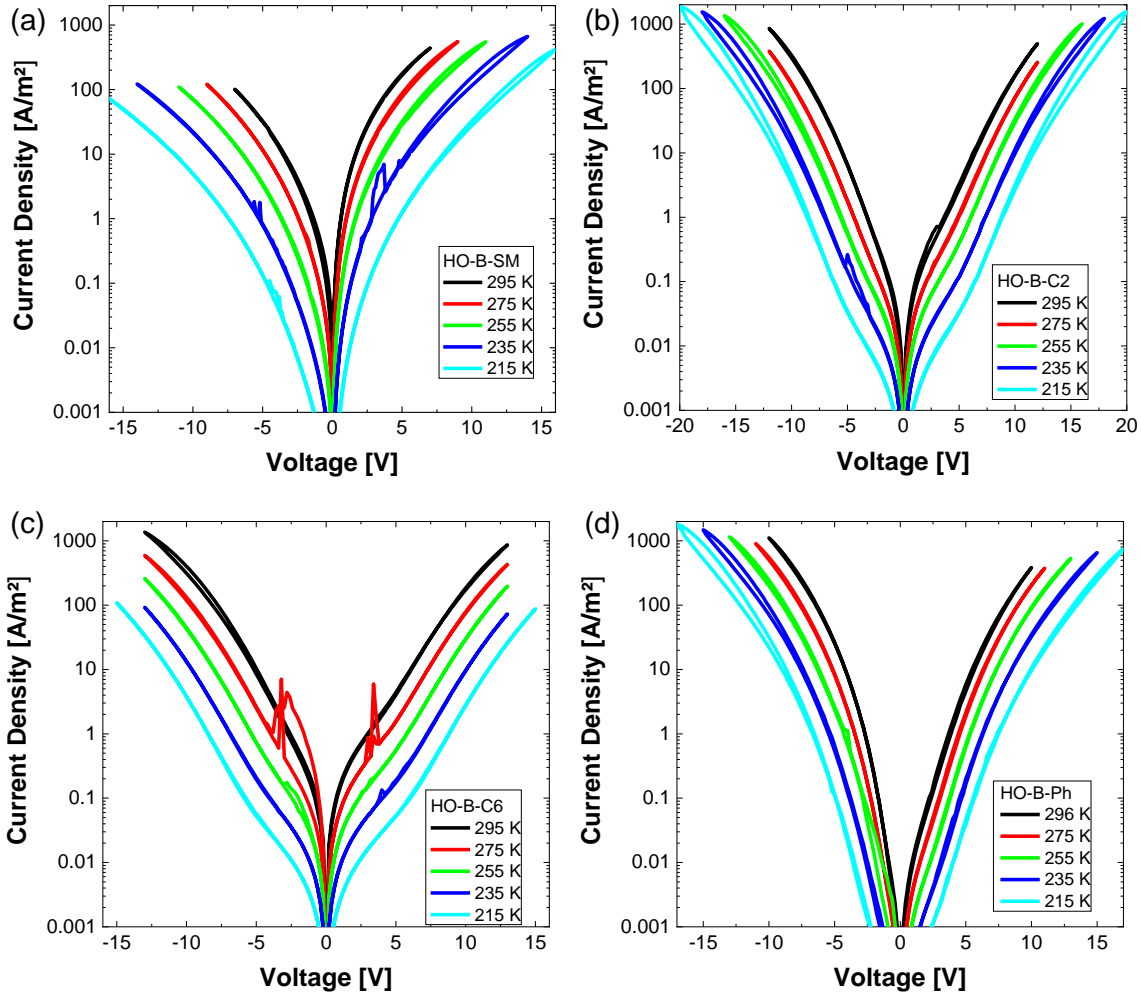


Figure 5.3. J - V characteristics of the hole only devices HO-B with p-pTFF-C₂F₅SIS as HIL layer of (a) **Tol-Mac-BP** (191 nm), (b) **P(C2-Mac-BP)** (77 nm), (c) **P(C6-Mac-BP)** (76 nm) and (d) **P(Ph-Mac-BP)** (77 nm) at various temperatures.

A conventional way of determining hole mobilities (μ) from the hole-only devices, is to fit the J - V characteristics with the expression for the space-charge limited current (SCLC) regime, which is described by the Mott-Gurney law.^[140,141]

$$J = \frac{9}{8} \varepsilon_0 \varepsilon_r \mu \frac{V^2}{L^3}, \quad (35)$$

where L is the thickness of the device, ε_0 is the permittivity of vacuum and ε_r is the permittivity of the semiconductor. **Equation 35** describes a quadratic relation between J and V , which is valid for a

trap-free semiconductor without doping and Ohmic contacts. However, the presence of charge traps will give rise to a stronger voltage dependence. Only when all traps are filled, achieved by applying a sufficiently high voltage, the quadratic dependence on voltage is restored. A quadratic J-V regime could not be reached, making a reliable determination of the hole mobility via the Mott-Gurney law impossible. The high voltage dependence of the current indicates the presence of strong charge trapping. In order to characterize the hole transport in more detail, **P(C2-MAc-BP)** with the hole-only device structure HO-B was chosen for a quantitative analysis via modelling using a numerical drift-diffusion simulator, which includes charge trapping and a temperature-, field-, and density dependent mobility described by the Extended-Gaussian-Disorder-Model (EGDM)^[142,143] (see **Figure 5.4**). The mobility is taken to be field- and density-dependent, which proved to be a vast improvement over the rather straightforward Mott-Gurney law (**Equation 35**).^[142] As mentioned before, a quadratic J-V regime is not reached in the investigated voltage range, making a quantitative determination of the charge-transport parameters impossible, since the individual roles of charge trapping and charge mobility on the current cannot be reliably discriminated. However, a rough estimate of the hole mobility and trapping characteristics can still be made. Since the *J-V* characteristics at first glance seem severely trap limited, they were fitted using a single level trap state with a trap density of $P_t = 7.2 \times 10^{23} \text{ m}^{-3}$ with effective trap energies ($E_{p,trap}$) between 0.26 eV and 0.34 eV, depending on the temperature. The reason for the temperature dependence is that the effective trap energy of a hole trap is measured relative to the temperature dependent density of occupied states (DOOS), rather than the middle of the Gaussian density of states (DOS). A hole mobility of $4 \times 10^{-10} \text{ m}^2 \text{ V}^{-1} \text{ s}^{-1}$ was determined (parameters are shown in **Table A5.1** in Appendix 5.4). The energetic disorder of the DOS was subsequently determined by plotting the effective trap energy against the reciprocal temperature (see **Figure 5.4b**). The width of the Gaussian DOS (σ_{DOS}) was calculated to be 0.1 eV, similar to 0.08 eV as used in the EGDM mobility function.^[10]

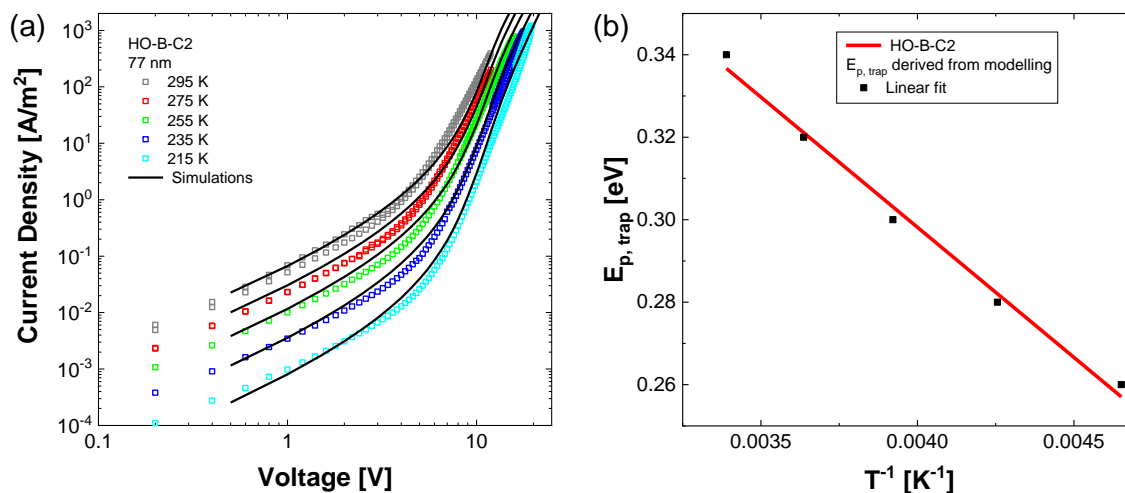


Figure 5.4. J - V characteristics of the hole only devices HO-B with p-pTFF-C₂F₅SIS as HIL layer of P(C2-Mac-BP) at various temperatures and visualized simulation.

The high trap density indicates that the hole transport is indeed severely trap limited. There is a wide variety of possible origins of these traps. These could be caused by small impurities like remaining catalyst. In contrast to small molecules, the purification of polymeric emitters and small molecules with long alkyl chains like **Tol-Mac-BP**, which are not suitable for sublimation, is more challenging. Another possible cause are defects in the molecular structure of the polymeric emitters itself. These trap forming species could be generated by side reactions in the polymerization or stemming from incomplete end-capping reactions. The intramolecular defects based on unreacted halide moieties as well as the transition metal catalyst necessary limit the use of Suzuki polycondensation reaction as polymerization reaction for polymers in optoelectronic application.

5.1. Electron Transport Characteristics

While the characterization of the hole-only devices of the TADF materials showed severely trap-limited hole transport, the efficiency of an OLED is based on the balance between hole and electron

transport. In electron-only devices (glass/ Al (30nm)/ TADF emitter/ Ba (5 nm)/Al (100 nm); see **Figure 5.10**) the TADF materials are sandwiched between an aluminum and a barium/aluminum electrode leading to efficient electron injection while preventing hole injection, enabling the characterization of the electron transport properties. The electron-only J - V characteristics of **Tol-MAc-BP**, **P(C2-MAc-BP)**, **P(C6-MAc-BP)** and **P(Ph-MAc-BP)** are shown in **Figure 5.5b**. In contrast to the hole-only devices, a higher layer thickness was necessary to prevent short circuits. While a slightly higher driving voltage in comparison to the hole-only devices could be stemming from the difference in layer thickness, the relatively high voltages needed in order to measure electron currents point to a low electron transport of all four materials. Similarly to the hole-only devices, stronger-than-quadratic voltage dependence was observed, pointing again to trap-limited transport.

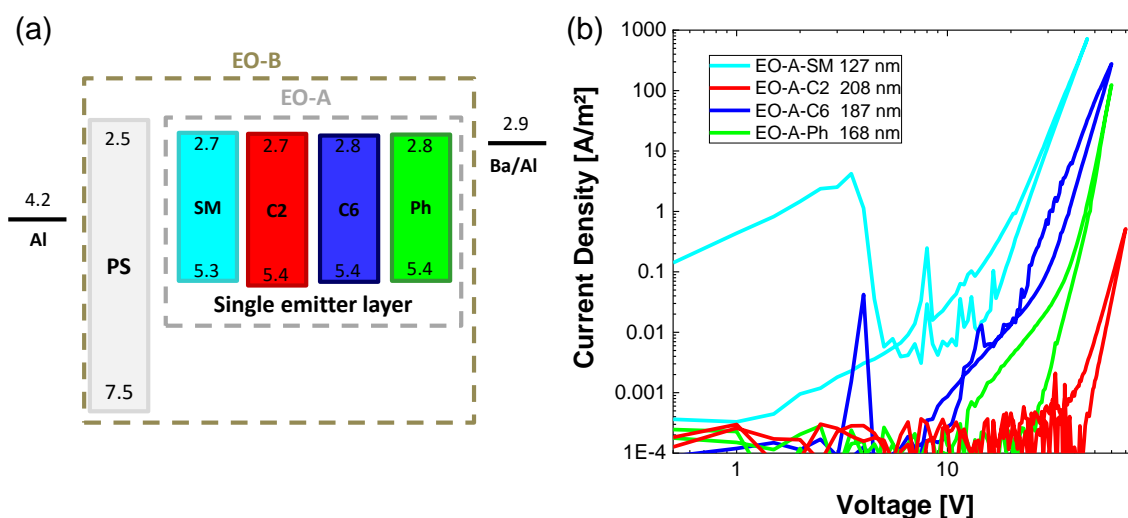


Figure 5.5. (a) Energy level diagram showing the HOMO/LUMO levels and structures of the electron-only devices EO-A and EO-B. (b) J - V characteristics of the electron-only devices EO-A. Layer thicknesses are shown in the legend.

Following the same approach as outlined for the HO-devices, we try to estimate the hole mobility and trap parameters. No temperature dependent curves were available and therefore the field and concentration-dependent electron mobility could not be determined, instead a constant mobility

(μ_{n0}), which generally leads to an overestimation, was used for modelling. The fit parameters are summarized in **Table 5.1**. Despite the fact that the accuracy of this estimation is limited, the determined electron mobilities ranging from $4 - 30 \times 10^{-12} \text{ m}^2 \text{ V}^{-1} \text{ s}^{-1}$ are about two orders of magnitudes lower than the hole mobility determined for **P(C2-Mac-BP)**. The electron transport was also found to be trap limited, with trap densities ($\sim 10^{23} \text{ m}^{-3}$) comparable to fluorescent polymer emitters.^[134]

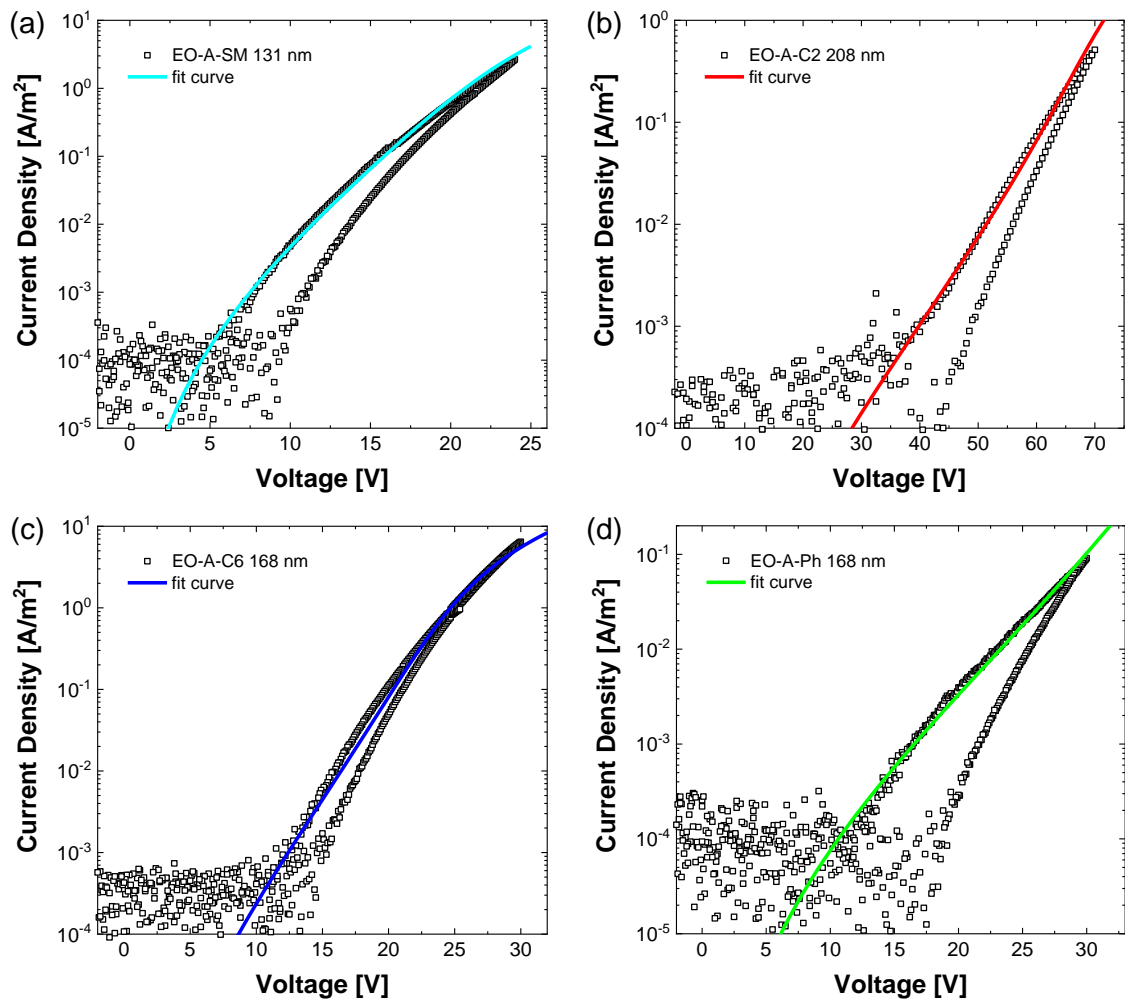


Figure 5.6. Simulated J - V characteristics of electron-only devices EO-A of (a) **Tol-Mac-BP**, (b) **P(C2-Mac-BP)**, (c) **P(C6-Mac-BP)** and (d) **P(Ph-Mac-BP)**. Layer thicknesses are shown in the legend.

Table 5.1. Fit parameters of the electron-only devices EO-A.

Compound	μ_{n0} [$10^{-12} \text{ m}^2 \text{ V}^{-1} \text{ s}^{-1}$]	N_t [10^{23} m^{-3}]	$E_{n,Gauss}$ [eV]	$\sigma_{n,Gauss}$ [eV]
EO-A-SM	8	5.6	0.36	0.12
EO-A-C2	4	6.1	0.45	0.12
EO-A-C6	30	4.0	0.42	0.11
EO-A-Ph	9	5.1	0.42	0.11

In order to be able to compare the imbalance between both charge carriers in an OLED, the electron current was modeled for the same layer thickness as the hole-only devices HO-B (see **Figure 5.7**). The direct comparison between hole and electron current in the same device thickness indicates a strong imbalance with higher hole currents in all the four materials. The difference in hole and electron current ranges from a factor of 3 to 10 for **P(C6-MAc-BP)** to more than one order of magnitude for **P(C2-MAc-BP)** and **P(PH-MAc-BP)**. The most pronounced difference was observed for **Tol-MAc-BP** with seven orders of magnitudes difference. While the electron mobility is similar to the TADF polymers, this is mostly caused by the comparably high hole mobility of Tol-MAc-BP.

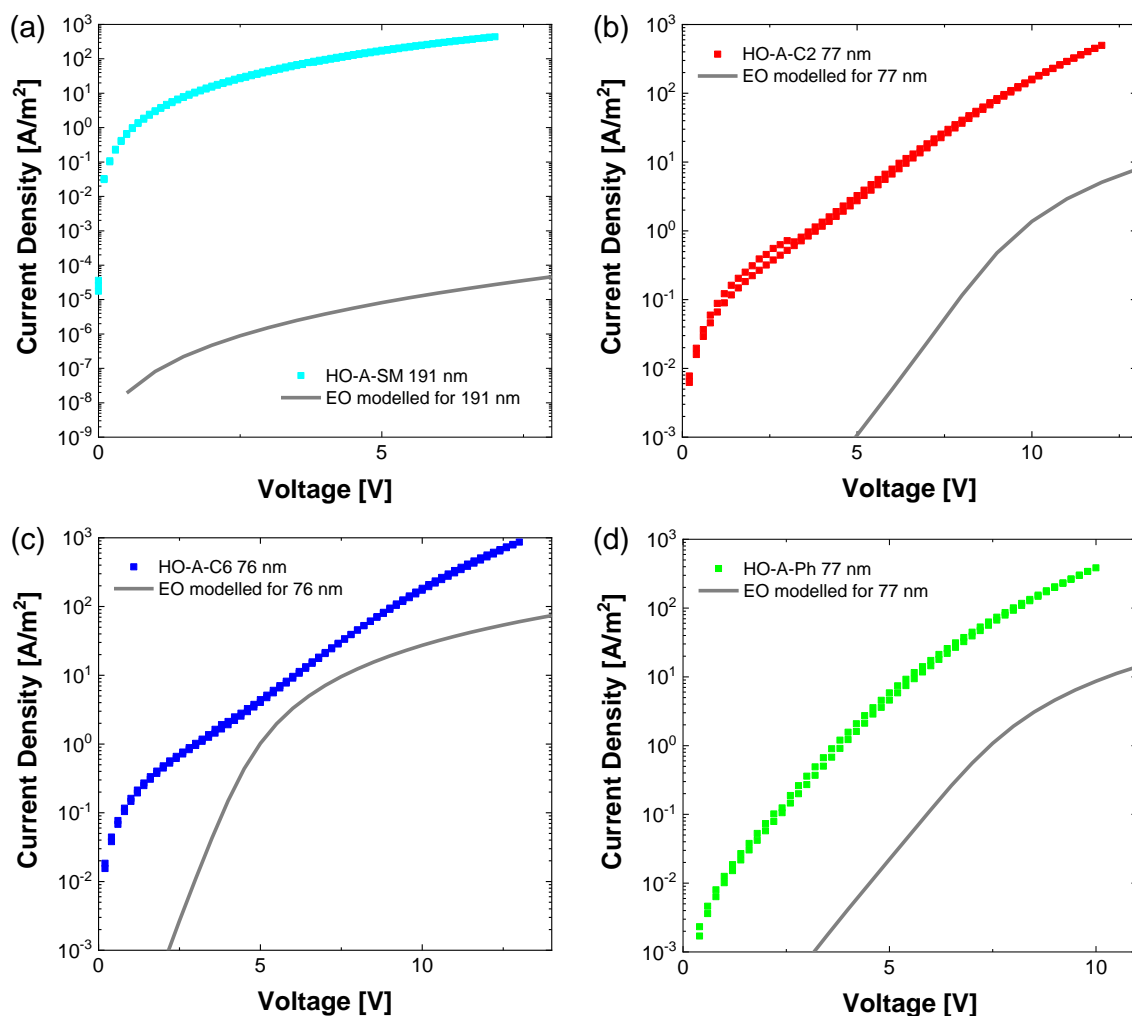


Figure 5.7. J - V characteristics of the hole-only devices HO-A with simulated EO curve for same layer thickness of (a) Tol-MAc-BP, (b) P(C2-MAc-BP), (c) P(C6-MAc-BP) and (d) P(Ph-MAc-BP). Layer thicknesses are shown in the legend.

While an improved OLED performance based on the increase in PLQY upon blending the emitter with an insulator found in chapter 4 is expected, a different phenomenon called ‘trap dilution’, which boosts the electron current, could play a role in the OLED performance. This effect was previously discovered for poly(*p*-phenylene vinylene) (PPV) polymers in this group and leads to an increase in electron current by simultaneous dilution of transport and trapping sites. This phenomenon can be explained with the trap limited current (J_{TL}) formula by Mark and Helfrich:^[144]

$$J_{TL} = N_c q \mu_e \left(\frac{\varepsilon_0 \varepsilon_r}{q N_t e^{kT_t}} \right)^r \left[\left(\frac{2r+1}{r+1} \right)^{r+1} \left(\frac{r}{r+1} \right)^r \right] \frac{V^{r+1}}{L^{2r+1}} \quad (36)$$

where q is the elementary charge, μ_e the free electron mobility, E_{tc} is the mean trap depth, T_t is the trap temperature describing the width of the trap distribution and $r = T_t/T$. This equation can be summarized to the proportionality

$$J_{TL} \sim \frac{N_c}{N_t^r} \quad (37)$$

showing a more pronounced influence of the dilution on the density of trapping sites (N_t) than on the density of transport sites (N_c) because r is usually 4 or more in organic semiconductors.^[134] The amount of dilution is expected to exhibit an optimum. Too much dilution removes the percolating pathway for the carriers, hindering the charge transport, ultimately lowering the current. Too little dilution will not reduce the density of trapping sites in a meaningful manner. Because dilution of the PPV polymers with low molecular weight PS reduces N_c and N_t simultaneously, a rise in electron current can be obtained.

Although a significant increase in electron current based on trap dilution was observed for these PPV polymers, the electron only devices of **Tol-MAc-BP**, **P(C2-MAc-BP)**, **P(C6-MAc-BP)** and **P(Ph-MAc-BP)** did not show a trap dilution effect, which could originate from the relatively small molecular weight, reducing percolating pathways for charge transport. The polymers **P(C2-MAc-BP)** and **P(C6-MAc-BP)** only showed a small difference in electron current between the pristine devices and the blending ratios emitter:PS of 1:1 and 1:3 (see **Figure 5.14**). In contrast, the small molecule **Tol-MAc-BP** exhibited a decrease in electron current upon blending with PS in 1:1 and 1:3. This observation is most likely the result of a gradual loss of percolation pathways, and is further discussed for the current densities of the OLED devices in the next section 5.2.

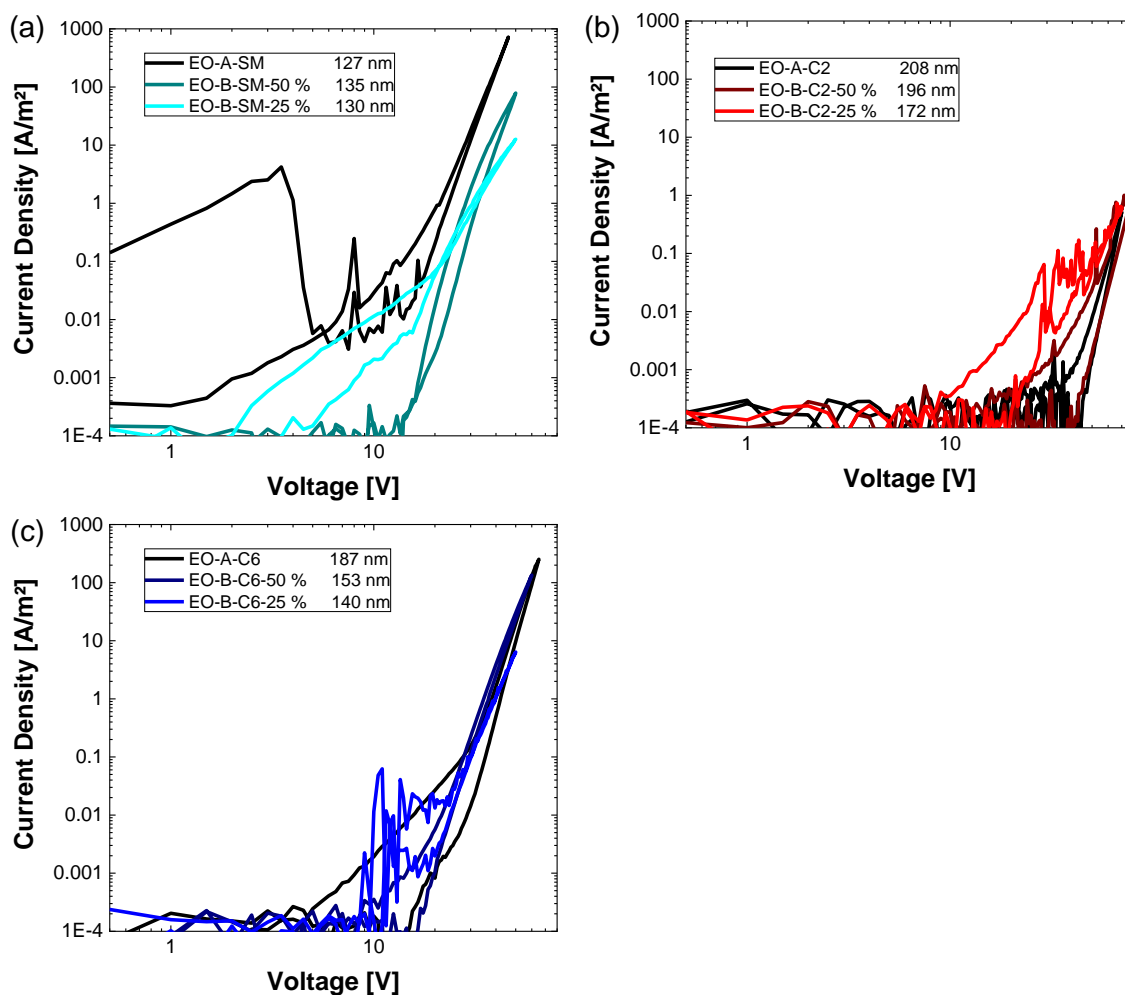


Figure 5.8. J - V characteristics of the electron-only devices EO-A and in comparison to EO-B with 50 % and 25 % weight content of (a) Tol-MAc-BP, (b) P(C2-MAc-BP) and (c) P(C6-MAc-BP). Layer thicknesses are shown in the legend.

5.2. Organic Light-Emitting Diode Performances

Although the imbalanced charge transport of all of the materials independent of the polymer structure, which was revealed in the previous section, potentially limits the maximum efficiency and life times of OLEDs, significant performance improvements can be obtained via optimization of the device structure. For this optimization, polymer LEDs were fabricated with the polymers P(C2-MAc-BP), P(C6-MAc-BP) and P(Ph-MAc-BP), whereas the small molecule Tol-MAc-BP was

just used in the final architecture to act as a reference. The detailed performance characteristics of the different sets of devices that led to the optimized OLED architecture are shown in the Appendix 5.4 (Table A5.2 and Figure A5.1-Figure A5.5).

Single-layer OLEDs, in which the polymer emitter is sandwiched directly between the hole- and electron-injection layer, showed maximum EQE below 1 %, likely indicating substantial quenching of the holes at the cathode due to the imbalanced charge transport. In order to suppress this loss process, 2,2',2''-(1,3,5-Benzinetriyl)-tris(1-phenyl-1-H-benzimidazole) (TPBi) was introduced as ETL via thermal evaporation (see molecular structures in Figure 5.9). TPBi not only enhances the transport of electrons but also acts as hole blocking layer stemming from its low HOMO of -6.2 eV. The additional layer leads to an accumulation of holes at the EML-ETL interface at which most of the charge recombination takes place, increasing the maximum EQE by almost an order of magnitude to 2.1 % - 7.1 %, while reducing the leakage current significantly. After these optimization steps, the replacing the PEDOT:PSS HIL with p-pTFF-C₂F₅SIS reduced the driving voltage significantly due to improved hole injection.

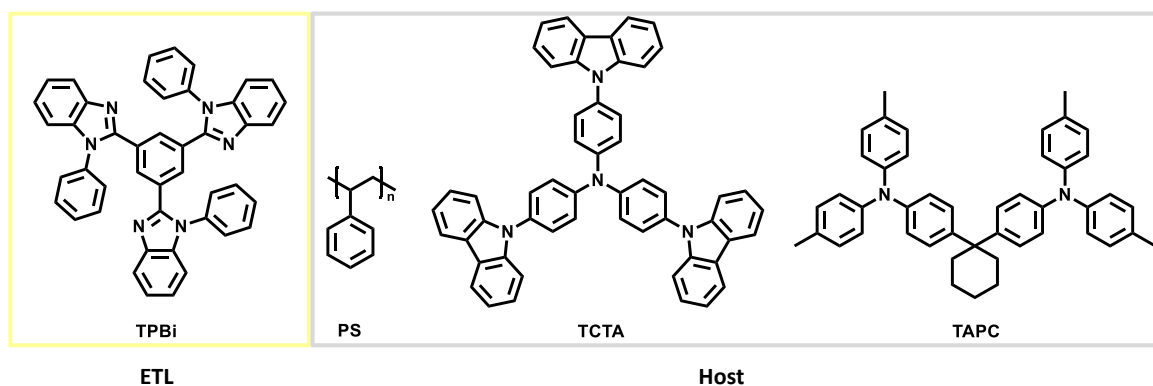


Figure 5.9. Molecular structures of TPBi, PS, TCTA and TAPC.

In order to investigate the influence of the linker strategy and the concentration quenching effect observed in chapter 4, OLEDs with the optimized device structure and EML consisting of the

TADF emitters in various blending ratios with PS were fabricated and are analyzed in section 5.2.1. In the subsequent section the performances of OLEDs with identical architecture but small molecule host are discussed. As host for these devices tris(4-carbazoyl-9-ylphenyl)amine (TCTA) as well as a mixed host with TCTA and 1,1-Bis[(di-4-tolylamino)phenyl]cyclohexane (TAPC) were chosen. This second set of devices enables the evaluation of the blending strategy with a nonconductive insulator like PS against the small molecule host systems used in literature.

5.2.1. OLEDs with PS Host

Analogous to the photophysical characterization in the previous chapter, the TADF materials were diluted in PS with blending ratios of 1:1, 1:3 and 1:9 and compared with pristine EML OLEDs. PS is an insulator with HOMO and LUMO of -7.5 eV and -2.5 eV, respectively. Therefore, injection of holes and electrons into PS is hindered and electronic effects based on the host can be excluded in the blends, enabling a comparison of the TADF material properties. Low molecular weight PS ($M_n = 1.2 \text{ kg mol}^{-1}$) was used in the device fabrication, since using high molecular weight PS ($M_n = 170 \text{ kg mol}^{-1}$) resulted in lower device efficiencies and phase separation detected by AFM (see Appendix 5.4). The optimized device structure of ITO (100 nm)/p-pTFF-C₂F₅SIS (40 nm)/ EML (30 nm)/ TPBi (60 nm)/ Ba (5nm)/ Al (100 nm) was used for **Tol-MAc-BP** (devices A), **P(C2-MAc-BP)** (devices B), **P(C6-MAc-BP)** (devices C) and **P(Ph-MAc-BP)** (devices D; see **Figure 5.10**).

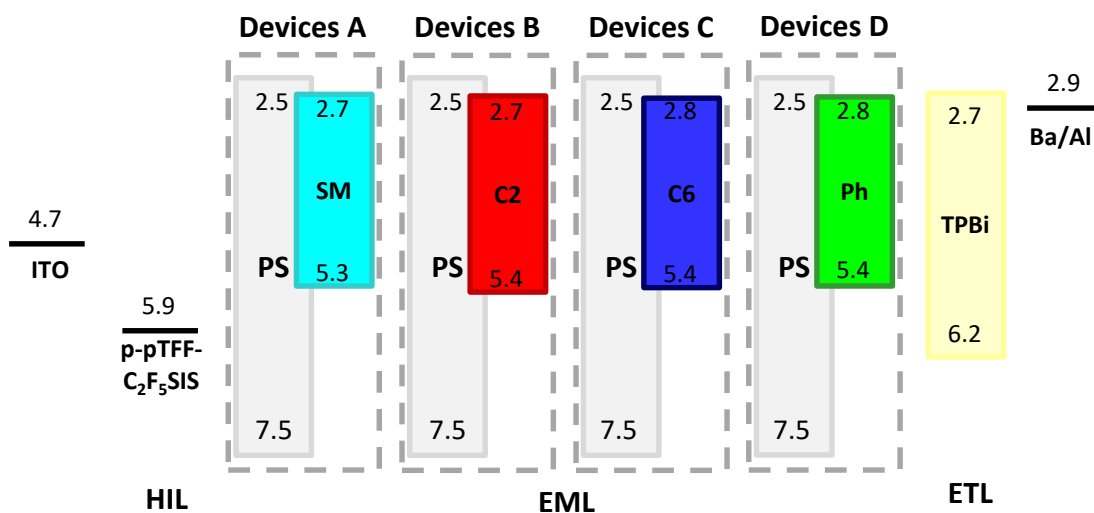


Figure 5.10. Energy level diagram showing the HOMO/LUMO levels and structures of the OLED devices A, B, C and D.

The current-voltage-luminescence (J - V - L) characteristics of the devices show the expected shape for a light-emitting diode (see **Figure 5.11** and summarized results in **Table 5.2**): All OLEDs show a low leakage current at low voltage, followed by a strong exponential increase in the diffusion regime, where a decrease in slope after reaching the built-in voltage marks the transition to the drift regime. As an estimate for the turn-on voltage V_{on} , the voltage at which the luminance reached 1 cd m^{-2} was chosen. The pristine EML devices of all materials exhibit a similarly low V_{on} of $3.0 \text{ V} - 3.2 \text{ V}$ showing a steady increase with higher PS blending ratios with $3.8 \text{ V} - 4.3 \text{ V}$ at 10 %. The devices further reached high luminance close to or above 1000 cd m^{-2} for the polymeric emitters and even $10,000 \text{ cd m}^{-2}$ in case of **Tol-Mac-BP** with a 50 % blended EML.

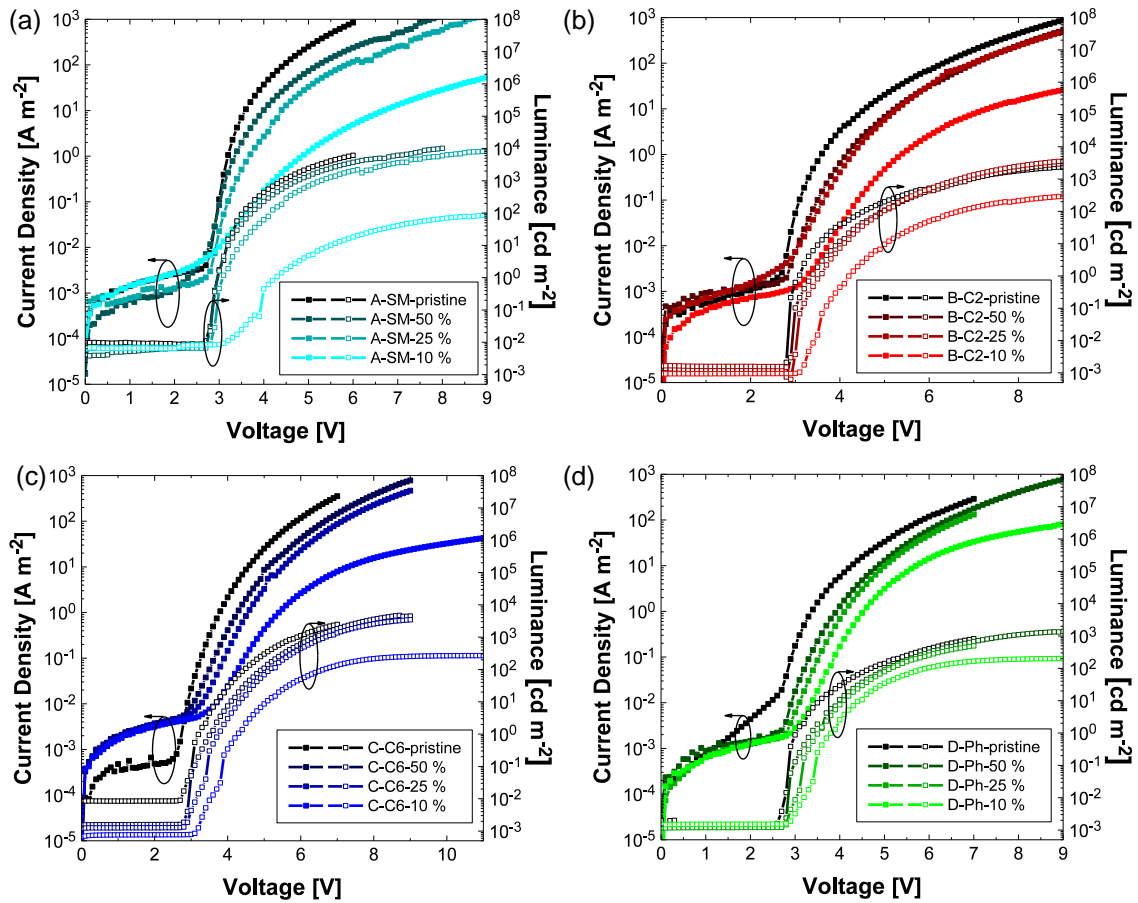


Figure 5.11. J-V-L characteristics of (a) devices A with Tol-MAC-BP, (b) devices B with P(C2-Mac-BP), (c) devices C with P(C6-Mac-BP) and (d) devices D with P(Ph-Mac-BP) with various PS blending ratios.

Table 5.2: Summary of device performance devices A with **Tol-MAc-BP**, devices B with **P(C2-MAc-BP)**, devices C with **P(C6-MAc-BP)** and devices D with **P(Ph-MAc-BP)** EML layers of varying doping concentrations.

Device	V_{on} [V] at 1 cd m ⁻²	V_d [V]	CE [cd A ⁻¹] max./ 100 /1000 cd m ⁻²	PE [Lm W ⁻¹]	EQE [%]	λ_{em} [nm]	FWHM [nm]	CIE (x, y)
A-SM-pristine	3.0	3.0/ 3.6/ 4.5	15.5/ 12.9/ 10.8	16.2/ 11.5/ 7.7	7.5/ 6.3/ 5.3	528	91	0.34, 0.59
A-SM-50 %	3.0	3.5/ 3.8/ 4.8	23.1/ 22.9/ 20.4	22.2/ 19.3/ 13.5	12.6/ 12.5/ 11.1	522	86	0.32, 0.59
A-SM-25 %	3.1	3.7/ 4.2/ 5.3	23.4/ 23.4/ 22.8	22.8/ 17.3/ 11.9	12.9/ 12.6/ 11.0	520	86	0.31, 0.59
A-SM-10 %	4.3	5.3/ -/ -	3.9/ -/ -	2.4/ -/ -	2.4/ -/ -	513	81	0.27, 0.56
B-C2-pristine	3.1	3.2/ 4.6/ 6.9	13.1/ 10.7/ 6.0	12.8/ 7.4/ 2.7	6.7/ 5.5/ 3.1	545	100	0.39, 0.57
B-C2-50 %	3.4	3.7/ 5.0/ 7.0	18.8/ 16.5/ 10.8	16.8/ 10.5/ 4.9	9.7/ 8.5/ 5.6	535	96	0.37, 0.58
B-C2-25 %	3.6	4.5/ 5.0/ 6.7	18.9/ 18.6/ 13.2	14.4/ 11.7/ 6.2	9.9/ 9.8/ 6.9	530	93	0.35, 0.59
B-C2-10 %	4.2	5.0/ 6.7/ -	20.4/ 17.4/ -	13.9/ 8.21/ -	11.2/ 9.6/ -	523	89	0.32, 0.59
C-C6-pristine	3.2	3.5/ 4.5/ 6.0	13.9/ 12.6/ 9.7	12.5/ 8.9/ 5.2	7.1/ 6.5/ 5.0	537	94	0.37, 0.58
C-C6-50 %	3.5	4.1/ 5.0/ 6.4	18.1/ 14.9/ 14.1	15.0/ 9.5/ 7.0	9.7/ 8.0/ 7.5	526	92	0.34, 0.59
C-C6-25 %	3.7	4.6/ 5.2/ 6.7	21.3/ 16.2/ 16.9	16.3/ 9.9/ 7.9	11.8/ 9.1/ 9.4	520	87	0.32, 0.59
C-C6-10 %	4.3	5.3/ 6.7/ -	20.0/ 18.1/ -	13.2/ 8.6/ -	11.4/ 10.4/ -	518	85	0.30, 0.58

D-Ph-pristine	3.0	3.5/ 4.7/	5.5/ 4.7/ -	5.3/ 3.1/ -	2.9/ 2.5/ -	399,	105	0.39,
		-				548		0.56
D-Ph-50 %	3.4	3.5/ 5.1/	8.6/ 6.7/	7.8/ 4.2/	4.5/ 3.5/	399,	101	0.37,
		7.8	2.9	1.2	1.5	542		0.57
D-Ph-25 %	3.5	3.6/ 5.2/	11.3/ 7.8/ -	9.8/ 4.7/ -	6.1/ 4.2/ -	399,	98	0.35,
		-				534		0.57
D-Ph-10 %	3.8	4.0/ 6.0/	11.4/ 7.5/ -	11.9/ 4.0/ -	8.4/ 4.2/ -	399,	94	0.34,
		-				528		0.57

The J - V - L characteristics of the devices with a pristine EML (see **Figure 5.11**) further show a lower driving voltage for the small molecule **Tol-MAc-BP** (845 A m^{-2} at 6 V) in comparison to the polymer counterparts **P(C2-MAc-BP)**, **P(C6-MAc-BP)** and **P(Ph-MAc-BP)** ranging from 70 A m^{-2} to 118 A m^{-2} at 6 V. Upon dilution of the TADF small molecule **Tol-MAc-BP** in PS the current density at the same voltage drops about one order of magnitude to 117 A m^{-2} at 1:3 blending ratio and about two orders of magnitude for 1:9 to 5 A m^{-2} . While the currents detected for the small molecule devices A are higher than in the devices B-D at identical blending ratios, the TADF polymers show an overall smaller relative decrease in current density upon dilution (see **Figure 5.12a**). In contrast to the drop in current density of one order of magnitude for devices A at 25 % blending ratio, a smaller reduction by 55 % for **P(Ph-MAc-BP)**, 62 % for **P(C2-MAc-BP)** and 80 % for **P(C6-MAc-BP)** were observed. This trend can be explained by the nature of the hopping charge transport mechanism. Based on the highly localized HOMO and LUMO distribution, hole transport happens between the donor and electron transport between acceptor moieties. This results in a gradual loss of percolation pathways upon dilution stemming from an increase in hopping distance. In case of a small molecule-polymer blend, an even distribution of the small molecule and therefore of the hopping sites can be assumed, which leads to a strong reduction in percolation pathways at high dilution (see **Figure 5.12b**). In contrast, the linkers in the polymers limit the distance between the D-A-D triads within a polymer molecule and due to a

higher probability of intersections between the polymer chains, the decrease of percolation pathways is not as pronounced compared to the small molecule.

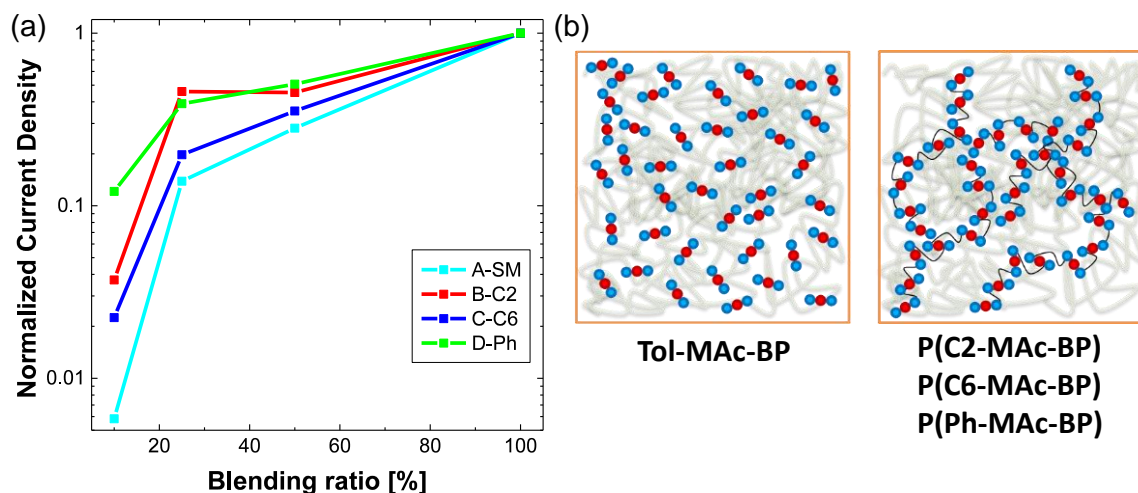


Figure 5.12. (a) Normalized current densities of devices A-D at 6 V in various blending ratios. (b) Illustration of blended films of **Tol-MAC-BP**, **P(C2-MAC-BP)**, **P(C6-MAC-BP)** and **P(Ph-MAC-BP)** at high dilution (cycles represent donor (blue) and acceptor (red)).

The electroluminescence spectra of the devices A-D are shown in **Figure 5.13a-d** and show a similar shift upon blending in PS host as observed in PL in chapter 4. The EL maximum shifts from 528 nm to 513 nm for **Tol-MAC-BP**, from 545 nm to 523 nm for **P(C2-MAC-BP)**, from 537 nm to 518 nm for **P(C6-MAC-BP)** and from 548 nm and 528 nm for **P(Ph-MAC-BP)** going from pristine EML devices to blending ratios of 1:9. The Commission Internationale de L'Eclairage (CIE) chromaticity diagram (see **Figure 5.13e**), which takes the perceived color in human vision into account, shows that the hypsochromic shift upon blending leads to a transition from a more yellow to a yellowish-green color emitted by the OLEDs. While except for the shift no change in spectral line shape was observed for these OLEDs, devices D with **P(Ph-MAC-BP)** showed a low intensity second emission maximum at 399 nm that increases in intensity at higher dilution (see **Figure 5.13d** inset). This emission might be caused by a LE emission from the acridine donors, similar to the results found

in PL from solution in high polarity solvents (see chapter 4). Another contributing emission might stem from the TPBi molecules at the EML-ETL interface. The injection of holes into the ETL with a HOMO of -6.2 eV requires a high accumulation of holes at the interface, which is caused by the imbalanced charge transport.^[145] TPBi does show a EL emission maximum of 385 nm^[131]. While this emission was not observed for the devices A-C, an EL emission with this maximum stemming from TPBi was also detected for **P(C6-MAc-BP)** when using high molecular weight PS as host exhibiting phase separation (shown in Appendix 5.4).

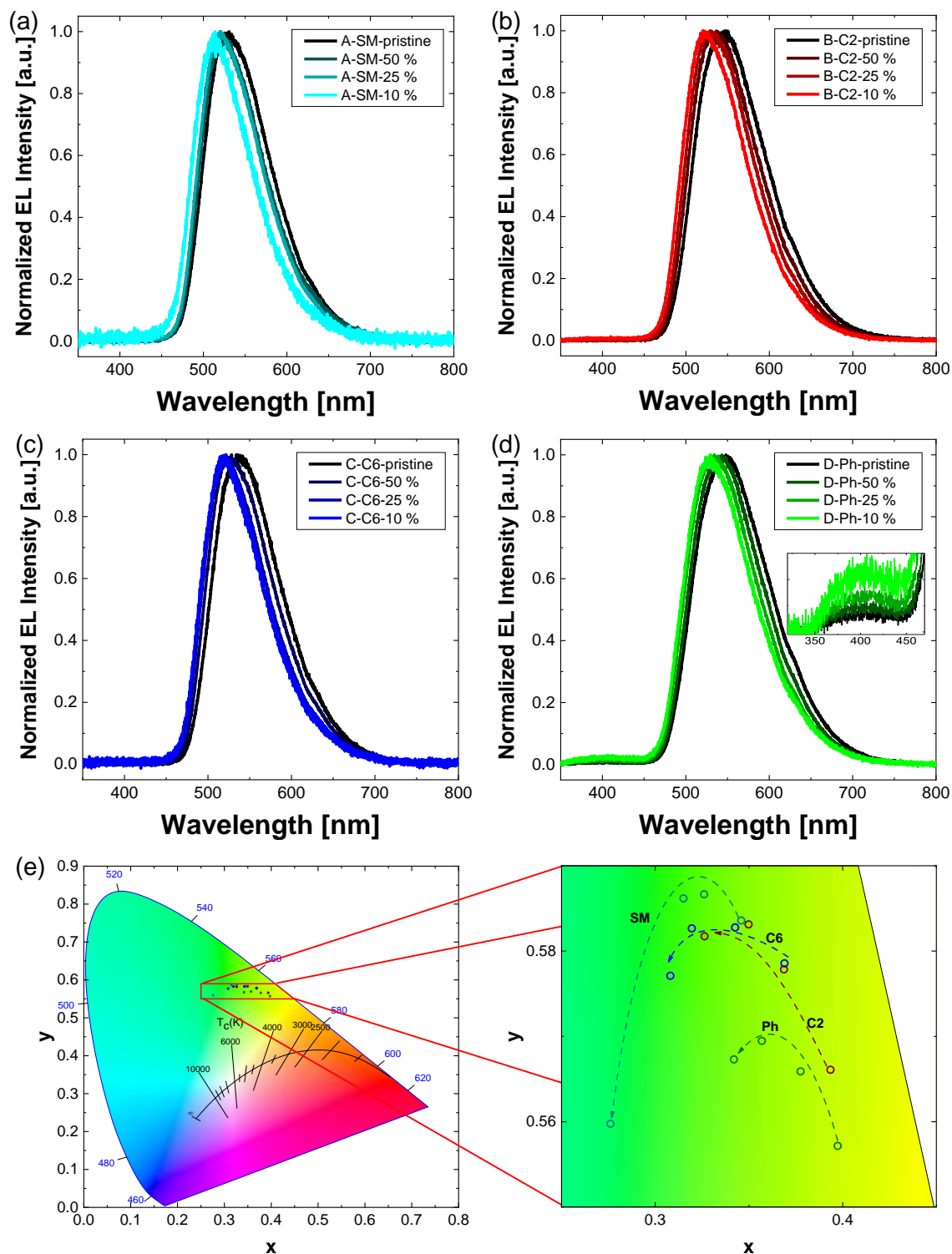


Figure 5.13. EL spectra of (a) devices A with Tol-Mac-BP, (b) devices B with P(C2-Mac-BP), (c) devices C with P(C6-Mac-BP) and (d) devices D with P(Ph-Mac-BP) with various PS blending ratios and an inset zoomed in on the second emission. (e) Diagram of the Commission International de L'Eclairage (CIE) chromaticity with zoomed in area. The CIE coordinates of the EL emission of Tol-Mac-BP (dark cyan), P(C2-Mac-BP) (dark red), P(C6-Mac-BP) (dark blue) and P(Ph-Mac-BP) (dark green) are shown in circles with arrows indicating the change from pristine EML to 1:9 blended EML.

By using a calibrated photodiode measuring the EL emission intensity using the method described by Forrest et al.^[146], it is possible to determine the EQE from the J - V - L characteristics and the EL spectra shown in **Figure 5.14**. The undoped devices already surpass the theoretical EQE limit of 5 % for conventional fluorescent emitters and show maximum EQE values of 7.5 % for **Tol-MAc-BP**, 6.7 % for **P(C2-MAc-BP)**, 7.1 % for **P(C6-MAc-BP)** and 2.9 % for **P(Ph-MAc-BP)**. Despite a strong influence of concentration quenching on these materials, which reduces their PLQY in the pristine film as determined in the previous chapter, the performance of pristine EML devices of the small molecule and the nonconjugated polymer were similar.

A significant performance enhancement was observed for all materials with the introduction of PS as insulating polymer host, reaching EQE_{max} of 12.9 % for **Tol-MAc-BP**, 9.9 % for **P(C2-MAc-BP)**, 11.8 % for **P(C6-MAc-BP)** and 6.1 % for **P(Ph-MAc-BP)** at blending ratios of 25 wt%. For **P(C2-MAc-BP)** and **P(Ph-MAc-BP)** the EQE further increases at a blending ratio of 1:9 to 11.2 % and 8.4 %, respectively. In contrast, the performance of the small molecule in the highest dilution drops significantly to 2.4 %. A possible explanation could again be the reduction of percolation paths at high dilution mentioned earlier. The decrease in percolation paths further leads to a higher exciton concentration on the remaining paths. This could be a possible explanation for the rapid and steep EQE roll-off observed for the devices with the most dilute EML layer, while the maximum EQE at low luminescence is still high.

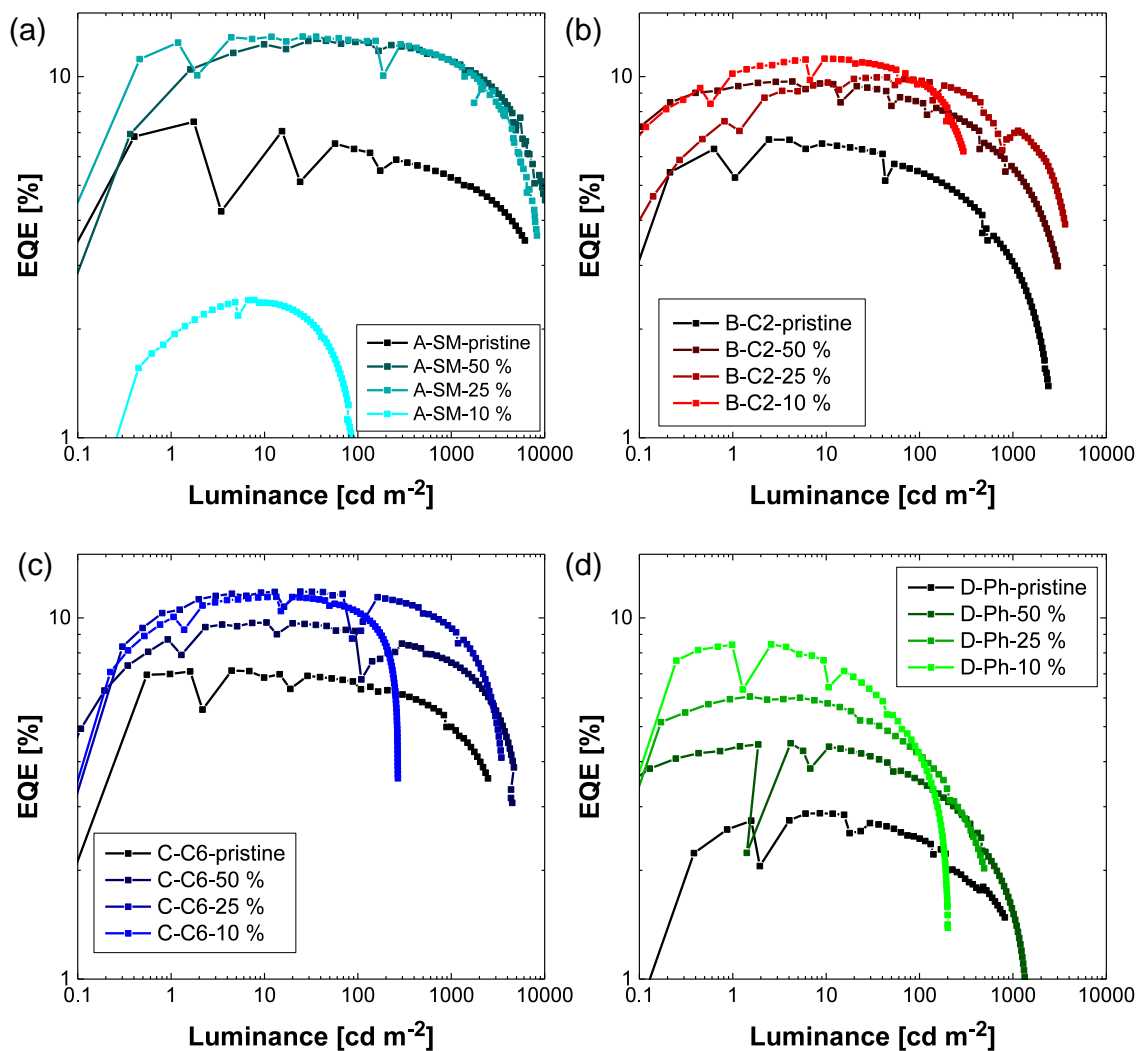


Figure 5.14. EQE-luance characteristics of (a) devices A with Tol-Mac-BP, (b) devices B with P(C2-Mac-BP), (c) devices C with P(C6-Mac-BP) and (d) devices D with P(Ph-Mac-BP) with various PS blending ratios.

The direct comparison of the relative increase in PLQY measured in chapter 4 with the relative increase in maximum EQE for devices A-D upon dilution in PS is shown in **Figure 5.15a**. The change in PLQY and in EQE are very similar for P(C6-Mac-BP) and P(Ph-Mac-BP) which indicates the suppression of concentration quenching to be the main reason for the performance improvement. The lower PLQY difference between pristine film and diluted films of the small molecule Tol-Mac-BP

compared to the EQE increase can be explained by the poor film quality of the pristine EML device. Despite this difference, the overall trend of a steady increase in both values is consistent.

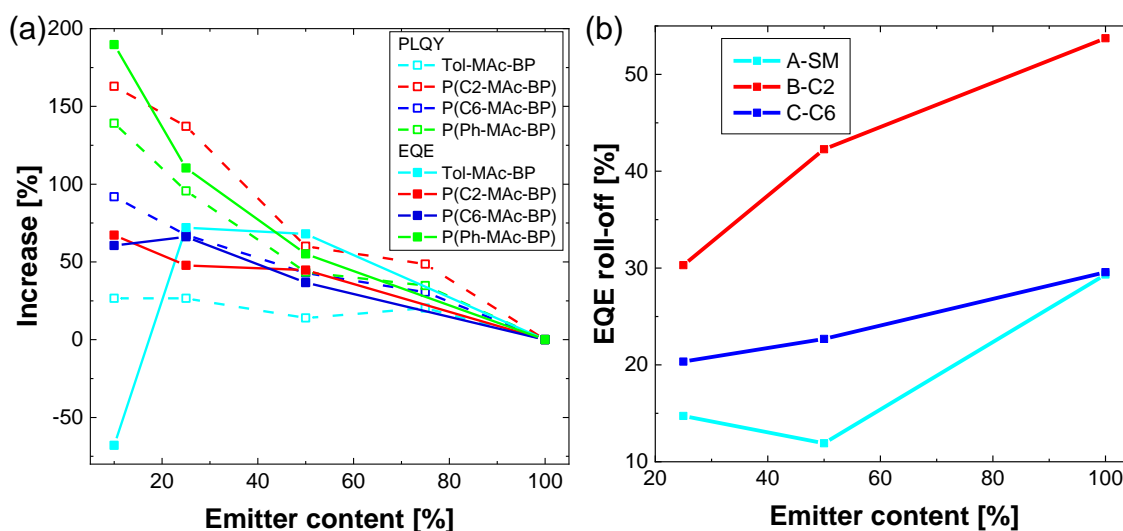


Figure 5.15. (a) Comparison of the increase upon blending with PS in PLQY of **Tol-MAC-BP**, **P(C2-MAC-BP)**, **P(C6-MAC-BP)** and **P(Ph-MAC-BP)** and maximum EQE of devices A-D. (b) EQE roll-off of devices A-C at 1000 cd m⁻².

The impact of concentration quenching can be estimated by the efficiency roll-off at high current densities, which stems from triplet exciton accumulation and resulting quenching processes like triplet-triplet or triplet-polaron annihilation.^[54,147] The efficiency roll-off is measured as the relative drop in EQE from its maximum to a luminance of 1000 cd m⁻². For C2 and C6, the roll-off decreases significantly when decreasing the emitter concentration to 25 wt% (see **Figure 5.15b**). The effect is even more pronounced for SM, which shows a reduction in roll-off from 29 % to 12 % already at an emitter concentration of 50 wt%. In contrast, a luminance of 1000 cd m⁻² is only achieved for **P(Ph-MAC-BP)** with 50 % blending ratio and the EQE roll-off at 100 cd m⁻² shows an opposite trend in comparison to the other TADF materials. With increasing emitter concentration, the roll-off increases from 14 % in the pristine film to 50 % at an emitter concentration of 10 wt%. This observation is in

agreement with a longer triplet lifetime observed for **P(Ph-MAc-BP)** reaching high triplet exciton concentrations and subsequent quenching at lower voltages.

The increase in EQE upon blending further leads to an improved PE (see **Figure 5.16**). The devices exhibit an enhancement of the PE maximum going from the pristine EML to a 1:3 blend, reaching 22.8 lm W^{-1} for **Tol-MAc-BP**. However, for **P(C2-MAc-BP)** the maximum PE is observed at 50 wt% emitter concentration with 16.8 lm W^{-1} , while **P(Ph-MAc-BP)** reaches its maximum at 10 wt% emitter concentration, reaching 11.9 lm W^{-1} . The increase in power efficiency of 30 % - 41 % for devices A-C upon blending with PS is lower than the enhancement in EQE. This difference can be explained by the voltage dependence of PE (see **Equation 3**). While an increase in EQE leads to an increase in PE, the simultaneous rise in driving voltage with polystyrene concentration has an adverse effect on the power efficiency. Since higher luminance requires a higher applied voltage, the PE-*L* characteristics show a stronger roll-off than the EQE-*L* plot.

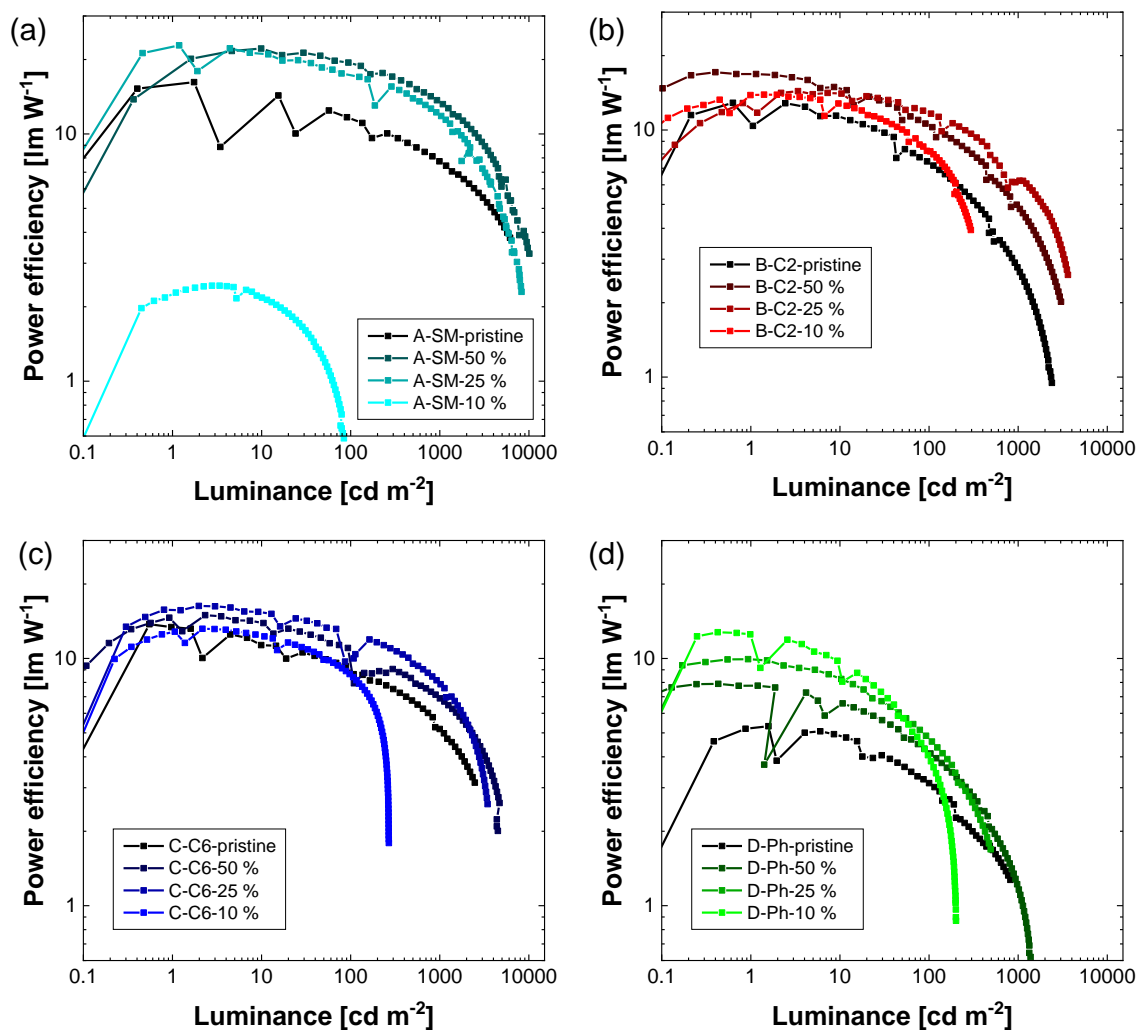


Figure 5.16. Power efficiency-luminescence characteristics of (a) devices A with **Tol-MAc-BP**, (b) devices B with **P(C2-MAc-BP)**, (c) devices C with **P(C6-MAc-BP)** and (d) devices D with **P(Ph-MAc-BP)** with various PS blending ratios.

To summarize, the increased EQE and PE with decreasing emitter concentration seems to be mostly caused by an increase in PLQY. Due to the loss of percolation pathways at low emitter concentrations of 10 wt%, the driving voltage is increased, while the maximal attainable luminance decreases, leading to a decline in performance. This indicates that the trade-off between concentration quenching and charge transport is obtained at emitter concentrations in the range of 25 wt%-50 wt%. The small molecule **Tol-MAc-BP** and nonconjugated polymers **P(C2-MAc-BP)** and **P(C6-MAc-BP)**

show similar performances and are superior to the fully conjugated polymer **P(Ph-MAc-BP)** when applied in OLEDs.

5.2.2. OLEDs with Small Molecule Host

In the previous section, an enhancement in OLED performance was achieved by blending the TADF materials with PS as an electrically insulating host, resulting in a suppression of concentration quenching. While the low cost of PS and the excellent solution processability are advantages of the chosen polymer host, the fact that it is an electrical insulator also increases the driving voltage and lowers the performance at high dilution unless a trap dilution effect is apparent. In order to investigate if the increased driving voltage can be mitigated by using more conventional semiconducting hosts, two sets of OLEDs were fabricated for each of the TADF materials. For the first set, TCTA was used as a host (devices E), while the second set consists of a mixed host of TCTA and TAPC (devices F), which has been used in combination with TADF polymers in solution processing.^[59,81] For both devices the doping concentration of the TADF materials is 10 %, resulting in a ratio of TADF:TCTA:TAPC of 10:65:25. The EMLs were spincoated from chlorobenzene solution and, due to the low solubility of TCTA and TAPC, the solutions had to be heated to 80 °C to fully dissolve the materials. Because of the dilute solutions, film thicknesses beyond 50 nm were not achieved, limiting the potential for solution processability. The HOMO and LUMO energies, as well as the device structure are shown in **Figure 5.17**.

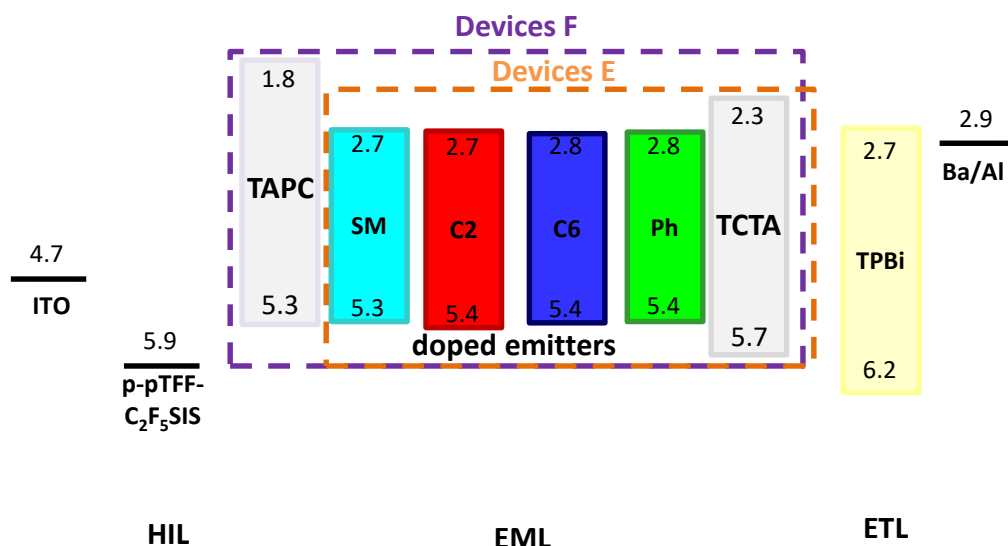


Figure 5.17. Energy level diagram showing the HOMO/LUMO levels and structures of the OLED devices E and F.

The OLED characteristics of devices E and F are shown in **Figure 5.18** and summarized in **Table 5.3**. Apart from the OLEDs based on the small molecule emitter, the current densities of the OLEDs containing polymer emitters are virtually identical, indicating that charge transport is dominated by the host. The addition of TAPC to the host mixture appears to have negligible impact on the overall charge transport. However, it appears that the SM also contributes to the hole transport, in agreement with the clearly better hole-transport properties as compared to the polymer counterparts (see section 5.1). In direct comparison to the PS blended EML devices with a dilution of 1:9, these current densities are between one and two orders of magnitude higher. Furthermore, the turn-on voltage stays low in the range of 2.8 V – 3.0 V. In contrast to the PS blended devices, all devices E and F reach luminances above 1000 cd m⁻². While the PS blending increased the driving voltage significantly, a luminance of 1000 cd m⁻² was achieved at low voltages between 4.6 V and 6.4 V.

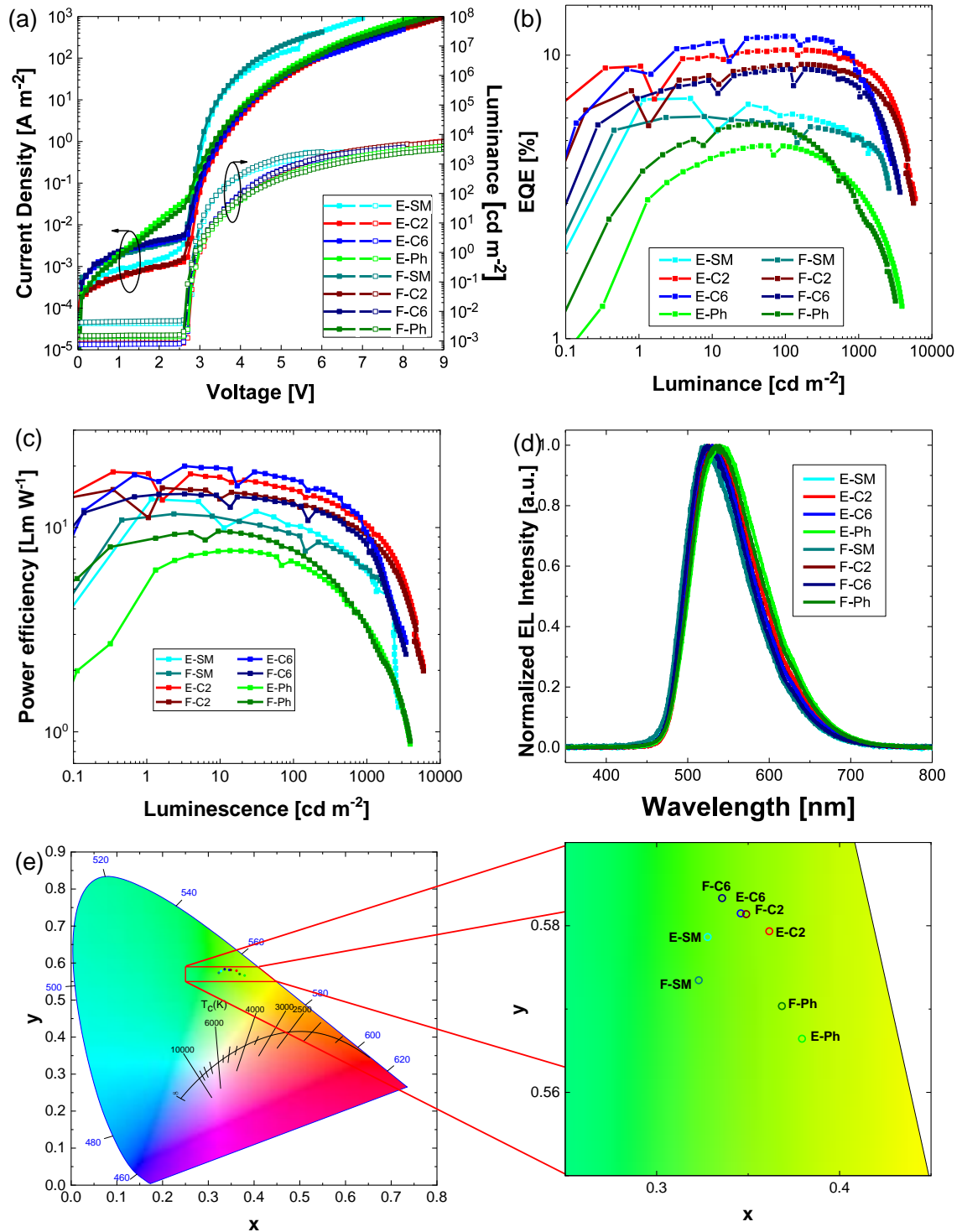


Figure 5.18. (a) J - V - L characteristics, (b) EQE- L characteristics, (c) PE- L characteristics and (d) EL spectra. (e) CIE chromaticity diagram with zoomed in area of devices E and F

In terms of EQE, similarly high values in comparison to the devices B and C with 25 % dilution with PS host are obtained for **P(C2-MAc-BP)** and **P(C6-MAc-BP)** with EQE_{max} of 10.5 % and 11.7 % in TCTA host and 9.3 % and 8.9 % for the two-component host. In contrast, devices based on the small molecule emitter **Tol-MAc-BP** on the other hand showed a lower maximum EQE of 7.0 % and 6.1 % similar to the pristine EML device A. This inferiority in performance can be ascribed to the poor film formation properties of a small molecule mixture of host and guest limiting the achievable performance. In all examples, except for the fully conjugated **P(Ph-MAc-BP)**, the TCTA host showed better performance than the TCTA:TAPC host system. Although the fully conjugated TADF polymer **P(Ph-MAc-BP)** exhibited a lower EQE with 4.8 % and 5.7 % than in the 1:9 blended EML, the maximum is further shifted to higher luminescence. The similar EQE and improved driving voltages lead to higher PE for the TCTA host devices of 18.4 lm W^{-1} for **P(C2-MAc-BP)** and even 20.0 lm W^{-1} for **P(C6-MAc-BP)** in comparison to the PS blended EML devices. Due to the slightly lower EQE values in the two component host system TCTA:TAPC, the PE is 15.6 lm W^{-1} and 14.6 lm W^{-1} for **P(C2-MAc-BP)** and **P(C6-MAc-BP)**, respectively, similar to the best PS blended EML devices. The maxima of the EL spectra range from 521 nm - 541 nm with no additional host emission around 400 nm detected.

Table 5.3: Summary of device performance of the devices E and F.

Device	V_{on} [V] at 1 cd m ⁻²	V_d [V]	CE [cd A ⁻¹] max./ 100 /1000 cd m ⁻²	PE [Lm W ⁻¹]	EQE [%]	λ_{em} [nm]	FWHM [nm]	CIE (x, y)
E-SM	2.9	3.0/ 3.5/ 4.8	12.8/ 11.2/ 9.4	13.8/ 10.2/ 6.2	7.0/ 6.1/ 5.2	523	89	0.33, 0.58
E-C2	3.0	4.2/ 4.2/ 5.5	20.1/ 20.1/ 17.9	18.4/ 15.3/ 10.3	10.5/ 10.5/ 9.4	533	95	0.36, 0.58
E-C6	2.9	4.0/ 4.1/ 5.5	21.8/ 21.8/ 16.3	20.0/ 17.1/ 9.5	11.7/ 11.7/ 8.7	527	92	0.34, 0.59
E-Ph	3.0	3.9/ 4.3/ 6.1	9.2/ 9.1/ 6.3	7.7/ 6.8/ 3.3	4.8/ 4.8/ 3.3	541	101	0.38, 0.57
F-SM	2.8	3.0/ 3.5/ 4.6	10.9/ 10.2/ 9.1	11.7/ 9.3/ 6.3	6.1/ 5.7/ 5.0	521	89	0.32, 0.58
F-C2	2.9	4.3/ 4.1/ 5.5	17.5/ 17.5/ 15.9	15.6/ 13.5/ 9.1	9.3/ 9.2/ 8.4	529	92	0.35, 0.58
F-C6	2.9	4.3/ 4.1/ 5.4	16.6/ 16.5/ 14.3	14.6/ 12.9/ 8.3	8.9/ 8.9/ 7.7	524	90	0.33, 0.59
F-Ph	2.9	3.8/ 4.3/ 6.4	10.9/ 10.5/ 5.5	9.6/ 7.8/ 2.7	5.7/ 5.5/ 2.9	536	98	0.37, 0.57

5.3. Conclusion

In this chapter, the OLED performance of the yellowish-green emitting TADF polymers **P(C2-MAc-BP)** and **P(C6-MAc-BP)** with alkyl linker and **P(Ph-MAc-BP)** with conjugated linker were determined and compared with their small molecule counterpart **Tol-MAc-BP**. Ohmic hole injection was obtained for all materials using the high work function HIL p-pTFF-C₂F₅-SIS. For the polymers trap-limited hole and electron transport was observed. The hole transport seems to decrease

significantly upon polymerization independent of the linker used. The electron transport was observed to be inferior to hole transport, causing imbalanced charge transport and limiting the efficiency of OLEDs. To counteract the inferior electron transport, TPBi was added as an ETL, increasing the efficiency by an order of magnitude in comparison to the single-layer device.

Using this optimized device structure, the OLED performance of the TADF materials in various blending ratios with PS was investigated. All materials showed an increase in EQE with dilution stemming from the suppression of concentration quenching, which both increased the PLQY and reduced the EQE roll-off. The nonconjugated polymers **P(C2-MAc-BP)** and **P(C6-MAc-BP)** showed high EQE maxima of 11.8 % at an emitter concentration of 25 wt%, while the small molecule **Tol-MAc-BP** reached its maximum EQE of 12.9 % at an emitter concentration of 50 wt%. The small molecule **Tol-MAc-BP** further showed the strongest decrease in current density upon with decreasing emitter concentration, ascribed to a loss in percolation pathways for charge transport. Compared to the nonconjugated polymers, a lower EQE of 8.4 % at an optimized 10 wt% emitter concentration was obtained for the fully conjugated polymer **P(Ph-MAc-BP)** overall showing a significantly more pronounced EQE roll-off and lower maximum luminance. This result for **P(Ph-MAc-BP)** is in agreement with the reduced PLQY and higher singlet and triplet quenching processes observed in chapter 4.

Using the small molecule host systems TCTA and TCTA:TAPC known from literature resulted in lower driving voltages for low emitter concentrations, as compared to using PS as a host. While the TCTA:TAPC host was inferior to a PS host in terms of OLED efficiency, the OLEDs with a TCTA host exhibited an improved PE stemming from similar EQE values but lower driving voltage compared to the PS blended devices. Interestingly, using a semiconducting (TCTA) host did not improve the overall performance in case of the small-molecular emitter **Tol-MAc-BP** at optimized concentration in a PS host. The excellent solution processability of PS and cheap price might outweigh the small improvement in power efficiency observed for the TCTA host in combination with polymer emitters. The fact that high efficiencies were obtained for **P(C2-MAc-BP)** and **P(C6-MAc-BP)** upon dilution

and that the performance is just slightly worse than their small molecule counterpart **Tol-Mac-BP** indicates the use of alkyl linker as a feasible strategy to develop highly efficient polymer OLEDs based on TADF polymers.

5.4. Appendix of Chapter 5

5.4.1. Contributions to Chapter 5

All devices were fabricated and characterized by Kai Philipps (Molecular Electronics Department, MPIP Mainz). The single carrier devices were modeled by [REDACTED] (Molecular Electronics Department, MPIP Mainz). p-pTFF-C₂F₅SIS was supplied by [REDACTED] (Department of Chemistry and Department of Physics, National University of Singapore). Experimental results were regularly discussed with Paul Blom (Molecular Electronics Department, MPIP Mainz), Jasper Michels (Molecular Electronics Department, MPIP Mainz), [REDACTED] (Faculty of Science, Vrije Universiteit Amsterdam and Molecular Electronics Department, MPIP Mainz) and [REDACTED] (Molecular Electronics Department, MPIP Mainz).

5.4.2. Figures and Tables

Table A5.1. Modelling parameters of HO-B-C2 hole-only devices using EGDM.

Device	P_t [10 ²³ m ⁻³]	μ_{n0} [10 ⁻¹² m ² V ⁻¹ s ⁻¹]	a_p [10 ⁻¹⁰ m]	$\sigma_{n,Gauss}$ [eV]
HO-A-C2	7.2	1.50	8	0.08

Table A5.2. Summary of device performance of the TADF emitters with varying doping concentrations.

Device	V_{on} [V] at 1 cd m ⁻²	V_d [V]	CE [cd A ⁻¹] max./ 100 /1000 cd m ⁻²	PE [Lm W ⁻¹]	EQE [%]	λ_{em} [nm]	FWHM [nm]	CIE (x, y)
G-C2	9.3	14.5/	0.82/ 0.78/	0.19/	0.43/ 0.42/	550	0.43	0.41,
		13.7/-	-	0.18/ -	-			0.56
G-C6	9.4	15.5/	0.92/ 0.81/	0.20/	0.48/ 0.42/	545	0.41	0.39,
		13.4/	0.89	0.19/ 0.17	0.47			0.57
		17.0						
G-Ph	8.6	12.5/	0.45/ 0.44/	0.12/	0.24/ 0.24/	550	0.42	0.41,
		13.0/ -	-	0.11/ -	-			0.56
H-SM	5.8	8.0/ -/ -	0.02/ -/ -	0.01/ -/ -	0.01/ -/ -	529	0.33	0.33, 0.61
H-C2	9.4	13.5/	0.97/ 0.93/	0.24/	0.52/ 0.50/	553	0.43	0.42,
		14.2/ -	-	0.21/ -	-			0.55
H-C6	7.8	13.5/	1.06/ 1.00/	0.27/	0.55/ 0.52/	543	0.41	0.39,
		11.9/ -	-	0.27/ -	-			0.57
H-Ph	8.2	12.0/	0.48/ 0.47/	0.14/	0.25/ 0.25/	554	0.42	0.42,
		12.8/ -	-	0.12/ -	-			0.55
I-C2	5.5	7.0/ 8.0/ -	5.79/ 5.45/	2.78/	3.13/ 2.95/	549	0.42	0.41,
			-	2.14/ -	-			0.56
I-C6	5.0	6.1/ 6.4/	13.56/	6.99/	7.09/ 5.77/	538	0.40	0.38,
		7.9	11.04/ 7.71	5.47/ 3.08	4.03			0.58
I-Ph	4.9	5.0/ 7.2/ -	3.88/ 2.79/	2.44/	2.11/ 1.50/	542,	0.42	0.38,
			-	1.21/ -	-			380
J-C6-50 %	4.3	4.8/ 5.5/	16.52/	10.81/	8.43/ 6.10/	534	0.40	0.36,
		7.8	11.98/ 7.32	6.81/ 3.02	3.67			0.58

J-C6-25 %	5.3	7.0/ 10.7/	11.21/	5.68/	6.84/ 4.53/	524,	0.40	0.32,
		-	7.46/ -	2.20/ -	-	385		0.57
J-C6-10 %	8.3	11.0/	3.65/ 3.22/	1.12/	2.36/ 2.09/	523,	0.40	0.31,
		13.4/ -	-	0.76/ -	-	382		0.56
K-C6-pristine	3.6	6.0/ 5.3/	9.21/ 8.84/	5.53/	4.72/ 4.51/	536	0.39	0.38,
		7.6	8.74	5.22/ 3.61	4.48			0.58
K-C6-50 %	3.8	6.6/ 5.3/	11.90/	6.92/	6.31/ 6.04/	527	0.39	0.35,
		7.2	11.38/	6.71/ 4.94	5.97			0.59
			11.26					
K-C6-25 %	4.3	6.0/ 5.9/	10.38/	5.64/	5.62/ 5.57/	524	0.39	0.34,
		7.5	10.27/ 9.56	5.44/ 3.99	5.17			0.59
K-C6-10 %	4.8	6.0/ 7.3/ -	10.25/	5.56/	5.73/ 5.57/	520	0.39	0.32,
			9.96/ -	4.30/ -	-			0.59
L-C6	5.1	9.6/ 8.5/	21.85/	9.63/	11.44/	528	0.38	0.35,
		11.1	21.15/	7.88/ 4.20	11.10/			0.59
			14.83		7.77			
M-C6	6.0	10.2/	17.06/	5.92/	9.06/ 9.01/	526	0.36	0.34,
		10.7/ -	16.94/ -	4.97/ -	-			0.60

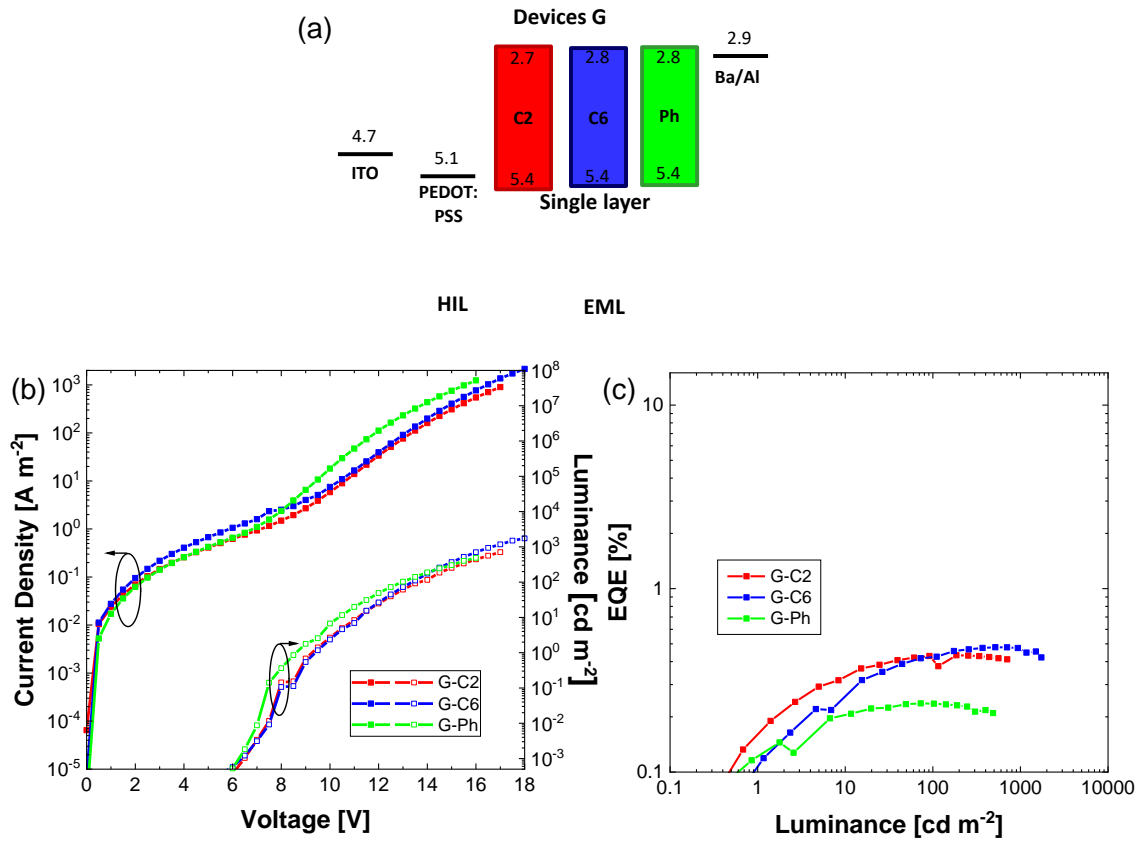


Figure A5.1. (a) Energy level diagram showing the HOMO/LUMO levels and structures of the OLED devices G (glass/ITO (100 nm)/PEDOT:PSS (60 nm)/TADF emitter (100 nm)/Ba (5 nm)/Al (100 nm)). (b) $J-V-L$ and (c) EQE-L characteristics of devices G.

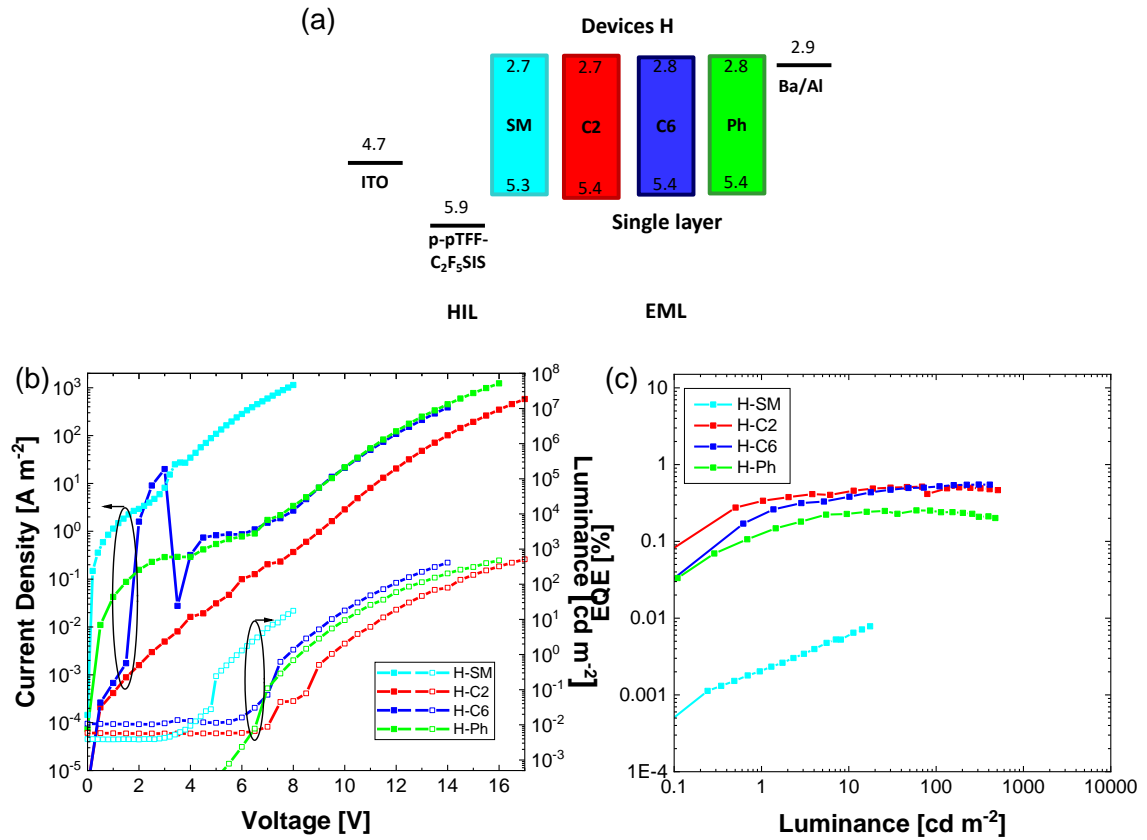


Figure A5.2. (a) Energy level diagram showing the HOMO/LUMO levels and structures of the OLED devices H (glass/ ITO (100 nm)/ p-pTFF-C₂F₅SIS (40 nm)/TADF emitter (100 nm) / Ba (5 nm)/Al (100 nm)). (b) *J-V-L* and (c) *EQE-L* characteristics of devices H.

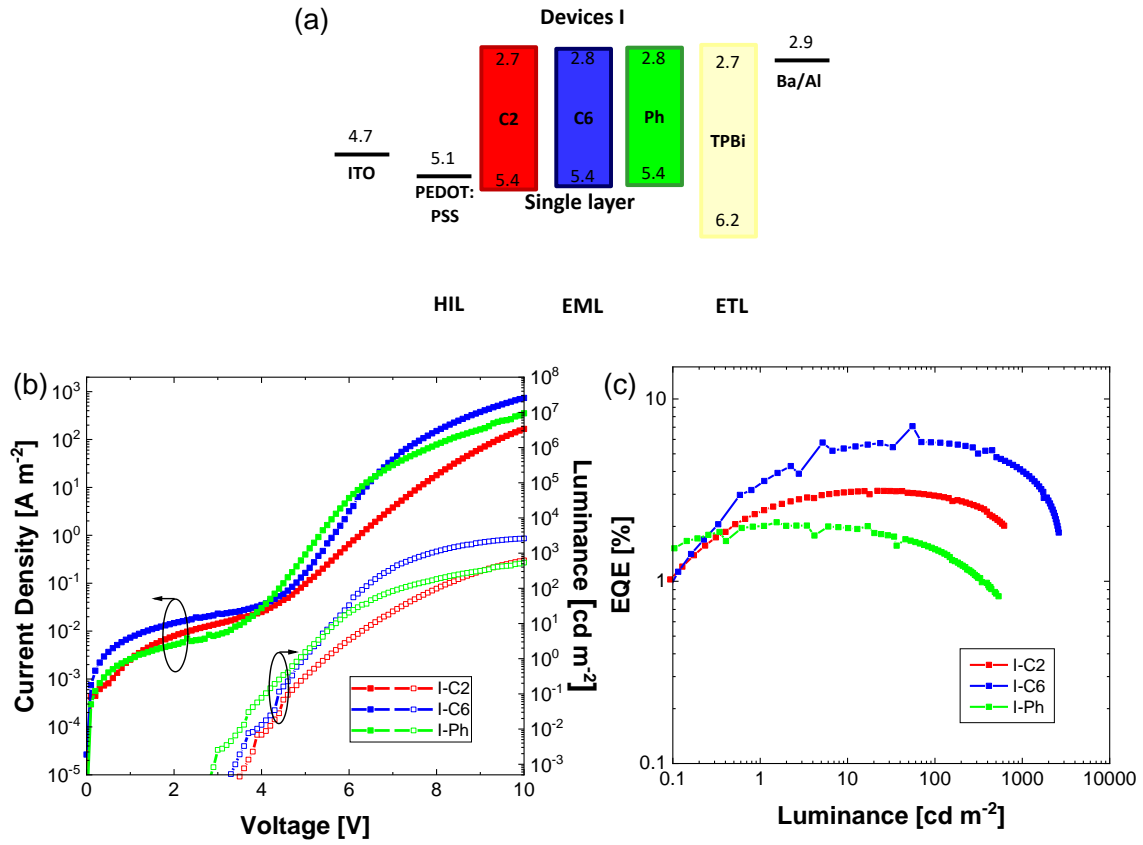


Figure A5.3. (a) Energy level diagram showing the HOMO/LUMO levels and structures of the OLED devices I (glass/ITO (100 nm)/ PEDOT:PSS (60 nm)/TADF emitter (40 nm)/ TPBi (60 nm)/ Ba (5 nm)/Al (100 nm)). (b) J - V - L and (c) EQE- L characteristics of devices I.

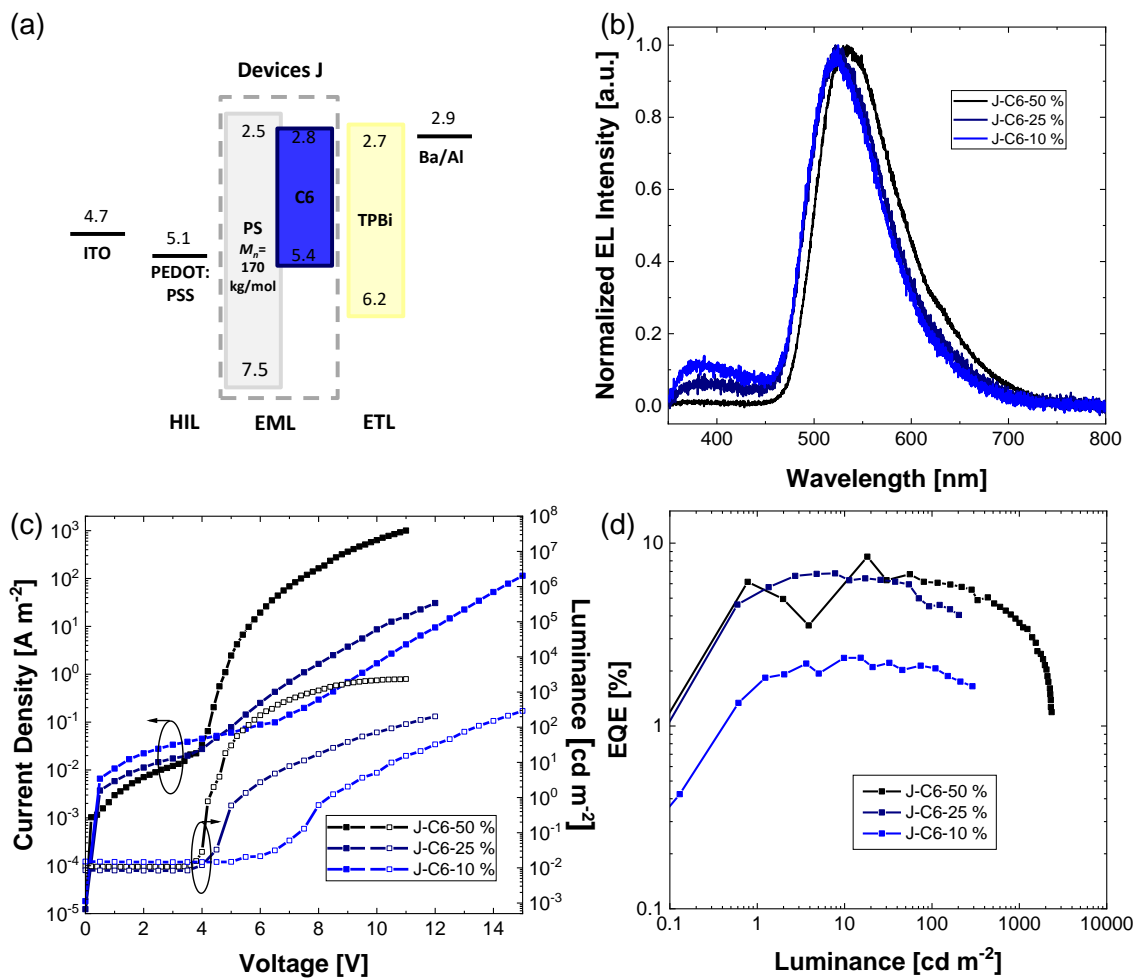


Figure A5.4. (a) Energy level diagram showing the HOMO/LUMO levels and structures of the OLED devices J (glass/ITO (100 nm)/ PEDOT:PSS (60 nm)/TADF emitter: PS ($M_n = 170$ kg/mol) (30 nm)/ TPBi (60 nm)/ Ba (5 nm)/Al (100 nm)). (b) EL spectra, (c) J - V - L and (d) EQE- L characteristics of devices J.

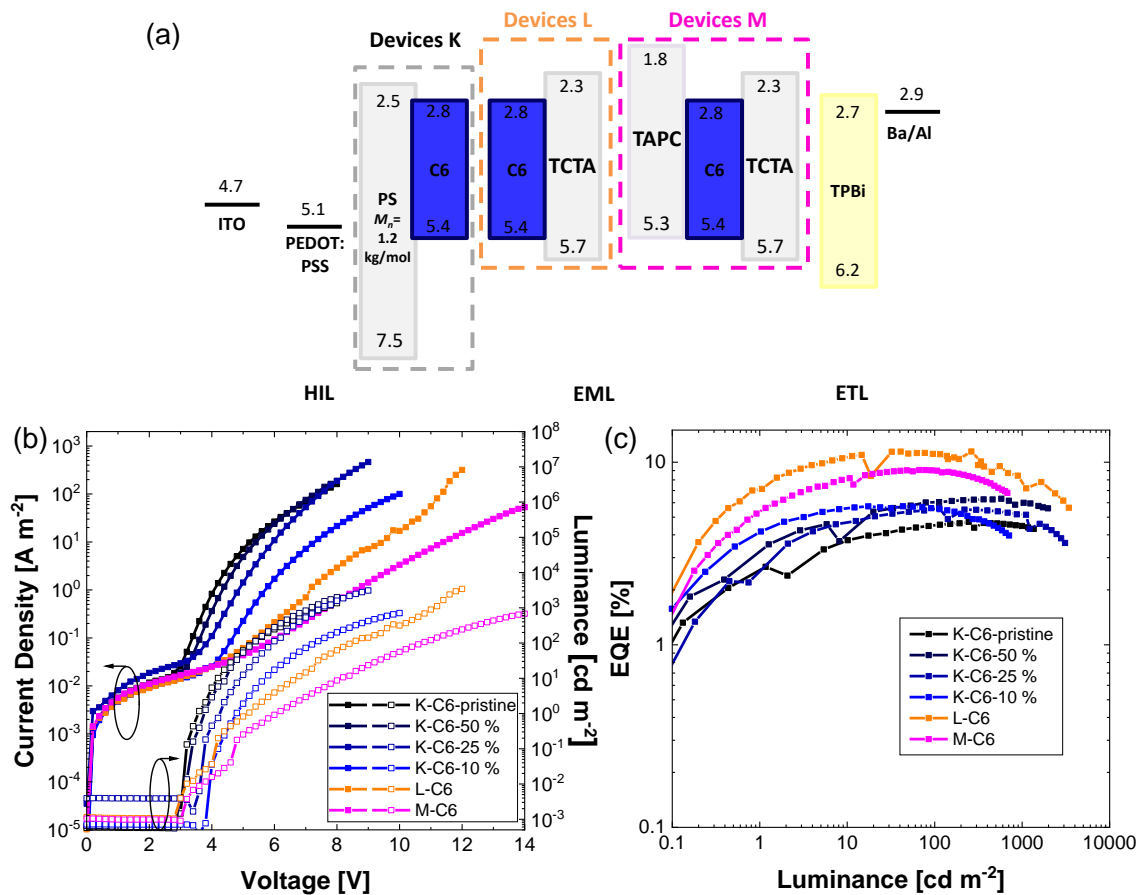


Figure A5.5. (a) Energy level diagram showing the HOMO/LUMO levels and structures of the OLED devices (glass/ITO (100 nm)/ PEDOT:PSS (60 nm)/ EML / TPBi (60 nm)/ Ba (5 nm)/Al (100 nm): Devices K (EML (30 nm) = TADF emitter: PS ($M_n = 170$ kg/mol)), L (EML (45 nm) = TADF emitter:TCTA (1:9)) and M (EML (70 nm) = TADF emitter:TCTA:TAPC (1:6.5:2.5)). (b) $J-V-L$ and (c) EQE-L characteristics of devices K, L and M.

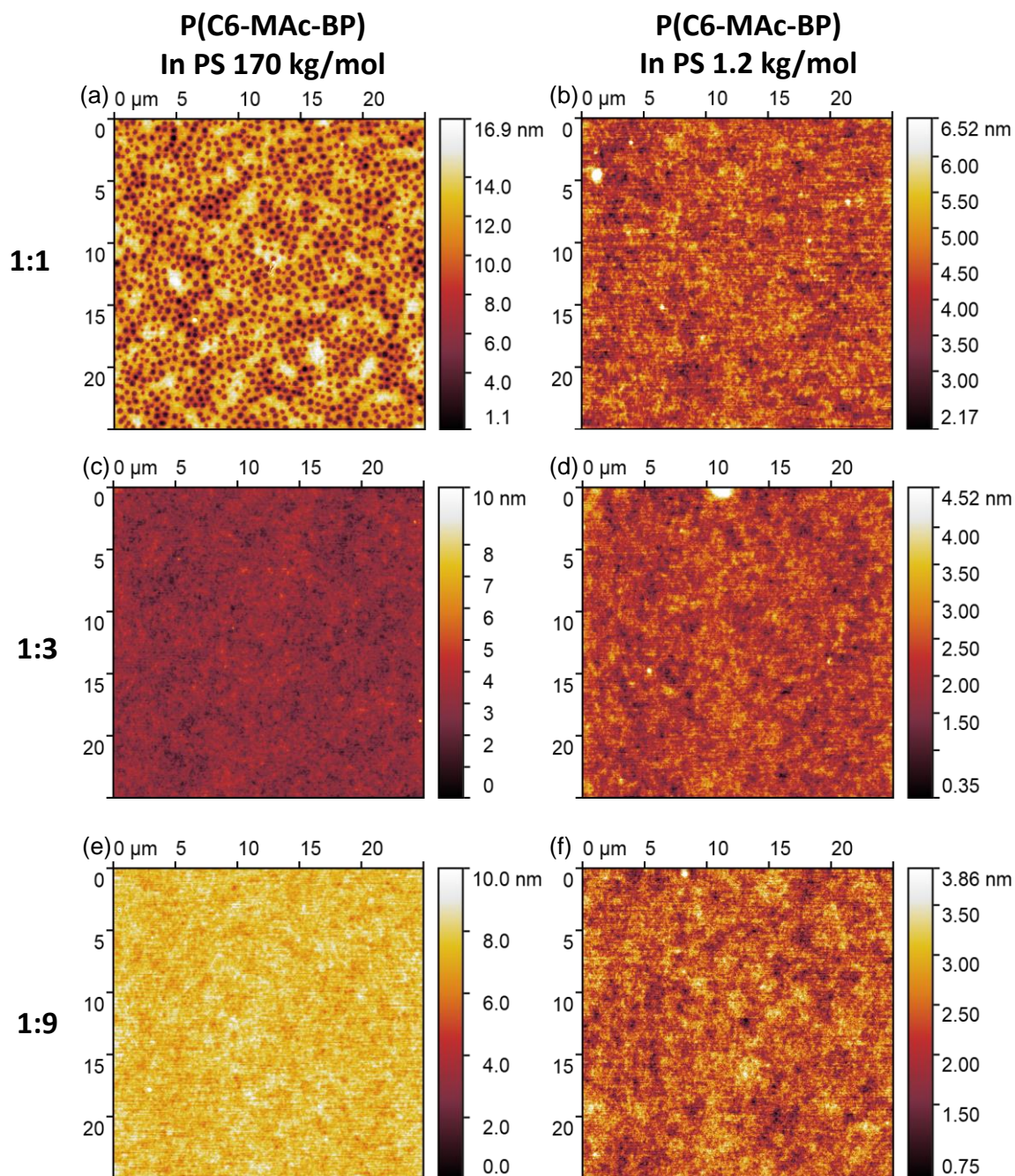


Figure A5.6. Topology AFM images (25 μm x 25 μm) of films of **P(C6-MAc-BP)** in high molecular weight PS ($M_n = 170 \text{ kg mol}^{-1}$) host in (a) 1:1, (c) 1:3 and (e) 1:9 blending ratio, as well as in low molecular weight PS ($M_n = 1.2 \text{ kg mol}^{-1}$) (b) 1:1, (d) 1:3 and (f) 1:9 blending ratio.

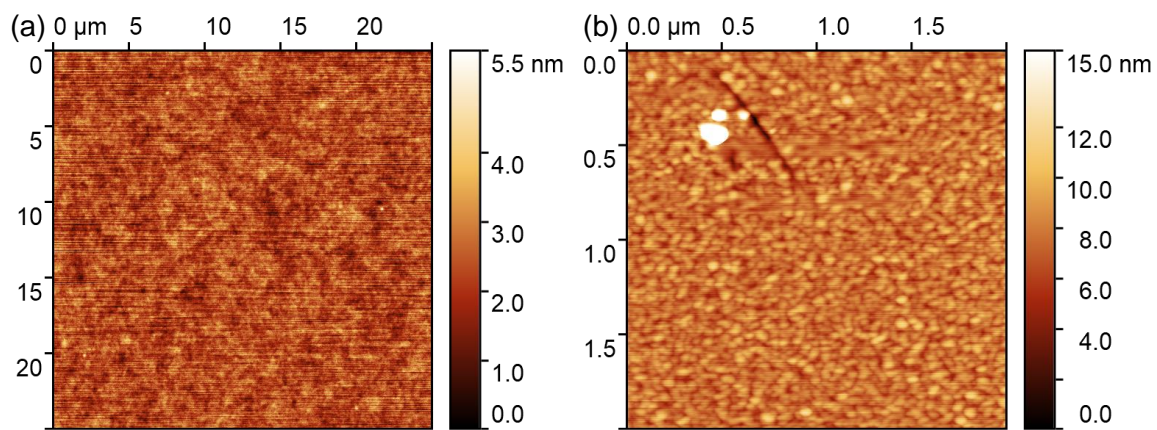


Figure A5.7. (a) Topology AFM images (25 μm x 25 μm) of a 1:9 blended film of **P(C6-Mac-BP):TCTA** and (b) Topology AFM images (2 μm x 2 μm) of a 1:6.5:2.5 blended film of **P(C6-Mac-BP):TCTA:TAPC**.

6. Supramolecular TADF Polymer

TADF emitters based on through-space charge transfer stemming from spatial π - π interactions require donor and acceptor to be in close proximity to one another. At the same time similarly to the through-bond charge transfer emitters, concentration quenching between the D-A units was identified to act as a loss process for the PL and EL emission. While the control of the relative position between donor and acceptor is limited in amorphous films obtained from solution processing, a self-assembling supramolecular polymer system promises exactly this control. Fine-tuning of the molecular structures utilized in this field of research enables the self-assembly of molecules based on different non-covalent interactions. Combining both areas of research as done in this chapter affords an ideal model upon introducing donor and acceptor moieties to the supramolecular comonomers for the systematic investigation of the TSCT mechanism.

For this investigation, the supramolecular ABA-type peptide-polymer conjugate described in detail in the introduction (see section 1.4) was utilized with donor and acceptor groups attached to the amine moiety (N-terminus) at the ends of the FHFHF pentapeptide sequence (see **Figure 6.1**). This supramolecular polymer system shows selective self-assembly in aqueous solution at pH above 6 while the polysarcosine polymer increases the water solubility and forms a hydrophilic shell around the rod-like aggregates formed. Within these nanostructures, the hydrophobicity of the introduced donor and acceptor moieties further ensures a small distance between them facilitating the TSCT stemming from the hydrophobic effect. Based on the reported TSCT polymer developed by Shao et al.^[76] (see section 1.3.4 for a detailed description), DMAC was selected as donor and 2,4,6-triphenyl-1,3,5-triazine (TRZ) as acceptor moiety. The emissive CT excited state formed between these moieties showed a characteristic bathochromic shift in emission with solvent polarity (solvatochromism), TADF in time-resolved photoluminescence spectroscopy and a PLQY of 60 % allowing a wide variety of photophysical characteristics that can be evaluated upon assembly. In order to be able to vary the D to A ratio, for example to assess concentration quenching, two separate supramolecular comonomers with

two donor end groups (**D-PSar-D**) and with one donor and one acceptor end group (**D-PSar-A**) were synthesized (see **Figure 6.1**).

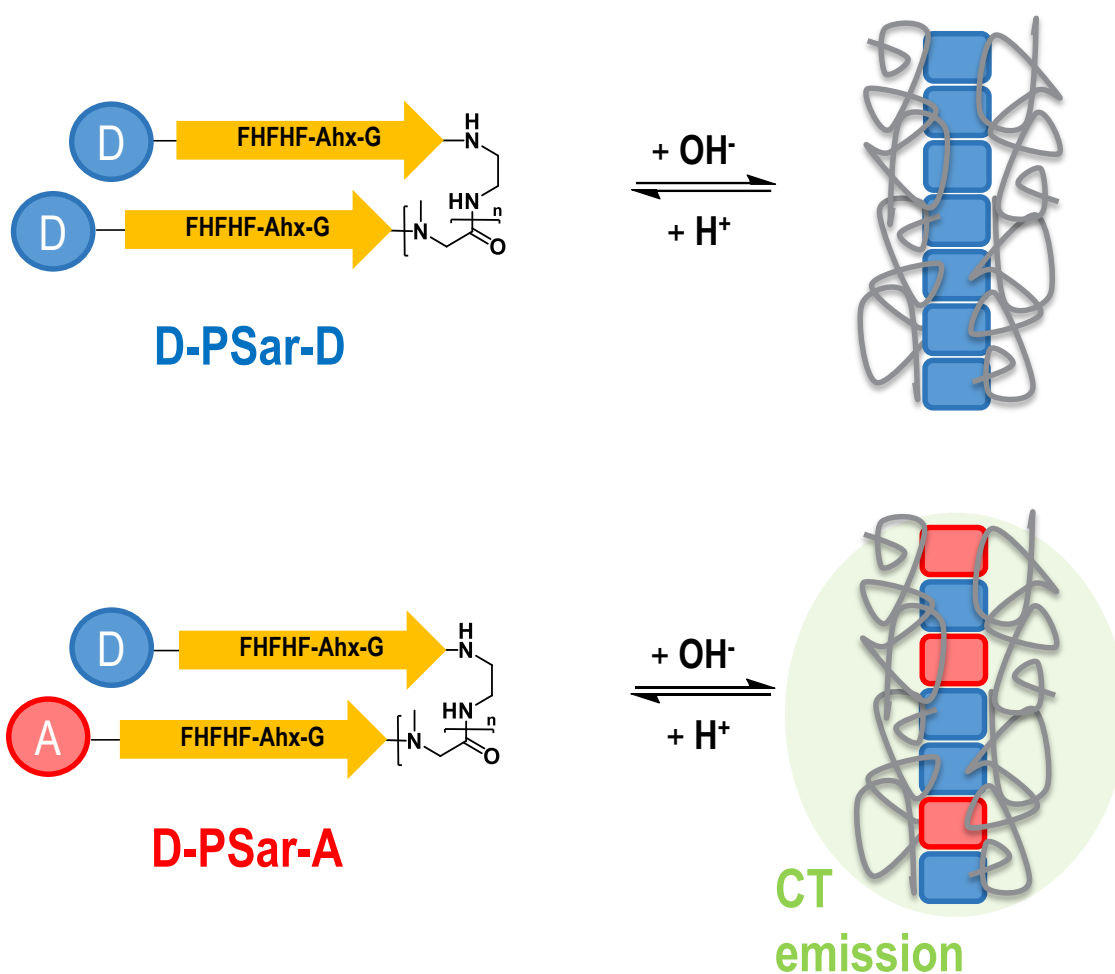


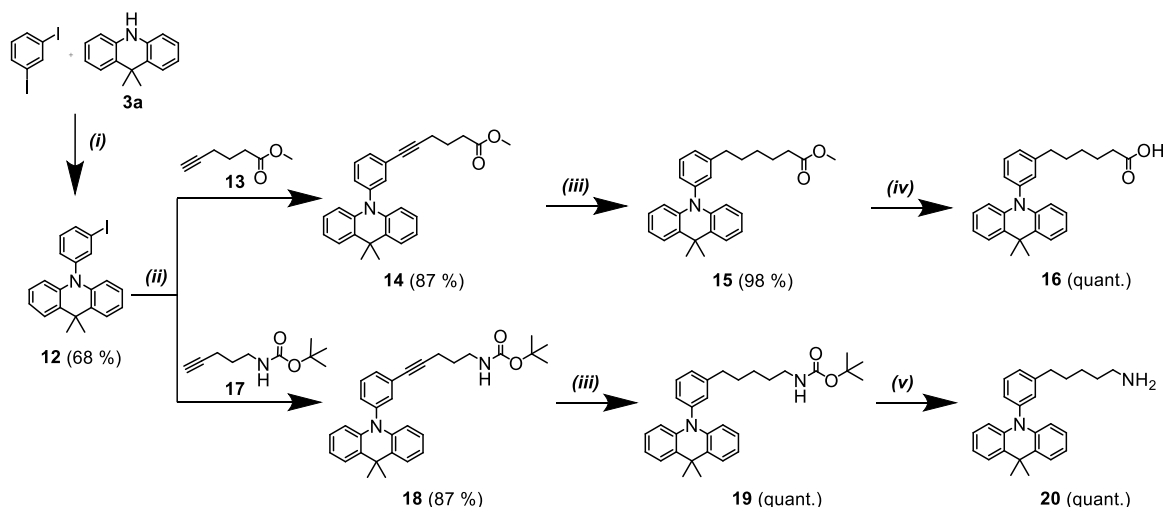
Figure 6.1. Schematic representation of pH responsive self-assembly of **D-PSar-D** and **D-PSar-A**. Ahx is an abbreviation for amniohexanoic acid and G for glycine.

6.1. Synthesis of **D-PSar-D** and **D-PSar-A**

The syntheses of the peptide-polymer conjugates **D-PSar-D** and **D-PSar-A** can be divided in three parts: At first, the DMAC donor and TRZ acceptor with carboxylic acid and amine functionalization were synthesized (see **Scheme 6.1** - **Scheme 6.3**). These reactive moieties enabled

the coupling to the pentapeptide in the next part to afford the initiator peptide **37** and the peptides **33** and **34** used for endgroup functionalization (see **Scheme 6.4**). In the last part, the **D-PSar-D** as well as **D-PSar-A** polymers were synthesized (see **Scheme 6.5**).

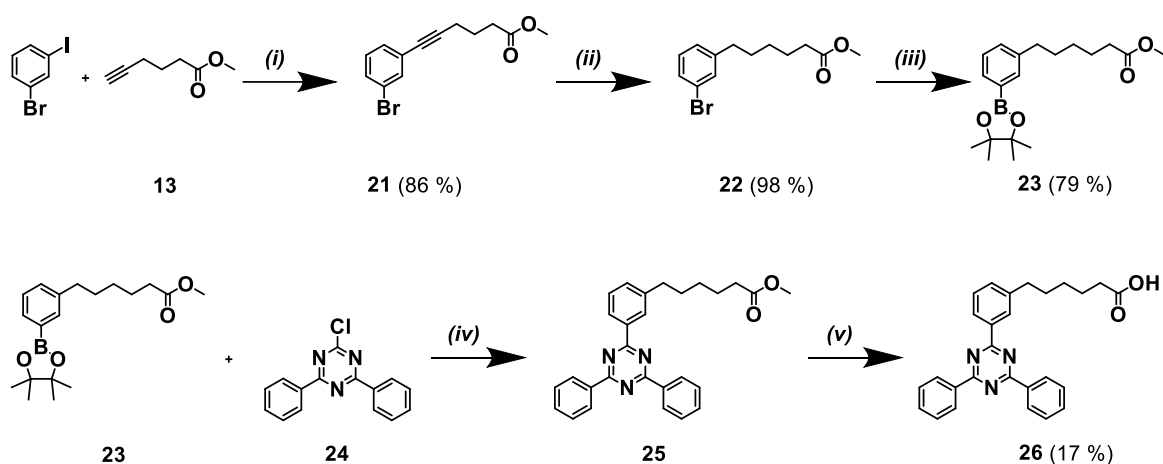
As a first step **3a** was coupled with 1,3-diiodobenzene in a copper-catalyzed amination to **12**. This monoiodinated acridine derivative **12** was used as a starting material for two Sonogashira reactions reacting with the terminal alkynes **13** and **17** to afford compounds **14** and **18**, respectively. In a subsequent step, the triple bond was hydrogenated with palladium on carbon (10 %) in a hydrogen atmosphere and the donor derivatives **15** with a methyl ester protected carboxylic acid and **19** with a *tert*-butyloxycarbonyl (Boc) protected amine moiety were obtained. The deblocking of these protection moieties were done via saponification of the ester affording **16** and under acidic conditions obtaining **20**. Both acridine donor derivatives were successfully synthesized in an overall yield of 58 % and 61 % for **16** and **20**, respectively.



Scheme 6.1. Synthesis of donor compounds **16** and **20**: i) Cu powder, K₂CO₃, dichlorobenzene, reflux; ii) PdCl₂(PPh₃)₂, THF, r.t.; iii) Pd-C (10 %), H₂, THF; iv) LiOH, THF:H₂O (1:1), r.t.; v) DCM:TFA (1:1), r.t.

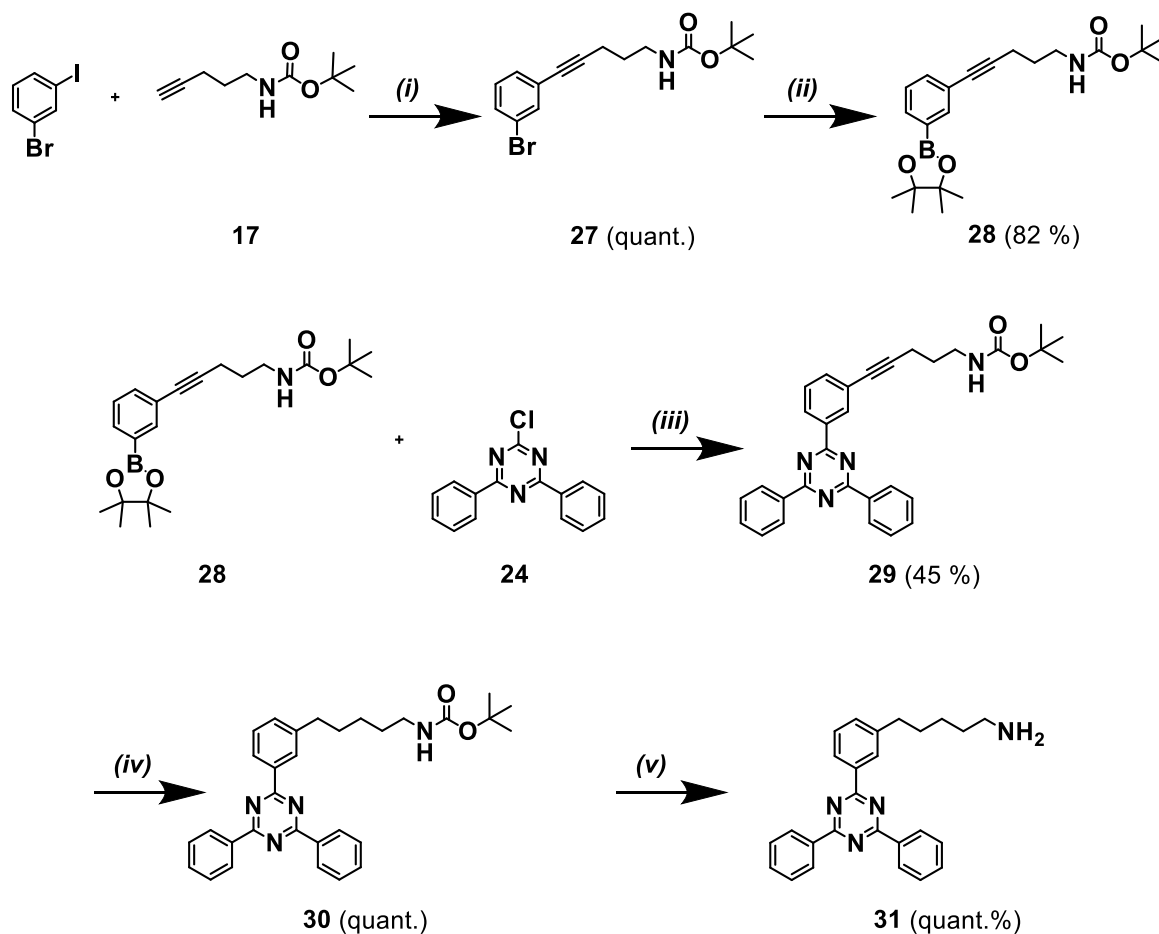
The first step for the synthesis of the carboxylic acid functionalized acceptor compound **26** was a Sonogashira reaction of **13** with 1-bromo-3-iodobenzene affording **21**. In the second step the alkyne

was hydrogenated with Raney®-nickel as a catalyst, which did not show a dehalogenation as observed for palladium on carbon and **22** was obtained. After borylation affording **23**, a subsequent Suzuki condensation lead to the methyl ester protected acceptor compound **25**. Due to the base used in this reaction the product was already partially saponificated, which is why **25** was not isolated but directly fully converted to the unprotected product **26** using LiOH as base. **26** was obtained in an overall yield of 11 %.



Scheme 6.2. Synthesis of acceptor **26**: i) CuI, PdCl₂(PPh₃)₂, NEt₃, THF, 80 °C; ii) Raney®-Nickel slurry, H₂, THF, r.t.; iii) bis-(pinakolato)-diboran, [1,1'-bis(diphenylphosphino)ferrocene]palladium(II) dichloride dichloromethane adduct, KOAc, dioxane, 80 °C; iv) Na₂CO₃, Pd(PPh₃)₄, toluene:EtOH:H₂O (4:1:1), 120 °C; v) LiOH, THF:H₂O (1:1), r.t.

The synthesis of the amine-functionalized acceptor compound **31** is similar to the previous synthetic route. Starting with a Sonogashira reaction between **17** and 1-bromo-3-iodobenzene affording **27** and a subsequent borylation yielding **28**. After a Suzuki coupling with **24**, the alkyne moiety of **29** was hydrogenated using palladium on carbon (10 %) as a catalyst and the Boc-protected acceptor amine **30** was obtained. The deblocking of the amine moiety of **30** was achieved under acidic conditions affording **31** with an overall yield of 37 %.

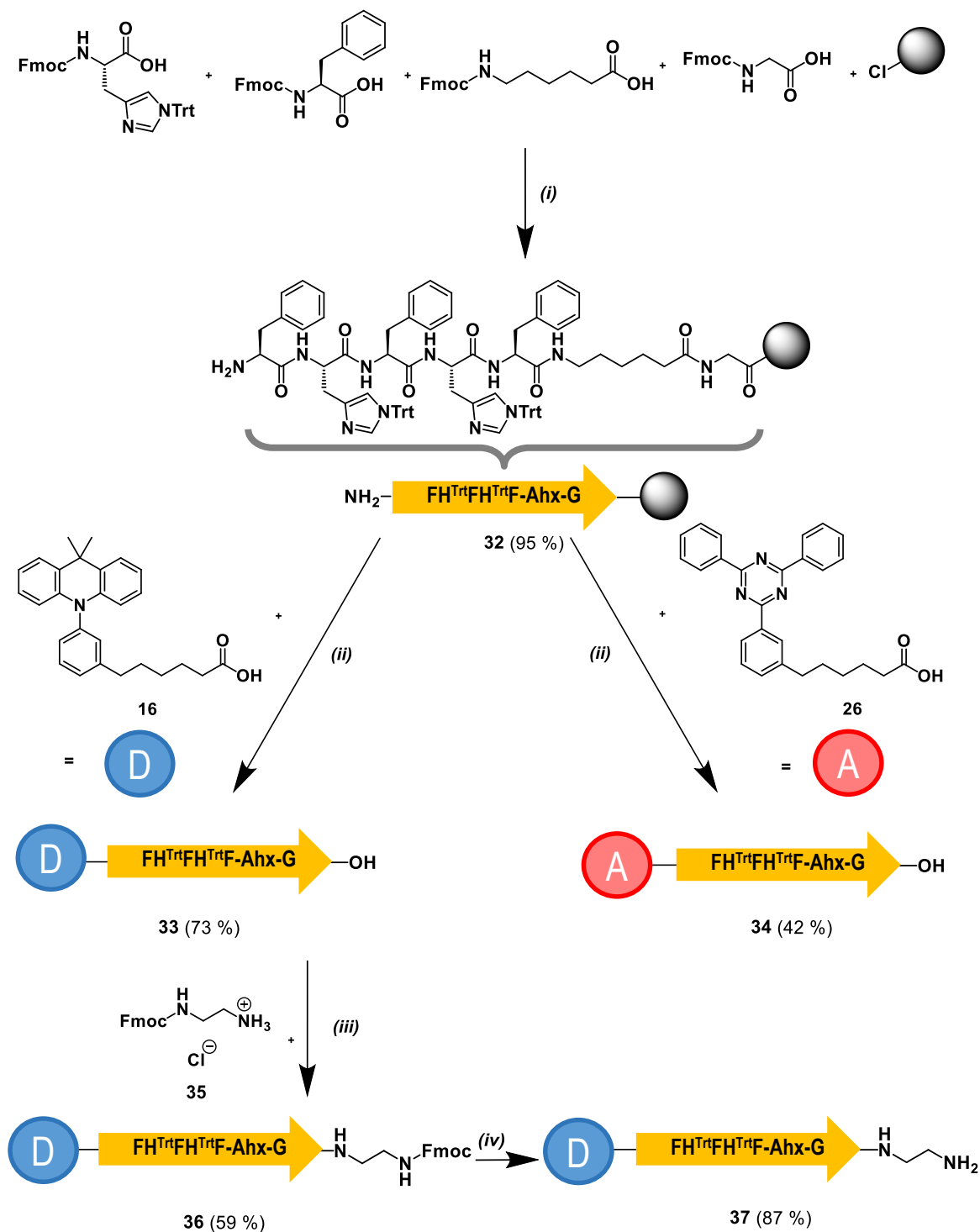


Scheme 6.3. Synthesis of acceptor **31**: i) CuI, PdCl₂(PPh₃)₂, NEt₃, THF, 80 °C; ii) bis-(pinacolato)-diboran, [1,1'-bis(diphenylphosphino)ferrocene]palladium(II) dichloride dichloromethane adduct, KOAc, dioxane, 80 °C; iii) Na₂CO₃, Pd(PPh₃)₄, toluene:EtOH:H₂O (4:1:1), 120 °C; iv) Raney®-Nickel slurry, H₂, THF, r.t.; v) DCM:TFA (1:1), r.t.

After the syntheses of the amine- and carboxylic acid-functionalized donor and acceptor, the peptide **32** was obtained using a solid-phase peptide synthesis (SPPS) as a next step. This synthetic procedure is based on a selective peptide coupling reaction performed by an automated synthesizer using fluorenylmethoxycarbonyl (Fmoc) protected amino acids as starting materials. While the amine moieties are blocked by Fmoc, the first amino acid is coupled to a solid phase resin with its carboxylic acid moiety. In subsequent deblocking and peptide coupling reactions, the peptide sequence is built up step-by-step from carboxylic acid (C-terminus) to the amine moiety (N-terminus) of the peptide. The

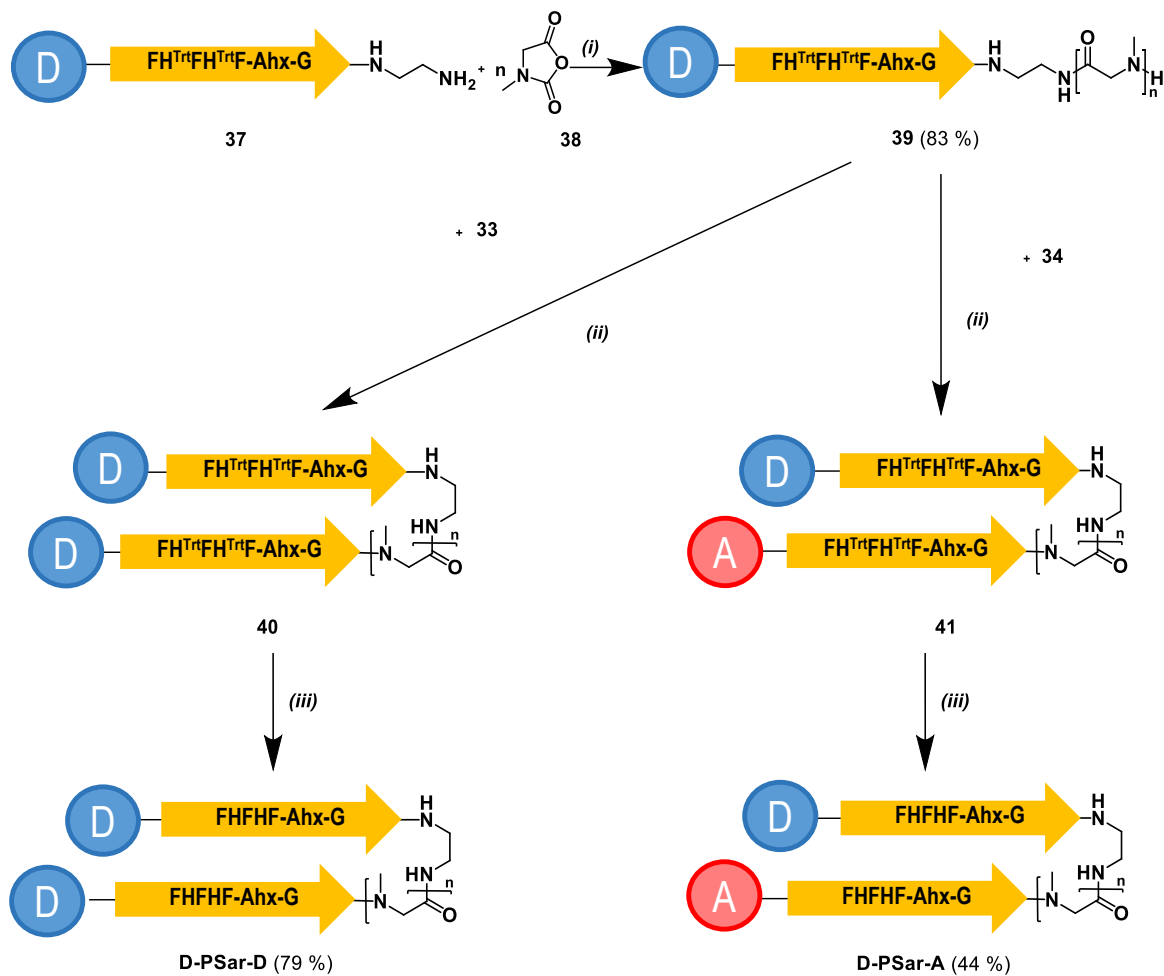
peptide **32** consists of the β -sheet encoded peptapeptide FHFHF with the amines of the histidines being trityl-protected (Trt), as well as an aminohexanoic acid (Ahx) and glycine (G) acting as spacer groups.

In the next step, the carboxylic acid-functionalized donor and acceptor compounds **16** and **26** were coupled to the peptide **32**, which was still loaded on the resin. After cleaving the peptide off the resin using 2,2,2-trifluoroethanol (TFE), the compounds **33** and **34** were obtained enabling the endgroup functionalization after the upcoming N-carboxyanhydride (NCA) polymerization. Based on **33**, the amine functionalized initiator **37** was afforded upon coupling Fmoc ethylene diamine hydrochloride (**35**) to the C-terminus and a subsequent Fmoc-deblocking of **36**.



Scheme 6.4. Synthesis of the peptides **33** and **34** as well as the peptide initiator **36**: i) SPPS coupling steps: 2-(1H-benzotriazol-1-yl)-1,1,3,3-tetramethyluronium-hexafluorophosphat (HBTU), 1-hydroxybenzotriazol (HOBT), N,N-diisopropylethylamine (DIPEA), DCM/DMF, r.t.; SPPS Fmoc-deprotection steps: piperidine, DMF, r.t.; ii) 1) HBTU, HOBT, DIPEA, DCM/DMF, r.t. 2) TFE:DCM (4:1); iii) PyBOP, HOBT, DIPEA, DMF, r.t.; iv) piperidine, DCM, r.t.

The amine moiety of **37** initiates the ring opening NCA polymerization via a nucleophilic attack of the carbonyl group in **38** and the peptide-polymer conjugate **39** was obtained. The batch of **39** was split in two and endgroup functionalized with the-peptides **33** and **34**. After the deprotection of the histidine side chains of **40** and **41**, the ABA'-type peptide-polymer conjugates **D-PSar-D** with two donor moieties and **D-PSar-A** with one donor and one acceptor moiety were obtained as final products. Both products were characterized using ^1H NMR spectroscopy and the spectra with signals assigned to hydrogen atoms of the molecular structures are shown in **Figure 6.2**. A broad singlet signal with a chemical shift of around 12 ppm indicates a carboxylic acid moiety stemming from water impurities in the NCA polymerization that act as initiator. It was not possible to separate this small impurity from the polymer sample.



Scheme 6.5. Synthesis of the peptide-polymer conjugates **D-PSar-D** and **D-PSar-A**: i) DMF, r.t.; ii) HBTU, HOBT, DIPEA, DMF, r.t.; iii) TFA: triisopropylsilane (TIPS):H₂O (95:2.5:2.5), r.t.

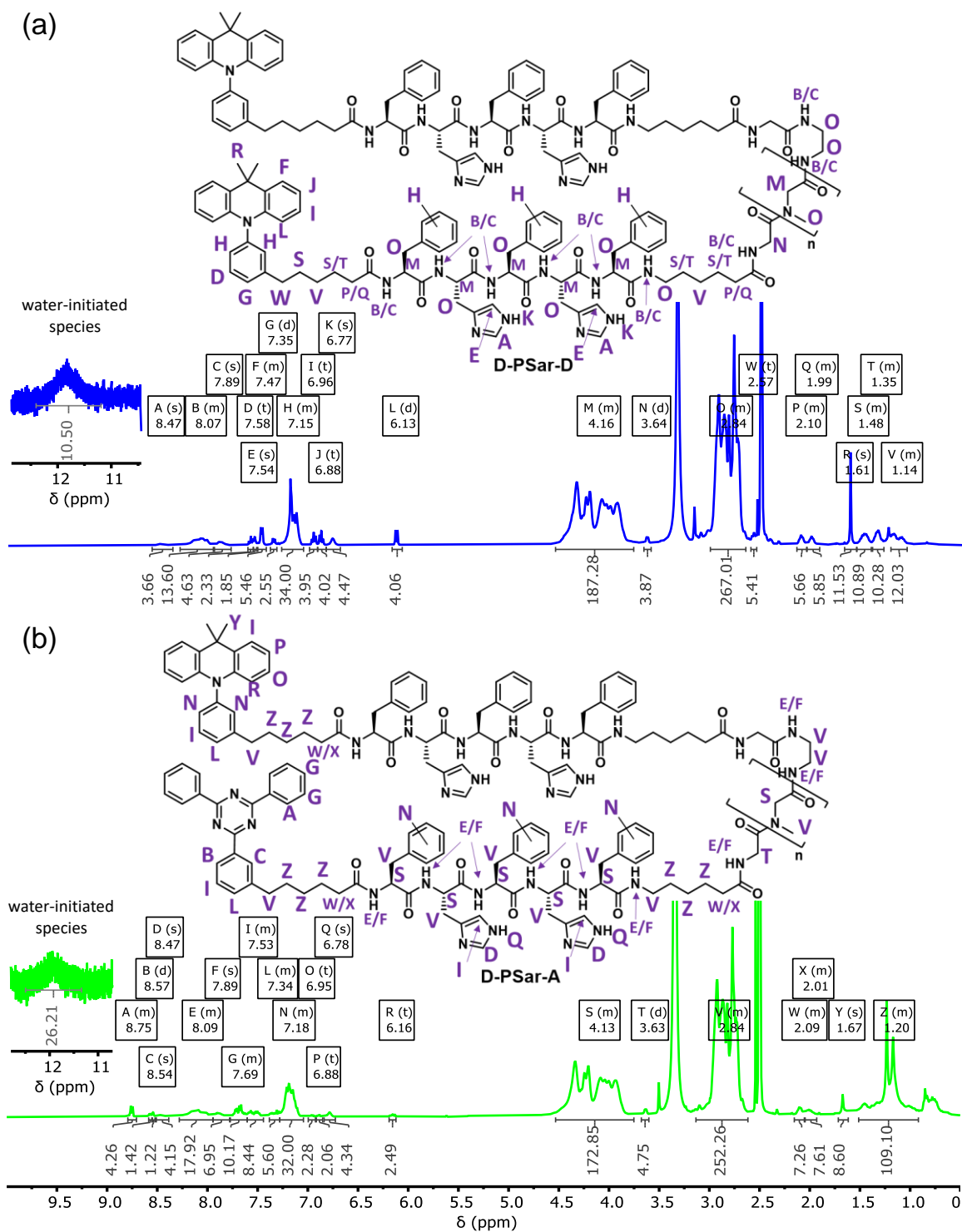


Figure 6.2. ^1H NMR spectra of (a) D-PSar-D and (b) D-PSar-A in DMSO-d_6 .

Synthesizing both **D-PSar-D** and **D-PSar-A** from the same batch of **39** ensured a matching PSar polymer length in both peptide-polymer conjugates. The molecular weight distributions as well as dispersity of all three peptide-polymer conjugates have been characterized using end group analysis, SEC and matrix assisted laser desorption/ionization (MALDI; see **Table 6.1**). In the NMR-based end-group analysis, the degree of polymerization was calculated from the integral of the signals assigned to the CH_2 of the PSar ($\delta = 3.75$ ppm - 4.50 ppm) after subtracting the superimposed CH in α -position to the amino acid moieties (5H for **39** and 10H for **D-PSar-D** and **D-PSar-A**). Using this method, X_n of the polysarcosine in **39**, **D-PSar-D** and **D-PSar-A** were determined to be 76-89, which is close to the monomer to initiator ratio (M/I) of 75 employed in synthesis. This corresponds to an M_n of 8.9 kg mol⁻¹ for **D-PSar-D** and 8.4 kg mol⁻¹ for **D-PSar-A**.

Table 6.1. Characterization of **39**, **D-PSar-D** and **D-PSar-A**.

Compound	M/I	$X_n(PSar)$		M_n		\bar{D}
		[kg mol ⁻¹]		[kg mol ⁻¹]		
		NMR/ SEC ^a / MALDI	NMR/ SEC ^a / MALDI	NMR/ SEC ^a / MALDI	NMR/ SEC ^a / MALDI	
39	75	76/ -/ 69	6.7/ 28.7/ 6.7	-/ 1.15/ 1.01		
D-PSar-D	-	89/ -/ 72	8.9/ 30.0/ 7.1	-/ 1.3/ 1.01		
D-PSar-A	-	81/ -/ -	8.4/ 35.5/ -	-/ 1.5/ -		

^aRefractive index detector signal used, relative to poly(methyl methacrylate) (PMMA) standard calibration.

While end-group analysis in NMR only enables the calculation of a number average molecular weight, the whole molecular weight distribution can be determined via SEC as well as MALDI (see **Figure 6.3**). In both methods, the molecular weights determined cannot be taken at face value: In SEC, the PMMA that was used as polymer calibration standard seems to be a poor standard in comparison to the peptide-polymer conjugates, which leads to significant overestimates of their molecular weights (about a factor of 3). In terms of MALDI, molecules with higher molecular weights

usually show a lower probability of being transferred into the gas phase and therefore detected. Nonetheless both methods enable a qualitative analysis of the molecular weight distribution.

The water-initiated PSar impurity that was already identified in NMR can be observed as a small shoulder in both the SEC elugram as well as the MALDI spectrum (see **Figure 6.3**). The tailing observed in SEC for **D-PSar-D** and **D-PSar-A** can be assigned to interactions of the deprotected peptide moieties with the stationary phase, as it was previously reported for this supramolecular polymer system.^[99] This effect as well as the low sensitivity of MALDI for higher molecular weights explains the difference in dispersity between both methods: In MALDI, \mathcal{D} was determined to be 1.01 for **D-PSar-D** indicating a very narrow molecular weight distribution. It was not possible to record a MALDI spectrum of **D-PSar-A** with sufficient intensities. In contrast to the MALDI results, a higher dispersity of 1.3 for **D-PSar-D** and 1.5 for **D-PSar-A** was obtained in SEC.

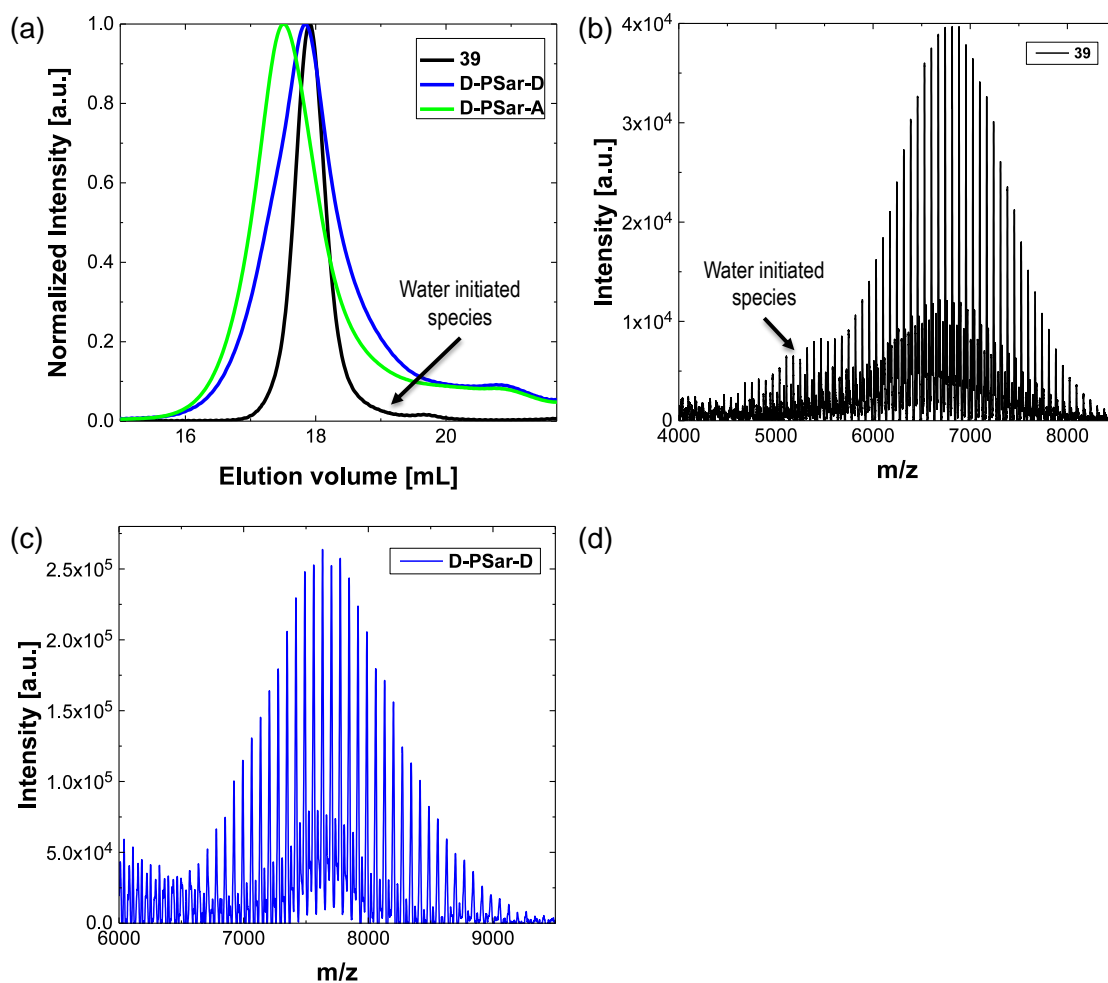


Figure 6.3. (a) SEC of **39**, **D-PSar-D** and **D-PSar-A** using HFIP with 3 g L⁻¹ potassium trifluoroacetate (KTFA) as eluent and MALDI spectra of (b) **39** and (c) **D-PSar-D**.

6.2. Self-Assembly Investigation via Transmission Electron Microscopy (TEM)

In transmission electron microscopy, high resolution images can be recorded that enable the visualization of self-assembled aggregates and the determination of their morphology. For the sample preparation, solutions of the peptide-polymer conjugates **D-PSar-D** (50 μM , in tris(hydroxymethyl)aminomethane (Tris) buffer) and **D-PSar-A** (10 μM , in DI water) in acidic and basic pH were prepared. After transferring a droplet of the solutions on copper grid substrates that were

coated with a carbon layer, a negative staining solution consisting of uranyl acetate (2 % v/v) was applied. The dimensions of the aggregates were statistically analyzed with the number average length (L_n) being

$$L_n = \frac{\sum_{i=1}^n n_i L_i}{\sum_{i=1}^n n_i} \quad (38)$$

With L being the length and n being the sample size. The standard deviation (σ), as well as the weight average polymer length (L_w) and D were calculated with the following equations:

$$\sigma = \sqrt{\frac{1}{n} \sum_{i=1}^n (L_i - L_n)^2} \quad (39)$$

$$L_w = \frac{\sum_{i=1}^n n_i L_i^2}{\sum_{i=1}^n n_i L_i} \quad (40)$$

$$D = \frac{L_w}{L_n} \quad (41)$$

At pH 1, the TEM images of the peptide-polymer conjugate **D-PSar-D** showed small spherical objects that indicate micelle formation in solution (see **Figure 6.4a-b**). The statistic analysis of these aggregates results in an average diameter of $D_n = 37$ nm ($\sigma = 10$ nm, $n = 19$), which was calculated with **Equations 38** and **39** substituting the diameter (D) for the length variables. Next to the spherical particles, small anisotropic aggregates have been observed (see **Figure 6.4c-d**). The small rod-like objects show a number average length of $L_n = 38$ nm ($\sigma = 9$ nm, $n = 123$) similar to the micelles observed at different spots of the substrate. The aggregates show a low dispersity of $D = 1.05$ indicating a narrow size distribution calculated from a weight average polymer length of $L_w = 40$ nm. The width of these aggregates was determined to be quite uniform with a thickness of $d = 15$ nm.

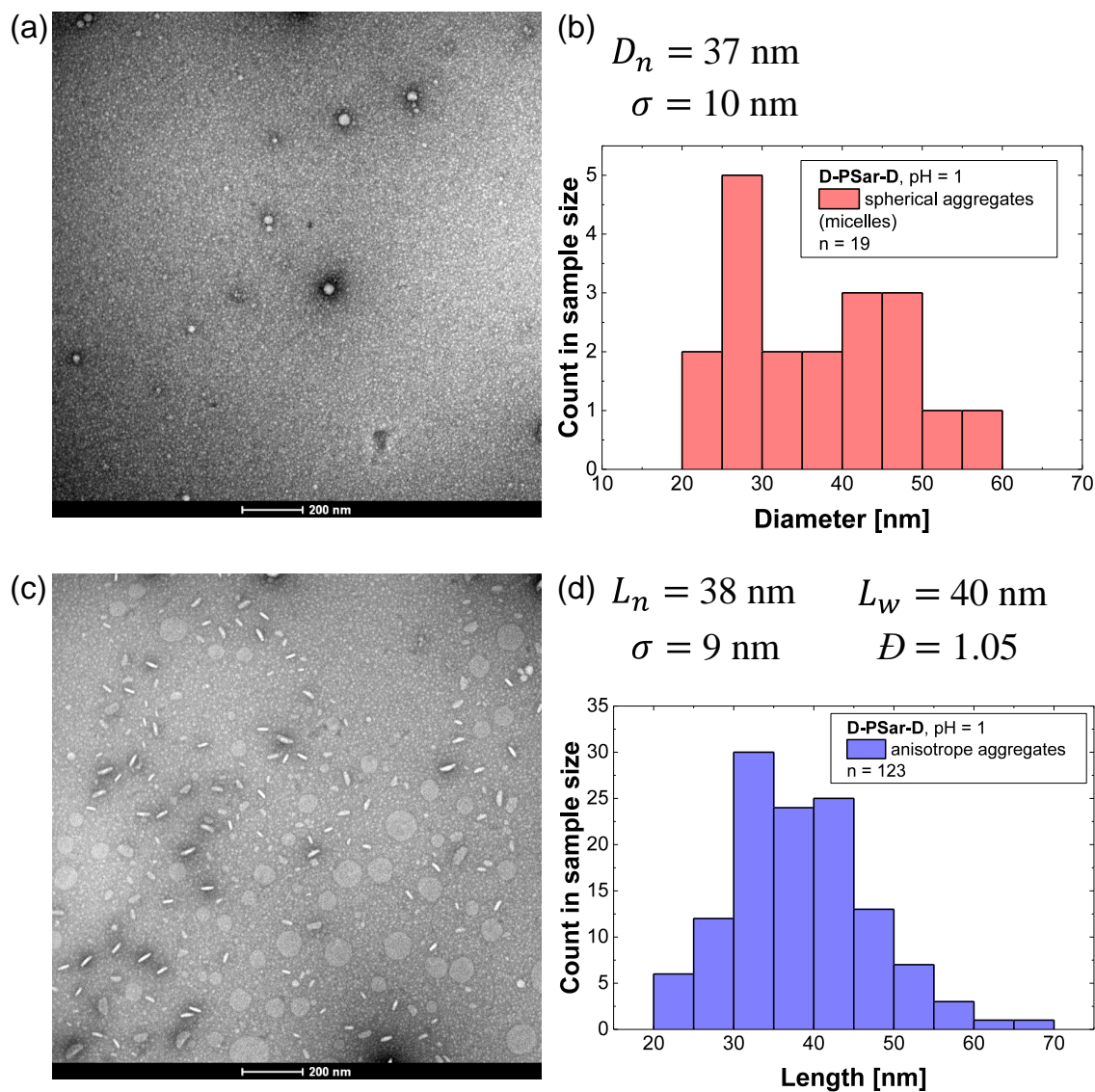


Figure 6.4. Negative stain TEM images of **D-PSar-D** ($50 \mu\text{M}$) in Tris buffer (10 mM) at $\text{pH} = 1$ showing (a) micelles and (b) anisotrope objects with the statistical analysis and histogram of the measured diameter/length in (c) and (d).

At $\text{pH} 8$, significantly longer rod-like aggregates and a few residual spherical objects were observed (see **Figure 6.5**). An average length of $L_n = 91 \text{ nm}$ ($\sigma = 35 \text{ nm}$, $L_w = 104 \text{ nm}$, $n = 72$) indicates a controlled self-assembly upon pH increase. The dispersity of these aggregates is slightly higher with $\mathcal{D} = 1.15$ in comparison to the short anisotropic structures recorded at acidic pH . In contrast to the anisotrope aggregates at acidic pH , the width of these 1D nanostructures was determined to be

smaller with 9 nm. These nanorods further showed a tendency for aggregation along their long side (lateral aggregation).

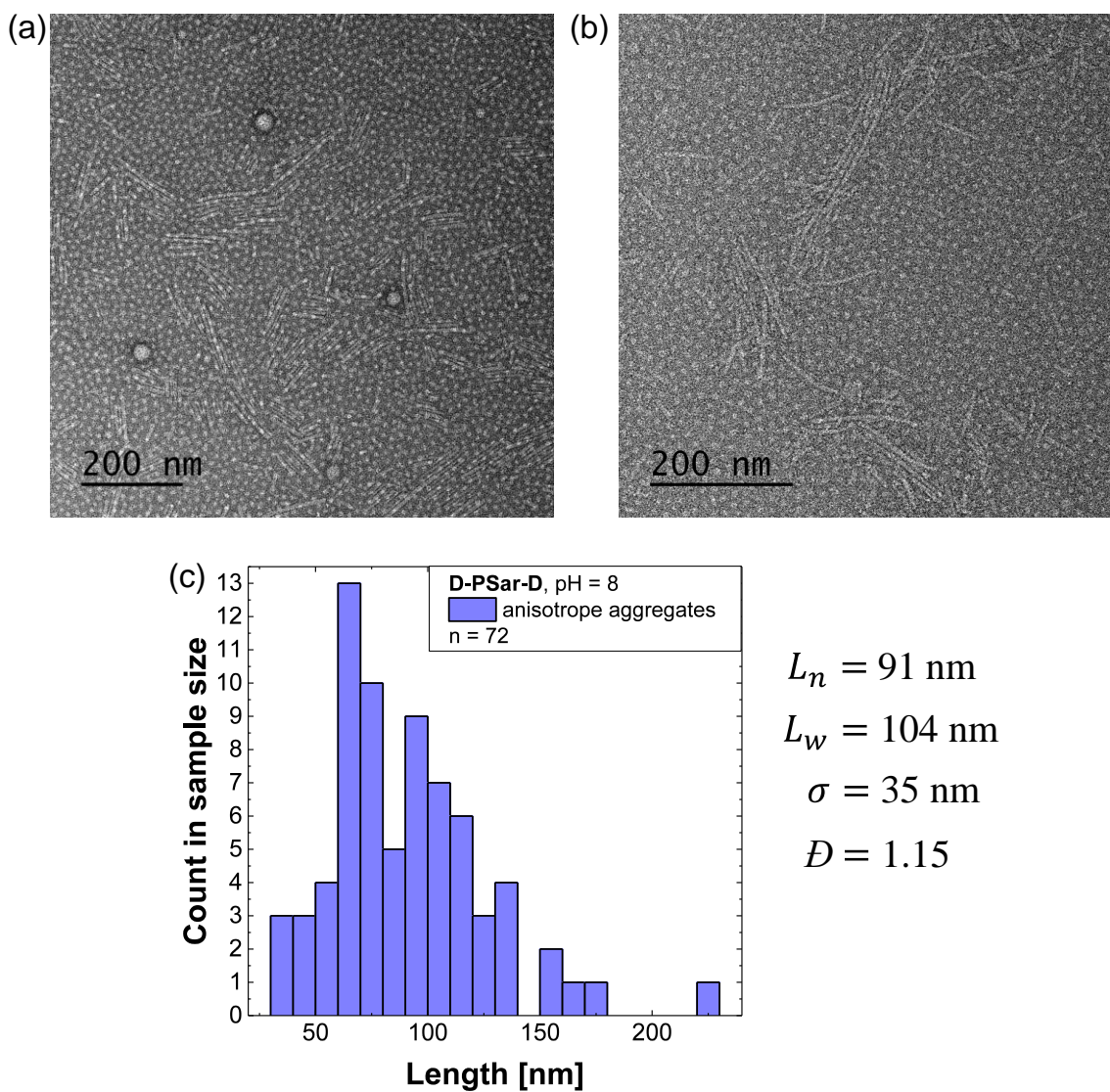


Figure 6.5. Negative stain TEM images of **D-PSar-D** (50 μM) in Tris buffer (10 mM) at pH = 8 showing (a) micelles and (a), (b) 1D nanostructures. (c) Histogram of the length of the rod-like aggregates.

The second peptide-polymer conjugate **D-PSar-A** showed small spherical aggregates at a pH of 3 with a diameter of $D_n = 16 \text{ nm}$ ($\sigma = 4 \text{ nm}$, $n = 138$) that can be assigned as micelles (see **Figure**

6.6). Upon pH increase, mainly big, shapeless aggregates were observed indicating a precipitation of **D-PSar-A**. The limited solubility might be explained by a stronger hydrophobic effect of the TRZ acceptor group then in **D-PSar-D**.

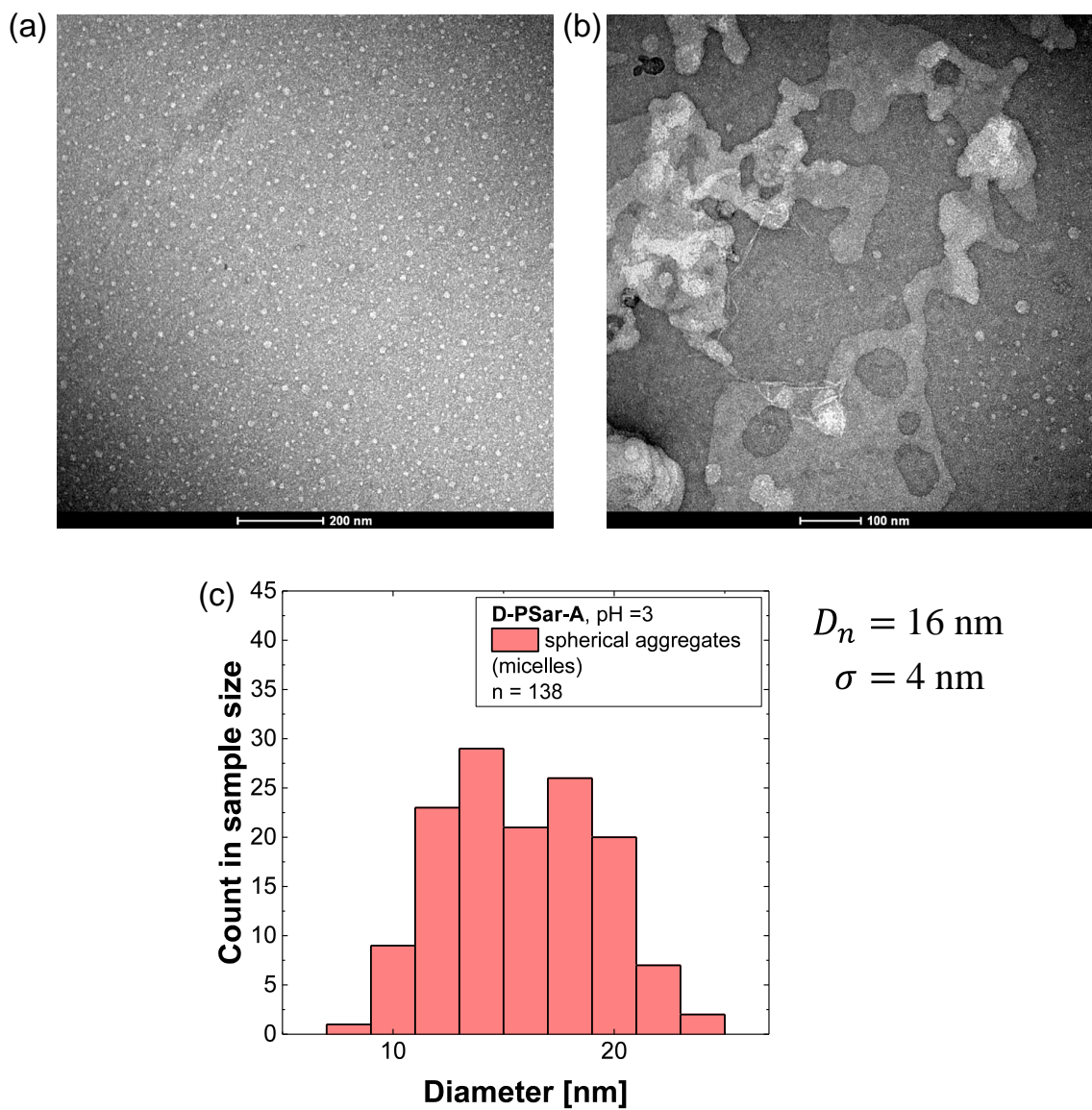


Figure 6.6. Negative stain TEM images of **D-PSar-A** (10 μM) in DI water at (a) pH = 3 and (b) pH = 10. (c) Histogram of the diameter of the observed micelles.

6.3. Photophysical Characterization

As a first step the donor and acceptor compounds **16** and **26** were characterized with absorption and photoluminescence spectroscopy in order to compare them to the functionalized polysarcosine-peptide conjugates **D-PSar-D** and **D-PSar-A** (see **Figure 6.7a** and **b**). Due to the fact that **16** and **26** are not soluble in water, toluene was used as a substitute solvent to determine their photophysical properties in solution. The absorption of both acceptor and donor increase steadily from 340 nm going to lower wavelength with a maximum at around 285 nm for **16**. The absorption maximum of **26** is at higher energies than the toluene absorption cut-off of 284 nm. Upon excitation, a high energy emission with a maximum at 360 nm was recorded for the donor derivative **16**. As expected, the acceptor compound **26** shows lower energy blue PL emission with a maximum at 469 nm.

For a first comparison, the PL emission of **D-PSar-D** and **D-PSar-A** were measured in solid state (see **Figure 6.7c** and **d**). For this purpose, a small amount the **D-PSar-D** was dissolved in DMF, drop-casted on a glass substrate and dried in high vacuum to enable the PL measurements in film state. Despite the strong background observed, a blue emission was recorded that is bathochromically shifted in comparison to **16** and exhibits a maximum at 413 nm. In contrast, the PL spectrum of **D-PSar-A** in solid state was measured on the solid directly using a quartz cuvette under argon atmosphere to exclude oxygen based quenching processes. The solid of **D-PSar-A** showed a green emission with a maximum at 538 nm. This PL emission shows a significant red shift in comparison to the donor **16** and acceptor **26** that are identical to the terminal moieties of **D-PSar-A**. This emission can be directly linked to the acceptor donor interaction and proves the formation of a through-space charge transfer excited state. The minor emission at 413 nm at the same PL maximum as exhibited by **D-PSar-D** further indicates a dominant but incomplete charge transfer.

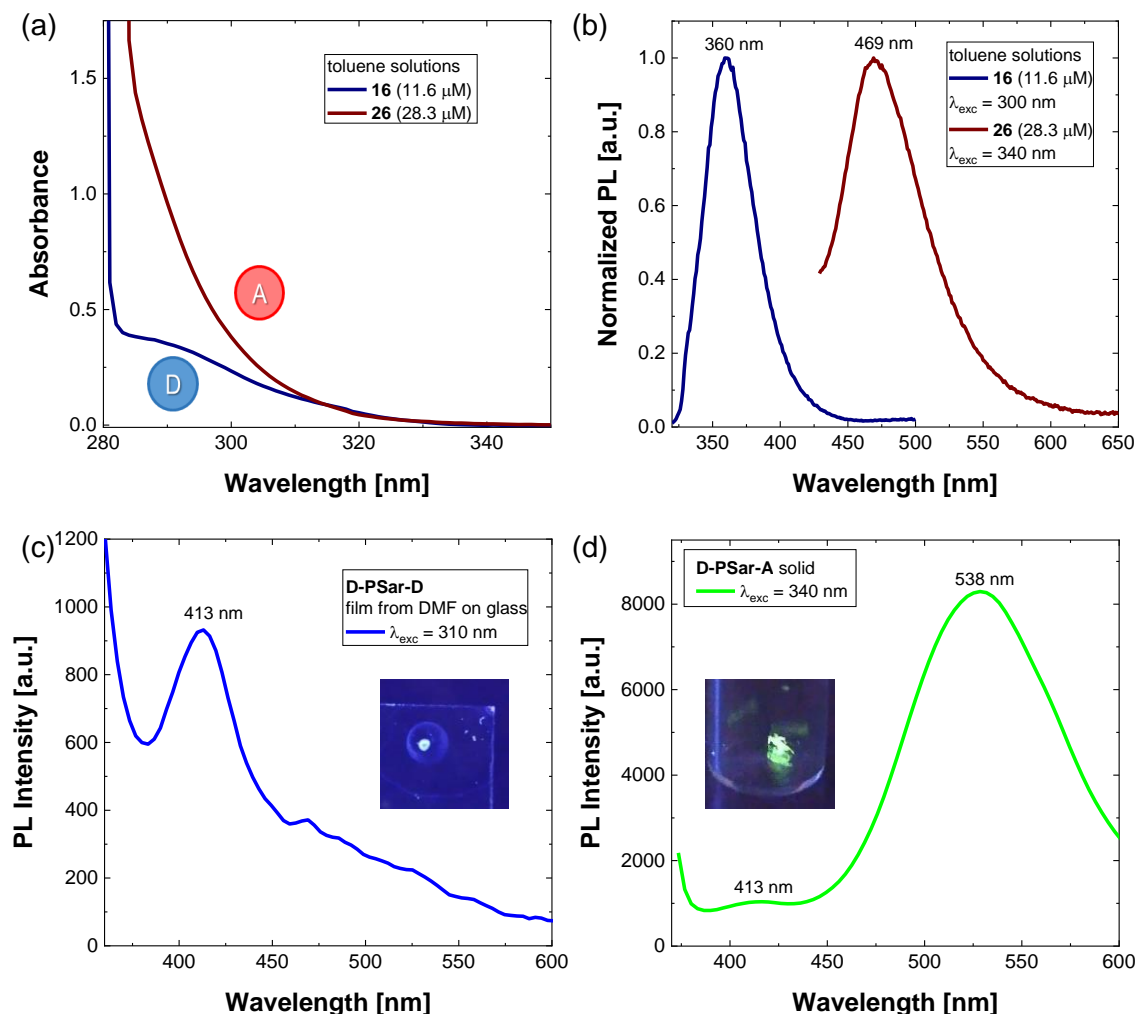


Figure 6.7. (a) Absorption spectra and (b) PL spectra of donor and acceptor compounds **16** and **26** in toluene. PL spectra of (c) **D-PSar-D** drop-casted from DMF on glass substrate and (d) of **D-PSar-A** as solid with photograph as inset.

In order to investigate supramolecular assembly of **D-PSar-D** and **D-PSar-A** that is expected to be pH responsive based on the polysarcosine–peptide conjugate system used, the absorption and emission spectra in aqueous solution at various pH were measured. Starting with **D-PSar-D**, a concentration of 10 μM in deionized (DI) water was chosen for the characterization. As **Figure 6.8c** shows, the solid did not fully dissolve in pure water at r.t. despite mixing. Upon lowering the pH to 2.97 with diluted HCl solution **D-PSar-D** was fully dissolved and no precipitation was observed upon increasing to a basic pH of 11.07 again. This initial insolubility of **D-PSar-D** might be based on the

formation of long stable self-assembled aggregates as a result of the lyophilization used as the last step of the purification procedure. The absorption as well as PL spectra showed no significant difference between the pH values and the dispersed solid in pure DI water (see **Figure 6.8a** and **b**). While the absorption maximum at 286 nm shows the same maximum as observed for the donor compound **16**, the PL emission exhibits a bathochromic shift to 381 nm. In contrast to the Gaussian line shape of the fluorescence of **16**, **D-PSar-D** shows two additional features around 400 nm and 420 nm.

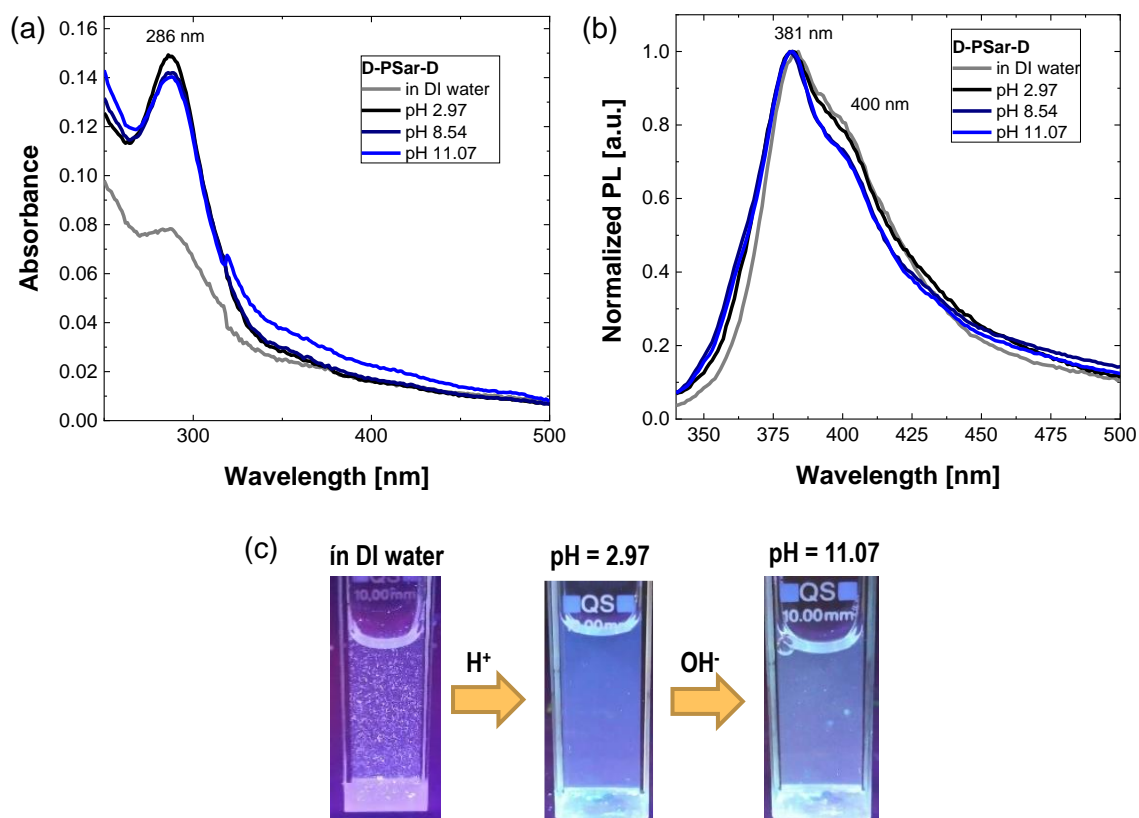


Figure 6.8. (a) Absorption and (b) PL spectra of **D-PSar-D** dispersed in pure DI water and dissolved at different pH values. (c) photographs of the solutions under excitation with a UV lamp ($\lambda_{exc} = 356$ nm).

While **D-PSar-D** does not show any significant change in PL emission upon self-assembly, a shift in PL emission based on a CT excited state formed as soon as donor and acceptor come into close proximity is expected for **D-PSar-A**. Similar to the procedure used for **D-PSar-D**, **D-PSar-A** did not

dissolve in pure DI water at a concentration of 10 μM (see **Figure 6.9c**). Despite changing the pH to acidic conditions to increase the solubility based on the histidine protonation, **D-PSar-A** was not fully dissolved and a few particles at the bottom of the cuvette could still be observed. This poor solubility in comparison to **D-PSar-D** indicates that the TRZ acceptor moiety either facilitates the self-assembly or limits the solubility based on its hydrophobicity. As expected, the amount of not dissolved particles increases at upon adding base at a pH of 11.40, which is in agreement with the observation of large aggregates in TEM in the previous section.

The absorption spectra of **D-PSar-A** show two absorption bands (see **Figure 6.9a**): The stronger signal exhibits a maximum at 276 nm, which can be attributed to the donor excitation. The maximum of the second absorption band is located at 347 nm and was not observed for **D-PSar-D**. In addition, the acceptor compound **26** also did not show an absorption maximum at higher wavelengths than the cut-off of toluene at 284 nm. This observation implies an involvement of both acceptor and donor moieties. In the absorption spectrum a weak absorption band at around 400 nm appeared upon changing from acidic to basic pH, that can be assigned to the direct CT excitation. While the difference in absorption was small between high and low pH values, the PL spectra change completely: At pH 1.82 a blue emission with a maximum at 391 nm similar to the donor emission observed for **D-PSar-D** was observed that is quenched under basic conditions. At pH 11.40 a second weak emission appears that exhibits a maximum PL at 517 nm (determined by Gaussian deconvolution, see **Figure 6.9c**). This green emission can be assigned to the CT state resulting from the through-space charge transfer upon self-assembly at high pH.

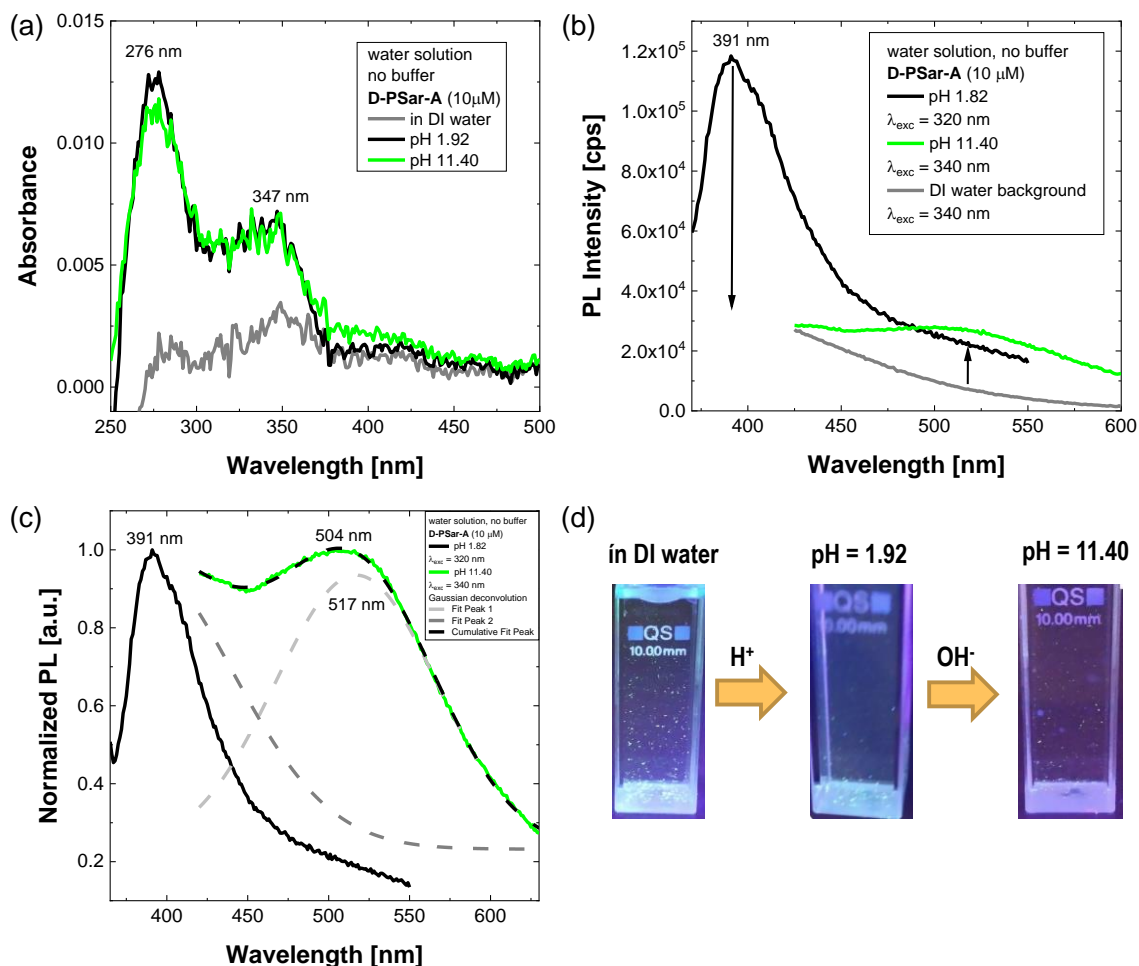


Figure 6.9. (a) Absorption, (b) unnormalized and (c) normalized PL spectra of **D-PSar-A** dispersed in pure DI water and in aqueous solution at acidic and basic pH. (d) Photographs of the solutions under excitation with a UV lamp ($\lambda_{exc} = 356$ nm).

Due to the limited solubility observed for **D-PSar-A**, a systematic investigation of optimal dissolving conditions with a higher concentration of 20 μ M was performed in direct comparison to **D-PSar-D** (see **Figure 6.10**). While both polymers do not dissolve in pure DI water, only changing the pH to acidic conditions was sufficient to fully dissolve **D-PSar-D**. After heating the solution to 80 $^{\circ}$ C at acidic pH also **D-PSar-A** was dissolved without visible dispersed particles left in the solution and showed precipitation again after changing to a pH of 11.20. Under acidic as well as basic pH, bimodal PL spectra were recorded. The strong CT emission that was in contrast to the identical measurements

at concentrations of 10 μM also observed under acidic conditions indicates an important concentration dependency on the self-assembly. The PL intensity of the CT emission at 515 nm further increases upon increasing excitation wavelengths from 350 nm to 390 nm showing a slightly higher intensity relative to the donor-based emission at basic pH.

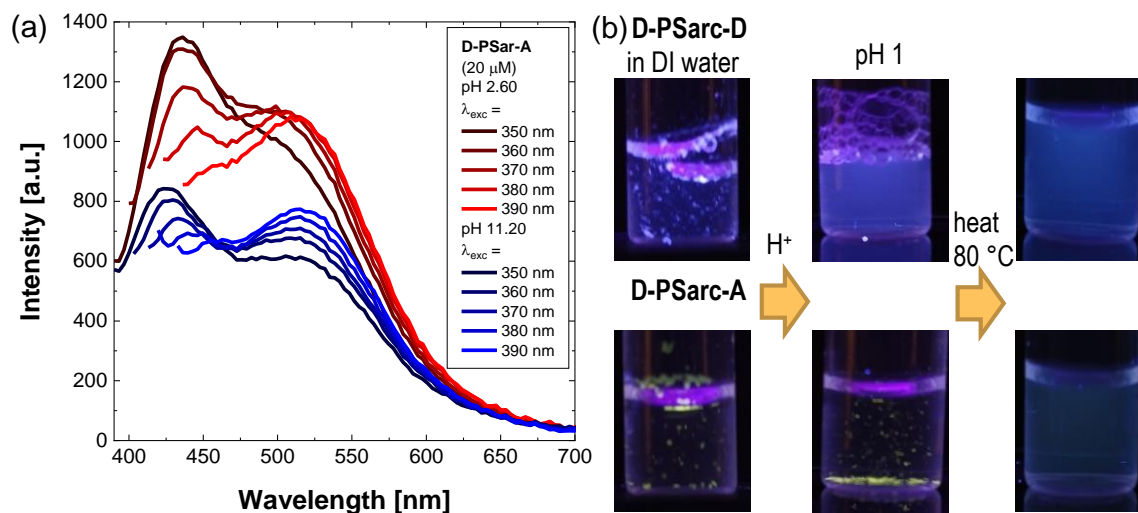


Figure 6.10. a) PL spectra of **D-PSar-A** dissolved in aqueous solution at acidic and basic pH (20 μM). (b) Photographs of **D-PSar-D** and **D-PSar-A** dispersions and solutions in water under excitation with a UV lamp ($\lambda_{exc} = 356 \text{ nm}$).

6.4. Conclusion and Outlook

As a first step in this chapter, DMAC as donor and TRZ as acceptor were synthesized with amine (**20** and **31**) as well as carboxylic acid functionality (**16** and **26**). Based on the compounds **16** and **26**, two ABA'-type peptide-polymer conjugates (**D-PSar-D** and **D-PSar-A**) were obtained. The degree of polymerization of the PSar polymer in these products as well as the intermediate **39** were determined to be $X_n = 76 - 89$ by NMR end-group analysis and confirmed by MALDI. Furthermore, a small water-initiated polysarcosin impurity was identified. Both products showed a narrow molecular weight distribution with a dispersity ranging from 1.3 to 1.5 obtained by SEC in hexafluoroisopropanol (HFIP).

TEM images of **D-PSar-D** and **D-PSar-A** revealed the formation of micelles under acidic conditions in solution with **D-PSar-D** additionally showing short anisotropic aggregates. At basic pH, **D-PSar-D** self-assembled into 1D nanostructures with an average length of $L_n = 91$ nm and a dispersity of 1.15. In contrast, **D-PSar-A** formed big shapeless aggregates assigned to the limited solubility caused by the TRZ acceptor. No significant change in absorption as well as PL emission ($\lambda_{PL} = 381$ nm) was observed for **D-PSar-D** between acidic and basic conditions in aqueous solutions. In contrast, **D-PSar-A** showed an additional absorption band at 347 nm in comparison to **D-PSar-D** and the blue emission at low pH is quenched and a yellowish-green PL emission with a maximum at 517 nm was detected upon changing to basic conditions. A similar emission can also be observed in solid state being bathochromically shifted compared to the separate donor and acceptor moieties, which indicates it stemming from an emissive CT state.

In order to investigate the CT character of the emissive state and to confirm the delayed fluorescence expected for the donor acceptor combination, time-resolved photoluminescence measurements are going to be the next step of future work. Another objective of upcoming experiments is going to be mixtures of both peptide-polymer conjugates. While the co-assembly might prevent the precipitation of **D-PSar-A** at basic pH, the dilution of acceptor groups in the supramolecular polymer structure might also increase the PL emission intensity based on reduced concentration quenching as has previously been observed for through space TADF emitters.^[76]

6.5. Appendix of Chapter 6

6.5.1. Contributions to Chapter 6

The syntheses of **16**, **20**, **26** and **31** as well as all photophysical measurements were performed by Kai Philipps. The syntheses of **D-PSar-D** and **D-PSar-A** were performed by [REDACTED] (Department of Chemistry, Johannes Gutenberg University Mainz). The MALDI spectra of **39**,

D-PSar-D and **D-PSar-A** were measured by [REDACTED] (Department of Chemistry, Johannes Gutenberg University Mainz). The TEM measurements were performed by [REDACTED] (Department of Chemistry, Johannes Gutenberg University Mainz). Experimental results were regularly discussed with Paul Blom (Molecular Electronics Department, MPIP Mainz), Jasper Michels (Molecular Electronics Department, MPIP Mainz), [REDACTED] (Faculty of Science, Vrije Universiteit Amsterdam and Molecular Electronics Department, MPIP Mainz) and [REDACTED] (Molecular Electronics Department, MPIP Mainz) and [REDACTED] (Department of Chemistry, Johannes Gutenberg University Mainz).

7. General Methods

7.1. Synthetic, Purification and Sample Preparation Methods

7.1.1. Solvents and Chemicals

All solvents and reagents were obtained from commercial sources at the highest purity available and used without further purification unless otherwise noted. TAPC was purified using thermal gradient sublimation. For use in moisture sensitive reactions dry solvents were purchased and transferred into the reaction vessels with a septum and a syringe. Unless otherwise stated, solvents and chemicals were not degassed prior to use. Polystyrene ($M_w = 1.100$ g/mol, $D = 1.15$, atactic and $M_w = 174000$ g/mol, $D = 1.06$, atactic) was synthesized via anionic polymerization of styrene.^[148] Dimethyl-formamide and piperidine used in solid phase peptide synthesis were used in peptide grade quality. Water for reactions and sample preparations in chapter 6 was purified via a *Veolia PURELAB flex 4* system (Paris, France).

7.1.2. Reaction Methods

All reactions were performed in a dry reaction flask (schlenk flask or pressure tube) using dry solvents in argon atmosphere (UN 1006 supplied by *Westfalen AG*), unless otherwise stated or water itself used as a solvent. For all reactions, the schlenk line technique was used. Liquids as well as solvents that are sensitive to air or moisture were transferred via a syringe and introduced into the flask using a septum. Solid compounds were added in argon counterflow. Hydrogenation reactions were performed using hydrogen supplied by *Westfalen AG*. The pressure tubes used for reactions were supplied by *ACE Glass Incorporated* and were equipped with a polytetrafluoroethylene (PTFE) cap.

7.1.3. Solid Phase Peptide Synthesis

Solid phase peptide synthesis was done using a CS136XT peptide synthesizer from *CS Bio Co* (Menlo Park, USA). A 2-chlorotriptyl chloride modified polystyrene resin with a loading capacity of 1.6 mmol/g from *Iris Biotech* (Marktredwitz, Germany) and SPPS-grade solvents and reagents were used.

7.1.4. pH-Electrodes

A MI-410 Micro-Combination pH-probe by *Microelectrodes* (Bedford, USA) or a fiveEasy™ pH Meter F20 by *Mettler Toledo* were used to measure and adjust pH-values. Buffer solutions at pH 4.01 and pH 10 by *Mettler-Toledo* (Columbus, USA) were used for calibration. All pH-values were adjusted by adding aqueous sodium hydroxide and hydrochloric acid solutions and measured, after the pH-value stabilized.

7.1.5. Soxhlet Purification

Soxhlet extraction is also known as continuous extraction and was used for the purification of the polymer compounds in chapter 3. The sample is first placed inside an extraction thimble and placed inside the set-up consisting of the soxhlet extractor, a cooler and a flask. Then the flask is filled with the solvent used in the process and heated until reflux (**Figure 7.1a**). The evaporated solvent condenses in the cooler and drops into the sample containing thimble (**Figure 7.1b**). The warm extracting solvent rises above the siphon glass tubing and is drained back into the flask (**Figure 7.1c and d**). These steps are now repeated continuously until the desired impurity is fully extracted, which for example can be indicated by the color of the extracting solvent.

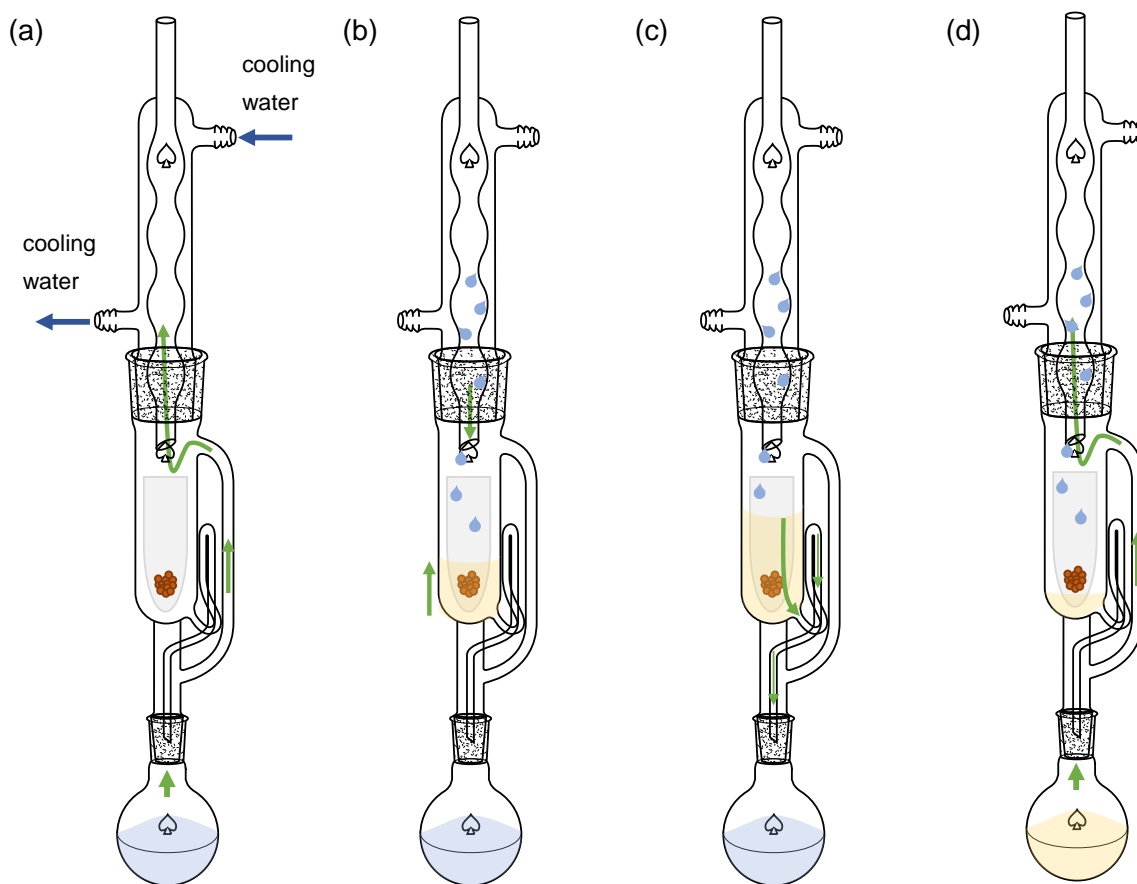


Figure 7.1. Operation steps of a Soxhlet extraction. Description of each step in the text.

7.1.6. Chromatography

Analytical thin-layer chromatography (TLC) was used for reaction control (Alugram® SIL G/UV 254 from *Macherey-Nagel*). TLC plates were visualized using a UV lamp (254 nm and 365 nm) or exposure to iodine in a closed chamber. Preparative flash column chromatography was performed with silica 60 M (0.04-0.063 mm) from *Macherey-Nagel*. The chromatography columns were then packed with the slurried silica gel in the solvent mixture previously determined by TLC. Using a manual pump, the excess of solvent was drained while simultaneously compressing the silica layer. After this the packed silica was covered with about 1-2 cm of sand and the product dissolved in the solvent

mixture used for the as mobile phase was added on-top. After carefully flushing the sample into the silica layer with several small portions of the solvent mixture, the column was filled and fitted with a solvent reservoir. After discarding an amount of solvent smaller than the column volume, the eluted fractions were collected in test tubes. The contents of the test tubes were evaluated by TLC and pure fractions combined to obtain the purified products.

Preparative size exclusion chromatography was performed using two JAIGEL-2HR columns in series for small molecules (optimal molecular weight $\sim 1000 \text{ g mol}^{-1}$) and JAIGEL-2.5HR and JAIGEL-3HR columns in series for polymers (optimal molecular weight $\sim 10000 \text{ g mol}^{-1}$) on a *Japan Analytical Industry Labo ACE LC-5060* using JAI scan software (Version 0.281). Chloroform stabilized with ethanol was used as a solvent for all uses of preparative SEC reported in this thesis.

Purification via size exclusion chromatography with DMF as mobile phase was done using the liquid chromatography medium *BioBeads® SX-1* by BioRad (Hercules, USA) as stationary phase.

7.1.7. Sublimation

For the purification of small molecules the thermal gradient sublimation set-up shown in **Figure 7.2** was used. The sample was placed in a small vial within a glass tube. This inner tube was then placed into an outer quartz glass tube, that was surrounded by a brass metal case. The quartz tube was then fitted to a high vacuum pump (TurboDrag TC600 supplied by *Pfeifer Vacuum*) with a condensation trap between them. After a pressure of 1×10^{-4} mbar was reached, the temperature was increased using the heat jackets with a difference to one another of $20 \text{ }^\circ\text{C}$. This leads to a temperature gradient along the quartz tube and the temperature was steadily increased until a separation of the sublimed materials along the length of the glass tube was observed. After cooling down the set-up, the inner glass tube was removed and cut into pieces separating the different sublimed fractions.

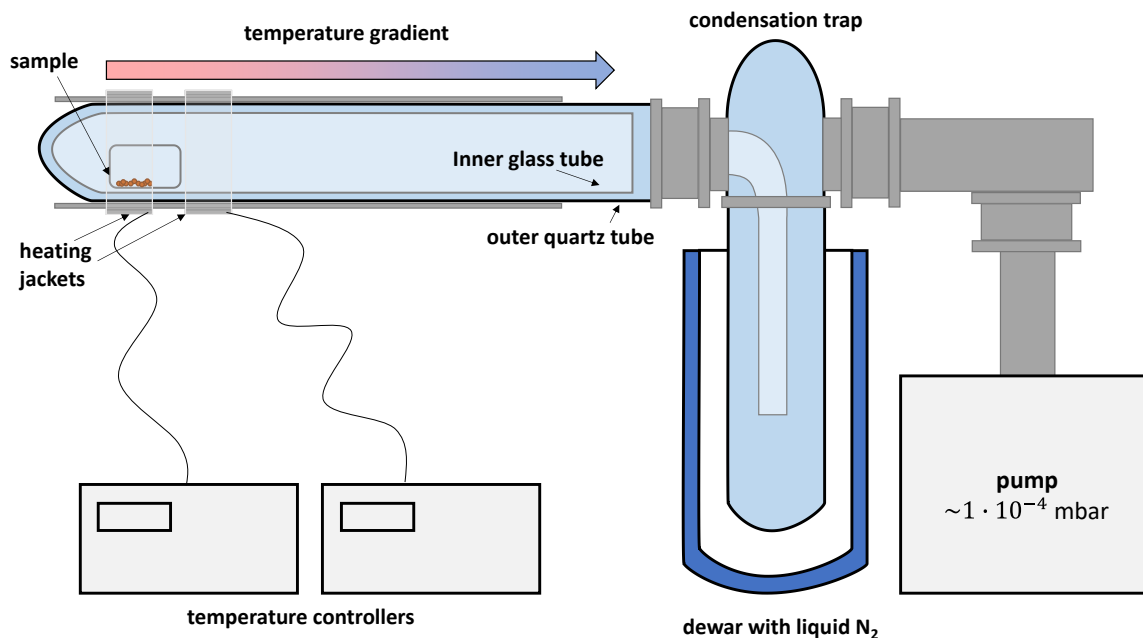


Figure 7.2. Schematic representation of the thermal gradient sublimation set-up.

7.1.8. Film Preparation

The substrates (quartz: 10 x 20 x 1 mm, supplied by *Präzisions Glas & Optik GmbH*; glass: 30 x 30 x 1 mm, BF33 supplied by *Schott AG*; ITO-glass substrates: 30 x 30 x 1 mm, supplied by *Phillips*) for thin films optical characterization were cleaned with acetone followed by 2-propanol in an ultrasonic bath for 20 min. After drying in a N₂ stream, the substrates received a UV-ozone treatment of 20 min. After this, the thin films were spincoated within a 20 min period. The specific spin coating methods and solvents used as well as the film thicknesses are shown in **Table 7.1**. The thicknesses were determined by using a DektakXT surface profilometer from *Bruker*.

Table 7.1. Fabrication details of the film fabricated for photophysical characterization.

Compounds	Host	Conc. (solvent) [mg mL⁻¹]	Method	Film thickness [nm]	Figures
Tol-MAc-BP	-	15.0 (CHCl ₃)	1) 60 s, 800 rpm, 500 acc 2) 20 s, 2000 rpm, 1000 acc	134	Figure 4.6, Figure 4.7, Figure 4.9, Figure 4.13, Figure A4.15, Figure A4.16
P(C2-MAc-BP)				165	
P(C6-MAc-BP)				114	
P(Ph-MAc-BP)				111	
Tol-HAc-BP				180	
P(C2-HAc-BP)				139	
P(C6-MAc-BP)				154	
P(Ph-HAc-BP)				182	
Tol-MAc-BP	2 wt% in PS (170 kg mol ⁻¹)	21.5 (toluene)	120 s, 2000 rpm, 1000 acc	117	Figure 4.7, Figure 4.10, Figure 4.11, Figure A4.10
P(C2-MAc-BP)				110	
P(C6-MAc-BP)				122	
P(Ph-MAc-BP)				109	
Tol-HAc-BP				95	
P(C2-HAc-BP)				99	
P(C6-MAc-BP)				108	
P(Ph-HAc-BP)				98	
Tol-MAc-BP	2 wt% in Zeonex® 480	21.5 (toluene)	120 s, 2000 rpm, 1000 acc	95	Figure 4.7, Figure A4.10, Figure 4.8
P(C2-MAc-BP)				97	
P(C6-MAc-BP)				96	
P(Ph-MAc-BP)				87	
Tol-HAc-BP				101	
P(C2-HAc-BP)				117	

P(C6-MAc-BP)				119	
P(Ph-HAc-BP)				96	
Tol-MAc-BP	in various	9.5-11.0,	120 s, 2000 rpm, 1000 acc	30-40,	Figure 4.12,
P(C2-MAc-BP)	ratios in	39.0 for		90-110	Figure 4.14,
P(C6-MAc-BP)	PS (1.2 kg	1:9 ratio		for 1:9	Figure 4.15,
P(Ph-MAc-BP)	mol ⁻¹)	(chloro- benzene)			Figure 4.17,
					Figure 4.16,
					Figure 4.18,
					Figure
					A4.12,
					Figure
					A4.13,
					Figure
					A4.14

7.2. Analytical Methods

7.2.1. Nuclear Magnetic Resonance

Proton (¹H NMR) as well as carbon nuclear magnetic resonance (¹³C NMR) spectra were recorded on a Bruker Avance 250 (250 MHz), a Bruker Avance 300 (300 MHz), a Bruker Avance II 400 (400 MHz) or on Bruker Avance III 700 (700 MHz) NMR spectrometers. Proton chemical shifts (δ) are reported in parts per million (ppm) downfield from tetramethylsilane ($\delta_{\text{TMS}} = 0$) and are referenced to the residual protons of the deuterated solvent used ($\delta_{\text{DMSO}} = 2.50$; $\delta_{\text{acetone}} = 2.05$; $\delta_{\text{CDCl}_3} = 7.26$; $\delta_{\text{CD}_2\text{Cl}_2} = 5.32$). For the declaration of spin multiplicities the following abbreviations were used: s (singlet), br. s (broad singlet), d (doublet), t (triplet) and m (multiplet) as well as appropriate combinations of these. Coupling constants were reported in hertz (Hz) and signal area in natural

numbers. Carbon chemical shifts (δ) are reported in parts per million (ppm) downfield from tetramethylsilane ($\delta_{\text{TMS}} = 0$) and are referenced to deuterated solvent used ($\delta_{\text{CDCl}_3} = 77.16$; $\delta_{\text{CD}_2\text{Cl}_2} = 53.84$). The NMR spectra were analyzed using the software MestReNova v.14.0.0-23239 (*MestreLab Research S.L.*).

7.2.2. Mass Spectrometry

High resolution mass was determined either by electrospray ionization (ESI) on an Agilent 6545 QTOF-MS electrospray ionization spectrometer (*Agilent Technologies, Inc.*) or by matrix-assisted laser desorption ionization with time-of-flight analysis on a Time-of-flight MS-Reflex III or a rapifleX MALDI-ToF/ToF from *Bruker*. DCTB (trans-2-[3-(4-tert-butylphenyl)-2-methylpropenylidene]malodinitrile) served as the matrix. The mass spectrometer was calibrated against red phosphorus.

7.2.3. Differential Scanning Calorimetry

Differential scanning calorimetry (DSC) was performed on Thermal Analysis DSC 3+ from Mettler Toledo. Thermogravimetry was performed on a TGA/DSC 3+ - Thermogravimetric Analyzer with high temperature furnace (HT) from Mettler Toledo under nitrogen flow with a heating rate of 10 °C/min from 25 to 300 °C.

7.2.4. Cyclic Voltammetry

Cyclic voltammetry measurements were carried out on a *Metrohm* Autolab PGSTAT204 potentiostat/galvanostat with a three-electrode-cell system: glassy carbon electrode as the working electrode, Ag/AgCl electrode as the reference electrode, platinum wire as the counter electrode, and

Bu₄NPF₆ (0.1 M in dichloromethane) as supporting electrolyte with a scan rate of 100 mV s⁻¹ (**Figure 7.3a**). Before recording the CV the solution was sparked with Ar for 3 minutes and an Ar stream was kept on flushing the headspace during the measurement. Ferrocene was used as an internal reference. The electrochemically determined electron affinity and ionization potential can be determined from the onset of the reduction and oxidation, respectively (see **Figure 7.3b**).

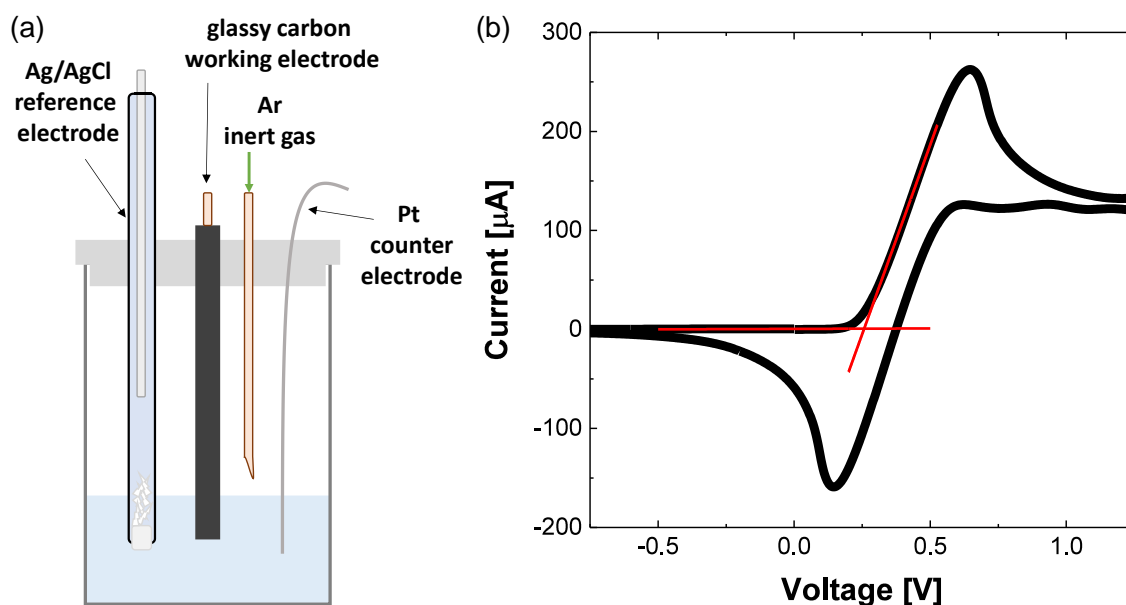


Figure 7.3. (a) Set-up for cyclic voltammetry. (b) Cyclic voltammogram of ferrocene in DCM with Bu₄NPF₆ as supporting electrolyte (0.1M).

7.2.5. Ultraviolet Photoelectron Spectroscopy

Using a helium discharge lamp, the sample is illuminated with high energy electromagnetic radiation of 21.22 eV (He(I) emission) and the kinetic energy of the photoelectrons it emits are recorded as UPS spectrum. Due to the excitation of these valence electrons above vacuum level, the kinetic energy (E_{kin}) detected depends on their energetic state, e.g. binding energy (E_B), in the valence band

$$E_{kin} = h\nu - E_B \quad (42)$$

with h being the Planck constant and ν is the frequency of the excitation radiation. Starting with a bare substrate, **Equation 42** allows it to assign electrons at the high kinetic energy cut-off ($E_{cut\ off}$) to the Fermi level and the low energy cutoff to the vacuum level.^[149] Repeating this type of measurement with a thin organic semiconductor layer on top of the metal surface affords a similar but shifted spectrum. Again, the high kinetic energy onset can now be assigned to the HOMO edge ($E_{HOMO\ edge}$) and its counterpart to the vacuum level at the surface of the organic layer. For sample preparation, a silicon wafer was covered with 2 nm of chromium and 50 nm of gold via vacuum thermal evaporation and the organic semiconductor investigated was spin-coated on-top of this substrate.

7.2.6. Ultraviolet-Visible Absorption Spectroscopy

The absorption of light by a compound is described by the Lambert-Beer law:

$$I = I_0 e^{-\epsilon lc} \quad (43)$$

where I_0 is the intensity of the incident light, I is the intensity of the transmitted light, ϵ is the molar absorptivity coefficient, c is the concentration of the analyte and l is the optical path length in cm. The absorption spectrum was recorded against a background, which was the spectral background radiation detected without a sample in the beam path as well as a blank solvent sample for solution measurements. The molar absorptivity coefficient was determined by measuring the absorption spectra in a set of various concentrations and determined with plotting the absorbance at one wavelength against the concentration and a fit with a straight line. Ultraviolet-visible (UV-vis) absorption spectra were recorded on a *Perkin Elmer* Lambda 900 UV/Vis/NIR spectrometer using the software *Perkin Elmer* UV Winlab (version 6.04.0738).

7.2.7. Steady State Photoluminescence Spectroscopy

Steady state PL spectra and related data shown in **Figure 4.1**, **Figure 4.2**, **Figure 4.3**, **Figure 4.4**, **Figure 4.6**, **Figure A4.1**, **Figure A4.2**, **Figure A4.8** and **Figure A4.9** were measured with a *J&M* TIDAS 9.5, FL305SL Spectrometer Mono RS232. The PL spectra and related data shown in **Figure 4.5**, **Figure 4.7**, **Figure 4.9**, **Figure 4.10**, **Figure 4.11** and **Figure 4.12** were recorded with a *HORIBA Jobin-Yvon* Fluorolog 3–22 Tau-3 using a photomultiplier tube (PMT) as detector and FluorEssence (version 3.9.0.1; Origin version 8.6001) as software. For the steady state temperature scans, the film samples were loaded into sample-in-vacuum cryostat (Optistat CF-V, *Oxford*), that was integrated in the aforementioned Fluorolog 3 system.

Photoluminescence quantum yield was measured using the aforementioned Fluorolog-3 with an integrating sphere (F-3018 from *Horiba Jobin Yvon*) under nitrogen flow using the method described in literature.^[127] The PLQY is defined as

$$\Phi_{PL} = \frac{\text{emitted photons}}{\text{absorbed photons}} \quad (44)$$

As a first step the scattered excitation light intensity at the desired excitation wavelength was calibrated to 1 million counts per second (cps) with the empty integrating sphere. Due to a lower sensitivity of the PMT detector above intensities of 1.5 million, a neutral-density filter was introduced between the excitation light beam and the integrating sphere excitation port. Then the scattered excitation light as well as the background emission of the integrating sphere was recorded with the same parameters as the samples that are measured in the next step. The sample is placed in a PTFE sample holder and arranged in the IN configuration (see **Figure 7.4**). In this set-up the excitation light directly hits the sample and the light emitted by the analyte as well as the excitation light that is not absorbed can reach the detector through the exit port due to the scattering material on the inside of the sphere. In case of film samples the sample holder is arranged in an 22.5 ° angle which ensures that reflected excitation light hits the scattering inside of the sphere. After recording the scattered excitation light as well as the emitted PL of the sample, the measurement is repeated in OUT configuration. In

this arrangement the PL emission detected is based on reabsorption of the scattered excitation light. With those three sets of measurements (empty sphere, IN and OUT configuration) the PLQY can be determined with

$$\Phi_{PL} = \frac{E_{IN}(\lambda) - (1-\alpha)E_{OUT}(\lambda)}{X_{empty}(\lambda)\alpha} \quad (45)$$

with

$$\alpha = \frac{X_{OUT}(\lambda) - X_{IN}(\lambda)}{X_{OUT}(\lambda)} \quad (46)$$

where $E_{IN}(\lambda)$ and $E_{OUT}(\lambda)$ are the integrated luminescence as well as $X_{IN}(\lambda)$, $X_{OUT}(\lambda)$ and $X_{empty}(\lambda)$ are the integrated scattered excitation light detected in each configuration.

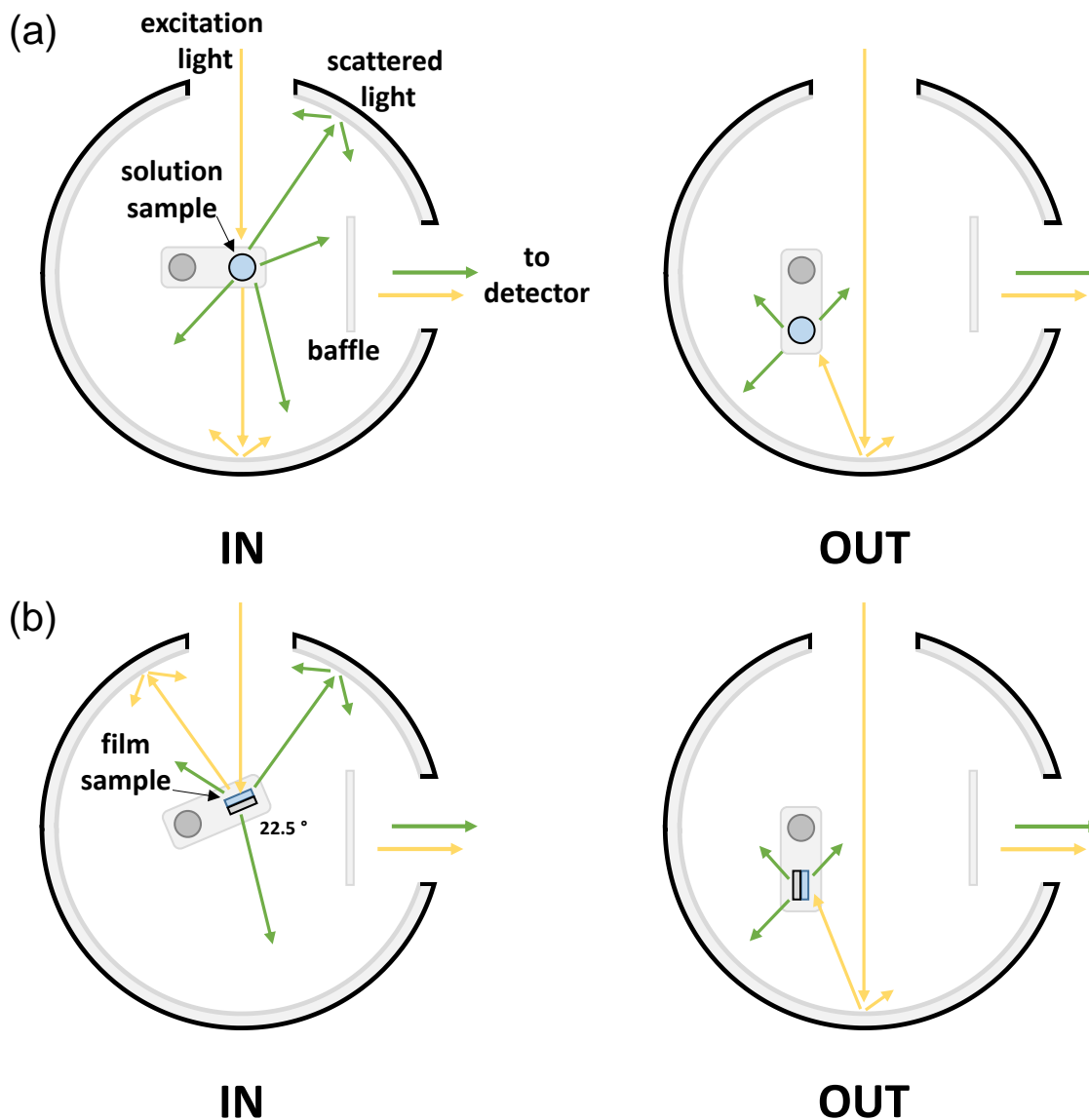


Figure 7.4. IN and OUT configuration for the PLQY measurements in an integrating sphere of (a) solution samples and (b) film samples. Excitation light is shown as yellow arrows and emission light shown as green arrows.

7.2.8. Time Resolved Photoluminescence Spectroscopy

In time-resolved photoluminescence spectroscopy, the lifetimes of emissive excited states can be determined by recording the PL spectra and photon count over time after the excitation. The

schematic set-up is shown in **Figure 7.5**. In order to get the precise excitation time, a high frequency pulsed laser has to be used. After the light pulses excite the sample, the emitted light reaches a spectrograph, in which gratings diffract the incoming light to a detector. This is usually an intensified charge-coupled device (iCCD) detector where the light of different wavelength hits different pixels of the detection area.

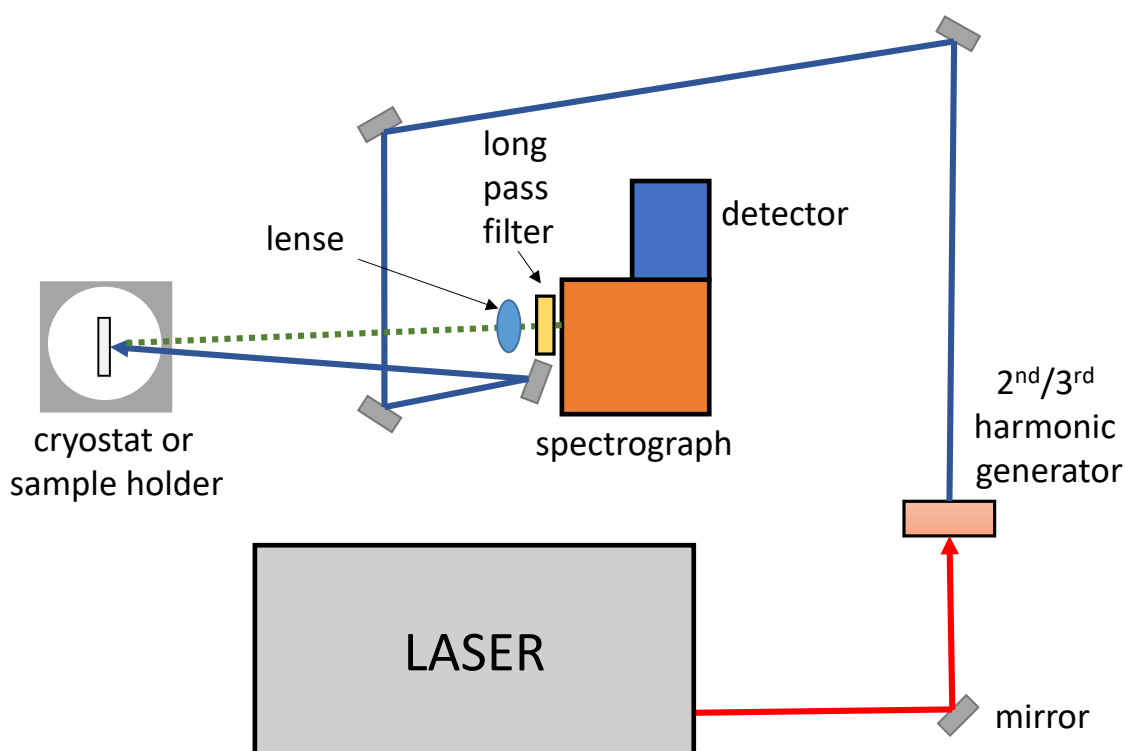


Figure 7.5. Schematic representation of a transient PL set-up.

In order to achieve time-resolved detection two different methods were used. The first one is a streak camera system, in which the photons hit a photocathode and electrons are released based on the photoelectric effect (see **Figure 7.6a**). These electrons are subsequently accelerated in a cathode ray tube and a time dependent electrical field is applied that deflect the photons differently depending on their time passing the plates generating this field. The following detection of these electrons results a

3D image with the wavelength on the x-axis, the detection time on the y-axis and the intensity on the z-axis (usually shown as contour plot; **Figure 7.6b**). In this plot the decay curve of each wavelength is shown along the y axis (**Figure 7.6c**). Dependent on the time window chosen, the instrument response changes and can be determined by measuring the scattered laser light.

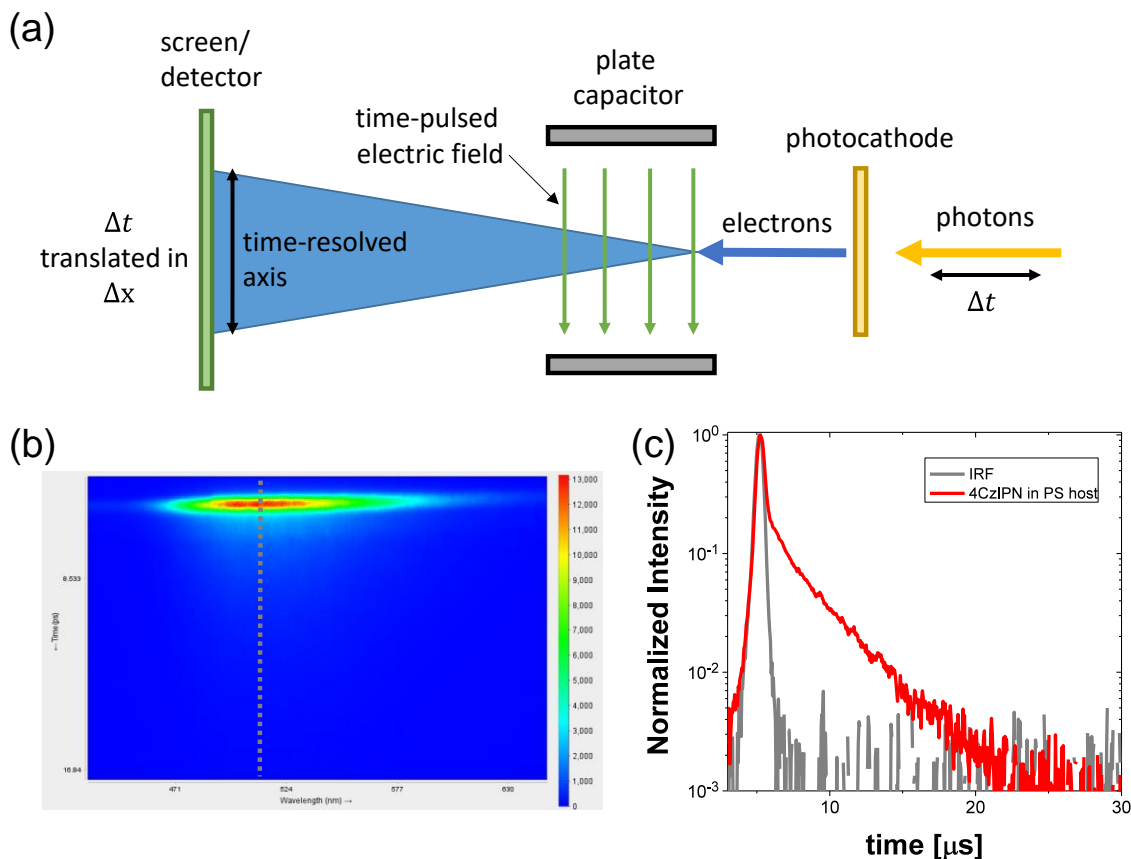


Figure 7.6. (a) Schematic work principle of a streak camera. (b) Contour plot of TRPL data derived from streak camera measurement and (b) decay curve of PL emission at 520 nm of 4CzIPN (TADF molecule) in PS host.

The second detection method used for TRPL was a gated ICCD camera system. In this set-up an electrical pulse from the laser triggers the camera in order to have both synchronized which allows it to specifically configure the detection time window (see **Figure 7.7a**). In this way, a PL spectrum for a set time delay can be recorded and by changing the detection window, the decay curve for all

wavelengths can be determined by dividing the intensity recorded with the detection window and the integration time (see **Figure 7.7b**).

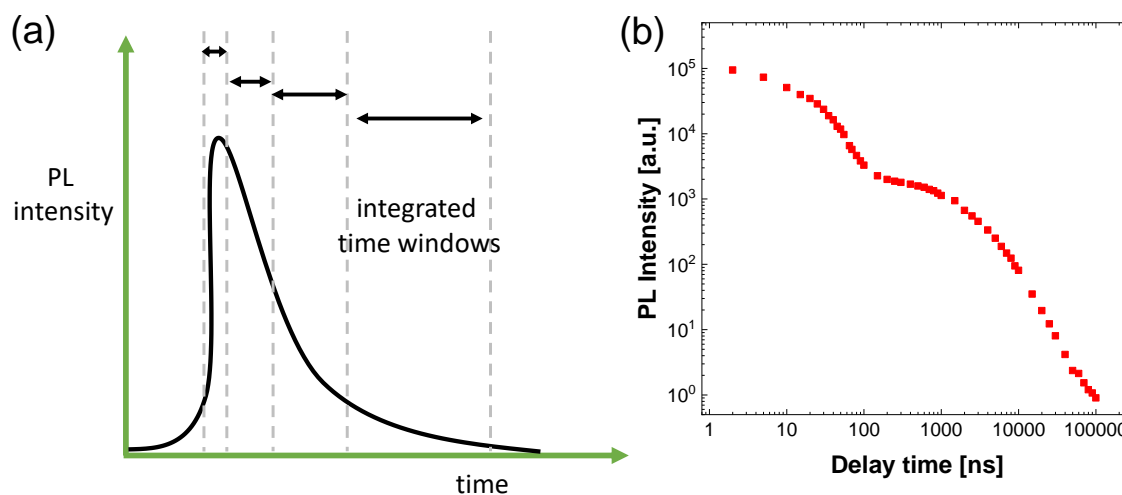


Figure 7.7. (a) Schematic representation of the emitted light intensity plotted against time with integration windows shown. (b) Example of a decay curve derived from the spectra recorded for different integration time windows.

For TRPL measurements shown in **Figure 4.13**, **Figure A4.15** and **Figure A4.16**, the film samples were placed in a nitrogen flow cryostat (*Cryovac*). PL was excited with a Nd:YAG (*Surelite I*, Continuum) pumped dye laser (*NARROWscan*, *Radiant Dyes*) with a repetition rate of 10 Hz and a pulse duration was 4 ns. The excitation intensity was measured with a thermoelectric detector (*Scientech*). The PL was focused on a monochromator (150 lines/mm, spectral resolution 1 nm) and an iCCD camera (operated in gated mode, minimum width 2 ns; *Roper Scientific*) was used for detection.

The TRPL spectra, decay curves and related data shown in **Figure 4.14**, **Figure 4.15**, **Figure 4.17**, **Figure 4.16**, **Figure A4.12** and **Figure A4.13** were excited with an excitation wavelength of 400 nm with the frequency-doubled output from a Ti:Sapphire laser (*Coherent*, *Libra HE*) supplying 100 fs pulses with a repetition rate of 1 kHz. The fluorescence emission was detected by streak camera

(Hamamatsu C5680, slow sweep mode; 100 ns time window: 0.45 ns instrument response, 50 μ s time window: 0.23 μ s instrument response) and HPDTA (version 9.5pf7) was used as operating software. The PL decay was collected at the PL maximum of the delayed fluorescence (520-540 nm). In order to limit triplet excited state quenching by oxygen, the sample was measured in an encapsulated sample holder in nitrogen atmosphere and loaded in a glovebox.

The TRPL spectra, decay curves and related data shown in **Figure 4.18** and **Figure A4.14** were measured using the same excitation but the PL was recorded by a 4 picos-DIG camera (*Stanford Computer Optics*). 4spec (version 2.30.0.2) was used as operating software. For the temperature scans, the film samples were loaded into a top load exchange gas closed cycle cryostat (GMX-19-OmniPlex, *Advanced Research Systems, Inc.*). To ensure a helium atmosphere, the cryostat was first flushed with dry nitrogen for 2 minutes and then with helium for 30 s. The measurements were performed under this helium (Helium 5.0 supplied by *Westfalen AG*) atmosphere for the entire temperature range.

7.2.9. Profilometer

The thicknesses of organic films were determined by using a DektakXT surface profilometer from *Bruker*. To determine the film thickness, the films were scratched with cannula and the profile was measured perpendicular to this scratch (see **Figure 7.8**). For higher precision, this procedure was repeated at three different spots and the mean thickness was calculated.

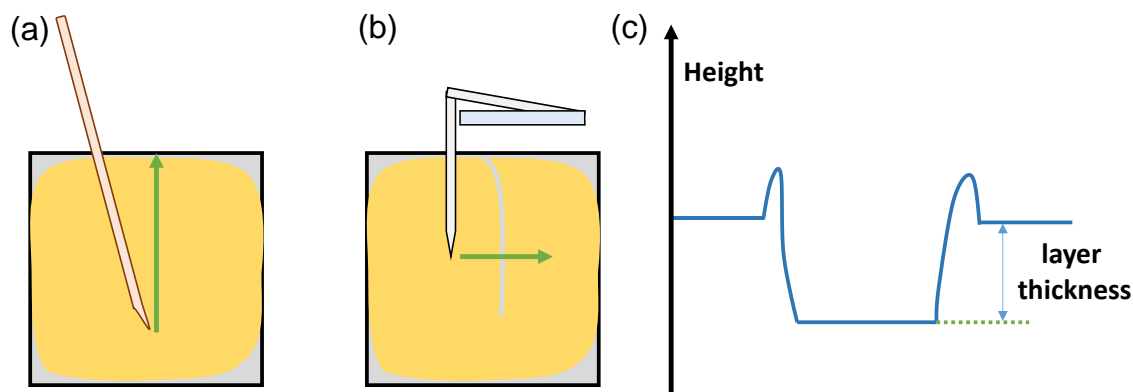


Figure 7.8. Profiler operation. (a) Scratching the surface. (b) Measurement perpendicular to the starch. (c) Profiletrace measured.

7.2.10. Atomic Force Microscopy

The AFM measurements were performed on a *Veeco* Dimension 3100 AFM in tapping mode using a cantilever with a force constant of 42 N/m and a resonance frequency of 300 kHz (supplied by *Bruker*) and operated by the software NanoScope® IIIa (version: 5-31R1, Digital Instruments, *Veeco Instruments, Inc.*).

7.2.11. Transmission Electron Microscopy

Transmission electron microscopy (TEM) samples were analyzed on a Tecnai T12 or a Tecnai G2 Spirit from *FEI* (Hillsboro, USA), both equipped with a LaB₆ cathode operating at 120 kV. The former is equipped with a BioTWIN objective lens whereas the latter makes use of a TWIN lens. Images were recorded either using a MegasyS 1k×1k or a Gatan US1000 2k×2k CCD sensor. 5 μL of the sample were left to absorb to freshly glow discharged copper grids (CF300-Cu, 300 mesh) coated with a 3–4 nm carbon film from *Electron Microscopy Sciences* (Hatfield, USA) for 1 min and negatively stained afterwards for 20 s with 5 μL of a 2 wt% solution of uranyl acetate. Excess liquid was removed

with Whatman® grade 1 filter papers from *GE Healthcare Bio-Sciences* (Uppsalla, Sweden) after each step.

7.2.12. Analytical Size Exclusion Chromatography

Analytical size exclusion chromatography in THF was performed with polystyrene as external and toluene as an internal standard to calculate the molecular weights. Both a refractive index detector (G 1362A RID, *Jasco*) and a UV-vis detector (UV-2075 Plus, *Jasco*) were used to detect the polymers.

Analysis via size exclusion chromatography in HFIP was performed on an Agilent 1100 Series from *Agilent Technologies* (Santa Clara, USA) with 3 g/L potassium trifluoroacetate as eluent at 40 °C and a flow rate of 0.8 mL/min. SEC columns were packed with modified silica (PFG columns, particle size: 7 µm porosity: 100 Å and 1000 Å, respectively). Poly(methyl methacrylate) standards from *PSS Polymer Standards Services* (Mainz, Germany) were used for calibration. A refractive index detector (G1362A RID) and an UV/Vis detector (230 nm; *Jasco* UV-2075 Plus) were used for detection.

7.3. Theoretical Computation

All quantum calculations were conducted by Gaussian 09W (Version 9.5) software package using GaussView 5.0.9. Due to the high molecular weights of the polymers, fragment molecules consisting of the linker connecting two D-A-D triads were used for the computations. The ground state geometries were optimized at B3LYP/6-31G(d,p) level of DFT. In subsequent TD-DFT calculations at B3LYP/6-31G(d,p) level of level of theory the energy of S₁ and T₁ were calculated. The molecular orbitals located at the end groups were not taken into account.

7.4. Fabrication of Optoelectronic Devices

The substrates were cleaned in a cleanroom. Glass as well as ITO substrates (see **Figure 7.9a**) were first cleaned with detergent (Extran® MA 02 supplied by *Merck KGaA*) with scrubbing the surface with gloves. After rinsing with DI water, the substrates were sonicated for 5 min each in acetone and 2-propanol. As a next step, the substrates were dried in nitrogen stream and in an oven (supplied by *HORO Dr. Hofmann GmbH*) at 140 °C for 10 min. Before spin-coating the first layers of the OLED the surface was activated with a UV-ozone cleaner (supplied by *FHR*) for 20 min.

As hole-injection layer poly(3,4-ethylenedioxythiophene):poly(styrene sulfonate) (PEDOT:PSS, *Heraeus Clevios 4083*) and p-pTFF-C₂F₅SIS were used. PEDOT:PSS was spincoated from water solution and subsequently heated for 10 min in an oven at 140 °C (see **Figure 7.9b**). In contrast, p-pTFF-C₂F₅SIS was weight in in a glovebox with a concentration of 10 mg ml⁻¹ in degassed and dry acetonitrile. To fully dissolve the material, the solution was heated in the closed vial in an oil bath for 30 s and then shaken with a vortex stirrer (supplied by *IKA*) for 30 s. Those two steps were repeated until the solid material was fully dissolved. Spin-coating from this solution afforded a film of 40 nm thickness (method: 60 s, 1000 rpm, 500 acc). All small molecules and polymers forming the EML were spin-coated from chlorobenzene solution (method: 1) 60s, 2000 rpm, 1000 acc, 2) 20 s, 4000 rpm, 1000 acc) and the thickness was controlled by the concentration of the solution (see **Figure 7.9c**).

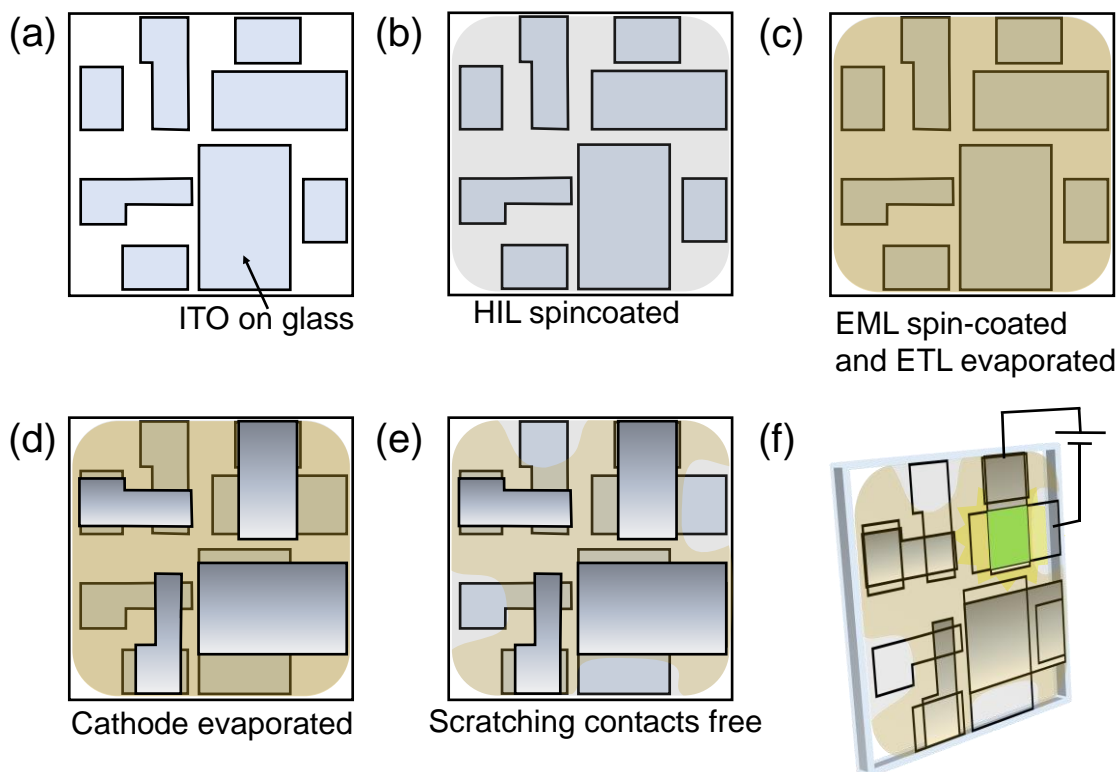


Figure 7.9. Schematic representation of the OLED device fabrication. (a) Bare substrate with ITO electrodes on glass. (b) Spin-coating of HIL. (c) Spincoating and ETL evaporation. (d) Thermal evaporation of cathode with a shadow mask perpendicular to the anode electrodes. (e) Scratching free of the ITO electrodes. (f) Light emission upon operation through the glass substrate.

The electron-transport layer 2,2',2''-(1,3,5-Benzinetriyl)-tris(1-phenyl-1-H-benzimidazole) (TPBi) was evaporated via thermal evaporation with a thickness of 60 nm. In this method organic small molecules, inorganic oxides and metals are heated in a high vacuum chamber until the materials sublime (see **Figure 7.10**). The devices and substrates were placed in a rotating sample holder and the quartz crystal microbalances at the sides of the chamber were used to control the evaporated layer thicknesses. Using the same method, the top electrode consisted of 5 nm of Ba and 100 nm Al for the OLEDs and 10 nm of MoO₃ and 100 nm Al for the hole-only (HO) devices (see **Figure 7.9d**). After scratching free the contacts of the anode, the optoelectronic device can be operated and characterized (see **Figure 7.9e** and **f**). In contrast, electron-only devices (EO) consist of a 30 nm Al layer using a shadow mask to form the bottom electrodes. The Al electrode was in a next step exposed to air for 5 min to form an oxide

layer and afterwards the organic semiconductor layer was spin-coated on-top. The top electrode in EO devices was identical to the one of OLEDs (Ba/Al).

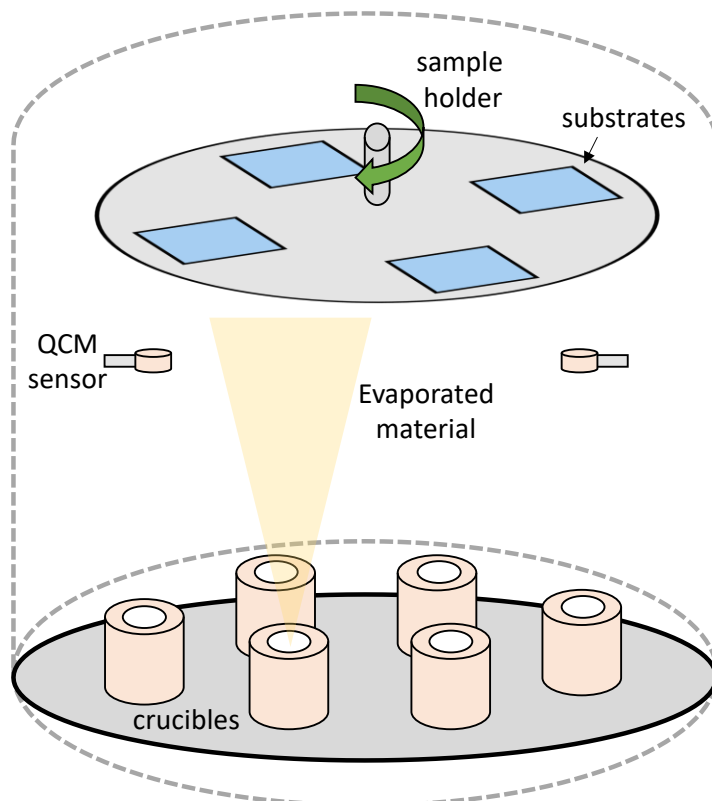


Figure 7.10. Schematic representation of the thermal vacuum evaporation set-up. The shutter preventing an uncontrolled deposition that is placed between the sources and the sample holder is not shown for reasons of clarity.

7.4.1. Characterization of Optoelectronic Devices

The current–voltage (J - V) measurements were carried out with a *Keithley* 2400 sourcemeter in a protected environment (O_2 and H_2O values below 0.1 ppm). The photocurrent–voltage measurements were carried out with a *Keithley* 6514 system electrometer recorded using a Si photodiode with NIST-traceable calibration, following a previously described procedure^[146] and the EQE as well as PE were calculated consequently. EL was recorded with a USB4000 UV–vis–ES spectrometer.

8. Synthetic Procedures and Characterization

8.1. Standard Operating Procedures (SOP)

8.1.1. Synthesis of Peptides via SPPS (SOP1)

Loading of the resin was done according to literature.^[150,151] 2 eq. relative to the resin loading capacity of the Fmoc-protected amino acid were dissolved in 10 mL/g resin of DCM and the solution was added to a Merrifield reactor containing the 2-chlorotrityl chloride resin. DIPEA (2 eq. relative to the resin loading capacity) was added and the mixture was placed on a shaker for 5 minutes. Afterwards, 3 eq. additional DIPEA were added and the mixture was placed on a shaker for 1 h. The reactor was drained and after addition of 1 mL/g resin of MeOH it was placed on a shaker for 15 min. Then, the vessel was drained and the resin was washed consecutively with DCM, DMF, DCM and MeOH three times each, dried and transferred to a SPPS-reactor vessel for the stepwise peptide synthesis via SPPS.

First the loaded resin was swollen in DCM and after draining, Fmoc-deprotection was achieved by adding a 20 vol% piperidine in DMF solution and shaking for 20 min. Afterwards, the vessel was drained and washed four times with DMF and two times with DCM. Each amino acid was coupled by premixing a 0.4 M solution of the Fmoc-protected amino acid in DMF (4 eq. relative to the resin loading capacity) with a solution of HOBt (4 eq. relative to the resin loading capacity), HBTU (4 eq. relative to the resin loading capacity) and DIPEA (6 eq. relative to the resin loading capacity) and adding this mixture to the reaction vessel. After shaking for 1 h, the vessel was drained and washed with DMF five times. This was repeated for each amino acid, starting each step with the Fmoc-deprotection of the last amino acid. In the last step, the beads were washed with DCM and dried under high vacuum.

8.1.2. Coupling of Carboxylic Acid-functionalized Dye to Peptide-loaded Resin and Cleavage from Resin (SOP2)

Coupling of the carboxylic acid-functionalized dye was done in a peptide reactor syringe by hand. 1 eq. of peptide-loaded resin was transferred into the peptide reactor syringe and swollen in DCM for 15 min. For the coupling step a solution of the carboxylic acid-functionalized dye (1 eq.) in DMF (0.4 mol/L) was mixed with a solution of HBTU (4 eq.) and HOBt (4 eq.) in DMF (0.4 mol/L) and a solution of DIPEA (6 eq.) in DMF (0.6 mol/L) for preactivation for 10 min and added to the drained reactor. The reactor was sealed with a plug and shaken for 2.5 h. Afterwards the reactor was drained and washed with DMF and DCM and the coupling and washing step was repeated one time.

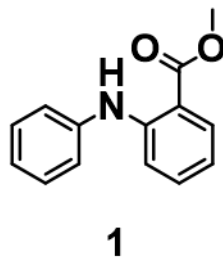
Finally, cleaving the peptide from the resin was performed according to literature^[152] by adding a solution of TFE and DCM (4:1) to the Merrifield reactor and shaking for 45 min. Afterwards the reactor was drained and washed with DCM, collecting the solutions. This step was repeated two times and all collected solutions were then concentrated under reduced pressure. The peptide was precipitated out in cold diethyl ether, separated via centrifugation and dried under vacuum.

8.1.3. End Group Modification and Deprotection of Polymer-peptide Conjugates (SOP3)

For the end group modification 1 eq. of the polymer was transferred into a pre-dried Schlenk flask equipped with a stir bar and dissolved in dry DMF (1 ml DMF per 65 mg polymer). The carboxylic acid-bearing peptide (3 eq.), HBTU (3.3 eq.), HOBt (3.3 eq.) and DIPEA (6.6 eq.) were added and the solution was stirred at room temperature for 3 days. Afterwards the polymer was precipitated from cold diethyl ether and separated *via* centrifugation.

Trt-deprotection was achieved by adding a solution of TFA, TIPS and water (95:2.5:2.5) and stirring for 45 min at room temperature. The mixture was concentrated under vacuum while stirring, co-distilled with toluene five times and lyophilized. Further purification was performed if needed.

8.2. Synthesis of Methyl 2-(phenylamino) benzoate (1)



2-(Phenylamino)benzoic acid (30.0 g, 140.7 mmol, 1.0 eq.) was dissolved in 500 mL methanol in inert gas atmosphere and was cooled to 0 °C with an ice bath. Thionylchloride (44 mL, 606.5 mmol, 4.33 eq.) was added dropwise and refluxed for 15 h. The solution was allowed to cool to r.t. and was quenched with deionized water (600 mL). The solution was extracted with EtOAc (6 × 250 mL). The combined organic phases were dried over MgSO₄ and concentrated *in vacuo*. The crude product was further purified by flash chromatography on silica gel (Hex:EtOAc = 6:4) followed by another flash chromatography on silica gel (Hex:EtOAc = 1:0 → 9:1) and light yellow crystals (19.56 g, 86.1 mmol, 61 %) were obtained.

Chemical formula: C₁₄H₁₃NO₂

R_f = 0.16 (SiO₂, Hexane).

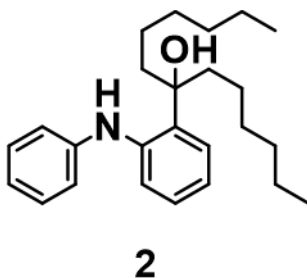
¹H NMR (300 MHz, Chloroform-*d*) δ 9.44 (br s, 1H, NH), 7.96 (d, *J* = 8.0 Hz, 1H, CH^{arom.}-C-COOCH₃), 7.40 – 7.20 (m, 6H, NH-C-CH^{arom.}-CH^{arom.}), 7.13 – 7.04 (m, 1H, CH^{arom.}-C-CH^{arom.}-CH^{arom.}-CH^{arom.}), 6.79 – 6.67 (m, 1H, CH^{arom.}-CH^{arom.}-C-COOCH₃), 3.90 (s, 3H, CH₃).

¹³C NMR (75 MHz, CDCl₃) δ 169.07 (C=O), 148.07 (NH-C-C), 140.89 (CH^{arom.}-C-CH^{arom.}), 134.23 (CH^{arom.}-CH^{arom.}-C-C-COOCH₃), 131.75 (CH^{arom.}-C-COOCH₃), 129.50 (CH^{arom.}-C-CH^{arom.}-CH^{arom.}), 123.70 (CH^{arom.}-C-CH^{arom.}-CH^{arom.}-CH^{arom.}), 122.65 (CH^{arom.}-C-CH^{arom.}), 117.24 (CH^{arom.}-CH^{arom.}-C-COOCH₃), 114.17 (CH^{arom.}-C-C-COOCH₃), 112.05 (C-COOCH₃), 51.91 (CH₃).

MALDI-MS (DCTB, DCM) (m/z): [M-MeOH]⁺: calc. 195.0684, found 195.0561; [M]⁺: calc. 227.0946, found 227.0817.

The characterization is in agreement with literature.^[153]

8.3. Synthesis of 7-(2-(Phenylamino)phenyl)tridecan-7-ol (2)



The modified procedure based on literature was carried out.^[154] Methyl 2-(phenylamino) benzoate (**1**; 10.0 g, 44.0 mmol, 1.0 eq.) was dissolved in dry inhibitor-free THF (45 mL) in inert gas atmosphere. Hexylmagnesium bromide (20 % in THF, 202.0 mL, 202 mmol, 4.6 eq.) was added dropwise while cooling the solution to r.t. with water. The solution was stirred for 17 h at r.t.. The solution was cooled with ice and slowly quenched with deionized water. The solution was extracted with EtOAc (3 × 200 mL) and the combined organic phases were dried over MgSO₄. Concentration *in vacuo* afforded the crude product which was further purified by flash chromatography on silica gel (Hex:EtOAc = 30:1) and the product was obtained as a light-yellow oil (16.17 g, 44.0 mmol, quant.).

Chemical formula: C₂₅H₃₇NO

R_f = 0.26 (SiO₂, Hex:EtOAc = 30:1).

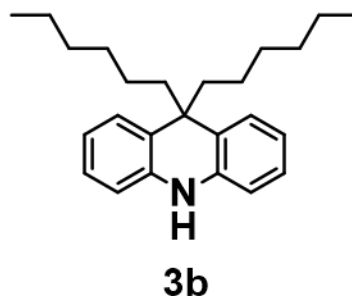
¹H NMR (300 MHz, DMSO-*d*₆) δ 8.52 (s, 1H, NH), 7.18 (t, *J* = 7.8 Hz, 4H, CH^{arom.}-C-C-CH^{arom.}, CH^{arom.}-C-CH^{arom.}-CH^{arom.}), 7.10 (d, *J* = 7.9 Hz, 1H, CH^{arom.}-CH^{arom.}-C-C-C-OH), 6.91 (d, *J* = 8.0 Hz, 2H, CH^{arom.}-C-CH^{arom.}), 6.85 (t, *J* = 7.5 Hz, 1H, CH^{arom.}-CH^{arom.}-C-C-OH), 6.77 (t, *J* = 7.4 Hz, 1H, CH^{arom.}-C-CH^{arom.}-CH^{arom.}-CH^{arom.}), 5.40 (s, 1H, OH), 1.86 – 1.72 (m, 4H, C₂-C-OH), 1.22 – 1.07 (m, 16H, CH₂-CH₂-CH₂-CH₂-CH₃), 0.78 (t, *J* = 6.5 Hz, 6H, CH₃).

¹³C NMR (75 MHz, DMSO) δ 144.58 (NH-C(CH^{arom.})₂), 142.13 (NH-C-C), 134.28 (NH-C-C), 129.14 (CH^{arom.}-C-CH^{arom.}-CH^{arom.}), 127.76 (NH-C-C-CH^{arom.}), 126.86 (OH-C-C-C-CH^{arom.}-CH^{arom.}), 120.23 (OH-C-C-CH^{arom.}-CH^{arom.}), 119.97 (OH-C-C-C-CH^{arom.}), 119.20 (CH^{arom.}-C-CH^{arom.}-CH^{arom.}-CH^{arom.}), 116.19 (CH^{arom.}-C-CH^{arom.}), 77.60 (C-OH), 31.13 (CH₂-CH₂-CH₃), 29.10 (CH₂-CH₂-CH₂-CH₃), 23.33

(OH-C-CH₂-CH₂), 21.96 (CH₂-CH₃), 13.86 (CH₃). The signal for OH-C-CH₂ was identified to have a chemical shift of $\delta \approx 39.2$ by heteronuclear single quantum coherence (HSQC) and heteronuclear multiple bond Correlation (HMBC) NMR experiment but is superimposed by the solvent signals.

MALDI-MS (DCTB, DCM) (m/z): [M-H₂O]⁺: calc. 349.2770, found 349.2640; [M]⁺: calc. 367.2875, found 367.2736.

8.4. Synthesis of 9,9-Dihexyl-9,10-dihydroacridine (3b)



The modified procedure based on literature was carried out.^[154] 7-(2-(phenylamino)phenyl)tridecan-7-ol (**2**; 6.73 g, 18.3 mmol, 1.0 eq.) was dissolved in acetic acid (70 mL) and conc. HCl was added (14 mL). The solution was refluxed for 48 h. The solution was allowed to cool to room temperature, quenched with ice and extracted with Et₂O (4 × 50 mL). The combined organic phases were washed with water twice and with brine once (100 mL each). The organic solution was dried over MgSO₄ and concentrated *in vacuo*. The crude product was further purified by flash chromatography on silica gel (Hex:EtOAc = 200:1 → 150:1) and a following recrystallization. The pure product was obtained as yellow crystals (4.70 g, 13.4 mmol, 73 %).

Chemical formula: C₂₅H₃₅N

R_f = 0.41 (SiO₂, Hex:EtOAc = 30:1).

¹H NMR (300 MHz, DMSO-*d*₆) δ 8.58 (s, 1H, NH), 7.17 (d, *J* = 7.8 Hz, 2H, CH₂-C-C-CH^{arom.}), 6.98 (t, *J* = 7.6 Hz, 2H, NH-C-CH^{arom.}-CH^{arom.}-CH^{arom.}), 6.72 (t, *J* = 7.5 Hz, 2H, NH-C-CH^{arom.}-CH^{arom.}-

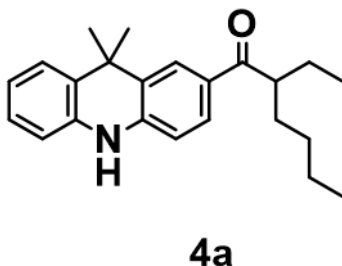
$CH^{arom.}$), 6.64 (d, $J = 8.0$ Hz, 2H, NH-C- $CH^{arom.}$), 1.89 – 1.71 (m, 4H, C(CH₂)₂), 1.18 – 0.94 (m, 12H, CH₂-CH₂-CH₂-CH₃), 0.93 – 0.78 (m, 4H, C-CH₂-CH₂), 0.73 (t, $J = 6.6$ Hz, 6H, CH₃).

¹³C NMR (75 MHz, DMSO) δ 139.65 (NH-C), 126.42 (NH-C- $CH^{arom.}$ - $CH^{arom.}$ - $CH^{arom.}$), 126.07 ($CH^{arom.}$ -C-C(CH₂)₂), 123.96 (NH-C-C), 119.10 (NH-C- $CH^{arom.}$ - $CH^{arom.}$), 112.90 (NH-C- $CH^{arom.}$), 45.29 (C(CH₂)₂), 43.80 (C(CH₂)₂), 31.08 (CH₂-CH₂-CH₃), 29.05 (CH₂-CH₂-CH₂-CH₃), 24.71 (C-CH₂-CH₂), 21.96 (CH₂-CH₃), 13.80 (CH₃).

MALDI-MS (DCTB, DCM) (m/z): [M-hexyl]⁺: calc. 264.1752, found 264.1625; [M-H]⁺: calc. 348.2691, found 248.2552; [M]⁺: calc. 349.2770, found 349.2588; [M+H]⁺: calc. 350.2848, found 350.2709.

The characterization is in agreement with literature. ^[154]

8.5. Synthesis of 1-(9,9-Dimethyl-9,10-dihydroacridin-2-yl)-2-ethylhexan-1-one (4a)



The modified procedure based on literature was carried out.^[59] Aluminum chloride (323 mg, 2.42 mmol, 2.0 eq.) was dispersed in dry DCM (30 mL) in inert gas atmosphere. The dispersion was cooled to 0 °C with an ice bath and 9,9-dimethyl-9,10-dihydroacridine (**3a**; 507 mg, 2.42 mmol, 2.0 eq.) was added under an argon counterflow. 2-Ethylhexanoyl chloride (210 μ L, 1.21 mmol, 1.0 eq.) was dissolved in dry DCM (2.5 mL). The solution was stirred at r.t. for 15 h. The solution was quenched with ice and extracted with DCM (4 \times 50 mL). The combined organic phases were dried over MgSO₄ and concentrated *in vacuo*. The crude product was purified by flash chromatography on silica gel (Hex:EtOAc = 20:1 \rightarrow 10:1) and the desired product was obtained as a light-yellow solid

(191 mg, 0.57 mmol, 47 %). Up-scaling led to a decrease in yield and therefore bigger amounts of product were synthesized by performing several reaction under the same conditions in parallel.

Chemical formula: C₂₃H₂₉NO

R_f = 0.18 (SiO₂, Hex:EtOAc = 10:1).

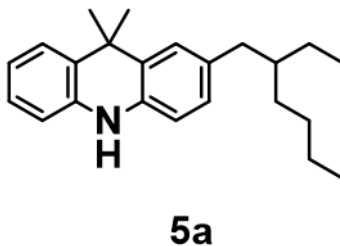
¹H NMR (300 MHz, DMSO-*d*₆) δ 9.45 (s, 1H, NH), 7.97 (d, *J* = 1.9 Hz, 1H, C=O-C-CH^{arom.}-C), 7.75 (dd, *J* = 8.4, 1.9 Hz, 1H, C=O-C-CH^{arom.}-CH^{arom.}), 7.39 (d, *J* = 7.8 Hz, 1H, (CH₃)₂-C-CH^{arom.}-CH^{arom.}), 7.10 (t, *J* = 7.5 Hz, 1H, NH-CH^{arom.}-CH^{arom.}-CH^{arom.}), 6.97 – 6.76 (m, 3H, CH^{arom.}-NH-CH^{arom.}-CH^{arom.}-CH^{arom.}), 3.50 – 3.35 (m, 1H, C=O-CH), 1.69 – 1.56 (m, 2H, C=O-CH-CH₂-CH₃), 1.53 (s, 6H, C(CH₃)₂), 1.50 – 1.34 (m, 2H, C=O-CH-CH₂-CH₂), 1.33 – 1.08 (m, 4H, CH₃-CH₂-CH₂), 0.98 – 0.70 (m, 6H, CH₃-CH₂).

¹³C NMR (75 MHz, DMSO) δ 201.40 (C=O), 142.77 (N-C-CH^{arom.}-CH^{arom.}-C), 137.09 (N-C-CH^{arom.}-CH^{arom.}-CH^{arom.}), 128.97 (O=C-C-CH₂), 128.30 (O=C-C-CH₂-C), 127.90 (N-C-CH^{arom.}-CH^{arom.}-C), 127.76 (N-C-CH^{arom.}-CH^{arom.}-CH^{arom.}), 126.90 ((CH₃)₂C-C-CH^{arom.}-CH^{arom.}), 126.49 ((CH₃)₂C-C-CH^{arom.}-CH^{arom.}), 125.81 ((CH₃)₂C-C-CH^{arom.}-C), 120.85 ((CH₃)₂C-C-CH^{arom.}-CH^{arom.}), 113.91 (N-C-CH^{arom.}-CH^{arom.}-C), 113.04 (N-C-CH^{arom.}-CH^{arom.}-CH^{arom.}), 45.44 ((CH₃)₂C), 35.62 (CH-CH₂-CH₃), 31.84 ((CH₃)₂C), 31.73 ((CH₃)₂C), 29.24 (CH-CH₂-CH₂), 25.38 (CH-CH₂-CH₂), 22.37 (CH-CH₂-CH₂-CH₂), 13.85 (CH₂-CH₂-CH₃), 11.78 (CH-CH₂-CH₃).

MALDI-MS (DCTB, DCM) (m/z): [M-CH₃]⁺: calc. 320.2014, found 320.1862; [M+H]⁺: calc. 336.2327, found 336.2325.

The characterization is in agreement with literature.^[59]

8.6. Synthesis of 2-(2-Ethylhexyl)-9,9-dimethyl-9,10-dihydroacridine (5a)



The modified procedure based on literature was carried out.^[59] Dry THF (50 mL) was cooled to 0 °C with an ice bath and aluminum chloride (610 mg, 4.58 mmol, 2.0 eq.). Lithium aluminum hydride (1 mol/L in THF, 9.17 mL, 9.17 mmol, 4.0 eq.) was added dropwise. 1-(9,9-dimethyl-9,10-dihydroacridin-2-yl)-2-ethylhexan-1-one (**4a**; 769 g, 2.29 mmol, 1.0 eq.) was dissolved in 5 mL dry THF and added dropwise. The solution was stirred at r.t. for 20 h. The solution was cooled with an ice bath and EtOAc (20 mL) and 5 wt% HCl (2 mL) was added. The precipitated solid was filtered off and the solution was concentrated *in vacuo*. The crude product was further purified by flash chromatography on silica gel (Hex:EtOAc = 20:1) and the desired product was obtained as a light-yellow solid (737 mg, 2.29 mmol, quant.).

Chemical formula: C₂₃H₃₁N

R_f = 0.45 (SiO₂, Hex:EtOAc = 20:1).

¹H NMR (300 MHz, Acetone-*d*₆) δ 7.93 (s, 1H, NH), 7.37 (d, *J* = 7.7 Hz, 1H, C(CH₃)₂-C-CH^{arom.}-CH^{arom.}), 7.20 (d, *J* = 1.9 Hz, 1H, CH₂-C-CH^{arom.}-C), 7.03 (ddd, *J* = 7.4, 1.4 Hz, 1H, NH-C-CH^{arom.}-CH^{arom.}), 6.87 (dd, *J* = 8.0, 1.9 Hz, 1H, CH₂-C-CH^{arom.}-CH^{arom.}), 6.84 – 6.76 (m, 2H, NH-C-CH^{arom.}-CH^{arom.}-CH^{arom.}), 6.73 (d, *J* = 8.0 Hz, 1H, CH₂-C-CH^{arom.}-CH^{arom.}), 2.49 (d, *J* = 7.0 Hz, 2H, CH₂-C-CH^{arom.}), 1.55 (s, 7H, C(CH₃)₂, (CH₂)₂-CH-C), 1.39 – 1.21 (m, 8H, CH₃-CH₂-CH-CH₂-CH₂-CH₂-CH₃), 0.95 – 0.80 (m, 6H, CH₃-CH₂).

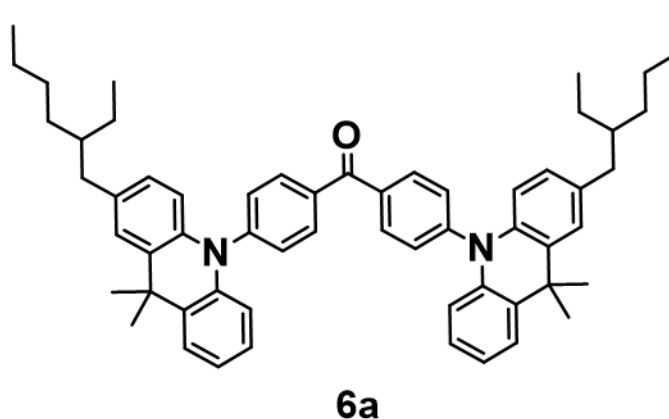
¹³C NMR (75 MHz, Acetone) δ 140.23 (N-C-CH^{arom.}-CH^{arom.}-CH^{arom.}), 137.76 (N-C-CH^{arom.}-CH^{arom.}-C), 133.73 (CH₂-C-CH^{arom.}), 129.52 (N-C-CH^{arom.}-CH^{arom.}-C), 129.26 (CH₂-C-CH^{arom.}-C), 128.31 (N-C-CH^{arom.}-CH^{arom.}-CH^{arom.}), 127.53 ((CH₃)₂C-C-CH^{arom.}-CH^{arom.}), 127.02 ((CH₃)₂C-C-CH^{arom.}-CH^{arom.}),

126.35 ((CH₃)₂C-C-CH^{arom.}-C), 120.66 (N-C-CH^{arom.}-CH^{arom.}-CH^{arom.}), 114.37 (N-C-CH^{arom.}-CH^{arom.}-CH^{arom.}), 114.26 (N-C-CH^{arom.}-CH^{arom.}-C), 42.28 ((CH₂)₃-CH), 40.45 (C-CH₂-CH), 36.87 ((CH₃)₂C), 33.13 (CH-CH₂-CH₂), 32.43 (CH-CH₂-CH₂), 31.35 ((CH₃)₂C), 31.28 ((CH₃)₂C), 26.36 (CH-CH₂-CH₃), 23.89 (CH₂-CH₂-CH₂-CH₃), 23.42 (CH₂-CH₂-CH₂-CH₃), 14.52 (CH₂-CH₂-CH₂-CH₃), 14.47 (CH₂-CH₂-CH₂-CH₃), 11.31 (CH-CH₂-CH₃).

MALDI-MS (DCTB, DCM) (m/z): [M-CH₃]⁺: calc. 306.2038 , found 306.2222; [M+H]⁺: calc. 320.2187 , found 320.2378.

The characterization is in agreement with literature.^[59]

8.7. Synthesis of Bis(4-(2-(2-ethylhexyl)-9,9-dimethylacridin-10(9H)-yl)phenyl)methanone (6a)



The modified procedure based on literature was carried out.^[59] Bis(4-bromophenyl)methanone (270 mg, 0.80 mmol, 1.0 eq.), sodium *tert*-butoxide (305 mg, 3.16 mmol, 4.0 eq.) and bis(tri-*tert*-butylphosphine) palladium (0) (41 mg, 80 μmol, 0.1 eq.) were transferred into a pressure tube under inert gas atmosphere. 2-(2-ethylhexyl)-9,9-dimethyl-9,10-dihydroacridine (**5a**; 538 mg, 1.67 mmol, 2.2 eq.) was dissolved in dry toluene (7 mL) and added. The solution was stirred at 120 °C for 21 h. The solution was allowed to cool to r.t., quenched with deionized water (5 mL), extracted with hexane (3 × 5 mL) and dried over MgSO₄. The solution was concentrated *in vacuo* and the crude product was

further purified by flash chromatography on silica gel (Hex:EtOAc = 50:1) as a yellow solid (624 mg, 0.76 mmol, 96 %).

Chemical formula: C₅₉H₆₈N₂O

R_f = 0.22 (SiO₂, Hex:EtOAc = 50:1).

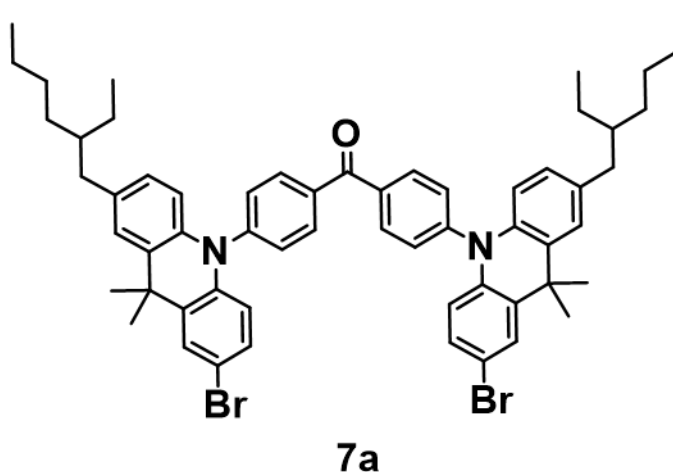
¹H NMR (300 MHz, Methylene Chloride-*d*₂) δ 8.14 (d, *J* = 8.3 Hz, 4H, C=O-C-CH^{arom.}), 7.53 (d, *J* = 8.3 Hz, 4H, C=O-C-CH^{arom.}-CH^{arom.}), 7.48 (dd, *J* = 7.6, 1.9 Hz, 2H, C(CH₃)₂-C-CH^{arom.}-CH^{arom.}), 7.26 (d, *J* = 2.0 Hz, 2H, C(CH₃)₂-C-CH^{arom.}-C), 7.07 – 6.91 (m, 4H, CH^{arom.}-CH^{arom.}-CH^{arom.}-CH^{arom.}), 6.80 (dd, *J* = 8.3, 2.0 Hz, 2H, CH₂-C-CH^{arom.}-CH^{arom.}), 6.39 (dd, *J* = 7.9, 1.5 Hz, 2H, NH-C-CH^{arom.}-CH^{arom.}-CH^{arom.}), 6.31 (d, *J* = 8.3 Hz, 2H, CH₂-C-CH^{arom.}-CH^{arom.}), 2.50 (d, *J* = 7.0 Hz, 4H, CH₂-C-CH^{arom.}), 1.68 (s, 12H, C(CH₃)₂), 1.58 – 1.48 (m, 2H, (CH₂)₃-CH), 1.39 – 1.20 (m, 16H, CH₂-CH₂-CH₂-CH₃, CH-CH₂-CH₃), 0.88 (t, *J* = 7.2 Hz, 12H, CH₂-CH₃).

¹³C NMR (75 MHz, CD₂Cl₂) δ 194.59 (C=O), 146.27 (N-C-CH^{arom.}-CH^{arom.}-C-C=O), 141.15 (N-C-CH^{arom.}-CH^{arom.}-CH^{arom.}), 138.81 (N-C-CH^{arom.}-CH^{arom.}-C-CH₂), 136.99 (C-C=O), 134.91 (CH₂-C-CH^{arom.}), 132.97 (CH^{arom.}-C-C=O), 131.45 (CH^{arom.}-CH^{arom.}-C-C=O), 131.04 (CH₂-C-CH^{arom.}-C), 130.90 (CH₂-C-CH^{arom.}-CH^{arom.}), 127.43 ((CH₃)₂C-C-CH^{arom.}-CH^{arom.}), 126.70 ((CH₃)₂C-C-CH^{arom.}-CH^{arom.}), 126.48 (N-C-CH^{arom.}-CH^{arom.}-CH^{arom.}), 125.74 ((CH₃)₂C-C-CH^{arom.}-C), 121.26 ((CH₃)₂C-C-CH^{arom.}-CH^{arom.}), 114.92 (N-C-CH^{arom.}-CH^{arom.}-CH^{arom.}), 114.78 (N-C-CH^{arom.}-CH^{arom.}-C), 41.60 ((CH₂)₃CH), 39.77 (CH₂-C-CH^{arom.}), 36.45 ((CH₃)₂C), 32.64 (CH-CH₂-CH₂), 31.21 (CH-CH₂-CH₂), 29.20 ((CH₃)₂C), 25.83 (CH-CH₂-CH₃), 23.51 (CH₂-CH₂-CH₃), 14.32 (CH-CH₂-CH₃), 11.00 (CH₂-CH₂-CH₃).

MALDI-MS (DCTB, DCM) (m/z): [M-CH₃]⁺: calc. 805.5097, found 805.5134; [M]⁺: calc. 820.5332, found 820.5365

The characterization is in agreement with literature.^[59]

8.8. Synthesis of Bis(4-(2-bromo-7-(2-ethylhexyl)-9,9-dimethylacridin-10(9H)-yl)phenyl)methanone (7a)



The modified procedure based on literature was carried out.^[59] Bis(4-(2-(2-ethylhexyl)-9,9-dimethylacridin-10(9H)-yl)phenyl)methanone (**6a**; 517 mg, 0.63 mmol, 1.0 eq.) was dissolved in CHCl_3 under inert gas atmosphere. *N*-Bromosuccinimide (250 mg, 1.38 mmol, 2.2 eq.) was dissolved in CHCl_3 under inert gas atmosphere and added to the solution. The solution was stirred at 50 °C in the dark for 42 h. The mixture was allowed to cool to r.t., quenched with saturated $\text{Na}_2\text{S}_2\text{O}_3$ solution and extracted with DCM (3×100 mL). The combined organic phases were dried over MgSO_4 and concentrated *in vacuo*. The crude product was further purified by flash chromatography on silica gel (Hex:EtOAc = 60:1) and a following size exclusion chromatography (in CHCl_3). The pure product was obtained as a yellow solid (591 mg, 0.60 mmol, 96 %).

Chemical formula: $\text{C}_{59}\text{H}_{66}\text{Br}_2\text{N}_2\text{O}$

$R_f = 0.22$ (SiO_2 , Hex:EtOAc = 60:1).

^1H NMR (250 MHz, Chloroform-*d*) δ 8.15 (d, $J = 8.1$ Hz, 4H, C=O-C- $\text{CH}^{\text{arom.}}$), 7.55 (d, $J = 2.3$ Hz, 2H, $\text{C}(\text{CH}_3)_2$ -C- $\text{CH}^{\text{arom.}}$ -C-Br), 7.51 (d, $J = 8.0$ Hz, 4H, C=O-C- $\text{CH}^{\text{arom.}}$ - $\text{CH}^{\text{arom.}}$), 7.22 (d, $J = 1.9$ Hz, 2H, $\text{C}(\text{CH}_3)_2$ -C- $\text{CH}^{\text{arom.}}$ -C- CH_2), 7.09 (dd, $J = 8.8, 2.3$ Hz, 2H, N-C- $\text{CH}^{\text{arom.}}$ - $\text{CH}^{\text{arom.}}$ -C-Br), 6.80 (dd, $J = 8.1, 1.7$ Hz, 2H, N-C- $\text{CH}^{\text{arom.}}$ - $\text{CH}^{\text{arom.}}$ -C- CH_2), 6.35 – 6.15 (m, 4H, N-C- $\text{CH}^{\text{arom.}}$ - $\text{CH}^{\text{arom.}}$ -C-Br, N-C- $\text{CH}^{\text{arom.}}$ - $\text{CH}^{\text{arom.}}$ -C- CH_2), 2.49 (d, $J = 6.8$ Hz, 4H, CH_2 -C- $\text{CH}^{\text{arom.}}$), 1.67 (s, 12H, $\text{C}(\text{CH}_3)_2$), 1.57 – 1.40

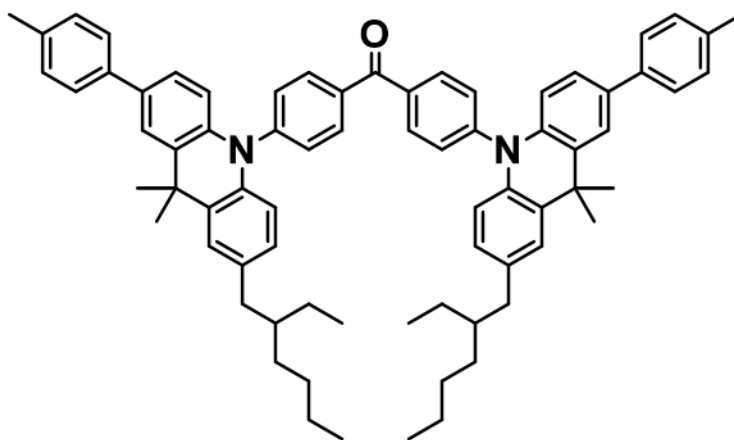
(m, 2H, $(\text{CH}_2)_3\text{-CH}$), 1.38 – 1.13 (m, 16H, $\text{CH}_2\text{-CH}_2\text{-CH}_2\text{-CH}_3$, $\text{CH-CH}_2\text{-CH}_3$), 0.98 – 0.75 (m, 12H, $\text{CH}_2\text{-CH}_3$).

^{13}C NMR (75 MHz, CDCl_3) δ 194.51 (C=O), 146.42 ($\text{N-C-CH}^{\text{arom.}}\text{-CH}^{\text{arom.}}\text{-C-C=O}$), 142.66 ($\text{N-C-CH}^{\text{arom.}}\text{-CH}^{\text{arom.}}\text{-C-Br}$), 140.07 ($\text{N-C-CH}^{\text{arom.}}\text{-CH}^{\text{arom.}}\text{-C-CH}_2$), 138.10 (C-C=O), 136.52 ($(\text{CH}_3)_2\text{C-C-CH}^{\text{arom.}}\text{-C-Br}$), 135.13 ($\text{CH}^{\text{arom.}}\text{-C-CH}_2$), 133.15 ($\text{CH}^{\text{arom.}}\text{-C-C=O}$), 132.84 ($\text{CH}^{\text{arom.}}\text{-CH}^{\text{arom.}}\text{-C-C=O}$), 130.86 ($(\text{CH}_3)_2\text{C-C-CH}^{\text{arom.}}\text{-C-CH}_2$), 130.07 ($\text{CH}_2\text{-C-CH}^{\text{arom.}}\text{-CH}^{\text{arom.}}$), 129.26 ($(\text{CH}_3)_2\text{C-C-CH}^{\text{arom.}}\text{-C-Br}$), 127.43 ($\text{N-C-CH}^{\text{arom.}}\text{-CH}^{\text{arom.}}\text{-C-Br}$), 126.19 ($(\text{CH}_3)_2\text{C-C-CH}^{\text{arom.}}\text{-C-CH}_2$), 116.11 (C-Br), 114.46 ($\text{N-C-CH}^{\text{arom.}}\text{-CH}^{\text{arom.}}\text{-C-Br}$), 113.43 ($\text{N-C-CH}^{\text{arom.}}\text{-CH}^{\text{arom.}}\text{-C-CH}_2$), 41.25 ($(\text{CH}_2)_3\text{CH}$), 39.58 ($\text{CH}_2\text{-C-CH}^{\text{arom.}}$), 36.41 ($(\text{CH}_3)_2\text{C}$), 32.38 ($\text{CH-CH}_2\text{-CH}_2$), 31.09 ($\text{CH-CH}_2\text{-CH}_2$), 28.96 ($(\text{CH}_3)_2\text{C}$), 25.54 ($\text{CH-CH}_2\text{-CH}_3$), 23.24 ($\text{CH}_2\text{-CH}_2\text{-CH}_3$), 14.31 ($\text{CH-CH}_2\text{-CH}_3$), 10.97 ($\text{CH}_2\text{-CH}_2\text{-CH}_3$).

MALDI-MS (DCTB, DCM) (m/z): $[\text{M-CH}_3]^+$: calc. 961.3307, found 961.3160; $[\text{M}]^+$: calc. 976.3542, found 976.3378.

The characterization is in agreement with literature.^[59]

8.9. Synthesis of Tol-MAc-BP



Tol-MAc-BP

The modified procedure based on literature was carried out.^[59] 4,4,5,5-Tetramethyl-2-(p-tolyl)-2,1,3,2-dioxaborolane (**11**; 130 mg, 0.59 mmol, 3.5 eq.), Na_2CO_3 (358 mg, 3.38 mmol, 20.0 eq.) and $\text{Pd}(\text{PPh}_3)_4$

(9.8 mg, 8.4 μmol , 0.05 eq.) were transferred into a pressure tube under inert atmosphere (Ar). Degassed EtOH (0.5 mL), and degassed, deionized water (0.5 mL) were added. Bis(4-(2-(2-ethylhexyl)-9,9-dimethyl-7-bromoacridin-10(9H)-yl)phenyl)methanone (**7a**; 165 mg, 0.17 mmol, 1.0 eq.) was dissolved in degassed toluene (1.8 mL) and added to the mixture. The pressure tube was closed and the solution was stirred at 120 °C for 72 h. The solution was allowed to cool to r.t. and extracted with CHCl_3 . The combined organic fractions were washed with water and HCl solution (5 mL, 2 M). The organic phase was dried over MgSO_4 and the solvent was evaporated under reduced pressure. The crude product was further purified by flash chromatography on flash silica gel (Hex:EtOH 50:1) and a subsequent preparative SEC in CHCl_3 . The desired product was obtained as a yellow solid (88 mg, 0.09 mmol, 52 %).

Chemical formula: $\text{C}_{73}\text{H}_{80}\text{N}_2\text{O}$

$R_f = 0.30$ (SiO_2 , Hex:EtOAc = 50:1).

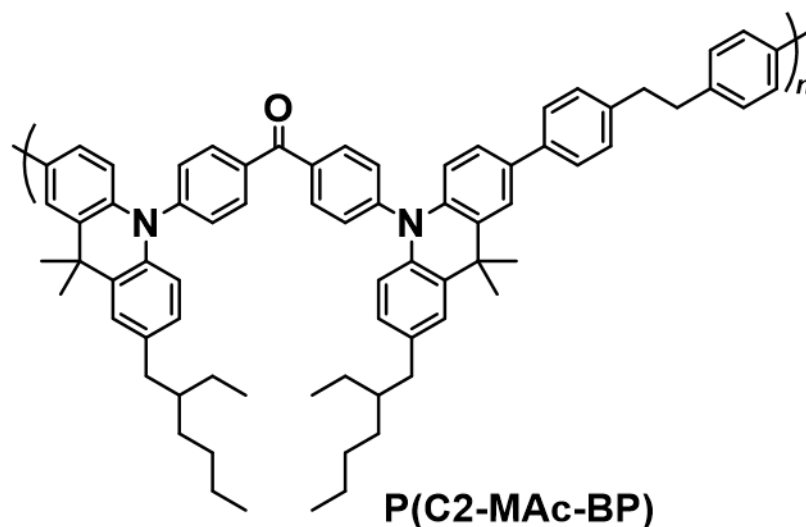
$^1\text{H NMR}$ (700 MHz, Methylene Chloride- d_2) δ 8.19 – 8.15 (m, 4H, $\text{C}=\text{O}-\text{C}-\text{CH}^{\text{arom.}}$), 7.71 (d, $J = 2.1$ Hz, 2H, $\text{C}(\text{CH}_3)_2-\text{C}-\text{CH}^{\text{arom.}}-\text{C}-\text{Tol}$), 7.59 – 7.55 (m, 4H, $\text{C}=\text{O}-\text{C}-\text{CH}^{\text{arom.}}-\text{CH}^{\text{arom.}}$), 7.47 (d, $J = 7.8$ Hz, 4H, $\text{CH}_3-\text{C}-\text{CH}^{\text{arom.}}-\text{CH}^{\text{arom.}}$), 7.29 (d, $J = 2.1$ Hz, 2H, $\text{C}(\text{CH}_3)_2-\text{C}-\text{CH}^{\text{arom.}}-\text{C}-\text{CH}_2$), 7.26 – 7.21 (m, 6H, $\text{CH}_3-\text{C}-\text{CH}^{\text{arom.}}-\text{CH}^{\text{arom.}}$), 6.82 (dd, $J = 8.3, 2.0$ Hz, 2H, $\text{N}-\text{C}-\text{CH}^{\text{arom.}}-\text{CH}^{\text{arom.}}-\text{C}-\text{Tol}$), 6.45 (dd, $J = 8.6, 3.6$ Hz, 2H, $\text{N}-\text{C}-\text{CH}^{\text{arom.}}-\text{CH}^{\text{arom.}}-\text{C}-\text{EtHex}$), 6.32 (dd, $J = 8.4, 3.4$ Hz, 2H, $\text{N}-\text{C}-\text{CH}^{\text{arom.}}-\text{CH}^{\text{arom.}}-\text{C}-\text{EtHex}$), 2.51 (d, $J = 7.0$ Hz, 4H, $\text{CH}_2-\text{C}-\text{CH}^{\text{arom.}}$), 2.37 (s, 6H, $\text{CH}_3-\text{C}-\text{CH}^{\text{arom.}}$), 1.75 (s, 12H, $\text{C}(\text{CH}_3)_2$), 1.53 (d, $J = 12.1$ Hz, 2H, $\text{CH}-(\text{CH}_2)_3$), 1.35 – 1.20 (m, 16H, $\text{CH}_2-\text{CH}_2-\text{CH}_2-\text{CH}_3$, $\text{CH}-\text{CH}_2-\text{CH}_3$), 0.91 – 0.86 (m, 12H, CH_2-CH_3).

$^{13}\text{C NMR}$ (176 MHz, CD_2Cl_2) δ 195.16 ($\text{C}=\text{O}$), 146.21 ($\text{N}-\text{C}-\text{CH}^{\text{arom.}}-\text{CH}^{\text{arom.}}-\text{C}-\text{C}=\text{O}$), 140.36 ($\text{N}-\text{C}-\text{CH}^{\text{arom.}}-\text{CH}^{\text{arom.}}-\text{C}-\text{Tol}$), 138.66 ($\text{N}-\text{C}-\text{CH}^{\text{arom.}}-\text{CH}^{\text{arom.}}-\text{C}-\text{EtHex}$), 138.57 ($\text{N}-\text{C}-\text{CH}^{\text{arom.}}-\text{CH}^{\text{arom.}}-\text{C}-\text{Tol}$), 137.14 ($\text{C}-\text{C}=\text{O}$), 136.78 ($\text{CH}_3-\text{C}-\text{CH}^{\text{arom.}}$), 135.00 ($\text{N}-\text{C}-\text{CH}^{\text{arom.}}-\text{CH}^{\text{arom.}}-\text{C}-\text{EtHex}$), 133.94 ($\text{CH}_3-\text{C}-$

$\text{CH}^{\text{arom.}}-\text{CH}^{\text{arom.}}-\text{C}$, 133.03 ($\text{CH}^{\text{arom.}}-\text{C}-\text{C}=\text{O}$), 131.66 ($\text{C}(\text{CH}_3)_2-\text{C}-\text{CH}^{\text{arom.}}-\text{C}-\text{Tol}$), 131.07 ($\text{N}-\text{C}-\text{CH}^{\text{arom.}}-\text{C}-\text{C}=\text{O}$), 130.84 ($\text{C}(\text{CH}_3)_2-\text{C}-\text{CH}^{\text{arom.}}-\text{C}-\text{EtHex}$), 129.81 ($\text{CH}_3-\text{C}-\text{CH}^{\text{arom.}}$), 127.53 ($\text{N}-\text{C}-\text{CH}^{\text{arom.}}-\text{C}-\text{EtHex}$), 126.66 ($\text{C}(\text{CH}_3)_2-\text{C}-\text{CH}^{\text{arom.}}-\text{C}-\text{EtHex}$), 125.14 ($\text{N}-\text{C}-\text{CH}^{\text{arom.}}-\text{CH}^{\text{arom.}}-\text{C}-\text{Tol}$), 124.42 ($\text{C}(\text{CH}_3)_2-\text{C}-\text{CH}^{\text{arom.}}-\text{C}-\text{Tol}$), 115.24 ($\text{N}-\text{C}-\text{CH}^{\text{arom.}}-\text{CH}^{\text{arom.}}-\text{C}-\text{Tol}$), 114.75 ($\text{N}-\text{C}-\text{CH}^{\text{arom.}}-\text{CH}^{\text{arom.}}-\text{C}-\text{EtHex}$), 41.63 ($\text{CH}(\text{CH}_2)_3$), 39.80 ($\text{CH}^{\text{arom.}}-\text{C}-\text{CH}_2-\text{CH}$), 36.63 ($\text{C}(\text{CH}_3)_2$), 32.67 ($\text{CH}_2-\text{CH}_2-\text{CH}_2-\text{CH}_3$), 31.57 ($\text{C}(\text{CH}_3)_2$), 31.56 ($\text{C}(\text{CH}_3)_2$), 29.23 ($\text{CH}_2-\text{CH}_2-\text{CH}_2-\text{CH}_3$), 25.86 ($\text{CH}-\text{CH}_2-\text{CH}_3$), 23.53 ($\text{CH}_2-\text{CH}_2-\text{CH}_3$), 21.15 ($\text{CH}_3-\text{C}-\text{CH}^{\text{arom.}}$), 14.33 ($\text{CH}_2-\text{CH}_2-\text{CH}_2-\text{CH}_3$), 11.01 ($\text{CH}-\text{CH}_2-\text{CH}_3$).

MALDI-MS (DCTB, DCM) (m/z): $[\text{M}-\text{CH}_3]^+$: calc. 985.6036, found 985.6100; $[\text{M}]^+$: calc. 1000.6271, found 1000.6333.

8.10. Synthesis of P(C2-MAc-BP)



The modified procedure based on literature was carried out.^[59] 1,2-Bis(4-(4,4,5,5-tetramethyl-1,3,2-dioxaborolan-2-yl)phenyl)ethane (**10d**; 133.2 mg, 0.307 mmol, 1.0 eq.), Na_2CO_3 (650 mg, 6.13 mmol, 20 eq.) and $\text{Pd}(\text{PPh}_3)_4$ (18 mg, 15 μmol , 0.05 eq.) were transferred into a pressure tube under inert

atmosphere (Ar). Degassed EtOH (0.5 mL), and degassed, deionized water (0.5 mL) were added. Bis(4-(2-(2-ethylhexyl)-9,9-dimethyl-7-bromoacridin-10(9H)-yl)phenyl)methanone (**7a**; 300.3 mg, 0.307 mmol, 1.0 eq.) was dissolved in degassed toluene (1.8 mL) and added to the mixture. The pressure tube was closed and the solution was stirred at 120 °C for 72 h. The solution was allowed to cool to r.t. and 4,4,5,5-tetramethyl-2-(p-tolyl)-2,1,3,2-dioxaborolane (**11**; 7 mg, 0.03 mmol, 0.1 eq.) and Pd(PPh₃)₄ (7 mg, 6 μmol, 0.02 eq.) were added in Ar counterflow for an endcapping reaction. The closed pressure tube was stirred at 120 °C for another 24 h. The mixture was cooled to r.t. and extracted with CHCl₃. The combined organic fractions were washed with water and HCl solution (5 mL, 2 M). The organic phase was dried over MgSO₄ and the solvent was evaporated under reduced pressure. The crude product was further purified by soxhlet extraction (1) methanol, 2) isopropanol, 3) hexane 4) CHCl₃) and a subsequent preparative SEC in CHCl₃. The desired product was obtained as a yellow solid (282 mg, 92 %).

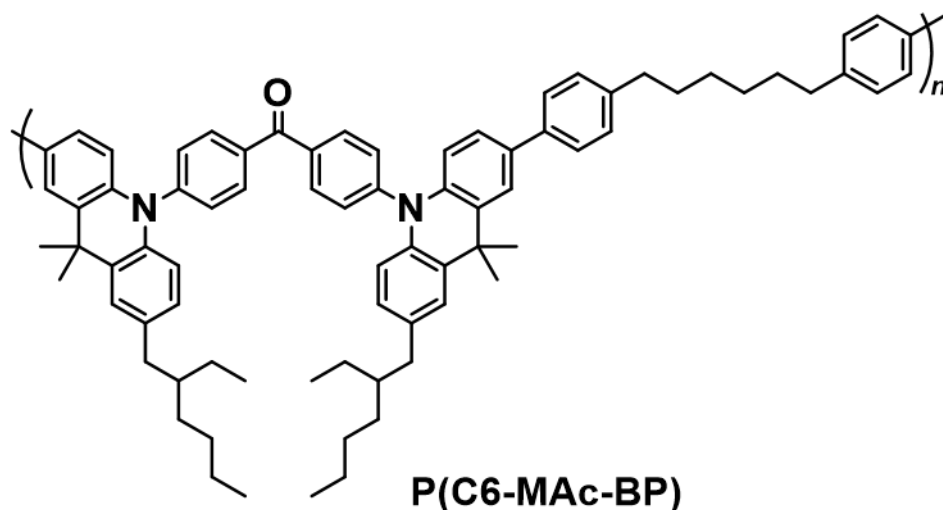
¹H NMR (700 MHz, Methylene Chloride-*d*₂) δ 8.23 – 8.09 (m, 4H, C=O-C-CH^{arom.}), 7.73 (s, 2H, C(CH₃)₂-C-CH^{arom.}-C-C-CH^{arom.}), 7.60 – 7.54 (m, 4H, C=O-C-CH^{arom.}-CH^{arom.}), 7.54 – 7.48 (m, 4H, CH₂-CH₂-C-CH^{arom.}-CH^{arom.}), 7.33 – 7.19 (m, 8H, C(CH₃)₂-C-CH^{arom.}-C-CH₂, N-C-CH^{arom.}-CH^{arom.}-C-CH^{arom.}-CH^{arom.}), 6.82 (d, *J* = 8.3 Hz, 2H, N-C-CH^{arom.}-CH^{arom.}-C-CH₂), 6.46 (d, *J* = 8.5 Hz, 2H, N-C-CH^{arom.}-CH^{arom.}-C-C-CH^{arom.}), 6.33 (d, *J* = 8.3 Hz, 2H, N-C-CH^{arom.}-CH^{arom.}-C-CH₂), 3.03 – 2.91 (m, 4H, CH₂-CH₂-C-CH^{arom.}), 2.56 – 2.43 (m, 4H, CH-CH₂-C-CH^{arom.}), 1.74 (s, 11H, C(CH₃)₂), 1.68 (s, 1H, C(CH₃)₂), 1.64 (s, 1H, C(CH₃)₂), 1.59 – 1.50 (m, 5H, CH(CH₂)₃), 1.38 – 1.17 (m, 18H, CH₂-CH₂-CH₂-CH₃, CH-CH₂-CH₃), 0.95 – 0.78 (m, 13H, CH₂-CH₃).

¹³C NMR (176 MHz, CD₂Cl₂) δ 195.16 (C=O), 146.18 (N-C-CH^{arom.}-CH^{arom.}-C-C=O), 140.70 (CH^{arom.}-C-CH₂-CH₂), 140.42 (N-C-CH^{arom.}-CH^{arom.}-C-C-CH^{arom.}), 139.13 (N-C-CH^{arom.}-CH^{arom.}-C-C-CH^{arom.}), 138.65 (N-C-CH^{arom.}-CH^{arom.}-C-CH₂), 137.15 (C-C=O), 135.01 (N-C-CH^{arom.}-CH^{arom.}-C-CH₂), 133.83 (N-C-CH^{arom.}-CH^{arom.}-C-C-CH^{arom.}), 133.04 (CH^{arom.}-C-C=O), 131.65 (C(CH₃)₂-C-CH^{arom.}-C-C-CH^{arom.}), 131.10 (N-C-CH^{arom.}-CH^{arom.}-C-C=O), 130.81 (C(CH₃)₂-C-CH^{arom.}-C-CH₂), 129.27 (CH₂-CH₂-C-CH^{arom.}), 127.53 (N-C-CH^{arom.}-CH^{arom.}-C-CH₂), 126.75 (CH₂-CH₂-C-CH^{arom.}-CH^{arom.}), 126.66

(C(CH₃)₂-C-CH^{arom.}-C-CH₂), 125.18 (N-C-CH^{arom.}-CH^{arom.}-C-C-CH^{arom.}), 124.48 (C(CH₃)₂-C-CH^{arom.}-C-C-CH^{arom.}), 115.24 (N-C-CH^{arom.}-CH^{arom.}-C-C-CH^{arom.}), 114.73 (N-C-CH^{arom.}-CH^{arom.}-C-CH₂), 41.62 (CH(CH₂)₃), 39.79 (CH^{arom.}-C-CH₂-CH), 37.77 (CH^{arom.}-C-CH₂-CH₂), 36.63 (C(CH₃)₂), 32.67 (CH₂-CH₂-CH₂-CH₃), 31.76 (C(CH₃)₂), 31.57 (C(CH₃)₂), 29.22 (CH₂-CH₂-CH₂-CH₃), 25.85 (CH-CH₂-CH₃), 23.52 (CH₂-CH₂-CH₂-CH₃), 14.34 (CH₂-CH₂-CH₂-CH₃), 11.02 (CH-CH₂-CH₃).

SEC (THF, UV detection, PS calibration): $M_n = 6.6 \text{ kg mol}^{-1}$, $D = 1.86$.

8.11. Synthesis of P(C6-MAc-BP)



The modified procedure based on literature was carried out.^[59] 1,6-Bis(4-(4,4,5,5-tetramethyl-1,3,2-dioxaborolan-2-yl)phenyl)hexane (**10e**; 177 mg, 0.36 mmol, 1.0 eq.), Na₂CO₃ (766 mg, 7.22 mmol, 20 eq.) and Pd(PPh₃)₄ (21 mg, 19 μmol, 0.05 eq.) were transferred into a pressure tube under inert atmosphere (Ar). Degassed EtOH (0.5 mL), and degassed, deionized water (0.5 mL) were added. Bis(4-(2-(2-ethylhexyl)-9,9-dimethyl-7-bromoacridin-10(9H)-yl)phenyl)methanone (**7a**; 353.5 mg, 0.361 mmol, 1.0 eq.) was dissolved in degassed toluene (1.8 mL) and added to the mixture. The pressure tube was closed and the solution was stirred at 120 °C for 72 h. The solution was allowed to cool to r.t. and 4,4,5,5-tetramethyl-2-(p-tolyl)-2,1,3,2-dioxaborolane (**11**; 8 mg, 0.04 mmol, 0.1 eq.) and Pd(PPh₃)₄ (8 mg, 7 μmol, 0.02 eq.) were added in Ar counterflow for an endcapping reaction. The closed pressure

tube was stirred at 120 °C for another 24 h. The mixture was cooled to r.t. and extracted with CHCl₃. The combined organic fractions were washed with water and HCl solution (5 mL, 2 M). The organic phase was dried over MgSO₄ and the solvent was evaporated under reduced pressure. The crude product was further purified by soxhlet extraction (1) methanol, 2) isopropanol, 3) hexane 4) CHCl₃) and a subsequent preparative SEC in CHCl₃. The desired product was obtained as a yellow solid (324 mg, 85 %).

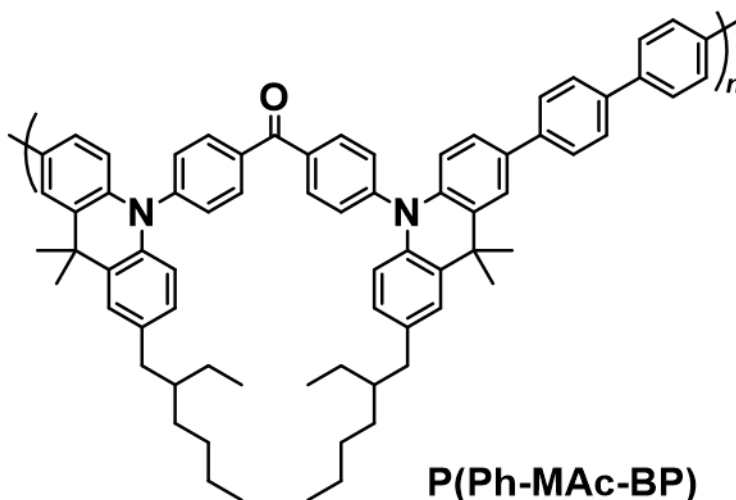
¹H NMR (700 MHz, Methylene Chloride-*d*₂) δ 8.19 – 8.12 (m, 4H, C=O-C-CH^{arom.}), 7.71 (s, 2H, C(CH₃)₂-C-CH^{arom.}-C-C-CH^{arom.}), 7.60 – 7.52 (m, 4H, C=O-C-CH^{arom.}-CH^{arom.}), 7.49 (d, *J* = 7.9 Hz, 4H, CH₂-CH₂-C-CH^{arom.}-CH^{arom.}), 7.28 (s, 2H, C(CH₃)₂-C-CH^{arom.}-C-CH₂), 7.26 – 7.16 (m, 6H, CH₂-CH₂-C-CH^{arom.}-CH^{arom.}), N-C-CH^{arom.}-CH^{arom.}-C-C-CH^{arom.}), 6.81 (d, *J* = 8.4 Hz, 2H, N-C-CH^{arom.}-CH^{arom.}-C-CH₂), 6.45 (d, *J* = 8.6 Hz, 2H, N-C-CH^{arom.}-CH^{arom.}-C-C-CH^{arom.}), 6.32 (d, *J* = 8.4 Hz, 2H, N-C-CH^{arom.}-CH^{arom.}-C-CH₂), 2.67 – 2.60 (m, 4H, CH₂-CH₂-CH₂-C-CH^{arom.}), 2.54 – 2.44 (m, 4H, CH-CH₂-C-CH^{arom.}), 1.74 (s, 12H, C(CH₃)₂), 1.70 – 1.60 (m, 6H, CH₂-CH₂-CH₂-C-CH^{arom.}), 1.58 – 1.47 (m, 6H, CH(CH₂)₃), 1.41 (s, 4H, CH₂-CH₂-CH₂-C-CH^{arom.}), 1.35 – 1.17 (m, 19H, CH₂-CH₂-CH₂-CH₃, CH-CH₂-CH₃), 0.93 – 0.80 (m, 14H, CH₂-CH₃).

¹³C NMR (176 MHz, CD₂Cl₂) δ 195.21 (C=O), 146.20 (N-C-CH^{arom.}-CH^{arom.}-C-C=O), 141.84 (CH^{arom.}-C-CH₂-CH₂), 140.35 (N-C-CH^{arom.}-CH^{arom.}-C-C-CH^{arom.}), 138.82 (N-C-CH^{arom.}-CH^{arom.}-C-C-CH^{arom.}), 138.66 (N-C-CH^{arom.}-CH^{arom.}-C-CH₂), 137.13 (C-C=O), 134.99 (N-C-CH^{arom.}-CH^{arom.}-C-CH₂), 133.99 (N-C-CH^{arom.}-CH^{arom.}-C-C-CH^{arom.}), 133.03 (CH^{arom.}-C-C=O), 131.65 (C(CH₃)₂-C-CH^{arom.}-C-C-CH^{arom.}), 131.06 (N-C-CH^{arom.}-CH^{arom.}-C-C=O), 130.84 (C(CH₃)₂-C-CH^{arom.}-C-EtHex), 129.19 (CH₂-CH₂-C-CH^{arom.}), 127.52 (N-C-CH^{arom.}-CH^{arom.}-C-CH₂), 127.23 (C(CH₃)₂-C-CH^{arom.}-C-CH₂), 126.67 (CH₂-CH₂-C-CH^{arom.}-CH^{arom.}), 125.17 (N-C-CH^{arom.}-CH^{arom.}-C-C-CH^{arom.}), 124.47 (C(CH₃)₂-C-CH^{arom.}-C-C-CH^{arom.}), 115.24 (N-C-CH^{arom.}-CH^{arom.}-C-C-CH^{arom.}), 114.75 (N-C-CH^{arom.}-CH^{arom.}-C-CH₂), 41.62 (CH(CH₂)₃), 39.80 (CH^{arom.}-C-CH₂-CH), 36.63 (C(CH₃)₂), 35.89 (CH₂-CH₂-CH₂-C-CH^{arom.}), 32.67 (CH₂-CH₂-CH₂-CH₃), 31.96 (CH₂-CH₂-CH₂-C-CH^{arom.}), 31.56 (C(CH₃)₂), 31.54 (C(CH₃)₂), 29.62

(CH₂-CH₂-CH₂-C-CH^{arom.}), 29.57 (CH₂-CH₂-CH₂-C-CH^{arom.}), 29.22 (CH₂-CH₂-CH₂-CH₃), 25.86 (CH-CH₂-CH₃), 23.52 (CH₂-CH₂-CH₂-CH₃), 14.34 (CH₂-CH₂-CH₂-CH₃), 11.02 (CH-CH₂-CH₃).

SEC (THF, UV detection, PS calibration): $M_n = 7.2 \text{ kg mol}^{-1}$, $D = 1.84$.

8.12. Synthesis of P(Ph-MAc-BP)



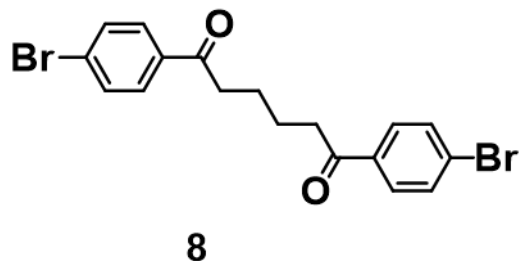
The modified procedure based on literature was carried out.^[59] 4,4'-Bis(4,4,5,5-tetramethyl-1,3,2-dioxaborolan-2-yl)-1,1'-biphenyl (**10c**; 105.2 mg, 0.259 mmol, 1.0 eq.), Na₂CO₃ (550 mg, 5.18 mmol, 20 eq.) and Pd(PPh₃)₄ (15 mg, 13 μmol, 0.05 eq.) were transferred into a pressure tube under inert atmosphere (Ar). Degassed EtOH (0.5 mL), and degassed, deionized water (0.5 mL) were added. Bis(4-(2-(2-ethylhexyl)-9,9-dimethyl-7-bromoacridin-10(9H)-yl)phenyl)methanone (**7a**; 253.5 mg, 0.259 mmol, 1.0 eq.) was dissolved in degassed toluene (1.8 mL) and added to the mixture. The pressure tube was closed and the solution was stirred at 120 °C for 72 h. The solution was allowed to cool to r.t. and 4,4,5,5-tetramethyl-2-(p-tolyl)-2,1,3,2-dioxaborolane (**11**; 6 mg, 0.03 mmol, 0.1 eq.) and Pd(PPh₃)₄ (6 mg, 5 μmol, 0.02 eq.) were added in Ar counterflow for an endcapping reaction. The closed pressure tube was stirred at 120 °C for another 24 h. The mixture was cooled to r.t. and extracted with CHCl₃. The combined organic fractions were washed with water and HCl solution (5 mL, 2 M).

The organic phase was dried over MgSO_4 and the solvent was evaporated under reduced pressure. The crude product was further purified by soxhlet extraction (1) methanol, 2) isopropanol, 3) hexane 4) CHCl_3) and a subsequent preparative SEC in CHCl_3 . The desired product was obtained as a yellow solid (156 mg, 62 %).

^1H NMR (700 MHz, Methylene Chloride- d_2) δ 8.22 – 8.18 (m, 4H, $\text{C}=\text{O}-\text{C}-\text{CH}^{\text{arom.}}$), 7.80 (s, 2H, $\text{C}(\text{CH}_3)_2-\text{C}-\text{CH}^{\text{arom.}}-\text{C}-\text{C}-\text{CH}^{\text{arom.}}$), 7.75 – 7.71 (m, 4H, $\text{C}-\text{C}-\text{CH}^{\text{arom.}}-\text{CH}^{\text{arom.}}-\text{C}-\text{C}$), 7.71 – 7.67 (m, 4H, $\text{C}-\text{C}-\text{CH}^{\text{arom.}}-\text{CH}^{\text{arom.}}-\text{C}-\text{C}$), 7.59 (d, $J = 8.0$ Hz, 4H, $\text{C}=\text{O}-\text{C}-\text{CH}^{\text{arom.}}-\text{CH}^{\text{arom.}}$), 7.35 – 7.29 (m, 4H, $\text{N}-\text{C}-\text{CH}^{\text{arom.}}-\text{CH}^{\text{arom.}}-\text{C}-\text{C}-\text{CH}^{\text{arom.}}$), $\text{C}(\text{CH}_3)_2-\text{C}-\text{CH}^{\text{arom.}}-\text{C}-\text{CH}_2$), 6.83 (d, $J = 8.5$ Hz, 2H, $\text{N}-\text{C}-\text{CH}^{\text{arom.}}-\text{CH}^{\text{arom.}}-\text{C}-\text{CH}_2$), 6.49 (d, $J = 8.6$ Hz, 2H, $\text{N}-\text{C}-\text{CH}^{\text{arom.}}-\text{CH}^{\text{arom.}}-\text{C}-\text{C}-\text{CH}^{\text{arom.}}$), 6.34 (d, $J = 8.2$ Hz, 2H, $\text{N}-\text{C}-\text{CH}^{\text{arom.}}-\text{CH}^{\text{arom.}}-\text{C}-\text{CH}_2$), 2.54 – 2.48 (m, 4H, $\text{CH}^{\text{arom.}}-\text{C}-\text{CH}_2$), 1.77 (s, 12H, $\text{C}(\text{CH}_3)_2$), 1.68 (s, 1H, $\text{C}(\text{CH}_3)_2$), 1.64 (s, 1H, $\text{C}(\text{CH}_3)_2$), 1.59 – 1.51 (m, 6H, $\text{CH}(\text{CH}_2)_3$), 1.34 – 1.21 (m, 20H, $\text{CH}_2-\text{CH}_2-\text{CH}_2-\text{CH}_3$, $\text{CH}-\text{CH}_2-\text{CH}_3$), 0.92 – 0.82 (m, 15H, CH_2-CH_3).

^{13}C NMR (176 MHz, CD_2Cl_2) δ 195.18 ($\text{C}=\text{O}$), 146.13 ($\text{N}-\text{C}-\text{CH}^{\text{arom.}}-\text{CH}^{\text{arom.}}-\text{C}-\text{C}=\text{O}$), 140.69 ($\text{N}-\text{C}-\text{CH}^{\text{arom.}}-\text{CH}^{\text{arom.}}-\text{C}-\text{C}-\text{CH}^{\text{arom.}}$), 140.39 ($\text{N}-\text{C}-\text{CH}^{\text{arom.}}-\text{CH}^{\text{arom.}}-\text{C}-\text{C}-\text{CH}^{\text{arom.}}$), 139.13 ($\text{C}-\text{C}-\text{CH}^{\text{arom.}}-\text{CH}^{\text{arom.}}-\text{C}-\text{C}$), 138.60 ($\text{N}-\text{C}-\text{CH}^{\text{arom.}}-\text{CH}^{\text{arom.}}-\text{C}-\text{CH}_2$), 137.24 ($\text{C}-\text{C}=\text{O}$), 135.09 ($\text{N}-\text{C}-\text{CH}^{\text{arom.}}-\text{CH}^{\text{arom.}}-\text{C}-\text{CH}_2$), 133.32 ($\text{C}-\text{C}-\text{CH}^{\text{arom.}}-\text{CH}^{\text{arom.}}-\text{C}-\text{C}$), 133.08 ($\text{CH}^{\text{arom.}}-\text{C}-\text{C}=\text{O}$), 131.68 ($\text{C}(\text{CH}_3)_2-\text{C}-\text{CH}^{\text{arom.}}-\text{C}-\text{C}-\text{CH}^{\text{arom.}}$), 131.21 ($\text{N}-\text{C}-\text{CH}^{\text{arom.}}-\text{CH}^{\text{arom.}}-\text{C}-\text{C}=\text{O}$), 130.75 ($\text{C}(\text{CH}_3)_2-\text{C}-\text{CH}^{\text{arom.}}-\text{C}-\text{CH}_2$), 127.53 ($\text{N}-\text{C}-\text{CH}^{\text{arom.}}-\text{CH}^{\text{arom.}}-\text{C}-\text{CH}_2$), 127.31 ($\text{C}-\text{C}-\text{CH}^{\text{arom.}}-\text{CH}^{\text{arom.}}-\text{C}-\text{C}$), 127.20 ($\text{C}-\text{C}-\text{CH}^{\text{arom.}}-\text{CH}^{\text{arom.}}-\text{C}-\text{C}$), 126.69 ($\text{C}(\text{CH}_3)_2-\text{C}-\text{CH}^{\text{arom.}}-\text{C}-\text{CH}_2$), 125.26 ($\text{N}-\text{C}-\text{CH}^{\text{arom.}}-\text{CH}^{\text{arom.}}-\text{C}-\text{C}-\text{CH}^{\text{arom.}}$), 124.55 ($\text{C}(\text{CH}_3)_2-\text{C}-\text{CH}^{\text{arom.}}-\text{C}-\text{C}-\text{CH}^{\text{arom.}}$), 115.27 ($\text{N}-\text{C}-\text{CH}^{\text{arom.}}-\text{CH}^{\text{arom.}}-\text{C}-\text{C}-\text{CH}^{\text{arom.}}$), 114.73 ($\text{N}-\text{C}-\text{CH}^{\text{arom.}}-\text{CH}^{\text{arom.}}-\text{C}-\text{CH}_2$), 41.63 ($\text{CH}(\text{CH}_2)_3$), 39.80 ($\text{CH}^{\text{arom.}}-\text{C}-\text{CH}_2-\text{CH}$), 36.65 ($\text{C}(\text{CH}_3)_2$), 32.68 ($\text{CH}_2-\text{CH}_2-\text{CH}_2-\text{CH}_3$), 31.64 ($\text{C}(\text{CH}_3)_2$), 29.23 ($\text{CH}_2-\text{CH}_2-\text{CH}_2-\text{CH}_3$), 25.86 ($\text{CH}-\text{CH}_2-\text{CH}_3$), 23.53 ($\text{CH}_2-\text{CH}_2-\text{CH}_2-\text{CH}_3$), 14.34 ($\text{CH}_2-\text{CH}_2-\text{CH}_2-\text{CH}_3$), 11.02 ($\text{CH}-\text{CH}_2-\text{CH}_3$).

SEC (THF, UV detection, PS calibration): $M_n = 7.3 \text{ kg mol}^{-1}$, $D = 1.83$.

8.13. Synthesis of 1,6-Bis(4-bromophenyl)hexane-1,6-dione (8)

The modified procedure based on literature was carried out.^[155] Aluminum chloride (5.90 g, 44.25 mmol, 2.1 eq.) was suspended in bromobenzene (25 mL, 238.8 mmol, 11.6 eq.) under inert gas atmosphere (Ar). Adipoyl chloride (3 mL, 20.57 mmol, 1.0 eq.) was dissolved in bromobenzene (5 mL, 47.76 mmol, 2.32 eq.) and slowly added to the solution. The solution was stirred at 50 °C for 1.5 h. The reaction was slowly quenched with a mixture of 50 g of ice and 50 mL conc. HCl. The precipitated solid separated from the solution by filtration and the solid was further washed with cold bromobenzene. The solid was dissolved in 20 mL CHCl₃, washed with water and the organic phase was dried over MgSO₄. After evaporation of the solvent the remaining solid was washed with cold EtOH and the product was obtained as a light yellow solid (1.48 g, 3.49 mmol, 17 %). The mixture was used in the following reaction without further purification.

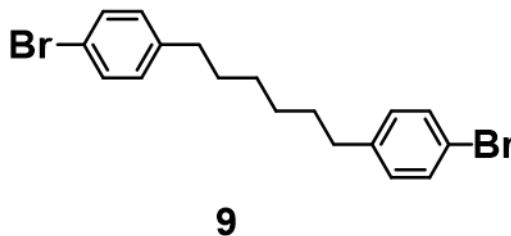
Chemical formula: C₁₈H₁₆Br₂O₂

¹H NMR (300 MHz, Chloroform-*d*) δ 7.81 (d, *J* = 8.3 Hz, 4H, CH^{arom.}-C-C=O), 7.60 (d, *J* = 8.2 Hz, 4H, Br-C-CH^{arom.}), 3.01 (q, *J* = 5.9 Hz, 4H, CH₂-C=O), 1.82 (h, *J* = 3.2 Hz, 4H, CH₂-CH₂-C=O).

¹³C NMR (75 MHz, CDCl₃) δ 198.96 (C=O), 135.76 (C-C=O), 132.06 (Br-C-CH^{arom.}), 129.70 (CH^{arom.}-C-C=O), 128.32 (C-Br), 38.48 (CH₂-C=O), 23.83 (CH₂-CH₂-C=O).

The characterization is in agreement with literature.^[156]

8.14. Synthesis of 1,6-Bis(4-bromophenyl)hexane (9)



The modified procedure based on literature was carried out.^[155] 1,6-Bis(4-bromophenyl)hexane-1,6-dione (**8**; 1.22 g, 2.88 mmol, 1.0 eq.) was dissolved in DCM (10 mL) under inert gas atmosphere (Ar). TFA (10 mL) and triethylsilane (4.5 mL, 28.20 mmol, 9.8 eq.) were added and the solution was stirred at r.t. for 17 h (overnight). The solution cooled to -20 °C with a salt-ice bath for 20 min and neutralized by slowly adding conc. NaOH. The mixture was extracted with DCM and the combined organic phase was washed with water (2x) and brine (1x). After drying the organic phase over MgSO₄, the solvent was evaporated under reduced pressure. The crude product was further purified by flash chromatography on silica gel (Hex) and the desired product was obtained as a colorless solid (1.02 g, 2.57 mmol, 89 %).

Chemical formula: C₁₈H₂₀Br₂

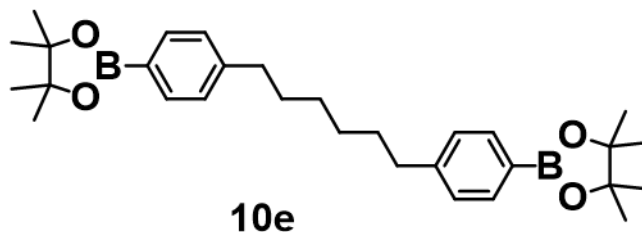
R_f = 0.51 (SiO₂, Hex).

¹H NMR (300 MHz, Chloroform-*d*) δ 7.38 (d, *J* = 8.0 Hz, 4H, Br-C-CH^{arom.}), 7.03 (d, *J* = 8.0 Hz, 4H, CH^{arom.}-C-CH₂), 2.54 (t, *J* = 7.7 Hz, 4H, CH^{arom.}-C-CH₂), 1.69 – 1.48 (m, 4H C-CH₂-CH₂), 1.43 – 1.22 (m, 4H, C-CH₂-CH₂-CH₂).

¹³C NMR (75 MHz, CDCl₃) δ 141.78 (CH^{arom.}-C-CH₂), 131.41 (Br-C-CH^{arom.}), 130.30 (CH^{arom.}-C-CH₂), 119.44 (C-Br), 35.42 (CH^{arom.}-C-CH₂), 31.31 (C-CH₂-CH₂), 29.07 (C-CH₂-CH₂-CH₂).

The characterization is in agreement with literature.^[156]

8.15. Synthesis of 4,4,5,5-Tetramethyl-2-(4-(6-(4-(4,4,5-trimethyl-1,3,2-dioxaborolan-2-yl)phenyl)hexyl)phenyl)-1,3,2-dioxaborolane (10e)



The modified procedure based on literature was carried out.^[155] 1,6-Bis(4-bromophenyl)hexane (**9**; 0.70 g, 1.77 mmol, 1 eq.) was dissolved in dry THF (30 mL) and cooled to -78 °C with an dry ice/acetone cooling bath under inert gas atmosphere (Ar). *n*-BuLi (2.5 mL, 1.6 M in hexane, 3.89 mmol, 2.2 eq.) was added dropwise and the solution was stirred at -78 °C for 1 h. After an addition of 2-isopropoxy-4,4,5,5-tetramethyl-1,3,2-dioxaborolane (1.5 mL, 7.35 mmol, 4.1 eq.) the mixture was stirred at -78 °C for another hour and then stirred at r.t. overnight (16 h). The reaction was quenched with deionized water (20 mL) and the solution extracted with DCM. The combined organic fractions were washed with water and brine, dried over MgSO₄ and the solvent was evaporated under reduced pressure. The crude product was further purified by size exclusion chromatography (in CHCl₃) and the product was obtained as colorless crystals (704.4 mg, 1.44 mmol, 81 %)

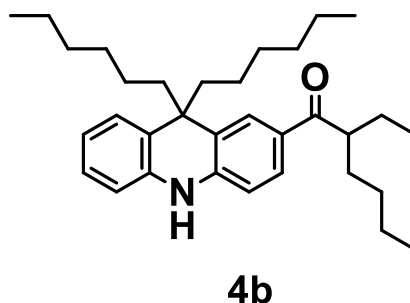
Chemical formula: C₃₀H₄₄B₂O₄

¹H NMR (300 MHz, Chloroform-*d*) δ 7.72 (d, *J* = 7.6 Hz, 4H, B-C-CH^{arom.}), 7.18 (d, *J* = 7.6 Hz, 4H, CH₂-C-CH^{arom.}), 2.60 (t, *J* = 7.6 Hz, 4H, CH₂-C-CH^{arom.}), 1.67 – 1.51 (m, 6H, CH^{arom.}-C-CH₂-CH₂), 1.34 (br s, 28H, CH₃, CH^{arom.}-C-CH₂-CH₂-CH₂).

¹³C NMR (75 MHz, CDCl₃) δ 146.44 (CH^{arom.}-C-CH₂), 134.96 (B-C-CH^{arom.}), 128.04 (CH^{arom.}-C-CH₂), 83.75 (C-O), 36.27 (CH^{arom.}-C-CH₂-CH₂-CH₂), 31.35 (CH^{arom.}-C-CH₂-CH₂-CH₂), 29.24 (CH^{arom.}-C-CH₂-CH₂-CH₂), 25.00 (CH₃). C-B signal was not observed.

The characterization is in agreement with literature.^[156]

8.16. Synthesis of 1-(9,9-Dihexyl-9,10-dihydroacridin-2-yl)-2-ethylhexan-1-one (4b)



The modified procedure based on literature was carried out.^[59] Aluminum chloride (232.1 mg, 1.74 mmol, 1.2 eq.) was dispersed in dry DCM (30 mL) in inert gas atmosphere. The dispersion was cooled to 0 °C with an ice bath and 9,9-dihexyl-9,10-dihydroacridine (**3b**; 508.9 mg, 1.46 mmol, 1.0 eq.) was added under an argon counterflow. 2-Ethylhexanoyl chloride (270 μ L, 1.57 mmol, 1.1 eq.) was dissolved in dry DCM (2.5 mL). The solution was stirred at r.t. for 15 h. The solution was quenched with ice and extracted with DCM (4 \times 50 mL). The combined organic phases were dried over MgSO₄ and concentrated *in vacuo*. The crude product was purified by flash chromatography on silica gel (Hex:EtOAc = 20:1) and the desired product was obtained as a yellow oil (393.3 mg, 1.43 mmol, 58 %). Up-scaling led to a decrease in yield and therefore bigger amounts of product were synthesized by performing several reaction under the same conditions in parallel.

Chemical formula: C₃₃H₄₉NO

R_f = 0.13 (SiO₂, Hex:EtOAc = 20:1).

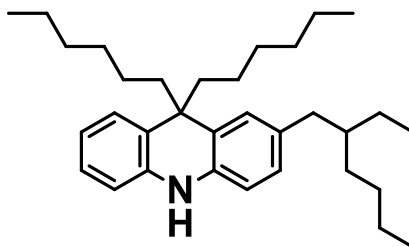
¹H NMR (300 MHz, DMSO-*d*₆) δ 9.24 (s, 1H, NH), 7.82 (s, 1H, C-CH^{arom.}-C-C=O), 7.67 (d, *J* = 8.5 Hz, 1H, CH^{arom.}-CH^{arom.}-C-C=O), 7.26 (d, *J* = 7.8 Hz, 1H, CH^{arom.}-CH^{arom.}-C-C(CH₂)₂), 7.04 (t, *J* = 7.5 Hz, 1H, NH-C-CH^{arom.}-CH^{arom.}-CH^{arom.}), 6.83 (t, *J* = 7.5 Hz, 1H, NH-C-CH^{arom.}-CH^{arom.}-CH^{arom.}), 6.73 (d, *J* = 8.3 Hz, 2H, CH^{arom.}-C-N-C-CH^{arom.}), 3.46 – 3.35 (m, 1H, (CH₂)₂-CH-C=O), 1.87 (dd, *J* = 11.1, 5.4 Hz, 4H, C(CH₂)), 1.71 – 1.52 (m, 2H, CH-CH₂-CH₃), 1.52 – 1.33 (m, 2H, CH-CH₂-CH₂), 1.31 – 1.12 (m, 4H, CH-CH₂-CH₂-CH₂-CH₃), 1.13 – 0.94 (m, 12H, CH₂-CH₂-CH₂-CH₂-CH₃), 0.91 – 0.82 (m,

4H, $\text{CH}_2\text{-CH}_2\text{-CH}_2\text{-CH}_2\text{-CH}_3$), 0.78 (t, $J = 7.0$ Hz, 6H, $\text{CH}_3\text{-CH}_2\text{-CH-CH}_2\text{-CH}_2\text{-CH}_2\text{-CH}_3$), 0.70 (t, 6H, $\text{CH}_2\text{-CH}_2\text{-CH}_2\text{-CH}_2\text{-CH}_3$).

^{13}C NMR (75 MHz, DMSO) δ 201.54 (C=O), 143.83 (NH-C- $\text{CH}^{\text{arom.}}$ - $\text{CH}^{\text{arom.}}$ -C), 138.38 (NH-C- $\text{CH}^{\text{arom.}}$ - $\text{CH}^{\text{arom.}}$ - $\text{CH}^{\text{arom.}}$), 128.91 (C-C=O), 127.56 (C- $\text{CH}^{\text{arom.}}$ -C-C=O), 127.44 ($\text{CH}^{\text{arom.}}$ - $\text{CH}^{\text{arom.}}$ -C-C=O), 126.77 (NH-C- $\text{CH}^{\text{arom.}}$ - $\text{CH}^{\text{arom.}}$ - $\text{CH}^{\text{arom.}}$), 126.26 ($\text{CH}^{\text{arom.}}$ - $\text{CH}^{\text{arom.}}$ -C-C(CH₂)₂), 124.57 ($\text{CH}^{\text{arom.}}$ - $\text{CH}^{\text{arom.}}$ -C-C(CH₂)₂), 123.52 (CH₂-C- $\text{CH}^{\text{arom.}}$ -C-C(CH₂)₂), 120.67 ($\text{CH}^{\text{arom.}}$ - $\text{CH}^{\text{arom.}}$ -C-C(CH₂)₂), 113.63 (NH-C- $\text{CH}^{\text{arom.}}$ - $\text{CH}^{\text{arom.}}$ -C), 112.88 (NH-C- $\text{CH}^{\text{arom.}}$ - $\text{CH}^{\text{arom.}}$ - $\text{CH}^{\text{arom.}}$), 45.49 (C(CH₂)₂), 43.95 (C(CH₂)₂), 32.06 (CH-CH₂-CH₃), 30.93/ 30.87 (CH₂-CH₂-CH₂-CH₂-CH₃), 29.23 (CH-CH₂-CH₂-CH₂-CH₃), 28.90/ 28.80 (CH₂-CH₂-CH₂-CH₂-CH₃), 25.54 (CH-CH₂-CH₂-CH₂-CH₃), 24.65/ 24.57 (CH₂-CH₂-CH₂-CH₂-CH₃), 22.35 (CH-CH₂-CH₂-CH₂-CH₃), 21.88/ 21.82 (CH₂-CH₂-CH₂-CH₂-CH₃), 13.79 (CH-CH₂-CH₂-CH₂-CH₃), 13.74 (CH₂-CH₂-CH₂-CH₂-CH₃), 11.81 (CH-CH₂-CH₃).

MALDI-MS (DCTB, DCM) (m/z): [M-hexyl]⁺: calc. 390.2797, found 390.2639; [M-H]⁺: calc. 474.3736, found 474.3572; [M]⁺: calc. 475.3814, found 475.3598; [M+H]⁺: calc. 476.3892, found 476.3732.

8.17. Synthesis of -(2-Ethylhexyl)-9,9-dihexyl-9,10-dihydroacridine (5b)



5b

The modified procedure based on literature was carried out.^[59] Dry THF (50 mL) was cooled to 0 °C with an ice bath and aluminum chloride (685.0 mg, 5.14 mmol, 2.0 eq.). Lithium aluminum hydride (1 mol/L in THF, 10.5 mL, 10.5 mmol, 4.0 eq.) was added dropwise. 1-(9,9-dihexyl-9,10-

dihydroacridin-2-yl)-2-ethylhexan-1-one (**4b**; 1.22 g, 2.57 mmol, 1.0 eq.) was dissolved in 5 mL dry THF and added dropwise. The solution was stirred at r.t. for 20 h. The solution was cooled with an ice bath and EtOAc (20 mL) and 5 wt% HCl (2 mL) was added. The precipitated solid was filtered off and the solution was concentrated *in vacuo*. The crude product was further purified by flash chromatography on silica gel (Hex:EtOAc = 50:1) and the desired product was obtained as a light yellow oil (1.13, 2.44 mmol, 95 %).

Chemical formula: C₃₃H₅₁N

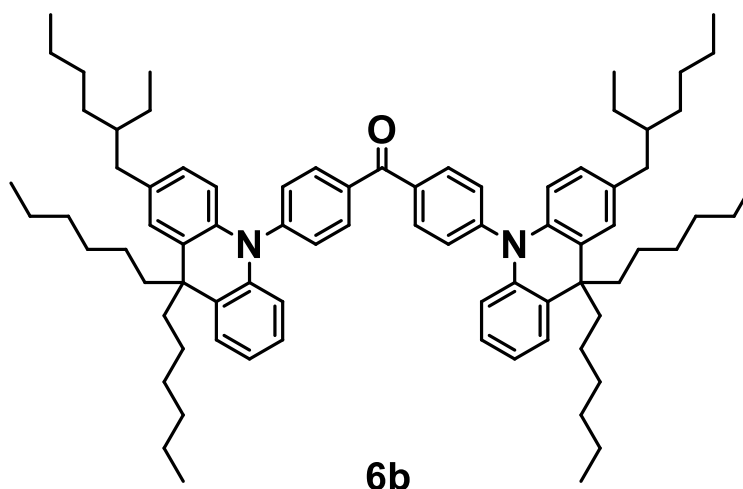
R_f = 0.44 (SiO₂, Hex:EtOAc = 50:1).

¹H NMR (300 MHz, Acetone-*d*₆) δ 7.74 (s, 1H, NH), 7.26 (d, *J* = 7.8 Hz, 1H, CH^{arom.}-CH^{arom.}-C-C(CH₂)₂), 7.07 (s, 1H, C-CH^{arom.}-C-C(CH₂)₂), 6.98 (t, *J* = 7.6 Hz, 1H, CH^{arom.}-CH^{arom.}-CH^{arom.}-C-NH), 6.82 (d, *J* = 8.1 Hz, 1H, NH-C-CH^{arom.}-CH^{arom.}-C), 6.75 (t, *J* = 7.5 Hz, 1H, CH^{arom.}-CH^{arom.}-C-C(CH₂)₂), 6.67 (d, *J* = 8.0 Hz, 1H, CH^{arom.}-CH^{arom.}-CH^{arom.}-C-NH), 6.62 (d, *J* = 8.0 Hz, 1H, C-CH^{arom.}-CH^{arom.}-C-NH), 2.60 – 2.35 (m, 2H, CH^{arom.}-C-CH₂), 1.98 – 1.84 (m, 4H, C(CH₂)₂), 1.62 – 1.44 (m, 1H, CH(CH₂)₃), 1.38 – 1.22 (m, 8H, CH-CH₂-CH₂-CH₂-CH₃, CH-CH₂-CH₃), 1.21 – 1.06 (m, 12H, CH₂-CH₂-CH₂-CH₂-CH₃), 1.06 – 0.95 (m, 4H, C-C-CH₂-CH₂), 0.89 (t, *J* = 7.5 Hz, 6H, CH-CH₂-CH₂-CH₂-CH₃, CH-CH₂-CH₃), 0.78 (t, *J* = 6.7 Hz, 6H, CH₂-CH₂-CH₂-CH₂-CH₃).

¹³C NMR (75 MHz, Acetone) δ 141.38 (CH^{arom.}-CH^{arom.}-CH^{arom.}-C-NH), 139.01 (C-CH^{arom.}-CH^{arom.}-C-NH), 133.23 (C-CH^{arom.}-CH^{arom.}-C-NH), 128.37 (C-CH^{arom.}-CH^{arom.}-C-NH), 128.08 (C-CH^{arom.}-C-C-NH), 127.52 (CH^{arom.}-CH^{arom.}-CH^{arom.}-C-NH), 127.40 (CH^{arom.}-CH^{arom.}-C-C(CH₂)₂), 125.59 (CH^{arom.}-CH^{arom.}-C-C(CH₂)₂), 125.21 (C-CH^{arom.}-C-C(CH₂)₂), 120.27 (CH^{arom.}-CH^{arom.}-C-C(CH₂)₂), 114.06 (CH^{arom.}-CH^{arom.}-CH^{arom.}-C-NH), 114.02 (C-CH^{arom.}-CH^{arom.}-C-NH), 46.92 (C(CH₂)₂), 46.89 (C(CH₂)₂), 45.29 (C(CH₂)₂), 42.51 (CH(CH₂)₃), 40.55 (CH^{arom.}-C-CH₂), 33.30 (CH-CH₂-CH₂-CH₂-CH₃), 32.70 (CH₂-CH₂-CH₂-CH₂-CH₃), 30.73 (CH₂-CH₂-CH₂-CH₂-CH₃), 29.92 (CH-CH₂-CH₂-CH₂-CH₃), 26.44 (CH-CH₂-CH₃), 26.12 (CH₂-CH₂-CH₂-CH₂-CH₃), 24.01 (CH-CH₂-CH₂-CH₂-CH₃), 23.47 (CH₂-CH₂-CH₂-CH₂-CH₃), 14.64 (CH-CH₂-CH₂-CH₂-CH₃), 14.48 (CH₂-CH₂-CH₂-CH₂-CH₃), 11.46 (CH-CH₂-CH₃).

MALDI-MS (DCTB, DCM) (m/z): [M-hexyl]⁺: calc. 376.3004, found 376.2851; [M-H]⁺: calc. 460.3943, found 460.3791; [M]⁺: calc. 461.4022, found 461.3825; [M+H]⁺: calc. 462.4100, found 462.3947.

8.18. Synthesis of Bis(4-(2-(2-ethylhexyl)-9,9-dihexylacridin-10(9H)-yl)phenyl)methanone (**6b**)



The modified procedure based on literature was carried out.^[59] Bis(4-bromophenyl)methanone (350.5 mg, 1.03 mmol, 1.0 eq.), sodium *tert*-butoxide (396.2 mg, 4.12 mmol, 4.0 eq.) and bis(*tri-tert*-butylphosphine) palladium (0) (52.0 mg, 101.8 μ mol, 0.10 eq.) were transferred into a pressure tube under inert gas atmosphere. 2-(2-ethylhexyl)-9,9-dihexyl-9,10-dihydroacridine (**5b**; 1.05 g, 2.27 mmol, 2.2 eq.) was dissolved in dry toluene (7 mL) and added. The solution was stirred at 120 °C for 21 h. The solution was allowed to cool to r.t., quenched with deionized water (5 mL), extracted with hexane (3 \times 5 mL) and dried over MgSO₄. The solution was concentrated *in vacuo* and the crude product was further purified by flash chromatography on silica gel (Hex:EtOAc = 100:1) as a yellow viscose oil (1.02 g, 921.5 μ mol, 89 %).

Chemical formula: C₇₉H₁₀₈N₂O

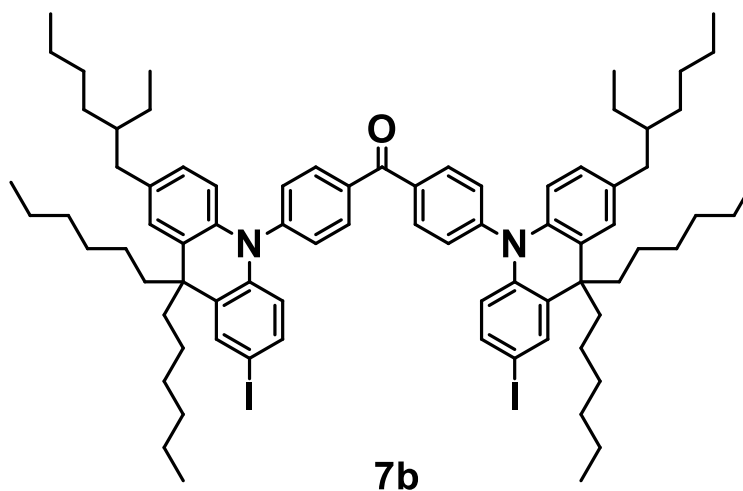
R_f = 0.15 (SiO₂, Hex:EtOAc = 100:1).

^1H NMR (300 MHz, Methylene Chloride- d_2) δ 8.14 (d, $J = 8.1$ Hz, 4H, $\text{CH}^{\text{arom.}}-\text{C}-\text{C}=\text{O}$), 7.45 (d, $J = 8.0$ Hz, 4H, $\text{CH}^{\text{arom.}}-\text{CH}^{\text{arom.}}-\text{C}-\text{C}=\text{O}$), 7.34 (d, $J = 7.5$ Hz, 2H, $\text{CH}^{\text{arom.}}-\text{CH}^{\text{arom.}}-\text{CH}^{\text{arom.}}-\text{C}-\text{C}(\text{CH}_2)_2$), 7.11 (s, 2H, $\text{C}-\text{CH}^{\text{arom.}}-\text{C}-\text{C}(\text{CH}_2)_2$), 6.99 – 6.81 (m, 4H, $\text{CH}^{\text{arom.}}-\text{CH}^{\text{arom.}}-\text{CH}^{\text{arom.}}-\text{C}-\text{C}(\text{CH}_2)_2$), 6.72 (d, $J = 8.4$ Hz, 2H, $\text{CH}^{\text{arom.}}-\text{C}-\text{CH}^{\text{arom.}}-\text{C}-\text{C}(\text{CH}_2)_2$), 6.19 (d, $J = 8.0$ Hz, 2H, $\text{N}-\text{C}-\text{CH}^{\text{arom.}}-\text{CH}^{\text{arom.}}-\text{CH}^{\text{arom.}}$), 6.11 (d, $J = 8.3$ Hz, 2H, $\text{N}-\text{C}-\text{CH}^{\text{arom.}}-\text{CH}^{\text{arom.}}-\text{C}-\text{CH}_2$), 2.46 (d, $J = 7.0$ Hz, 4H, $\text{CH}^{\text{arom.}}-\text{C}-\text{CH}_2$), 2.04 – 1.88 (m, 8H, $\text{C}(\text{CH}_2)_2$), 1.51 – 1.43 (m, 2H, $\text{CH}(\text{CH}_2)_3$), 1.35 – 1.22 (m, 16H, $\text{CH}-\text{CH}_2-\text{CH}_2-\text{CH}_2-\text{CH}_3$, $\text{CH}-\text{CH}_2-\text{CH}_3$), 1.17 (d, $J = 5.9$ Hz, 24H, $\text{CH}_2-\text{CH}_2-\text{CH}_2-\text{CH}_2-\text{CH}_3$), 1.11 – 0.99 (m, 8H, $\text{C}-\text{C}-\text{CH}_2$), 0.88 (t, $J = 7.2$ Hz, 12H, $\text{CH}-\text{CH}_2-\text{CH}_2-\text{CH}_2-\text{CH}_3$, $\text{CH}-\text{CH}_2-\text{CH}_3$), 0.80 (t, 12H, $\text{CH}_2-\text{CH}_2-\text{CH}_2-\text{CH}_2-\text{CH}_3$).

^{13}C NMR (75 MHz, CD_2Cl_2) δ 195.29 ($\text{C}=\text{O}$), 146.68 ($\text{N}-\text{C}-\text{CH}^{\text{arom.}}-\text{CH}^{\text{arom.}}-\text{C}-\text{C}=\text{O}$), 142.37 ($\text{N}-\text{C}-\text{CH}^{\text{arom.}}-\text{CH}^{\text{arom.}}-\text{CH}^{\text{arom.}}$), 140.13 ($\text{N}-\text{C}-\text{CH}^{\text{arom.}}-\text{CH}^{\text{arom.}}-\text{C}-\text{CH}_2$), 137.26 ($\text{C}-\text{C}=\text{O}$), 134.10 ($\text{CH}^{\text{arom.}}-\text{C}-\text{CH}_2$), 133.10 ($\text{CH}^{\text{arom.}}-\text{C}-\text{C}=\text{O}$), 132.04 ($\text{CH}^{\text{arom.}}-\text{CH}^{\text{arom.}}-\text{C}-\text{C}=\text{O}$), 127.63 ($\text{C}-\text{CH}^{\text{arom.}}-\text{C}-\text{C}(\text{CH}_2)_2$), 127.37 ($\text{N}-\text{C}-\text{CH}^{\text{arom.}}-\text{CH}^{\text{arom.}}-\text{C}-\text{CH}_2$), 126.95 ($\text{CH}^{\text{arom.}}-\text{CH}^{\text{arom.}}-\text{CH}^{\text{arom.}}-\text{C}-\text{C}(\text{CH}_2)_2$), 126.65 ($\text{CH}^{\text{arom.}}-\text{CH}^{\text{arom.}}-\text{CH}^{\text{arom.}}-\text{C}-\text{C}(\text{CH}_2)_2$), 126.54 ($\text{CH}^{\text{arom.}}-\text{CH}^{\text{arom.}}-\text{CH}^{\text{arom.}}-\text{C}-\text{C}(\text{CH}_2)_2$), 126.11 ($\text{C}-\text{CH}^{\text{arom.}}-\text{C}-\text{C}(\text{CH}_2)_2$), 120.62 ($\text{CH}^{\text{arom.}}-\text{CH}^{\text{arom.}}-\text{CH}^{\text{arom.}}-\text{C}-\text{C}(\text{CH}_2)_2$), 114.13 ($\text{CH}^{\text{arom.}}-\text{C}-\text{N}-\text{C}-\text{CH}^{\text{arom.}}$), 46.46 ($\text{C}(\text{CH}_2)_2$), 44.47 ($\text{C}(\text{CH}_2)_2$), 41.72 ($\text{C}(\text{CH}_2)_3$), 39.72 ($\text{CH}^{\text{arom.}}-\text{C}-\text{CH}_2$), 32.72 ($\text{CH}-\text{CH}_2-\text{CH}_2-\text{CH}_2-\text{CH}_3$), 32.16 ($\text{CH}_2-\text{CH}_2-\text{CH}_2-\text{CH}_2-\text{CH}_3$), 30.22 ($\text{CH}_2-\text{CH}_2-\text{CH}_2-\text{CH}_2-\text{CH}_3$), 29.35 ($\text{CH}-\text{CH}_2-\text{CH}_2-\text{CH}_2-\text{CH}_3$), 25.77 ($\text{CH}-\text{CH}_2-\text{CH}_3$), 25.48 ($\text{CH}_2-\text{CH}_2-\text{CH}_2-\text{CH}_2-\text{CH}_3$), 23.53 ($\text{CH}-\text{CH}_2-\text{CH}_2-\text{CH}_2-\text{CH}_3$), 23.07 ($\text{CH}_2-\text{CH}_2-\text{CH}_2-\text{CH}_2-\text{CH}_3$), 14.35 ($\text{CH}-\text{CH}_2-\text{CH}_2-\text{CH}_2-\text{CH}_3$), 14.22 ($\text{CH}_2-\text{CH}_2-\text{CH}_2-\text{CH}_2-\text{CH}_3$), 11.00 ($\text{CH}-\text{CH}_2-\text{CH}_3$).

MALDI-MS (DCTB, DCM) (m/z): [M-hexyl] $^+$: calc. 1015.7444, found 1015.7497.

8.19. Synthesis of Bis(4-(2-(2-ethylhexyl)-9,9-dihexyl-7-iodoacridin-10(9H)-yl)phenyl)methanone (7b)



The modified procedure based on literature was carried out.^[59] Bis(4-(2-(2-ethylhexyl)-9,9-dihexylacridin-10(9H)-yl)phenyl)methanone (**6b**; 1.02 g, 921.3 μmol , 1.0 eq.) was dissolved in CHCl_3 under inert gas atmosphere. *N*-Iodosuccinimide (1.09 g, 4.84 mmol, 5.25 eq.) was dissolved in CHCl_3 under inert gas atmosphere and added to the solution. The solution was stirred at 50 $^\circ\text{C}$ in the dark for 42 h. The mixture was allowed to r.t., quenched with saturated $\text{Na}_2\text{S}_2\text{O}_3$ solution and extracted with DCM ($3 \times 100 \text{ mL}$). The combined organic phases were dried over MgSO_4 and concentrated *in vacuo*. The crude product was further purified by flash chromatography on silica gel (Hex:EtOAc = 100:1) and a following size exclusion chromatography (in CHCl_3). The pure product was obtained as a yellow viscose oil (905.2 mg, 669.0 μmol , 73 %).

Chemical formula: $\text{C}_{79}\text{H}_{106}\text{I}_2\text{N}_2\text{O}$

$R_f = 0.21$ (SiO_2 , Hex:EtOAc = 100:1).

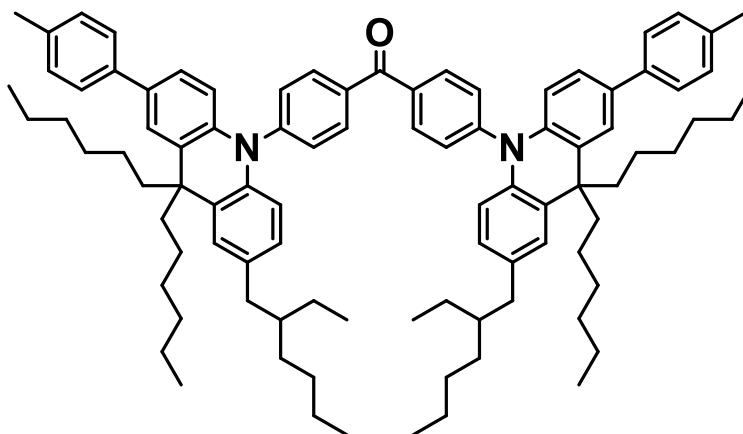
$^1\text{H NMR}$ (300 MHz, Methylene Chloride- d_2) δ 8.13 (d, $J = 7.9 \text{ Hz}$, 4H, $\text{CH}^{\text{arom.}}\text{-C-C=O}$), 7.58 (s, 2H, $\text{C-CH}^{\text{arom.}}\text{-C-I}$), 7.43 (d, $J = 7.8 \text{ Hz}$, 4H, $\text{CH}^{\text{arom.}}\text{-CH}^{\text{arom.}}\text{-C-C=O}$), 7.19 (d, $J = 8.8 \text{ Hz}$, 2H, $\text{I-C-CH}^{\text{arom.}}\text{-CH}^{\text{arom.}}$), 7.09 (s, 2H, $\text{C-CH}^{\text{arom.}}\text{-C-C(CH}_2)_2$), 6.73 (d, $J = 8.4 \text{ Hz}$, 2H, $\text{CH}^{\text{arom.}}\text{-C-CH}^{\text{arom.}}\text{-C-C(CH}_2)_2$), 6.10 (d, $J = 8.3 \text{ Hz}$, 2H, $\text{N-C-CH}^{\text{arom.}}\text{-CH}^{\text{arom.}}\text{-C-CH}_2$), 5.96 (d, $J = 8.7 \text{ Hz}$, 2H, $\text{N-C-CH}^{\text{arom.}}\text{-CH}^{\text{arom.}}\text{-C-}$

I), 2.46 (d, $J = 7.0$ Hz, 4H, $\text{CH}^{\text{arom.}}\text{-C-CH}_2$), 2.09 – 1.77 (m, 8H, $\text{C}(\text{CH}_2)_2$), 1.64 – 1.41 (m, 2H, $\text{CH}(\text{CH}_2)_3$), 1.36 – 1.21 (m, 16H, $\text{CH-CH}_2\text{-CH}_2\text{-CH}_2\text{-CH}_3$, $\text{CH-CH}_2\text{-CH}_3$), 1.22 – 1.13 (m, 24H, $\text{CH}_2\text{-CH}_2\text{-CH}_2\text{-CH}_3$), 1.12 – 0.99 (m, 4H, C-C-CH_2), 0.88 (t, $J = 7.2$ Hz, 12H, $\text{CH-CH}_2\text{-CH}_2\text{-CH}_2\text{-CH}_3$, $\text{CH-CH}_2\text{-CH}_3$), 0.82 (t, $J = 6.2$ Hz, 13H, $\text{CH}_2\text{-CH}_2\text{-CH}_2\text{-CH}_2\text{-CH}_3$).

^{13}C NMR (75 MHz, CD_2Cl_2) δ 195.19 (C=O), 146.04 ($\text{N-C-CH}^{\text{arom.}}\text{-CH}^{\text{arom.}}\text{-C-C=O}$), 142.20 ($\text{CH}^{\text{arom.}}\text{-CH}^{\text{arom.}}\text{-C-I}$), 139.60 ($\text{N-C-CH}^{\text{arom.}}\text{-CH}^{\text{arom.}}\text{-C-CH}_2$), 137.44 (C-C=O), 135.59 ($(\text{CH}_2)_2\text{-C-C-CH}^{\text{arom.}}\text{-C-I}$), 135.33 ($\text{N-CH}^{\text{arom.}}\text{-CH}^{\text{arom.}}\text{-C-I}$), 134.60 ($\text{CH}^{\text{arom.}}\text{-C-CH}_2$), 133.21 ($\text{CH}^{\text{arom.}}\text{-C-C=O}$), 131.84 ($\text{CH}^{\text{arom.}}\text{-CH}^{\text{arom.}}\text{-C-C=O}$), 129.56 ($\text{I-C-CH}^{\text{arom.}}\text{-C-C}(\text{CH}_2)_2$), 127.58 ($\text{CH}_2\text{-C-CH}^{\text{arom.}}\text{-C-C}(\text{CH}_2)_2$, $\text{N-C-CH}^{\text{arom.}}\text{-CH}^{\text{arom.}}\text{-C-CH}_2$), 125.85 ($\text{CH}_2\text{-C-CH}^{\text{arom.}}\text{-C-C}(\text{CH}_2)_2$), 116.40 ($\text{N-C-CH}^{\text{arom.}}\text{-CH}^{\text{arom.}}\text{-C-I}$), 114.26 ($\text{N-C-CH}^{\text{arom.}}\text{-CH}^{\text{arom.}}\text{-C-CH}_2$), 82.45 (C-I), 46.62 ($\text{C}(\text{CH}_2)_2$), 44.57 ($\text{C}(\text{CH}_2)_2$), 41.69 ($\text{C}(\text{CH}_2)_3$), 39.69 ($\text{CH}^{\text{arom.}}\text{-C-CH}_2$), 32.71 ($\text{CH-CH}_2\text{-CH}_2\text{-CH}_2\text{-CH}_3$), 32.10 ($\text{CH}_2\text{-CH}_2\text{-CH}_2\text{-CH}_2\text{-CH}_3$), 30.10 ($\text{CH}_2\text{-CH}_2\text{-CH}_2\text{-CH}_2\text{-CH}_3$), 29.33 ($\text{CH-CH}_2\text{-CH}_2\text{-CH}_2\text{-CH}_3$), 25.76 ($\text{CH-CH}_2\text{-CH}_3$), 25.41 ($\text{CH}_2\text{-CH}_2\text{-CH}_2\text{-CH}_2\text{-CH}_3$), 23.52 ($\text{CH-CH}_2\text{-CH}_2\text{-CH}_2\text{-CH}_3$), 23.05 ($\text{CH}_2\text{-CH}_2\text{-CH}_2\text{-CH}_2\text{-CH}_3$), 14.34 ($\text{CH-CH}_2\text{-CH}_2\text{-CH}_2\text{-CH}_3$), 14.25 ($\text{CH}_2\text{-CH}_2\text{-CH}_2\text{-CH}_2\text{-CH}_3$), 10.99 ($\text{CH-CH}_2\text{-CH}_3$).

MALDI-MS (DCTB, DCM) (m/z): $[\text{M-hexyl}]^+$: calc. 1267.5377, found 1267.5517.

8.20. Synthesis of Tol-HAc-BP



Tol-HAc-BP

The modified procedure based on literature was carried out.^[59] 4,4,5,5-Tetramethyl-2-(p-tolyl)-2,1,3,2-dioxaborolane (**11**; 24.0 mg, 110.1 μmol , 3.4 eq.), Na_2CO_3 (131.7 mg, 1.24 mmol, 19.1 eq.) and $\text{Pd}(\text{PPh}_3)_4$ (4.8 mg, 4.15 mmol, 0.06 eq.) were transferred into a pressure tube under inert atmosphere (Ar). Degassed EtOH (0.5 mL), and degassed, deionized water (0.5 mL) were added. Bis(4-(2-(2-ethylhexyl)-9,9-dihexyl-7-iodoacridin-10(9H)-yl)phenyl)methanone (**7b**; 88.2 mg, 65.2 μmol , 1.0 eq.) was dissolved in degassed toluene (1.8 mL) and added to the mixture. The pressure tube was closed and the solution was stirred at 120 $^\circ\text{C}$ for 23 h. The solution was allowed to cool to r.t. and extracted with CHCl_3 . The combined organic fractions were washed with water and HCl solution (5 mL, 2 M). The organic phase was dried over MgSO_4 and the solvent was evaporated under reduced pressure. The crude product was further purified by flash chromatography on flash silica gel (Hex:EtOH 100:1) and the desired product was obtained as a yellow, sticky solid (83.5 mg, 65.2 μmol , quant.).

Chemical formula: $\text{C}_{93}\text{H}_{120}\text{N}_2\text{O}$

$R_f = 0.19$ (SiO_2 , Hex:EtOAc = 100:1).

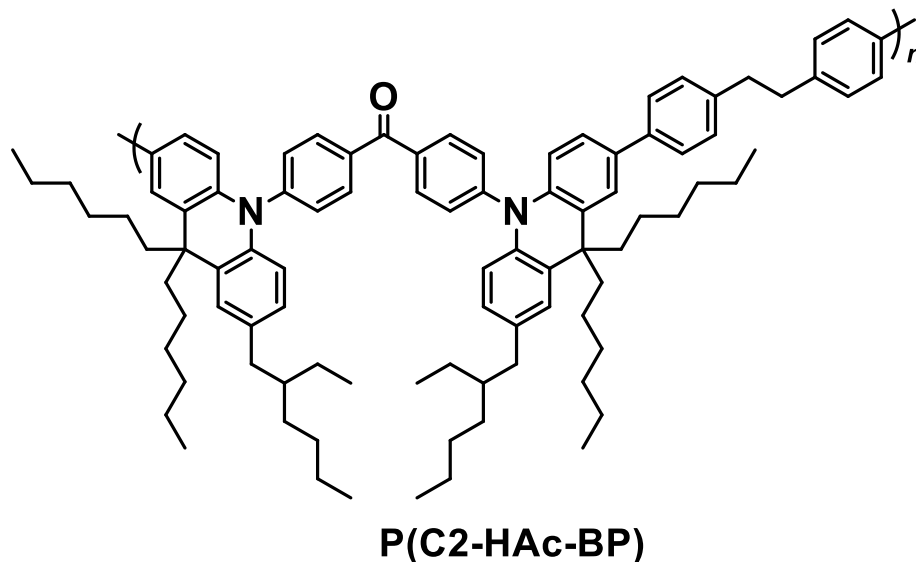
$^1\text{H NMR}$ (300 MHz, Chloroform-*d*) δ 8.17 (d, $J = 8.1$ Hz, 4H, $\text{CH}^{\text{arom.}}\text{-C-C=O}$), 7.55 (d, $J = 2.2$ Hz, 2H, $(\text{CH}_2)_2\text{C-CH}^{\text{arom.}}\text{-C-C-CH}^{\text{arom.}}$), 7.49 (d, $J = 8.1$ Hz, 4H, $\text{CH}^{\text{arom.}}\text{-CH}^{\text{arom.}}\text{-C-C=O}$), 7.45 (d, $J = 8.0$ Hz, 4H, $\text{CH}_3\text{-C-CH}^{\text{arom.}}\text{-CH}^{\text{arom.}}$), 7.24 (d, $J = 8.3$ Hz, 4H, $\text{CH}_3\text{-C-CH}^{\text{arom.}}\text{-CH}^{\text{arom.}}$), 7.17 (dd, $J = 8.6, 2.1$ Hz, 2H, $\text{N-C-CH}^{\text{arom.}}\text{-CH}^{\text{arom.}}\text{-C-C-CH}^{\text{arom.}}$), 7.10 (d, $J = 2.0$ Hz, 2H, $(\text{CH}_2)_2\text{C-CH}^{\text{arom.}}\text{-C-CH}_2$), 6.73 (dd,

$J = 8.4, 1.9$ Hz, 2H, N-C-CH^{arom.}-CH^{arom.}-C-CH₂), 6.24 (d, $J = 8.5$ Hz, 2H, N-C-CH^{arom.}-CH^{arom.}-C-CH^{arom.}), 6.12 (d, $J = 8.3$ Hz, 2H, N-C-CH^{arom.}-CH^{arom.}-C-CH₂), 2.48 (d, $J = 6.9$ Hz, 4H, CH^{arom.}-C-CH₂-CH), 2.39 (s, 6H, CH₃-C-CH₂), 2.12 – 1.91 (m, 8H, C-C(CH₂)₂), 1.54 – 1.43 (m, 2H, CH(CH₂)₃), 1.37 – 1.23 (m, 16H, CH₃-CH₂-CH-CH₂-CH₂-CH₂-CH₃), 1.23 – 1.04 (m, 32H, CH₂-CH₂-CH₂-CH₂-CH₃), 0.88 (t, 12H, CH₃-CH₂-CH-CH₂-CH₂-CH₂-CH₃), 0.79 (t, $J = 7.1$ Hz, 12H, CH₂-CH₂-CH₂-CH₂-CH₃).

¹³C NMR (75 MHz, CDCl₃) δ 146.32 (N-C-CH^{arom.}-CH^{arom.}-C-C=O), 141.12 (N-C-CH^{arom.}-CH^{arom.}-C-C-CH^{arom.}), 139.50 (N-C-CH^{arom.}-CH^{arom.}-C-CH₂), 138.45 (N-C-CH^{arom.}-CH^{arom.}-C-C-CH^{arom.}), 136.78 (C-C=O), 136.12 (CH^{arom.}-C-CH₃), 133.76 (N-C-CH^{arom.}-CH^{arom.}-C-CH₂), 132.98 (N-C-CH^{arom.}-CH^{arom.}-C-C-CH^{arom.}), 132.75 (CH^{arom.}-C-C=O), 131.72 ((CH₂)₂C-C-CH^{arom.}-C-C-CH^{arom.}), 129.42 (CH^{arom.}-CH^{arom.}-C-C=O), 127.26 ((CH₂)₂C-C-CH^{arom.}-C-CH₂), 127.03 (CH^{arom.}-C-CH₃), 126.54 (N-C-CH^{arom.}-CH^{arom.}-C-CH₂), 126.29 ((CH₂)₂C-C-CH^{arom.}-C-CH₂), 125.72 (N-C-CH^{arom.}-CH^{arom.}-C-C-CH^{arom.}), 124.79 ((CH₂)₂C-C-CH^{arom.}-C-C-CH^{arom.}), 114.04 (N-C-CH^{arom.}-CH^{arom.}-C-C-CH^{arom.}), 113.71 (N-C-CH^{arom.}-CH^{arom.}-C-CH₂), 46.14 ((CH₂)₂C), 44.29 ((CH₂)₂C), 41.27 ((CH₂)₃CH), 39.47 (CH^{arom.}-C-CH₂-CH), 32.36 (CH-CH₂-CH₂-CH₂-CH₃), 31.69 (CH₂-CH₂-CH₂-CH₂-CH₃), 29.81 (CH₂-CH₂-CH₂-CH₂-CH₃), 28.98 (CH-CH₂-CH₂-CH₂-CH₃), 25.36 (CH-CH₂-CH₃), 24.97 (CH₂-CH₂-CH₂-CH₂-CH₃), 23.11 (CH-CH₂-CH₂-CH₂-CH₃), 22.67 (CH₂-CH₂-CH₂-CH₂-CH₃), 21.06 (CH^{arom.}-C-CH₃), 14.17 (CH-CH₂-CH₂-CH₂-CH₃), 14.05 (CH₂-CH₂-CH₂-CH₂-CH₃), 10.83 (CH-CH₂-CH₃). The C=O signal was not observed in ¹³C but coupling at around 195 ppm was observed in the HMBC spectrum.

MALDI-MS (DCTB, DCM) (m/z): [M-hexyl]⁺: calc. 1195.8383, found 1195.8472; [M]⁺: calc. 1280.9401, found 1280.9479.

8.21. Synthesis of P(C2-HAc-BP)



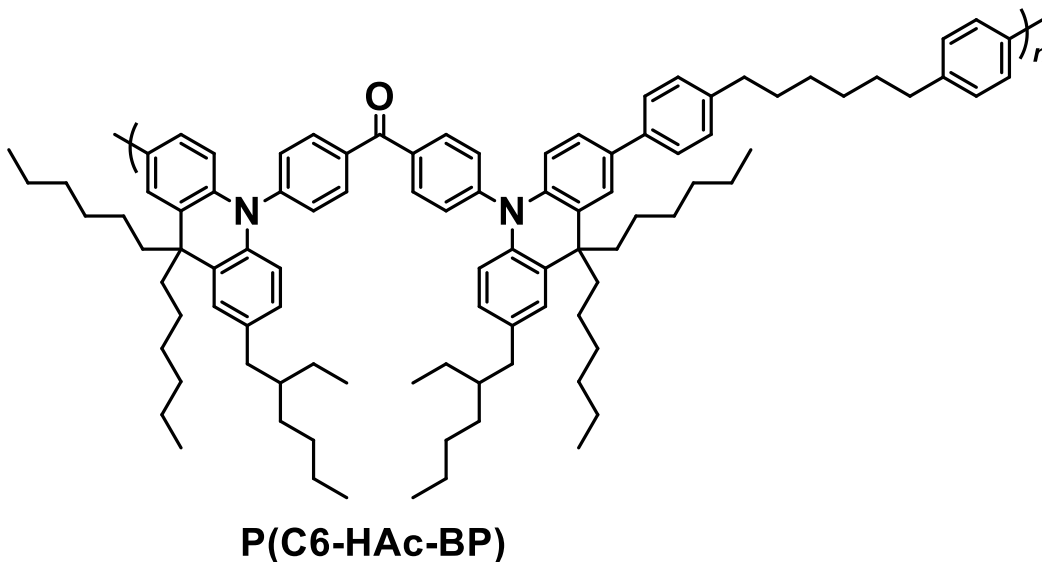
The modified procedure based on literature was carried out.^[59] The modified procedure based on literature was carried out.^[59] 1,2-Bis(4-(4,4,5,5-tetramethyl-1,3,2-dioxaborolan-2-yl)phenyl)ethane (**10d**; 228.8 mg, 0.527 mmol, 1.0 eq.), Na₂CO₃ (998.7 mg, 9.423 mmol, 17.9 eq.) and Pd(PPh₃)₄ (37.6 mg, 33 μmol, 0.06 eq.) were transferred into a pressure tube under inert atmosphere (Ar). Degassed EtOH (1.5 mL), and degassed, deionized water (1 mL) were added. Bis(4-(2-(2-ethylhexyl)-9,9-dihexyl-7-iodoacridin-10(9H)-yl)phenyl)methanone (**7b**; 714.5 mg, 0.527 mmol, 1.0 eq.) was dissolved in degassed toluene (5.5 mL) and added to the mixture. The pressure tube was closed and the solution was stirred at 120 °C for 72 h. The solution was allowed to cool to r.t. and 4,4,5,5-tetramethyl-2-(p-tolyl)-2,1,3,2-dioxaborolane (**11**; 69.3 mg, 0.318 mmol, 0.6 eq.) and Pd(PPh₃)₄ (20.7 mg, 18 μmol, 0.03 eq.) were added in Ar counterflow for an endcapping reaction. The closed pressure tube was stirred at 120 °C for another 24 h. The mixture was cooled to r.t. and extracted with CHCl₃. The combined organic fractions were washed with water and HCl solution (5 mL, 2 M). The organic phase was dried over MgSO₄ and the solvent was evaporated under reduced pressure. The crude product was further purified by soxhlet extraction (1) methanol, 2) isopropanol, 3) CHCl₃) and a subsequent preparative SEC in CHCl₃. The desired product was obtained as a yellow solid (358.5 mg, 53 %).

¹H NMR (700 MHz, Methylene Chloride-*d*₂) δ 8.24 – 8.07 (m, 4H, $CH^{\text{arom.}}-C-C=O$), 7.59 (s, 2H, $(CH_2)_2C-C-CH^{\text{arom.}}-C-C-CH^{\text{arom.}}$), 7.55 – 7.41 (m, 9H, $CH^{\text{arom.}}-CH^{\text{arom.}}-C-C=O$, $CH_2-CH_2-C-CH^{\text{arom.}}-CH^{\text{arom.}}-C$), 7.33 – 7.25 (m, 3H, $CH_2-CH_2-C-CH^{\text{arom.}}-CH^{\text{arom.}}-C$), 7.24 – 7.16 (m, 2H, $N-C-CH^{\text{arom.}}-CH^{\text{arom.}}-C-C-CH^{\text{arom.}}$), 7.14 (s, 2H, $(CH_2)_2C-C-CH^{\text{arom.}}-C-CH_2$), 6.84 – 6.65 (m, 2H, $CH_2-C-CH^{\text{arom.}}-CH^{\text{arom.}}-C-N$), 6.30 – 6.22 (m, 2H, $N-C-CH^{\text{arom.}}-CH^{\text{arom.}}-C-C-CH^{\text{arom.}}$), 6.21 – 6.06 (m, 2H, $N-C-CH^{\text{arom.}}-CH^{\text{arom.}}-C-CH_2$), 3.03 – 2.92 (m, 3H, $CH_2-CH_2-C-CH^{\text{arom.}}-CH^{\text{arom.}}-C$), 2.53 – 2.40 (m, 4H, $N-C-CH^{\text{arom.}}-CH^{\text{arom.}}-C-CH_2$), 2.12 – 1.88 (m, 8H, $(CH_2)_2C-C-CH^{\text{arom.}}$), 1.51 – 1.45 (m, 2H, $(CH_2)_3CH$), 1.36 – 1.22 (m, 32H, $CH_3-CH_2-CH-CH_2-CH_2-CH_2-CH_3$), 1.22 – 0.99 (m, 40H, $CH_2-CH_2-CH_2-CH_2-CH_3$), 0.94 – 0.83 (m, 16H, $CH_3-CH_2-CH-CH_2-CH_2-CH_2-CH_3$), 0.83 – 0.74 (m, 14H, $CH_2-CH_2-CH_2-CH_2-CH_3$).

¹³C NMR (176 MHz, CD₂Cl₂) δ 194.27 (C=O), 146.58 ($N-C-CH^{\text{arom.}}-CH^{\text{arom.}}-C-C=O$), 141.73 ($CH_2-CH_2-C-CH^{\text{arom.}}-CH^{\text{arom.}}-C$), 140.00 ($N-C-CH^{\text{arom.}}-CH^{\text{arom.}}-C-C-CH^{\text{arom.}}$), 139.16 ($N-C-CH^{\text{arom.}}-CH^{\text{arom.}}-C-C-CH^{\text{arom.}}$), 137.38 (C-C=O), 134.31 ($N-C-CH^{\text{arom.}}-CH^{\text{arom.}}-C-CH_2$), 133.15 ($CH^{\text{arom.}}-C-C=O$), 132.02 ($CH^{\text{arom.}}-CH^{\text{arom.}}-C-C=O$), 129.22 ($CH_2-CH_2-C-CH^{\text{arom.}}-CH^{\text{arom.}}-C$), 127.70 ($N-C-CH^{\text{arom.}}-CH^{\text{arom.}}-C-CH_2$), 127.45 ($(CH_2)_2C-C-CH^{\text{arom.}}-C-CH_2$), 127.02 ($(CH_2)_2C-C-CH^{\text{arom.}}-C-C-CH^{\text{arom.}}$), 126.62 ($CH_2-CH_2-C-CH^{\text{arom.}}-CH^{\text{arom.}}-C$), 126.09 ($(CH_2)_2C-C-CH^{\text{arom.}}-C-CH_2$), 125.39 ($N-C-CH^{\text{arom.}}-CH^{\text{arom.}}-C-C-CH^{\text{arom.}}$), 125.07 ($(CH_2)_2C-C-CH^{\text{arom.}}-C-C-CH^{\text{arom.}}$), 114.59 ($N-C-CH^{\text{arom.}}-CH^{\text{arom.}}-C-C-CH^{\text{arom.}}$), 114.19 ($N-C-CH^{\text{arom.}}-CH^{\text{arom.}}-C-CH_2$), 46.61 ($(CH_2)_2C-C-CH^{\text{arom.}}$), 44.73 ($(CH_2)_2C-C-CH^{\text{arom.}}$), 41.74 ($(CH_2)_3CH$), 39.75 ($N-C-CH^{\text{arom.}}-CH^{\text{arom.}}-C-CH_2$), 37.77 ($CH_2-CH_2-C-CH^{\text{arom.}}-CH^{\text{arom.}}-C$), 32.74 ($CH-CH_2-CH_2-CH_2-CH_3$), 32.16 ($CH_2-CH_2-CH_2-CH_2-CH_3$), 30.11 ($CH_2-CH_2-CH_2-CH_2-CH_3$), 29.36 ($CH-CH_2-CH_2-CH_2-CH_3$), 25.80 ($CH-CH_2-CH_3$), 25.51 ($CH_2-CH_2-CH_2-CH_2-CH_3$), 23.54 ($CH-CH_2-CH_2-CH_2-CH_3$), 23.08 ($CH_2-CH_2-CH_2-CH_2-CH_3$), 14.32 ($CH_2-CH_2-CH_2-CH_2-CH_3$), 11.04 ($CH-CH_2-CH_3$).

SEC (THF, UV detection, PS calibration): $M_n = 4.7 \text{ kg mol}^{-1}$, $D = 1.55$.

8.1. Synthesis of P(C6-HAc-BP)



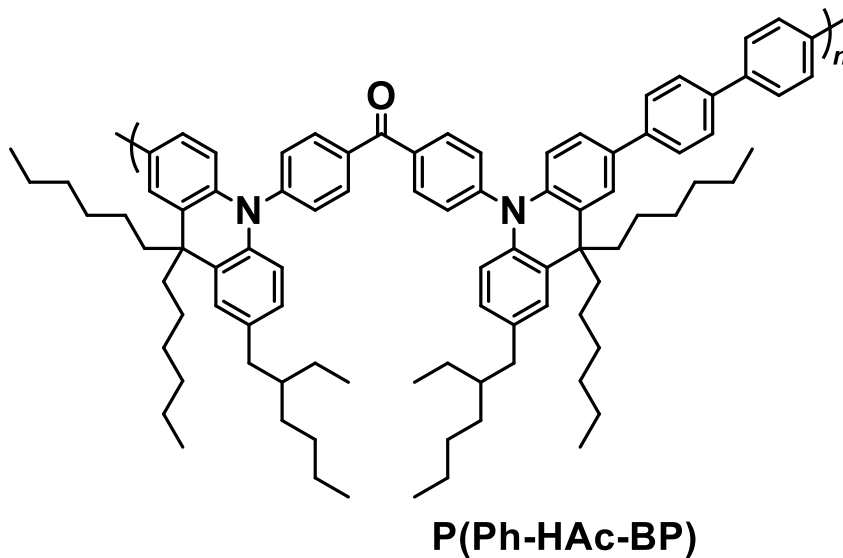
The modified procedure based on literature was carried out.^[59] The modified procedure based on literature was carried out.^[59] 1,6-Bis(4-(4,4,5,5-tetramethyl-1,3,2-dioxaborolan-2-yl)phenyl)hexane (**10e**; 287.3 mg, 0.586 mmol, 1.0 eq.), Na₂CO₃ (994.4 mg, 9.382 mmol, 16.0 eq.) and Pd(PPh₃)₄ (36.4 mg, 31 μmol, 0.05 eq.) were transferred into a pressure tube under inert atmosphere (Ar). Degassed EtOH (1.5 mL), and degassed, deionized water (1.0 mL) were added. Bis(4-(2-(2-ethylhexyl)-9,9-dihexyl-7-iodoacridin-10(9H)-yl)phenyl)methanone (**7b**; 793.25 mg, 0.586 mmol, 1.0 eq.) was dissolved in degassed toluene (5.0 mL) and added to the mixture. The pressure tube was closed and the solution was stirred at 120 °C for 72 h. The solution was allowed to cool to r.t. and 4,4,5,5-tetramethyl-2-(p-tolyl)-2,1,3,2-dioxaborolane (**11**; 71.7 mg, 0.329 mmol, 0.56 eq.) and Pd(PPh₃)₄ (10.1 mg, 9 μmol, 0.01 eq.) were added in Ar counterflow for an endcapping reaction. The closed pressure tube was stirred at 120 °C for another 24 h. The mixture was cooled to r.t. and extracted with CHCl₃. The combined organic fractions were washed with water and HCl solution (5 mL, 2 M). The organic phase was dried over MgSO₄ and the solvent was evaporated under reduced pressure. The crude product was further purified by soxhlet extraction (1) methanol, 2) isopropanol, 3) CHCl₃) and a subsequent preparative SEC in CHCl₃. The desired product was obtained as a yellow solid (271.2 mg, 35 %).

¹H NMR (700 MHz, CD₂Cl₂) δ 8.31 – 8.01 (m, 4H, CH^{arom.}-C-C=O), 7.58 (s, 1H, (CH₂)₂C-C-CH^{arom.}-C-C-CH^{arom.}), 7.53 – 7.38 (m, 8H, CH^{arom.}-CH^{arom.}-C-C=O, N-C-CH^{arom.}-CH^{arom.}-C-C-CH^{arom.}), 7.27 – 7.20 (m, 3H, CH₂-CH₂-C-CH^{arom.}), 7.18 (d, $J = 8.5$ Hz, 1H, N-C-CH^{arom.}-CH^{arom.}-C-C-CH^{arom.}), 7.14 (s, 2H, (CH₂)₂C-C-CH^{arom.}-C-CH₂), 6.73 (d, $J = 11.5$ Hz, 2H, N-C-CH^{arom.}-CH^{arom.}-C-CH₂), 6.29 – 6.21 (m, 1H, N-C-CH^{arom.}-CH^{arom.}-C-C-CH^{arom.}), 6.19 – 6.06 (m, 2H, N-C-CH^{arom.}-CH^{arom.}-C-CH₂), 2.63 (s, 3H, CH₂-CH₂-C-CH^{arom.}), 2.47 (s, 4H, CH^{arom.}-C-CH₂-CH), 2.10 – 1.88 (m, 8H, (CH₂)₂C), 1.65 (s, 4H, CH₂-CH₂-C-CH^{arom.}), 1.50 (s, 2H, (CH₂)₃CH), 1.41 (s, 3H, CH₂-CH₂-CH₂-C-CH^{arom.}), 1.31 – 1.22 (m, 17H, CH-CH₂-CH₃), 1.22 – 0.99 (m, 38H, CH₂-CH₂-CH₂-CH₂-CH₃), 0.90 – 0.83 (m, 13H, CH₃-CH₂-CH-CH₂-CH₂-CH₂-CH₃), 0.83 – 0.76 (m, 13H, CH₂-CH₂-CH₂-CH₂-CH₃).

¹³C NMR (176 MHz, CD₂Cl₂) δ 195.36 (C=O), 146.53 (N-C-CH^{arom.}-CH^{arom.}-C-C=O), 141.68 (CH₂-CH₂-C-CH^{arom.}), 140.01 (N-C-CH^{arom.}-CH^{arom.}-C-C-CH^{arom.}), 138.86 (N-C-CH^{arom.}-CH^{arom.}-C-C-CH^{arom.}, N-C-CH^{arom.}-CH^{arom.}-C-CH₂), 137.35 (C-C=O), 134.28 (N-C-CH^{arom.}-CH^{arom.}-C-CH₂), 133.27 (N-C-CH^{arom.}-CH^{arom.}-C-C-CH^{arom.}), 133.14 (CH^{arom.}-C-C=O), 132.02 (CH^{arom.}-CH^{arom.}-C-C=O), 129.15 (CH₂-CH₂-C-CH^{arom.}), 127.70 (N-C-CH^{arom.}-CH^{arom.}-C-CH₂), 127.23 ((CH₂)₂C-C-CH^{arom.}-C-CH₂), 126.98 ((CH₂)₂C-C-CH^{arom.}-C-C-CH^{arom.}), 126.53 (CH₂-CH₂-C-CH^{arom.}-CH^{arom.}), 126.09 ((CH₂)₂C-C-CH^{arom.}-C-CH₂), 125.38 (N-C-CH^{arom.}-CH^{arom.}-C-C-CH^{arom.}), 125.04 ((CH₂)₂C-C-CH^{arom.}-C-C-CH^{arom.}), 114.57 (N-C-CH^{arom.}-CH^{arom.}-C-C-CH^{arom.}), 114.17 (N-C-CH^{arom.}-CH^{arom.}-C-CH₂), 46.58 ((CH₂)₂C(C-CH^{arom.})₂), 44.72 ((CH₂)₂C(C-CH^{arom.})₂), 41.73 ((CH₂)₃CH), 39.75 (CH-CH₂-C-CH^{arom.}), 35.90 (CH₂-CH₂-C-CH^{arom.}), 32.74 (CH-CH₂-CH₂-CH₂-CH₃), 32.15 (CH₂-CH₂-CH₂-CH₂-CH₃), 32.00 (CH₂-CH₂-C-CH^{arom.}), 30.20 (CH₂-CH₂-CH₂-CH₂-CH₃), 29.57 (CH₂-CH₂-CH₂-C-CH^{arom.}), 29.36 (CH-CH₂-CH₂-CH₂-CH₃), 25.79 (CH-CH₂-CH₃), 25.50 (CH₂-CH₂-CH₂-CH₂-CH₃), 23.54 (CH-CH₂-CH₂-CH₂-CH₃), 23.07 (CH₂-CH₂-CH₂-CH₂-CH₃), 14.31 (CH₂-CH₂-CH₂-CH₂-CH₃), 10.99 (CH₃-CH₂-CH-CH₂-CH₂-CH₂-CH₃).

SEC (THF, UV detection, PS calibration): $M_n = 5.9$ kg mol⁻¹, $D = 1.53$.

8.1. Synthesis of P(Ph-HAc-BP)



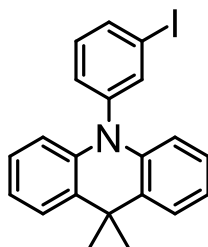
The modified procedure based on literature was carried out.^[59] The modified procedure based on literature was carried out.^[59] 4,4'-Bis(4,4,5,5-tetramethyl-1,3,2-dioxaborolan-2-yl)-1,1'-biphenyl (**10c**; 245.3 mg, 0.604 mmol, 1.0 eq.), Na₂CO₃ (929.4 mg, 8.769 mmol, 14.5 eq.) and Pd(PPh₃)₄ (34.4 mg, 30 μmol, 0.05 eq.) were transferred into a pressure tube under inert atmosphere (Ar). Degassed EtOH (1.5 mL), and degassed, deionized water (1 mL) were added. Bis(4-(2-(2-ethylhexyl)-9,9-dihexyl-7-iodoacridin-10(9H)-yl)phenyl)methanone (**7b**; 817.6 mg, 0.604 mmol, 1.0 eq.) was dissolved in degassed toluene (5.0 mL) and added to the mixture. The pressure tube was closed and the solution was stirred at 120 °C for 72 h. The solution was allowed to cool to r.t. and 4,4,5,5-tetramethyl-2-(p-tolyl)-2,1,3,2-dioxaborolane (**11**; 75.2 mg, 0.345 mmol, 0.57 eq.) and Pd(PPh₃)₄ (8.5 mg, 7 μmol, 0.01 eq.) were added in Ar counterflow for an endcapping reaction. The closed pressure tube was stirred at 120 °C for another 24 h. The mixture was cooled to r.t. and extracted with CHCl₃. The combined organic fractions were washed with water and HCl solution (5 mL, 2 M). The organic phase was dried over MgSO₄ and the solvent was evaporated under reduced pressure. The crude product was further purified by soxhlet extraction (1) methanol, 2) isopropanol, 3) CHCl₃) and a subsequent preparative SEC in CHCl₃. The desired product was obtained as a yellow solid (276.1 mg, 37 %).

¹H NMR (700 MHz, Methylene Chloride-*d*₂) δ 8.25 – 8.07 (m, 4H, CH^{arom.}-C-C=O), 7.81 – 7.69 (m, 3H, C-C-CH^{arom.}-CH^{arom.}-C-C), 7.69 – 7.60 (m, 5H, C-C-CH^{arom.}-CH^{arom.}-C-C, (CH₂)₂C-C-CH^{arom.}-C-C-CH^{arom.}), 7.55 – 7.39 (m, 4H, CH^{arom.}-CH^{arom.}-C-C=O), 7.30 – 7.22 (m, 1H, N-C-CH^{arom.}-CH^{arom.}-C-C-CH^{arom.}), 7.20 – 7.12 (m, 2H, (CH₂)₂C-C-CH^{arom.}-C-CH₂), 6.79 – 6.69 (m, 2H, N-C-CH^{arom.}-CH^{arom.}-C-CH₂), 6.36 – 6.23 (m, 1H, N-C-CH^{arom.}-CH^{arom.}-C-C-CH^{arom.}), 6.22 – 6.06 (m, 2H, N-C-CH^{arom.}-CH^{arom.}-C-CH₂), 2.57 – 2.38 (m, 4H, CH^{arom.}-C-CH₂-CH), 2.14 – 1.90 (m, 7H, (CH₂)₂C-C-CH^{arom.}), 1.70 – 1.43 (m, 2H, (CH₂)₃CH), 1.40 – 1.24 (m, 17H, CH₃-CH₂-CH-CH₂-CH₂-CH₂-CH₃), 1.24 – 0.99 (m, 35H, CH₂-CH₂-CH₂-CH₂-CH₃), 0.93 – 0.84 (m, 12H, CH₃-CH₂-CH-CH₂-CH₂-CH₂-CH₃), 0.84 – 0.75 (m, 12H, CH₂-CH₂-CH₂-CH₂-C₃).

¹³C NMR (176 MHz, CD₂Cl₂) δ 195.18 (C=O), 146.53 (N-C-CH^{arom.}-CH^{arom.}-C-C=O), 142.01 (N-C-CH^{arom.}-CH^{arom.}-C-C-CH^{arom.}), 140.42 (N-C-CH^{arom.}-CH^{arom.}-C-C-CH^{arom.}, N-C-CH^{arom.}-CH^{arom.}-C-CH₂), 139.96 (N-C-CH^{arom.}-CH^{arom.}-C-C-CH^{arom.}), 139.03 (N-C-CH^{arom.}-CH^{arom.}-C-C-CH^{arom.}), 137.42 (C-C=O), 134.43 (CH^{arom.}-C-CH₂), 133.19 (CH^{arom.}-C-C=O), 132.03 (CH^{arom.}-CH^{arom.}-C-C=O), 129.25 (CH^{arom.}-CH^{arom.}-C-C=O), 127.72 ((CH₂)₂C-C-CH^{arom.}-C-CH₂), 127.58 (N-C-CH^{arom.}-CH^{arom.}-C-CH₂), 127.48 (C-C-CH^{arom.}-CH^{arom.}-C-C), 127.15 ((CH₂)₂C-C-CH^{arom.}-C-C-CH^{arom.}), 127.07 (C-C-CH^{arom.}-CH^{arom.}-C-C), 126.12 ((CH₂)₂C-C-CH^{arom.}-C-CH₂), 125.49 (N-C-CH^{arom.}-CH^{arom.}-C-C-CH^{arom.}), 125.15 ((CH₂)₂C-C-CH^{arom.}-C-C-CH^{arom.}), 114.68 (N-C-CH^{arom.}-CH^{arom.}-C-C-CH^{arom.}), 114.24 (N-C-CH^{arom.}-CH^{arom.}-C-CH₂), 46.65 ((CH₂)₂C-C-CH^{arom.}), 44.77 ((CH₂)₂C-C-CH^{arom.}), 41.75 ((CH₂)₃CH), 39.77 (CH^{arom.}-C-CH₂-CH), 32.75 (CH-CH₂-CH₂-CH₂-CH₃), 32.17 (CH₂-CH₂-CH₂-CH₂-CH₃), 30.22 (CH₂-CH₂-CH₂-CH₂-CH₃), 29.37 (CH-CH₂-CH₂-CH₂-CH₃), 25.81 (CH-CH₂-CH₃), 25.52 (CH₂-CH₂-CH₂-CH₂-CH₃), 23.55 (CH-CH₂-CH₂-CH₂-CH₃), 23.08 (CH₂-CH₂-CH₂-CH₂-CH₃), 14.30 (CH₂-CH₂-CH₂-CH₂-CH₃, CH-CH₂-CH₂-CH₂-CH₃), 11.00 (CH-CH₂-CH₃).

SEC (THF, UV detection, PS calibration): $M_n = 7.1 \text{ kg mol}^{-1}$, $D = 1.49$.

8.1. Synthesis of 10-(3-Iodophenyl)-9,9-dimethyl-9,10-dihydroacridine (12)



12

The modified procedure based on literature was carried out.^[157] 9,9-Dimethyl-9,10-dihydroacridine (**3a**; 502 mg, 2.40 mmol, 1.0 eq.), 1,3-diiodobenzene (2.313 g, 7.01 mmol, 2.9 eq.), Cu powder (149 mg, 2.35 mmol, 1.0 eq.) and K₂CO₃ (1.307 g, 9.46 mmol, 3.9 eq.) were dissolved/ dispersed in dry dichlorobenzene (20 mL) under argon atmosphere. The solution was stirred under reflux for 50 h with a sand bath. The solution was allowed to cool to r.t., water was added (100 mL) and the solution was extracted with DCM (2x 100 mL). The combined organic fractions were washed with brine (20 mL), dried over MgSO₄ and the solvent was evaporated under reduced pressure. The residue was purified by flash chromatography on silica gel (Hex). The product was obtained as a colorless solid (672 mg, 1.63 mmol, 68 %).

Chemical formula: C₂₁H₁₈IN

R_f = 0.40 (SiO₂, Hex).

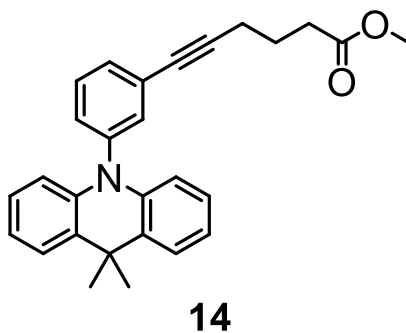
¹H NMR (300 MHz, Chloroform-*d*) δ 7.86 (ddd, *J* = 6.8, 2.1 Hz, 2.1 Hz, 1H, I-C-CH^{arom.}-CH^{arom.}), 7.72 (d, *J* = 2.2 Hz, 1H, I-C-CH^{arom.}-C), 7.46 (dd, *J* = 7.3, 1.9 Hz, 2H, C(CH₃)₂-C-CH^{arom.}), 7.39 – 7.32 (m, 2H, I-C-CH^{arom.}-CH^{arom.}-CH^{arom.}), 7.05 – 6.89 (m, 4H, C(CH₃)₂-C-CH^{arom.}-CH^{arom.}-CH^{arom.}), 6.25 (dd, *J* = 7.8, 1.7 Hz, 2H, C(CH₃)₂-C-C-CH^{arom.}), 1.69 (s, 6H, CH₃).

¹³C NMR (75 MHz, CDCl₃) δ 142.62 (N-C-CH^{arom.}-C), 140.66 (N-C-CH^{arom.}-C), 140.52 (N-C-C), 137.55 (CH^{arom.}-CH^{arom.}-C-I), 132.32 (CH^{arom.}-CH^{arom.}-C-I), 131.13 (CH^{arom.}-CH^{arom.}-CH^{arom.}-C-I), 130.24 (C(CH₃)₂-C), 126.57 (C(CH₃)₂-C-CH^{arom.}), 125.46 (C(CH₃)₂-C-CH^{arom.}-CH^{arom.}-CH^{arom.}), 121.02 (C(CH₃)₂-C-CH^{arom.}-CH^{arom.}), 114.13 (C(CH₃)₂-C-C-CH^{arom.}), 95.45 (C-I), 36.10 (C(CH₃)₂), 31.42 (C(CH₃)₂).

MALDI-MS (DCTB, DCM) (m/z): $[M-CH_3]^+$: calc. 396.0249, found 396.0207; $[M]^+$: calc. 411.0484, found 411.0423.

Characterization is in agreement with literature. ^[157]

8.2. Synthesis of Methyl 6-(3-(9,9-dimethylacridin-10(9H)-yl)phenyl)hex-5-ynoate (14)



The modified procedure based on literature was carried out.^[158,159] 10-(3-iodophenyl)-9,9-dimethyl-9,10-dihydroacridine (**12**; 245 mg, 0.60 mmol, 1 eq.) and $PdCl_2(PPh_3)_2$ (25 mg, 0.04 mmol, 0.06 eq.) were dissolved in dry THF (5 mL) and the solution was sparged with argon for 2 min in a vial with septum (vial 1). Methyl-5-hexynoate (**13**; 129 mg, 1.03 mmol, 1.7 eq.), CuI (22 mg, 0.12 mmol, 0.2 eq.) and trimethylamine (249 mg, 2.46 mmol, 4.1 eq.) were dissolved/ dispersed in dry THF (5 mL) in a separate vial with septum (vial 2) and sparged with argon for 2 min. Vial 2 was cooled to 0 °C with an ice bath and the solution of vial 1 was added via a syringe. The solution was allowed to heat to r.t. and stirred at r.t. for 52 h. Saturated NH_4Cl solution (20 mL) was added and the mixture was stirred for 30 min at r.t. The solution was extracted with EtOAc (3x 50 mL). The combined organic phase was washed with brine, dried over $MgSO_4$ and the solvent was evaporated under reduced pressure. The residue was purified by flash column chromatography on silica gel (Hex:EtOAc = 20:1). The product was obtained as a colorless solid (213 mg, 0.52 mmol, 87 %).

Chemical formula: $C_{28}H_{27}NO_2$

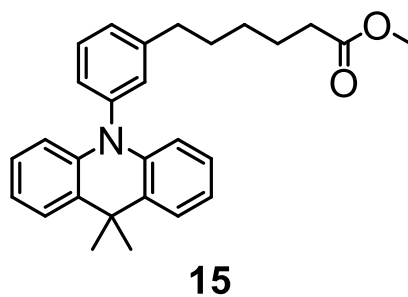
R_f = 0.28 (SiO_2 , Hex:EtOAc = 20:1).

¹H NMR (300 MHz, Chloroform-*d*) δ 7.59 – 7.50 (m, 2H, $CH^{\text{arom.}}-CH^{\text{arom.}}-C-C\equiv C$), 7.45 (dd, $J = 7.4$, 2.0 Hz, 2H, $C(CH_3)_2-C-CH^{\text{arom.}}$), 7.39 (s, 1H, $C-CH^{\text{arom.}}-C-C\equiv C$), 7.32 – 7.21 (m, 1H, $CH^{\text{arom.}}CH^{\text{arom.}}-CH^{\text{arom.}}-C-C\equiv C$), 7.03 – 6.84 (m, 4H, $C(CH_3)_2-C-CH^{\text{arom.}}-CH^{\text{arom.}}-CH^{\text{arom.}}$), 6.26 (dd, $J = 8.0$, 1.7 Hz, 2H, $C(CH_3)_2-C-C-CH^{\text{arom.}}$), 3.68 (s, 3H, $COOCH_3$), 2.59 – 2.42 (m, 4H, $C\equiv C-CH_2-CH_2-CH_2$), 1.93 (p, $J = 7.1$ Hz, 2H, $C\equiv C-CH_2-CH_2-CH_2$), 1.68 (s, 6H, $C(CH_3)_2$).

¹³C NMR (75 MHz, $CDCl_3$) δ 173.70 ($C=O$), 141.36 ($N-C-CH^{\text{arom.}}-C$), 140.81 ($N-C-C$), 134.66 ($N-C-CH^{\text{arom.}}-C$), 131.51 ($CH^{\text{arom.}}-CH^{\text{arom.}}-C-C\equiv C$), 131.14 ($CH^{\text{arom.}}-CH^{\text{arom.}}-C-C\equiv C$), 130.89 ($CH^{\text{arom.}}-CH^{\text{arom.}}-CH^{\text{arom.}}-C-C\equiv C$), 130.15 ($C(CH_3)_2-C$), 126.77 ($C-C\equiv C$), 126.51 ($C(CH_3)_2-C-CH^{\text{arom.}}$), 125.35 ($C(CH_3)_2-C-CH^{\text{arom.}}-CH^{\text{arom.}}-CH^{\text{arom.}}$), 120.78 ($C(CH_3)_2-C-CH^{\text{arom.}}-CH^{\text{arom.}}$), 114.19 ($C(CH_3)_2-C-C-CH^{\text{arom.}}$), 90.68 ($C-C\equiv C-CH_2$), 80.68 ($C-C\equiv C-CH_2$), 51.76 ($COOCH_3$), 36.10 ($C(CH_3)_2$), 33.01 ($CH_2-COOCH_3$), 31.37 ($C(CH_3)_2$), 23.92 ($CH_2-CH_2-COOCH_3$), 19.01 ($C\equiv C-CH_2$).

MALDI-MS (DCTB, DCM) (m/z): $[M-CH_3]^+$: calc. 394.1807, found 394.1836; $[M]^+$: calc. 409.2042, found 409.2049.

8.3. Synthesis of Methyl 6-(3-(4,6-diphenyl-1,3,5-triazin-2-yl)phenyl)hexanoate (15)



Methyl 6-(3-(9,9-dimethylacridin-10(9H)-yl)phenyl)hex-5-ynoate (**14**; 597 mg, 1.46 mmol, 98 %) and palladium on carbon (10 wt%, 327 mg) was dissolved/ dispersed in dry and degassed THF under argon atmosphere. The solution was sparged with H_2 for 2 min and mounted with a second balloon. The solution was shaken on a shaker for 17 h in H_2 atmosphere. EtOAc (10 mL) was added to the solution

and it was filtered through a silica plug (THF:Hex = 1:1). The product was obtained as colorless oil (591 mg, 1.43 mmol, 98 %)

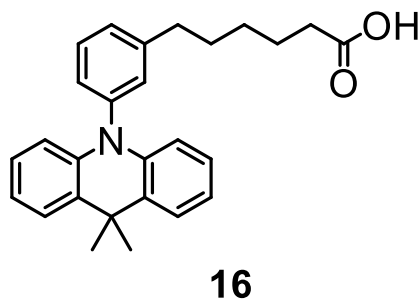
Chemical formula: C₂₈H₃₁NO₂

¹H NMR (300 MHz, Chloroform-*d*) δ 7.55 (t, *J* = 7.9 Hz, 1H, CH^{arom.}-CH^{arom.}-C-CH₂), 7.48 (dd, *J* = 7.4, 1.8 Hz, 2H, C(CH₃)₂-C-CH^{arom.}), 7.34 (d, *J* = 7.6 Hz, 1H, CH^{arom.}-C-CH₂), 7.22 – 7.14 (m, 2H, CH^{arom.}-C-CH^{arom.}-C-CH₂), 7.04 – 6.90 (m, 4H, C(CH₃)₂-C-CH^{arom.}-CH^{arom.}-CH^{arom.}), 6.30 (d, *J* = 7.9 Hz, 2H, C(CH₃)₂-C-C-CH^{arom.}), 3.68 (s, 3H, COOCH₃), 2.72 (t, *J* = 7.7 Hz, 2H, CH^{arom.}-C-CH₂), 2.34 (t, *J* = 7.5 Hz, 2H, CH₂-COOCH₃), 1.78 – 1.63 (m, 10H, C(CH₃)₂, CH₂-CH₂-CH₂-CH₂-COOCH₃), 1.49 – 1.36 (m, 2H, CH₂-CH₂-CH₂-COOCH₃).

¹³C NMR (75 MHz, CDCl₃) δ 174.25 (C=O), 145.77 (CH^{arom.}-C-CH₂), 141.20 (N-C-CH^{arom.}-C), 141.06 (N-C-CH^{arom.}-CH^{arom.}-CH^{arom.}-CH^{arom.}), 131.13 (N-C-CH^{arom.}-C), 130.72 (CH^{arom.}-CH^{arom.}-C-CH₂), 130.00 ((CH₃)₂C), 128.54 (CH^{arom.}-CH^{arom.}-CH^{arom.}-C-CH₂), 128.35 (CH^{arom.}-CH^{arom.}-C-CH₂), 126.44 ((CH₃)₂C-C-CH^{arom.}), 125.30 (N-C-CH^{arom.}-CH^{arom.}-CH^{arom.}-CH^{arom.}), 120.52 (N-C-CH^{arom.}-CH^{arom.}-CH^{arom.}-CH^{arom.}), 114.12 (N-C-CH^{arom.}-CH^{arom.}-CH^{arom.}-CH^{arom.}), 51.59 (O-CH₃), 36.08 ((CH₃)₂C), 35.65 (CH^{arom.}-C-CH₂), 34.11 (CH₂-C=O), 31.44 ((CH₃)₂C), 31.07 (CH^{arom.}-C-CH₂-CH₂), 28.85 (CH₂-CH₂-CH₂-C=O), 24.87 (CH₂-CH₂-C=O).

MALDI-MS (DCTB, DCM) (m/z): [M-CH₃]⁺: calc. 398.2120, found 398.2153; [M]⁺: calc. 413.2355, found 413.2375.

8.4. Synthesis of 6-(3-(9,9-Dimethylacridin-10(9H)-yl)phenyl)hexanoic acid (**16**)



Methyl 6-(3-(4,6-diphenyl-1,3,5-triazin-2-yl)phenyl)hexanoate (**15**; 590 mg, 1.35 mmol, 1.0 eq.) was added to a solution of LiOH (69 mg, 2.88 mmol, 2.1 eq.) in THF:water (1:1, 10 mL) and stirred at r.t. for 44 h and conversion was monitored via TLC. The solution was washed with saturated NH_4Cl solution (100 mL) and extracted with EtOAc (3x 100 mL). The combined organic phases was dried over MgSO_4 and the solvent was evaporated under reduced pressure. The product was obtained as a colorless solid (539 mg, 1.35 mmol, quant.).

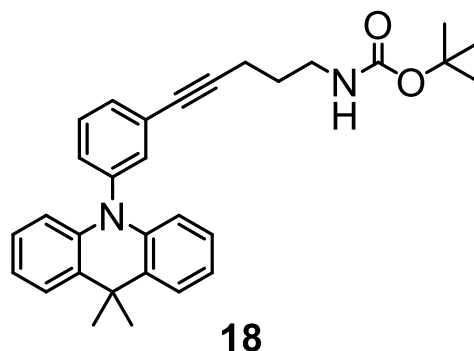
Chemical formula: $\text{C}_{27}\text{H}_{29}\text{NO}_2$

^1H NMR (300 MHz, Chloroform-*d*) δ 10.95 (br s, 1H, COOH), 7.52 (t, $J = 7.6$ Hz, 1H, $\text{CH}^{\text{arom.}}$ - $\text{CH}^{\text{arom.}}$ -C- CH_2), 7.45 (dd, $J = 7.4, 1.8$ Hz, 2H, $\text{C}(\text{CH}_3)_2$ -C- $\text{CH}^{\text{arom.}}$), 7.30 (d, $J = 7.7$ Hz, 1H, $\text{CH}^{\text{arom.}}$ - $\text{CH}^{\text{arom.}}$ -C- CH_2), 7.19 – 7.11 (m, 2H, $\text{CH}^{\text{arom.}}$ -C- $\text{CH}^{\text{arom.}}$ -C- CH_2), 7.02 – 6.87 (m, 4H, $\text{C}(\text{CH}_3)_2$ -C- $\text{CH}^{\text{arom.}}$ - $\text{CH}^{\text{arom.}}$ - $\text{CH}^{\text{arom.}}$), 6.26 (dd, $J = 7.9, 1.5$ Hz, 2H, $\text{C}(\text{CH}_3)_2$ -C-C- $\text{CH}^{\text{arom.}}$), 2.69 (t, $J = 7.7$ Hz, 2H, $\text{CH}^{\text{arom.}}$ -C- CH_2), 2.35 (t, $J = 7.4$ Hz, 2H, CH_2 -COOH), 1.83 – 1.60 (m, 10H, $\text{C}(\text{CH}_3)_2$, CH_2 - CH_2 - CH_2 - CH_2 -COOH), 1.51 – 1.34 (m, 2H, CH_2 - CH_2 - CH_2 -COOH).

^{13}C NMR (75 MHz, CDCl_3) δ 179.31 (C=O), 145.72 ($\text{CH}^{\text{arom.}}$ -C- CH_2), 141.23 (N-C- $\text{CH}^{\text{arom.}}$ -C), 141.07 ($\text{C}(\text{CH}_3)_2$ -C-C), 131.13 (N-C- $\text{CH}^{\text{arom.}}$ -C), 130.75 ($\text{CH}^{\text{arom.}}$ - $\text{CH}^{\text{arom.}}$ -C- CH_2), 130.02 ($\text{C}(\text{CH}_3)_2$ -C), 128.60 ($\text{CH}^{\text{arom.}}$ -C- $\text{CH}^{\text{arom.}}$ -C- CH_2), 128.36 ($\text{CH}^{\text{arom.}}$ - $\text{CH}^{\text{arom.}}$ -C- CH_2), 126.46 ($\text{C}(\text{CH}_3)_2$ -C- $\text{CH}^{\text{arom.}}$), 125.33 ($\text{C}(\text{CH}_3)_2$ -C- $\text{CH}^{\text{arom.}}$ - $\text{CH}^{\text{arom.}}$ - $\text{CH}^{\text{arom.}}$), 120.54 ($\text{C}(\text{CH}_3)_2$ -C- $\text{CH}^{\text{arom.}}$ - $\text{CH}^{\text{arom.}}$ - $\text{CH}^{\text{arom.}}$), 114.13 ($\text{C}(\text{CH}_3)_2$ -C-C- $\text{CH}^{\text{arom.}}$), 36.10 ($\text{C}(\text{CH}_3)_2$), 35.64 ($\text{CH}^{\text{arom.}}$ -C- CH_2), 33.94 (CH_2 -COOH), 31.46 ($\text{C}(\text{CH}_3)_2$), 31.06 ($\text{CH}^{\text{arom.}}$ -C- CH_2 - CH_2), 28.77 (CH_2 - CH_2 - CH_2 -COOH), 24.60 (CH_2 - CH_2 -COOH).

MALDI-MS (DCTB, DCM) (m/z): $[M-CH_3]^+$: calc. 384.1964, found 384.2003; $[M]^+$: calc. 399.2198, found 399.2219.

8.5. Synthesis of *tert*-Butyl (5-(3-(9,9-dimethylacridin-10(9H)-yl)phenyl)pent-4-yn-1-yl)carbamate (**18**)



The modified procedure based on literature was carried out.^[158,159] 10-(3-Iodophenyl)-9,9-dimethyl-9,10-dihydroacridine (**12**; 338.4 mg, 0.823 mmol, 1.0 eq.) and $PdCl_2(PPh_3)_2$ (28.1 mg, 0.040 mmol, 0.05 eq.) were dissolved in dry THF (5 mL) in an argon atmosphere in a Schlenk flask (flask 1). The solution was sparged with argon for 3 min. In a separate Schlenk flask CuI (34.9 mg, 0.183 mmol, 0.22 eq.) and *tert*-butyl pent-4-yn-1-ylcarbamate (**17**; 146.8 mg, 0.801 mmol, 0.97 eq.) were dissolved in dry THF (5 mL) and triethylamine (360 mg, 3.558 mmol, 4.32 eq.) were added (flask 2). After sparging the second flask with argon for 3 min the solution was cooled to 0 °C with an ice bath and flask 1 was added under Ar counterflow. The combined solution was allowed to heat to r.t. and stirred at r.t. overnight (15 h). Saturated NH_4Cl solution (50 mL) was added and the solution was stirred for 30 min. The solution was extracted with EtOAc (3x 50 mL). The combined organic fraction was washed with brine (50 mL), dried over $MgSO_4$ and the solvent was evaporated. The crude product was further purified by flash chromatography on silica gel (Hex:EtOAc = 7:1) and the desired product was obtained as a yellow-orange solid (333.7 mg, 0.72 mmol, 87 %).

Chemical formula: $C_{31}H_{34}N_2O_2$

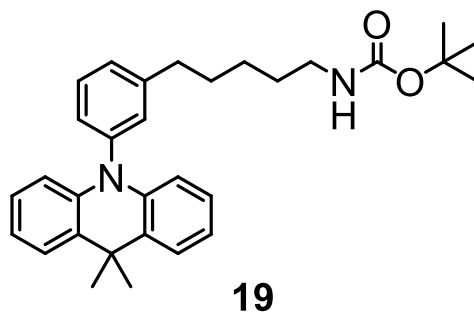
R_f = 0.32 (SiO_2 , Hex:EtOAc = 7:1).

¹H NMR (300 MHz, CDCl₃) δ 7.54 (d, *J* = 4.7 Hz, 2H, CH^{arom.}-CH^{arom.}-C-C≡C), 7.45 (dd, *J* = 7.4, 1.9 Hz, 2H, (CH₃)₂C-C-CH^{arom.}), 7.38 (s, 1H, N-C-CH^{arom.}-C-C≡C), 7.30 – 7.21 (m, 1H, CH^{arom.}-CH^{arom.}-CH^{arom.}-C-C≡C), 7.03 – 6.87 (m, 4H, (CH₃)₂C-C-CH^{arom.}-CH^{arom.}-CH^{arom.}), 6.26 (dd, *J* = 7.9, 1.7 Hz, 2H, N-C-CH^{arom.}-CH^{arom.}-CH^{arom.}-CH^{arom.}), 4.68 (s, 1H, NH), 3.28 (t, *J* = 6.8 Hz, 2H, N-CH₂), 2.47 (t, *J* = 7.0 Hz, 2H, C≡C-CH₂), 1.79 (p, *J* = 6.9 Hz, 2H, C≡C-CH₂-CH₂), 1.68 (s, 6H, (CH₃)₂C), 1.43 (s, 9H, (CH₃)₃C).

¹³C NMR (75 MHz, CDCl₃) δ 156.11 (C=O), 141.37 (N-C-CH^{arom.}-C), 140.81 (N-C-CH^{arom.}-CH^{arom.}-CH^{arom.}-CH^{arom.}), 134.62 (N-C-CH^{arom.}-C), 131.52 (CH^{arom.}-CH^{arom.}-C-C≡C), 131.15 (CH^{arom.}-CH^{arom.}-C-C≡C), 130.89 (CH^{arom.}-CH^{arom.}-CH^{arom.}-C≡C), 130.14 ((CH₃)₂C-C-CH^{arom.}), 126.75 (CH^{arom.}-C-C≡C), 126.50 ((CH₃)₂C-C-CH^{arom.}), 125.35 (N-C-CH^{arom.}-CH^{arom.}-CH^{arom.}-CH^{arom.}), 120.77 ((CH₃)₂C-C-CH^{arom.}-CH^{arom.}), 114.19 (N-C-CH^{arom.}-CH^{arom.}-CH^{arom.}-CH^{arom.}), 90.89 (C≡C-CH₂), 80.51 (C≡C-CH₂), 79.47 ((CH₃)₃C), 36.09 ((CH₃)₂C-C), 31.38 ((CH₃)₂C-C), 28.93 (C≡C-CH₂-CH₂), 28.54 ((CH₃)₃C), 17.10 (C≡C-CH₂). The CH₂-NH signal was not observed.

MALDI-MS (DCTB, DCM) (m/z): [M-CH₃]⁺: calc. 451.2386, found 351.2351; [M]⁺: calc. 466.2620, found 466.2573.

8.6. Synthesis of *tert*-Butyl (5-(3-(9,9-dimethylacridin-10(9H)-yl)phenyl)pentyl)carbamate (**19**)



tert-Butyl (5-(3-(9,9-dimethylacridin-10(9H)-yl)phenyl)pent-4-yn-1-yl)carbamate (**18**; 313.7 mg, 0.672 mmol, 1.0 eq.) was dissolved in dry THF (3 mL) in a vial with septum and palladium on carbon

(10 wt%, 137.6 mg) was added under Ar counterflow. The solution was sparged with H₂ for 2 min and shaken in a shaker in H₂ atmosphere for 15 h. The product was obtained after flushing the solution through a short flash silica column (Hex: EtOAc = 1:1) as a colorless oil (336.2 mg, quant.).

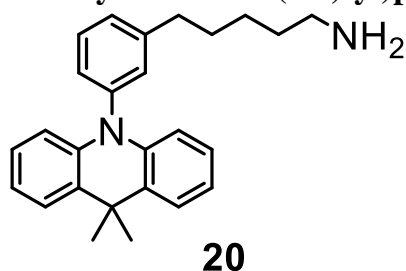
Chemical formula: C₃₁H₃₈N₂O₂

¹H NMR (300 MHz, CDCl₃) δ 7.52 (t, *J* = 7.6 Hz, 1H, CH^{arom.}-CH^{arom.}-C-CH₂), 7.48 – 7.42 (m, 2H, (CH₃)₂C-C-CH^{arom.}), 7.30 (d, *J* = 7.4 Hz, 1H, N-C-CH^{arom.}-CH^{arom.}-CH^{arom.}-C-CH₂), 7.15 (d, *J* = 8.5 Hz, 2H, N-C-CH^{arom.}-C-CH₂), 7.01 – 6.87 (m, 3H, N-C-CH^{arom.}-CH^{arom.}-CH^{arom.}-CH^{arom.}), 6.26 (d, *J* = 7.9 Hz, 2H, N-C-CH^{arom.}-CH^{arom.}-CH^{arom.}-CH^{arom.}), 4.49 (s, 1H, NH), 3.10 (d, *J* = 8.0 Hz, 2H, CH₂-NH), 2.69 (t, *J* = 7.7 Hz, 2H, CH^{arom.}-C-CH₂), 1.70 (s, 6H, (CH₃)₂C-C), 1.44 (s, 9H, (CH₃)₃C), 1.57 – 1.33 (m, 4H, CH₂-CH₂-CH₂-CH₂-CH₂-N), 1.25 (d, *J* = 11.3 Hz, 2H, CH₂-CH₂-CH₂-CH₂-CH₂-N).

¹³C NMR (75 MHz, CDCl₃) δ 156.11 (C=O), 145.78 (CH^{arom.}-C-CH₂), 141.21 (N-C-CH^{arom.}-C-CH₂), 141.07 (N-C-CH^{arom.}-CH^{arom.}-CH^{arom.}-CH^{arom.}), 131.11 (N-C-CH^{arom.}-C-CH₂), 130.74 (N-C-CH^{arom.}-CH^{arom.}-CH^{arom.}-C-CH₂), 130.01 ((CH₃)₂C-C-CH^{arom.}), 128.57 (N-C-CH^{arom.}-CH^{arom.}-CH^{arom.}-C-CH₂), 128.35 (CH^{arom.}-CH^{arom.}-C-CH₂), 126.46 ((CH₃)₂C-C-CH^{arom.}), 125.32 (N-C-CH^{arom.}-CH^{arom.}-CH^{arom.}-CH^{arom.}), 120.53 (N-C-CH^{arom.}-CH^{arom.}-CH^{arom.}-CH^{arom.}), 114.12 (N-C-CH^{arom.}-CH^{arom.}-CH^{arom.}-CH^{arom.}), 36.09 ((CH₃)₂C-C), 35.79 (CH^{arom.}-C-CH₂), 31.47 (CH^{arom.}-C-CH₂-CH₂), 31.11 ((CH₃)₂C-C), 30.09 (CH₂-CH₂-NH), 28.57 (CH₃)₃C, 26.58 (CH₂-CH₂-CH₂-NH). (CH₃)₃C-O and NH-C signals were not observed.

MALDI-MS (DCTB, DCM) (m/z): [M-CH₃]⁺: calc. 455.2699, found 455.2670; [M]⁺: calc. 470.2933, found 470.2891.

8.7. Synthesis of 5-(3-(9,9-Dimethylacridin-10(9H)-yl)phenyl)pentan-1-amine (20)



tert-Butyl (5-(3-(9,9-dimethylacridin-10(9H)-yl)phenyl)pentyl)carbamate (**19**; 226.3 mg, 0.480 mmol, 1.0 eq.) was dissolved in DCM:trifluoroacetic acid 1:1 (5 mL) under Ar atmosphere. The solution was stirred at r.t. for 1 h. After evaporating the solvent residue, the product was obtained as a light green oil (176.7 mg, quant.).

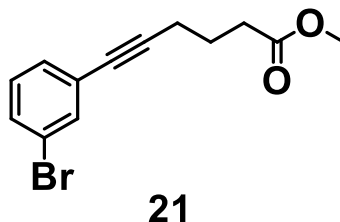
Chemical formula: C₂₆H₃₀N₂

¹H NMR (300 MHz, CDCl₃) δ 8.13 (s, 3H, NH), 7.49 (dd, *J* = 9.9, 6.1 Hz, 1H, N-C-CH^{arom.}-CH^{arom.}-CH^{arom.}-C-CH₂), 7.44 (d, *J* = 7.5 Hz, 2H, (CH₃)₂C-CH^{arom.}), 7.27 (d, *J* = 7.2 Hz, 1H, N-C-CH^{arom.}-CH^{arom.}-C-CH₂), 7.14 (d, *J* = 8.2 Hz, 1H, N-C-CH^{arom.}-CH^{arom.}-CH^{arom.}-C-CH₂), 7.10 (s, 1H, N-C-CH^{arom.}-C-CH₂), 7.02 – 6.84 (m, 4H, (CH₃)₂C-C-CH^{arom.}-CH^{arom.}-CH^{arom.}), 6.24 (d, *J* = 7.8 Hz, 2H, N-C-CH^{arom.}-CH^{arom.}-CH^{arom.}-CH^{arom.}), 2.95 (s, 2H, CH₂-NH₂), 2.75 – 2.56 (m, 4H, CH^{arom.}-C-CH₂), 1.69 (d, *J* = 5.2 Hz, 6H, CH₂-CH₂-CH₂-CH₂-NH₂, (CH₃)₂C-C), 1.45 (q, *J* = 7.8 Hz, 2H, CH₂-CH₂-CH₂-CH₂-NH₂).

¹³C NMR (75 MHz, CDCl₃) δ 145.26 (CH^{arom.}-C-CH₂), 141.29 (N-C-CH^{arom.}-C-CH₂), 141.04 (N-C-CH^{arom.}-CH^{arom.}-CH^{arom.}-CH^{arom.}), 131.07 (N-C-CH^{arom.}-C-CH₂), 130.83 (CH^{arom.}-CH^{arom.}-C-CH₂), 130.03 ((CH₃)₂C-C-CH^{arom.}), 128.77 (N-C-CH^{arom.}-CH^{arom.}-CH^{arom.}-C-CH₂), 128.29 (CH^{arom.}-CH^{arom.}-C-CH₂), 126.47 ((CH₃)₂C-C-CH^{arom.}), 125.32 (N-C-CH^{arom.}-CH^{arom.}-CH^{arom.}-CH^{arom.}), 120.58 ((CH₃)₂C-C-CH^{arom.}-CH^{arom.}), 114.09 (N-C-CH^{arom.}-CH^{arom.}-CH^{arom.}-CH^{arom.}), 39.96 (CH₂-NH₂), 36.09 ((CH₃)₂C-C), 35.52 (CH^{arom.}-C-CH₂), 31.43 ((CH₃)₂C-C), 30.75 (CH^{arom.}-C-CH₂-CH₂), 27.59 (CH₂-CH₂-NH₂), 26.19 (CH₂-CH₂-CH₂-NH₂).

MALDI-MS (DCTB, DCM) (m/z): $[M-CH_3]^+$: calc. 355.2174, found 355.2113; $[M]^+$: calc. 371.2487, found 371.2425.

8.8. Synthesis of Methyl-6-(3-bromophenyl)hex-5-ynoate (**21**)



The modified procedure based on literature was carried out.^[158,159] 1-Bromo-3 iodobenzene (4.490 g, 8.09 mmol, 2.0 eq.) and $PdCl_2(PPh_3)_2$ (231 mg, 0.33 mmol, 0.04 eq.) were dissolved in dry THF (20 mL) in an argon atmosphere in a Schlenk flask (flask 1). The solution was sparged with argon for 3 min. In a separate Schlenk flask CuI (308 mg, 1.62 mmol, 0.2 eq.) and methyl-5-hexynoate (**13**; 1.021 g, 8.09 mmol, 1.0 eq.) were dissolved in dry THF (20mL) and triethylamine (3.22 g, 31.82 mmol, 3.9 eq.) were added (flask 2). After sparging the second flask with argon for 3 min the solution was cooled to 0 °C with an ice bath and flask 1 was added under Ar counterflow. The combined solution was allowed to heat to r.t. and stirred at r.t. overnight (16 h). Saturated NH_4Cl solution (50 mL) was added and the solution was stirred for 30 min. The solution was extracted with EtOAc (3x 50 mL). The combined organic fraction was washed with brine (50 mL), dried over $MgSO_4$ and the solvent was evaporated. The crude product was further purified by flash chromatography on silica gel (Hex:EtOAc = 20:1) and the desired product was obtained as a colorless oil (1.949 g, 6.93 mmol, 86 %).

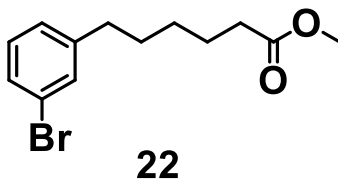
Chemical formula: $C_{13}H_{13}BrO_2$

R_f = 0.24 (SiO₂, Hex:EtOAc = 20:1).

¹H NMR (300 MHz, Chloroform-*d*) δ 7.54 (s, 1H, C-CH^{arom.}-C), 7.40 (d, J = 8.0 Hz, 1H, CH^{arom.}-BrC-CH^{arom.}-C), 7.31 (d, J = 7.6 Hz, 1H, CH^{arom.}-CH^{arom.}-C-C), 7.14 (t, J = 7.8 Hz, 1H, CH^{arom.}-CH^{arom.}-C-C), 3.69 (s, 3H, O-CH₃), 2.49 (q, 4H, C \equiv C-CH₂, CH₂-COOCH₃), 1.93 (p, 2H, CH₂-CH₂-CH₂).

^{13}C NMR (75 MHz, CDCl_3) δ 173.63 (C=O), 134.47 (Br-C- $\text{CH}^{\text{arom.}}$ -C), 130.97 (BrC- $\text{CH}^{\text{arom.}}$ - $\text{CH}^{\text{arom.}}$), 130.24 ($\text{CH}^{\text{arom.}}$ - $\text{CH}^{\text{arom.}}$ -C-C), 129.76 ($\text{CH}^{\text{arom.}}$ - $\text{CH}^{\text{arom.}}$ - $\text{CH}^{\text{arom.}}$), 125.85 (C-C \equiv C), 122.13 (C-Br), 90.53 (C \equiv C- CH_2), 80.17 (C-C \equiv C), 51.74 (CH_3), 32.96 (CH_2 -COO CH_3), 23.87 (C \equiv C- CH_2 - CH_2), 18.95 (C \equiv C- CH_2).

8.9. Synthesis of Methyl 6-(3-bromophenyl)hexanoate (22)



Raney®-Nickel slurry in water (414 mg) was transferred into a 40 mL vial with a septum cap (vial 1) and the vial was flushed with argon for 3 min. In a separate vial with a septum cap (vial 2) methyl-6-(3-bromophenyl)hex-5-ynoate (**21**; 543 mg, 3.63 mmol, 1.0 eq.) was dissolved in dry THF (5 mL) and sparged with argon for 3 min. The solution in vial 2 was added to the Raney®-Nickel catalyst via a syringe. The solution was sparged for 1 min with hydrogen gas. The vial was mounted with a balloon of H_2 and placed on a shaker overnight (15.5 h). The solution was filtered through a silica plug (Hex:EtOAc = 10:1) and the solvent was evaporated under reduced pressure. The pure product was obtained without further purification as colorless oil (536 mg, 1.88 mmol, 97 %)

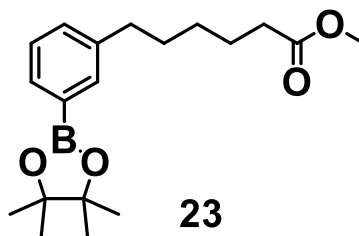
Chemical formula: $\text{C}_{13}\text{H}_{17}\text{BrO}_2$

^1H NMR (300 MHz, Chloroform-*d*) δ 7.38 – 7.19 (m, 2H, BrC- $\text{CH}^{\text{arom.}}$ -C, BrC- $\text{CH}^{\text{arom.}}$ - $\text{CH}^{\text{arom.}}$), 7.21 – 6.89 (m, 2H, CH_2 -C- $\text{CH}^{\text{arom.}}$ - $\text{CH}^{\text{arom.}}$), 3.65 (s, 3H, CH_3), 2.58 (t, $J = 7.9$ Hz, 2H, CH_2 -C- $\text{CH}^{\text{arom.}}$), 2.30 (t, $J = 7.5$ Hz, 2H, CH_2 -COO CH_3), 1.79 – 1.50 (m, 4H, CH_2 - CH_2 - CH_2 - CH_2 - CH_2), 1.48 – 1.18 (m, 2H, CH_2 - CH_2 - CH_2 - CH_2 - CH_2).

^{13}C NMR (75 MHz, CDCl_3) δ 174.25 (C=O), 144.96 ($\text{CH}^{\text{arom.}}$ -C- CH_2), 131.54 (BrC- $\text{CH}^{\text{arom.}}$ -C), 129.96 (BrC- $\text{CH}^{\text{arom.}}$ - $\text{CH}^{\text{arom.}}$), 128.94 (BrC- $\text{CH}^{\text{arom.}}$ - $\text{CH}^{\text{arom.}}$), 127.18 ($\text{CH}^{\text{arom.}}$ - $\text{CH}^{\text{arom.}}$ -C- CH_2), 122.49 (BrC),

51.61 (CH₃), 35.47 (CH^{arom.}-C-CH₂), 34.06 (CH₂-COOCH₃), 30.95 (CH^{arom.}-C-CH₂-CH₂), 28.74 (CH₂-CH₂-CH₂-CH₂), 24.84 (CH₂-CH₂-COOCH₃).

8.10. Synthesis of Methyl 6-(3-(4,4,5,5-tetramethyl-1,3,2-dioxaborolan-2-yl)phenyl)hexanoate (23)



The modified procedure based on literature was carried out.^[160] Methyl 6-(3-bromophenyl)hexanoate (**22**; 897 mg, 3.15 mmol, 1.0 eq.), 4,4,4',4',5,5,5',5'-octamethyl-2,2'-bi-1,3,2-dioxaborolane (982 mg, 3.88 mmol, 1.2), [1,1'-bis(diphenylphosphino)ferrocene]palladium(II) dichloride dichloromethane adduct (78 mg, 0.11 mmol, 0.03 eq.) and potassium acetate (890 mg, 9.07 mmol, 2.9 eq.) were dissolved in dry dioxane (10 mL) under argon atmosphere. The solution was sparged with argon for 3 min. The solution was stirred at 80 °C over the weekend (52.5 h). DI water was added (50 mL) and the solution was extracted with EtOAc (3x 50 mL). The combined organic fractions were washed with brine (50 mL), dried over MgSO₄ and the solvent was evaporated under reduced pressure. The residue was further purified with a silica plug (Hex:EtOAc = 5:1) and subsequent flash chromatography on silica gel (Hex:EtOAc = 20:1). The pure product was obtained as colorless oil (824 mg, 2.48 mmol, 79 %).

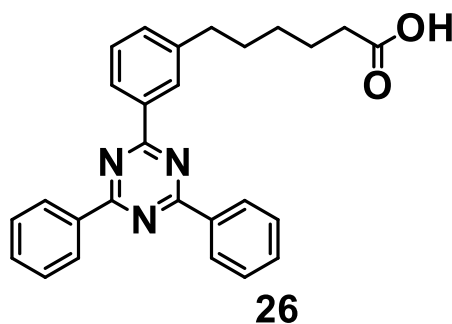
Chemical formula: C₁₉H₂₉BO₄

R_f = 0.35 (SiO₂, Hex:EtOAc = 20:1).

¹H NMR (300 MHz, Chloroform-*d*) δ 7.60 – 7.51 (m, 2H, CH^{arom.}-CB-CH^{arom.}), 7.26 – 7.15 (m, 2H, CH^{arom.}-CH^{arom.}-C-CH₂), 3.59 (s, 3H, O-CH₃), 2.54 (t, *J* = 7.8 Hz, 2H, CH^{arom.}-C-CH₂), 2.23 (t, *J* = 7.5 Hz, 2H, CH₂-COOCH₃), 1.66 – 1.46 (m, 4H, CH₂-CH₂-CH₂-CH₂-CH₂), 1.36 – 1.30 (m, 2H, CH₂-CH₂-CH₂-CH₂-CH₂), 1.28 (s, 12H, C(CH₃)₂).

^{13}C NMR (75 MHz, CDCl_3) δ 174.36 (C=O), 141.93 ($\text{CH}^{\text{arom.}}\text{-C-CH}_2$), 134.85 (C- $\text{CH}^{\text{arom.}}\text{-C}$), 132.34 (B-C- $\text{CH}^{\text{arom.}}\text{-CH}^{\text{arom.}}$), 131.52 ($\text{CH}^{\text{arom.}}\text{-CH}^{\text{arom.}}\text{-C-CH}_2$), 127.85 ($\text{CH}^{\text{arom.}}\text{-CH}^{\text{arom.}}\text{-CH}^{\text{arom.}}$), 83.86 ($\text{C}(\text{CH}_3)_2$), 51.60 (COOCH_3), 35.82 ($\text{CH}^{\text{arom.}}\text{-C-CH}_2$), 34.16 ($\text{CH}_2\text{-COOCH}_3$), 31.35 ($\text{CH}^{\text{arom.}}\text{-C-CH}_2\text{-CH}_2$), 29.00 ($\text{CH}_2\text{-CH}_2\text{-CH}_2\text{-CH}_2\text{-CH}_2$), 25.01 ($\text{C}(\text{CH}_3)_2$), 24.96 ($\text{CH}_2\text{-CH}_2\text{-COOCH}_3$). The C-B signal was not detected.

8.11. Synthesis of 6-(3-(4,6-Diphenyl-1,3,5-triazin-2-yl)phenyl)hexanoic acid (26)



The modified procedure based on literature was carried out.^[59] Methyl 6-(3-(4,4,5,5-tetramethyl-1,3,2-dioxaborolan-2-yl)phenyl)hexanoate (**23**; 374 mg, 1.12 mmol, 1.0 eq.), 2-chloro-4,6-diphenyl-1,3,5-triazine (**24**; 331 mg, 1.24 mmol, 1.1 eq.), Na_2CO_3 (1.79 mg, 16.87 mmol, 15.0 eq.) and $\text{Pd}(\text{PPh}_3)_4$ (65 mg, 0.06 mmol, 0.05 eq.) were dissolved/ dispersed in a mixture of degassed toluene (4 mL), degassed EtOH (1 mL) and water (1 mL) in a pressure tube under argon atmosphere. The solution was stirred in the dark at 120 °C for 42 h. After adding water (50 mL), the solution was extracted with EtOAc (3x 50 mL). The combined organic phases were washed with brine, dried over MgSO_4 and the solvent was evaporated under reduced pressure. The residual yellow oil was purified by flash chromatography on silica gel (Hex:EtOAc = 20:1). The partially hydrolyzed ester obtained was added to a solution of LiOH (138 mg, 5.75 mmol, 5.1 eq.) in THF:water (1:1, 20 mL) and stirred at r.t. for 44 h and conversion was monitored via TLC. The solution was washed with saturated NH_4Cl solution (100 mL) and extracted with EtOAc (3x 100 mL). The combined organic phases was dried over MgSO_4 and the

solvent was evaporated under reduced pressure. The product was obtained as a colorless solid (81 mg, 0.19 mmol, 17 %).

Chemical formula: C₂₇H₂₅N₃O₂

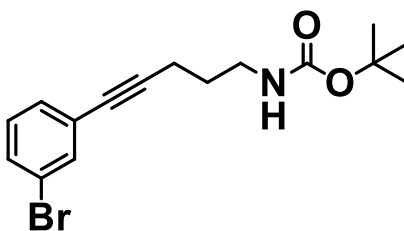
R_f (intermediate) = 0.21 (SiO₂, Hex:EtOAc = 20:1).

¹H NMR (300 MHz, Chloroform-*d*) δ 10.27 (s br, 1H, COOH), 8.78 (dd, *J* = 7.5, 2.2 Hz, 4H, N-C-C-CH^{arom.}, Ph), 8.61 (d, *J* = 7.7 Hz, 1H, CH^{arom.}-C-CH^{arom.}-C-CH₂), 8.56 (s, 1H, C-CH^{arom.}-C-CH₂), 7.67 – 7.54 (m, 6H, N-C-C-CH^{arom.}, Ph-CH^{arom.}, Ph-CH^{arom.}, Ph), 7.49 (t, *J* = 7.5 Hz, 1H, CH^{arom.}-CH^{arom.}-C-CH₂), 7.43 (d, *J* = 7.6 Hz, 1H, CH^{arom.}-CH^{arom.}-C-CH₂), 2.80 (t, *J* = 7.7 Hz, 2H, CH^{arom.}-C-CH₂), 2.39 (t, *J* = 7.4 Hz, 2H, CH₂-COOCH₃), 1.84 – 1.64 (m, 4H, CH₂-CH₂-CH₂-CH₂-CH₂), 1.56 – 1.38 (m, 2H, CH₂-CH₂-CH₂-CH₂).

¹³C NMR (75 MHz, CDCl₃) δ 178.44 (C=O), 171.98 (N-C-C-CH^{arom.}-C), 171.78 (N-C-C^{Ph}), 143.08 (CH^{arom.}-C-CH₂), 136.44 (N-C-C), 132.82 (CH^{arom.}-C-CH₂), 132.63 (N-C-C-CH^{arom.}, Ph-CH^{arom.}, Ph-CH^{arom.}, Ph), 129.12 (N-C-C-CH^{arom.}, Ph), 128.96 (C-CH^{arom.}-C-CH₂), 128.79 (CH^{arom.}-CH^{arom.}-C-CH₂, N-C-C-CH^{arom.}, Ph-CH^{arom.}, Ph), 126.76 (CH^{arom.}-CH^{arom.}-CH^{arom.}-C-CH₂), 35.91 (CH^{arom.}-C-CH₂), 33.83 (CH₂-COOH), 31.30 (CH^{arom.}-C-CH₂-CH₂), 28.86 (CH₂-CH₂-CH₂-CH₂-CH₂), 24.70 (CH₂-CH₂-COOH).

MALDI-MS (DCTB, DCM) (m/z): [M+H]⁺: calc. 424.2025, found 424.2025.

8.12. Synthesis of *tert*-Butyl (5-(3-bromophenyl)pent-4-yn-1-yl)carbamate (27)



27

The modified procedure based on literature was carried out.^[158,159] 1-Bromo-3 iodobenzene (652.0 mg, 2.305 mmol, 2.1 eq.) and PdCl₂(PPh₃)₂ (37.2 mg, 0.053 mmol, 0.05 eq.) were dissolved in dry THF

(5 mL) in an argon atmosphere in a Schlenk flask (flask 1). The solution was sparged with argon for 3 min. In a separate Schlenk flask CuI (43.7 mg, 0.230 mmol, 0.21 eq.) and tert-butyl pent-4-yn-1-ylcarbamate (**17**; 199.5 mg, 1.089 mmol, 1.0 eq.) were dissolved in dry THF (5 mL) and triethylamine (470 mg, 4.645 mmol, 4.27 eq.) were added (flask 2). After sparging the second flask with argon for 3 min the solution was cooled to 0 °C with an ice bath and flask 1 was added under Ar counterflow. The combined solution was allowed to heat to r.t. and stirred at r.t. overnight (17 h). Saturated NH₄Cl solution (50 mL) was added and the solution was stirred for 30 min. The solution was extracted with EtOAc (3x 50 mL). The combined organic fraction was washed with brine (50 mL), dried over MgSO₄ and the solvent was evaporated. The crude product was further purified by flash chromatography on silica gel (Hex:EtOAc = 10:1) and the desired product was obtained as a yellow-orange solid (378.3 mg, 1.119 mmol, quant.).

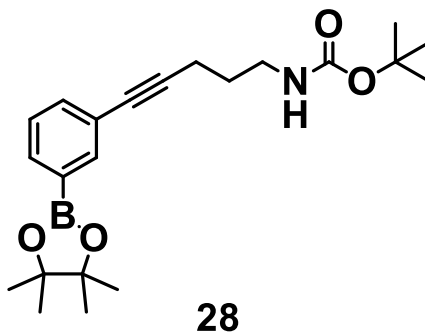
Chemical formula: C₁₆H₂₀BrNO₂

R_f = 0.24 (SiO₂, Hex:EtOAc = 10:1).

¹H NMR (300 MHz, CDCl₃) δ 7.54 (s, 1H, Br-C-CH^{arom.}-C), 7.40 (d, *J* = 8.0 Hz, 1H, Br-C-CH^{arom.}-CH^{arom.}), 7.31 (d, *J* = 7.8 Hz, 1H, CH^{arom.}-C-C≡C), 7.14 (t, *J* = 7.8 Hz, 1H, CH^{arom.}-CH^{arom.}-C-C≡C), 4.70 (s, 1H, NH), 3.28 (q, *J* = 6.6 Hz, 2H, CH₂-NH), 2.46 (t, *J* = 7.0 Hz, 2H, C≡C-CH₂), 1.79 (tt, *J* = 6.9, 6.8 Hz, 2H, C≡C-CH₂-CH₂), 1.45 (s, 9H, (CH₃)₂C).

¹³C NMR (75 MHz, CDCl₃) δ 156.08 (C=O), 134.48 (Br-C-CH^{arom.}-C), 131.02 (Br-C-CH^{arom.}), 130.27 (CH^{arom.}-C-C≡C), 129.78 (CH^{arom.}-CH^{arom.}-C-C≡C), 125.85 (C-C≡C), 122.17 (Br-C), 90.79 (C-C≡C), 80.04 ((CH₃)₃C), 40.02 (CH₂-NH), 28.88 (CH₂-CH₂-NH), 28.56 ((CH₃)₃C), 17.11 (C≡C-CH₂). The C≡C-CH₂ signal was not observed.

8.13. Synthesis of *tert*-Butyl (5-(3-(4,4,5,5-tetramethyl-1,3,2-dioxaborolan-2-yl)phenyl)pent-4-yn-1-yl)carbamate (**28**)



The modified procedure based on literature was carried out.^[160] *tert*-Butyl (5-(3-bromophenyl)pent-4-yn-1-yl)carbamate (**27**; 398.4 mg, 1.178 mmol, 1.0 eq.), Bis(pinacolato)diboron (560.5 mg, 2.216 mmol, 1.9 eq.), KOAc (344.3 mg, 3.508 mmol, 3.0 eq.) and 1,1'-Bis(diphenylphosphino)ferrocene] (54.0 mg, 0.074 mmol, 0.06 eq.) were dissolved in dry dioxane (10 mL). The solution was stirred at 80 °C for 43 h. The solution was cooled to r.t. and water was added (200 mL). The solution was extracted with EtOAc (3 x 100 mL) and the organic phase was washed with brine, dried over MgSO₄ and the solvent was evaporated under reduced pressure. The crude product was further purified via flash chromatography on silica gel (Hex:EtOAc = 5:1). The pure product was obtained as a light yellow oil (372.0 mg, 0.965 mmol, 82 %).

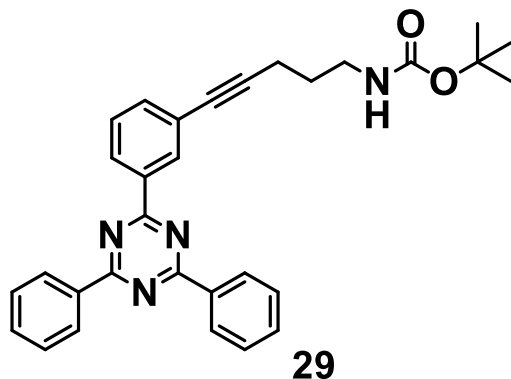
Chemical formula: C₂₂H₃₂BNO₄

R_f = 0.29 (SiO₂, Hex:EtOAc = 5:1).

¹H NMR (300 MHz, CDCl₃) δ 7.85 (s, 1H, B-C-CH^{arom.}-C), 7.70 (d, *J* = 7.5 Hz, 1H, B-C-CH^{arom.}-CH^{arom.}), 7.47 (d, *J* = 7.6 Hz, 1H, CH^{arom.}-C-C≡C), 7.29 (d, *J* = 7.6 Hz, 1H, B-C-CH^{arom.}-CH^{arom.}), 4.73 (s, 1H, NH), 3.29 (q, *J* = 6.5 Hz, 2H, CH₂-NH), 2.45 (t, *J* = 6.9 Hz, 2H, C≡C-CH₂), 1.78 (tt, *J* = 7.0, 6.9 Hz, 2H, C≡C-CH₂-CH₂), 1.45 (s, 9H, (CH₃)₃C), 1.34 (s, 12H, B-O-C(CH₂)₂).

¹³C NMR (75 MHz, CDCl₃) δ 138.14 (B-C-CH^{arom.}-C), 134.25 (CH^{arom.}-CH^{arom.}-C-C≡C), 133.97 (B-C-CH^{arom.}-CH^{arom.}), 127.74 (B-C-CH^{arom.}-CH^{arom.}), 123.35 (CH^{arom.}-C-C≡C), 89.13 (CH^{arom.}-C-C≡C), 84.08 (B-O-C(CH₃)₂), 81.39 ((CH₃)₃C), 40.04 (CH₂-NH), 28.96 (CH₂-CH₂-NH), 28.57 ((CH₃)₃C), 25.01 (B-O-C(CH₃)₂), 17.10 (C≡C-CH₂). The C≡C-CH₂ and C-B were not observed.

8.14. Synthesis of *tert*-Butyl (5-(3-(4,6-diphenyl-1,3,5-triazin-2-yl)phenyl)pent-4-yn-1-yl)carbamate (**29**)



The modified procedure based on literature was carried out.^[59] *tert*-Butyl (5-(3-(4,4,5,5-tetramethyl-1,3,2-dioxaborolan-2-yl)phenyl)pent-4-yn-1-yl)carbamate (**28**; 315.6 mg, 0.819 mmol, 1.0 eq.), 2-chloro-4,6-diphenyl-1,3,5-triazine (**24**; 241.5 mg, 0.902 mmol, 1.1 eq.), Na₂CO₃ (1.307 g, 12.337 mmol, 15.1 eq.) and Pd(PPh₃)₄ (53.9 mg, 0.047 mmol, 0.06 eq.) were dissolved in a mixture of degassed toluene (2 mL), EtOH (1 mL) and water (1 mL) under Ar atmosphere in a pressure tube. The solution was stirred at 120 °C for 140 h. The solution was allowed to cool to r.t. and after adding brine (100 mL), the solution was extracted with EtOAc (3x100 mL). The combined organic phases were washed with brine, dried over MgSO₄ and the solvents were evaporated under reduced pressure. The crude product was further purified via flash chromatography on silica gel (Hex:EtOAc = 5:1) and a subsequent preparative size exclusion chromatography in CHCl₃. The pure product was obtained as a colorless solid (179.16 mg, 0.365 mmol, 45 %).

Chemical formula: C₃₁H₃₀N₄O₂

R_f = 0.28 (SiO₂, Hex:EtOAc = 5:1).

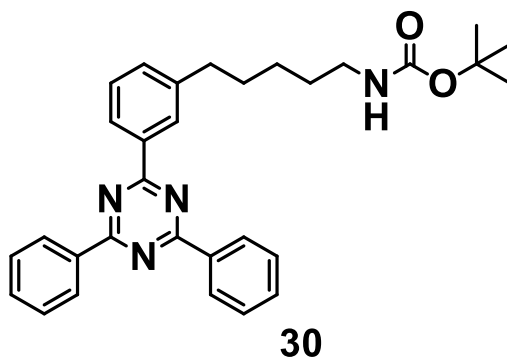
¹H NMR (300 MHz, CDCl₃) δ 8.87 – 8.65 (m, 7H, N-C-C-CH^{arom.}), 7.74 – 7.43 (m, 9H, CH^{arom.}-CH^{arom.}-C-C≡C), 4.71 (s, 1H, NH), 3.34 (q, *J* = 6.5 Hz, 2H, CH₂-NH), 2.55 (t, *J* = 7.0 Hz, 2H, C≡C-CH₂), 1.87 (tt, *J* = 7.0, 6.9 Hz, 2H, C≡C-CH₂-CH₂), 1.47 (s, 9H, (CH₃)₃C).

¹³C NMR (75 MHz, CDCl₃) δ 171.87 (N-C-Ph), 171.21 (N-C-C-CH^{arom.}-C), 156.13 (C=O), 136.56 (N-C-C-CH^{arom.}-C), 136.27 (N-C-C^{Ph}), 135.63 (N-C-C-CH^{arom.}-CH^{arom.}-CH^{arom.}-CH^{arom.}), 132.73 (CH^{arom.}-

$\text{CH}^{\text{arom.}}-\text{C}-\text{C}\equiv\text{C}$), 132.05 (N-C-C- $\text{CH}^{\text{arom.}}$ -C), 129.15 (N-C-C- $\text{CH}^{\text{arom.}}$ - $\text{CH}^{\text{arom.}}$ - $\text{CH}^{\text{arom.}}$ - $\text{CH}^{\text{arom.}}$), 128.81 (N-C-C- $\text{CH}^{\text{arom.}}$ - $\text{CH}^{\text{arom.}}$ - $\text{CH}^{\text{arom.}}$ - $\text{CH}^{\text{arom.}}$), 128.74 ($\text{CH}^{\text{arom.}}$ - $\text{CH}^{\text{arom.}}$ -C-C $\equiv\text{C}$), 128.41 ($\text{CH}^{\text{arom.}}$ - $\text{CH}^{\text{arom.}}$ - $\text{CH}^{\text{arom.}}$ -C-C $\equiv\text{C}$), 124.40 ($\text{CH}^{\text{arom.}}$ -C-C $\equiv\text{C}$), 89.98 ($\text{CH}^{\text{arom.}}$ -C-C $\equiv\text{C}$), 81.12 ($(\text{CH}_3)_3\text{C}$), 40.10 ($\text{CH}_2\text{-NH}$), 28.58 ($(\text{CH}_3)_3\text{C}$, C $\equiv\text{C}-\text{CH}_2-\text{CH}_2$), 17.22 (C $\equiv\text{C}-\text{CH}_2$). The C $\equiv\text{C}-\text{CH}_2$ signal was not observed.

MALDI-MS (DCTB, DCM) (m/z): [M+H]⁺: calc. 491.2447, found 491.2475.

8.15. Synthesis of *tert*-Butyl (5-(3-(4,6-diphenyl-1,3,5-triazin-2-yl)phenyl)pentyl)carbamate (**30**)



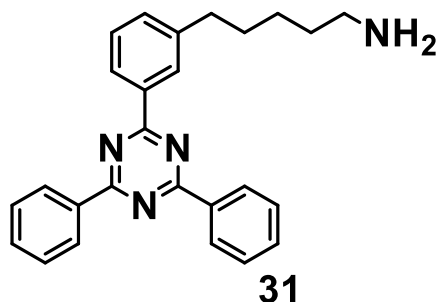
tert-Butyl (5-(3-(4,6-diphenyl-1,3,5-triazin-2-yl)phenyl)pent-4-yn-1-yl)carbamate (**29**; 148.6 mg, 0.303 mmol, 1.0 eq.) was dissolved in dry THF (3 mL) in a vial with septum and palladium on carbon (10 wt%, mg) was added under Ar counterflow. The solution was sparged with H₂ for 2 min and shaken in a shaker in H₂ atmosphere for 15 h. The product was obtained after flushing the solution through a short flash silica column (EtOAc) as a colorless solid (150.3 mg, quant.).

Chemical formula: C₃₁H₃₄N₄O₂

¹H NMR (300 MHz, CDCl₃) δ 8.86 – 8.72 (m, 4H, N-C-C- $\text{CH}^{\text{arom.}}$ - $\text{CH}^{\text{arom.}}$ - $\text{CH}^{\text{arom.}}$ - $\text{CH}^{\text{arom.}}$), 8.61 (d, *J* = 7.7 Hz, 1H, $\text{CH}^{\text{arom.}}$ - $\text{CH}^{\text{arom.}}$ - $\text{CH}^{\text{arom.}}$ -C-CH₂), 8.56 (s, 1H, N-C- $\text{CH}^{\text{arom.}}$ -C-CH₂), 7.60 (d, *J* = 6.9 Hz, 6H, N-C-C- $\text{CH}^{\text{arom.}}$ - $\text{CH}^{\text{arom.}}$ - $\text{CH}^{\text{arom.}}$ - $\text{CH}^{\text{arom.}}$), 7.49 (t, *J* = 7.6 Hz, 1H, $\text{CH}^{\text{arom.}}$ - $\text{CH}^{\text{arom.}}$ -C-CH₂), 7.42 (d, *J* = 7.5 Hz, 1H, $\text{CH}^{\text{arom.}}$ - $\text{CH}^{\text{arom.}}$ -C-CH₂), 4.51 (s, 1H, NH), 3.13 (d, *J* = 8.4 Hz, 2H, CH₂-NH), 2.79 (t, *J* = 7.7 Hz, 2H, $\text{CH}^{\text{arom.}}$ -C-CH₂), 1.76 (p, *J* = 7.6 Hz, 2H, $\text{CH}^{\text{arom.}}$ -C-CH₂-CH₂), 1.55 (q, *J* = 7.3 Hz, 3H, CH₂-CH₂-NH), 1.44 (br s, 11H, (CH₃)₃, CH₂-CH₂-CH₂-NH).

^{13}C NMR (75 MHz, CDCl_3) δ 171.98 (N-C-C- $\text{CH}^{\text{arom.}}$ -C), 171.77 (N-C-Ph), 143.13 ($\text{CH}^{\text{arom.}}$ -C- CH_2), 136.44 (N-C-C), 132.83 ($\text{CH}^{\text{arom.}}$ - $\text{CH}^{\text{arom.}}$ -C- CH_2), 132.63 (N-C-C- $\text{CH}^{\text{arom.}}$ - $\text{CH}^{\text{arom.}}$ - $\text{CH}^{\text{arom.}}$ - $\text{CH}^{\text{arom.}}$), 129.12 (N-C-C- $\text{CH}^{\text{arom.}}$, Ph), 128.96 (N-C- $\text{CH}^{\text{arom.}}$ -C- CH_2), 128.79 ($\text{CH}^{\text{arom.}}$ - $\text{CH}^{\text{arom.}}$ -C- CH_2 , N-C-C- $\text{CH}^{\text{arom.}}$ - $\text{CH}^{\text{arom.}}$ - $\text{CH}^{\text{arom.}}$ - $\text{CH}^{\text{arom.}}$), 126.73 ($\text{CH}^{\text{arom.}}$ - $\text{CH}^{\text{arom.}}$ - $\text{CH}^{\text{arom.}}$ -C- CH_2), 36.07 ($\text{CH}^{\text{arom.}}$ -C- CH_2), 31.36 ($\text{CH}^{\text{arom.}}$ -C- CH_2 - CH_2), 30.18 (CH_2 - CH_2 -NH), 28.57 ($(\text{CH}_3)_3\text{C}$), 26.65 (CH_2 - CH_2 - CH_2 -NH). The CH_2 -NH and $(\text{CH}_3)_3\text{C}$ signals were not detected.

8.16. Synthesis of 5-(3-(4,6-Diphenyl-1,3,5-triazin-2-yl)phenyl)pentan-1-amine (31)



tert-Butyl (5-(3-(4,6-diphenyl-1,3,5-triazin-2-yl)phenyl)pentyl)carbamate (**30**; 134.8 mg, 0.272 mmol, 1.0 eq.) was dissolved in DCM:trifluoroacetic acid 1:1 (5 mL) under Ar atmosphere. The solution was stirred at r.t. for 1 h. After evaporating the solvent residue, the product was obtained as a colorless solid (107.4 mg, quant.).

Chemical formula: $\text{C}_{26}\text{H}_{26}\text{N}_4$

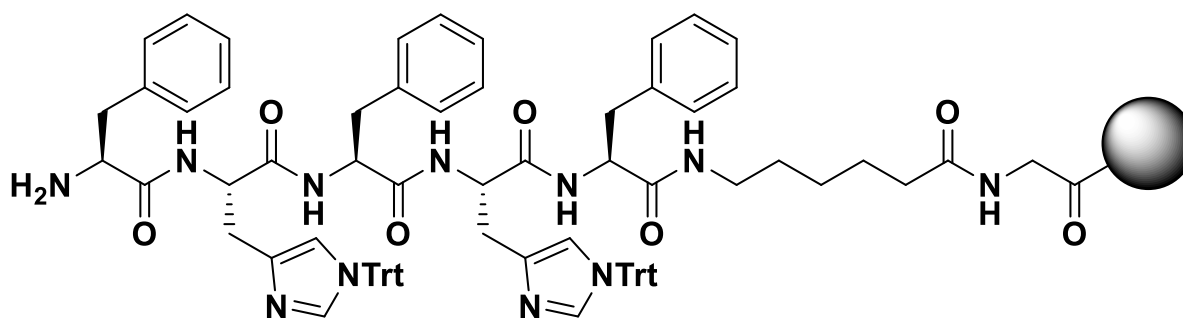
^1H NMR (300 MHz, CDCl_3) δ 8.86 – 8.63 (m, 4H, N-C-C- $\text{CH}^{\text{arom.}}$ - $\text{CH}^{\text{arom.}}$ - $\text{CH}^{\text{arom.}}$ - $\text{CH}^{\text{arom.}}$), 8.55 (d, J = 7.7 Hz, 1H, $\text{CH}^{\text{arom.}}$ - $\text{CH}^{\text{arom.}}$ - $\text{CH}^{\text{arom.}}$ -C- CH_2), 8.48 (s, 1H, N-C-C- $\text{CH}^{\text{arom.}}$ -C), 7.56 (d, J = 7.4 Hz, 8H, N-C-C- $\text{CH}^{\text{arom.}}$ - $\text{CH}^{\text{arom.}}$ - $\text{CH}^{\text{arom.}}$ - $\text{CH}^{\text{arom.}}$, NH_2), 7.43 (t, J = 7.6 Hz, 1H, $\text{CH}^{\text{arom.}}$ - $\text{CH}^{\text{arom.}}$ -C- CH_2), 7.34 (d, J = 7.5 Hz, 1H, $\text{CH}^{\text{arom.}}$ - $\text{CH}^{\text{arom.}}$ -C- CH_2), 3.00 (s, 2H, CH_2 - NH_2), 2.73 (t, J = 7.5 Hz, 2H, $\text{CH}^{\text{arom.}}$ -C- CH_2), 1.72 (s, 4H, CH_2 - CH_2 - CH_2 - CH_2 - NH_2), 1.45 (s, 2H, CH_2 - CH_2 - CH_2 - CH_2 - NH_2).

^{13}C NMR (75 MHz, CDCl_3) δ 171.80 (N-C-C- $\text{CH}^{\text{arom.}}$ -C), 171.73 (N-C-Ph), 142.44 ($\text{CH}^{\text{arom.}}$ -C- CH_2), 136.38 (N-C-C- $\text{CH}^{\text{arom.}}$ -C), 136.29 (N-C- C^{Ph}), 132.71 ($\text{CH}^{\text{arom.}}$ - $\text{CH}^{\text{arom.}}$ -C- CH_2), 132.67 (N-C-C-

$\text{CH}^{\text{arom.}}-\text{CH}^{\text{arom.}}-\text{CH}^{\text{arom.}}-\text{CH}^{\text{arom.}}$), 129.11 ($\text{N}-\text{C}-\text{C}-\text{CH}^{\text{arom.}}-\text{CH}^{\text{arom.}}-\text{CH}^{\text{arom.}}-\text{CH}^{\text{arom.}}$), 128.86 ($\text{N}-\text{C}-\text{C}-\text{CH}^{\text{arom.}}-\text{C}$), 128.82 ($\text{CH}^{\text{arom.}}-\text{CH}^{\text{arom.}}-\text{C}-\text{CH}_2$), 128.76 ($\text{N}-\text{C}-\text{C}-\text{CH}^{\text{arom.}}-\text{CH}^{\text{arom.}}-\text{CH}^{\text{arom.}}-\text{CH}^{\text{arom.}}$), 126.91 ($\text{CH}^{\text{arom.}}-\text{CH}^{\text{arom.}}-\text{CH}^{\text{arom.}}-\text{C}-\text{CH}_2$), 40.51 (CH_2-NH_2), 35.70 ($\text{CH}^{\text{arom.}}-\text{C}-\text{CH}_2$), 30.88 ($\text{CH}^{\text{arom.}}-\text{C}-\text{CH}_2-\text{CH}_2$), 27.54 ($\text{CH}_2-\text{CH}_2-\text{NH}_2$), 26.03 ($\text{CH}_2-\text{CH}_2-\text{CH}_2-\text{NH}_2$).

MALDI-MS (DCTB, DCM) (m/z): $[\text{M}+\text{H}]^+$: calc. 395.2236, found 395.2226.

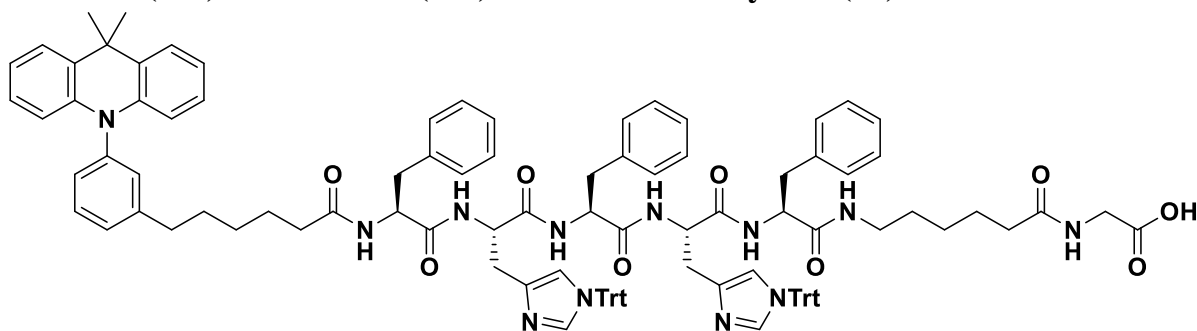
8.17. Synthesis of $\text{H}_2\text{N}-\text{L}-\text{Phe}-\text{L}-\text{His}(\text{Trt})-\text{L}-\text{Phe}-\text{L}-\text{His}(\text{Trt})-\text{L}-\text{Phe}-\text{Ahx}-[\text{L}-\text{Gly}]$ -resin (32)



32

Synthesis of the peptide-loaded resin was done according to SOP1 using of resin (2 g, 3.2 mmol, 1,0 eq.). The product was obtained as a pale yellow resin (6.01g, 3.04 mmol, 95 %)

8.18. Synthesis of 6-(3-(9,9-Dimethylacridin-10(9H)-yl)phenyl)hexanoyl-L-Phe-L-His(Trt)-L-Phe-L-His(Trt)-L-Phe-Ahx-L-Gly-OH (**33**)

**33**

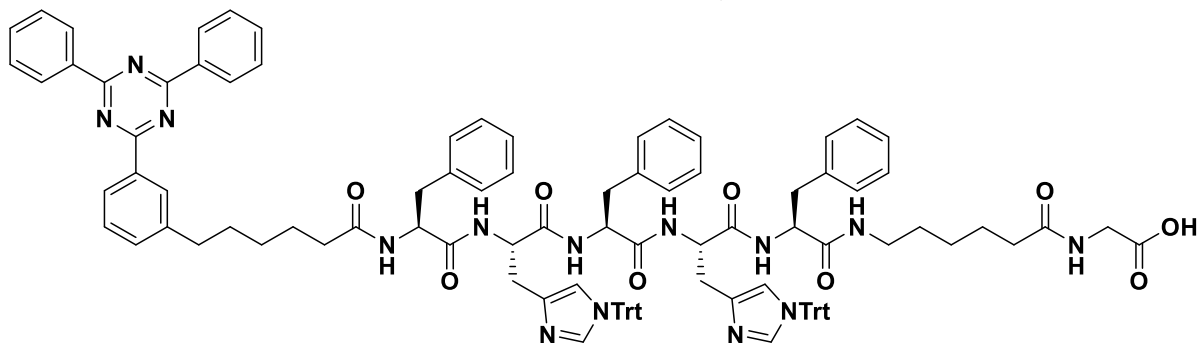
The donor functionalized peptide was synthesized according to SOP2 using **32** (148.4 mg, 75 μ mol, 1 eq.) and **16** (30 mg, 75 μ mol, 1 eq.). The product was obtained as a colorless solid (97.4 mg, 55 μ mol, 73 %).

Chemical formula: C₁₁₂H₁₁₂N₁₂O₉

¹H NMR (400 MHz, DMSO-*d*₆) δ 8.51 (s, 3H, (N-CH^{arom.}-NTrt)^{His}), 8.18 (s, 2H, O=C-NH), 8.03 (s, 2H, O=C-NH), 8.00 – 7.78 (m, 4H, O=C-NH), 7.57 (t, *J* = 7.8 Hz, 2H, N-C-CH^{arom.}-CH^{arom.}-CH^{arom.}-C-CH₂), 7.47 (dd, *J* = 7.6, 1.7 Hz, 2H, (CH₃)₂C-C-CH^{arom.}), 7.40 – 6.97 (m, 48H, CH^{arom., Phe, Trt}, CH^{arom.}-CH^{arom.}-C-CH^{arom.}-C-CH₂), 6.96 – 6.89 (m, 2H, (CH₃)₂C-C-CH^{arom.}-CH^{arom.}-CH^{arom.}-CH^{arom.}), 6.89 – 6.83 (m, 2H, (CH₃)₂C-C-CH^{arom.}-CH^{arom.}-CH^{arom.}-CH^{arom.}), 6.66 (s, 1H, (N-C-CH^{arom.}-NTrt)^{His}), 6.55 (s, 1H, (N-C-CH^{arom.}-NTrt)^{His}), 6.12 (dd, *J* = 8.1, 1.4 Hz, 2H, (CH₃)₂C-C-CH^{arom.}-CH^{arom.}-CH^{arom.}-CH^{arom.}), 4.48 – 4.27 (m, 8H, (O=C-CH-NH)^{Phe, His}), 3.68 (s, 2H, (N-CH₂-C=O)^{Gly}), 3.06 – 2.69 (m, 16H, CH₂^{His, Phe}, NH-CH₂-CH₂-CH₂), 2.63 (s, 1H, N-C-CH^{arom.}-C-CH₂), 2.04 (t, *J* = 7.3 Hz, 3H, CH₂-CH₂-C=O), 1.92 (d, *J* = 5.7 Hz, 3H, CH₂-CH₂-C=O), 1.60 (s, 5H, (CH₃)₂C), 1.49 – 1.42 (m, 3H, CH₂-CH₂-CH₂-CH₂-C=O), 1.42 – 1.36 (m, 2H, CH₂-CH₂-CH₂-CH₂-C=O), 1.34 – 1.18 (m, 7H, CH₂-CH₂-CH₂-CH₂-C=O), 1.15 – 1.02 (m, 12H, CH₂-CH₂-CH₂-C=O).

ESI-HRMS (MeOH, pos.) *m/z*: [M+H]⁺: calc. 1769.8748, found 1769.8691; [M+Na]⁺: calc. 1791.8573, found 1791.8508.

8.19. Synthesis of 6-(3-(4,6-Diphenyl-1,3,5-triazin-2-yl)phenyl)hexanoyl-L-Phe-L-His(Trt)-L-Phe-L-His(Trt)-L-Phe-Ahx-L-Gly-OH (34)



34

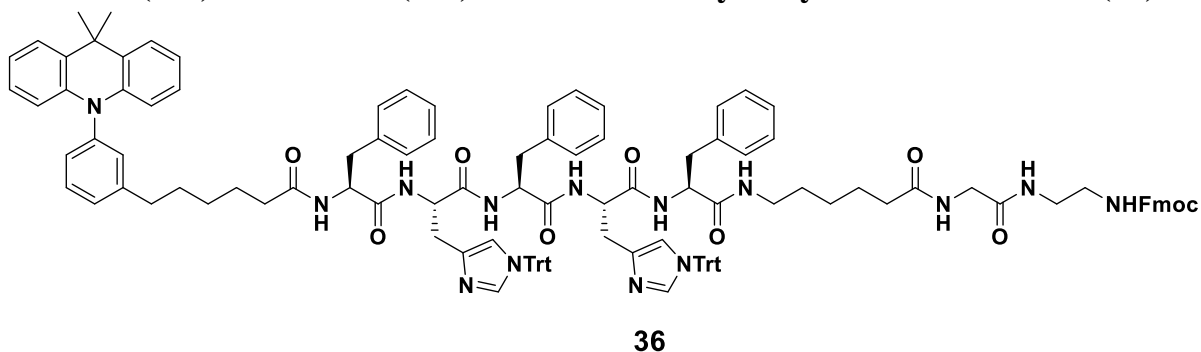
The donor functionalized peptide was synthesized according to SOP2 using **32** (59.4 mg, 30 μmol , 1 eq.) and **26** (13 mg, 30 μmol , 1 eq.). The product was obtained as a colorless solid (22.5 mg, 13 μmol , 42 %).

Chemical formula: $\text{C}_{112}\text{H}_{108}\text{N}_{14}\text{O}_9$

^1H NMR (400 MHz, DMSO- d_6) δ 8.79 – 8.69 (m, 3H, N-C-C- $\text{CH}^{\text{arom.}}$ - $\text{CH}^{\text{arom.}}$ - $\text{CH}^{\text{arom.}}$ - $\text{CH}^{\text{arom.}}$), 8.56 (dt, $J = 7.7, 1.5$ Hz, 1H, N-C-C- $\text{CH}^{\text{arom.}}$ - $\text{CH}^{\text{arom.}}$ - $\text{CH}^{\text{arom.}}$ -C- CH_2), 8.52 (s, 2H, N-C-C- $\text{CH}^{\text{arom.}}$ -C- CH_2 , (N- $\text{CH}^{\text{arom.}}$ -NTrt)^{His}), 8.17 (s, 1H, O=C-NH), 8.04 (s, 2H, O=C-NH), 7.95 (s, 3H, O=C-NH), 7.77 – 7.60 (m, 5H, N-C-C- $\text{CH}^{\text{arom.}}$ - $\text{CH}^{\text{arom.}}$ - $\text{CH}^{\text{arom.}}$ - $\text{CH}^{\text{arom.}}$), 7.55 (t, $J = 7.6$ Hz, 1H, N-C-C- $\text{CH}^{\text{arom.}}$ - $\text{CH}^{\text{arom.}}$ - $\text{CH}^{\text{arom.}}$ -C- CH_2), 7.52 – 7.45 (m, 1H, N-C-C- $\text{CH}^{\text{arom.}}$ - $\text{CH}^{\text{arom.}}$ - $\text{CH}^{\text{arom.}}$ -C- CH_2), 7.42 – 6.91 (m, 45H, $\text{CH}^{\text{arom., Phe, Trt}}$), 6.66 (s, 1H, (N-C- $\text{CH}^{\text{arom.}}$ -NTrt)^{His}), 6.55 (s, 1H, (N-C- $\text{CH}^{\text{arom.}}$ -NTrt)^{His}), 4.53 – 4.27 (m, 6H, (O=C- CH -NH)^{His, Phe}), 3.69 (d, $J = 5.7$ Hz, 3H, CH_2^{Gly}), 3.08 – 2.56 (m, 17H, $\text{CH}_2^{\text{His, Phe}}$, N-C-C- $\text{CH}^{\text{arom.}}$ -C- CH_2 , NH- CH_2 - CH_2 - CH_2), 2.10 – 2.01 (m, 2H, CH_2 - CH_2 - CH_2 -C=O), 2.01 – 1.88 (m, 2H, CH_2 - CH_2 - CH_2 -C=O), 1.60 – 1.47 (m, 2H, CH_2 - CH_2 - CH_2 - CH_2 -C=O), 1.46 – 1.29 (m, 4H, CH_2 - CH_2 - CH_2 - CH_2 -C=O), 1.29 – 1.18 (m, 3H, CH_2 - CH_2 - CH_2 - CH_2 -C=O), 1.18 – 1.07 (m, 6H, CH_2 - CH_2 - CH_2 - CH_2 -C=O).

ESI-HRMS (MeOH, pos.) m/z : [M+H]⁺: calc. 1793.8496, found 1793.8480; [M+Na]⁺: calc. 1815.8321, found 1815.8287.

8.20. Synthesis of 6-(3-(9,9-Dimethylacridin-10(9H)-yl)phenyl)hexanoyl-L-Phe-L-His(Trt)-L-Phe-L-His(Trt)-L-Phe-Ahx-L-Gly-Ethylenediamine-Fmoc (36)



33 (44.3 mg, 25 μ mol, 1.00 eq.) was dissolved in DMF (120 μ L) in a predried Schlenk flask equipped with a stir bar under an argon atmosphere. Fmoc ethylene diamine hydrochloride (**35**; 7.4 mg, 26 μ mol, 1.05 eq), PyBOP (14.3 mg, 28 μ mol, 1.10 eq.), HOBt (3.7 mg, 28 μ mol, 1.1 eq.) and DIPEA (9.15 μ L, 28 μ mol, 2.10 eq.) were added under argon counter flow. The mixture was stirred overnight at room temperature. After removal of the solvent through reduced pressure, the residue was purified via flash chromatography on silica gel (DCM/MeOH = 10:1). The product was obtained as a colorless solid (30.3 mg, 15 μ mol, 59 %).

Chemical formula: C₁₂₉H₁₂₈N₁₄O₁₀

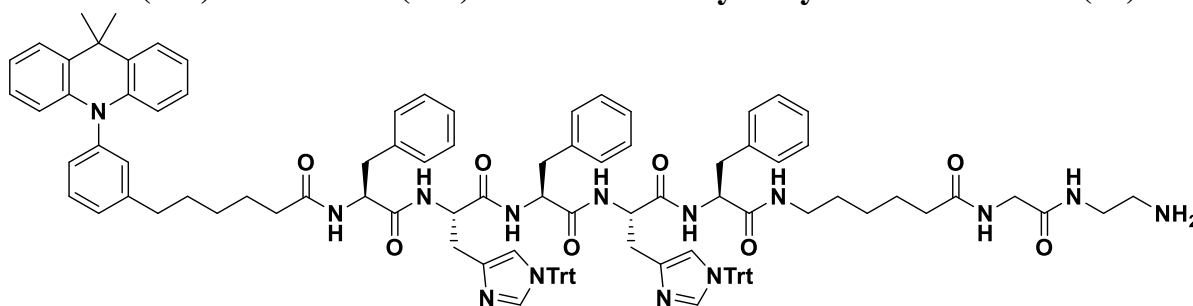
R_f = 0.6 (SiO₂, DCM/MeOH = 10:1).

¹H NMR (400 MHz, DMSO-*d*₆) δ 8.44 (d, *J* = 7.4 Hz, 1H, (N-CH^{arom.}-NTrt)^{His}), 8.16 (d, *J* = 7.5 Hz, 1H, O=C-NH), 8.03 (d, *J* = 7.0 Hz, 1H, O=C-NH), 8.00 – 7.81 (m, 8H, O=C-NH, (CH₂-CH-C-CH^{arom.}-CH^{arom.}-CH^{arom.}-CH^{arom.}-CH^{arom.})^{Fmoc}), 7.67 (d, *J* = 7.5 Hz, 2H, (CH₂-CH-C-CH^{arom.}-CH^{arom.}-CH^{arom.}-CH^{arom.})^{Fmoc}), 7.57 (t, *J* = 7.7 Hz, 1H, N-C-CH^{arom.}-CH^{arom.}-CH^{arom.}-C-CH₂), 7.46 (dd, *J* = 7.6, 1.7 Hz, 2H, (CH₃)₂C-C-CH^{arom.}), 7.40 (td, *J* = 7.6, 1.2 Hz, 3H, (CH₂-CH-C-CH^{arom.}-CH^{arom.}-CH^{arom.}-CH^{arom.})^{Fmoc}), 7.37 – 6.96 (m, 48H, CH^{arom.}-Phe,Trt, CH^{arom.}-CH^{arom.}-CH^{arom.}-C-CH^{arom.}-C-CH₂), 6.92 (td, *J* = 7.7, 1.7 Hz, 2H, (CH₃)₂C-C-CH^{arom.}-CH^{arom.}-CH^{arom.}-CH^{arom.}), 6.86 (td, *J* = 7.4, 1.4 Hz, 2H, (CH₃)₂C-C-CH^{arom.}-CH^{arom.}-CH^{arom.}-CH^{arom.}), 6.66 (s, 1H, N-C-CH^{arom.}-NTrt), 6.57 (s, 1H, N-C-CH^{arom.}-NTrt), 6.12 (dd, *J* = 8.1, 1.4 Hz, 2H, (CH₃)₂C-C-CH^{arom.}-CH^{arom.}-CH^{arom.}-CH^{arom.}), 4.49 – 4.31 (m, 6H, (O=C-CH-NH)^{His, Phe}), 4.29 (d, *J* = 6.9 Hz, 2H, CH₂^{Fmoc}), 4.20 (t, *J* = 6.8 Hz, 1H, CH^{Fmoc}), 3.63 (d, *J* = 5.8 Hz,

2H, (NH-CH₂-C=O)^{Gly}), 3.15 – 2.58 (m, 28H, CH₂^{Phe, His}, N-C-CH^{arom.}-C-CH₂, O=C-NH-CH₂-CH₂-CH₂, NH-CH₂-CH₂-NH), 2.06 (t, *J* = 7.6 Hz, 3H, CH₂-CH₂-CH₂-C=O), 1.99 – 1.81 (m, 4H, CH₂-CH₂-CH₂-C=O), 1.60 (s, 6H, (CH₃)₂C), 1.51 – 1.34 (m, 5H, CH₂-CH₂-CH₂-CH₂-C=O), 1.34 – 1.17 (m, 6H, CH₂-CH₂-CH₂-CH₂-C=O), 1.14 – 1.01 (m, 5H, CH₂-CH₂-CH₂-CH₂-C=O).

ESI-HRMS (MeOH, pos.) *m/z*: [M+H]⁺: calc. 2034.0011, found 2033.9960; [M+Na]⁺: calc. 2055.9836, found 2055.9790.

8.21. Synthesis of 6-(3-(9,9-Dimethylacridin-10(9H)-yl)phenyl)hexanoyl-L-Phe-L-His(Trt)-L-Phe-L-His(Trt)-L-Phe-Ahx-L-Gly-Ethylenediamine-NH₂ (37)



37

36 (27.3 mg, 13 μmol, 1.00 eq.) was dissolved in a mixture of DCM (65.4 μL) and piperidine (4.6 μL, 14 μmol, 1.05 eq.). After stirring for 45 minutes at room temperature the volatiles were removed via reduced pressure. The residue was dissolved in DCM and precipitated in diethyl ether. The solid residue was dissolved in DCM and washed with water, after the removal of the solvent through reduced pressure the product was obtained as a colorless solid (20.7 mg, 11 μmol, 87 %).

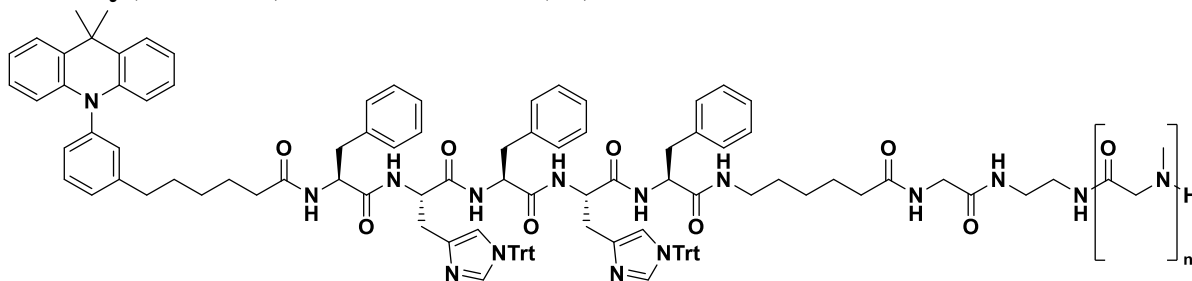
Chemical formula: C₁₁₄H₁₁₈N₁₄O₈

¹H NMR (400 MHz, DMSO-d₆) δ 8.44 (s, 1H, (N-CH^{arom.}-NTrt)^{His}), 8.16 (s, 1H, O=C-NH), 8.05 – 7.79 (m, 5H, O=C-NH), 7.57 (t, *J* = 7.7 Hz, 1H, N-C-CH^{arom.}-CH^{arom.}-CH^{arom.}-C-CH₂), 7.47 (d, *J* = 7.6 Hz, 2H, (CH₃)₂C-C-CH^{arom.}), 7.39 – 6.96 (m, 48H, CH^{arom.,Phe, Trt}, CH^{arom.}-CH^{arom.}-CH^{arom.}-C-CH^{arom.}-CH₂), 6.96 – 6.90 (m, 2H, (CH₃)₂C-C-CH^{arom.}-CH^{arom.}-CH^{arom.}-CH^{arom.}), 6.89 – 6.83 (m, 2H, (CH₃)₂C-C-CH^{arom.}-CH^{arom.}-CH^{arom.}-CH^{arom.}), 6.67 (s, 1H, (N-C-CH^{arom.}-NTrt)^{His}), 6.57 (s, 1H, (N-C-CH^{arom.}-

NTrt)^{His}), 6.16 – 6.09 (m, 2H, (CH₃)₂C-C-CH^{arom.}-CH^{arom.}-CH^{arom.}-CH^{arom.}), 4.48 – 4.28 (m, 7H, (O=C-CH-NH)^{Phe, His}), 3.65 (d, *J* = 5.6 Hz, 1H, (O=C-CH-NH)^{Gly}), 3.18 – 2.59 (m, 20H, NH-CH₂-CH₂-NH₂, CH₂^{Phe, His}, NH-CH₂-CH₂-CH₂, N-C-CH^{arom.}-C-CH₂), 2.12 – 1.84 (m, 6H, CH₂-CH₂-CH₂-C=O), 1.60 (s, 5H, (CH₃)₂C), 1.51 – 1.34 (m, 5H, CH₂-CH₂-CH₂-CH₂-C=O), 1.34 – 1.19 (m, 10H, CH₂-CH₂-CH₂-CH₂-C=O, NH-CH₂-CH₂-NH₂), 1.15 – 1.02 (m, 8H, CH₂-CH₂-CH₂-CH₂-C=O).

ESI-HRMS (MeOH, pos.) *m/z*: [M+H]⁺: calc. 1811.9330, found 1811.9282, [M+Na]⁺: calc. 1833.9155, found 1833.9121.

8.22. Synthesis of 6-(3-(9,9-Dimethylacridin-10(9H)-yl)phenyl)hexanoyl-L-Phe-L-His(Trt)-L-Phe-L-His(Trt)-L-Phe-Ahx-L-Gly-Ethylenediamine-NH-Poly(sarcosine)-COCH₂NCH₃H (39)



39

NCA polymerization was done according to literature procedures.^[98] **37** (16.7 mg, 9 μmol, 1 eq.) was put into a pre-dried Schlenk tube with equipped with a stir bar and closed with a septum and suspended in toluene (1 mL) via ultrasonification and stirring under nitrogen atmosphere. After freezing in liquid nitrogen, the solvent was removed under high vacuum overnight. Dry DMF was degassed *via* three freeze-pump-thaw cycles and **37** was dissolved in degassed, dry DMF (397.7 μL). Furthermore, a stock solution of sarcosine NCA (**38**) in degassed, dry DMF (200 mg/mL) was prepared in another pre-dried Schlenk flask under nitrogen atmosphere. The stock solution (397.7 μL, 697 μmol, 75 eq.) was added to the initiator solution through the septum *via* a syringe. The solution was stirred at room temperature while a constant stream of dry nitrogen was kept on the flask via the Schlenk line to allow CO₂ to

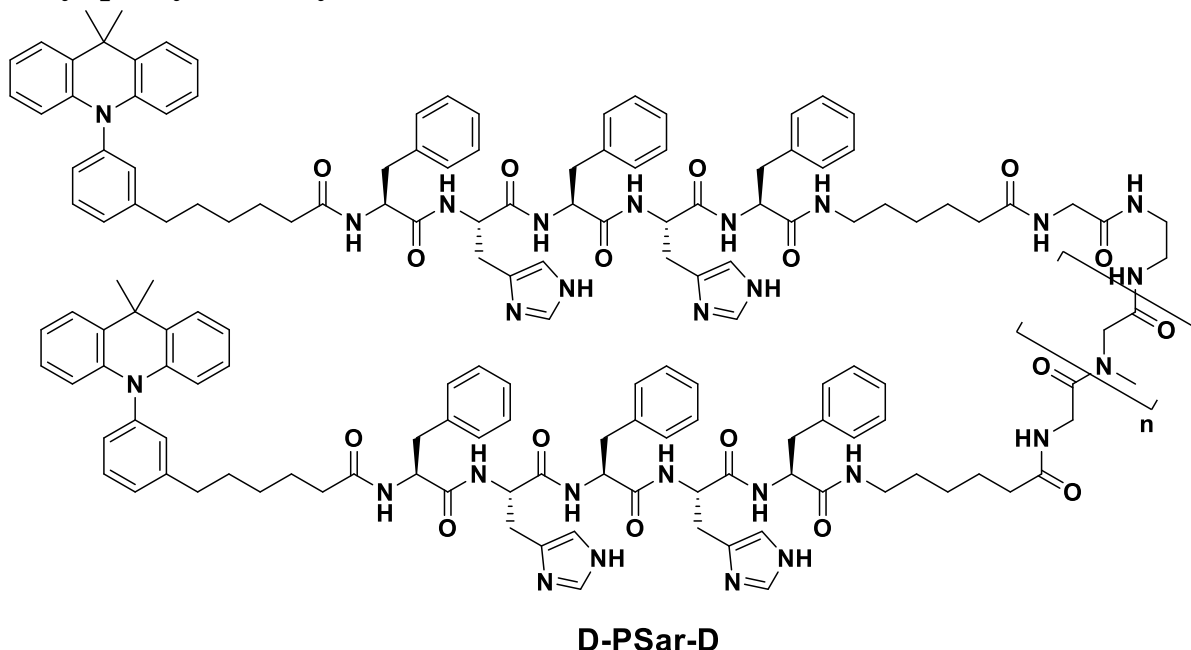
escape and to prevent impurities from entering the flask. The reaction progress of the polymerization was monitored by IR spectroscopy (disappearance of the NCA peaks (1853 and 1786 cm^{-1})). After 14 h the reaction was completed so the polymer was precipitated into cold diethyl ether and separated via centrifugation. The liquid fraction was discarded, and the polymer was resuspended in diethyl ether and separated via centrifugation again. Finally, the polymer was dissolved in water and lyophilized resulting in the isolated product as a colorless solid (57.7 mg, 7.6 μmol , 83 %).

^1H NMR (400 MHz, DMSO- d_6) δ 8.44 (d, $J = 7.5$ Hz, 1H, (N- $\text{CH}^{\text{arom.}}$ -NTrt)^{His}), 8.21 – 8.07 (m, 2H, O=C-NH), 8.06 – 7.82 (m, 12H, O=C-NH), 7.57 (t, $J = 7.7$ Hz, 1H, N-C- $\text{CH}^{\text{arom.}}$ - $\text{CH}^{\text{arom.}}$ - $\text{CH}^{\text{arom.}}$ -C- CH_2), 7.47 (dd, $J = 7.6, 1.7$ Hz, 2H, $(\text{CH}_3)_2\text{C-C-CH}^{\text{arom.}}$), 7.40 – 6.96 (m, 48H, $\text{CH}^{\text{arom.}}$ -Phe, Trt, $\text{CH}^{\text{arom.}}$ - $\text{CH}^{\text{arom.}}$ - $\text{CH}^{\text{arom.}}$ -C- CH_2), 6.96 – 6.89 (m, 2H, $(\text{CH}_3)_2\text{C-C-CH}^{\text{arom.}}$ - $\text{CH}^{\text{arom.}}$ - $\text{CH}^{\text{arom.}}$ - $\text{CH}^{\text{arom.}}$), 6.89 – 6.81 (m, 2H, $(\text{CH}_3)_2\text{C-C-CH}^{\text{arom.}}$ - $\text{CH}^{\text{arom.}}$ - $\text{CH}^{\text{arom.}}$ - $\text{CH}^{\text{arom.}}$), 6.66 (s, 1H, (N-C- $\text{CH}^{\text{arom.}}$ -NTrt)^{His}), 6.56 (s, 1H, (N-C- $\text{CH}^{\text{arom.}}$ -NTrt)^{His}), 6.12 (dd, $J = 8.1, 1.4$ Hz, 2H, $(\text{CH}_3)_2\text{C-C-CH}^{\text{arom.}}$ - $\text{CH}^{\text{arom.}}$ - $\text{CH}^{\text{arom.}}$ - $\text{CH}^{\text{arom.}}$), 4.55 – 3.76 (m, 157H, (O=C- CH_2 -NH)^{PSar}, (O=C- CH -NH)^{His, Phe}), 3.63 (d, $J = 5.6$ Hz, 3H, (NH- CH_2 -C=O)^{Gly}), 3.19 – 2.58 (m, 278H, N- $\text{CH}_3^{\text{PSar}}$, NH- CH_2 - CH_2 - CH_2 , N-C- $\text{CH}^{\text{arom.}}$ -C- CH_2 , CH_2^{His} , Phe, NH- CH_2 - CH_2 -NH), 2.07 (t, $J = 7.5$ Hz, 2H, CH_2 - CH_2 - CH_2 -C=O), 2.00 – 1.86 (m, 2H, CH_2 - CH_2 - CH_2 -C=O), 1.60 (s, 5H, $(\text{CH}_3)_2\text{C}$), 1.50 – 1.34 (m, 5H, CH_2 - CH_2 - CH_2 - CH_2 -C=O), 1.34 – 1.18 (m, 6H, CH_2 - CH_2 - CH_2 - CH_2 -C=O), 1.15 – 1.02 (m, 15H, CH_2 - CH_2 - CH_2 - CH_2 -C=O).

MALDI-MS (DCTB, MeOH): $M_n = 6.7 \text{ kg mol}^{-1}$, $D = 1.01$.

SEC (HFIP, KTFA 3 g/L, RI detection, PMMA calibration): $M_n = 28.7 \text{ kg mol}^{-1}$, $D = 1.15$.

8.23. Synthesis of 6-(3-(9,9-Dimethylacridin-10(9H)-yl)phenyl)hexanoyl-L-Phe-L-His-L-Phe-L-His-L-Phe-Ahx-L-Gly-Ethylenediamine-NH-Poly(sarcosine)-L-Gly-Ahx-L-Phe-L-His-L-Phe-L-His-L-Phe-6-(3-(9,9-dimethylacridin-10(9H)-yl)phenyl)hexanoyl (D-PSar-D)



End group modification and deprotection was done according to **SOP3** using **39** (27.4 mg, 3.8 μ mol, 1 eq.) and **33** (20.4 mg, 11.4 μ mol, 3 eq.). Purification was achieved via size exclusion chromatography (BioBeads SX-1, DMF). The obtained residue was dissolved in water and lyophilized, yielding the product as a colorless solid (23.6 mg, 3.0 μ mol, 79 %).

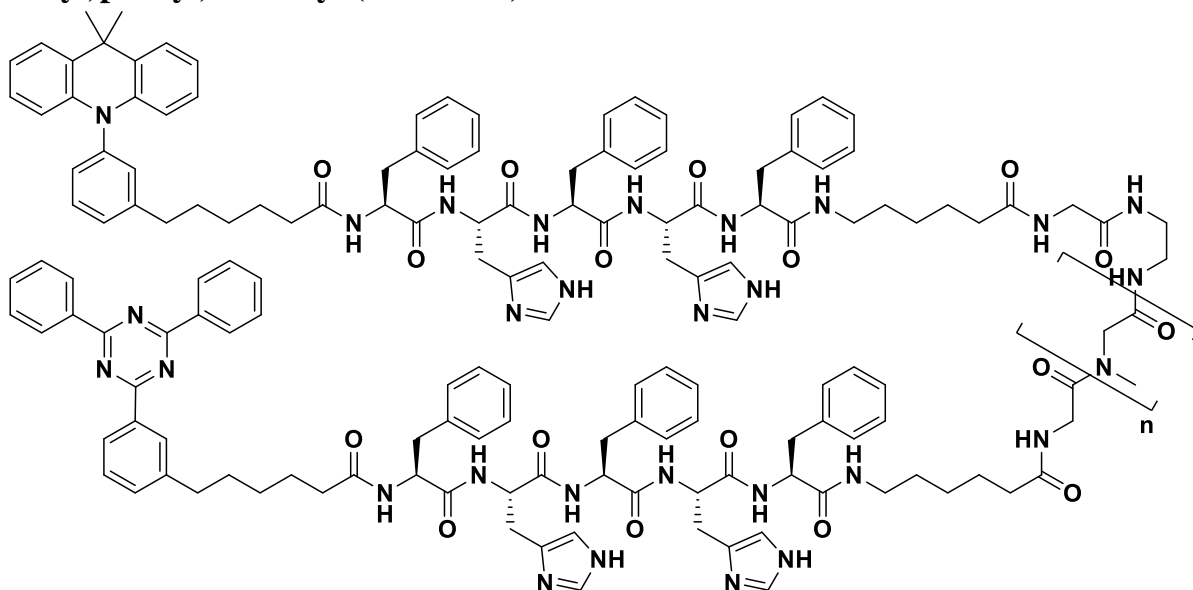
^1H NMR (400 MHz, DMSO- d_6) δ 8.47 (s, 4H, (N- $\text{CH}^{\text{arom.}}$ -NH)^{His}), 8.34 – 7.96 (m, 14H, NH-C=O), 7.89 (s, 5H, NH-C=O), 7.58 (t, $J = 7.7$ Hz, 2H, N-C- $\text{CH}^{\text{arom.}}$ - $\text{CH}^{\text{arom.}}$ - $\text{CH}^{\text{arom.}}$ -C-CH₂), 7.54 (s, 2H, (N-C- $\text{CH}^{\text{arom.}}$ -NH)^{His}), 7.51 – 7.44 (m, 5H, (CH₃)₂C-C- $\text{CH}^{\text{arom.}}$), 7.35 (d, $J = 7.6$ Hz, 3H, N-C- $\text{CH}^{\text{arom.}}$ - $\text{CH}^{\text{arom.}}$ -C-CH₂), 7.25 – 7.07 (m, 34H, $\text{CH}^{\text{arom.}}$.Phe, $\text{CH}^{\text{arom.}}$ -C- $\text{CH}^{\text{arom.}}$ -C-CH₂), 6.96 (t, $J = 7.6$ Hz, 4H, (CH₃)₂C-C- $\text{CH}^{\text{arom.}}$ - $\text{CH}^{\text{arom.}}$ - $\text{CH}^{\text{arom.}}$), 6.88 (t, $J = 7.4$ Hz, 4H, (CH₃)₂C-C- $\text{CH}^{\text{arom.}}$ - $\text{CH}^{\text{arom.}}$ - $\text{CH}^{\text{arom.}}$), 6.77 (s, 4H, NH^{His}), 6.13 (d, $J = 8.1$ Hz, 4H, (CH₃)₂C-C- $\text{CH}^{\text{arom.}}$ - $\text{CH}^{\text{arom.}}$ - $\text{CH}^{\text{arom.}}$ - $\text{CH}^{\text{arom.}}$), 4.52 – 3.81 (m, 187H, (O=C-CH-NH)^{His,Phe,PSar}), 3.64 (d, $J = 5.6$ Hz, 4H, (O=C-CH₂-NH)^{Gly}), 3.00 – 2.66 (m, 267H, (CH₂-CH-NH)^{Phe,His}, N-CH₃, NH-CH₂-CH₂-NH), 2.61 – 2.55 (m, 5H, N-C-CH₂-C-CH₂), 2.16 – 2.05 (m, 6H, CH₂-CH₂-C=O), 2.05 – 1.95 (m, 6H, CH₂-CH₂-C=O), 1.61 (s, 12H, (CH₃)₂C), 1.55 – 1.41 (m,

11H, N-C-CH^{arom.}-C-CH₂-CH₂-CH₂-CH₂, NH-CH₂-CH₂-CH₂-CH₂), 1.41 – 1.28 (m, 10H, N-C-CH^{arom.}-C-CH₂-CH₂-CH₂-CH₂, NH-CH₂-CH₂-CH₂-CH₂), 1.21 – 1.04 (m, 12H, CH₂-CH₂-CH₂-C=O).

MALDI-MS (DCTB, MeOH): $M_n = 7.1 \text{ kg mol}^{-1}$, $D = 1.01$.

SEC (HFIP, KTFA 3 g/L, RI detection, PMMA calibration): $M_n = 30.0 \text{ kg mol}^{-1}$, $D = 1.3$.

8.24. Synthesis of 6-(3-(9,9-Dimethylacridin-10(9H)-yl)phenyl)hexanoyl-L-Phe-L-His-L-Phe-L-His-L-Phe-Ahx-L-Gly-Ethylenediamine-NH-Poly(sarcosine)-L-Gly-Ahx-L-Phe-L-His-L-Phe-L-His-L-Phe-6-(3-(4,6-diphenyl-1,3,5-triazin-2-yl)phenyl)hexanoyl (D-PSar-A)



D-PSar-A

End group modification and deprotection was done according to **SOP3** using **39** (27.4 mg, 3.8 μmol , 1 eq.) and **34** (20.4 mg, 11.4 μmol , 3 eq.). Purification was achieved via size exclusion chromatography (BioBeads SX-1, DMF). The obtained residue was dissolved in water and lyophilized, yielding the product as a colorless solid (23.6 mg, 3.0 μmol , 79 %).

¹H NMR (400 MHz, DMSO-*d*₆) δ 8.83 – 8.69 (m, 4H, (N-C-C-CH^{arom.}-CH^{arom.}-CH^{arom.}-CH^{arom.})^{TRZ}), 8.57 (d, $J = 7.8 \text{ Hz}$, 1H, (N-C-C-CH^{arom.}-CH^{arom.}-CH^{arom.}-C-CH₂)^{TRZ}), 8.54 (s, 1H, (N-C-C-CH₂-C-CH₂)^{TRZ}), 8.47 (s, 4H, (N-CH^{arom.}-NH)^{His}), 8.29 – 7.96 (m, 18H, O=C-NH), 7.89 (s, 7H, O=C-NH), 7.77

– 7.61 (m, 10H, (N-C-C-CH^{arom.}-CH^{arom.}-CH^{arom.}-CH^{arom.})^{TRZ}), 7.60 – 7.46 (m, 8H, (N-C-CH^{arom.}-NH)^{His}, (CH^{arom.}-CH^{arom.}-CH^{arom.}-C-CH₂-CH₂)^{TRZ}, (CH₃)₂C-C-CH^{arom.}), 7.39 – 7.27 (m, 6H, CH^{arom.}-CH^{arom.}-CH^{arom.}-C-CH₂-CH₂), 7.26 – 7.07 (m, 32H, CH^{arom.,Phe}, (CH₃)₂C-C-C-N-C-CH^{arom.}), 6.95 (t, $J = 8.0$ Hz, 2H, (CH₃)₂C-C-CH^{arom.}-CH^{arom.}-CH^{arom.}-CH^{arom.}), 6.88 (t, $J = 7.4$ Hz, 2H, (CH₃)₂C-C-CH^{arom.}-CH^{arom.}-CH^{arom.}-CH^{arom.}), 6.78 (s, 4H, NH^{His}), 6.16 (t, $J = 10.0$ Hz, 2H, (CH₃)₂C-C-CH^{arom.}-CH^{arom.}-CH^{arom.}-CH^{arom.}), 4.57 – 3.81 (m, 173H, (O=C-CH-NH)^{His,Phe,PSar}), 3.63 (d, $J = 5.6$ Hz, 5H, (CH₂-CH₂-NH)^{Gly}), 3.01 – 2.64 (m, 252H, (CH₂-CH-NH)^{Phe,His}, N-CH₃, C-CH^{arom.}-C-CH₂-CH₂, N-CH₂-CH₂-N), 2.15 – 2.06 (m, 7H, CH₂-CH₂-C=O), 2.05 – 1.93 (m, 8H, CH₂-CH₂-C=O), 1.67 (s, 9H, (CH₃)₂C), 1.54 – 0.93 (m, 109H, CH₂-CH₂-CH₂-CH₂-C=O).

SEC (HFIP, KTFA 3 g/L, RI detection, PMMA calibration): $M_n = 35.5$ kg mol⁻¹, $D = 1.5$.

9. Appendix

9.1. NMR Spectra

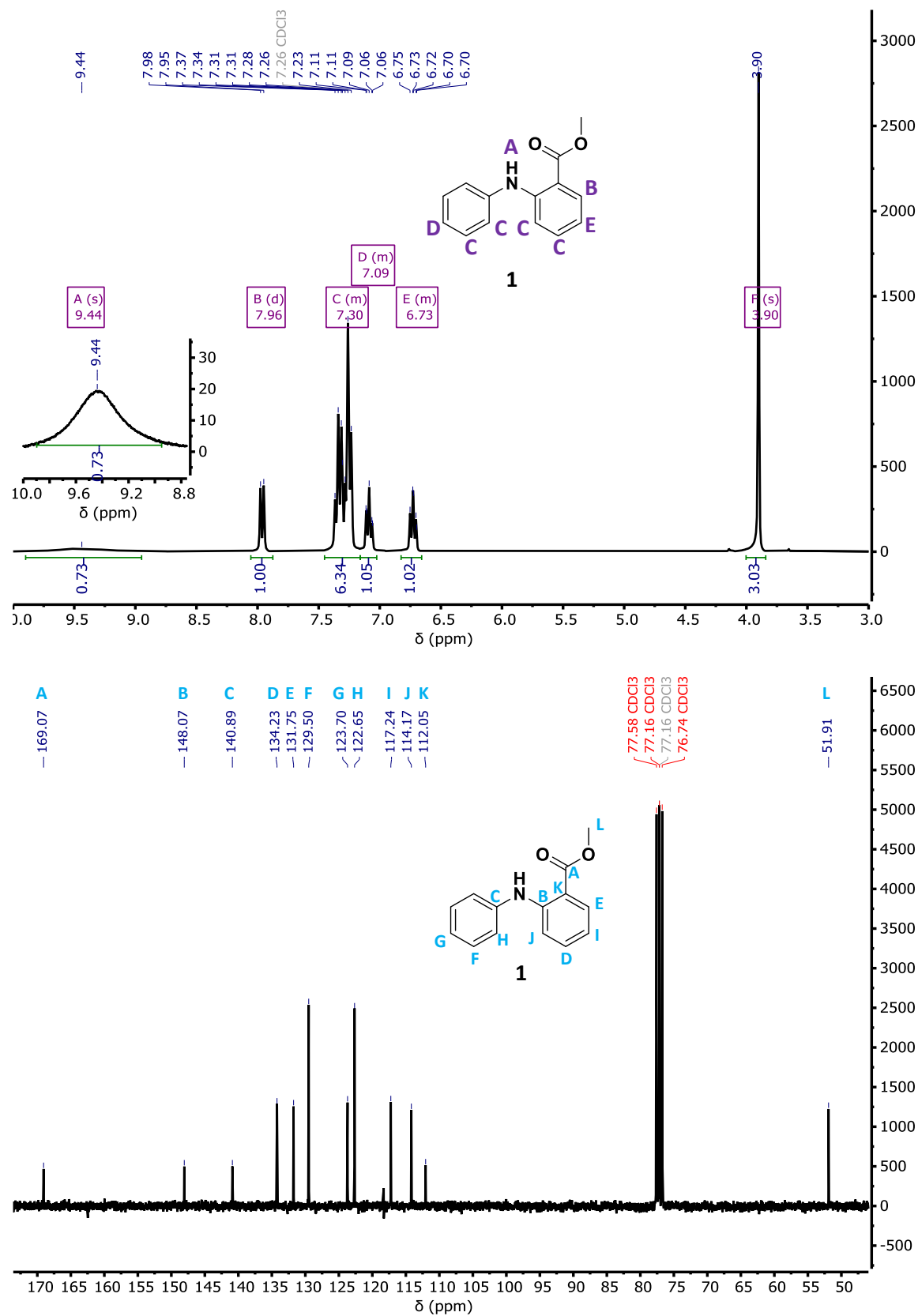


Figure 9.1. ¹H NMR (top) and ¹³C NMR spectrum (bottom) of compound 1.

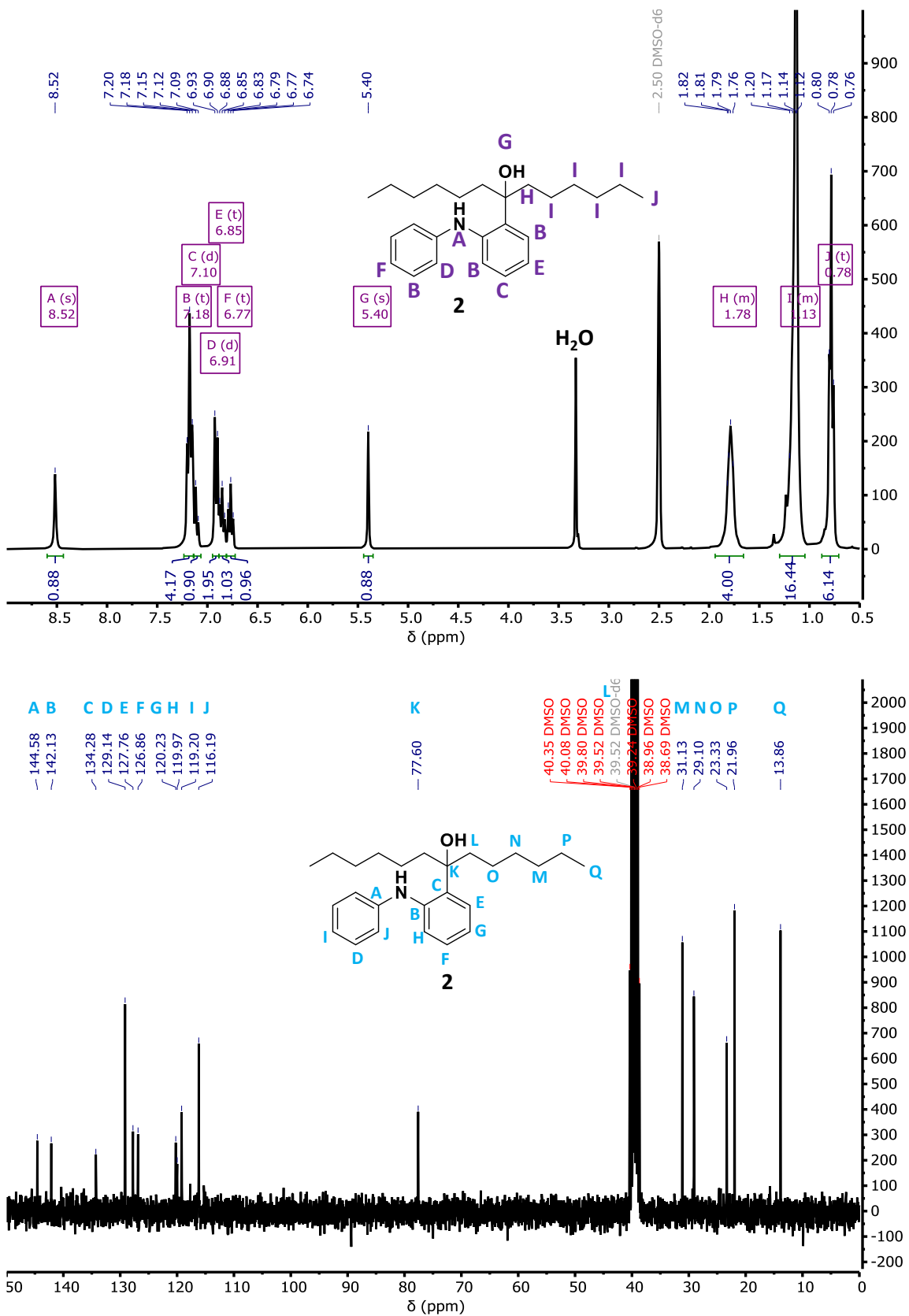


Figure 9.2. ¹H NMR (top) and ¹³C NMR spectrum (bottom) of compound 2.

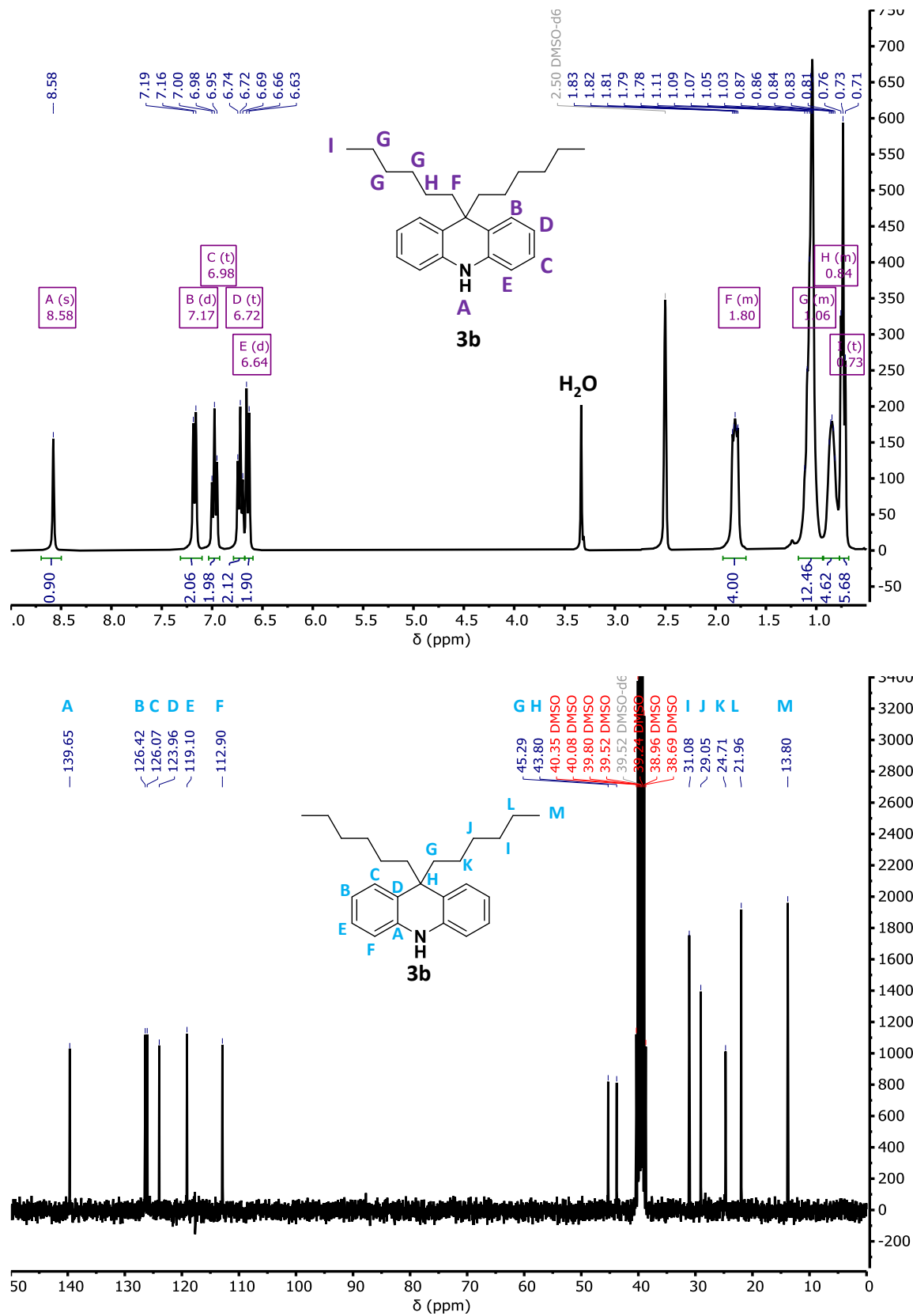


Figure 9.3. ¹H NMR (top) and ¹³C NMR spectrum (bottom) of compound **3b**.

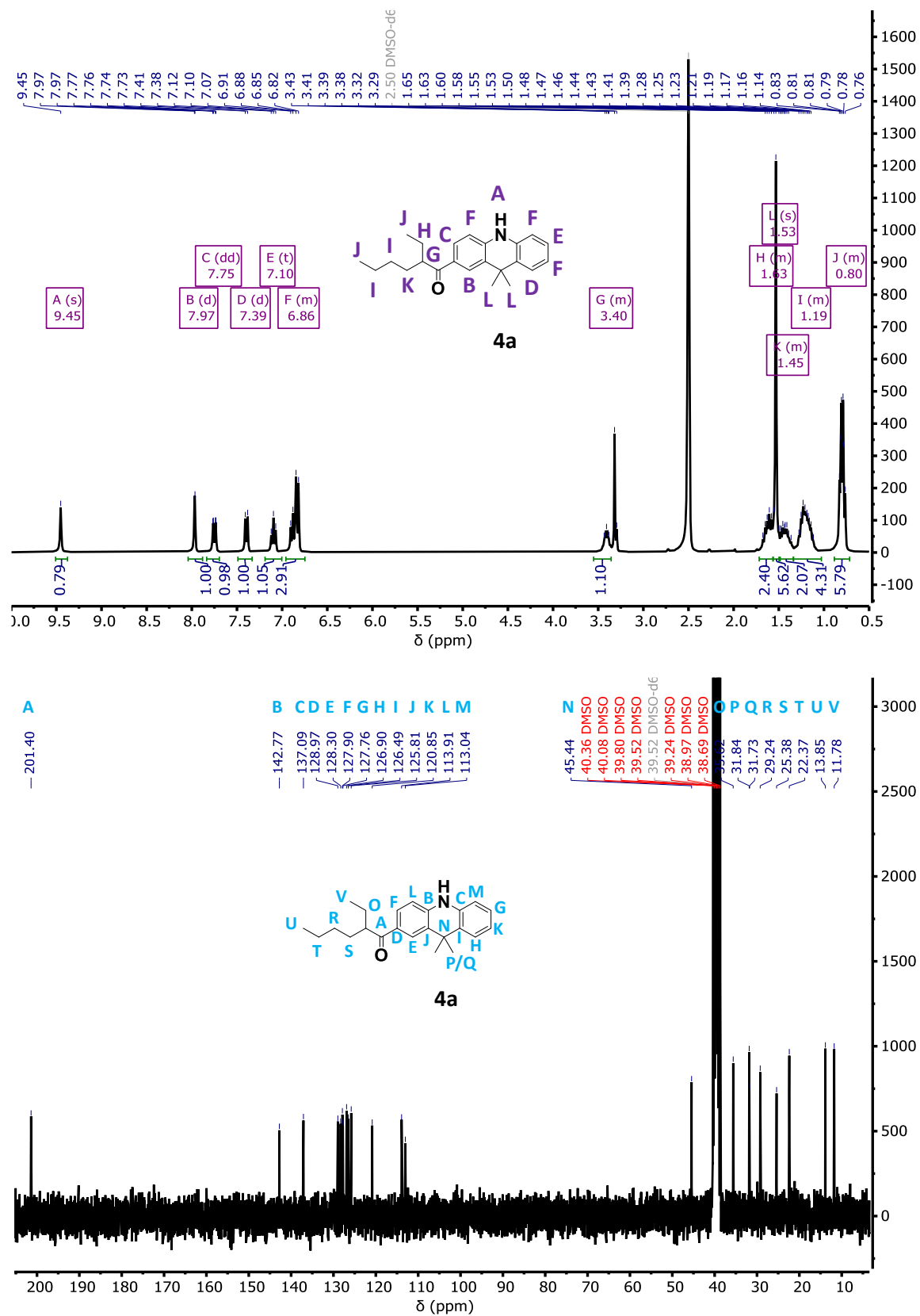


Figure 9.4. ^1H NMR (top) and ^{13}C NMR spectrum (bottom) of compound 4a.

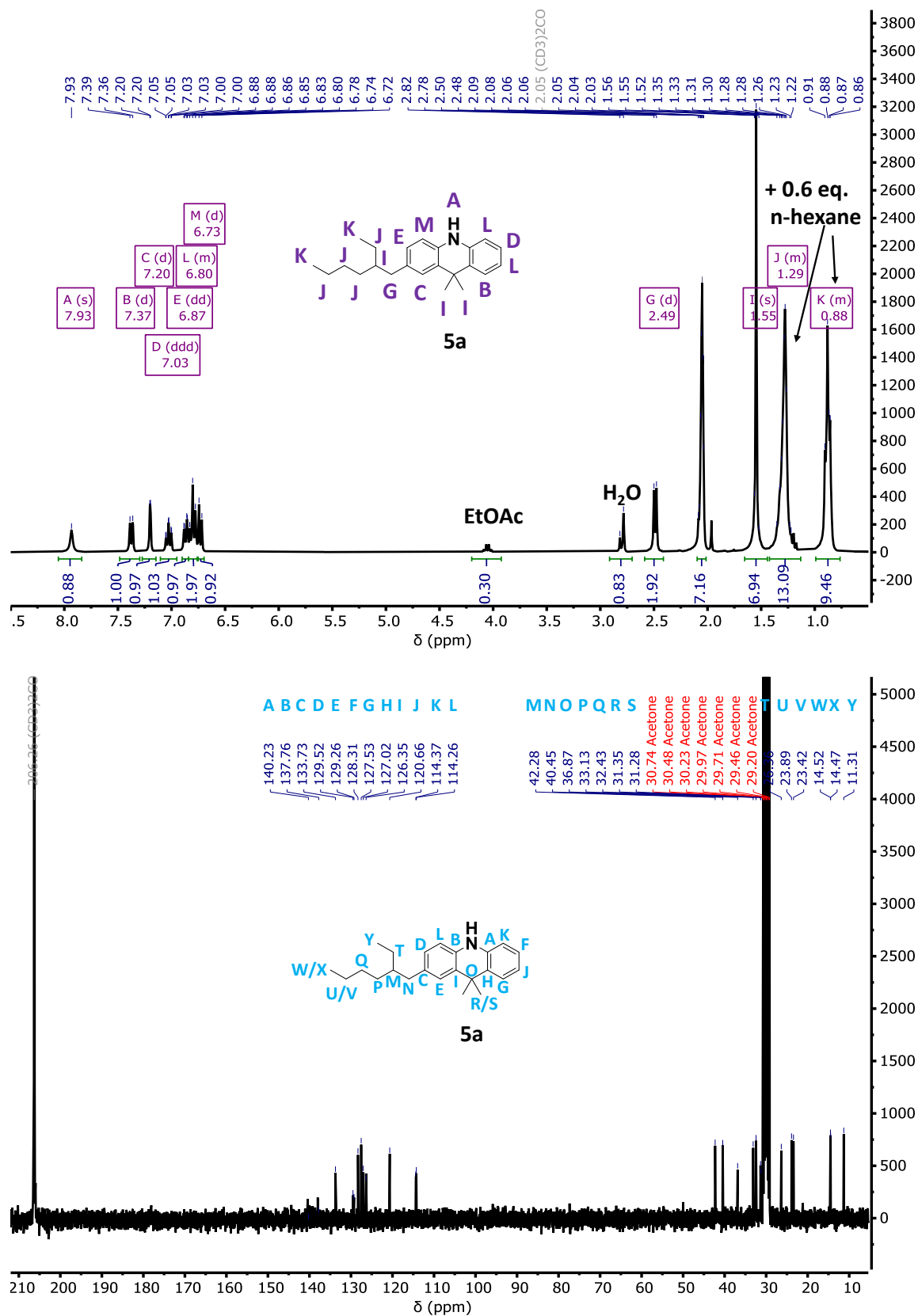


Figure 9.5. ¹H NMR (top) and ¹³C NMR spectrum (bottom) of compound **5a**.

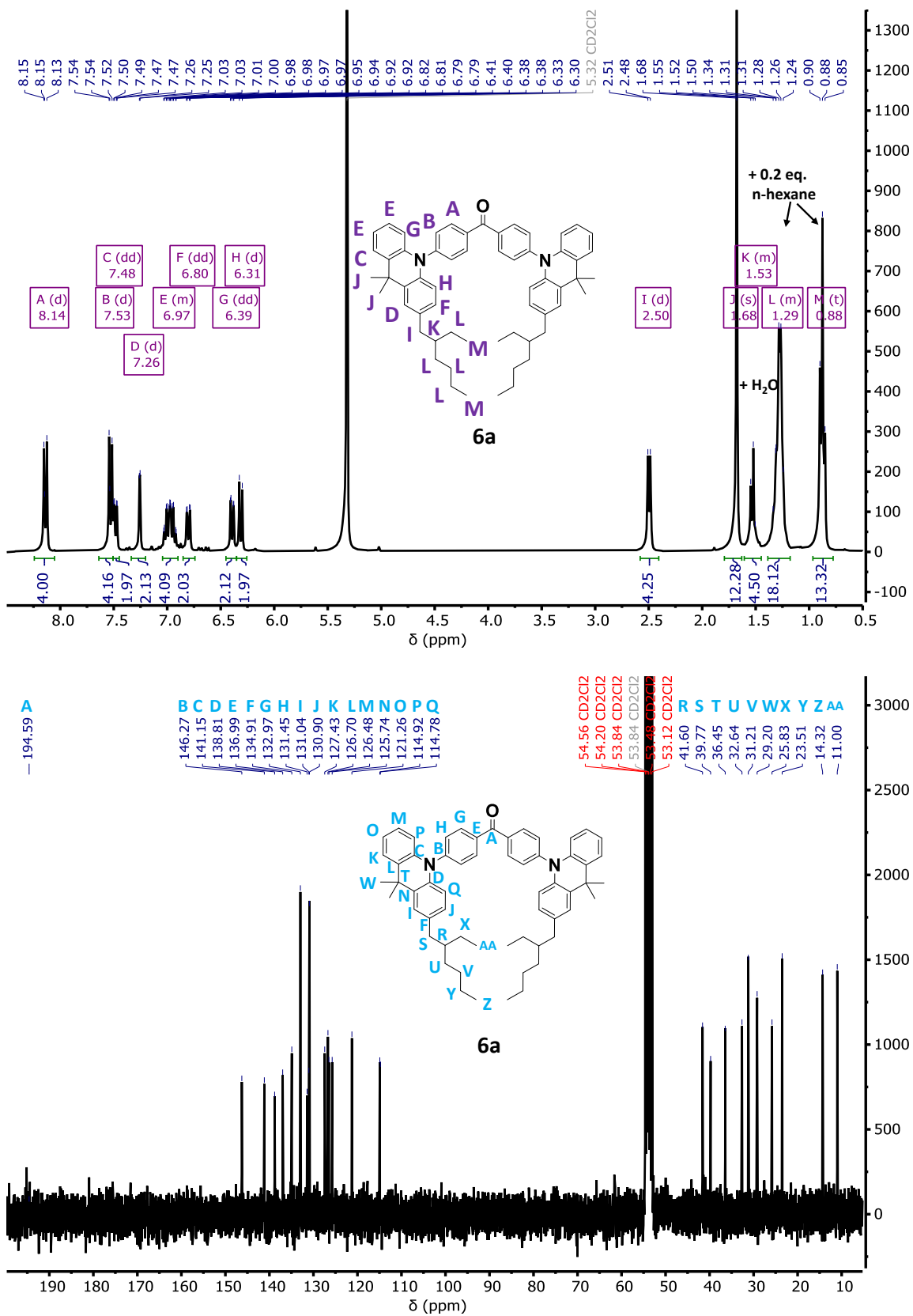


Figure 9.6. ¹H NMR (top) and ¹³C NMR spectrum (bottom) of compound 6a.

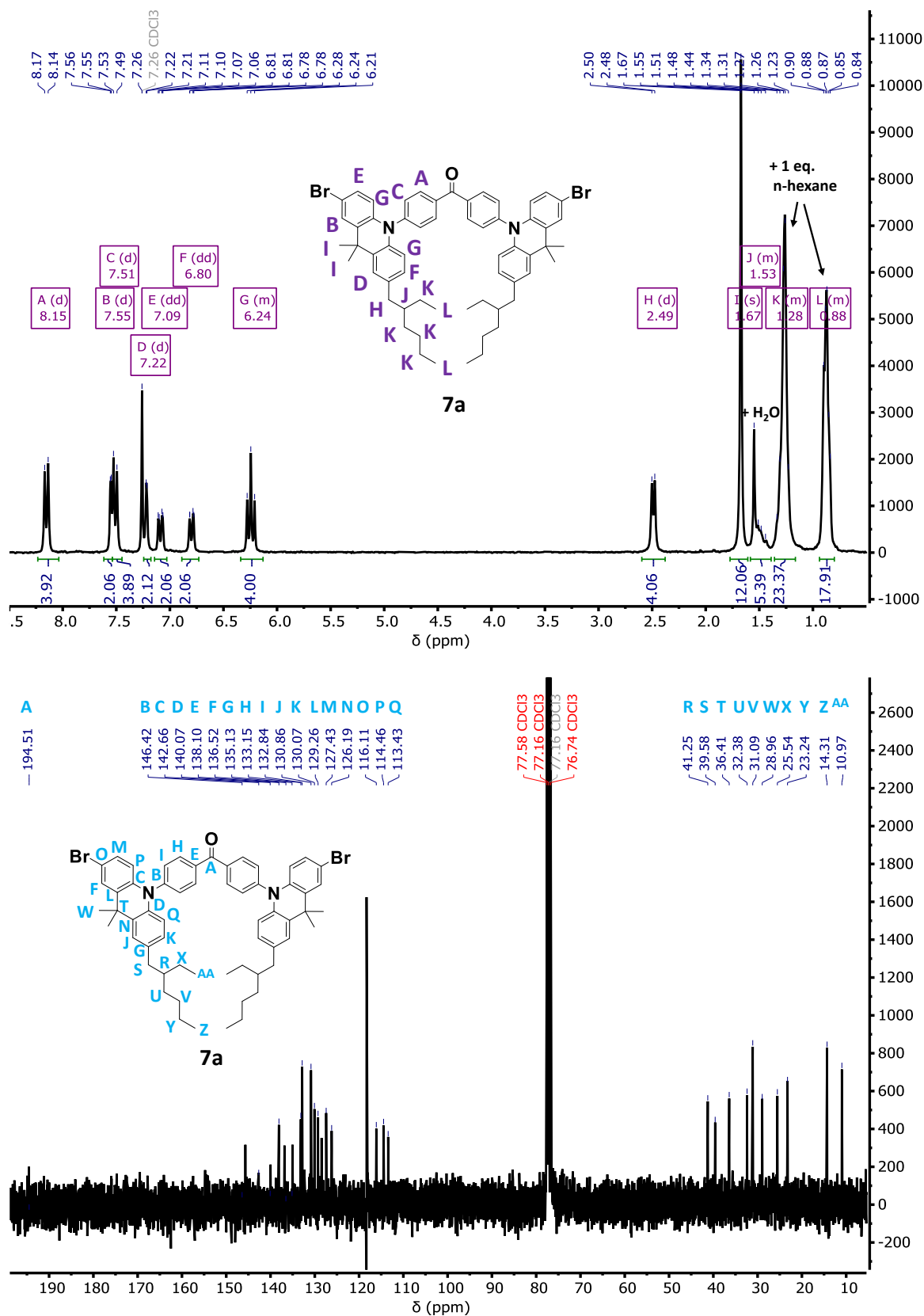


Figure 9.7. ¹H NMR (top) and ¹³C NMR spectrum (bottom) of compound **7a**.

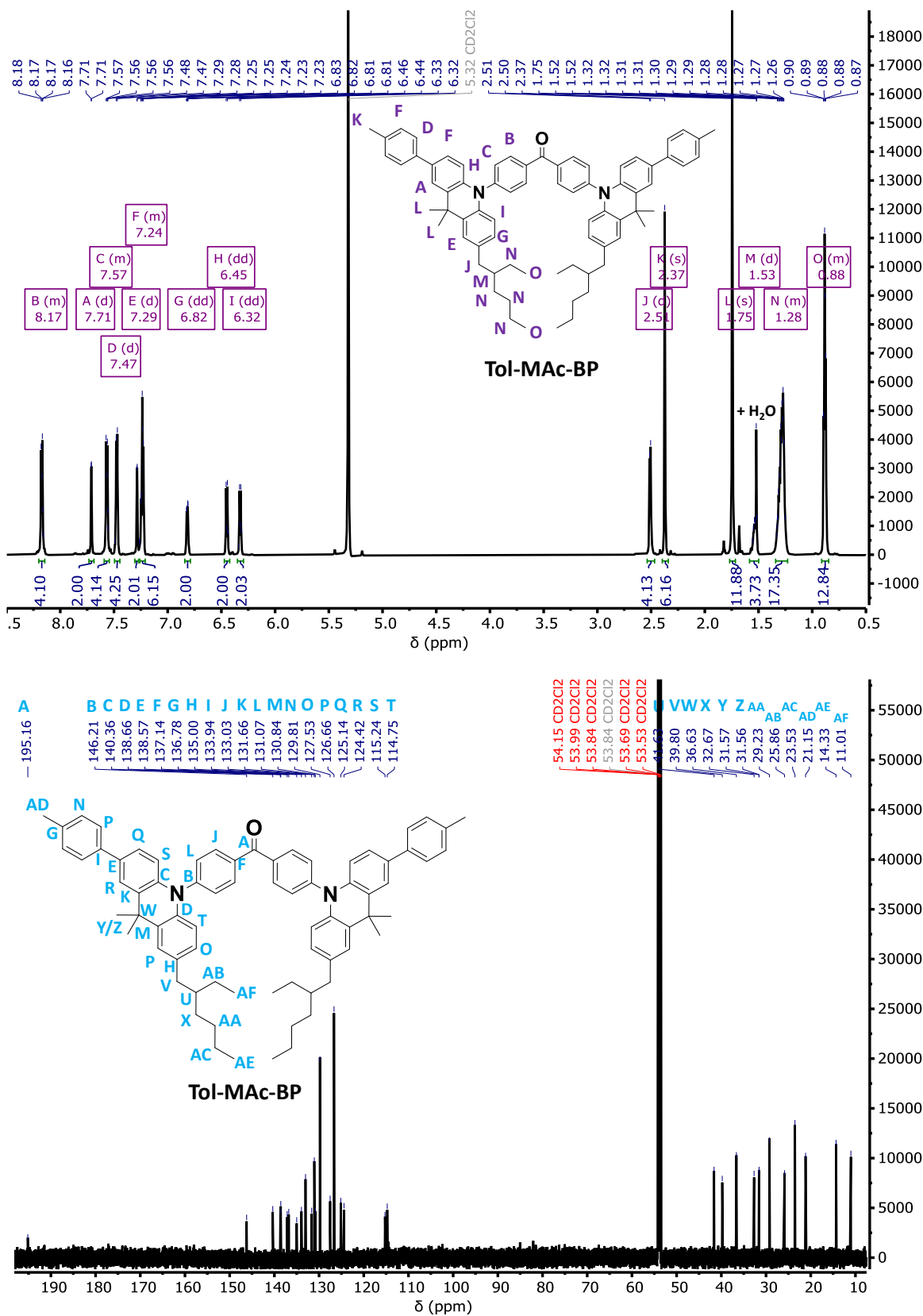


Figure 9.8. ¹H NMR (top) and ¹³C NMR spectrum (bottom) of compound Tol-Mac-BP.

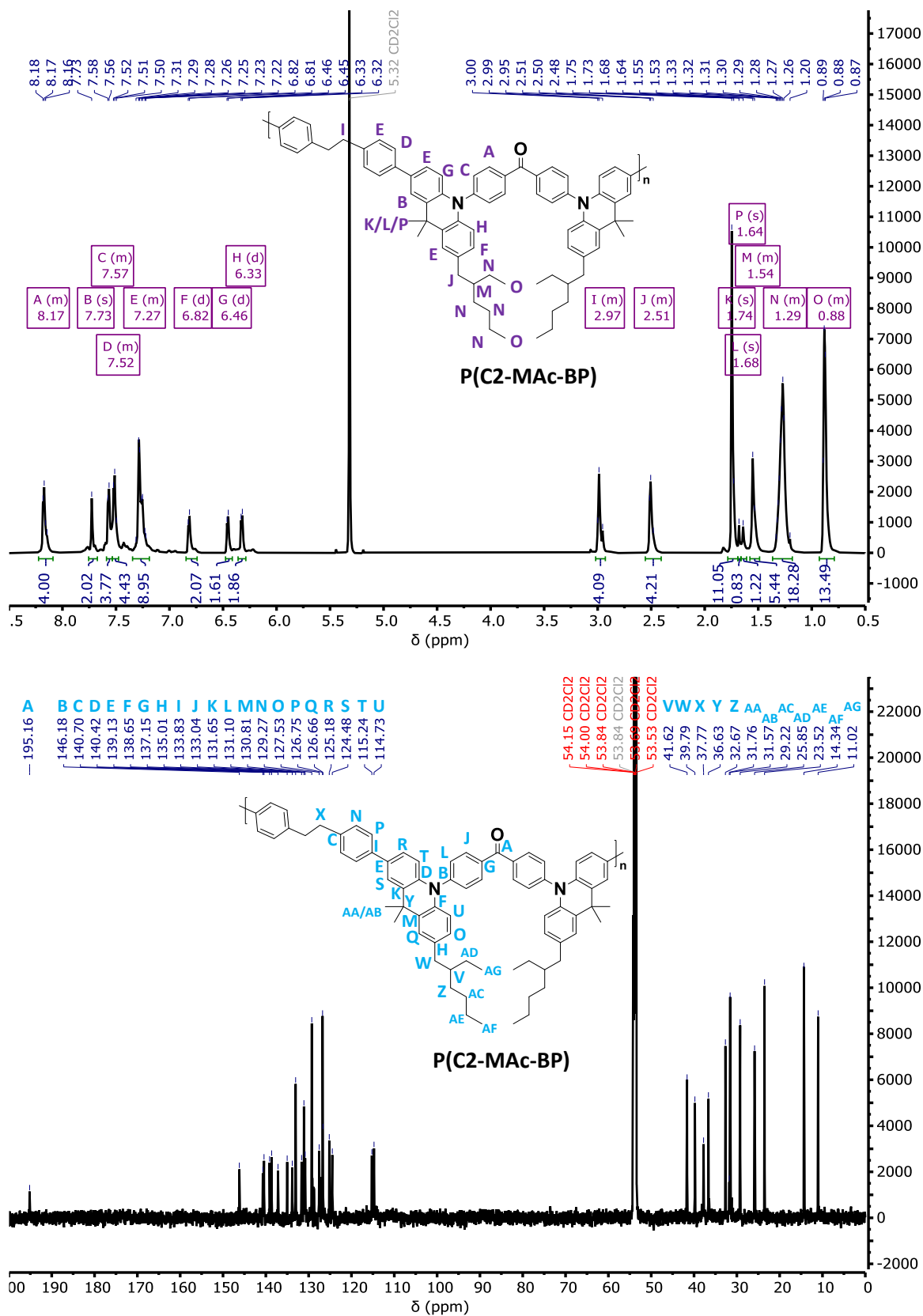


Figure 9.9. ¹H NMR (top) and ¹³C NMR spectrum (bottom) of compound P(C2-Mac-BP).

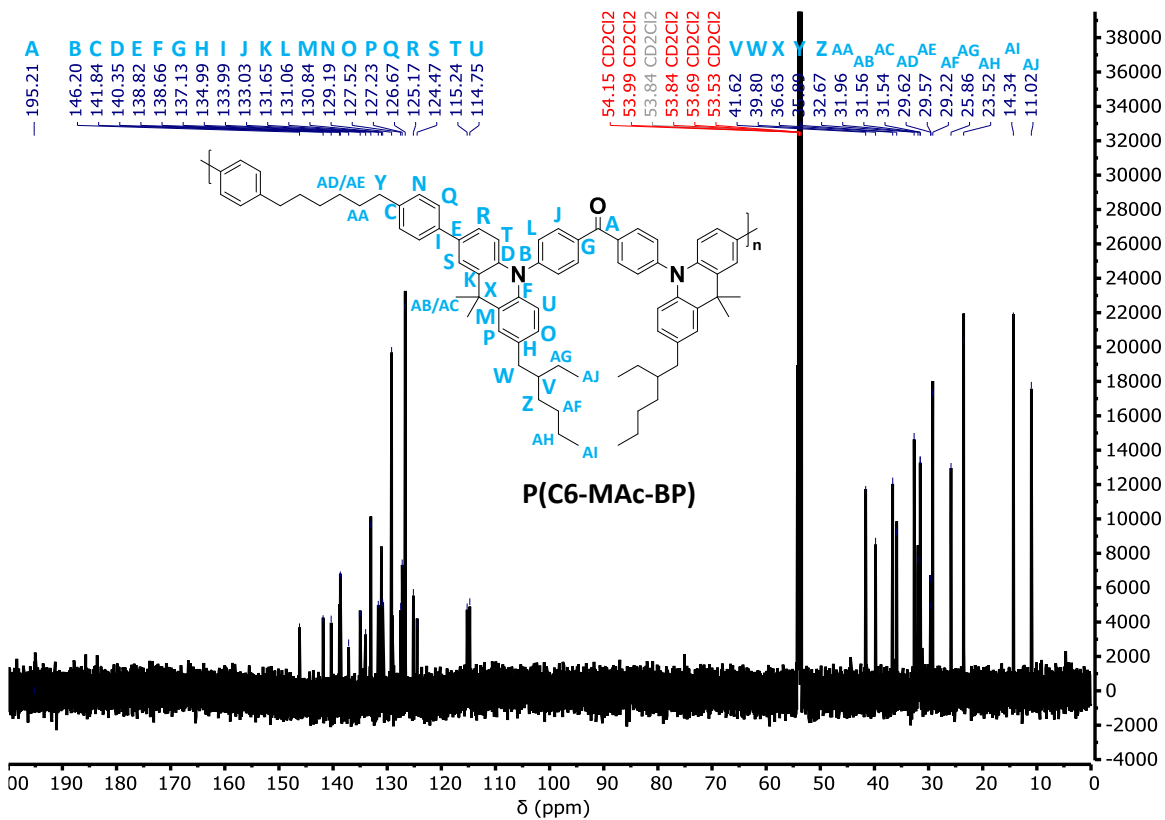
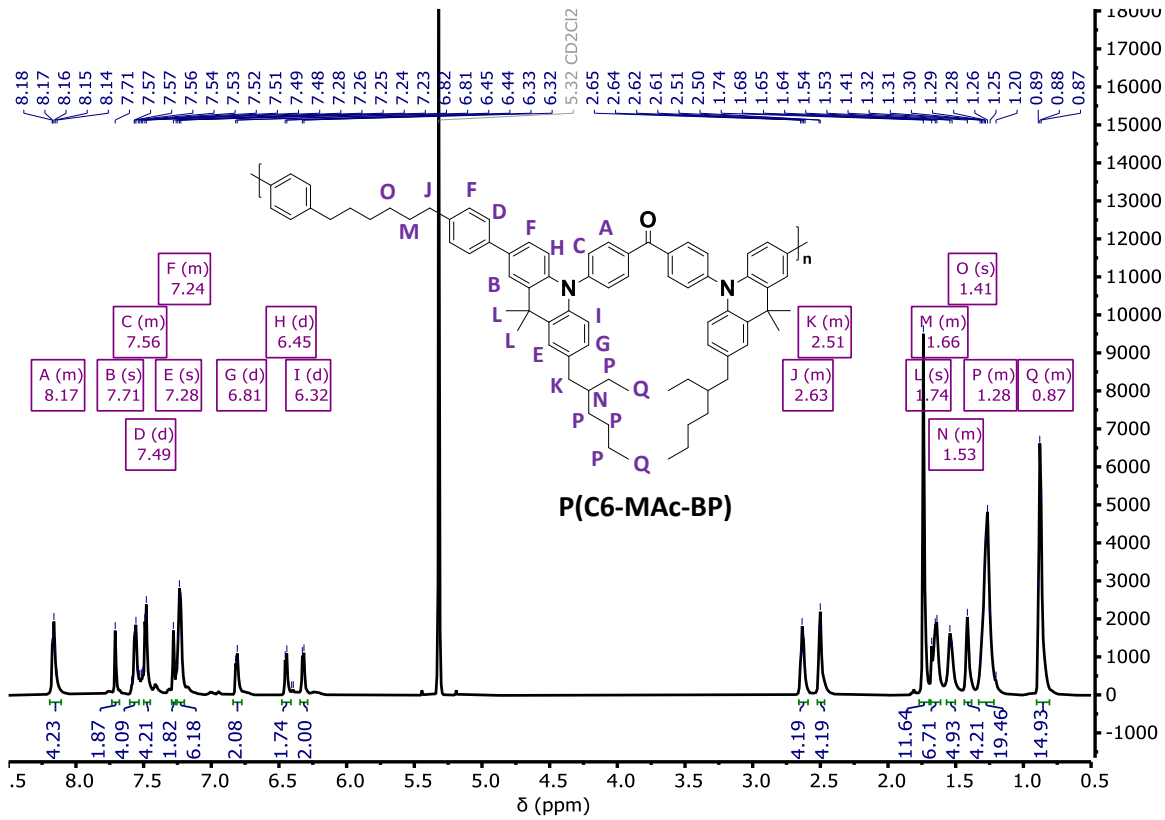


Figure 9.10. ¹H NMR (top) and ¹³C NMR spectrum (bottom) of compound P(C6-MAc-BP).

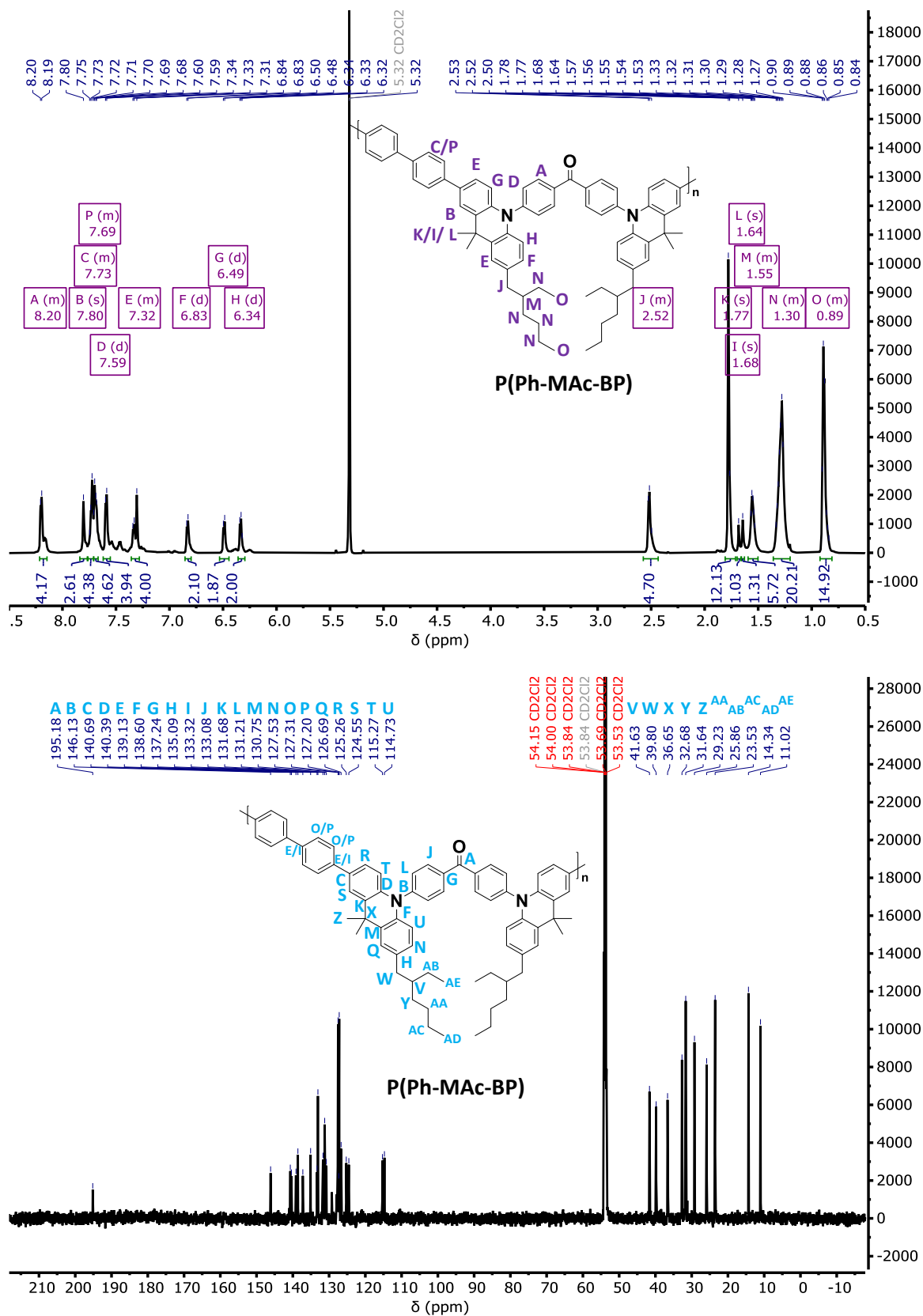


Figure 9.11. ¹H NMR (top) and ¹³C NMR spectrum (bottom) of compound P(Ph-MAc-BP).

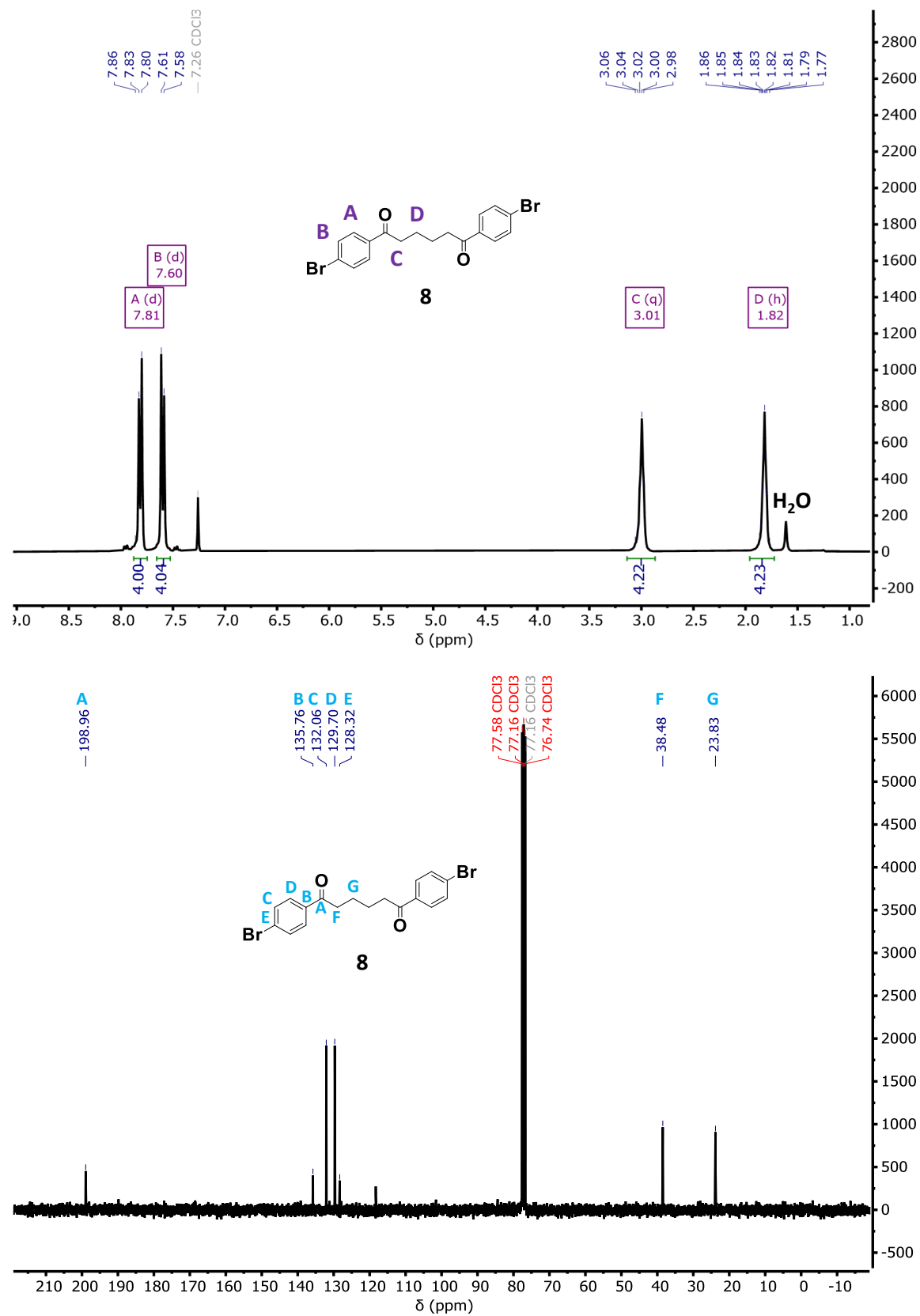


Figure 9.12. ¹H NMR (top) and ¹³C NMR spectrum (bottom) of compound 8.

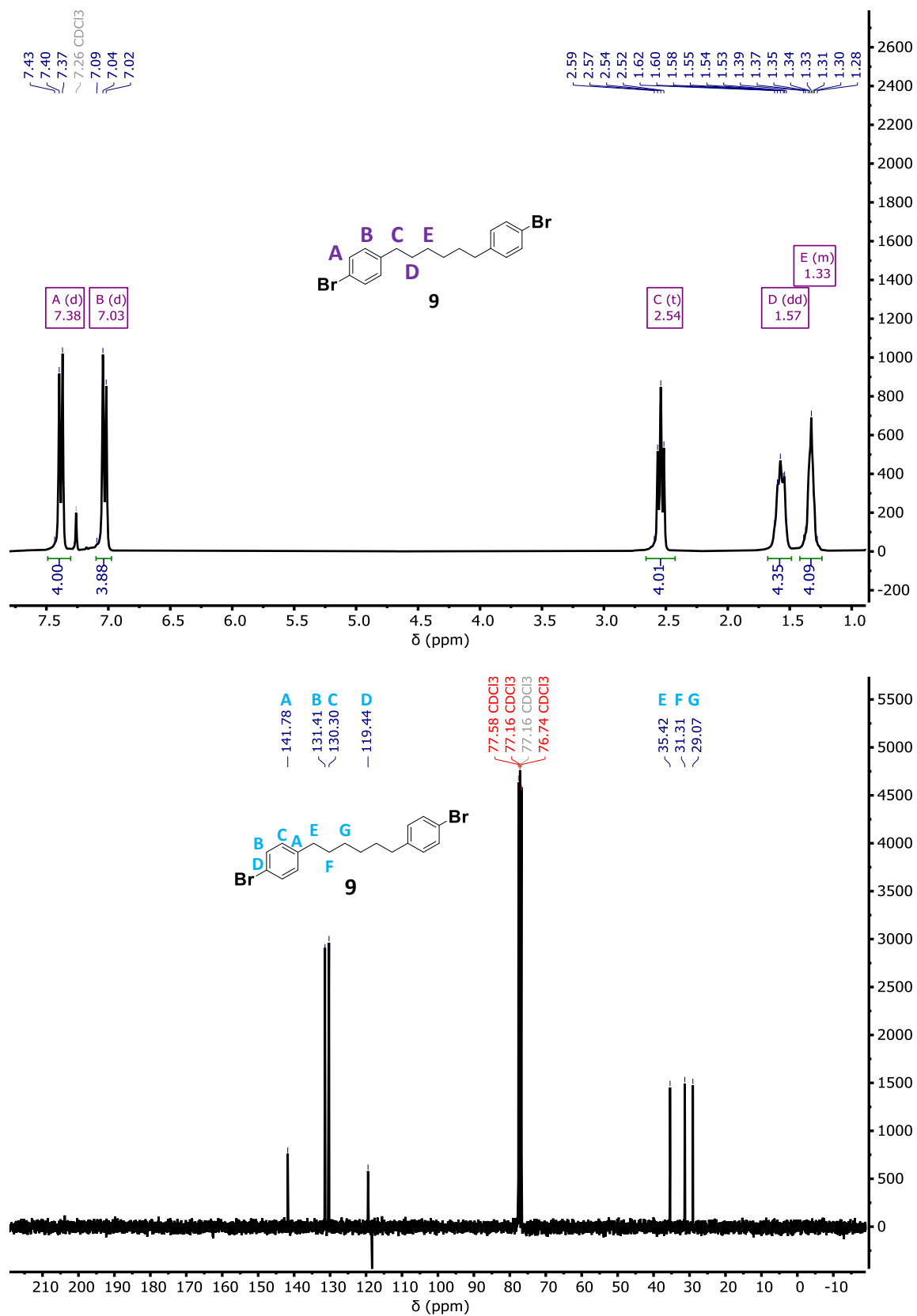


Figure 9.13. ¹H NMR (top) and ¹³C NMR spectrum (bottom) of compound 9.

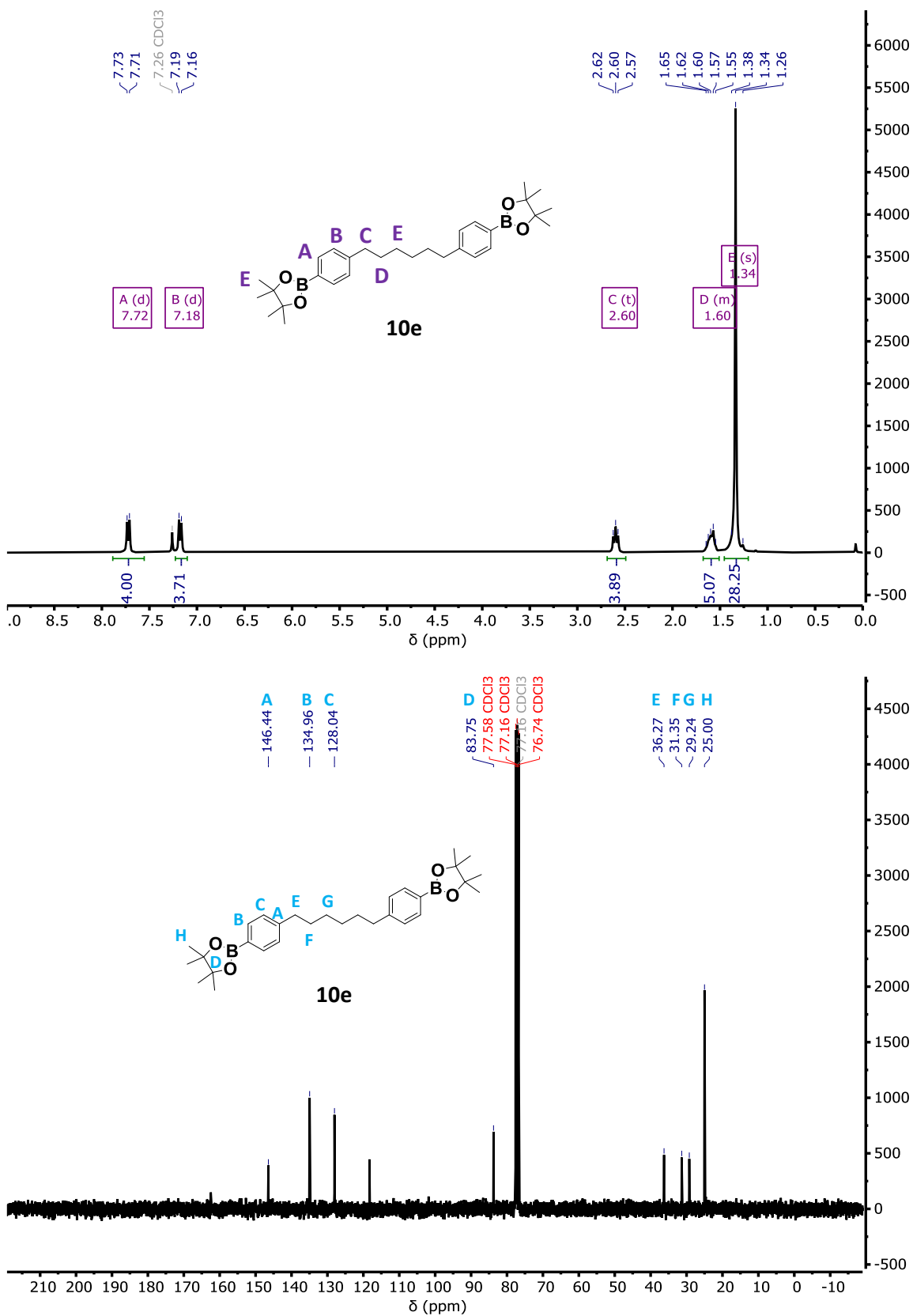


Figure 9.14. ¹H NMR (top) and ¹³C NMR spectrum (bottom) of compound 10e.

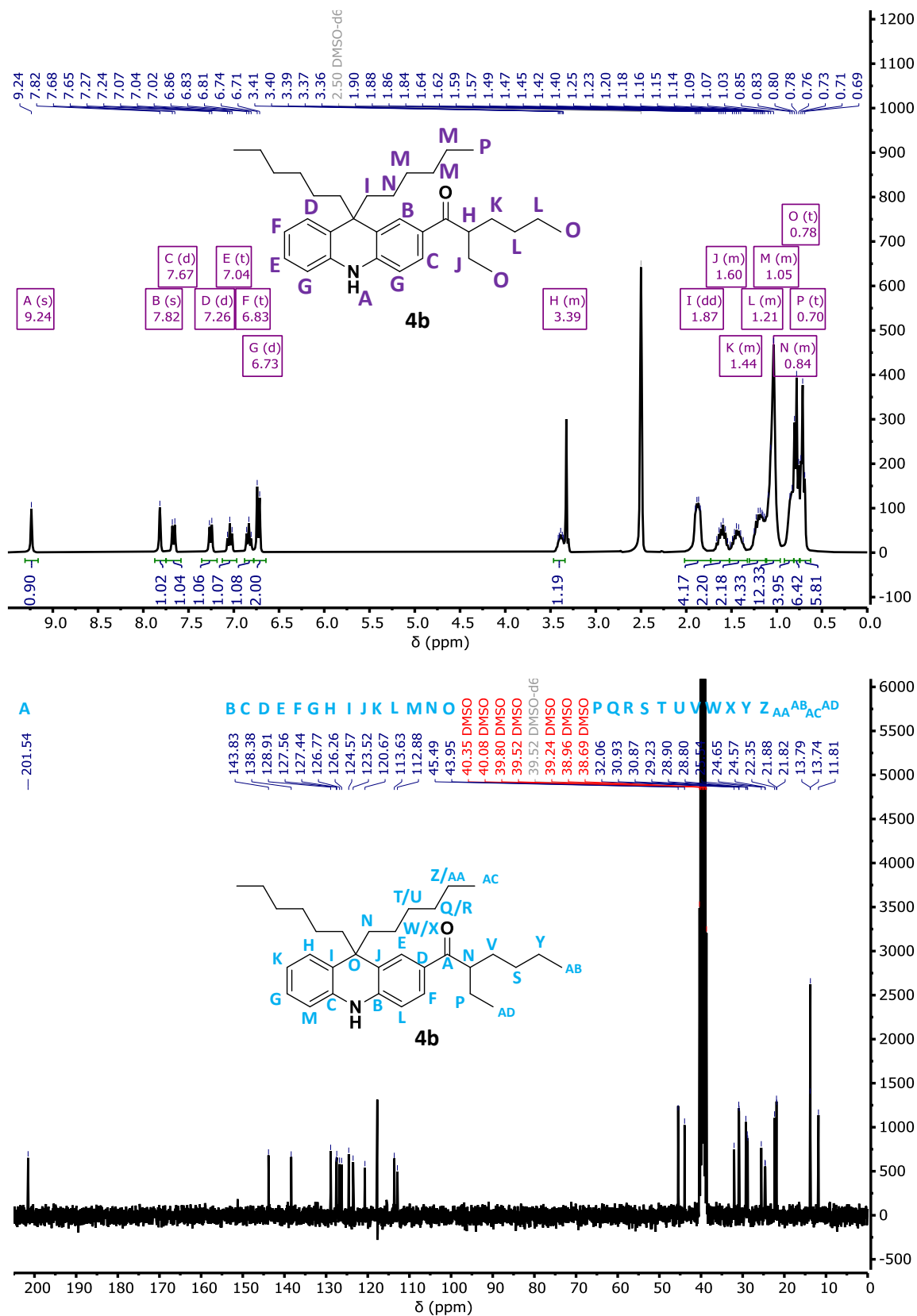


Figure 9.15. ^1H NMR (top) and ^{13}C NMR spectrum (bottom) of compound **4b**.

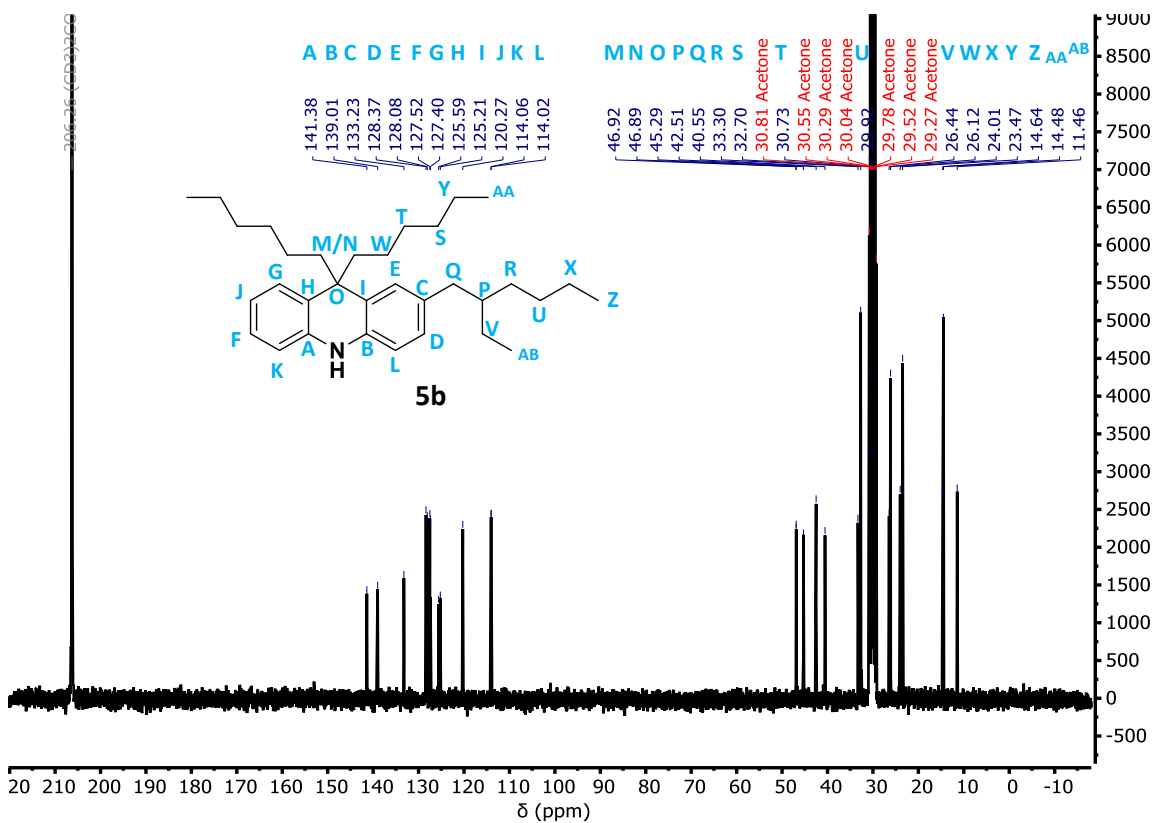
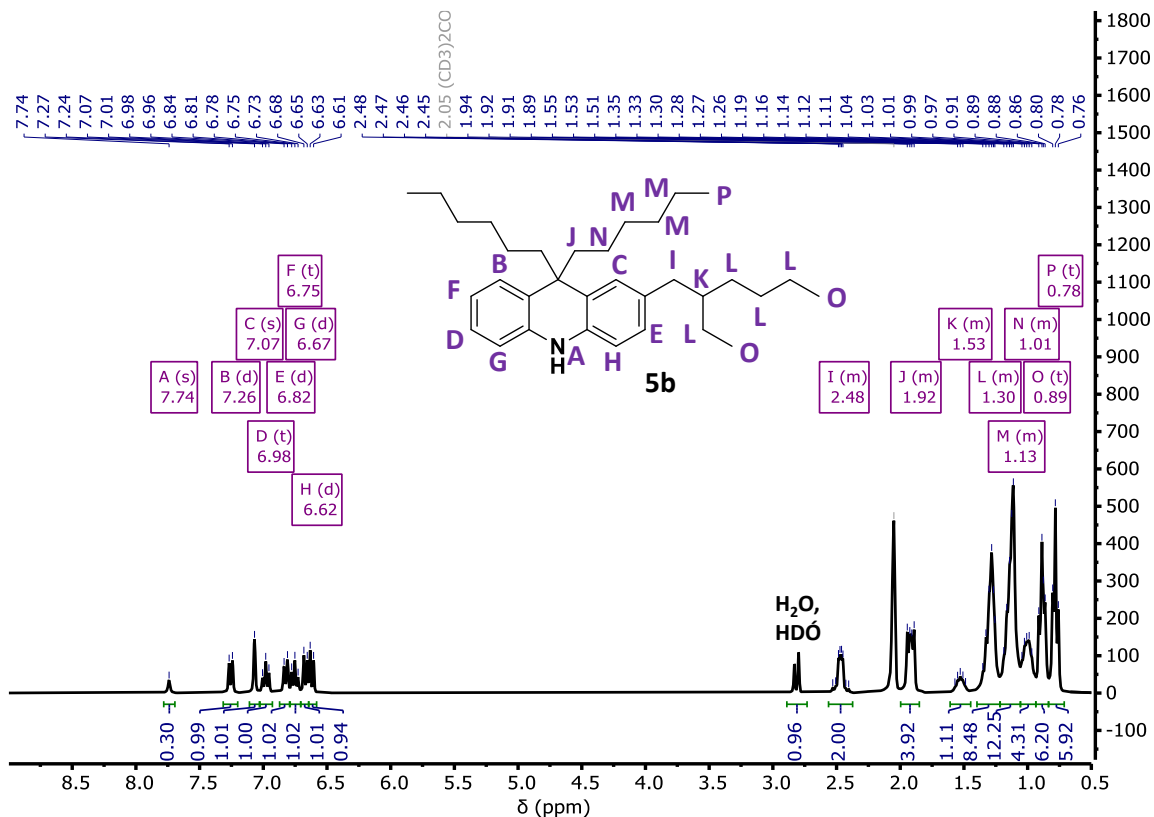


Figure 9.16. ¹H NMR (top) and ¹³C NMR spectrum (bottom) of compound 5b.

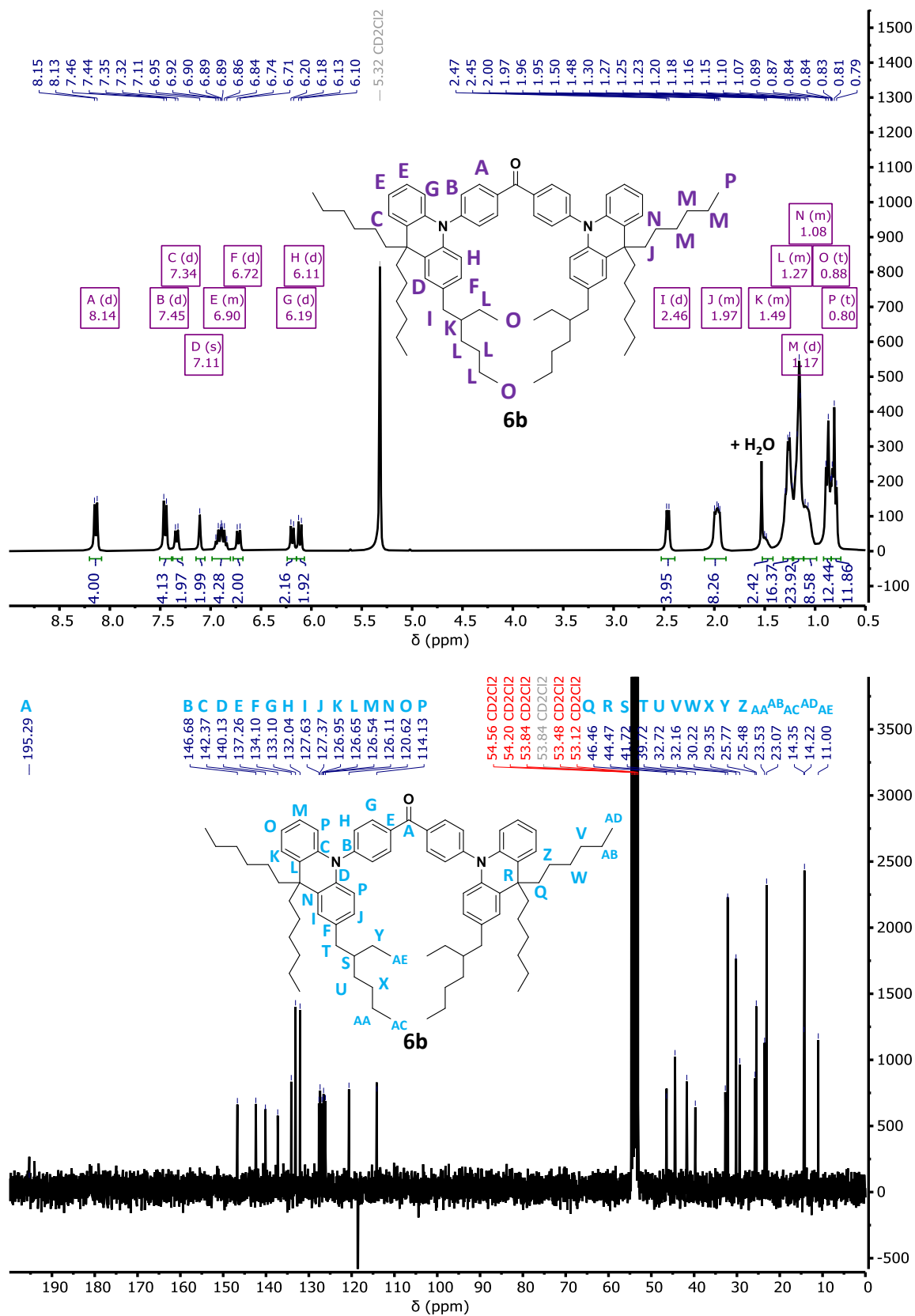


Figure 9.17. ^1H NMR (top) and ^{13}C NMR spectrum (bottom) of compound **6b**.

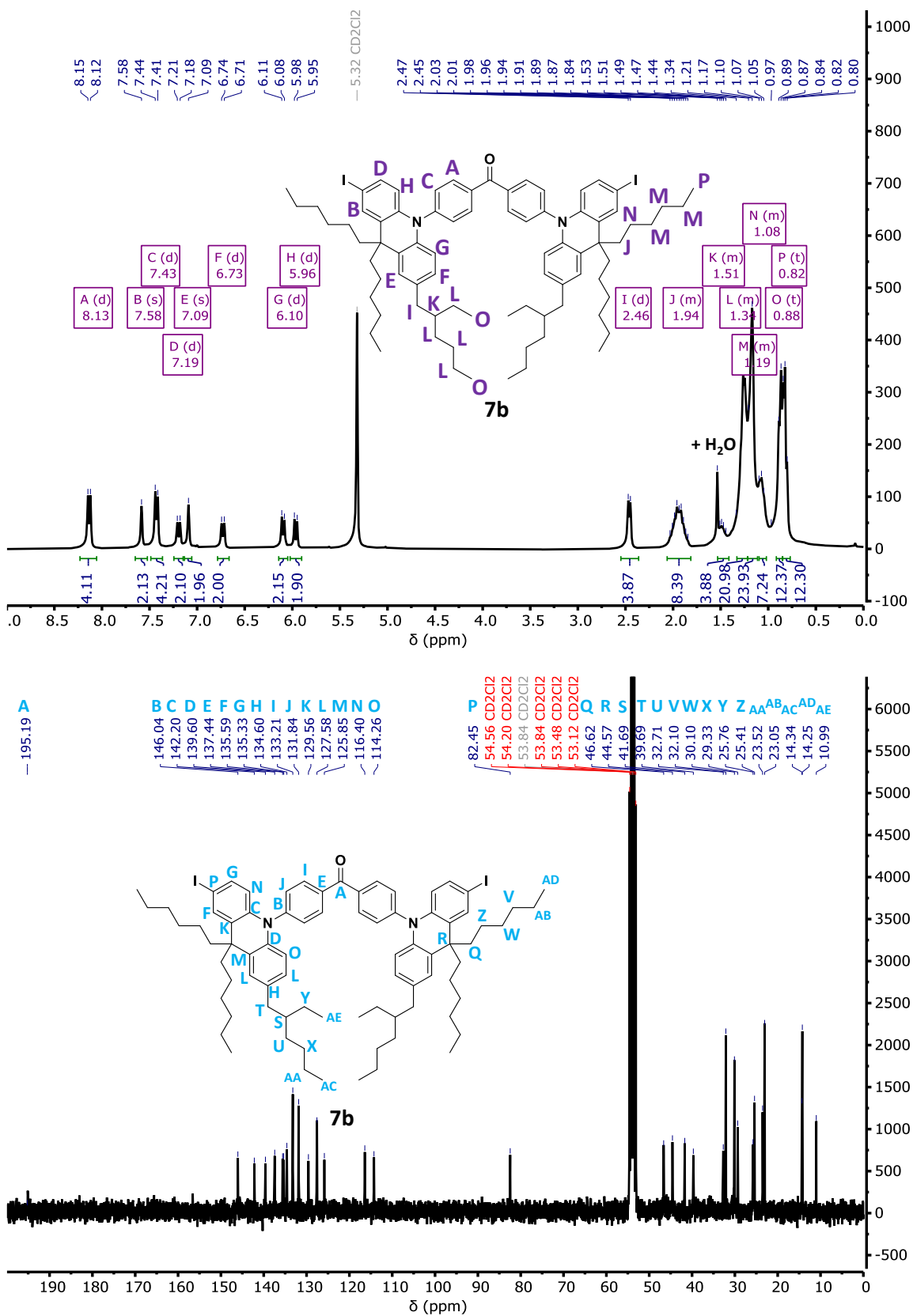


Figure 9.18. ¹H NMR (top) and ¹³C NMR spectrum (bottom) of compound **7b**.

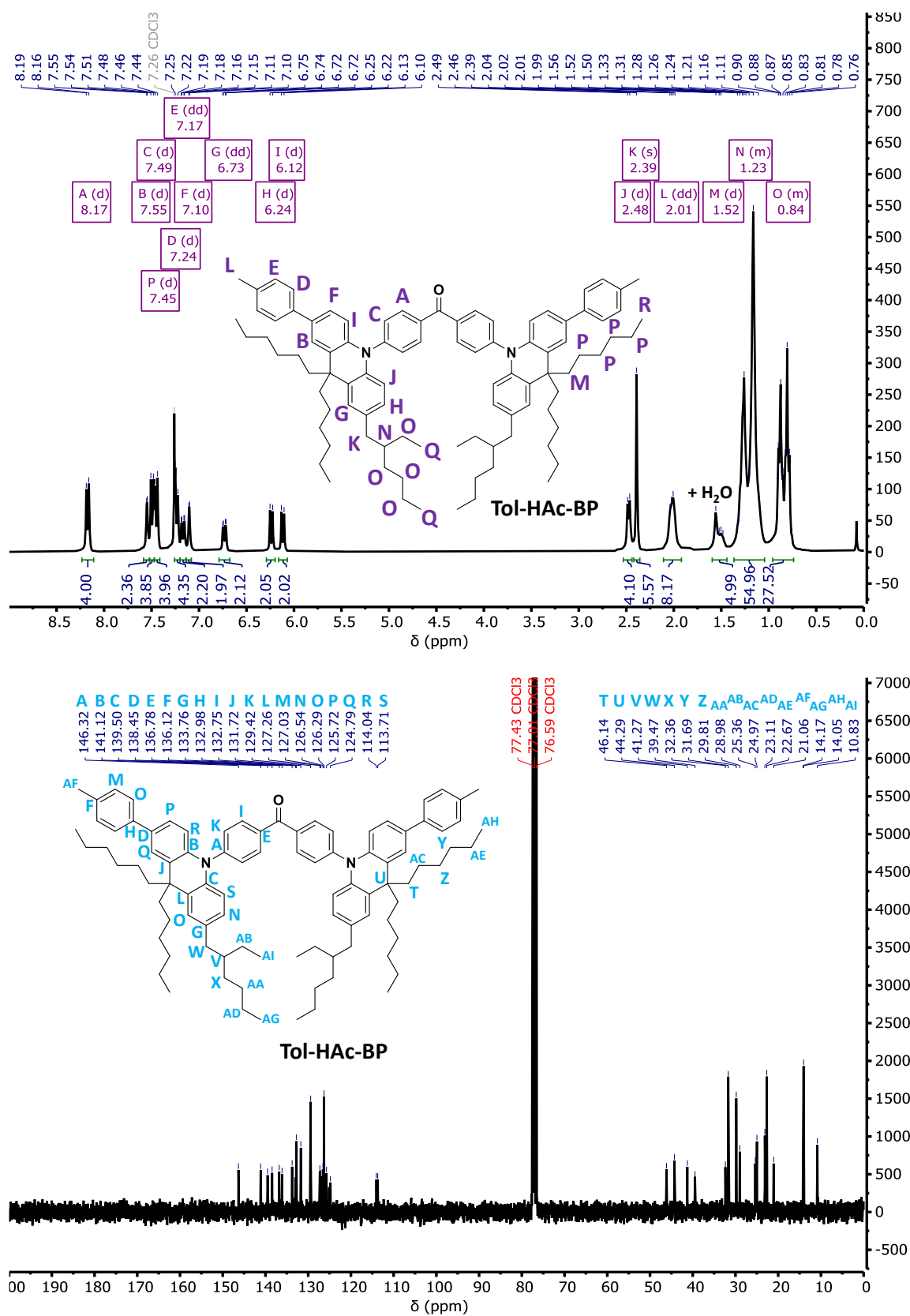


Figure 9.19. ¹H NMR (top) and ¹³C NMR spectrum (bottom) of compound Tol-HAc-BP.

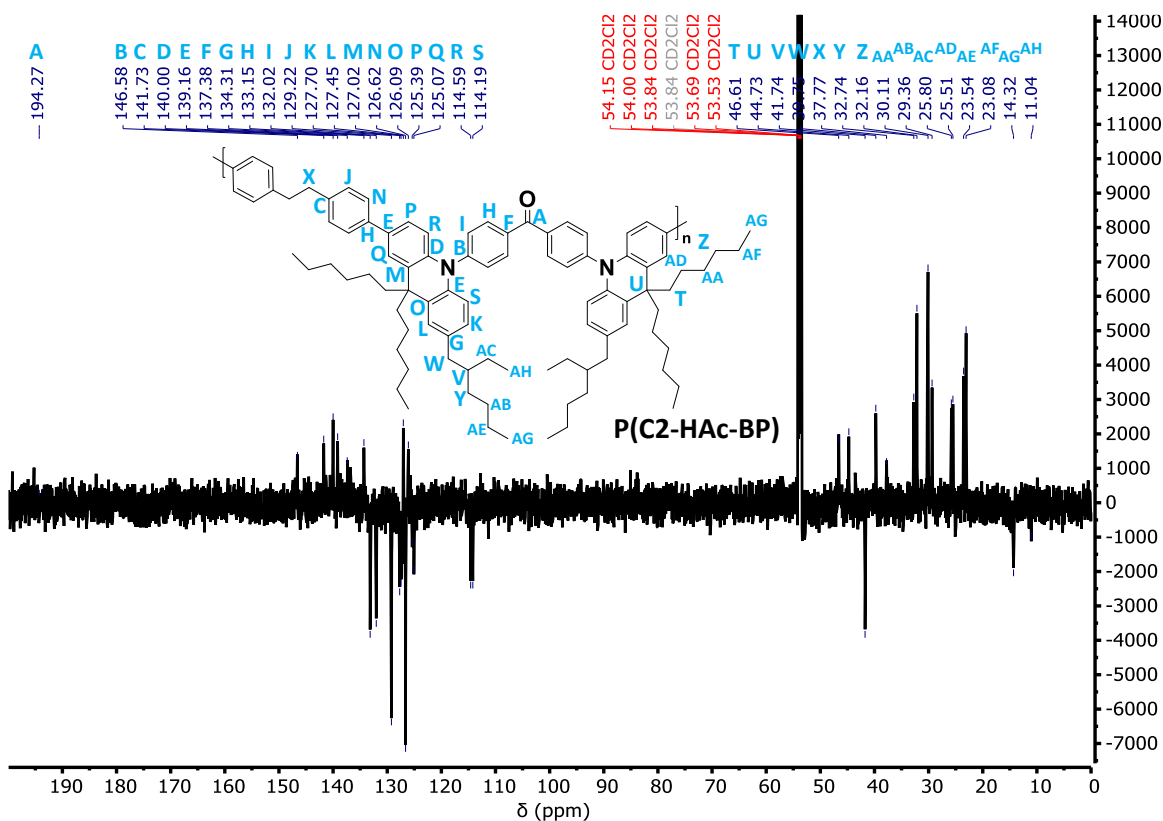
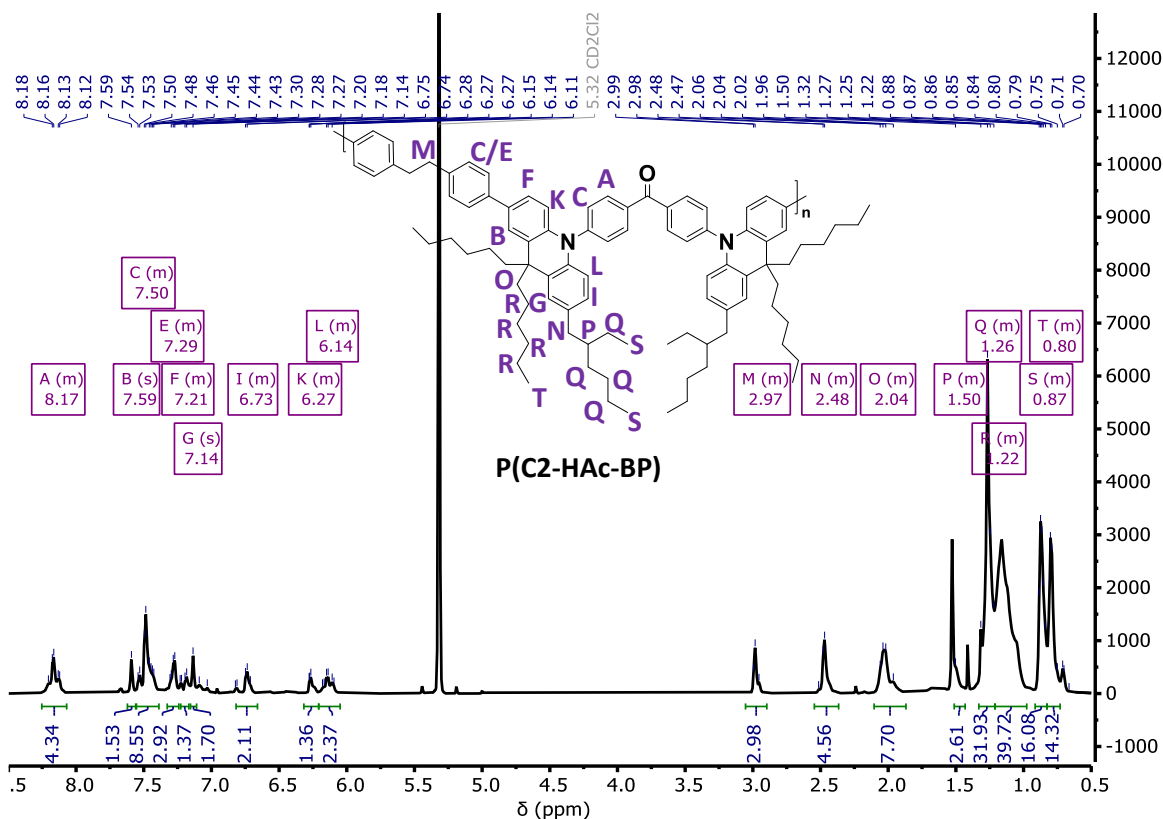


Figure 9.20. ¹H NMR (top) and ¹³C NMR J-mode spectrum (bottom) of compound P(C2-HAc-BP).

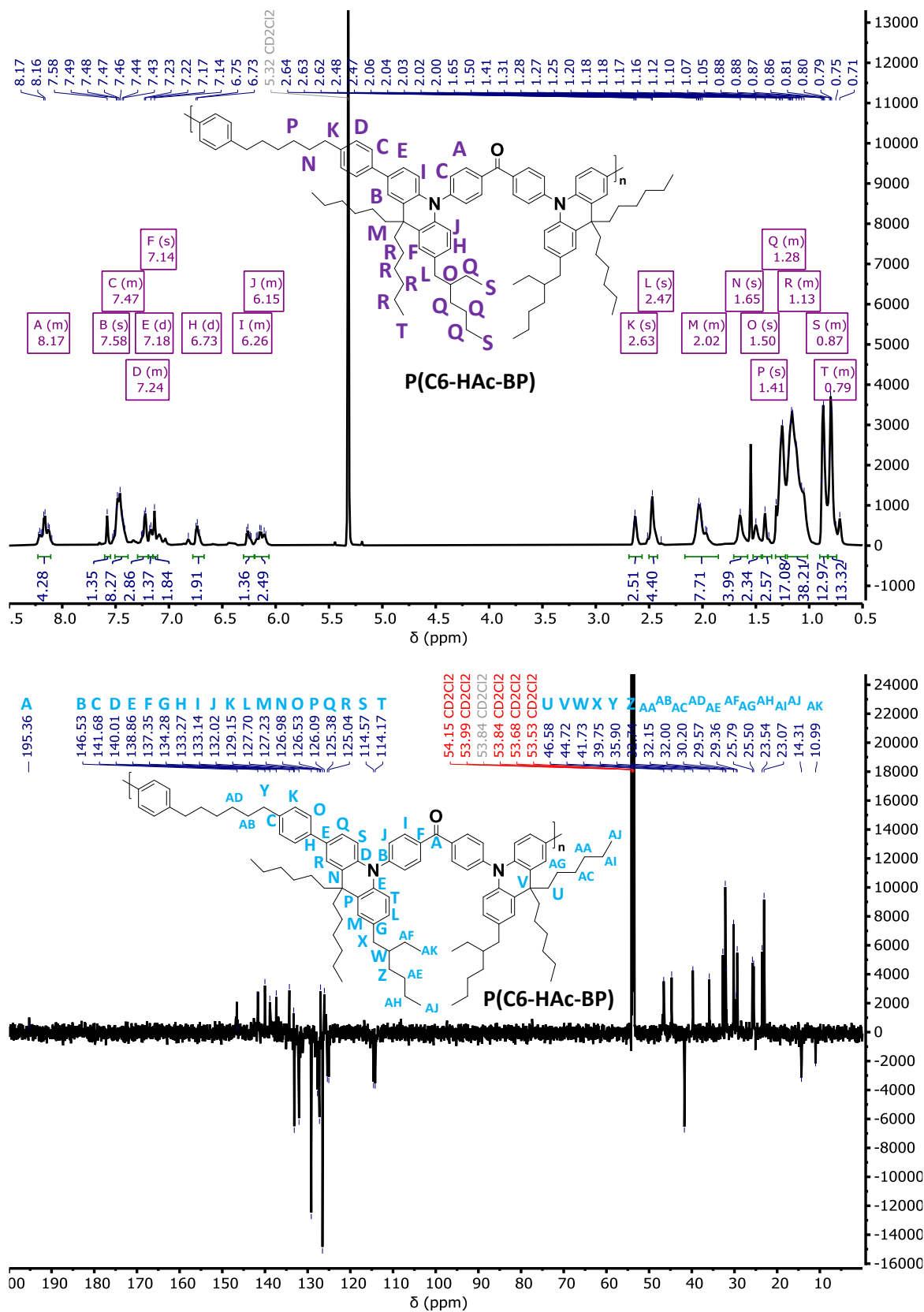


Figure 9.21. ^1H NMR (top) and ^{13}C NMR J -mode spectrum (bottom) of compound P(C6-HAc-BP).

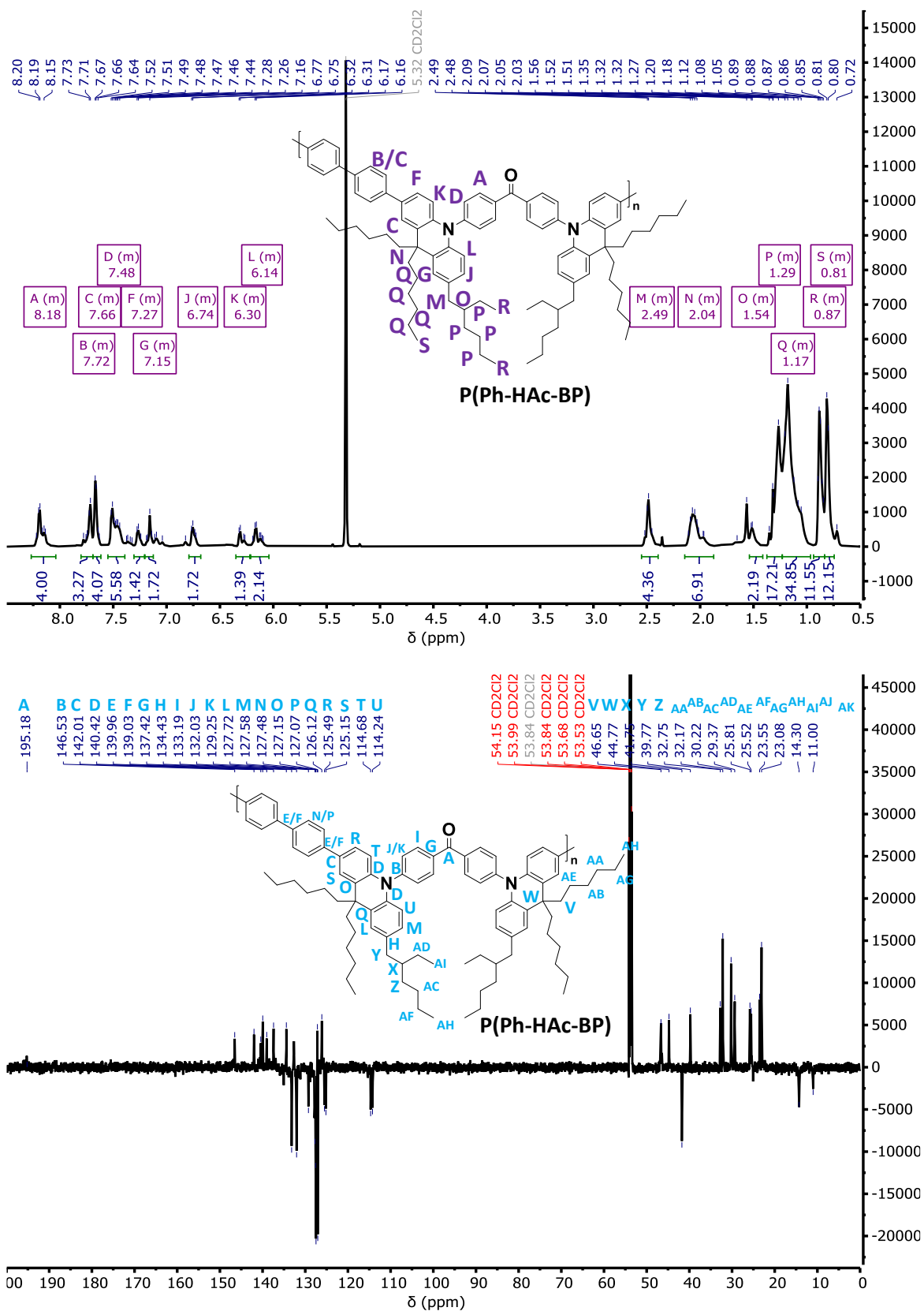


Figure 9.22. ^1H NMR (top) and ^{13}C NMR J -mode spectrum (bottom) of compound **P(Ph-HAc-BP)**.

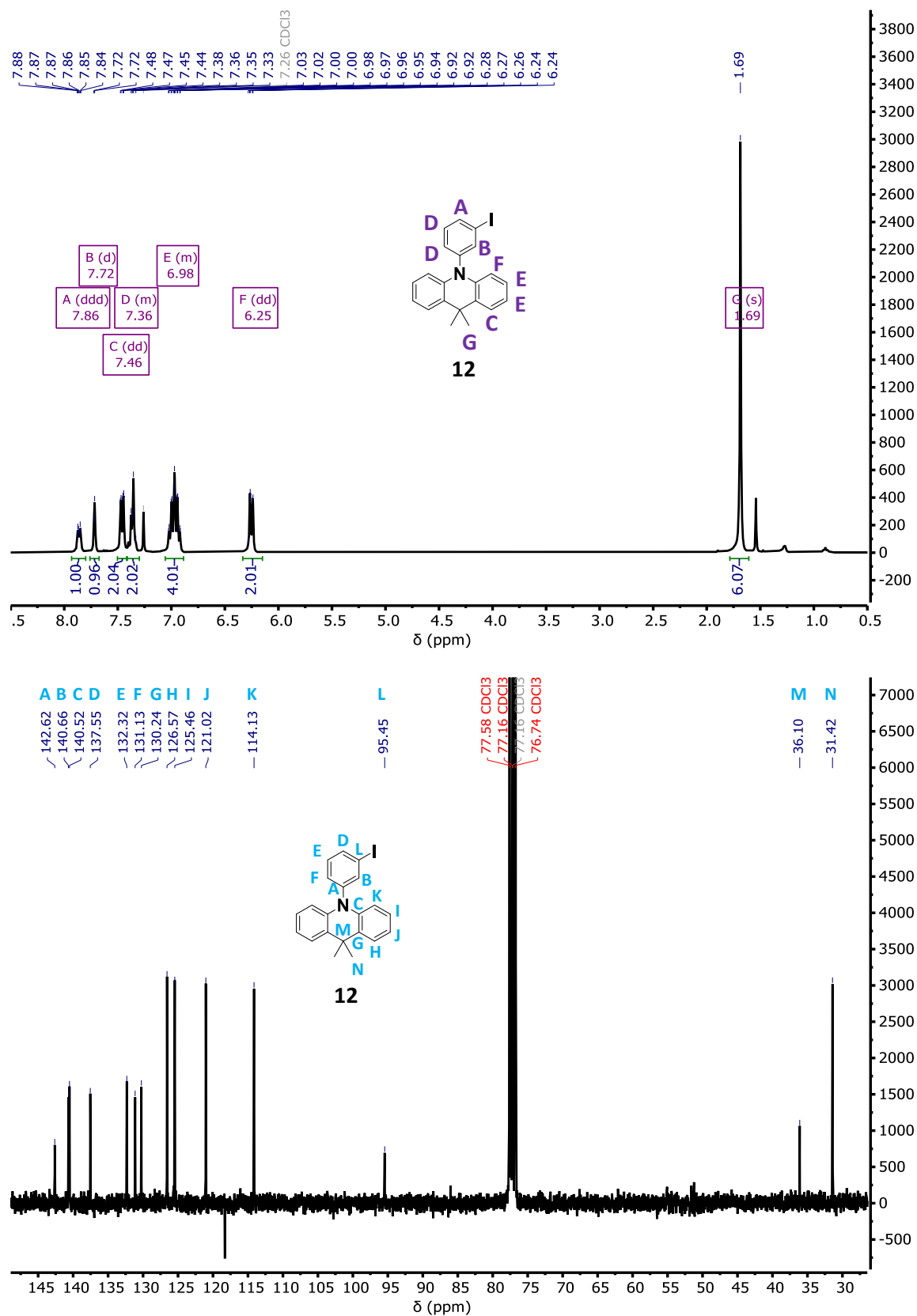


Figure 9.23. ¹H NMR (top) and ¹³C NMR spectrum (bottom) of compound **12**.

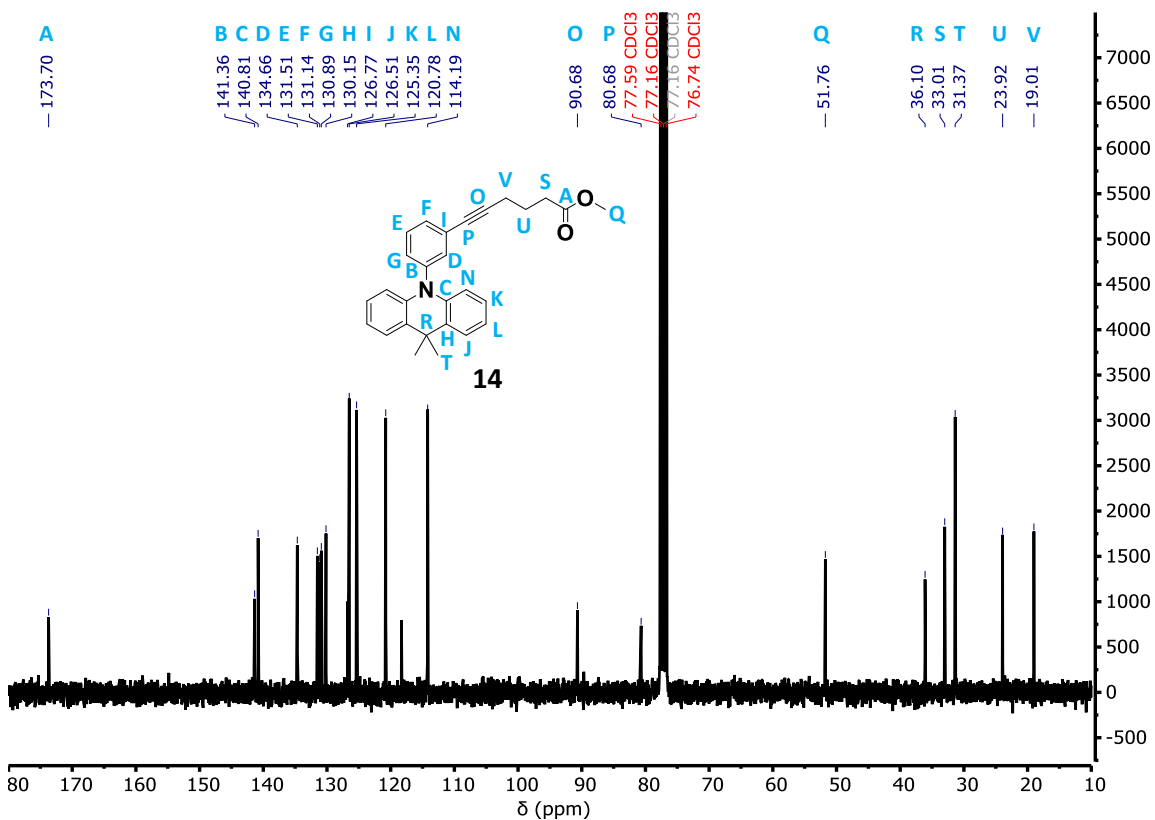
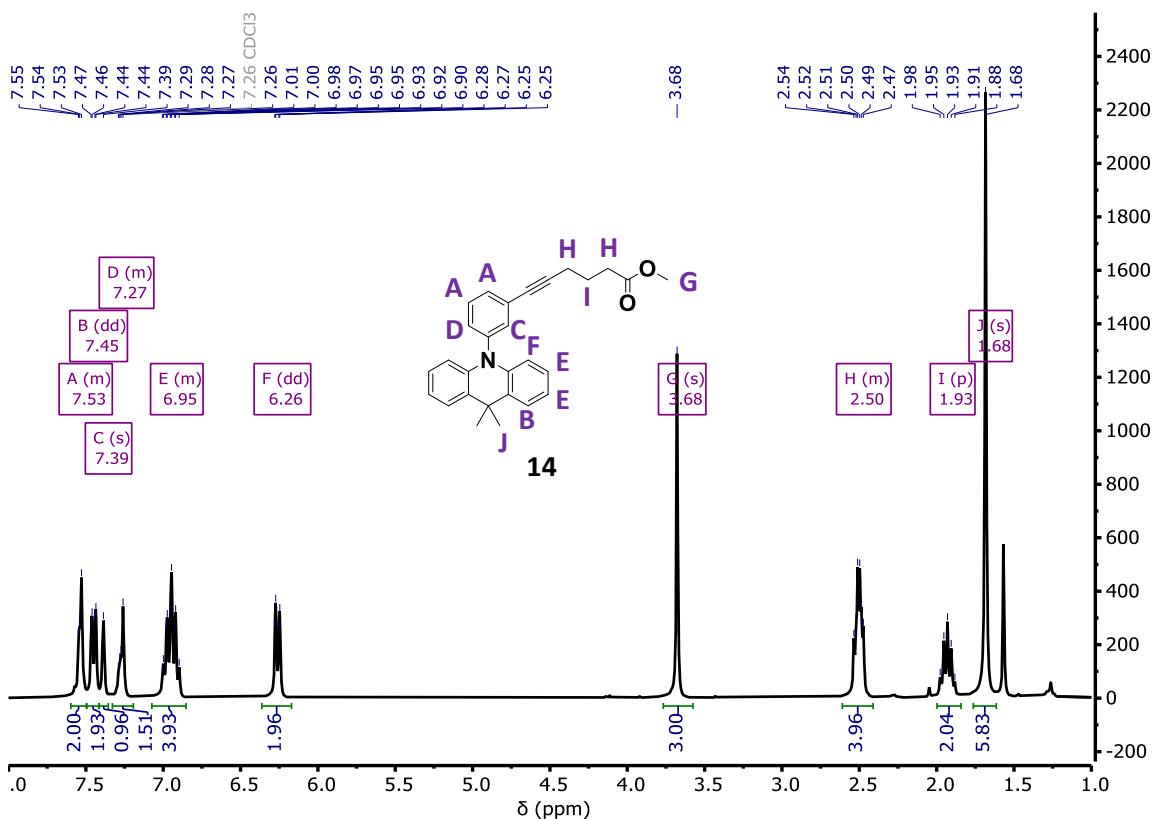


Figure 9.24. ¹H NMR (top) and ¹³C NMR spectrum (bottom) of compound 15.

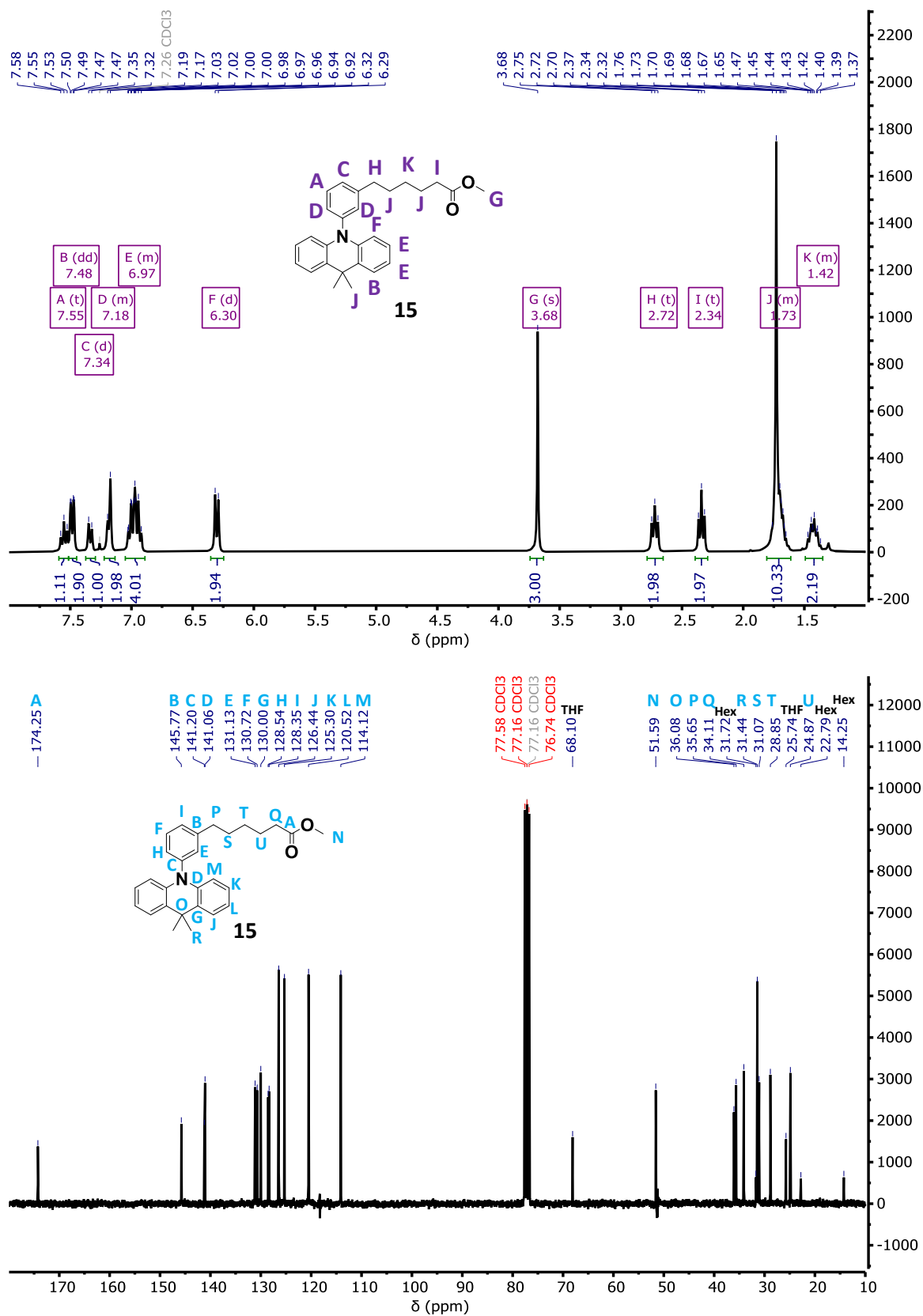


Figure 9.25. ¹H NMR (top) and ¹³C NMR spectrum (bottom) of compound **15**.

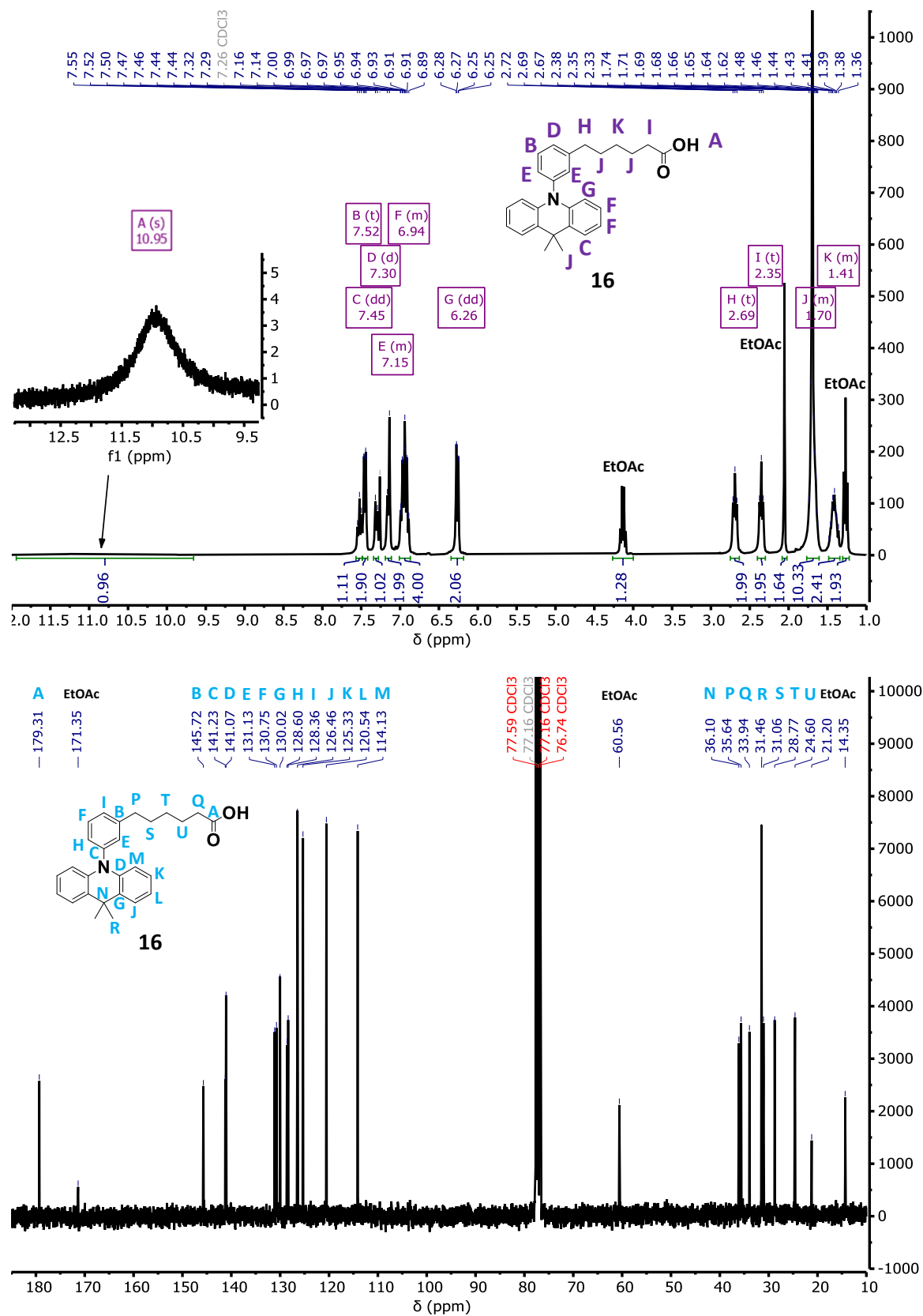


Figure 9.26. ¹H NMR (top) and ¹³C NMR spectrum (bottom) of compound 16.

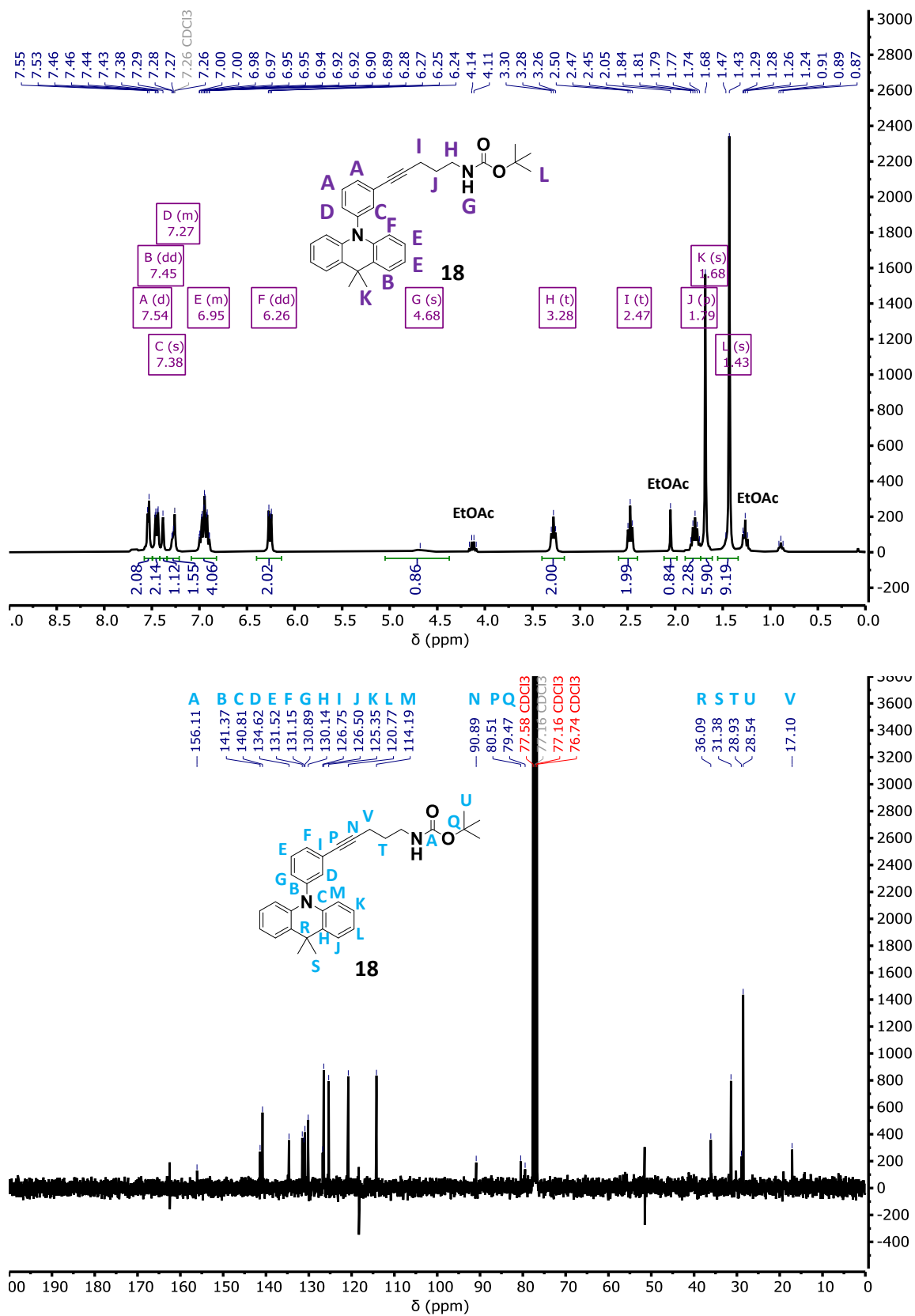


Figure 9.27. ¹H NMR (top) and ¹³C NMR spectrum (bottom) of compound **18**.

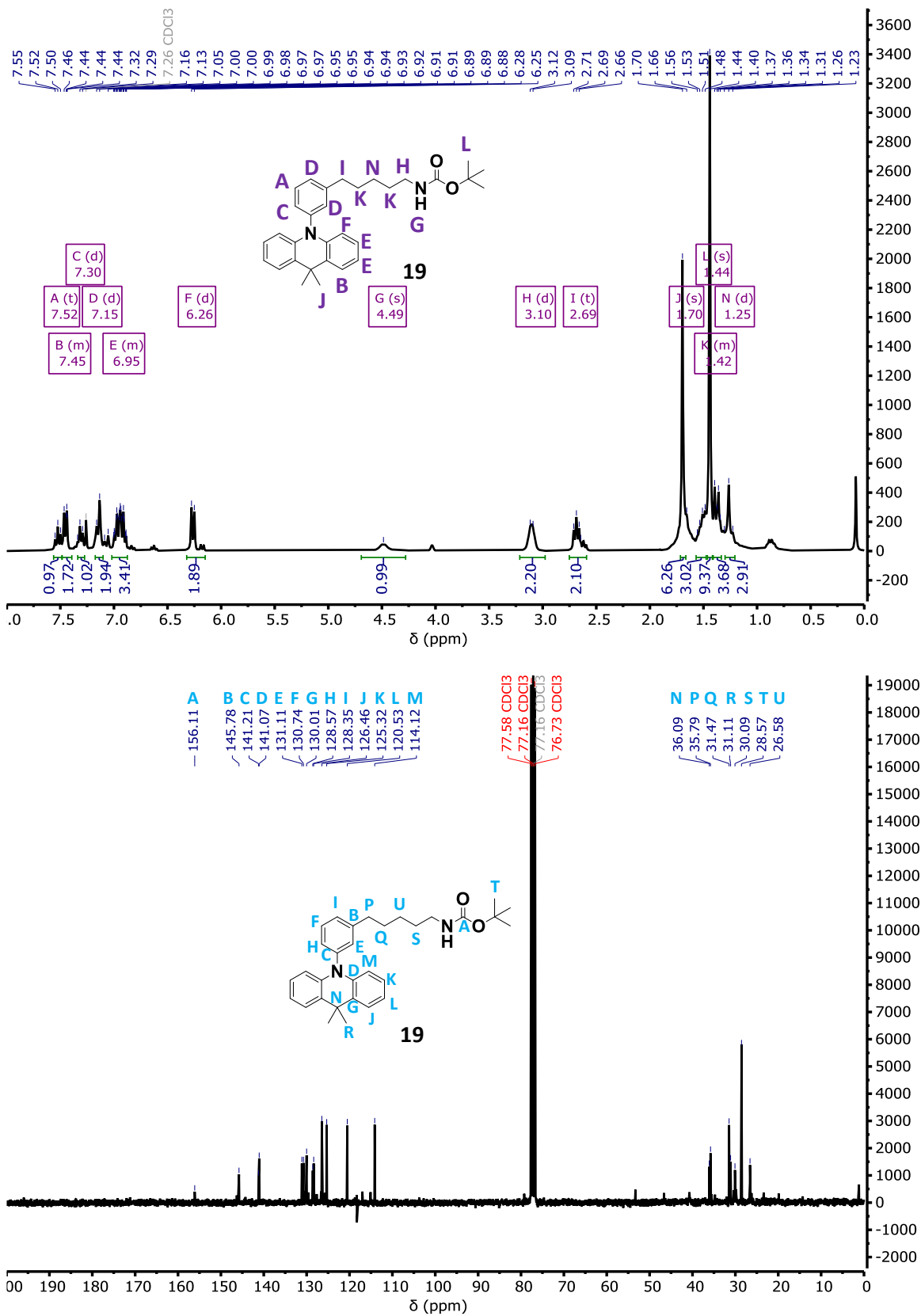


Figure 9.28. ¹H NMR (top) and ¹³C NMR spectrum (bottom) of compound **19**.

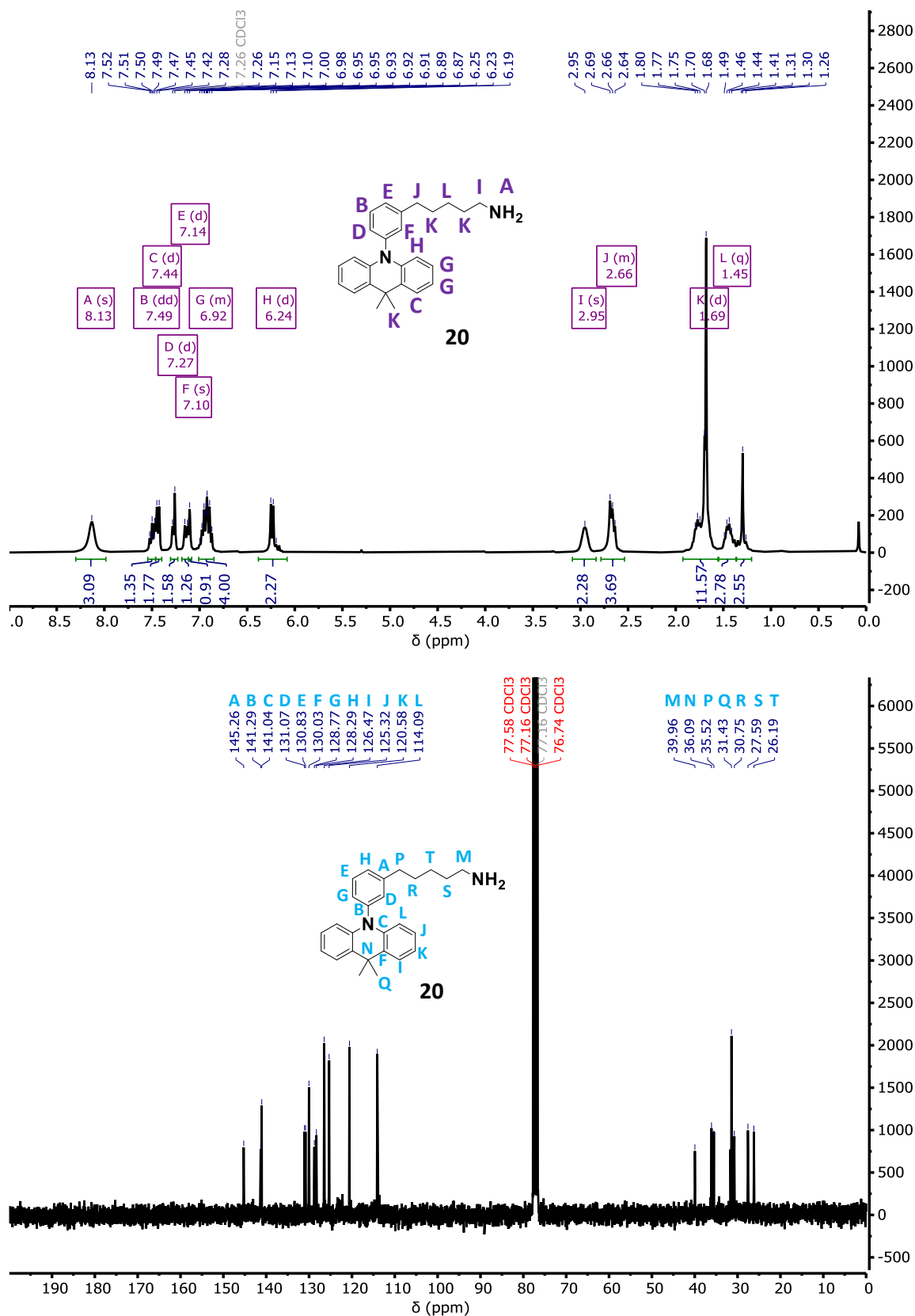


Figure 9.29. ¹H NMR (top) and ¹³C NMR spectrum (bottom) of compound 20.

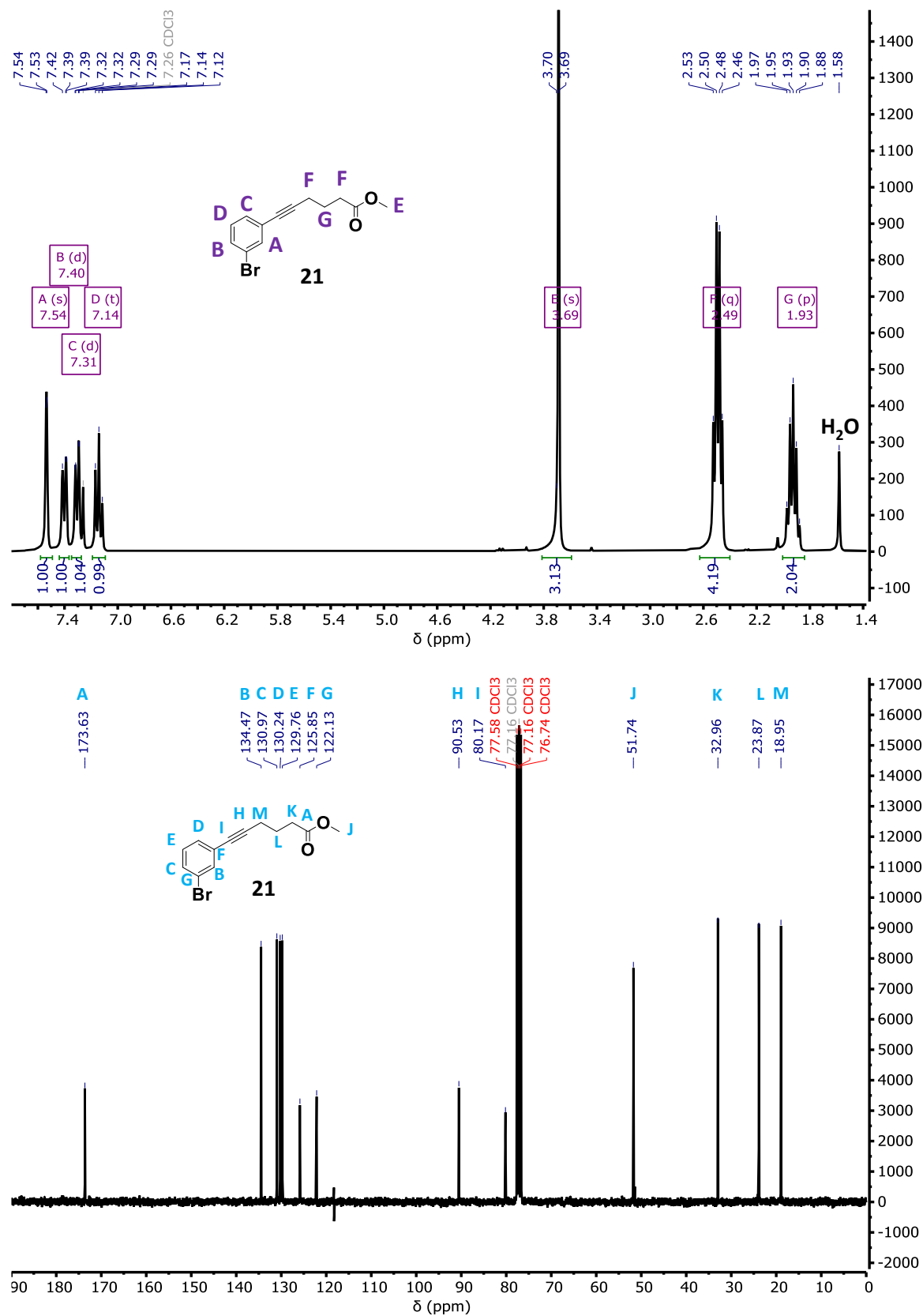


Figure 9.30. ¹H NMR (top) and ¹³C NMR spectrum (bottom) of compound 21.

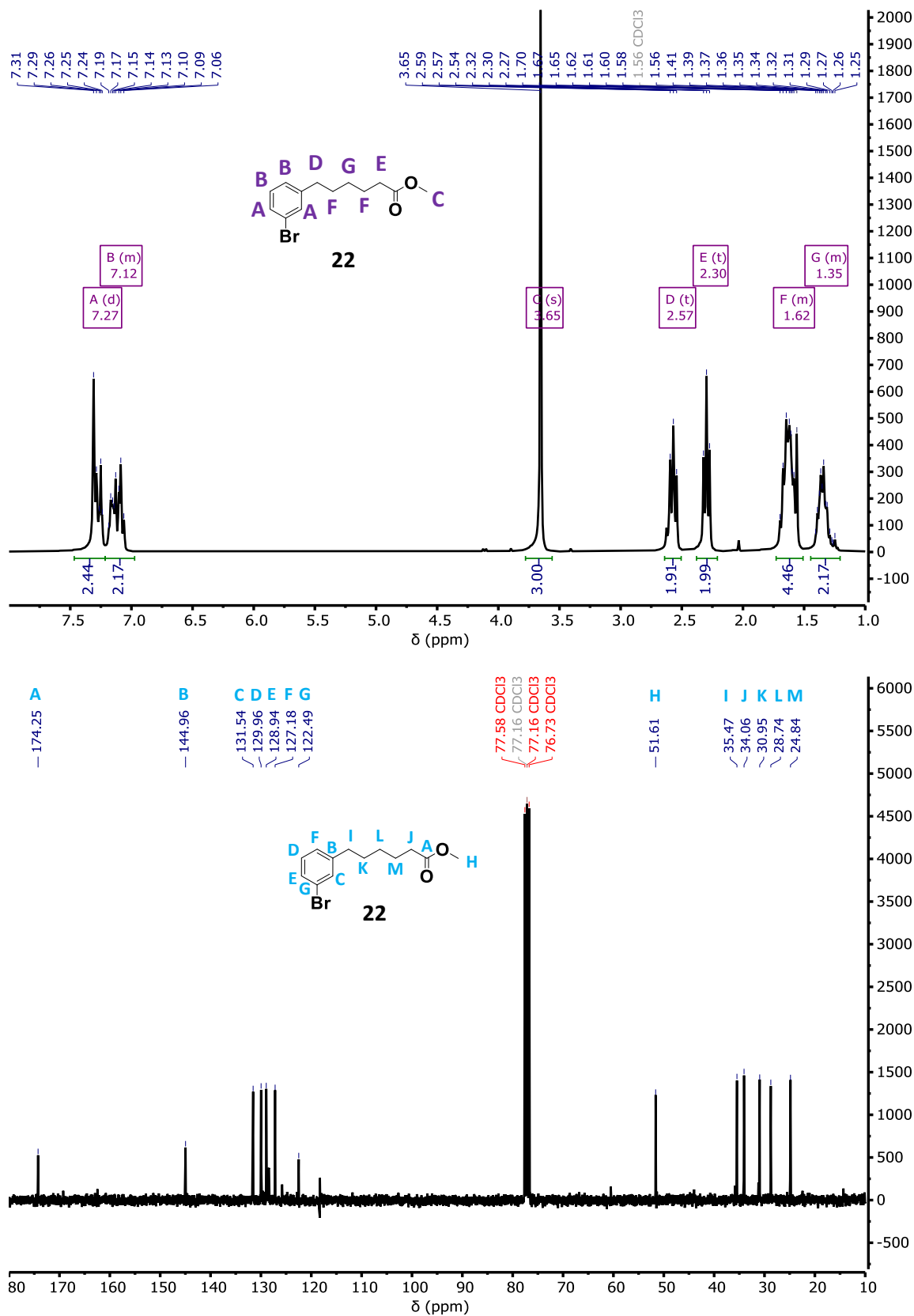


Figure 9.31. ¹H NMR (top) and ¹³C NMR spectrum (bottom) of compound **22**.

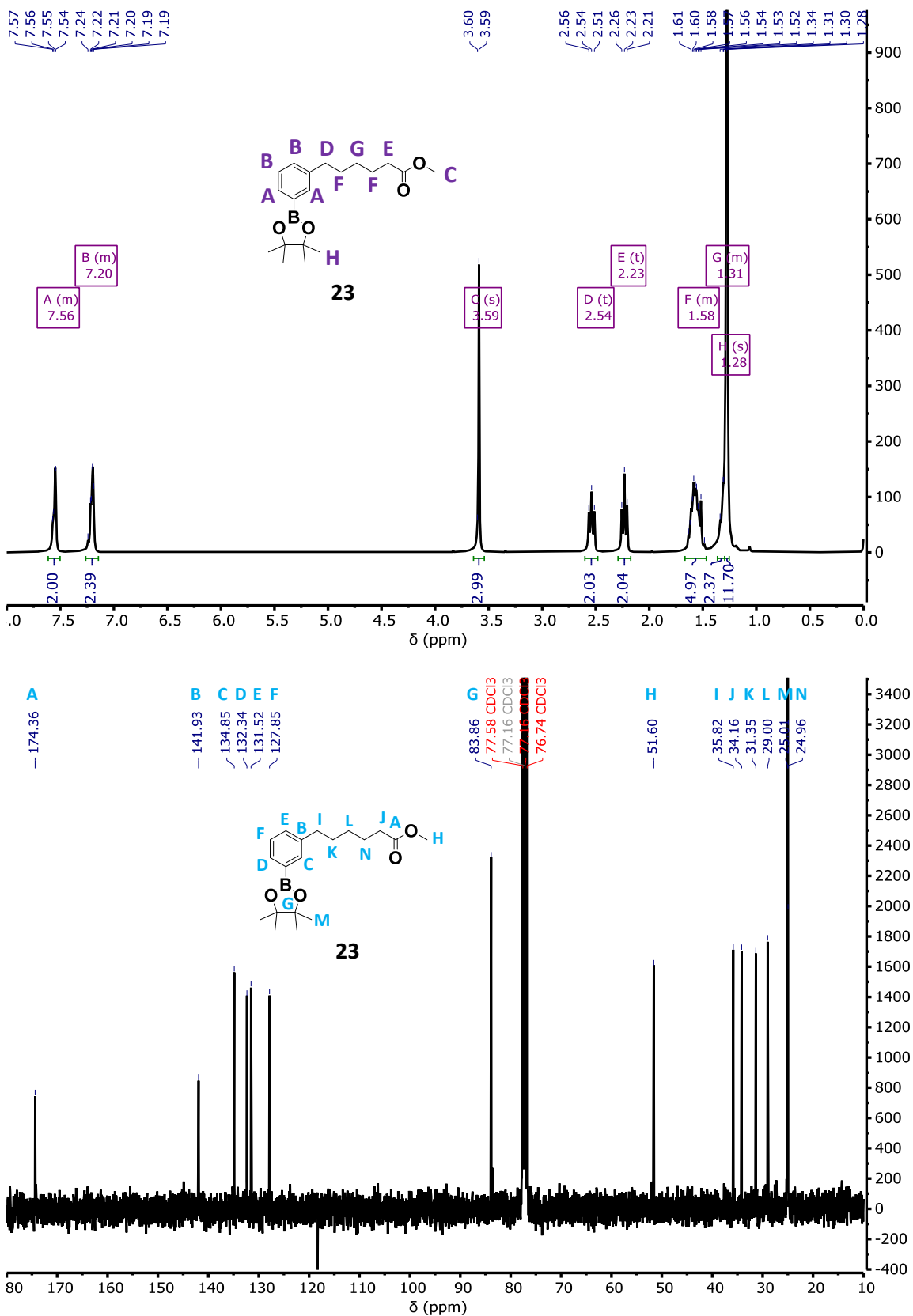


Figure 9.32. ¹H NMR (top) and ¹³C NMR spectrum (bottom) of compound 23.

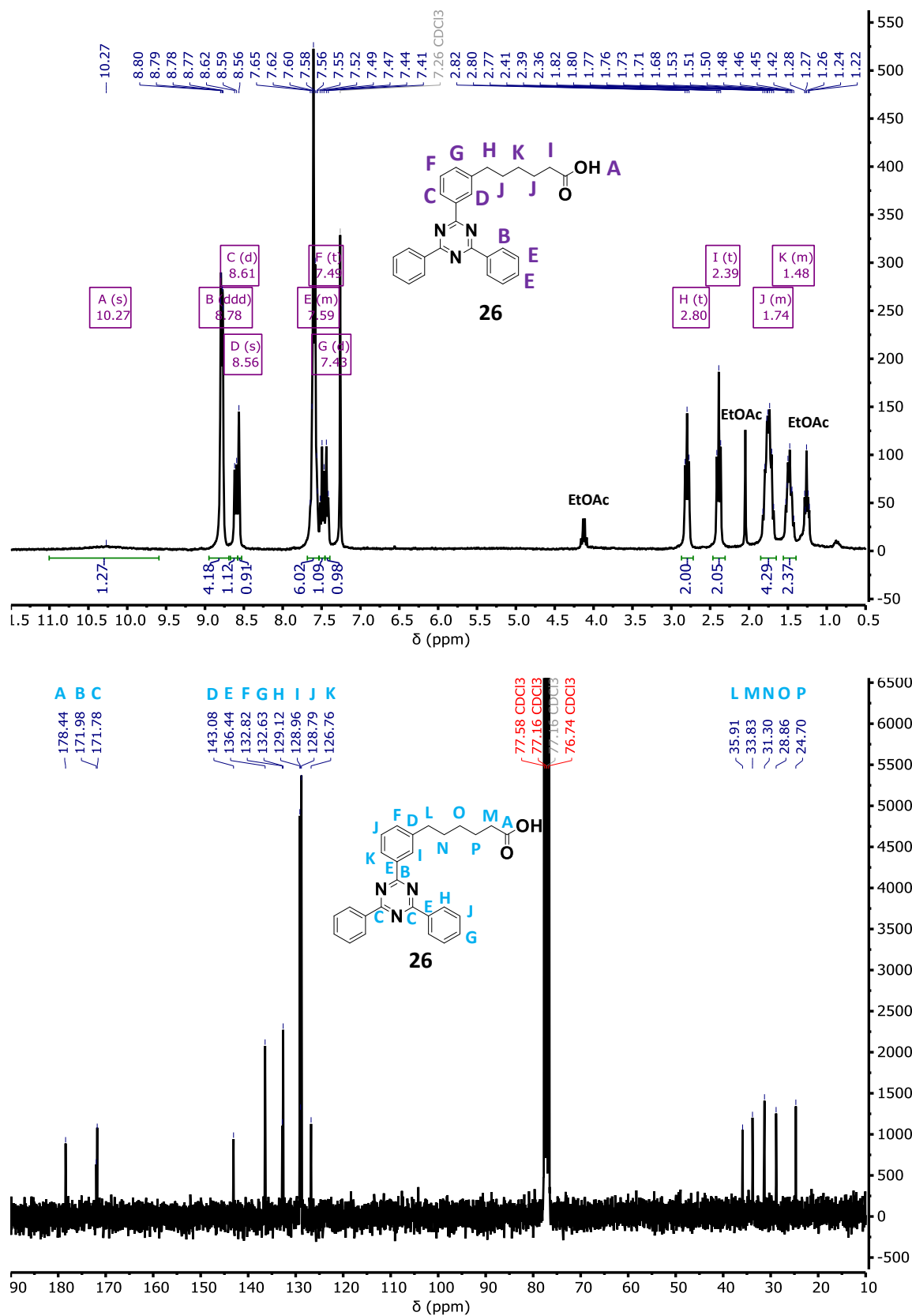


Figure 9.33. ¹H NMR (top) and ¹³C NMR spectrum (bottom) of compound 26.

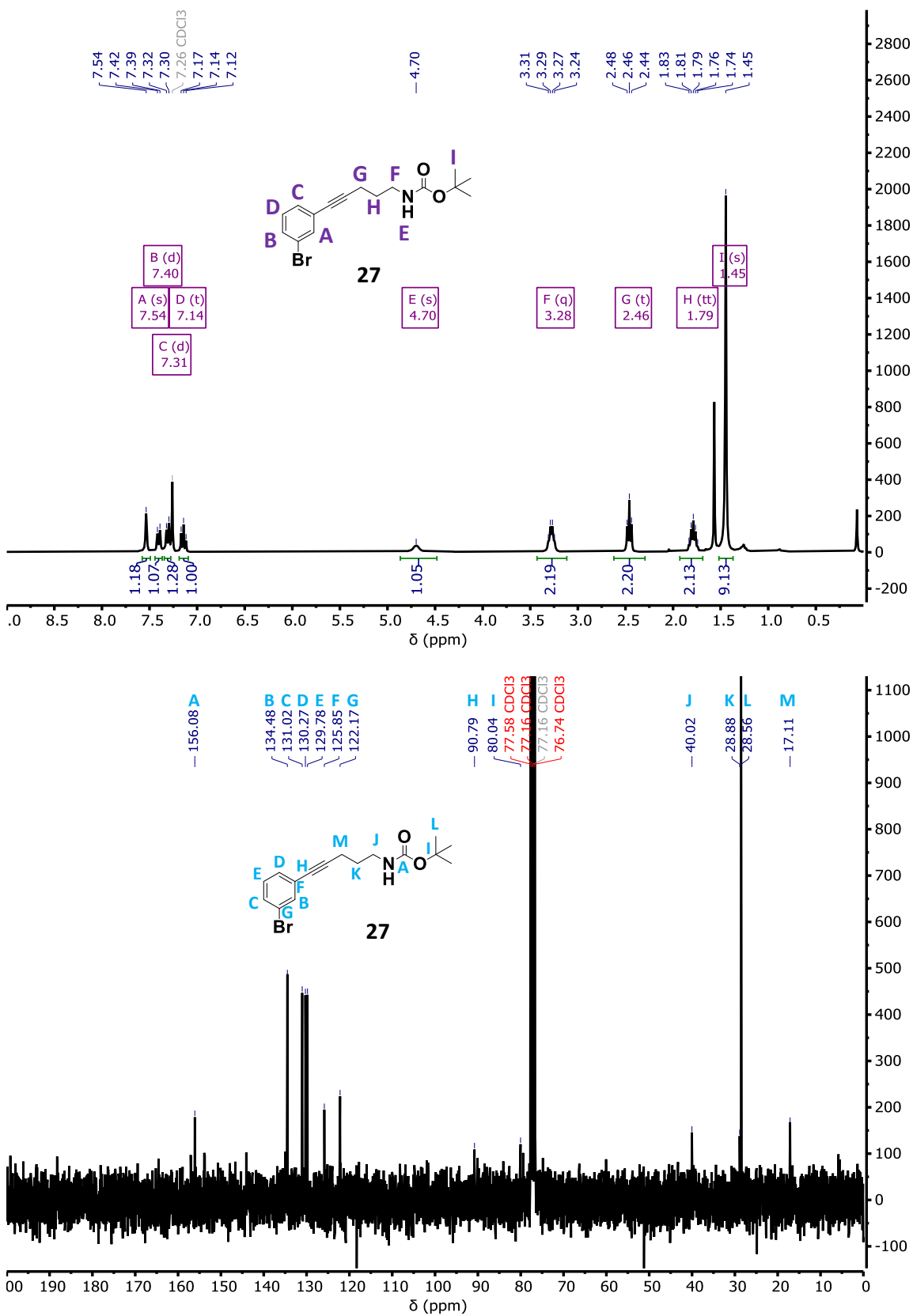


Figure 9.34. ¹H NMR (top) and ¹³C NMR spectrum (bottom) of compound 27.

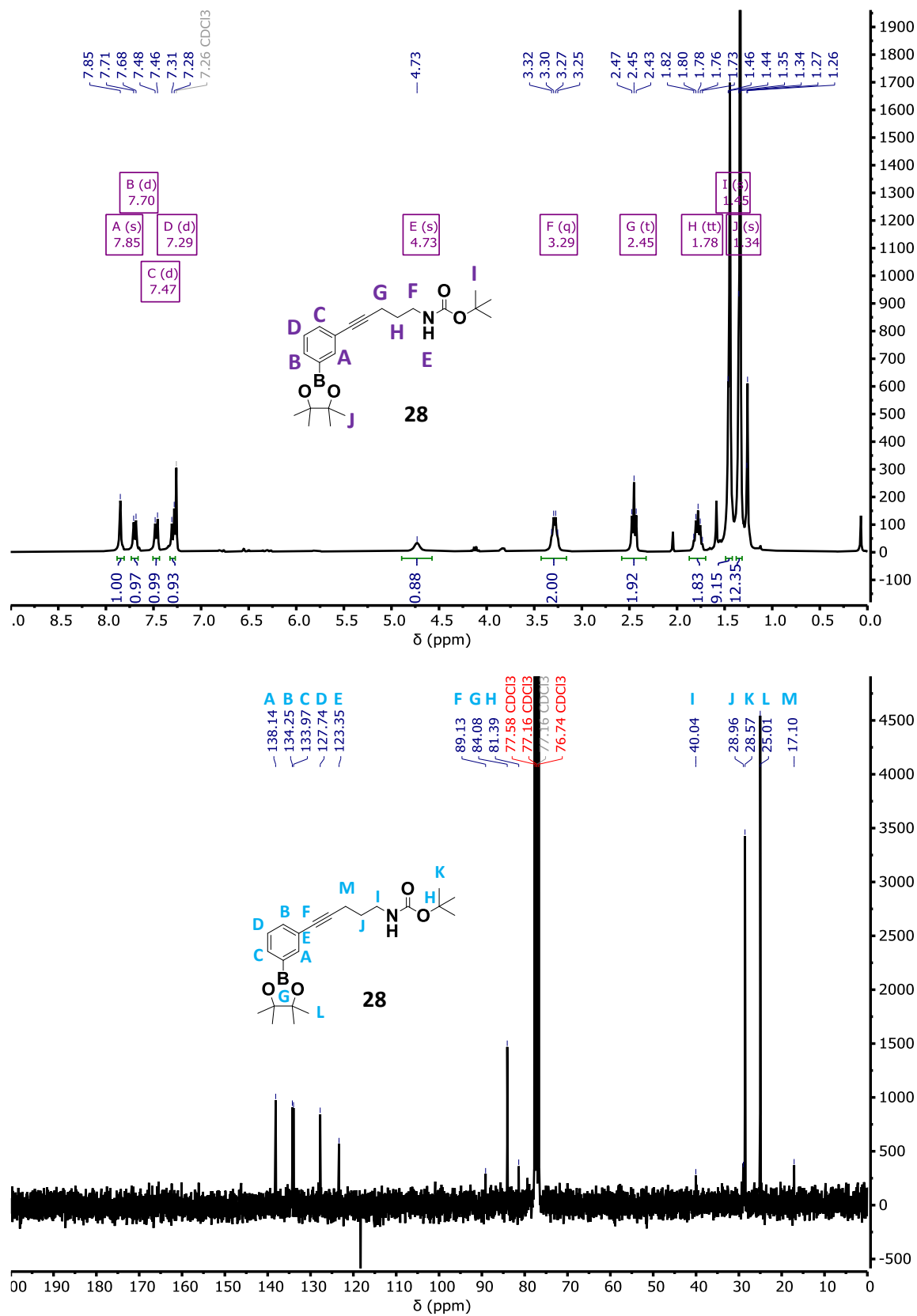


Figure 9.35. ^1H NMR (top) and ^{13}C NMR spectrum (bottom) of compound **28**.

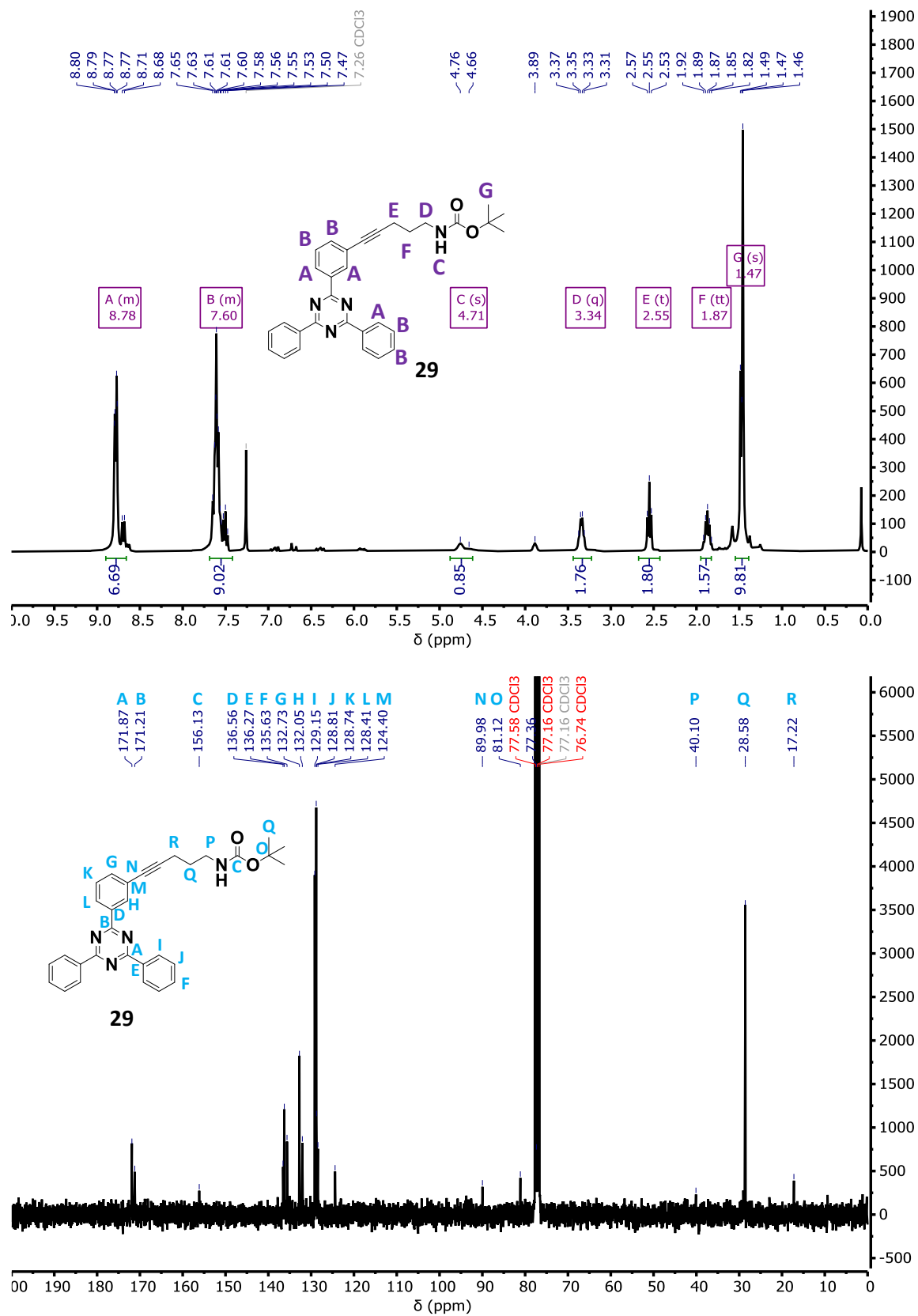


Figure 9.36. ^1H NMR (top) and ^{13}C NMR spectrum (bottom) of compound 29.

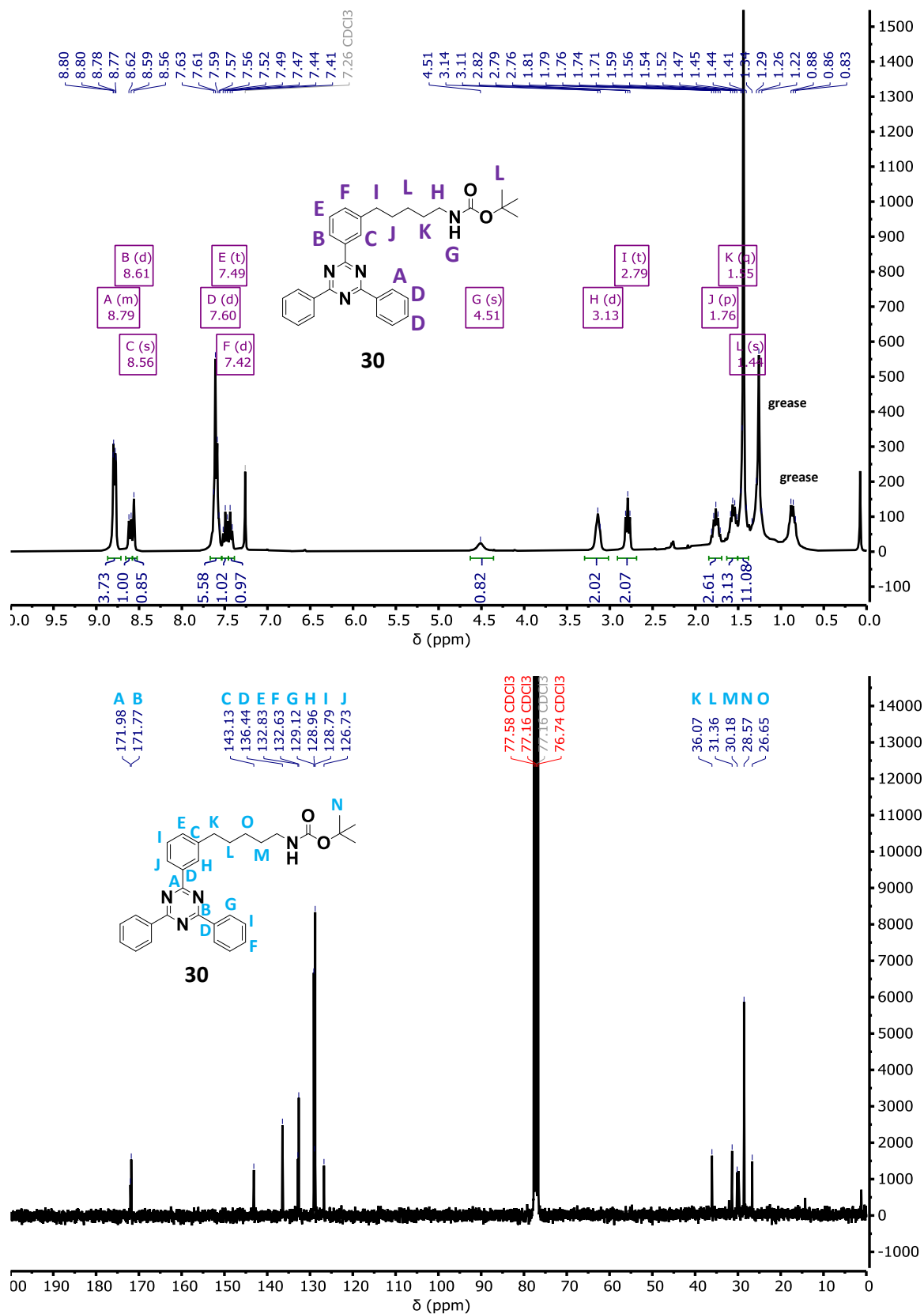


Figure 9.37. ^1H NMR (top) and ^{13}C NMR spectrum (bottom) of compound 30.

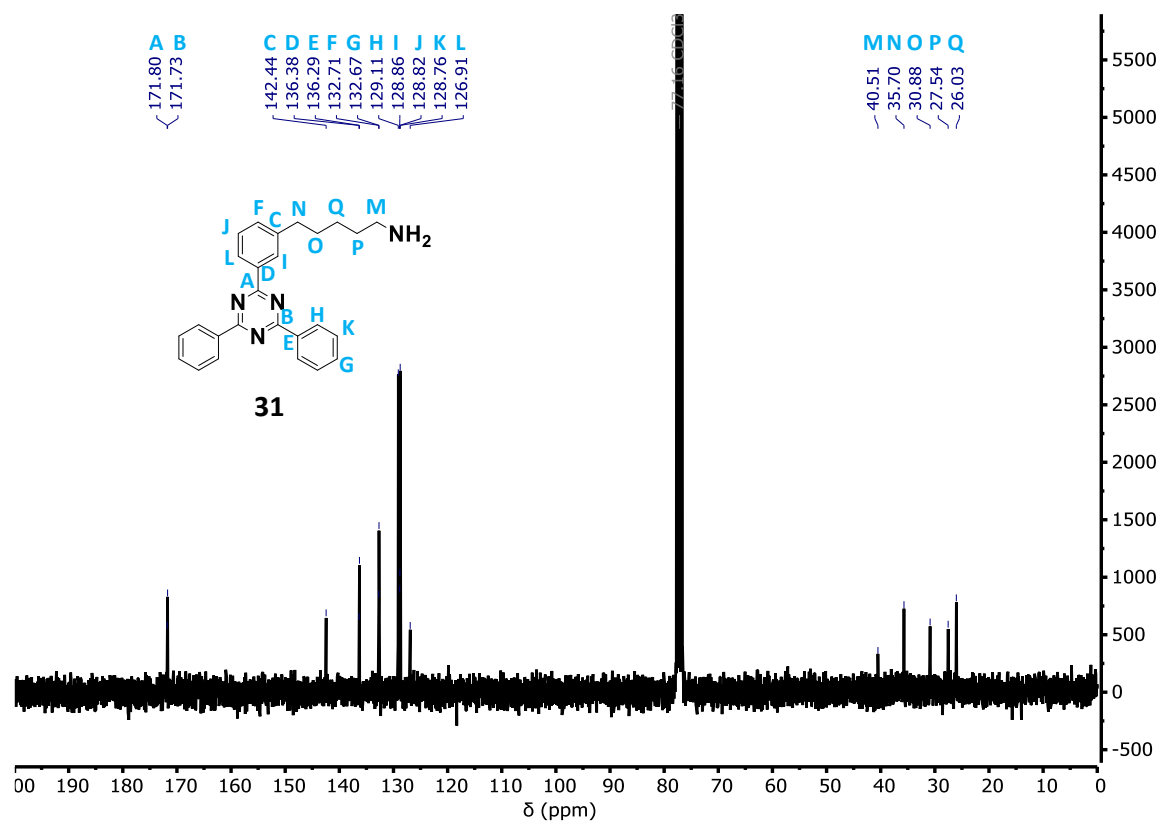
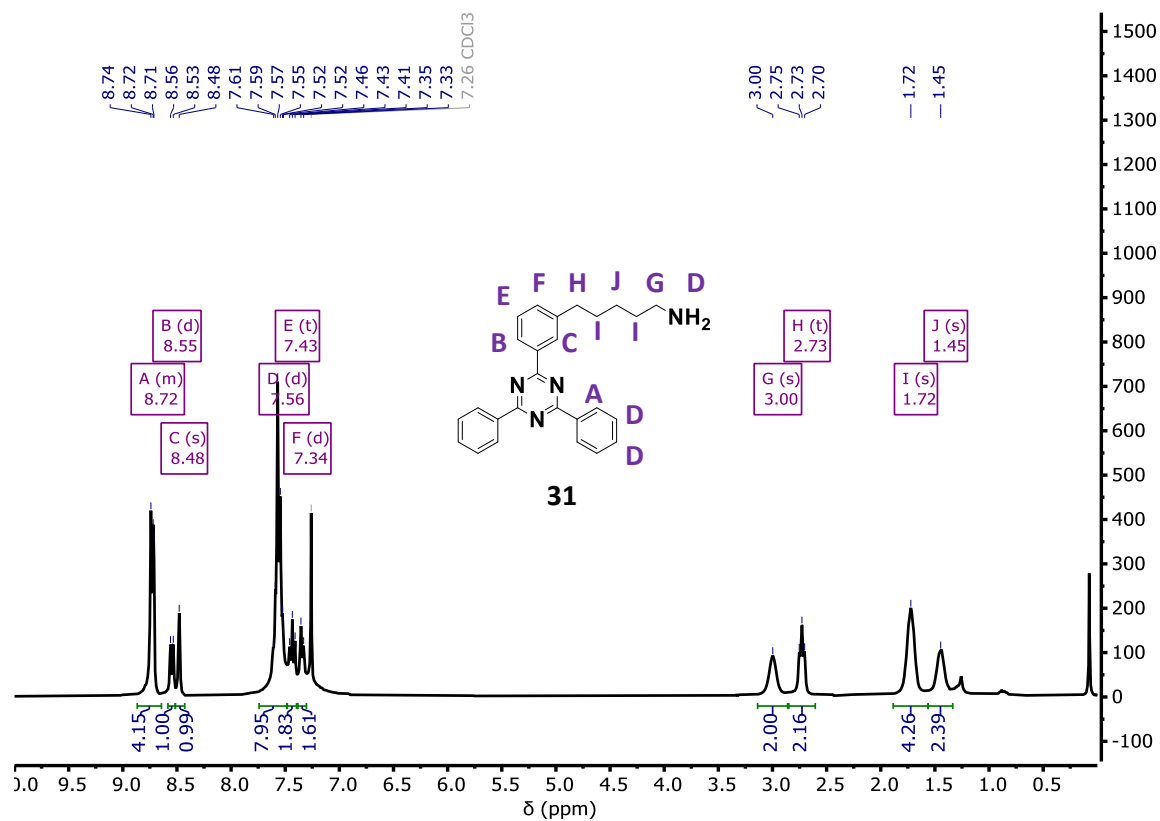


Figure 9.38. ¹H NMR (top) and ¹³C NMR spectrum (bottom) of compound 31.

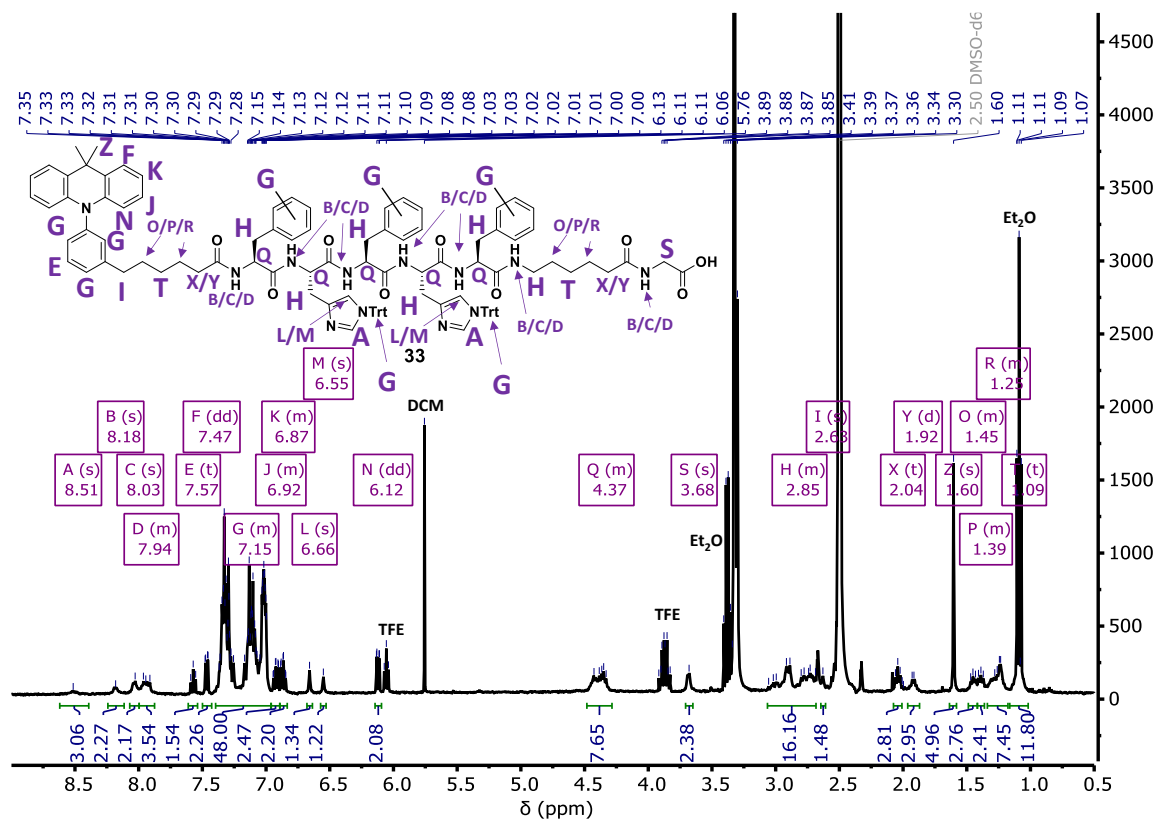


Figure 9.39. ^1H NMR of compound 33.

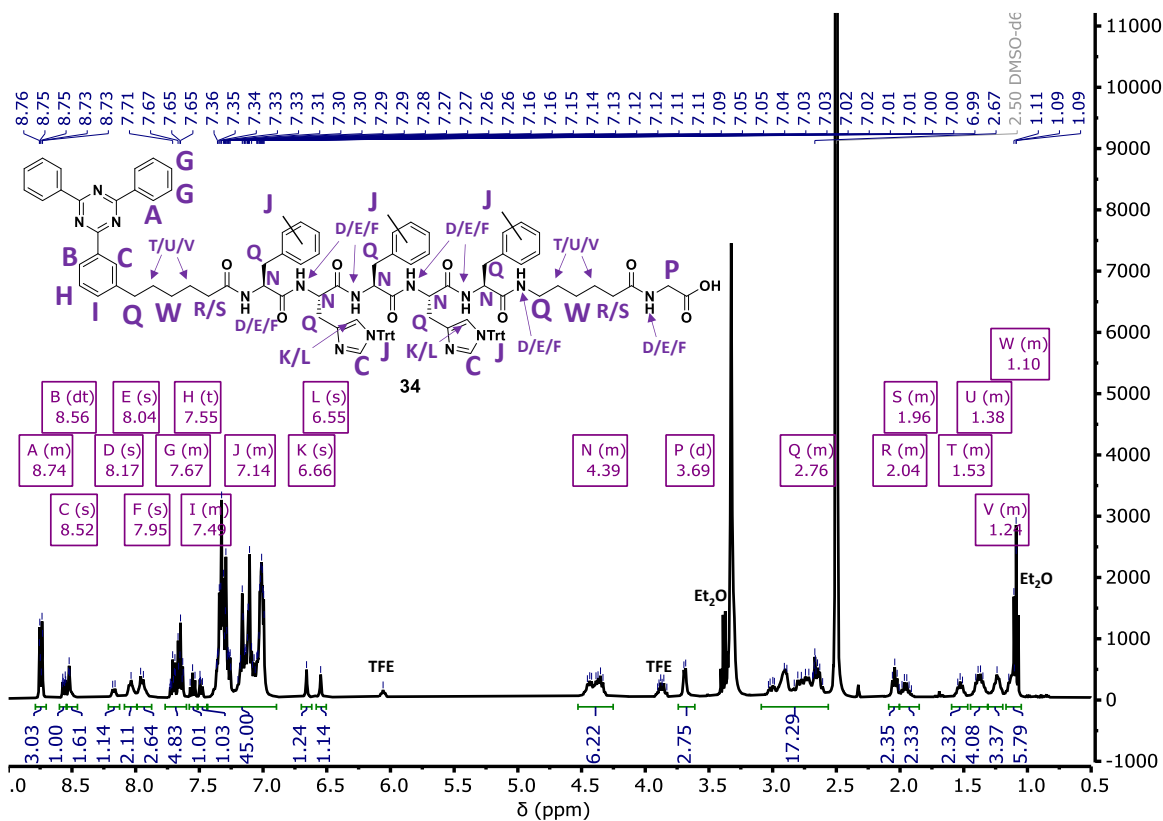


Figure 9.40. ¹H NMR of compound 34.

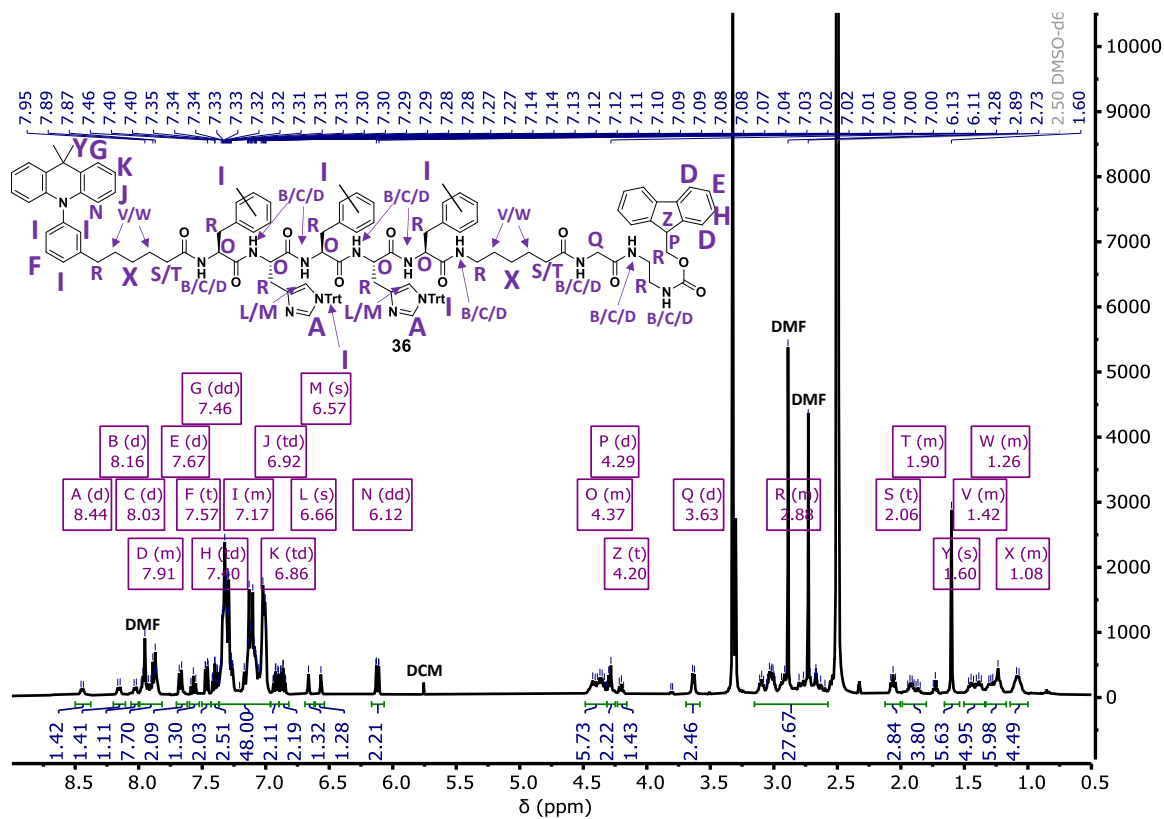


Figure 9.41. ¹H NMR of compound 36.

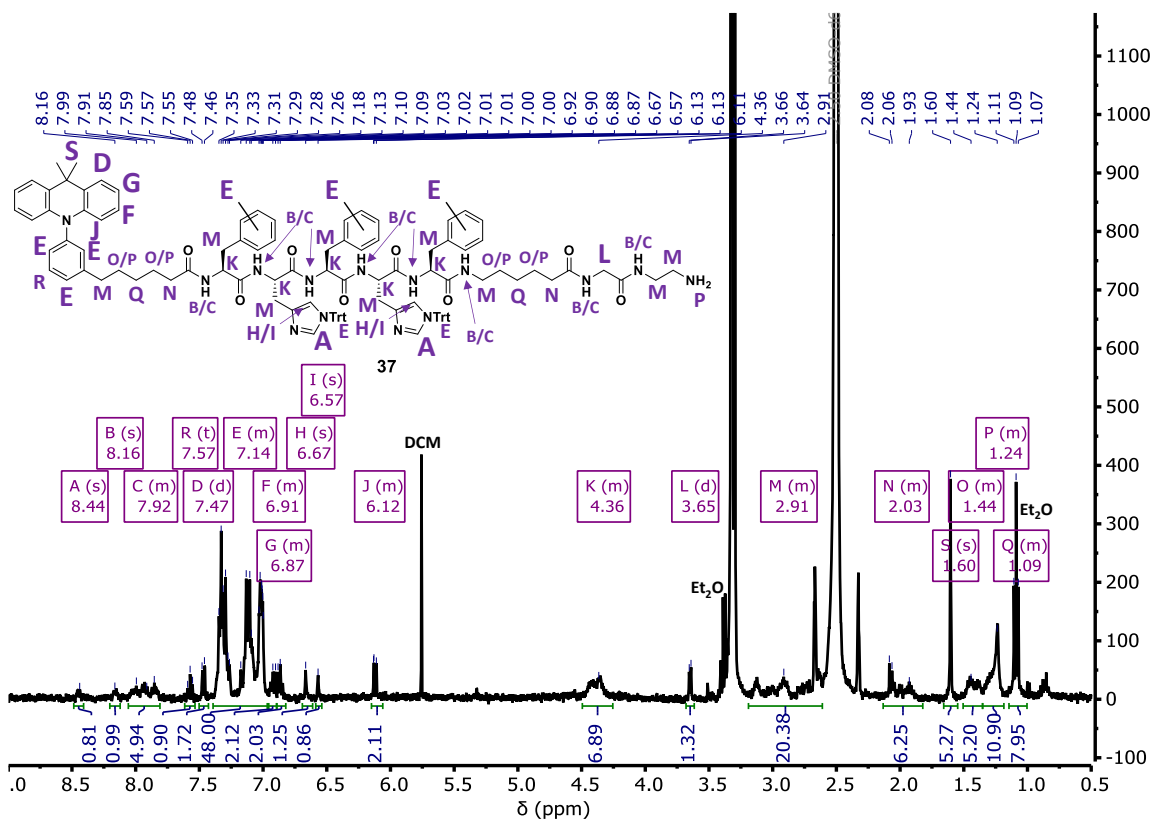


Figure 9.42. ¹H NMR of compound 37.

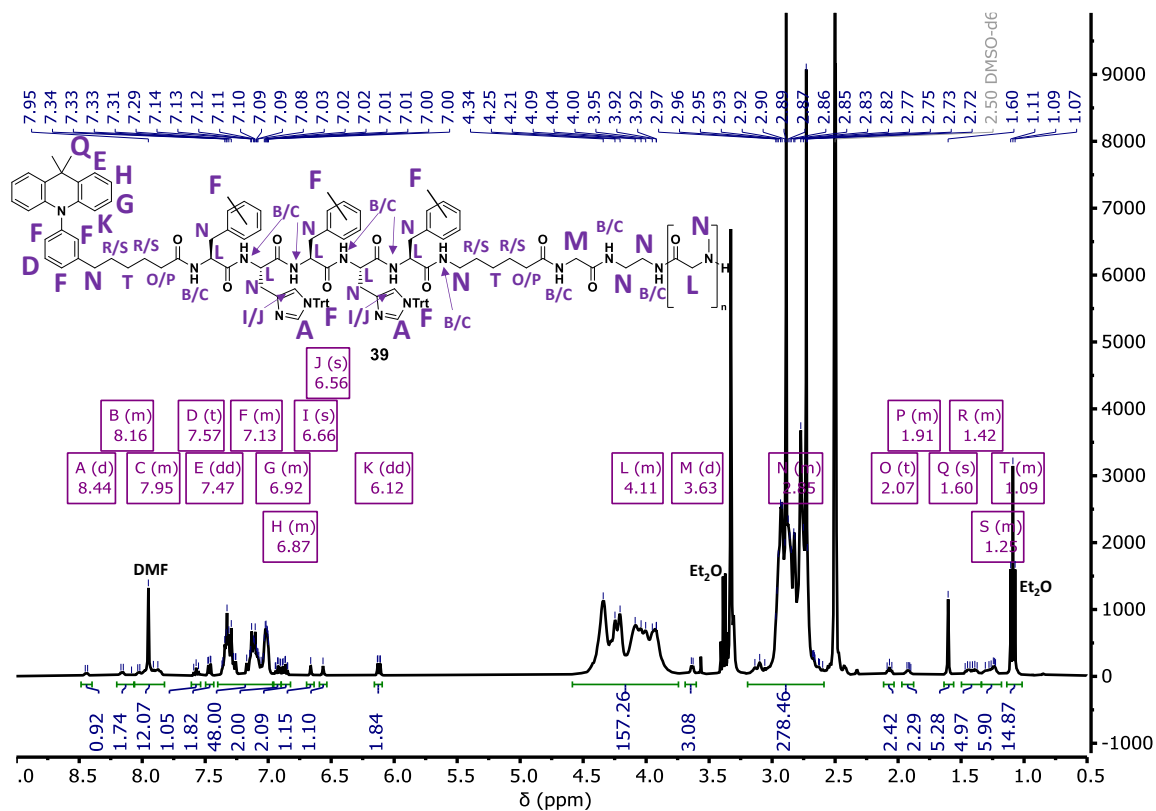


Figure 9.43. ¹H NMR of compound 39.

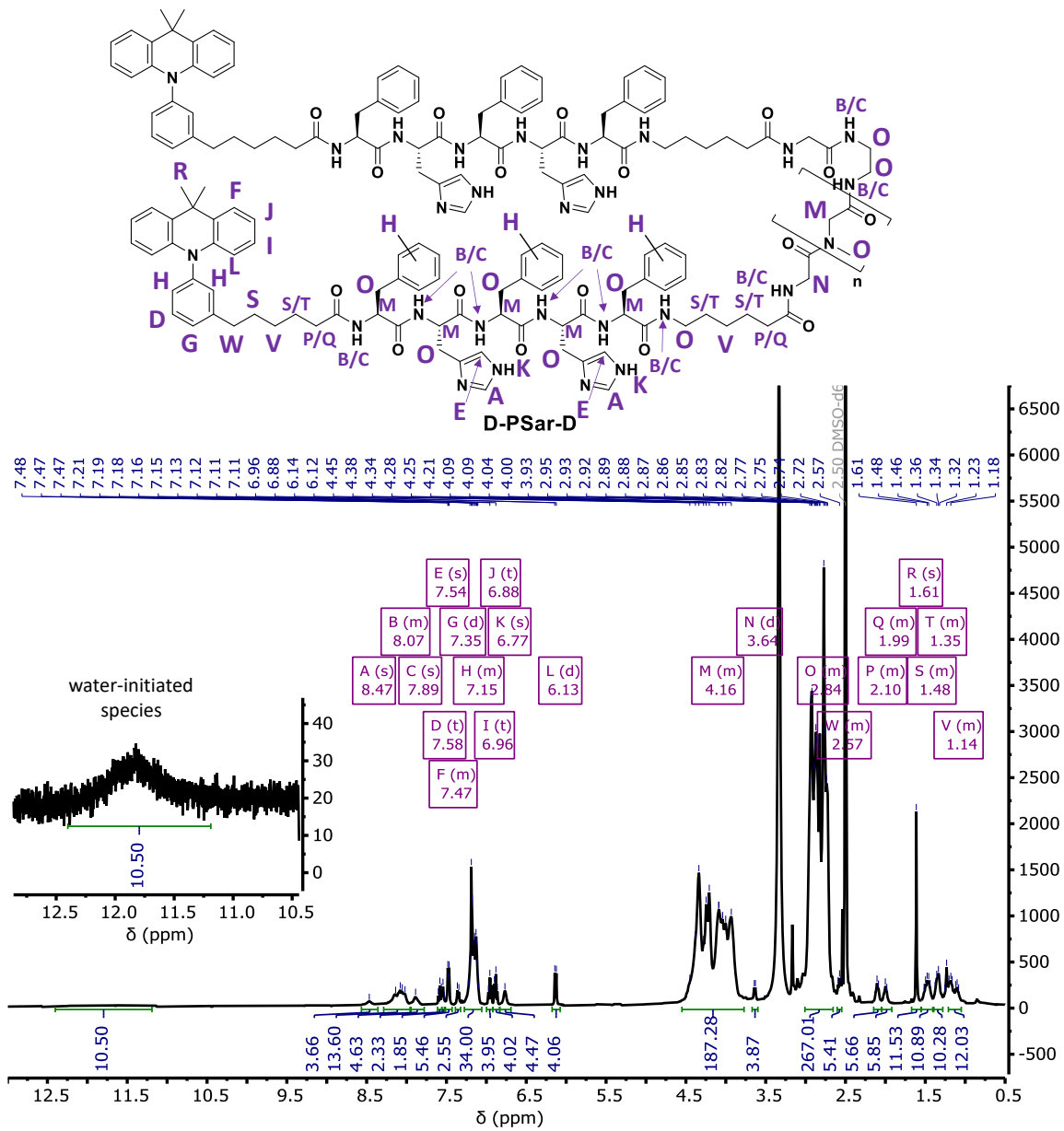


Figure 9.44. ^1H NMR of compound D-PSar-D.

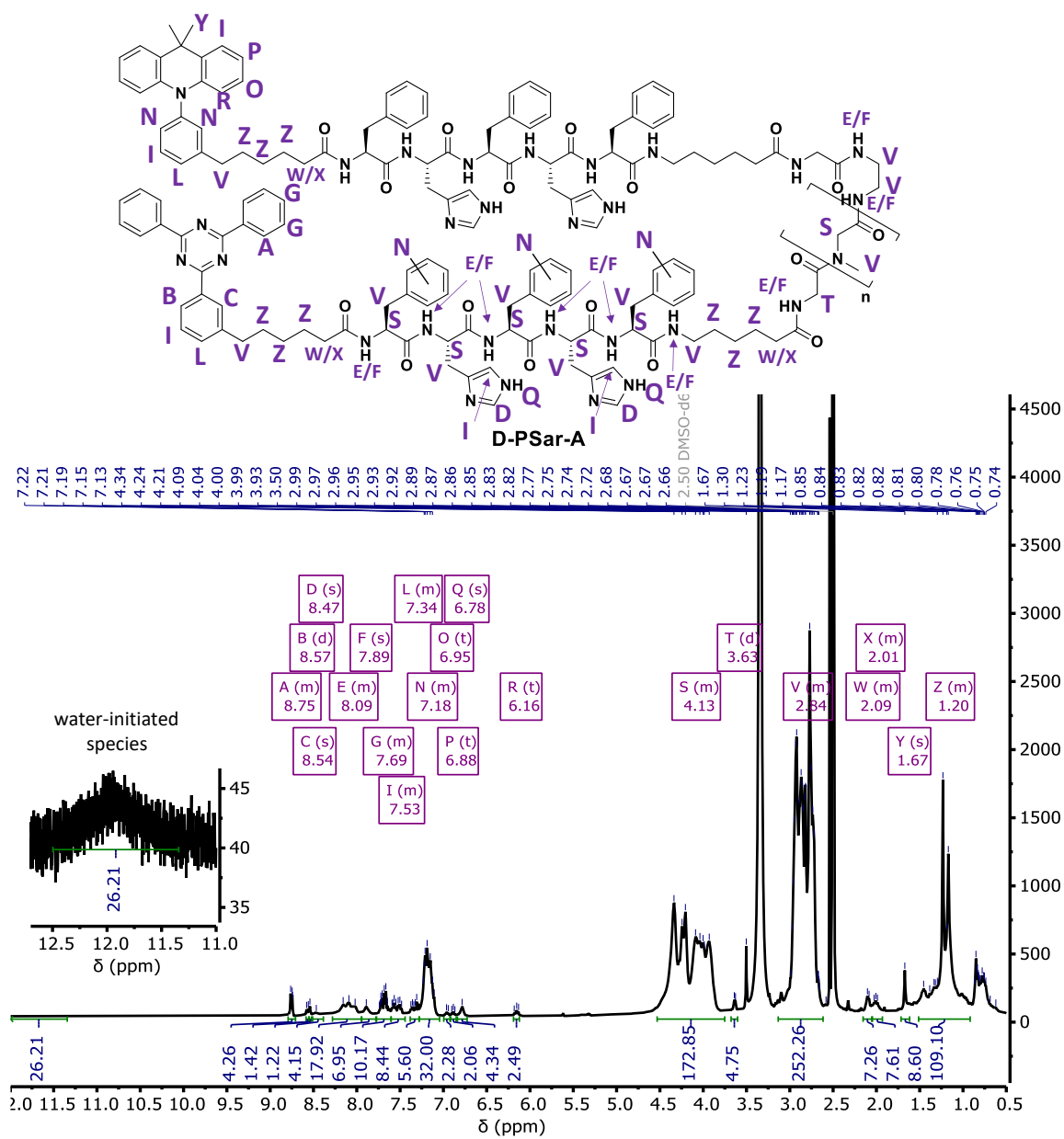


Figure 9.45. ^1H NMR of compound D-PSar-A.

9.2. MALDI-TOF Spectra

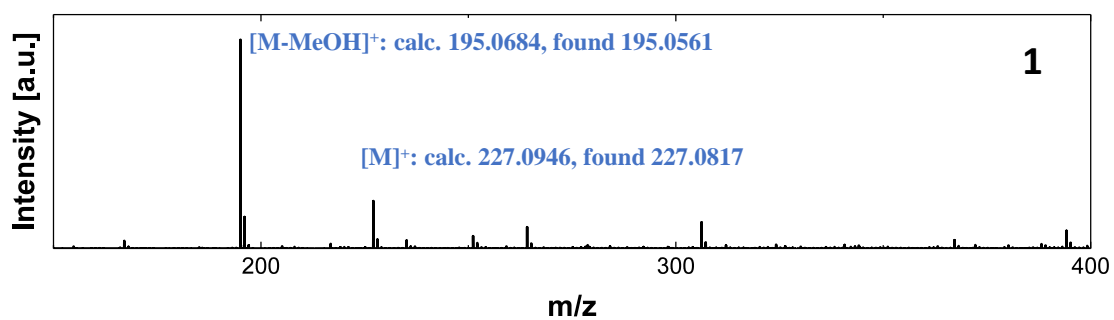


Figure 9.46. MALDI-TOF MS spectra of compound 1.

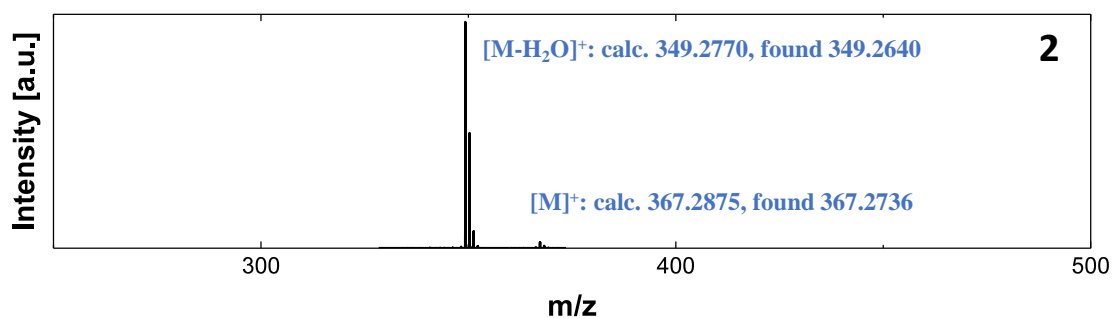


Figure 9.47. MALDI-TOF MS spectra of compound 2.

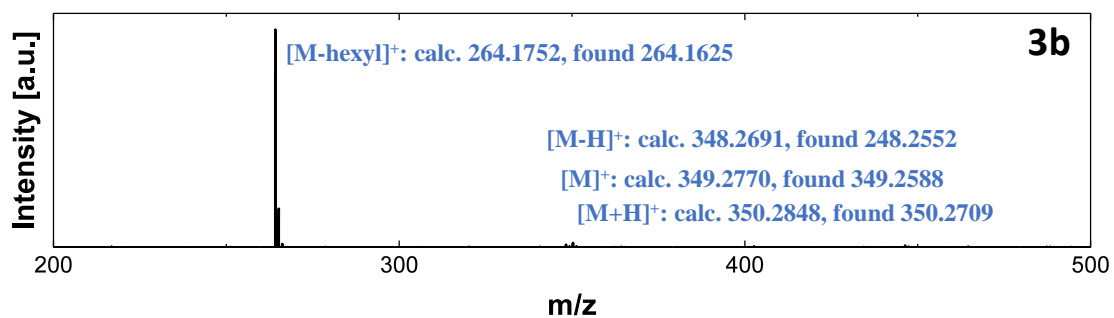


Figure 9.48. MALDI-TOF MS spectra of compound 3b.

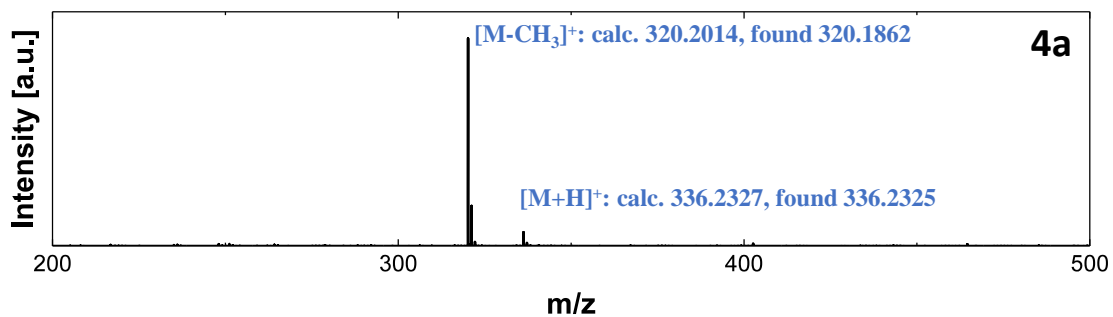


Figure 9.49. MALDI-TOF MS spectra of compound 4a.

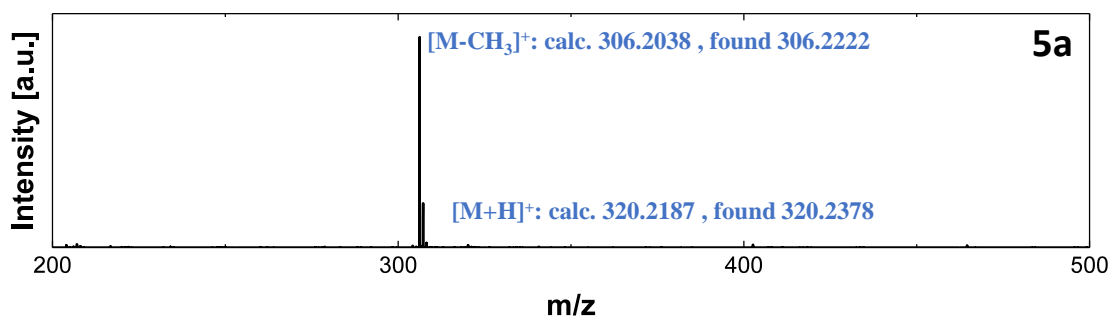


Figure 9.50. MALDI-TOF MS spectra of compound 5a.

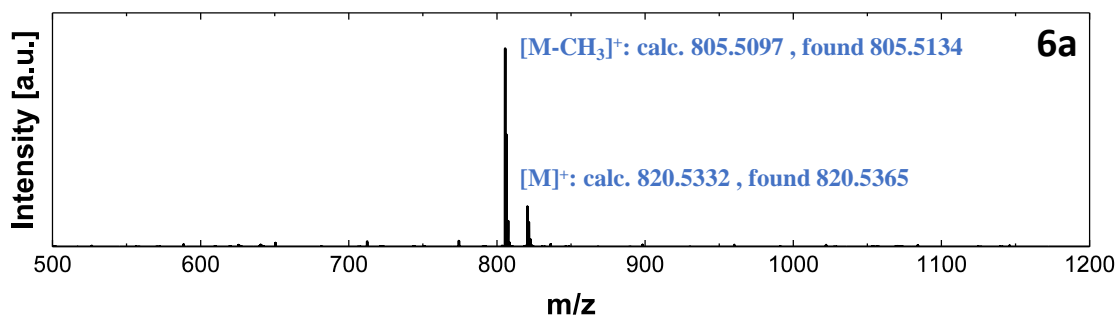


Figure 9.51. MALDI-TOF MS spectra of compound 6a.

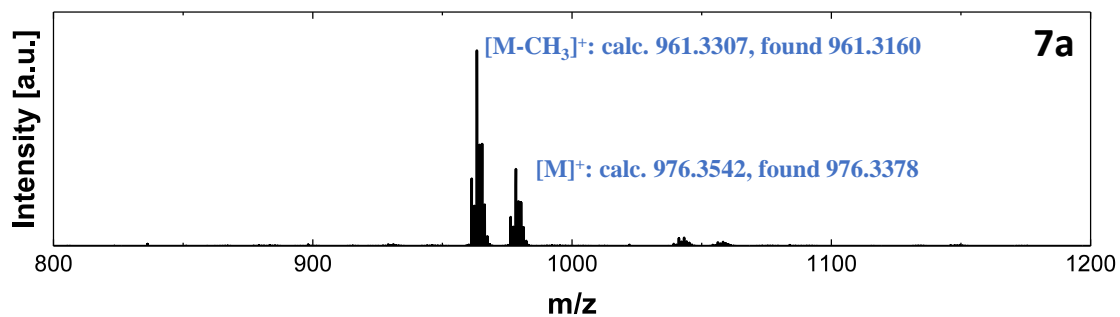


Figure 9.52. MALDI-TOF MS spectra of compound **7a**.

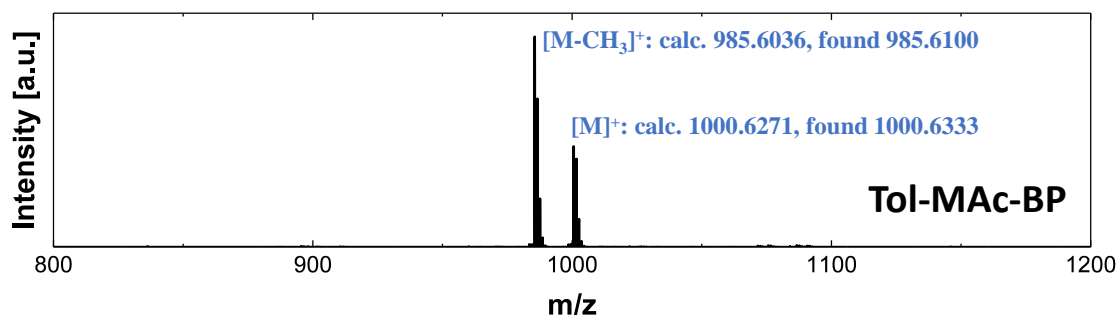


Figure 9.53. MALDI-TOF MS spectra of compound **Tol-Mac-BP**.

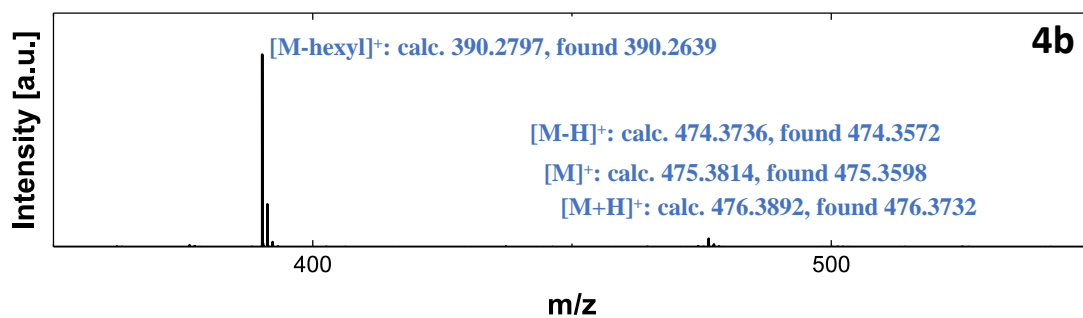


Figure 9.54. MALDI-TOF MS spectra of compound **4b**.

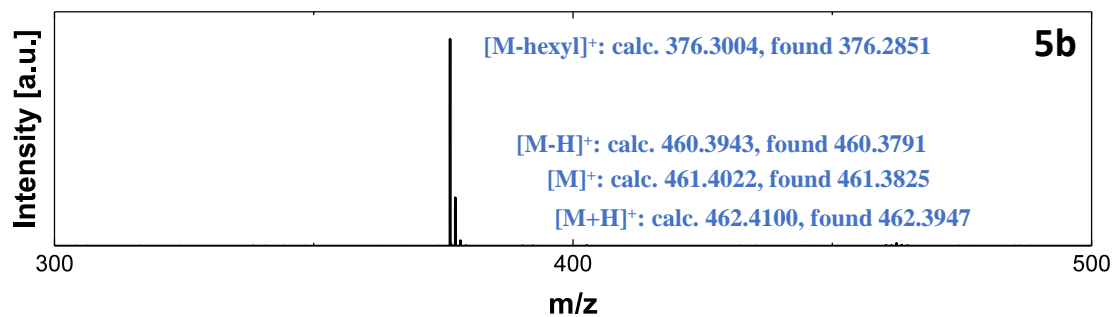


Figure 9.55. MALDI-TOF MS spectra of compound **5b**.

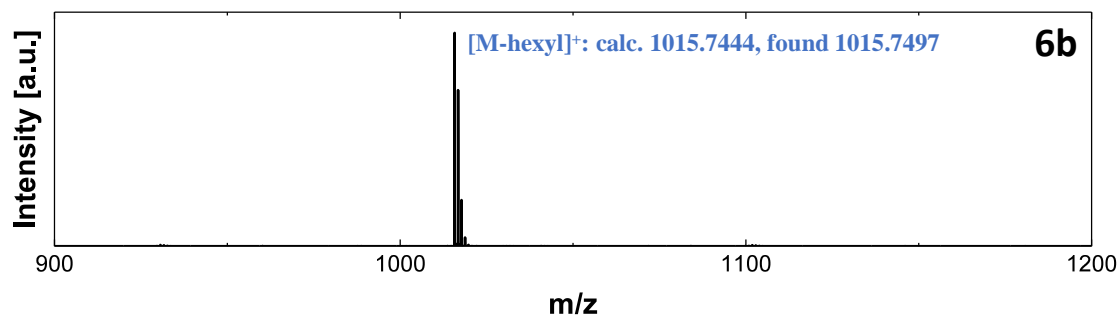


Figure 9.56. MALDI-TOF MS spectra of compound **6b**.

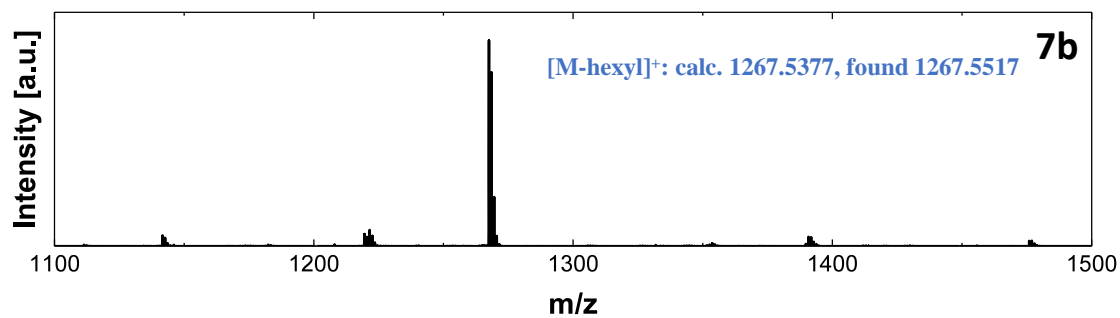


Figure 9.57. MALDI-TOF MS spectra of compound **7b**.

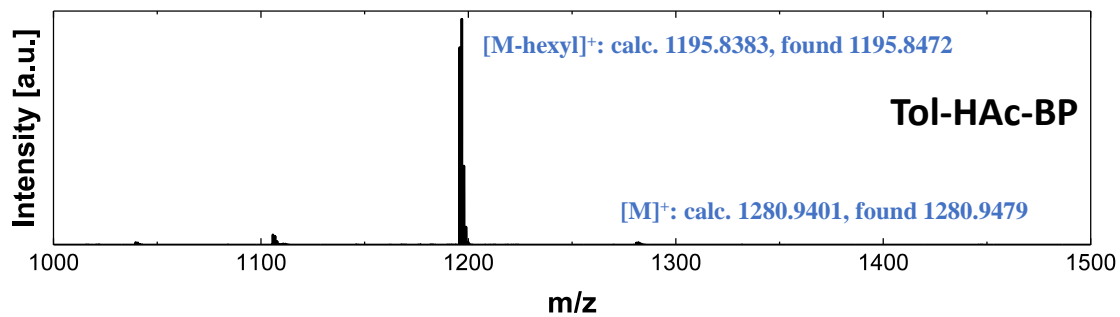


Figure 9.58. MALDI-TOF MS spectra of compound Tol-HAc-BP.

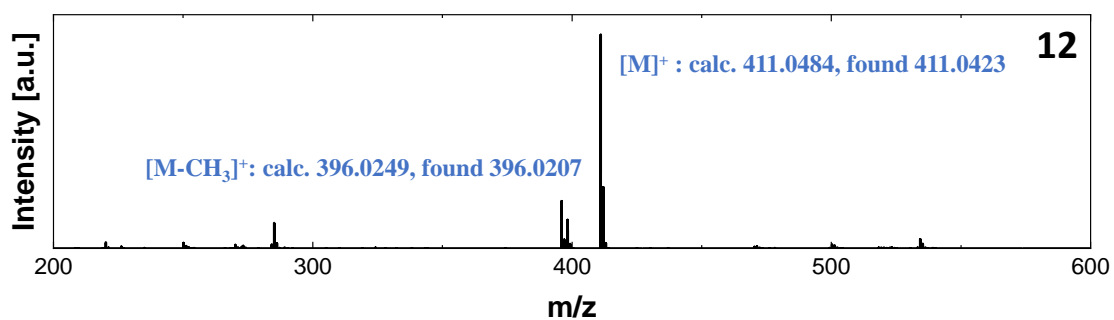


Figure 9.59. MALDI-TOF MS spectra of compound 12.

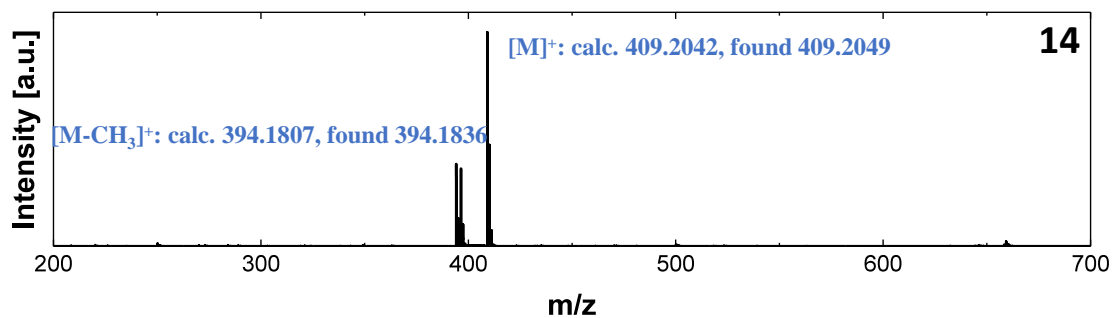


Figure 9.60. MALDI-TOF MS spectra of compound 14.

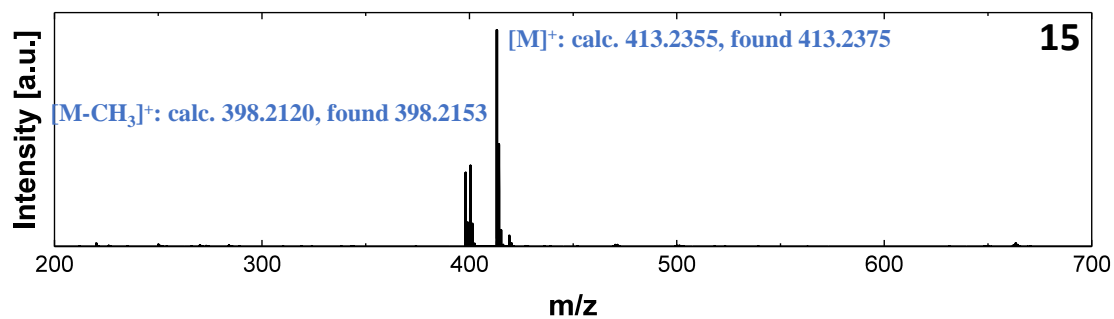


Figure 9.61. MALDI-TOF MS spectra of compound 15.

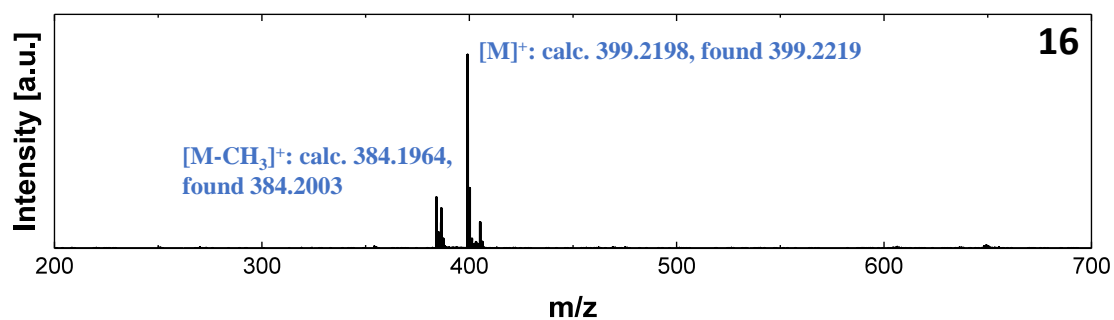


Figure 9.62. MALDI-TOF MS spectra of compound 16.

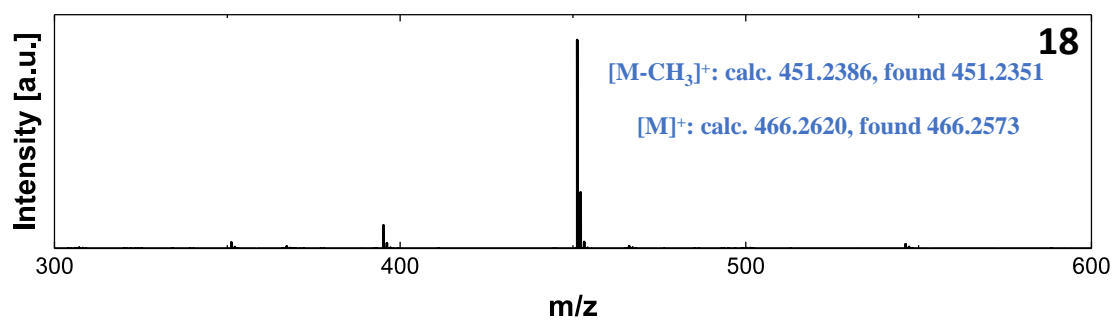


Figure 9.63. MALDI-TOF MS spectra of compound 18.

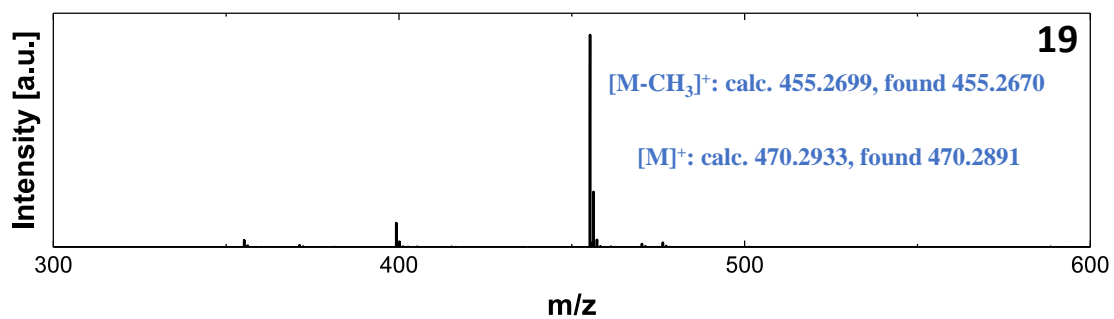


Figure 9.64. MALDI-TOF MS spectra of compound 19.

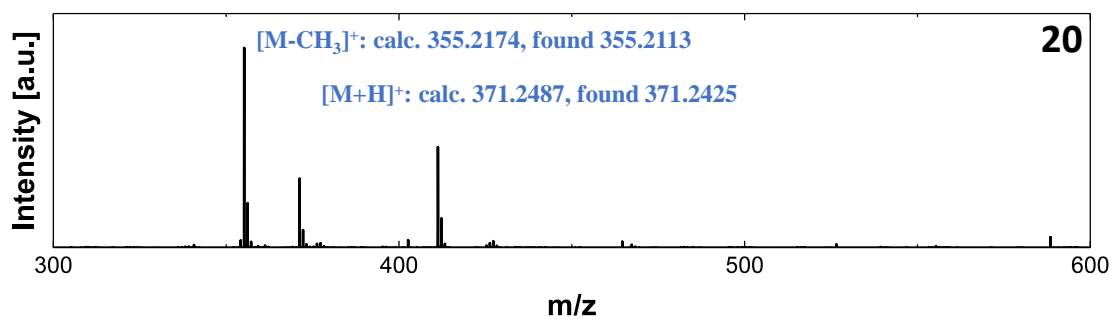


Figure 9.65. MALDI-TOF MS spectra of compound 20.

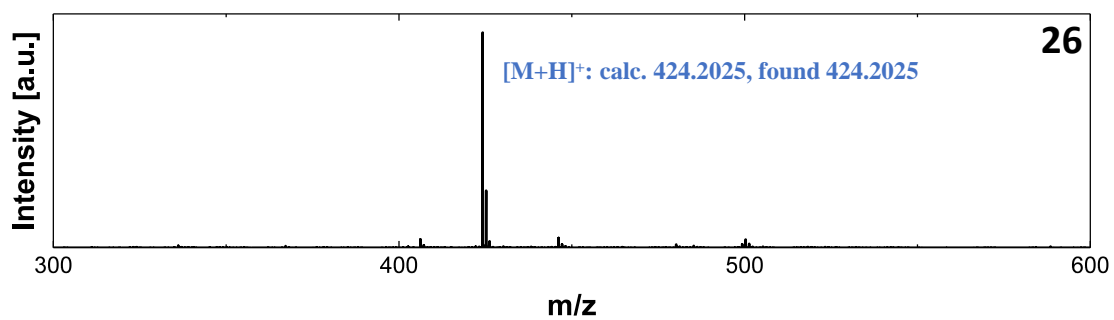


Figure 9.66. MALDI-TOF MS spectra of compound 26.

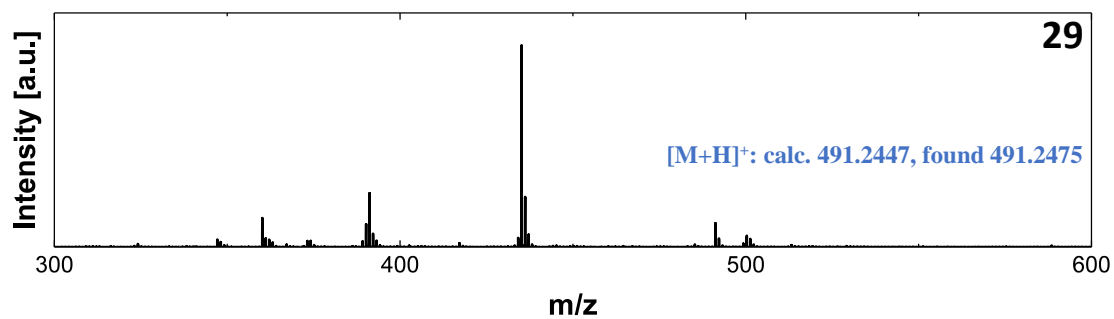


Figure 9.67. MALDI-TOF MS spectra of compound 29.

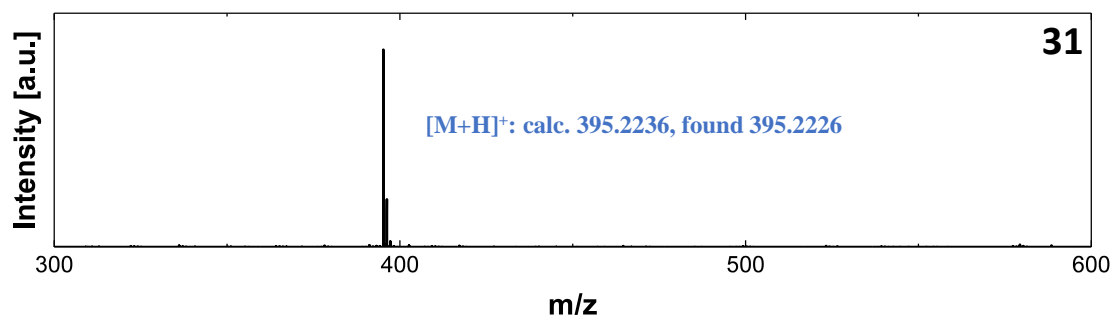


Figure 9.68. MALDI-TOF MS spectra of compound 31.

9.3. ESI HRMS Spectra

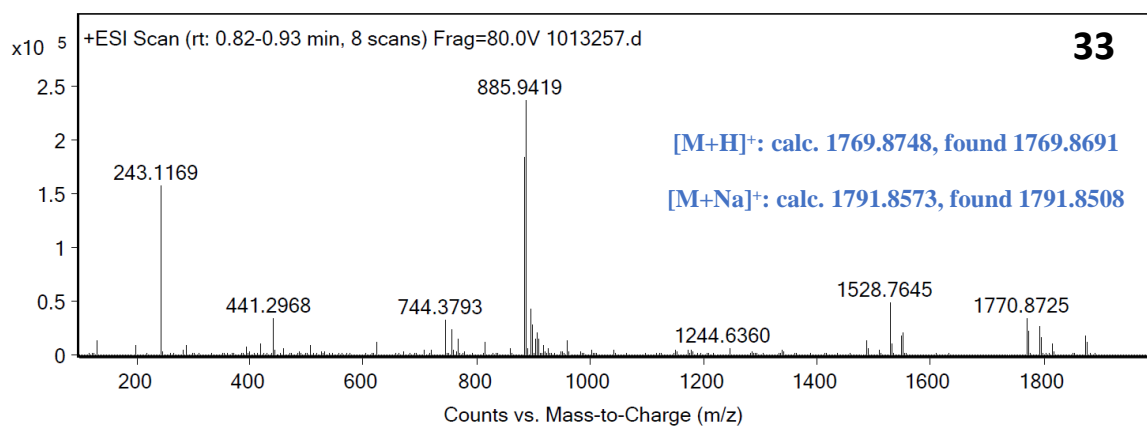


Figure 9.69. ESI-HRMS spectrum of compound **33**.

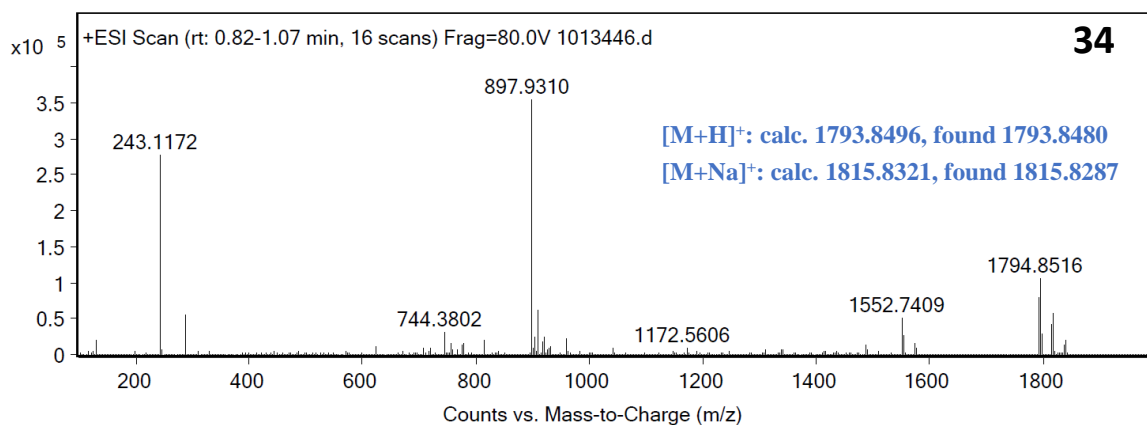


Figure 9.70. ESI-HRMS spectrum of compound **34**.

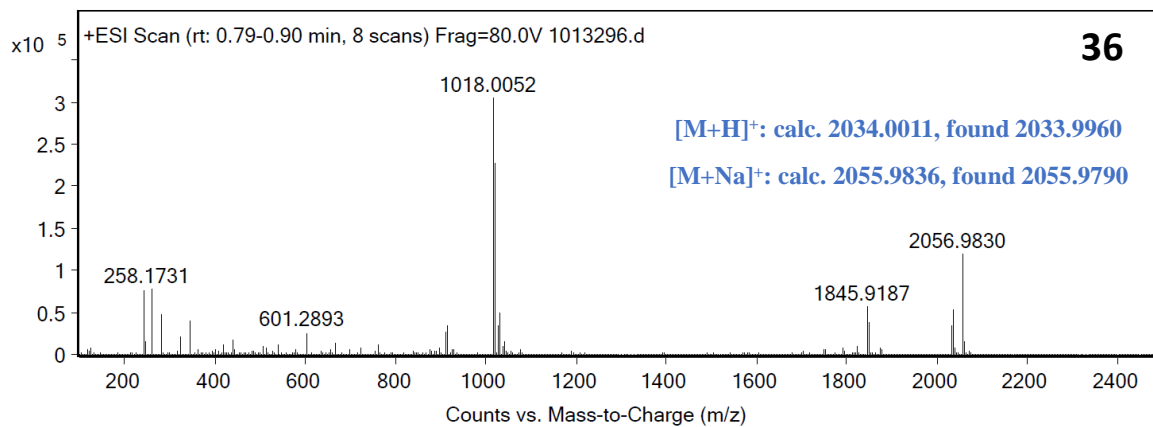


Figure 9.71. ESI-HRMS spectrum of compound 36.

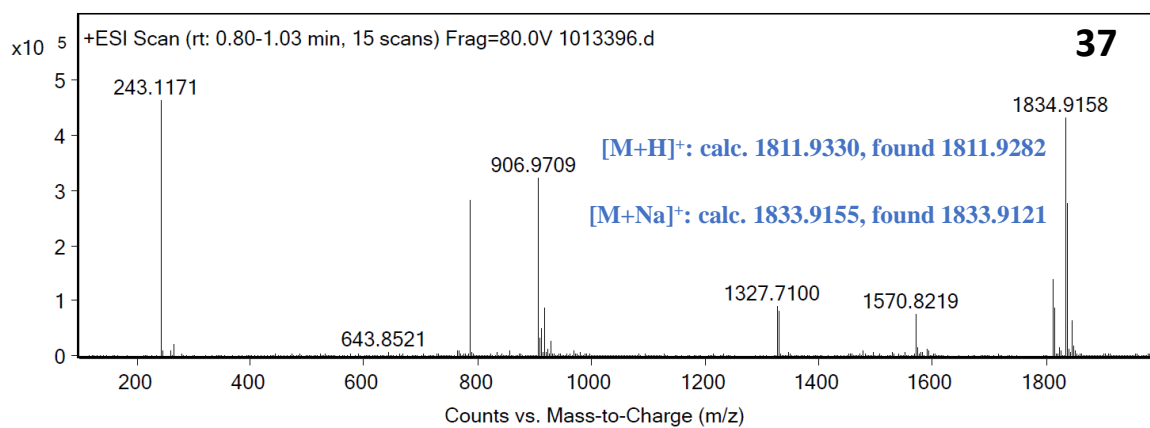


Figure 9.72. ESI-HRMS spectrum of compound 37.

10. Acknowledgement

[Redacted text block containing multiple paragraphs of blacked-out content]

[Redacted text block]

11. Publications and Presentations

Research Articles:

- [6] Results of chapters 3, 4, and 5 are planned to be submitted and the manuscript is currently in preparation. K. Philipps, [REDACTED]
[REDACTED] J. J. Michels, P. W. M. Blom
- [5] Results of chapter 6 are planned to be submitted and the manuscript is currently in preparation. K. Philipps, [REDACTED] J. J. Michels.
- [4] ‘Direct synthesis of light-emitting triblock copolymers from RAFT polymerization’, A. H. Ribeiro, J. Haven, A.-L. Buckinx, M. Beuchel, K. Philipps, T. Junkers, J. J. Michels, *Polym. Chem.* **2021**, *12*, 216–225.
- [3] ‘Polymer–perovskite blend light-emitting diodes using a self-compensated heavily doped polymeric anode’, A. G. Ricciardulli, B. van der Zee, K. Philipps, G. A. H. Wetzelaer, R.-Q. Png, P. K. H. Ho, L.-L. Chua, P. W. M. Blom, *APL Mater.* **2020**, *8*, 021101.
- [2] ‘An Easy-to-Machine Electrochemical FlowMicroreactor:Efficient Synthesis of Isoindolinone and Flow Functionalization’, A. A. Folgueiras-Amador, K. Philipps, S. Guilbaud, J. Poelakker, T. Wirth, *Angew. Chemie Int. Ed.* **2017**, *56*, 15446–15450.
- [1] ‘Colloidal Nanoplatelet/Conducting Polymer Hybrids: Excitonic and Material Properties’,B. Guzelturk, F. Menk, K. Philipps, Y. Kelestemur, M. Olutas, R. Zentel, H. V. Demir, *J. Phys. Chem. C* **2016**, *120*, 3573–3582.

Minireview Articles:

- [1] ‘The Block Copolymer Shuffle in Size Exclusion Chromatography: The Intrinsic Problem with Using Elugrams to Determine Chain Extension Success’, K. Philipps, T. Junkers, J. J. Michels, *Polym. Chem.* 2021, DOI: 10.1039/D1PY00210D.

Presentations:

- [2] ‘Investigation of Chain Connectivity on Thermally Activated Delayed Fluorescence (TADF) Polymers’, poster presentation, π 14- Symposium, 06/2019, Berlin, Germany
- [1] ‘Next Generation Organic Light-Emitting Diodes (OLED) based on Thermally Activated Delayed Fluorescence (TADF) Polymers’, oral presentation, Advanced Materials Workshop, Horizon 2020, 09/2018, Duni, Bulgaria

12. References

- [1] S. Reineke, M. Thomschke, B. Lüssem, K. Leo, *Rev. Mod. Phys.* **2013**, *85*, 1245–1293.
- [2] V. C. Bender, T. B. Marchesan, J. M. Alonso, *IEEE Ind. Electron. Mag.* **2015**, *9*, 6–16.
- [3] C. W. Tang, S. A. VanSlyke, *Appl. Phys. Lett.* **1987**, *51*, 913–915.
- [4] M.-K. Wei, C.-W. Lin, C.-C. Yang, Y.-W. Kiang, J.-H. Lee, H.-Y. Lin, *Int. J. Mol. Sci.* **2010**, *11*, 1527–1545.
- [5] Y.-H. Tak, K.-B. Kim, H.-G. Park, K.-H. Lee, J.-R. Lee, *Thin Solid Films* **2002**, *411*, 12–16.
- [6] A. L. Burin, M. A. Ratner, *J. Phys. Chem. A* **2000**, *104*, 4704–4710.
- [7] N. Chopra, J. Lee, Y. Zheng, S.-H. Eom, J. Xue, F. So, *ACS Appl. Mater. Interfaces* **2009**, *1*, 1169–1172.
- [8] G. Bagdziunas, M. Surka, K. Ivaniuk, *Org. Electron.* **2017**, *41*, 122–129.
- [9] H. Fujimoto, M. Yahiro, S. Yukiwaki, K. Kusuhara, N. Nakamura, T. Suekane, H. Wei, K. Imanishi, K. Inada, C. Adachi, *Appl. Phys. Lett.* **2016**, *109*, 243302.
- [10] P. W. M. Blom, N. I. Craciun, D. M. De Leeuw, G.-J. A. H. Wetzelaer, H. T. Nicolai, M. Kuik, *Adv. Mater.* **2014**, *26*, 512–531.
- [11] D. Abbaszadeh, A. Kunz, N. B. Kotadiya, A. Mondal, D. Andrienko, J. J. Michels, G. J. A. H. Wetzelaer, P. W. M. Blom, *Chem. Mater.* **2019**, *31*, 6380–6386.

- [12] T. Chatterjee, K. T. Wong, *Adv. Opt. Mater.* **2019**, *7*, 1–34.
- [13] A. Köhler, H. Bäessler, *Mater. Sci. Eng. R Reports* **2009**, *66*, 71–109.
- [14] Y. Li, Q. Wei, L. Cao, F. Fries, M. Cucchi, Z. Wu, R. Scholz, S. Lenk, B. Voit, Z. Ge, et al., *Front. Chem.* **2019**, *7*, 1–12.
- [15] M. C. Gather, S. Reineke, *J. Photonics Energy* **2015**, *5*, 057607.
- [16] W. Song, Y. Chen, Q. Xu, H. Mu, J. Cao, J. Huang, J. Su, *ACS Appl. Mater. Interfaces* **2018**, *10*, 24689–24698.
- [17] P. Vandersteegen, G. Schwartz, P. Bienstman, R. Baets, *Appl. Opt.* **2008**, *47*, 1947–1955.
- [18] B. Zhao, T. Zhang, B. Chu, W. Li, Z. Su, H. Wu, X. Yan, F. Jin, Y. Gao, C. Liu, *Sci. Rep.* **2015**, *5*, 10697.
- [19] X. Cai, S.-J. Su, *Adv. Funct. Mater.* **2018**, *28*, 1802558.
- [20] M. Tanaka, R. Nagata, H. Nakanotani, C. Adachi, *Commun. Mater.* **2020**, *1*, 1–9.
- [21] Q. Niu, G. J. A. H. Wetzelaer, P. W. M. Blom, N. I. Crăciun, *Adv. Electron. Mater.* **2016**, *2*, 1–10.
- [22] C. Adachi, M. A. Baldo, M. E. Thompson, S. R. Forrest, *J. Appl. Phys.* **2001**, *90*, 5048–5051.
- [23] C. Adachi, A. S. D. Sandanayaka, *CCS Chem.* **2020**, *2*, 1203–1216.
- [24] F. B. Dias, T. J. Penfold, A. P. Monkman, *Methods Appl. Fluoresc.* **2017**, *5*, 012001.
- [25] P. Pander, F. B. Dias, *Disp. Imaging* **2017**, *2*, 249–263.
- [26] A. Endo, K. Sato, K. Yoshimura, T. Kai, A. Kawada, H. Miyazaki, C. Adachi, *Appl. Phys. Lett.* **2011**, *98*, 2009–2012.
- [27] X. Yin, Y. He, X. Wang, Z. Wu, E. Pang, J. Xu, J. Wang, *Front. Chem.* **2020**, *8*, 1–23.
- [28] F. B. Dias, J. Santos, D. R. Graves, P. Data, R. S. Nobuyasu, M. A. Fox, A. S. Batsanov, T. Palmeira, M. N. Berberan-Santos, M. R. Bryce, et al., *Adv. Sci.* **2016**, *3*, 1600080.
- [29] P. L. dos Santos, J. S. Ward, A. S. Batsanov, M. R. Bryce, A. P. Monkman, *J. Phys. Chem. C* **2017**, *121*, 16462–16469.
- [30] J. S. Ward, A. Danos, P. Stachelek, M. A. Fox, A. S. Batsanov, A. P. Monkman, M. R. Bryce,

- Mater. Chem. Front.* **2020**, *4*, 3602–3615.
- [31] J. Gibson, A. P. Monkman, T. J. Penfold, *ChemPhysChem* **2016**, 2956–2961.
- [32] J. S. Ward, R. S. Nobuyasu, A. S. Batsanov, P. Data, A. P. Monkman, F. B. Dias, M. R. Bryce, *Chem. Commun.* **2016**, *52*, 2612–2615.
- [33] A. Endo, M. Ogasawara, A. Takahashi, D. Yokoyama, Y. Kato, C. Adachi, *Adv. Mater.* **2009**, *21*, 4802–4806.
- [34] R. Czerwieniec, M. J. Leitl, H. H. H. Homeier, H. Yersin, *Coord. Chem. Rev.* **2016**, *325*, 2–28.
- [35] W.-P. To, G. Cheng, G. S. M. Tong, D. Zhou, C.-M. Che, *Front. Chem.* **2020**, *8*, 1–7.
- [36] Z. Yang, Z. Mao, Z. Xie, Y. Zhang, S. Liu, J. Zhao, J. Xu, Z. Chi, M. P. Aldred, *Chem. Soc. Rev.* **2017**, *46*, 915–1016.
- [37] W. Zeng, H. Y. Lai, W. K. Lee, M. Jiao, Y. J. Shiu, C. Zhong, S. Gong, T. Zhou, G. Xie, M. Sarma, et al., *Adv. Mater.* **2018**, *30*, 1–8.
- [38] T. L. Wu, M. J. Huang, C. C. Lin, P. Y. Huang, T. Y. Chou, R. W. Chen-Cheng, H. W. Lin, R. S. Liu, C. H. Cheng, *Nat. Photonics* **2018**, *12*, 235–240.
- [39] H. Lim, H. J. Cheon, S. J. Woo, S. K. Kwon, Y. H. Kim, J. J. Kim, *Adv. Mater.* **2020**, *32*, 1–8.
- [40] Y. Kondo, K. Yoshiura, S. Kitera, H. Nishi, S. Oda, H. Gotoh, Y. Sasada, M. Yanai, T. Hatakeyama, *Nat. Photonics* **2019**, *13*, 678–682.
- [41] H. Nakanotani, T. Higuchi, T. Furukawa, K. Masui, K. Morimoto, M. Numata, H. Tanaka, Y. Sagara, T. Yasuda, C. Adachi, *Nat. Commun.* **2014**, *5*, 1–7.
- [42] T. T. Bui, F. Goubard, M. Ibrahim-Ouali, D. Gigmes, F. Dumur, *Beilstein J. Org. Chem.* **2018**, *14*, 282–308.
- [43] H. Noda, X. K. Chen, H. Nakanotani, T. Hosokai, M. Miyajima, N. Notsuka, Y. Kashima, J. L. Brédas, C. Adachi, *Nat. Mater.* **2019**, *18*, 1084–1090.
- [44] N. B. Kotadiya, P. W. M. Blom, G. J. A. H. Wetzelaer, *Nat. Photonics* **2019**, *13*, 765–769.
- [45] L. S. Cui, S. Bin Ruan, F. Bencheikh, R. Nagata, L. Zhang, K. Inada, H. Nakanotani, L. S. Liao, C. Adachi, *Nat. Commun.* **2017**, *8*, 1–8.

- [46] T. Jiang, Y. Liu, Z. Ren, S. Yan, *Polym. Chem.* **2020**, *11*, 1555–1571.
- [47] M. Colella, P. Pander, A. P. Monkman, *Org. Electron. physics, Mater. Appl.* **2018**, *62*, 168–173.
- [48] X. L. Chen, J. H. Jia, R. Yu, J. Z. Liao, M. X. Yang, C. Z. Lu, *Angew. Chemie - Int. Ed.* **2017**, *56*, 15006–15009.
- [49] T. Huang, W. Jiang, L. Duan, *J. Mater. Chem. C* **2018**, *6*, 5577–5596.
- [50] Q. Wei, Z. Ge, B. Voit, *Macromol. Rapid Commun.* **2019**, *40*, 1–19.
- [51] Y. Liu, C. Li, Z. Ren, S. Yan, M. R. Bryce, *Nat. Rev. Mater.* **2018**, *3*, 18020.
- [52] H. S. Kim, S.-R. Park, M. C. Suh, *J. Phys. Chem. C* **2017**, *121*, 13986–13997.
- [53] J. Lee, N. Aizawa, M. Numata, C. Adachi, T. Yasuda, *Adv. Mater.* **2017**, *29*, 1604856.
- [54] Y. Zhu, Y. Yang, Y. Wang, B. Yao, X. Lin, B. Zhang, H. Zhan, Z. Xie, Y. Cheng, *Adv. Opt. Mater.* **2018**, *6*, 1701320.
- [55] K. Masui, H. Nakanotani, C. Adachi, *Org. Electron.* **2013**, *14*, 2721–2726.
- [56] J. Guo, X.-L. Li, H. Nie, W. Luo, R. Hu, A. Qin, Z. Zhao, S.-J. Su, B. Z. Tang, *Chem. Mater.* **2017**, *29*, 3623–3631.
- [57] H. Abroshan, E. Cho, V. Coropceanu, J. L. Brédas, *Adv. Theory Simulations* **2020**, *3*, 1–12.
- [58] H. J. Kim, C. Lee, M. Godumala, S. Choi, S. Y. Park, M. J. Cho, S. Park, D. H. Choi, *Polym. Chem.* **2018**, *9*, 1318–1326.
- [59] S. Y. Lee, T. Yasuda, H. Komiyama, J. Lee, C. Adachi, *Adv. Mater.* **2016**, *28*, 4019–4024.
- [60] J. Rao, X. Liu, X. Li, L. Yang, L. Zhao, S. Wang, J. Ding, L. Wang, *Angew. Chemie - Int. Ed.* **2020**, *59*, 1320–1326.
- [61] P. J. Flory, *Principles of Polymer Chemistry*, Cornell University Press, Ithaca, N.Y., **1953**.
- [62] Y. Liu, Z. Ren, D. Ma, C. Li, S. Yan, Y. Wang, *Macromolecules* **2018**, *51*, 4615–4623.
- [63] J. Rao, L. Yang, X. Li, L. Zhao, S. Wang, J. Ding, L. Wang, *Angew. Chemie - Int. Ed.* **2020**, *650091*, 17903–17909.
- [64] Z. Wu, F. Ni, D. Wei, C. Zhong, D. Ma, K. An, K. Wu, Z. Zhu, C. Yang, T. Chen, *J. Mater. Chem. C* **2017**, *5*, 1363–1368.

- [65] Y. Liu, Y. Wang, C. Li, Z. Ren, D. Ma, S. Yan, *Macromolecules* **2018**, *51*, 4615–4623.
- [66] Y. Zhu, H. Zhan, B. Zhang, Y. Yang, Z. Xie, Y. Cheng, Y. Wang, X. Lin, *J. Mater. Chem. C* **2017**, *6*, 568–574.
- [67] Y. Yang, S. Wang, Y. Zhu, Y. Wang, H. Zhan, Y. Cheng, *Adv. Funct. Mater.* **2018**, *28*, 1–6.
- [68] H. Zhan, Y. Wang, K. Li, Y. Chen, X. Yi, K. Bai, G. Xie, Y. Cheng, *Front. Chem.* **2020**, *8*, 1–9.
- [69] T. Wang, B. Yao, K. Li, Y. Chen, H. Zhan, X. Yi, Z. Xie, Y. Cheng, *Adv. Opt. Mater.* **2021**, *2001981*, 2001981.
- [70] R. S. Nobuyasu, Z. Ren, G. C. Griffiths, A. S. Batsanov, P. Data, S. Yan, A. P. Monkman, M. R. Bryce, F. B. Dias, *Adv. Opt. Mater.* **2016**, *4*, 597–607.
- [71] Y. H. Park, H. J. Jang, J. Y. Lee, *Polym. Chem.* **2019**, *10*, 4872–4878.
- [72] C. Li, Z. Ren, X. Sun, H. Li, S. Yan, *Macromolecules* **2019**, *52*, 2296–2303.
- [73] X. Zeng, J. Luo, T. Zhou, T. Chen, X. Zhou, K. Wu, Y. Zou, G. Xie, S. Gong, C. Yang, *Macromolecules* **2018**, *51*, 1598–1604.
- [74] F. Chen, J. Hu, X. Wang, S. Shao, L. Wang, X. Jing, F. Wang, *Sci. China Chem.* **2020**, *63*, 1112–1120.
- [75] J. Hu, Q. Li, X. Wang, S. Shao, L. Wang, X. Jing, F. Wang, *Angew. Chemie Int. Ed.* **2019**, *58*, 8405–8409.
- [76] S. Shao, J. Hu, X. Wang, L. Wang, X. Jing, F. Wang, *J. Am. Chem. Soc.* **2017**, *139*, 17739–17742.
- [77] K. Albrecht, K. Matsuoka, K. Fujita, K. Yamamoto, *Angew. Chemie - Int. Ed.* **2015**, *54*, 5677–5682.
- [78] Y. Li, G. Xie, S. Gong, K. Wu, C. Yang, *Chem. Sci.* **2016**, *7*, 5441–5447.
- [79] X. Ban, W. Jiang, K. Sun, B. Lin, Y. Sun, *ACS Appl. Mater. Interfaces* **2017**, *9*, 7339–7346.
- [80] D. Liu, W. Tian, Y. Feng, X. Zhang, X. Ban, W. Jiang, Y. Sun, *ACS Appl. Mater. Interfaces* **2019**, *11*, 16737–16748.

- [81] C. Li, R. S. Nobuyasu, Y. Wang, F. B. Dias, Z. Ren, M. R. Bryce, S. Yan, *Adv. Opt. Mater.* **2017**, *5*, 1700435.
- [82] Y. Yang, L. Zhao, S. Wang, J. Ding, L. Wang, *Macromolecules* **2018**, *51*, 9933–9942.
- [83] Z. Ren, R. S. Nobuyasu, F. B. Dias, A. P. Monkman, S. Yan, M. R. Bryce, *Macromolecules* **2016**, *49*, 5452–5460.
- [84] Y. Wang, Y. Zhu, G. Xie, H. Zhan, C. Yang, Y. Cheng, *J. Mater. Chem. C* **2017**, *5*, 10715–10720.
- [85] X. Wang, S. Wang, J. Lv, S. Shao, L. Wang, X. Jing, F. Wang, *Chem. Sci.* **2019**, *10*, 2915–2923.
- [86] L. Brunsveld, B. J. Folmer, E. W. Meijer, R. P. Sijbesma, *Chem. Rev.* **2001**, *101*, 4071–98.
- [87] D. B. Amabilino, D. K. Smith, J. W. Steed, *Chem. Soc. Rev.* **2017**, *46*, 2404–2420.
- [88] R. P. M. Lafleur, S. M. C. Schoenmakers, P. Madhikar, D. Bochicchio, B. Baumeier, A. R. A. Palmans, G. M. Pavan, E. W. Meijer, *Macromolecules* **2019**, *52*, 3049–3055.
- [89] H. Frisch, E. C. Fritz, F. Stricker, L. Schmäser, D. Spitzer, T. Weidner, B. J. Ravoo, P. Besenius, *Angew. Chemie - Int. Ed.* **2016**, *55*, 7242–7246.
- [90] H. Frisch, J. P. Unsleber, D. Lüdeker, M. Peterlechner, G. Brunklaus, M. Waller, P. Besenius, *Angew. Chemie - Int. Ed.* **2013**, *52*, 10097–10101.
- [91] S. Amharar, S. Yuvayapan, A. Aydogan, *Chem. Commun.* **2018**, *54*, 829–832.
- [92] A. Osypenko, E. Moulin, O. Gavot, G. Fuks, M. Maaloum, M. A. J. Koenis, W. J. Buma, N. Giuseppone, *Chem. - A Eur. J.* **2019**, *25*, 13008–13016.
- [93] C. M. Berac, L. Zengerling, D. Straßburger, R. Otter, M. Urschbach, P. Besenius, *Macromol. Rapid Commun.* **2020**, *41*, 1900476.
- [94] D. Spitzer, L. L. Rodrigues, D. Straßburger, M. Mezger, P. Besenius, *Angew. Chemie - Int. Ed.* **2017**, *56*, 15461–15465.
- [95] X. Yan, F. Wang, B. Zheng, F. Huang, *Chem. Soc. Rev.* **2012**, *41*, 6042.
- [96] J. Y. Shu, B. Panganiban, T. Xu, *Annu. Rev. Phys. Chem.* **2013**, *64*, 631–657.
- [97] R. Otter, P. Besenius, *Org. Biomol. Chem.* **2019**, *17*, 6719–6734.

- [98] R. Otter, N. A. Henke, C. Berac, T. Bauer, M. Barz, S. Seiffert, P. Besenius, *Macromol. Rapid Commun.* **2018**, *39*, 1800459.
- [99] R. Otter, K. Klinker, D. Spitzer, M. Schinnerer, M. Barz, P. Besenius, *Chem. Commun.* **2018**, *54*, 401–404.
- [100] T. J. Moyer, J. A. Finbloom, F. Chen, D. J. Toft, V. L. Cryns, S. I. Stupp, *J. Am. Chem. Soc.* **2014**, *136*, 14746–14752.
- [101] G. Zissis, in *Handb. Adv. Light. Technol.* (Eds.: R. Karlicek, C.-C. Sun, G. Zissis, R. Ma), Springer International Publishing, Cham, **2016**, pp. 1–13.
- [102] B. Zhang, Y. Cheng, *Chem. Rec.* **2019**, *19*, 1624–1643.
- [103] X. Liu, J. Rao, X. Li, S. Wang, J. Ding, L. Wang, *iScience* **2019**, *15*, 147–155.
- [104] Q. Zhang, D. Tsang, H. Kuwabara, Y. Hatae, B. Li, T. Takahashi, S. Y. Lee, T. Yasuda, C. Adachi, *Adv. Mater.* **2015**, *27*, 2096–2100.
- [105] M. Y. Wong, E. Zysman-Colman, *Adv. Mater.* **2017**, *29*, 1605444.
- [106] R. Xie, A. R. Weisen, Y. Lee, M. A. Aplan, A. M. Fenton, A. E. Masucci, F. Kempe, M. Sommer, C. W. Pester, R. H. Colby, et al., *Nat. Commun.* **2020**, *11*, 4–11.
- [107] J. L. Bredas, *Mater. Horizons* **2014**, *1*, 17–19.
- [108] N. Elgrishi, K. J. Rountree, B. D. McCarthy, E. S. Rountree, T. T. Eisenhart, J. L. Dempsey, *J. Chem. Educ.* **2018**, *95*, 197–206.
- [109] Y. Llif, M. S. Liu, A. K. Jen, *Acta Polym.* **1999**, *50*, 105–108.
- [110] J. Sworakowski, *Synth. Met.* **2018**, *235*, 125–130.
- [111] E. Campioli, S. Sanyal, A. Marcelli, M. Di Donato, M. Blanchard-Desce, O. Mongin, A. Painelli, F. Terenziani, *ChemPhysChem* **2019**, *20*, 2860–2873.
- [112] L. Yu, Z. Wu, C. Zhong, G. Xie, K. Wu, D. Ma, C. Yang, *Dye. Pigment.* **2017**, *141*, 325–332.
- [113] R. Huang, N. A. Kukhta, J. S. Ward, A. Danos, A. S. Batsanov, M. R. Bryce, F. B. Dias, *J. Mater. Chem. C* **2019**, *7*, 13224–13234.
- [114] S. Nigam, S. Rutan, *Appl. Spectrosc.* **2001**, *55*, 362A–370A.

- [115] J. R. Lakowicz, *Principles of Fluorescence Spectroscopy*, Springer US, Boston, MA, **2006**.
- [116] F. B. Dias, S. Pollock, G. Hedley, L. O. Pålsson, A. Monkman, I. I. Perepichka, I. F. Perepichka, M. Tavasli, M. R. Bryce, *J. Phys. Chem. B* **2006**, *110*, 19329–19339.
- [117] F. B. Dias, T. J. Penfold, A. P. Monkman, *Methods Appl. Fluoresc.* **2017**, *5*, 012001.
- [118] J. Shi, M. A. Izquierdo, S. Oh, S. Y. Park, B. Milián-Medina, D. Roca-Sanjuán, J. Gierschner, *Inorg. Chem. Front.* **2019**, *6*, 1948–1954.
- [119] E. G. Demissie, E. T. Mengesha, G. W. Woyessa, *J. Photochem. Photobiol. A Chem.* **2017**, *337*, 184–191.
- [120] U. Subuddhi, S. Haldar, S. Sankararaman, A. K. Mishra, *Photochem. Photobiol. Sci.* **2006**, *5*, 459–466.
- [121] H. K. Sinha, P. C. P. Thomson, K. Yates, *Can. J. Chem.* **1990**, *68*, 1507–1513.
- [122] K. Stavrou, L. G. Franca, A. P. Monkman, *ACS Appl. Electron. Mater.* **2020**, *2*, 2868–2881.
- [123] G. Méhes, K. Goushi, W. J. Potscavage, C. Adachi, *Org. Electron.* **2014**, *15*, 2027–2037.
- [124] H. S. Kim, S. Park, M. C. Suh, *J. Phys. Chem. C* **2017**, *121*, 13986–13997.
- [125] S. Karabunarliev, E. R. Bittner, M. Baumgarten, *J. Chem. Phys.* **2001**, *114*, 5863–5870.
- [126] O. V. Mikhnenko, P. W. M. Blom, T. Q. Nguyen, *Energy Environ. Sci.* **2015**, *8*, 1867–1888.
- [127] L. Porrès, A. Holland, L. O. Pålsson, A. P. Monkman, C. Kemp, A. Beeby, *J. Fluoresc.* **2006**, *16*, 267–272.
- [128] Y. Y. Cheng, T. Houry, R. G. C. R. Clady, M. J. Y. Tayebjee, N. J. Ekins-Daukes, M. J. Crossley, T. W. Schmidt, *Phys. Chem. Chem. Phys.* **2010**, *12*, 66–71.
- [129] V. Jankus, E. W. Snedden, D. W. Bright, V. L. Whittle, J. A. G. Williams, A. Monkman, *Adv. Funct. Mater.* **2013**, *23*, 384–393.
- [130] M. Mamada, K. Inada, T. Komino, W. J. Potscavage, H. Nakanotani, C. Adachi, *ACS Cent. Sci.* **2017**, *3*, 769–777.
- [131] N. B. Kotadiya, H. Lu, A. Mondal, Y. Ie, D. Andrienko, P. W. M. Blom, G. J. A. H. Wetzelaer, *Nat. Mater.* **2018**, *17*, 329–334.

- [132] H. F. Haneef, A. M. Zeidell, O. D. Jurchescu, *J. Mater. Chem. C* **2020**, *8*, 759–787.
- [133] N. B. Kotadiya, A. Mondal, P. W. M. Blom, D. Andrienko, G.-J. A. H. Wetzelaer, *Nat. Mater.* **2019**, *18*, 1182–1186.
- [134] D. Abbaszadeh, A. Kunz, G. A. H. Wetzelaer, J. J. Michels, N. I. Crăciun, K. Koynov, I. Lieberwirth, P. W. M. Blom, *Nat. Mater.* **2016**, *15*, 628–633.
- [135] E. Khodabakhshi, J. J. Michels, P. W. M. Blom, *AIP Adv.* **2017**, *7*, 075209.
- [136] T. P. A. van der Pol, S. T. Keene, B. W. H. Saes, S. C. J. Meskers, A. Salleo, Y. van de Burgt, R. A. J. Janssen, *J. Phys. Chem. C* **2019**, *123*, 24328–24337.
- [137] M. Kröger, S. Hamwi, J. Meyer, T. Riedl, W. Kowalsky, A. Kahn, *Appl. Phys. Lett.* **2009**, *95*, 123301.
- [138] A. G. Ricciardulli, B. van der Zee, K. Philipps, G. A. H. Wetzelaer, R.-Q. Png, P. K. H. Ho, L.-L. Chua, P. W. M. Blom, *APL Mater.* **2020**, *8*, 021101.
- [139] R.-Q. Png, M. C. Y. Ang, M.-H. Teo, K.-K. Choo, C. G. Tang, D. Belaineh, L.-L. Chua, P. K. H. Ho, *Nat. Commun.* **2016**, *7*, 11948.
- [140] M. Kuik, G.-J. A. H. Wetzelaer, H. T. Nicolai, N. I. Craciun, D. M. De Leeuw, P. W. M. Blom, *Adv. Mater.* **2014**, *26*, 512–531.
- [141] J. A. Röhr, D. Moia, S. A. Haque, T. Kirchartz, J. Nelson, *J. Phys. Condens. Matter* **2018**, *30*, 105901.
- [142] W. F. Pasveer, J. Cottaar, C. Tanase, R. Coehoorn, P. A. Bobbert, P. W. M. Blom, D. M. de Leeuw, M. A. J. Michels, *Phys. Rev. Lett.* **2005**, *94*, 206601.
- [143] R. Coehoorn, W. F. Pasveer, P. A. Bobbert, M. A. J. Michels, *Phys. Rev. B* **2005**, *72*, 155206.
- [144] P. Mark, W. Helfrich, *J. Appl. Phys.* **1962**, *33*, 205–215.
- [145] R. Meerheim, S. Scholz, S. Olthof, G. Schwartz, S. Reineke, K. Walzer, K. Leo, *J. Appl. Phys.* **2008**, *104*, 014510.
- [146] S. R. Forrest, D. D. C. Bradley, M. E. Thompson, *Adv. Mater.* **2003**, *15*, 1043–1048.
- [147] C. Murawski, K. Leo, M. C. Gather, *Adv. Mater.* **2013**, *25*, 6801–6827.

- [148] E. Khodabakhshi, P. W. M. Blom, J. J. Michels, *Appl. Phys. Lett.* **2019**, *114*, 093301.
- [149] H. Ishii, K. Seki, *IEEE Trans. Electron Devices* **1997**, *44*, 1295–1301.
- [150] P. Athanassopoulos, K. Barlos, D. Gatos, O. Hatzi, C. Tzavara, *Tetrahedron Lett.* **1995**, *36*, 5645–5648.
- [151] K. Barlos, O. Chatzi, D. Gatos, G. Stavropoulos, *Int. J. Pept. Protein Res.* **1991**, *37*, 513–520.
- [152] W. C. Chan, P. D. White, *Fmoc Solid Phase Peptide Synthesis : A Practical Approach*, Oxford University Press, Oxford, **2000**.
- [153] J. Zhao, R. C. Larock, *J. Org. Chem.* **2007**, *72*, 583–588.
- [154] Y. Zhu, Y. Zhang, B. Yao, Y. Wang, Z. Zhang, H. Zhan, B. Zhang, Z. Xie, Y. Wang, Y. Cheng, *Macromolecules* **2016**, *49*, 4373–4377.
- [155] M. Linseis, S. Záliš, M. Zabel, R. F. Winter, *J. Am. Chem. Soc.* **2012**, *134*, 16671–16692.
- [156] P. Li, T. J. Sisto, E. R. Darzi, R. Jasti, *Org. Lett.* **2014**, *16*, 182–185.
- [157] D.-J. Jang, S. Jeong, J.-I. Hong, J. K. Kim, Y. Lee, *J. Mater. Chem. C* **2018**, *6*, 9049–9054.
- [158] J. V. N. Vara Prasad, F. E. Boyer, L. Chupak, M. Dermeyer, Q. Ding, K. Gavardinas, S. E. Hagen, M. D. Huband, W. Jiao, T. Kaneko, et al., *Bioorg. Med. Chem. Lett.* **2006**, *16*, 5392–5397.
- [159] F. S. Fouad, J. M. Wright, A. D. Purohit, J. K. Wyatt, A. El-Shafey, G. Hynd, C. F. Crasto, Y. Lin, G. B. Jones, *J. Org. Chem.* **2005**, *70*, 9789–9797.
- [160] G. L. Adams, F. Velazquez, C. Jayne, U. Shah, S. Miao, E. R. Ashley, M. Madeira, T. E. Akiyama, J. Di Salvo, T. Suzuki, et al., *ACS Med. Chem. Lett.* **2017**, *8*, 96–101.